Luminescence dating of sediments in Punjab, Pakistan: implications for the collapse of the Harappan Civilisation

Julie Ann Durcan

Thesis submitted in fulfilment of the requirements for the degree of PhD

Aberystwyth University

December 2012

Abstract

This study presents the first application of optically stimulated luminescence (OSL) dating in the lowlands of Pakistan. More specifically, the Pakistani section of the Ghaggar-Hakra palaeochannel is dated for the first time, having been the subject of research for over a century. The Ghaggar-Hakra is associated with a dense concentration of Mature and Late Harappan archaeological sites. The Mature Harappan are hypothesised to have collapsed at ~3.9 ka, and it has been hypothesised that changing fluvial activity and climatic variability were key factors in the demise of this civilisation. This thesis aims to use OSL dating to develop a chronology of fluvial activity for the palaeochannel and to establish whether there is a temporal link between changing fluvial activity and climatic variability. The chronology is also compared with records of archaeological change to ascertain whether changing fluvial activity contributed to the Mature Harappan collapse.

The majority of work presented in this thesis is concerned with the development of an accurate geochronological framework using OSL dating. The fast ratio is developed as a means for assessing the dominance of the fast component in the initial part of a quartz OSL signal and range-finder OSL dating is developed as a protocol for rapid age estimation using the quartz OSL signal, providing age estimates with uncertainties within 20%. Equivalent dose calculation using statistical models is discussed and the extent of incomplete bleaching in the dataset is considered. OSL ages dating predominantly from the Holocene are presented.

Based on the OSL ages calculated, strengthened fluvial activity in the Ghaggar-Hakra palaeochannel during the early and mid-Holocene is observed. Flow recession up-channel during the mid-Holocene is inferred, and a hiatus in fluvial deposition in the channel is observed between 4.5 and 1.4 ka. Changes in fluvial activity in the Ghaggar-Hakra are driven by the intensity of the Asian Monsoon, which fluctuates during the Holocene. Changing fluvial activity coincides with documented archaeological change and it is concluded that changing fluvial activity driven by climate was a significant factor in the collapse of the Mature Harappan at ~3.9 ka.

DECLARATION

This work has not previously been accepted in substance for any degree and is not being concurrently submitted in candidature for any degree.

Signed Julie Durcan (Candidate)

Date 17th December 2012

STATEMENT 1

This thesis is the result of my own investigations, except where otherwise stated. Where correction services have been used, the extent and nature of the correction is clearly marked in a footnote(s).

Other sources are acknowledged by footnotes giving explicit references.
A bibliography is appended.

Signed Julie Durcan (Candidate)

Date 17th December 2012

STATEMENT 2

I hereby give consent for my thesis, if accepted, to be available for photocopying and for inter-library loan, and for the title and summary to be made available to outside organisations.

Signed Julie Durcan (Candidate)

Date 17th December 2012

Acknowledgements

This PhD project has been funded by The Leverhulme Trust. I am grateful to the International Union for Quaternary Research, the Quaternary Research Association, the British Society for Geomorphology and Aberystwyth University, whose support has allowed my participation at national and international conferences.

I cannot thank my supervisors Professor Geoff Duller and Professor Mark Macklin enough for their guidance and encouragement throughout the course of my PhD - I consider myself extremely fortunate to have worked with such talented and prolific scientists. I would also like to thank Dr Helen Roberts, who I have always considered as a supervisor and who has helped and supported me throughout my PhD.

Dr Anwar Alizai (Geological Survey Pakistan) and Dr Muhammad Rabbani and colleagues at the National Institute of Oceanography Pakistan are thanked for their help with fieldwork logistics. Professor Peter Clift (Aberdeen University) and Dr Liviu Giosan (Woods Hole Oceanographic Institute) are also thanked for their support throughout the project. I am also extremely grateful to Mrs Lorraine Morrison and Ms Hollie Wynne for their support during laboratory work.

Thank you also to my friends and fellow residents of C66b and visitors to the ALRL, including Professor Ann Wintle, Dr Naomi Porat, Dr Femke Davids, Ms Laura Warington, Ms Hollie Wynne, Ms Rachel Smedley, Ms Rosie Stirling and Mrs Melissa Chapot for the many invaluable luminescence chats and coffees. I have been fortunate enough to make many good friends throughout my time at IGES and would like to thank them all for making my time in Aberystwyth so enjoyable. I am particularly grateful to my housemates Dr Mark Smith and Dr Duncan Quincey for keeping me well fed, watered and entertained throughout my time in Aber.

Thank you to my family for their love, support and patience throughout my studies.

This PhD thesis is dedicated to Tom Shaw, who inspires me every day.

Contents

List of contents

List of figures

List of tables

1. Introduction

This thesis utilises the optically stimulated luminescence (OSL) signal from quartz as a geochronological tool for dating the Holocene fluvial activity of the Ghaggar-Hakra palaeochannel in Punjab, Pakistan. Associated with this palaeochannel is a dense concentration of archaeological remains relating to the Mature and Late Harappan civilisation and pronounced change in settlement patterns and densities are seen during the mid-Holocene (e.g. Mughal, 1997; Possehl, 1997; Possehl 2002; Gangal et al., 2010; Giosan et al., 2012). The Mature Harappan civilisation is hypothesised to have collapsed approximately 4,000 years ago, and many authors have suggested that the weakening of the Asian monsoon resulted in reduced regional fluvial activity and contributed to this collapse. However, very little previous work has been attempted to study the chronology of fluvial change in this region. This thesis is primarily concerned with reconstructing periods of fluvial activity in the Ghaggar-Hakra palaeochannel and comparing this record with other proxies of regional climatic variability to ascertain whether changing fluvial regimes can be linked with records of climate change. By reconstructing past fluvial activity, this record can be compared to the documented archaeological record to ascertain whether a change in fluvial activity coincides with archaeological change, and the implications that this may have had on human societies in the region can be inferred.

In this chapter, the project research context and research aims are first presented. The collapse of mid-Holocene civilisations is discussed briefly, along with a summary of the Harappan civilisation and human occupation of the Indus Valley during the Holocene. The OSL signal from quartz is used for dating in this study because it provides the direct dating of sediments, and therefore deposition events, and because it has been successfully used to develop chronologies of fluvial activity in other semi-arid to arid regions, where the absence of organic material in large amounts precludes the use of radiocarbon dating. Dating using the quartz OSL signal is discussed further, along with the physical processes giving rise to the quartz luminescence signal. This chapter concludes with the project research objectives,

developed to address the research aims outlined in section 1.1.1 and the structure of this thesis is presented.

1.1 Research context

The Indus Valley has been occupied almost constantly throughout the Holocene, with remains of the earliest human settlements found in western Pakistan and eastern Afghanistan (Clift and Plumb, 2008). Early Neolithic farming settlements have been found near modern-day Quetta and dated to ~7000 BC, and as settled communities and pastoralism developed, more sophisticated technologies, such as the production of pottery and casting/firing techniques, emerged and are dated to ~5500 BC. Out of these early pastoralist societies, the Harappan civilisation developed, and in contrast to the earlier settlers, the Harappan occupied the fertile alluvial plains of Punjab and Cholistan (figure 1.1). The Mature Harappan (2500 – 1900 BC) was one of the largest and most complex human societies in the pre-industrial world (Possehl, 2002). Contemporaneous with the Akkadian, Egyptian and Chinese Neolithic, the Harappan flourished, building mega-cities which housed tens of thousands of residents (Kenoyer, 1998), and which were laid out in an orderly grid system (Jansen, 1989). These cities had water and waste disposal systems and the Mature Harappan had in place a productive agricultural system capable of sustaining many thousands of urban residents whose primary craft was not agriculture (Madella and Fuller, 2006). However, this civilisation collapsed at approximately 1900 BC and was succeeded by a post-urban phase (Possehl, 2002), and the reason for this collapse is not yet understood. Some authors hypothesise that the collapse of the Mature Harappan was founded in a reduction, and ultimately a cessation, of fluvial activity in the area, possibly due to a decline in the intensity of the summer monsoon (e.g. Staubwasser et al., 2003) or through more local hydrological factors (e.g. Agrawal and Sood, 1982). In contrast, some archaeologists have argued that climate change has been largely irrelevant for human societies during the Holocene (e.g. Possehl, 1999), and that a better understanding of past economic, social and political change is required.

Rather than being a period of relative climatic stability, the Holocene in the Indian sub-continent consists of a series of arid-humid alterations on centennial and millennial scales (e.g. Gupta et al., 2003; Morrill et al., 2003), along with short abrupt events (e.g. Bond et al., 1997; Cullen et al., 2000), such as the 4.2 ka event (e.g. Magny et al., 2009). These fluctuations were set against a backdrop of weakening of the Asian Monsoon (e.g. Berger and Loutre, 1999; Wang et al., 2005), which would have resulted in variable precipitation and the onset of enhanced aridity. Case studies from around the world have shown that unpredictable precipitation patterns and periods of prolonged drought placed ancient civilisations under stress (de Menocal, 2001) and when faced with environmental stresses, civilisations such as the Akkadian (Weiss et al., 1993; Cullen et al., 2000) and the Chinese Neolithic (e.g. Wenxiang and Tungsheng, 2004) responded with collapse and/or transformation to less complex social states. However, whilst the archaeology in Pakistan is well dated, mainly using radiocarbon dating (with references from the many hundreds of articles publishing radiocarbon dates including Agrawal and Sood, 1982; Possehl, 1994; Jarridge, 1995; Possehl 1998), the direct dating of the landscape is limited and therefore, the landscape response to external forcing factors such as climate has not been well investigated.

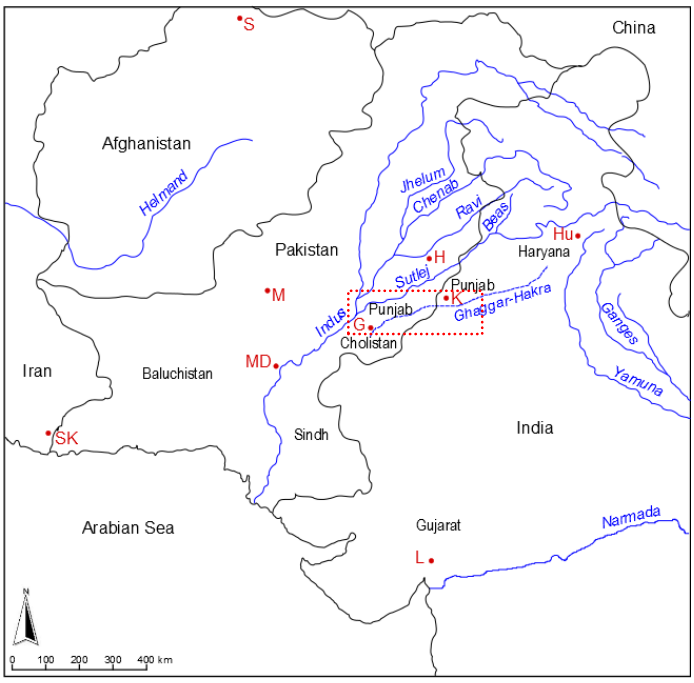

Figure 1.1: Map of the major rivers in Pakistan and western India. Regions mentioned in the text are shown, as well as some of the main Harappan sites: G – Ganweriwala, H – Harappa, Hu – Hulas, K – Kalibangan, L – Lothal, M – Merhgarh (early Neolithic site), MD – Mohenjo-Daro, S – Shortugai, SD – Sutkagen-dor. Note, the satellite image in figure 1.3 is shown by the boxed area.

Figure 1.2: Examples of the contemporary fluvial landscape of the Cholistan and Punjab regions. a) Aerial view of relict/ephemeral channel in Cholistan desert (photo taken by Julie Durcan). b) Relict channel of the Sutlej River near Bahawalpur (photo taken by Anwar Alizai). c) Ephemeral channel of the Sutlej River near Bahawalpur (photo taken by Mark Macklin). d) The Sutlej River at the Empress Bridge, north of Bahawalpur (Zaicha, 2007).

The fluvial landscape of Pakistan is dominated by the Indus River, which drains an area of approximately 970,000 km^2 (Inam et al., 2007) and has five major tributaries: the Jhelem, Chenab, Ravi, Beas and Sutlej Rivers (figure 1.1). Associated with the Indus and its tributaries are many relict channels, indicating that existing channels have been highly dynamic in the past, but also that some systems which were active in the past are no longer so, or have been reduced to ephemeral channels (e.g. figure 1.2a-c). A palaeochannel known as the Hakra in Pakistan and the Ghaggar in India (referred to in this study as the Ghaggar-Hakra) is evident in satellite imagery in Punjab (figure 1.3), and has been the subject of investigation since the early 1900s (Mughal, 1997). It has been described as a major river system for the Harappan (Wright, 2010), hosting one of the densest concentrations of Mature Harappan settlement in the region (Wright et al., 2008) and many archaeological sites relating to the Mature and Late Harappan are located along this channel (Mughal, 1997; figure 1.3). Many authors have suggested that a reduction

and/or cessation in flow in this channel is related to the collapse of the Mature Harappan (section 1.4.1). However, a firm chronology of past fluvial dynamics does not exist for the Ghaggar-Hakra palaeochannel (Wright, 2010), and this provides the opportunity for a focused study along one tributary of the system in an area considered as the 'bread-basket' of the Harappan civilisation (Possehl, 1997). With such a dense concentration of archaeological sites and a prominent change in the location and number of settlements of the Mature and Late Harappan and the later Grey Wares (1500 – 1000 BC) (e.g. figure 1.3), determining the timings of fluvial activity in this palaeochannel during the past will allow the timing of geomorphological and archaeological change to be compared.

1.1.1 Research aims

The primary research aim of this PhD is to develop a chronology of fluvial activity during the Holocene for the Ghaggar-Hakra palaeochannel in Pakistan. A key part of this thesis is to develop luminescence procedures appropriate for this and the majority of work presented is concerned with the development of a robust geochronological framework of past fluvial activity using OSL dating. One of the secondary aims of this PhD project is to place the fluvial chronology of this palaeochannel into the context of regional climatic variability. The presence of the Ghaggar-Hakra palaeochannel is indicative of wetter conditions in the past, and by comparing the luminescence chronology to other regional proxies of climatic variability, the influence of changing climate on the fluvial dynamism of the Ghaggar-Hakra can be assessed to ascertain whether fluvial activity in this palaeochannel has been affected by climate variability during the Holocene. The other secondary aim of the PhD is to compare the chronology of fluvial activity with the documented records of archaeological change along the Ghaggar-Hakra. Associated with this palaeochannel is a dense concentration of archaeological sites relating to the Mature Harappan civilisation (section 1.3.5) and to a lesser extent, the Late Harappan (e.g. Mughal, 1997). After the collapse of the Mature Harappan, settlements in this area are abandoned in favour of sites to the east, closer to the headwaters of the Yamuna and the Sutlej River systems (discussed further in

section 1.4.1). There is much detailed archaeological research on the topic of the Mature Harappan and their demise, including extensive field excavations and mapping (e.g. Mughal, 1996; 1997) and detailed texts which explore the lives of the Harappan (e.g. Kenoyer, 1998; Possehl, 2002: Agrawal, 2007; Wright, 2010). This work does not seek to add to this extensive literature. Instead, the documented archaeological change along the Ghaggar-Hakra channel provides a context in which to compare fluvial activity, and ascertain whether a reduction and/or cessation in flow coincides with settlement migration and the timing of civilisation collapse. The research objectives designed in order to achieve these research aims are presented in section 1.6.

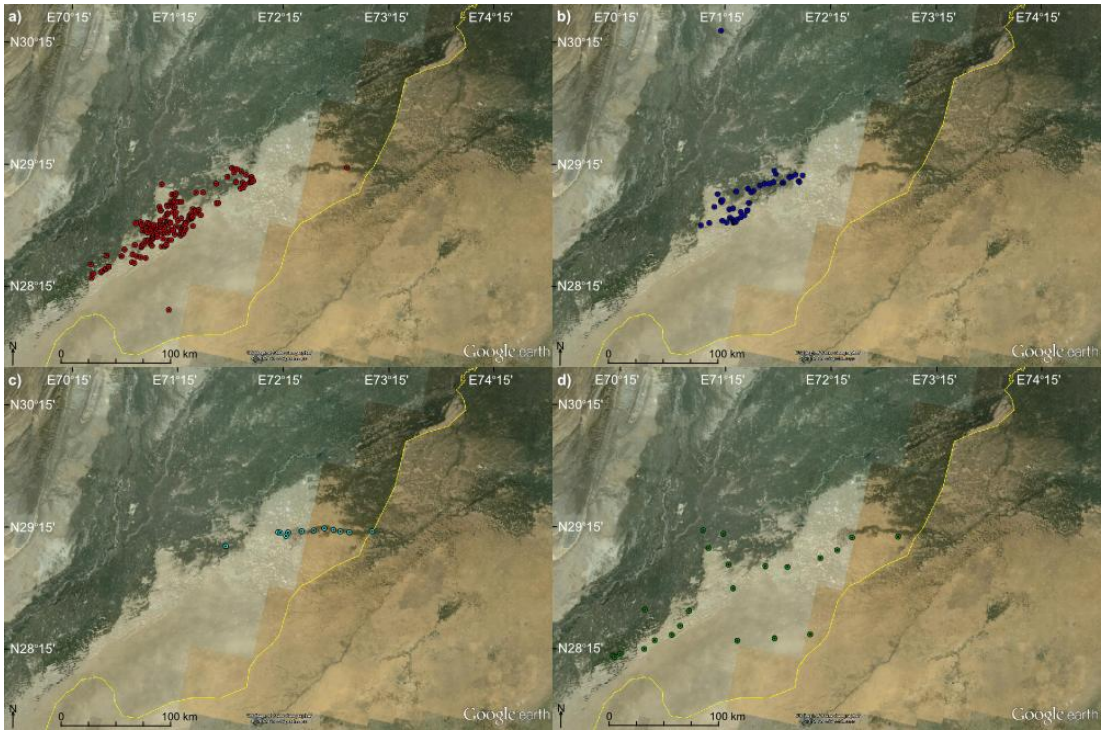

Figure 1.3: Satellite image of the Ghaggar-Hakra palaeochannel, with the Pakistani-Indian border shown by the solid yellow line. The archaeological sites reported by Mughal (1997) are shown in each image. a) The Mature Harappan (2500 – 1900 BC). b) The Late Harappan (1900 – 1500 BC). c) The Painted Grey Wares (1100 – 500 BC). d) Medieval period (1100 – 1700 AD). Images are from Google Earth, and the position of the area in relation to Pakistan is shown in figure 1.1.

1.1.2 Expression of time units

A task group aimed at updating the recommendations for the use of units for geochronological use was set up by the International Union of Pure and Applied Chemistry (IUPAC) and the International Union of Geological Sciences (IUGS) in

October 2006. The conclusions of this task group have been published by Holden et al. (2011) and it is recommended that time periods and ages are expressed in the SI unit 'a', with prefixes 'k' (x 10^3), M (x 10^6) and G (x 10^9) used as required to indicated thousands, millions and billions of years respectively (IUPAC-IUGS Task group 2006-06-1-200; Holden et al., 2011). These recommendations have been adopted by the journals *Quaternary Science Reviews* and *Quaternary Geochronology* (Rose, 2007), and therefore ages and time periods are reported using the SI unit 'ka' in this study. However, there are two notable exceptions in the reporting of ages within this thesis. The first is for calibrated radiocarbon (^{14}C) ages, where the term 'cal BP' is reserved for use (where BP refers to 1950 AD) and this unit is recommended for use for ^{14}C dates by Rose (2007) after Van der Plicht and Hogg (2006). In this study, ^{14}C ages are reported in thousands of years and therefore the unit 'cal kyr BP' is used where the age is reported. The second exception is for archaeological data. The use of 'Before Christ' (BC) and Anno Domino (AD) by archaeologists began in the nineteenth century (Taylor, 2008) and continues to be used by contemporary archaeologists. Therefore, to ensure that archaeological sources are quoted consistently, the BC/AD framework is used. BC and AD are preferred over BCE/CE (Before Common Era/Common Era) by the *Journal of Prehistory* (Taylor, 2008) and are therefore the units used in this thesis.

1.2 Civilisation collapse during the Holocene

Throughout the Holocene and across the globe, there is evidence for numerous prehistoric, ancient and pre-modern societies collapsing (Weiss and Bradley, 2001). In an early description of civilisation collapse, Renfrew (1979) described that the collapse of a civilisation or society entailed increasing socio-political dislocation followed by the collapse of centralised economic and political organisation, a decline in population and a shift to lower population densities, and a transition of communities to a less complex social organisation. Later, Diamond (2005) defined collapse as a drastic decrease in human population size and/or political/ economic/social complexity over a considerable area for an extended time. Both definitions imply a change in both population size and the level of socio-economic

complexity. However, the term collapse is used interchangeably to describe abrupt and rapid collapses, such as that of the Akkadian empire, where collapse seems to have occurred within a 100 year period during the third millennia BC (Weiss et al., 1993) and more gradual declines, such as the Greenland Norse, who flourished during the Medieval Warm Period, with population decline and dietary adaption leading to abandonment in the 15th Century AD.

In the past, climate scientists have presented 'culture-climate' hypotheses (e.g. Singh, 1971; Singh et al., 1974) where the flourishing and collapse of societies has hinged upon the variability of climatic conditions. Conversely, many archaeologists and anthropologists have considered the role of climate as largely irrelevant (e.g. Tainter, 1988), instead focusing upon the role of internal socio-political factors to explain the demise of civilisations. Madella and Fuller (2006) argue that both archaeologists and Quaternary scientists approach their arguments in a one-sided manner, stating that more effort should be made to provide a synthesis of the information available and a more critical assessment of the data without citing previous studies unsystematically. More recently, there has been an increase in interdisciplinary studies investigating the role of changing environments on social processes (e.g. Woodward et al., 2001; Wenxiang and Tungsheng, 2004; Madella and Fuller, 2006; Williams et al., 2010).

Diamond (2005) suggests a number of both internal and external factors that have the potential to have led to civilisation collapse, including: land degradation and unsustainable use of the environment, climate change, war, economics and societal response to these stresses. It is unlikely that these stresses occurred independently of each other and for Dearing (2006), climate, ecosystem and human society factors are intrinsically linked to causality and feedback. O'Sullivan (2008) argues that it is the inability to respond and adapt to both internal and external stresses that will ultimately lead to collapse. However, civilisation response to such factors are likely to have been non-linear both spatially and temporally, with response to the same stimuli varying between societies depending on population dynamics, activities and

societal structure (Leroy et al., 2006) and it is this that can make identifying a definitive cause challenging.

With concerns over the implications of global warming for human societies, the link between climate and ancient civilisations has become an important research focus (Caseldine and Turney, 2010). Quaternary scientists are moving away from the environmentally deterministic notion that fluctuations in the physical environment govern social and political change (Brooks, 2006), and instead there is a shift to seeing the physical environment as the setting for social and cultural expansion, innovation and decline (Chapman, 2003). Many case studies have been presented where climate is thought to have been one of the main, if not the most important, stresses on society, ultimately leading to civilisation collapse. These include the collapse of the Mayans around 900 AD (e.g. Hodell et al., 2001; 2005; 2007), the Akkadians during the 3rd millennium BC (e.g. Weiss et al., 1993; Cullen et al., 2000), and the Chinese Neolithic during the same period (e.g. Wenxiang and Tungsheng, 2004; An et al., 2005; Huang et al., 2010). Civilisation collapse appears to be prevalent towards the end of the mid-Holocene, with the period around 4 ka seeing the collapse of numerous large, complex civilisations, including the Akkadians, the Harappan and the Egyptians (figure 1.4).

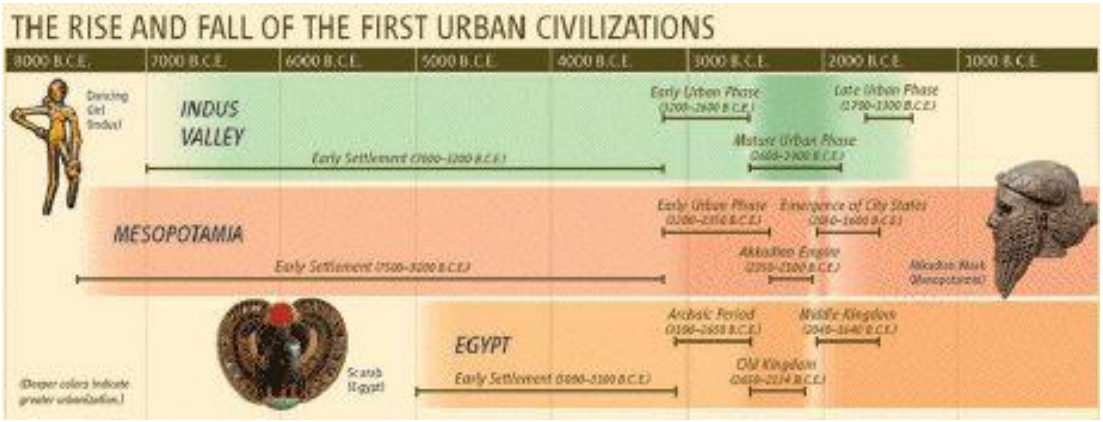

Figure 1.4: Summary of the settlement phases in the Indus Valley (including the Mature Harappan), Mesopotamia and Egypt from Lawler (2008). Deeper colours indicate more intensive urbanisation. In all three regions, de-urbanisation is observed between ~2200 and 1900 BC.

1.2.1 The Akkadians

The Akkadians occupied the alluvial plains between the Tigris and Euphrates Rivers in modern day Syria and Iraq, and under the rule of Sargon of Akkad, became one of the world's first united empires between 4.3 and 4.2 ka (Cullen et al., 2000). The Akkadians utilised fertile floodplains and a system of rain-fed agriculture to flourish (Cullen et al., 2000), however, after a relatively short-lived period of prosperity, the Akkadian empire collapsed at 4.2 ka (Weiss et al., 1993). The major Akkadian cities of Tell Leilan and Tell Brak were suddenly abandoned (Weiss et al., 1993), and abandonment can be seen at smaller sites across the region at this time (Matthews, 2003). At many sites, a hiatus in settlement is also observed before resettlement by smaller sedentary populations is seen at 3.9 ka (Cullen et al., 2000). At Tell Leilan and nearby sites, a 0.5 cm tephra layer is observed, which is overlain by a 100 cm unit of well-sorted, wind-blown silts, and this unit is undisturbed and contains no archaeological remains (Weiss et al., 1993). The archaeological remains directly beneath these units have been dated to 4.17 ± 0.15 cal kyr BP (Weiss et al., 1993). Whilst some authors have suggested that the collapse of the Akkadians is due to socio-political factors, such as war and/or political disintegration (e.g. Yoffee and Cowgill, 1998), this silt unit has been interpreted as evidence for the rapid onset of enhanced aridity, which may have contributed to collapse (Weiss et al., 1993). The timing of this collapse corresponds with evidence for regional climatic variability and the 4.2 ka event is widely reported across the Levant and Mediterranean as a severe climatic anomaly leading to increased aridity and drought (e.g. Magny et al., 2009). Lemcke and Sturm (1997) report a 30 – 50 m fall in Lake Van, Turkey at approximately 4.2 cal kyr BP and a decrease in the level of the Dead Sea is also reported at a similar time by Frumkin (1991). Bar-Matthews et al. (1997) document a decrease in precipitation of 20 – 30% at Soreq Cave in Israel using the U/Th record from cave speleothems between 4.2 and 4.0 ka. This rapid onset of aridity is generally considered as the cause, or at least, the stimulus for the collapse of the Akkadian civilisation.

1.2.2 The Chinese Neolithic

The term Chinese Neolithic refers to a number of cultures who occupied the eastern and central regions of China between ~8.0 – 4.0 ka (Maisels, 2001). The collapse of this group of societies is associated with the ending of a number of comparably complex cultures between ~4.3 – 4.0 ka (Wenxiang and Tungshen, 2004). These include the Liangzhu (5.3 – 4.2 ka) (Zhu et al., 1997; Stanley et al., 1999), the Shijiahe (4.6 – 4.2 ka) (Zhang et al., 2000), the Shangdong Longshang (4.6 – 4.2 ka) (Liu 1996; 2000) and the Laohushan (4.5 – 4.3 ka) (Tian, 2000). Many archaeologists have attributed the collapse to internal, socio-economic factors. Wu and Li (2001) believe the Shijiahe culture collapsed due to warfare and similarly Sun and Chen (1991) state the collapse of the Shandong Longshan is linked to invasion, whilst Zhu et al. (2008) argue that over-exploitation of the natural environment and/or of the labour supply accounts for the collapse of the Liangzhu culture. Wenxiang and Tungshen (2004) state that whilst these may be the internal factors which led to the collapse of each of these cultures individually, socio-economic stresses do not account for the regional collapse of multiple cultures at the same time. From the $\delta^{18}O$ record of a stalagmite from Dongge Cave, China, Wang et al. (2005) show that the Asian monsoon declines in intensity during the early- and mid-Holocene, driven by changes in solar insolation (e.g. Berger and Loutre, 1991; 1999). Their record shows a number of weak Asian monsoon events throughout the Holocene, coincident with north Atlantic ice-rafted debris events (e.g. Bond et al., 1997), one of which occurs at ~4.4 ka. In Wang et al.'s (2005) record, there is a large duration and magnitude shift in isotope values (by 0.8 – 1.0‰) between 4.5 – 4.0 ka, which would have resulted in a period of strongly enhanced aridity, resulting in both the drying and the cooling of the environment. It is this increase in aridity, centred at 4.2 ka, which is attributed to the collapse of the Chinese Neolithic by many researchers.

1.3 The Harappan civilisation

The Harappan civilisation (also known as the Indus Valley civilisation), along with the Akkadians and the Egyptians, is considered to be one of the three societies in the 'Ancient East' which made up the cradle of early civilisation in the Old World during the mid-Holocene (Childe, 1950). Gangal et al. (2010) comment that at its peak, the Mature Harappan civilisation was the largest urbanised Bronze Age civilisation in the world. It covered an area in excess of one million square kilometres, an area at least twice the size of ancient Egypt or Mesopotamia (Kenoyer, 1998) and extended north to south from Shortugai in northern Afghanistan to Daimabad in southern India and from east to west from Sutkagen-dor in eastern Iran, to Hulas in Uttar Pradesh, India (figure 1.1). Wright (2010) suggests that whilst the Egyptian and Akkadian civilisations have been relatively well studied, research into the Harappan civilisation is less advanced due to a lack of travel historically to Pakistan and India by western scholars and because the script of the Harappan is yet to be deciphered. The discovery of this civilisation occurred relatively recently. The city of Harappa was the first site to be discovered by Charles Masson in 1829 (Possehl, 2002), with archaeological exploration and excavation continuing throughout the nineteenth and twentieth centuries, including the discovery of the major urban centres of Mohenjo-Daro, Lothal and Kalibangan. In 1924, writing in the *Illustrated London News*, archaeologist John Marshall announced the discovery of Harappa and Mohenjo-Daro and a 'long lost civilisation' in the Indus Valley, which was roughly contemporaneous with Mesopotamia (Possehl, 2002; Wright, 2010).

Whilst the Mature Harappan is the most commonly referred to phase of occupation, human settlement in the Indus valley is evident throughout the Holocene. Typically, when referring to the Harappan, one is making reference to the Mature Harappan phase, between 2500 – 1900 BC (Possehl, 1997), who represent the most complex and advanced level of society during the Indus Age, albeit occupying the region during a relatively narrow window of time. The Indus Age has been subdivided into a series of phases by Possehl (2002) and is summarised in

figure 1.5, and these phases are based on archaeological materials, subsistence regime, trade patterns, socio-cultural institutions and geographic area. Possehl (2002) provides an extensive review of the key characteristics of the people of each phase, including settlement patterns, modes of food production and technology. This categorisation has been widely used in recent archaeological literature as a means for differentiating between the different cultural phases of the Indus Age (e.g. Madella and Fuller, 2006; Agrawal, 2007; McIntosh, 2007; Wright, 2010) and as an archaeological chronology used in many palaeoenvironmental studies (e.g. Staubwasser et al., 2003; Wright et al., 2008; MacDonald, 2011). Development of these phases would have occurred over different spatial and temporal scales, depending on local environmental and social conditions, however, the key characteristics of the different phases are summarised in the following sections.

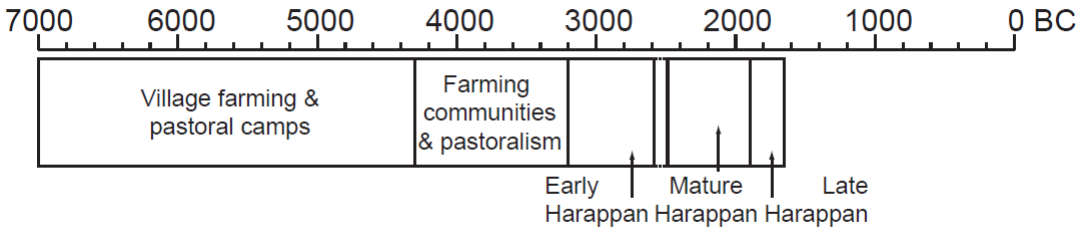

Figure 1.5: Chronology of the Indus Valley civilisation, summarised from Possehl (2002).

1.3.1 Chronology

Early timeframes for the Holocene occupation of the Indus Valley were based on correlation with Mesopotamian chronologies (Kenoyer, 1991). The Mesopotamians kept records of monarchs using the cuneiform script, and once this script was deciphered in the nineteenth century, they were translated and correlated with other historical events, providing a general chronology for Mesopotamian cities (Kenoyer, 1998). As Harappan seals and motifs were discovered in Mesopotamian urban centres, a general timeframe for the Harappan phases was developed, which was based on these Mesopotamian sequences. Sir John Marshall was one of the first researchers to propose a period for the Mature Harappan, with his phase of 3250 – 2750 BC (Marshall, 1931) later revised to 2500 – 1500 BC by Wheeler (1953). The development of the radiocarbon (^{14}C) dating technique in the 1950s allowed

Harappan sequences to be directly dated for the first time, with the archaeologist George Dales taking the first samples for ^{14}C dating from Mohenjo-Daro in his 1964-65 excavations (Kenoyer, 1998). As ^{14}C dating became a more established dating technique, the number of samples taken increased, with over seventy radiocarbon dates calculated at Harappa alone between 1986 and 1990 (Kenoyer, 1991), and hundreds of dates calculated from across the geographic area (Possehl, 1994). In general, the suite of radiocarbon dates is in agreement with the chronology developed through correlation with Mesopotamia, with the occupation of the urban centres of the Mature Harappan dated to 2500 – 1900 BC (Possehl, 1997).

1.3.2 Village farming and pastoral camps (7000 – 4300 BC)

The earliest phase of settled human occupation in the Indus Valley region is not well documented (Possehl, 2002) and it is likely that preservation and discovery issues means that the 53 recorded sites from this period is only a small proportion of the true number. Settlements from this period are relatively small in size (2 – 3 hectares), with sites concentrated in the highlands of Baluchistan, Quetta and the Northwest frontier, with a small number of sites in Sindh (figure 1.6), and these settlements appear to have been simple, compartmentalised buildings made from mud (Possehl, 2002). Palynological remains of both wild and domestic species at the Merhgarh type site near the city of Quetta, indicate the local domestication of barley (Wright, 2010), as well as domestication of exotic species of einkorn and emmer wheat from the Near East (Meadow, 1993). The domestication of cattle and goat is inferred from animal remains at Merhgarh (Meadow, 1998) and it is likely that sheep were also domesticated. From the same archaeological units, sickle blades and grinding tools have been recovered (Fairservis, 1956), providing further evidence of floral and faunal domestication. Technology during this phase is indicative of a transition from hunting to farming (Wright, 2010), with artefacts for food preparation (such as grinding tools and pots for storage) found alongside stone tools used for hunting and butchery (Vaughan, 1995). Remains of ornamental jewellery, such as necklaces and headbands fashioned from materials including shell, tortoise and lapis lazuli, as well as human figurines have been discovered from

this period (Kenoyer, 1998). This period represents the transition from hunting and gathering to farming and domestication in the region, with the people at this time developing the tools to cultivate, prepare and store crops and the skills to fashion raw materials for decorative purposes.

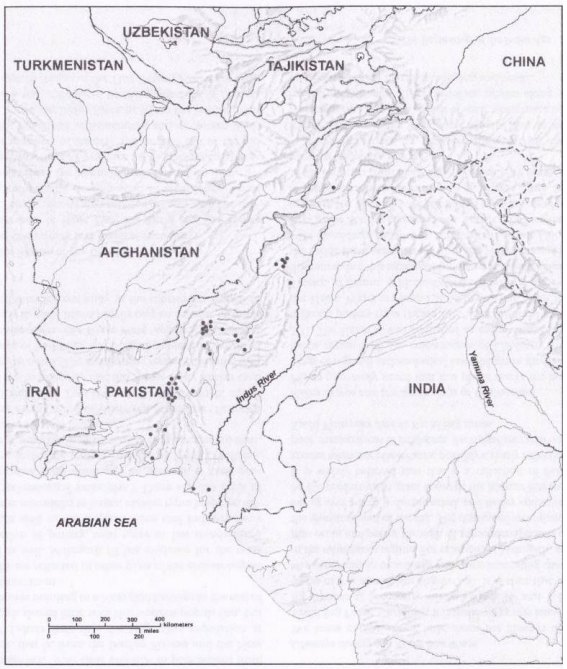

Figure 1.6: Sites relating to the village farming and pastoral camps phase of Indus Valley occupation (7000 – 4300 BC). From Possehl (2002).

1.3.3 Farming communities and pastoralism (4300 – 3200 BC)

The period between 4300 – 3200 BC represents a continuation from the village farming and camps phase, is a period of growth and expansion and sees the development of settled village farming communities and pastoral societies (Possehl, 2002), with increasing numbers of larger settlements. By 2002, 340 sites from this phase had been discovered with an average settlement size of 4.8 ha (Possehl, 2002). Settlement in Baluchistan continues, however sites dating from this period are also found in the Cholistan region (figure 1.7). Pastoralism is still evident, particularly in Cholistan, with a number of campsites observed (Mughal, 1997). Evidence for the domestication of local flora and fauna species is more widespread during this period (Meadow, 1998), indicating the establishment and spread of agriculture (Wright, 2010). The role of pottery becomes increasingly developed,

with the development of a potters wheel (Possehl, 2002) and technologies to allow the firing of clay, allowing ceramic pots to be used as cooking utensils and as storage for both food and water (Wright, 2010). Pottery becomes more ornate (Fairservis, 1956), with flanged rims and decoration becoming more prevalent (Possehl, 2002). Human figurines also become increasingly elaborate, both in terms of how they were modelled, but also by the decorations added which included hairstyles, headdresses and jewellery (Kenoyer, 1998). This phase represents the expansion and settlement of the Indus Valley people, with the continued domestication of local flora and fauna and the development of technologies to allow diversification in food preparation and storage. Expansion of people into Cholistan is evident, with a focus of settlement around the area where Fort Derawar stands today.

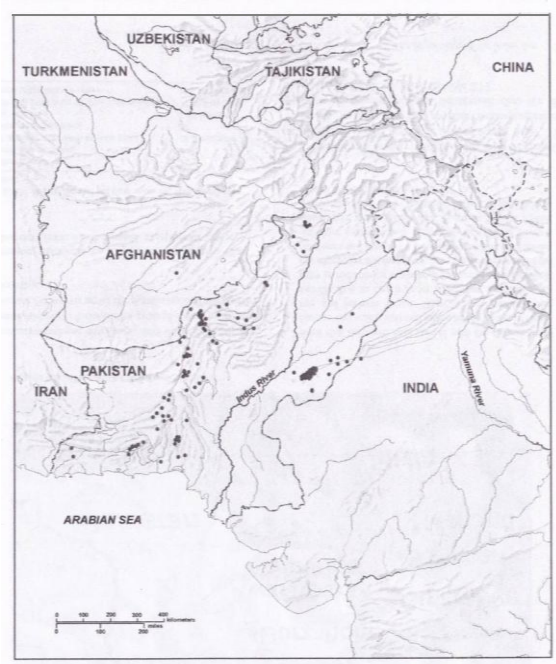

Figure 1.7: Sites relating to the farming communities and pastoralism phase of Indus Valley occupation (4300 – 3200 BC). From Possehl (2002).

1.3.4 The Early Harappan (3200 – 2600 BC)

The Early Harappan (3200 – 2600 BC) represent a cultural continuity from the early pastoral phases (section 1.3.2 and 1.3.3), with a focus on expansion and growth and minimal technological change (Possehl, 2002). A total of 477 sites, with an average

settlement size of 4.5 ha are reported by Possehl (2002) and in this phase, an increasing number of Early Harappan sites are seen in Cholistan, with expansion into the Punjab and Haryana provinces of modern-day India observed for the first time (figure 1.8). There is no evidence during this stage for significant social differentiation, career specialisation and there is no public architecture, which would indicate political or religious institutions (Possehl, 1998). The end of this phase is marked by disruption and/or abandonment with ^{14}C dates at some sites indicating a hiatus in occupation of a few hundred years (Possehl, 1997). At some sites, such as Kot Diji in Sindh, there is evidence for massive burning, with thick deposits of burnt and charred material such as charcoal, bones and pot shards within an ashy horizon (Khan, 1965). Whether caused accidentally, as part of widespread clearance or as part of warfare has not been established, but there is a trend for marked abandonment of Early Harappan sites at the end of this phase (Mughal, 1997; Possehl, 2002).

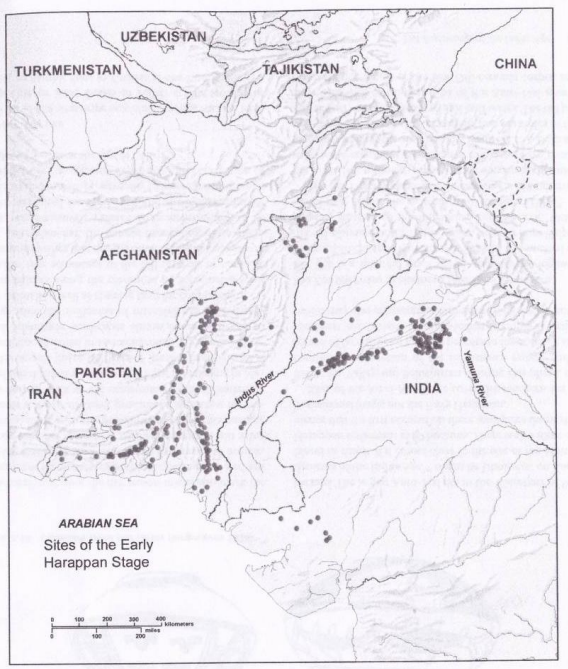

Figure 1.8: Sites relating to the Early Harappan phase of Indus Valley occupation (3200 – 2600 BC). From Possehl (2002).

1.3.5 The Mature Harappan (2500 – 1900 BC)

The Mature Harappan (2500 – 1900 BC) were a well-developed, complex society, inferred from the geographic scale of the civilisation, urbanisation and technological developments (Possehl, 2002). The Mature Harappan are associated with mega-cities such as Mohenjo-Daro, Harappa and Ganweriwala, and Mohenjo-Daro is estimated to have been approximately 250 ha in area, with a population in excess of 40,000 people, (Fairservis, 1956), although Kenoyer (1998) suggests that this number is likely to have been higher. By 2002, 1019 sites (with an average area of 7.25 ha) had been documented (Possehl, 2002). These urban centres were well planned, with buildings and streets organised along north-south and west-east orientations (Kenoyer, 1998), with the cities subdivided into separate areas, each containing larger public buildings, market areas, private housing and craft workshops (Jansen, 1979). Buildings were typically composed of mud bricks and baked bricks, wood and reeds, with a standard size of brick used for house construction and a larger size used for larger buildings and the city walls. These building materials and sizes appear to have been standard throughout the Mature Harappan phase (Kenoyer, 1998). Within the mega-cities, wells were built in both public and private areas and many households had latrines, and even smaller towns and villages had impressive drainage systems to remove polluted water and sewage (Jansen, 1989). Settlement is concentrated in the Cholistan region, as well as Sindh, and Gujarat in India (figure 1.9). Not all Mature Harappan occupied mega-cities, and Possehl (2002) notes that a range of settlement sizes from these mega-cities which are in excess of 100 ha to small villages and campsites, which are 2 – 3 ha in size have been excavated.

The Harappan script was invented at ~2600 BC and was used widely on pottery, copper-bronze tablets, tools and weapons. The script was both inscribed directly on to artefacts and stamped on, using seals made from steatite (Kenoyer, 1996). Whilst the script was widely used, scribes and seal cutters were part of a suite of complex trades, including metalworkers, architects and/or engineers (Possehl, 2002). Other crafts undertaken at the time include the continuation of ceramics and pottery,

bead making and metallurgy, utilising a variety of naturally available materials, including copper, iron, lapis lazuli, limestone and chert (e.g. Possehl, 2002). The Mature Harappan had an established, productive agricultural system in place, capable of producing surpluses to support many thousands of urban residents (Madella and Fuller, 2006). The main crops utilised included cereals (wheat and barley), millet, linseed and cotton, as well as dates and grapes (Wright et al., 2008). Wright (2010) suggests that the diversity of crops used indicates the development of a multi-cropping system, where drought-resistant barley was grown in the winter, with fruits and cotton grown during the summer. Sheep, goat and cattle continued to be domesticated, and it has been suggested that dogs and cats were kept (Possehl, 1999). The Mature Harappan civilisation collapsed at 1900 BC (Possehl, 2002) and this is discussed in section 1.4.

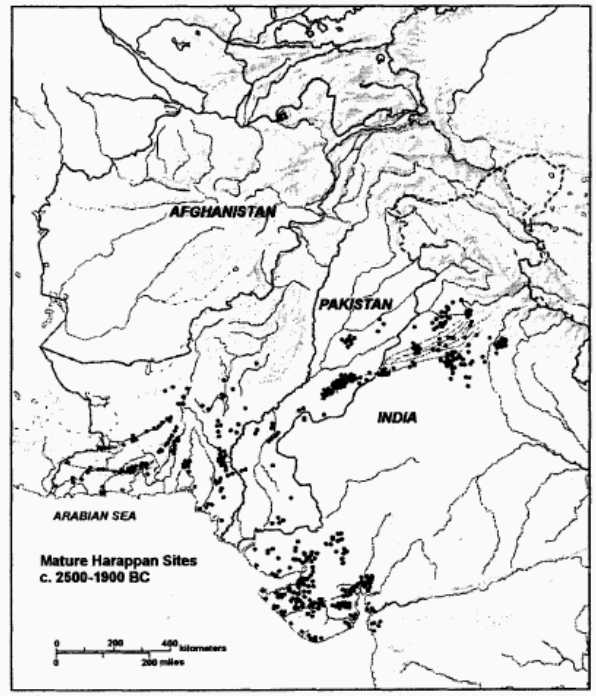

Figure 1.9: Sites relating to the Mature Harappan phase of Indus Valley occupation (2500 – 1900 BC). From Possehl (1997).

1.3.6 The Late Harappan (1900 – 1500 BC)

During the Late Harappan phase (1900 – 1500 BC) the majority of sites are located in the upper tributaries of the Ghaggar-Hakra and Yamuna river systems (figure 1.10; Possehl, 2002), and whereas Cholistan was one of the most densely populated

areas of the Mature Harappan phase (figure 1.9), relatively few Late Harappan sites have been found along the Ghaggar-Hakra palaeochannel. The mega-cities of Mohenjo-Daro and Ganweriwala were abandoned (Lahiri, 2000), although there is evidence for continued occupation of Harappa (Wright, 2010), with a decrease in site size and population (Possehl, 2002). The average settlement size decreases in comparison to the Mature Harappan phase, although there are more Late Harappan sites (Gangal et al., 2010). Whilst wheat and barley continued to be principle crops for the Late Harappan (Wright, 2010), the more drought resistant barley became more dominant (Weber, 2003). Crop detritus, such as chaff and weeds, are found in Late Harappan domestic settlements, which Weber (1999) and Fuller and Madella (2000) suggest is evidence of a socio-political change away from the communal/centralised cropping practices of the Mature Harappan. During this period, the presence of high-status objects is reduced, along with the technologically elaborate crafts used to make objects (Wright, 2010) and notably, the Indus script disappears between 1900 – 1700 BC (Kenoyer, 1998), and whilst some of the crafts practiced by the Mature Harappan prevailed, they are not inscribed (Kenoyer, 1998). The Late Harappan phase represents de-urbanisation and a return to a more village-based, less complex, mode of society (Wright, 2010).

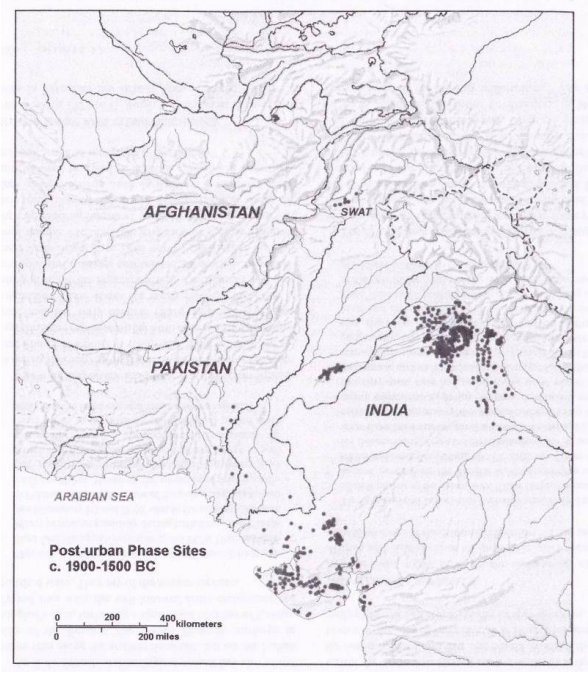

Figure 1.10: Sites relating to the Late Harappan phase of Indus Valley occupation (1900 – 1500 BC). From Possehl (2002).

1.4 Collapse of the Mature Harappan

Between ~2000 – 1900 BC, Mohenjo-Daro and many other of the large urban centres of the Mature Harappan are abandoned in Sindh and Cholistan (e.g. Possehl, 1996), and whilst Harappa remained occupied, it was not an urban centre after the end of the Mature Harappan phase (Possehl, 1997). The Harappan economy appears to have been disrupted, with the production of luxury items (e.g. beads and seals) curtailed and long-distance trade reduced (Possehl, 2002), and as stated in section 1.3.6, the Harappan script is lost during the Late Harappan phase (Kenoyer, 1998). The Late Harappan period sees an increase in the number of sites (figure 1.11), however a decrease in net occupied area in comparison to the Mature Harappan phase, suggesting de-urbanisation. According to Possehl (1997), this implies substantial change in the political and economic organisation of the society. Migration in an eastwards direction can be observed (e.g. figures 1.8 and 1.9). Settlement patterns are discussed in more detail in section 1.4.1, and hypotheses for the cause of the collapse/transformation of the Mature Harappan are presented in section 1.4.2.

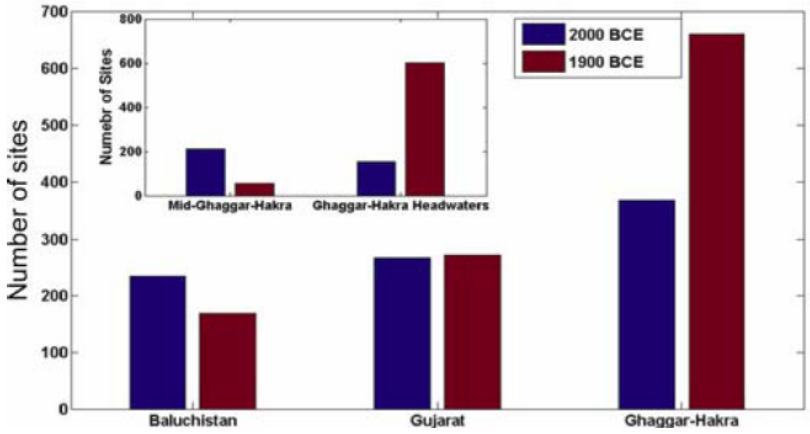

Figure 1.11: Histogram comparing the site distribution in Baluchistan, Gujurat and the Ghaggar-Hakra (Cholistan) regions. Inset, the Mid-Ghaggar-Hakra (in Pakistan) and the Ghaggar-Hakra headwaters (in India). From Gangal et al. (2010), who used data from Possehl (1999) to construct the diagram. Data consists of 1874 sites, with typical errors of approximately 100 – 200 years on radiocarbon dates used by Possehl (1999).

1.4.1 Settlement patterns

The change in distribution and density of settlement is an important factor for identifying and describing civilisation collapse (Renfrew, 1979) and is observed in the transition between the Mature and the Late Harappan at ~1900 BC. The distribution of Harappan archaeological sites documented during the period 4.5 – 3.0 ka has been collated by Giosan et al. (2012) and is shown in figure 1.12, incorporating records from Mughal (1996; 1997), Possehl (1999), Wright et al. (2005) and Gangal et al. (2010). Settlement data is shown in four time slices and although changes in settlement patterns would have been a gradual process, there is a distinct change in the location of archaeological sites between 4.5 ka (e.g. the beginning of the Mature Harappan), 3.9 ka (the transition between the Mature and Late Harappan) and 3.5 ka (the end of the Late Harappan phase). Generally, there is a significant shift in site numbers towards the east. In the Sindh region, the number of sites decreases from 90 to 19 (Possehl, 1997; Possehl, 1999; Mallah, 2010; Gangal et al., 2010) and a fall in the number of sites is also observed in areas beyond the core Mature Harappan settled area, such as Baluchistan and Gujarat (e.g. figure 1.11; Gangal et al., 2010; Giosan et al., 2012). Significant changes also occur in Cholistan and Punjab (e.g. figure 1.12), where in the western part of the area, there are 174 Mature Harappan sites (with a settled area of 974 ha), which reduces to 41 Late Harappan sites (209 ha). Conversely, to the east, the number of Mature Harappan sites increases from 218 to 853 Late Harappan sites (Gangal et al., 2010). Interestingly, the occupied area increases only slightly from 2943 to 2985 ha (Possehl, 1999), reflecting the decrease in average site size between the Mature and Late Harappan (Giosan et al., 2012) and the abandonment of the large urban centres of the Mature Harappan.

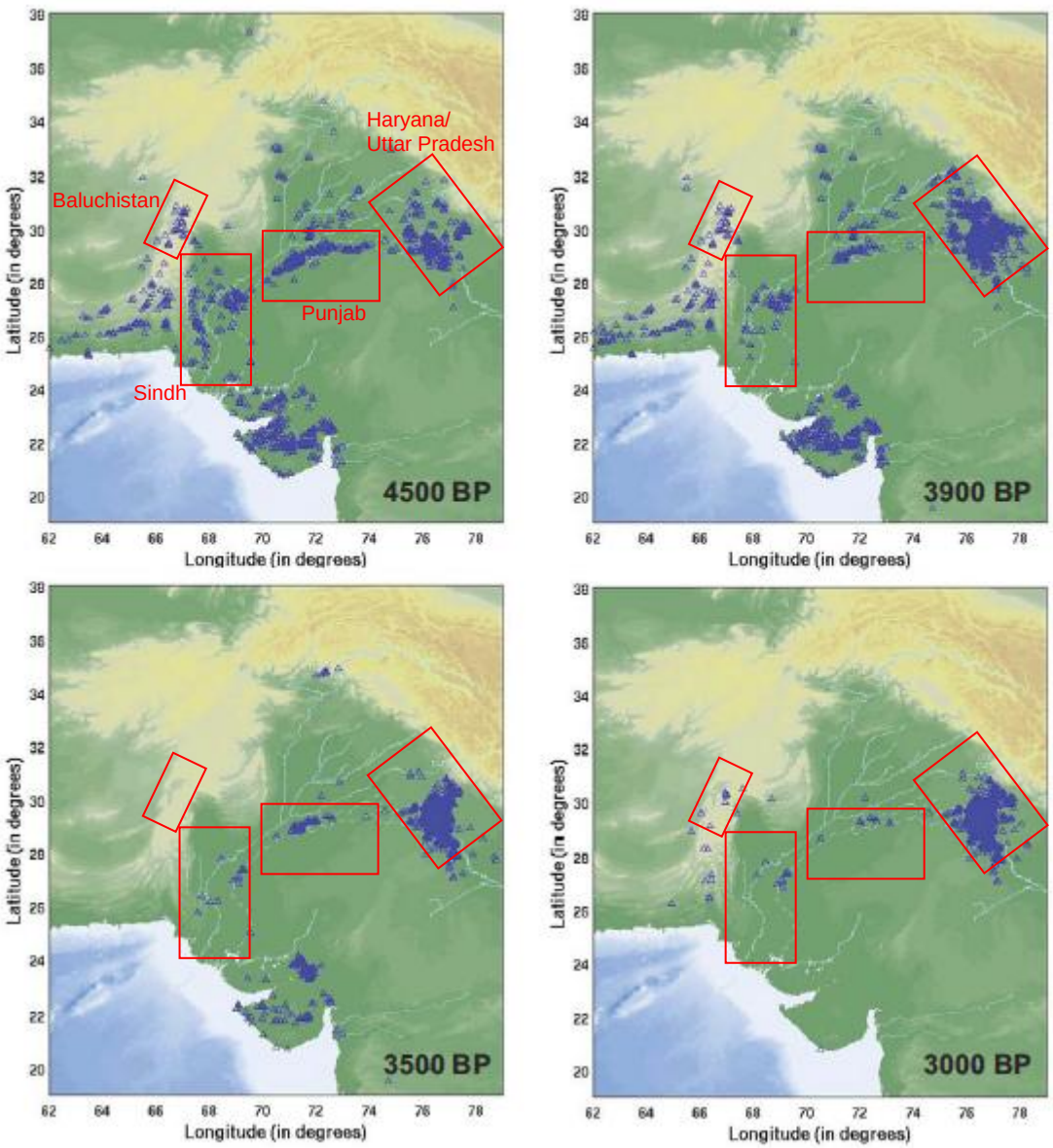

Figure 1.12: Distribution of Harappan sites at 4.5, 3.9, 3.5 and 3.0 ka from Giosan et al. (2012). Data collated from Mughal (1996; 1997), Possehl (1999), Wright et al. (2005) and Gangal et al. (2010). The distribution at 4.5 ka represents Mature Harappan settlements. At 3.9 ka, the transformation between the Mature and Late Harappan phases was underway, and 3.5 ka sees the end of the Late Harappan phase. Key areas of change are highlighted by the red boxes.

1.4.2 Proposed collapse hypotheses

The manner of the collapse (or transformation) of the Mature Harappan suggests that it is likely that there was more than one explanation for the demise of this civilisation (Allchin and Allchin, 1997; Lahiri, 2000). The collapse is unlikely to have been a simultaneous process and the manner of the collapse is different between different urban centres, with steady declines observed at Mohenjo-Daro and

Dholavira (Bhan, 1989), in contrast to apparently abrupt de-population at Kalibangan and Banawali (e.g. Raikes, 1969). Lahiri (2000) suggests the collapse was staggered over time, with some sites deteriorating from 2200 BC, and some lasting until ~1900 – 1800 BC. With a wide range of researchers approaching the enigma of this collapse with historical, archaeological and geographic backgrounds, many hypotheses have been suggested to explain the reasons behind this change. Explanations have been suggested ever since the discovery of the civilisation (Marshall, 1931) and fall broadly into three groups: climate and environment; economic and social; invasion and war. Many authors have suggested reasons for the collapse and below the main hypotheses and key references are outlined briefly.

1.4.2.1 Climate and environment

Gurdip Singh was the first to suggest a link between climatic variability and the collapse of the Mature Harappan (Singh 1971; Singh et al., 1974). Investigating the palynology of lake cores from Lakes Sambhar, Didwana and Lunkaransar in Rajasthan, India, Singh notes an increase in the salinity of these lakes at approximately 4 ka. He suggests that the change in lake conditions is due to a period of enhanced aridity, coinciding with the Harappan collapse. Critics of Singh's hypothesis include Possehl (1997), who suggests that lake salinity is not solely driven by precipitation, and that the hydrology of even small lake systems is difficult to attribute to one sole variable. Possehl (1997) also states that some of the lakes Singh studied are controlled by subsurface drainage and hence tectonics. Despite the rejection of the climate hypothesis by many archaeologists, there is a case to be made that the collapse of the Harappan occurs during a period of climatic variability tending towards increased aridity. This trend during the mid-Holocene has been observed by many researchers in India and Pakistan (e.g. Srivastava et al., 2003; Schuldenrein et al., 2004) and Enzel et al. (1999) comments that the Harappan civilisation flourished along river channels in a period of semi-aridity and that the Harappan would have been reliant on water for food security and urban dwelling. Using stable isotope records from foraminifera from the Indus Delta to produce a

palaeodischarge proxy for the Indus River, Staubwasser et al. (2003) identify a sharp drought at 4.2 ka, followed by quasi-periodic phases of drought with a cyclicity of 200 – 800 years. It appears that the flourishing and collapse of the Mature Harappan occurs against a backdrop of the weakening of the monsoon system and a period of oscillating climatic conditions. Weiss and Bradley (2001) hypothesised that the larger-scale climatic event at 4.2 ka, which is thought to have contributed to the collapse of the Chinese Neolithic, Akkadians and Egyptians, is also responsible for the beginning of the decline of the Harappan.

Investigations of the Ghaggar-Hakra palaeochannel, sometimes referred to as the 'lost' Saraswati, have been undertaken since the first study by Auriel Stein (Stein, 1942), and are reviewed in more detail in section 2.6. Agrawal and Sood (1982) and Misra (1984) propose that the loss of flow to this channel was triggered by avulsion and/or tectonic uplift, resulting in the capture of the Ghaggar-Hakra headwaters by the Yamuna River, and suggest that climate variability had little influence on the fluvial dynamics of the Ghaggar-Hakra system. Using the U-Pb dating of zircons from river sediments, Clift et al. (2012) present evidence that the Yamuna River did flow west, but prior to 49 ka, and conclude that although at some point in the geological past, the Ghaggar-Hakra may have lost waters to headwater capture by the Yamuna, this did not occur during the Holocene, and therefore reject Misra's hypothesis. Other early hypotheses relating to river dynamics were presented by Raikes (1964; 1965), Dales (1966a,b) and Dales and Raikes (1968), who suggested that the Indus River was damned by sediment in Sindh, causing severe flooding at Mohenjo-Daro and regional disruption. Critics of this hypothesis, including Wasson (1984; 1987), suggest that the unconsolidated sediments of the Indus floodplain would not have been suitable for building a dam with sufficient structural integrity to dam the Indus River.

Other researchers have questioned whether the Mature Harappan over-exploited their environment, with misuse of natural resources leading to environmental degradation (Vishnu-Mittre, 1993). Over-grazing and over-cultivation may have resulted in the removal of vegetation cover, increased soil erosion and the onset of

desertification (Vishnu-Mittre, 1993) and Fairservis (1967) suggested that overgrazing and the removal of material for brick-making would have placed an enormous strain on the landscape. He proposed that this strain led to precarious economic conditions, contributing to the eventual collapse of the Harappan. Lahiri (2000) argues however, that whilst these were probably key considerations for the Harappan, there has been no evidence put forward to substantiate claims of environmental degradation by the Harappan.

1.4.2.2 Economy and society

Allchin and Allchin (1997) propose that economic factors were influential in the decline of the Mature Harappan, suggesting that the demise of the Egyptians and the Akkadians at ~2000 BC left the Harappan with no major trading partners. Allchin and Allchin (1997) acknowledge that this itself probably would not have led to the decline of the Harappan, but believe that it was part of a set of circumstances (which may have included changing fluvial systems and tectonic activity), which disrupted the Harappan way of life. Wright (2010) suggests that social breakdown may have contributed to the migration and de-population of the Harappan, with archaeological evidence at Mohenjo-Daro and Harappa for socio-political breakdown. City structures were not maintained and squatting is observed in previously ordered domestic areas. Wright (2010) believes that these changes may signal a shift in leadership, but could also imply political acts of defiance, signalling a rejection of the integrated Mature Harappan society and the leadership that promoted and maintained order.

1.4.2.3 Invasion

Wheeler (1947) was one of the first researchers to suggest that the decline of the Mature Harappan was due to conflict (Possehl, 2002), and whilst earlier researchers had suggested Aryan invasion as a reason for collapse (e.g. Chanda, 1916; Childe, 1934), Wheeler was the first to present documented evidence to support this idea. Reading the Rig Veda as a historical document, Wheeler (1947) hypothesises that

whilst changing political and environmental conditions may have led to the weakening of the Harappan, ultimately the collapse occurred due to deliberate destruction by the Aryans. However, this hypothesis has been widely discounted, not only because of the scale of the Harappan civilisation (Dales, 1964), but also because the Rig Veda has now been dated to approximately 1000 BC (Possehl, 2002), approximately one millennium after the fall of the Harappan. In addition, the chronology of the Aryans in Asia has not been well defined (Allchin, 1990).

1.5 Developing chronologies of fluvial activity

Fluvial systems are responsive to variability in geology, geomorphology, climate, hydrology, vegetation and tectonics (e.g. Schumm, 1977) and fluvial deposits and landforms represent important archives of response to changing climate, sea level, glaciations and tectonics (Rittenour, 2008). Recent advances in developing fluvial chronologies has been through the development and analyses of regional databases of radiocarbon (^{14}C) dates (Lewin et al., 2005; Macklin et al., 2005, 2006), with emphasis given to dates marking the modification of sedimentation rate/style, which can be attributed to changes in fluvial dynamics (Turner et al., 2010). Suites of calibrated, fluvial ^{14}C dates are plotted as cumulative probability density functions, with the emphasis on 'river change dates' (Macklin et al., 2005), in order to identify temporal and spatial variability in fluvial dynamics from large databases of ^{14}C ages (Macklin et al., 2011). This meta-analysis approach has been successfully employed in many environments, including the UK (Macklin et al., 2005; 2010), Spain (Thorndycraft and Benito, 2006), the USA (Harden et al., 2008) and India (Kale, 2007), and has highlighted a strong underlying climate forcing of Holocene fluvial activity in Europe and the Indian subcontinent (Turner et al., 2010).

Developing fluvial chronologies in dryland environments can be problematic (Stokes, 1999), with relatively low amounts of biomass produced and preserved in arid and semi-arid regions. It is also possible that ancient carbon is reworked in many fluvial settings (e.g. Blong and Gillespie, 1978; Gillespie et al., 1992). Therefore, in many arid contexts, it is not possible to develop and analyse large

suites of ^{14}C dates using the approach applied by Macklin et al. (2005) and Lewin et al. (2005). Rittenour (2008) comments that other dating techniques, such as the cosmogenic nuclide dating of terrace surfaces and U-series dating of pedogenic carbonate, may be useful for providing minimum ages for sediment deposition and landform abandonment. However, the luminescence dating of non-biogenic material (e.g. quartz and/or feldspar) provides an advantage over these techniques, not only because of the availability of material for dating, but also because the most recent deposition event is directly dated. The development of the single aliquot regenerative dose (SAR) protocol (Murray and Wintle; 2000; Wintle and Murray, 2006) and the advances in the statistical treatment of complex dose distributions (e.g. Galbraith et al., 1999) has seen OSL dating increasingly applied to define fluvial chronologies. Not only has OSL dating helped improve temporal frameworks for arid geomorphological research (Tooth, 2012), but it is being increasingly applied in geoarchaeological contexts to help improve understanding of how variability in the natural environment impacted upon past human civilisations (e.g. Williams et al., 2010).

In this study, the optically stimulated luminescence signal from quartz is used to develop a chronology of past fluvial activity in the Ghaggar-Hakra, in order to satisfy the primary research aim (section 1.1.1). Luminescence dating in Pakistan has been limited to the dating of glacigenic deposits in the Himalaya (e.g. Richards, 2000; Owen et al., 2002; Spencer and Owen, 2004) and to date, there are no published luminescence ages from the floodplains of the Indus River or its tributaries. The work in this thesis presents the first luminescence chronology for fluvial activity in a system in the lowlands of Pakistan and therefore, the majority of work in this thesis is concerned with the development of a robust geochronological framework using the OSL signal. The following sections discuss the physical processes which give rise to the luminescence signal used for dating (section 1.5.2) and recent applications of luminescence dating to fluvial deposits (section 1.5.4).

1.5.1 Using the luminescence signal for dating

The luminescence signal from quartz and feldspar can be used for the dating of unfired sediments and heated ceramics and offers a means of directly dating geological events and archaeological artefacts from the late Quaternary period. Despite being a relatively new technique, it has become a widely applied dating technique for establishing geochronological control in Quaternary environments (Wintle, 2010). The historical development of luminescence dating has been outlined in detail by Wintle (2008a), starting with the development of the first thermoluminescence (TL) dating technique in the 1960s, which was applied to archaeological ceramics to determine the time elapsed since firing. The direct dating of sediments (using quartz and feldspar mineral grains) using the TL signal was developed during the early 1980s, and was followed by the first OSL dating of quartz grains by Huntley et al. (1985). The luminescence signals from quartz and feldspar are most commonly used for dating (Wintle, 1997), however, signals from other minerals, such as zircons (e.g. Smith, 1988; Templar and Smith, 1988) and calcite (Wintle, 1978; Debenham, 1983; Duller et al., 2009; Stirling et al., 2012) have also been observed.

As a dating tool, OSL dating offers a potential dateable range between one year and several hundred thousand years (Rhodes, 2011), and with the most commonly dated minerals, quartz and feldspar, being virtually ubiquitous, OSL dating is suited to a wide range of applications (table 1.1). Reviews of the application of OSL dating to geomorphological studies have recently been published in a special issue of the journal *Boreas* and cover settings including aeolian environments (Roberts, 2008; Singhvi and Porat, 2008), fluvial (Rittenour, 2008), glacial (Fuchs and Owen, 2008) and periglacial (Bateman, 2008). Rhodes (2011) summarises some of the common environments that OSL dating is applied to in table 1.1. As detailed in table 1.1, OSL dating has been increasingly applied in archaeological settings, both as a means for dating the sediments which encase archaeological finds (e.g. Jacobs, 2003a; 2003b; 2006) and for determining the timing of environmental change to ascertain a relationship with civilisation collapse (e.g. Williams et al., 2010).

Table 1.1: The applications and sedimentary environments for OSL dating. From Rhodes (2011).

Applications	Comments	Contexts
Tectonic and paleoseismic	Relatively recently applied	Marine, fluvial, lacustrine, slope deposits
Paleoclimatic and paleoenvironmental	Now widely used	Wide range of sediments
Geomorphic and Quaternary	Now widely used	Wide range of sediments
Environmental and process studies	Relatively recently applied	Soils, fluvial, potential for wider range
Archaeological and paleoanthropological	Now widely used	Fluvial, colluvial, soils, heated/fired materials
Environments		
Eolian (wind transported)	Usually successful	Sand dunes, loess
Fluvial, alluvial, lacustrine (water-lain)	Zeroing can be problematic	River terraces, alluvial fans, flood plains, lakes
Marine: coastal and offshore	Zeroing issue in deep water	Raised beaches, beach ridges, deeper water
Glacigenic	Zeroing and characteristics can be problematic	Moraine and till, outwash, glaciomarine
Slope deposits	Zeroing and characteristics can be problematic	Colluvium, rockfall, debris flows
Caves (karstic)	Zeroing can be problematic	Shallow cave sediments, sands and silts
Anthropomorphic	Zeroing can be problematic	Artificial fill, anthropomorphic soils
Volcanic rocks, precipitation	Characteristics are often problematic	Opal, biogenic opal, phenocrysts, xenocrysts
Soils	Grain movement studies	Modern, compound and buried soils
Heated materials	Usually successful	Ceramics, wild fires, thermochronology
Strained and shocked materials	Little research to date	Impact craters, fault movement

1.5.2 The physical processes giving rise to the luminescence signal

The basic physical principles of luminescence have been described by Aitken (1985) in his book *Thermoluminescence Dating* and the description of these principles which follows has been written with reference to this text. Luminescence is a phenomenon which arises from the interaction of ionising radiation and a mineral grain through the release and trapping of electrons in the crystal lattice of the dosimeter mineral (Preusser et al., 2009). The crystal lattice of a mineral such as quartz is made up of a framework of alternating positive and negative ions. However, defects in this lattice can occur and may result due to impurities in the crystal and from radiation damage. Defects which have occurred due to the absence of a negative ion are known as electron traps, because electrons that have become separated from their parent nuclei are attracted to that negative-ion vacancy. Once trapped, an electron remains in the defect until realised by thermal or optically induced vibrations in the crystal lattice. Once free, the electron can diffuse within the crystal in the conduction band (figure 1.13), and can either be re-trapped and re-evicted from the same trap, trapped in a more stable trap or can re-combine with an ion which had previously lost an electron. This type of recombination may result in the production of light (radiative recombination), and ions or atoms at which radiative recombination occurs are known as luminescence centres, where

the thermoluminescence (TL) and optically stimulated luminescence (OSL) signals are produced.

Aitken (1990) summarises these luminescence processes using the energy-level diagram in figure 1.13. During both natural and laboratory induced irradiation (figure 1.13i), negative ions are removed from their parent nuclei in the valence band, leaving positively charged 'holes'. Whilst sufficient energy remains, the excited electrons diffuse in their excited state in the conduction band before recombination occurs. The excited electrons attracted to the defects or traps (L and T in figure 1.13) are stored as long as there is insufficient energy to re-excite them into the conduction band (figure 1.13ii). Upon contact with heat or light (figure 1.13iii), the probability of the trapped electron being evicted from the defect increases and some of these electrons will reach luminescence centres and combine to produce luminescence. The number of electrons that combine with luminescence centres is directly proportional to the total trapped electron population, which is in turn proportional to the amount of irradiation that the crystal has been exposed to.

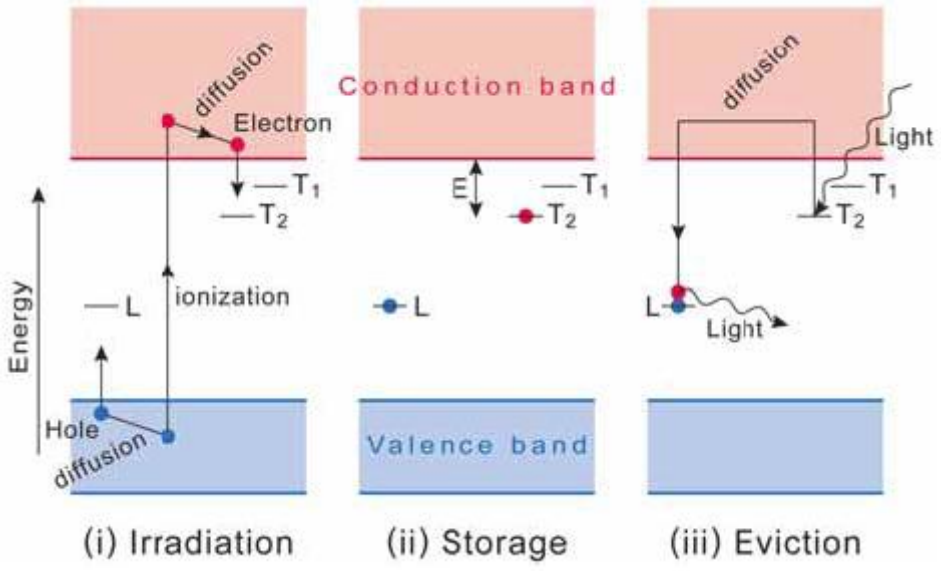

Figure 1.13: Energy-level representation of the processes involved during i) irradiation, ii) storage and iii) heating or exposure to light, resulting in eviction. T and L refer to traps and holes respectively (with T_2 referring to a deeper trap, which is more stable over time) and E refers to the depth of the trap below the conduction band. From Duller (2008a), modified from Aitken (1990).

1.5.3 Use of the quartz OSL signal

In sedimentary and geomorphological contexts, the OSL signal is usually preferred over the TL signal because it is bleached much more rapidly. In figure 1.14a, the TL and OSL signals observed from both quartz and feldspar after various periods of exposure to sunlight have been plotted by Godfrey-Smith et al. (1988). These data were re-plotted by Duller (2008a) as a percentage of signal remaining after exposure of an aliquot to sunlight for various different periods (figure 1.14b). Duller (2008a) observes that whilst the quartz OSL has reduced to approximately 0.1% of its initial signal after exposure to sunlight for 100 s, more than 85% of the TL signal remains after the same exposure period. The same pattern is observed for feldspar, with the OSL signal bleached much more rapidly than then TL signal.

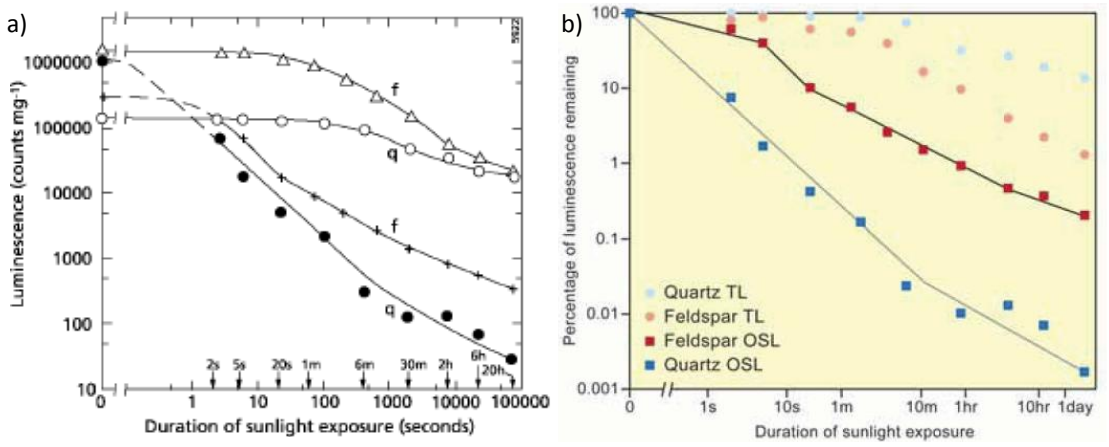

Figure 1.14: a) The sunlight bleaching of the natural TL (open symbols) and OSL (filled symbols) signals of quartz (q) and feldspar (f) from Godfrey-Smith et al. (1988). b) The data of Godfrey-Smith et al. (1988) re-plotted by Duller (2008a).

Wallinga (2002) states that mineral selection for the luminescence dating of fluvial sediments is an important consideration. From figure 1.14, it is clear that the quartz OSL signal is bleached much more rapidly than the feldspar OSL signal, and in a fluvial context, where incomplete bleaching of the luminescence signal is a potential issue (section 1.5.4), Wallinga (2002) suggests that quartz should be preferred over feldspar because the OSL signal is more likely to be bleached effectively. In addition to the feldspar OSL signal being bleached much less rapidly (Godfrey-Smith et al., 1998), many feldspar OSL signals are subject to anomalous fading (Wintle 1973), which can result in age underestimation. Anomalous fading can be corrected for

(e.g. Lamothe and Auclair, 1999), however the application of this correction is not straight forward, and can be problematic (Wallinga, 2002). In addition, when dating using K-feldspars, calculation of the environmental dose rate (section 1.5.2) must take into account the internal potassium concentration of the grain, which can add complexity to dose rate calculations (Rhodes, 2011; Smedley et al., 2012).

The sediments of interest in this study are likely to be Holocene in age, and are therefore well within the dateable age range of quartz OSL dating. The sediments sampled are from floodplain alluvium in Punjab, and the quartz OSL signal is likely to have been sensitised since the sediments were first eroded from their source in the Himalaya. Therefore, assuming that the signals measured are dominated by the fast component (e.g. Smith and Rhodes, 1994; Bailey et al., 1997), the quartz OSL signal has been selected for use for developing a fluvial chronology in this study.

1.5.3.1 The 325°C TL peak in quartz

The energy-level model in figure 1.13 (Aitken, 1990) represents a simplified model of the physical processes relating to the production of luminescence. In reality, there are a number of different types of traps that give rise to the quartz OSL signal. The energy required to evict an electron from its trap and into the conduction band is defined by the depth of the trap, with shallower traps requiring less energy and deeper traps requiring higher energies. By gradually heating a sample and recording the TL, a number of peaks, relating to traps of different depths, are evident (e.g. figure 1.15). The most commonly observed peaks in quartz are observed at temperatures of around 110°C, 230°C, 270°C, 325°C and 375°C (see Preusser et al., 2009 and references within), depending on the experimental conditions (e.g. the heating rate), but not all peaks are observed in all samples. The 325°C TL electron trap is usually of most interest when considering the quartz OSL signal because this is the source of the majority of the OSL signal when stimulating with blue or green light wavelengths at elevated temperatures (Smith et al., 1990; Spooner, 1994; Wintle and Murray 1997, 2006). The 325°C trap is stable, with a life-time in excess of 20 Ma (at temperatures of 20°C) (Spooner and Questiaux, 2000) and the electron

population associated with this trap can be evicted rapidly with light stimulation (Spooner et al., 1988), making this signal suitable for geochronological applications (Duller and Wintle, 2012).

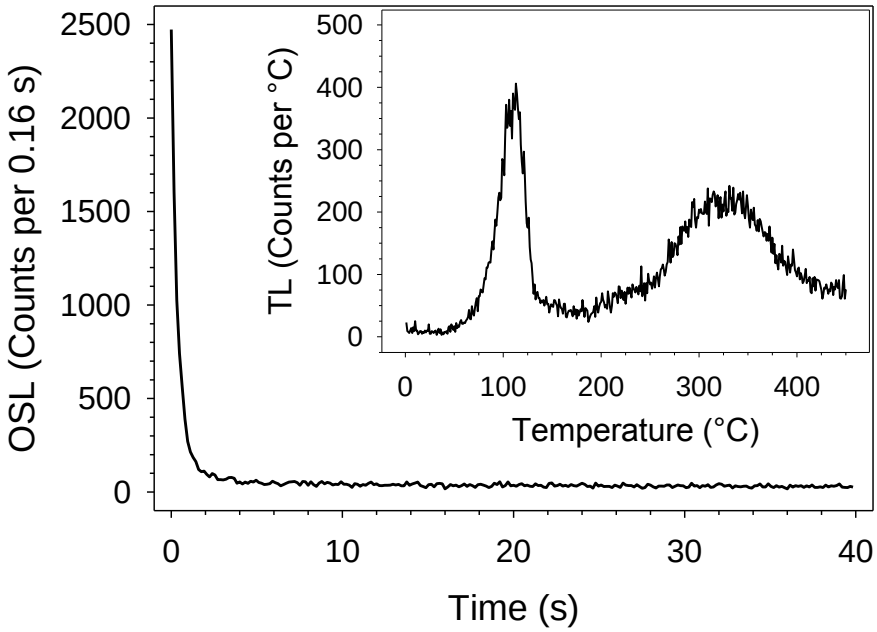

Figure 1.15: OSL signal from an aliquot of Pakistan quartz (sample 136-3-9) after a 5 Gy dose, and inset a TL signal from the same aliquot after a 5 Gy dose. In the TL signal, the 110°C and 325°C TL peaks are prominent. The 110°C peak has a short lifetime and therefore is only present in signals after laboratory irradiation and is not seen during the measurement of natural signals.

1.5.3.2 Calculation of a quartz OSL age

In the majority of geomorphological systems, a cycle of erosion, transportation and deposition of sediment over numerous spatial and temporal scales can be observed. Luminescence dating allows the direct dating of the timing and rates of such events by providing the time elapsed since a sediment grain was last exposed to light. During burial, the mineral grain is exposed to ionising radiation. Figure 1.16 provides a schematic representation of the trapped charge population during these cycles in nature. As discussed in section 1.5.2, this ionising radiation results in electron trapping and it is this process which leads to the luminescence signal increasing over time. During a bleaching event (e.g. exposure to light), energy absorption results in the release of charge and the reduction of the trapped charge population (Bøtter-Jensen et al., 2003b). Subsequent cycles of burial, transport and

deposition will result in the trapped charge population increasing, being reset and increasing once more.

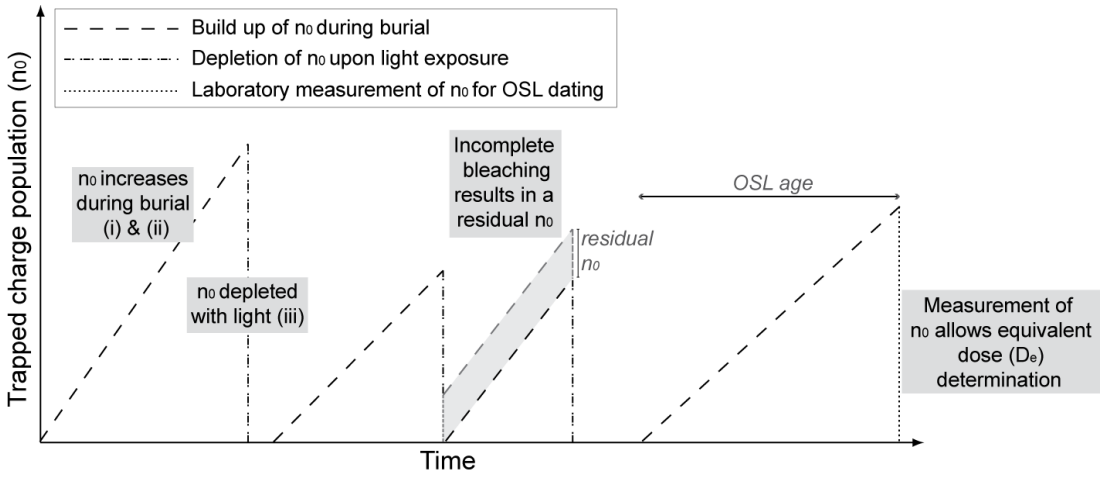

Figure 1.16: A schematic representation of the build up and depletion of the trapped charge population (n_0) over time. i), ii) and iii) relate to the energy-level diagram in figure 1.13 to describe the physical processes resulting in the accumulation and resetting of the trapped charge population.

During burial, a grain is exposed to radiation in the form of alpha and beta particles and gamma rays emitted by the sediment matrix. For the majority of samples, this radiation flux originates from Uranium, Thorium and Potassium in approximately equal parts, with a small contribution from Rubidium (Aitken, 1985). There is also a contribution from extra-terrestrial cosmic rays (Aitken, 1985). The sum of the radiation delivered from these sources during burial is termed the environmental dose rate, which is the rate of energy absorption from the ionising radiation in the environment (Aitken, 1988), measured in Gray per millennia ($Gy.ka^{-1}$). The amount of accrued luminescence also requires measurement in order to calculate the age of a sample. The OSL signal of quartz is most frequently measured using the single-aliquot regenerative-dose (SAR) protocol (Murray and Wintle, 2000; 2003; Wintle and Murray, 2006), where the natural signal is measured, and is followed by a series of luminescence measurements after applying a number of increasing laboratory irradiations. By constructing a dose response curve, the natural luminescence signal can be interpolated to assess the amount of laboratory irradiation required to reproduce a luminescence signal equivalent to the natural signal. Once the equivalent dose and the environmental dose rate have been quantified, the luminescence age of a sample can be calculated using equation 1.1.

$$Age\ (ka) = \frac{Equivalent\ dose\ (Gy)}{Environmental\ dose\ rate\ (Gy.ka^{-1})} \qquad \text{(Equation 1.1)}$$

1.5.4 OSL dating of fluvial deposits

A number of recent methodological and analytical developments have seen OSL dating increasingly used as a geochronological tool for the dating of fluvial sediments. One of the main challenges when dating fluvial sediments is the incomplete bleaching of the luminescence signal, where either the luminescence signal for all grains in a sample is not completely reset during the burial event or when the OSL signal from grains from the same sample are bleached to a different degree, resulting in different equivalent dose (D_e) values calculated from aliquots of the same sample (Duller, 1994). For fluvial sediments, where individual grains are likely to have had unique paths of transport within the water column, and therefore will have been exposed to varying amounts of light at varying degrees (Rodnight et al., 2006), incomplete bleaching is likely (Rittenour, 2008).

Predicting the extent of bleaching in a fluvial environment is complicated (Murray and Olley, 2002), with factors such as mixing, saltation, turbidity, sediment load and water column depth all contributing to the probability that, for an individual grain, the luminescence signal (used for dating) is completely reset. Therefore, when dating fluvial sediments, the complete bleaching of the luminescence signal cannot be assumed, and careful measurement of the luminescence signal and interpretation and analysis of the sample dose distribution must be undertaken to calculate an appropriate D_e. Duller (2008b) notes that using single-aliquot methods to make replicate measurements of the same sample allows incomplete bleaching to be identified. For a well bleached sample (e.g. figure 1.17a), the majority of equivalent dose measurements will be consistent (within errors) with one value, whereas for a sample which has not been well bleached at deposition (e.g. figure 1.17b), there will be a broad range of D_e values, with asymmetry of the distribution observed towards higher equivalent doses (Olley et al., 1998). The overdispersion parameter of Galbraith et al. (1999) is a measure of the relative standard deviation

of the underlying dose distribution after measurement uncertainties have been taken into account. It is frequently used by the OSL dating community to help inform the extent of bleaching, with Olley et al. (2004a) concluding that dose distributions with an overdispersion of less than 20% can be considered well bleached. Aliquot size is a key consideration when assessing the extent of incomplete bleaching. As Olley et al. (1999) observe, when the OSL signal from an aliquot is composed of signal from a high number of grains, less variation in D_e will be observed, and therefore, incomplete bleaching will be difficult to identify, which could result in age overestimation. Olley et al. (1999) suggest that the measurements of single grains will give the most complete assessment of the extent of incomplete bleaching, but in settings where this is not practicable, small aliquots should be used for samples where incomplete bleaching of the OSL signal is a possibility (e.g. Rittenour, 2008).

Comprehensive reviews of the application of the luminescence dating of fluvial sediments have been published by Murray and Olley (2002), Wallinga (2002), Jain et al. (2004) and Rittenour (2008) amongst others. These authors report on a wide range of applications of the OSL dating technique to fluvial deposits, including flood deposits in Australia (Murray et al., 1995), slackwater deposits in India (Kale et al., 2000), river terrace sequences (e.g. Lewis et al., 2001; Rittenour et al., 2003; Briant et al., 2006;) and palaeochannel sediments to assess rates of channel migration (Rodnight et al., 2006; Tooth et al., 2009). More recent applications of OSL dating to fluvial deposits include palaeochannel sediments in Sudan (Williams et al., 2010) and India (Saini et al., 2010), arroyo deposits in Utah, USA (Summa-Nelson and Rittenour, 2012) and river aggradation sediments in Germany (Lauer et al., 2010). It is clear from the vast number of studies published that many applications of OSL dating to fluvial deposits provide ages in good agreement with independent age control (e.g. Murray and Olley, 2002; Rittenour, 2008; Rhodes, 2011) and in the instances when incomplete bleaching is present, measurements of the signal from small aliquots and/or single grains, as well as the application of statistical methods facilitates the reliable dating of fluvial sediments (Rittenour, 2008).

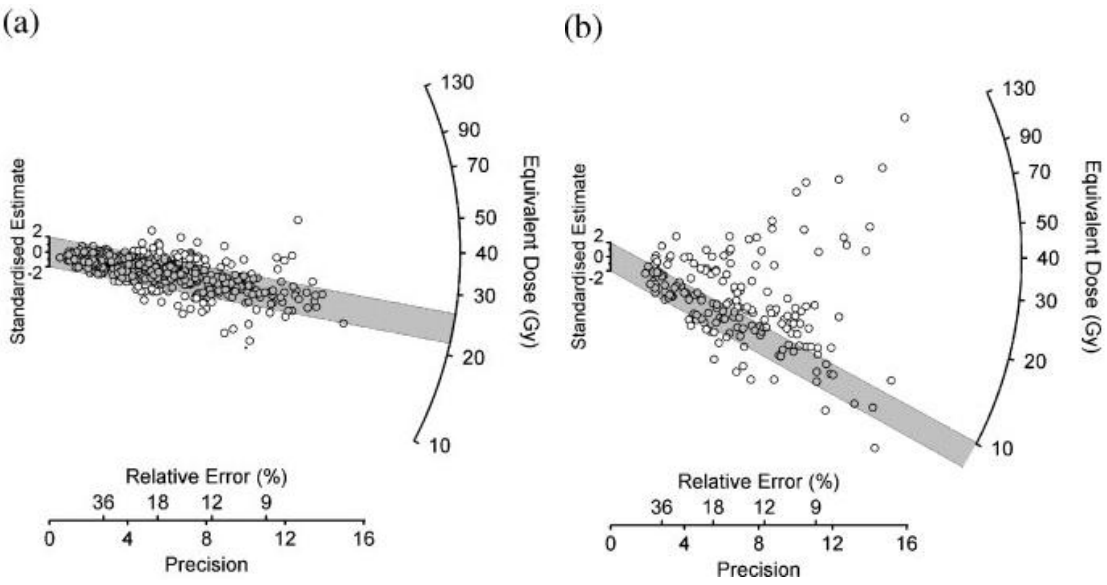

Figure 1.17: Two single-grain equivalent dose distributions measured plotted by Duller (2004). a) The D_e distribution from a dune deposit, where D_e values are consistent within a relatively narrow band, indicating that the sample was well bleached at deposition. b) The D_e distribution from a colluvial deposit, where the majority of individual D_e determinations are not consistent with one value, indicating the sample was incompletely bleached at deposition.

Despite the assertion of Jain et al. (2004) that incomplete bleaching is only a problem for modern and young sediments (less than 1 ka), there are many examples where older samples appear to be incompletely bleached (Juyal et al., 2006) and conversely, where younger samples are well bleached (DeLong and Arnold, 2007). Clearly, for all sediments sampled from fluvial units, there is the potential that not all grains were completely bleached at burial. The degree of bleaching depends on many factors including sediment load, turbidity, water column depth and transport distance and mode (Stone and Thomas, in press), making it impractical to predict the extent of bleaching (Murray and Olley, 2002) and therefore Rodnight (2006) suggests that all samples should be checked individually for heterogeneous bleaching. Despite this, OSL dating can be a valuable tool for the dating of fluvial sediments, as long as appropriate sampling and careful analysis is undertaken (Rodnight et al., 2006).

1.6 Research objectives

The research objectives of this study have been designed in order that the research aims outlined in section 1.1.1 can be achieved. The overall aim of this thesis is to

develop a chronology of fluvial activity for the Ghaggar-Hakra palaeochannel using quartz OSL dating. Further aims are to compare this chronology to published records of regional climate change and the documented archaeological record and to assess whether a change in fluvial activity may have been a factor in the collapse of the Mature Harappan at 1900 BC. To achieve these aims, a number of research objectives have been developed. These are listed below and the chapters in which they are addressed are shown in parentheses.

1. To identify sites where fluvial and aeolian processes have been active in the past using sedimentological and stratigraphic investigation in the field and to sample these sediments for OSL dating and where applicable, ^{14}C dating. (Chapter 2).
2. To calculate OSL dates for the collected samples, using thick source alpha and beta counting measurements to determine radionuclide concentrations and from these, derive the environmental dose rate and using the quartz OSL signal for the equivalent dose calculation. (Chapter 3 and 4).
3. To check that all OSL ages are based on signals which are dominated by the fast component of quartz and to develop a technique which assesses the dominance of the fast component within a quartz OSL signal. (Chapter 5).
4. To use OSL dating to provide a chronology of fluvial activity along the palaeochannel Ghaggar-Hakra. (Chapter 6).
5. To develop and test a protocol for rapid age estimation using the quartz OSL signal, which will allow the age of a sample to be rapidly approximated to help inform laboratory sampling strategy. (Chapter 7).
6. To place the fluvial chronology into the context of published records of regional climatic variability to determine whether changes in the fluvial dynamics of the Ghaggar-Hakra can be related to climate change. (Chapter 8).
7. To compare the fluvial chronology to the documented archaeological record along the Ghaggar-Hakra channel. (Chapter 8).

2. The Ghaggar-Hakra palaeochannel: physiography and study area

2.1 Introduction

Pakistan is geographically diverse. Extending from 24° – 37° N latitude and 61° – 76° E longitude, it consists of many varied physiographical settings, including marine, coastal, desert, riverine and high altitude mountain environments (Singhvi et al., 2010a). Therefore, the climate and geomorphology varies significantly across the country. The South Asian Monsoon dominates the climate of the region (e.g. Kale et al., 2003), providing the majority of precipitation to the central and southern provinces of Pakistan, and is an important factor in the society, ecology and economy of both the modern region and for ancient civilisations (Singhvi and Kale, 2009).

This chapter outlines the geomorphological and climatological setting of the study area, before discussing the Ghaggar-Hakra palaeochannel and previous work on this channel in more detail. The study area selected is outlined and the two transects taken across this area are defined. A number of sites along these transects were selected for sampling, and these are discussed in further detail in sections 2.6 and 2.7. At each of the twelve study sites, samples were taken for optically stimulated luminescence (OSL) dating, and where appropriate material was available, samples for radiocarbon (^{14}C) dating were also taken.

2.2 Physiography of Pakistan

Pakistan is located within the Indian sub-continent, bordered by Iran and India to the west and east, and sharing borders with Afghanistan and China to the north. The Indus River drains into the Indus Delta in the Arabian Sea from the Himalayas in the north, and whilst the climate of Pakistan is predominantly controlled by the Asian Monsoon, mid-latitude cyclones driven by the westerlies influence the climate at higher latitudes (e.g. Thamban et al., 2007; Bookhagen, 2010). Pakistan can be broadly divided into three distinctive geographic areas; the highlands in the north,

the Baluchistan rock plateau to the west and the Indus Plain. The geography of the northern part of Pakistan is dominated by some of the highest mountain ranges in the world, including the Himalaya, the Karakorum and the Hindu Kush. The upper tributaries of the Indus River are sourced in these ranges and the climate is influenced by westerly weather systems and the monsoon to some extent (Owen et al., 2002). To the west, the Baluchistan rock plateau marks the eastern edge of the Iranian plateau and is a high altitude, arid region which is tectonically active due to the current collision/subduction of the Indian and Eurasian plates. The Indus plain is the semi-arid region to the east of the current channel of the Indus River in Punjab and Sindh. This region is intensively cultivated, with the Indus and its tributaries utilised for irrigation and farming, and this area has supported human occupation throughout the Holocene (e.g. Possehl, 2002; section 1.3). To the east of the Indus Plain, the Cholistan Desert represents the western most extent of the Thar Desert, and is a flat, arid region characterised by small dune fields and abandoned channels, such as the Ghaggar-Hakra.

2.2.1 Fluvial landscape of Pakistan

The fluvial systems of Pakistan form part of the Indo-Gangetic Plain, which was constructed during the Cenozoic by the erosion of the Himalayas (Burbank et al., 1996). Using Shuttle Radar Topography Mission (SRTM) data, Giosan et al. (2012) plot the large scale morphology of the Indo-Gangetic Plain (figure 2.1). They observe that the major Pakistani river channels are largely degradational after emerging from the Himalaya, with the Indus and its tributaries characterised by wide, shallow incised valleys separated by interfluves (e.g. figure 2.1d; Giosan et al., 2012). This is in contrast to the aggradational systems in the east (e.g. the Ganges and its tributaries), which have highly seasonal sediment discharge and low stream power (Sinha et al., 2007; Sinha and Sarkar, 2009). Giosan et al. (2012) suggest that the differences in morphology are largely driven by the regional precipitation gradient driven by the monsoon.

The Indus River drainage basin is one of the largest in the world, draining an area of 970,000 km^2 from its source in Tibet to the Indus delta in southern Pakistan (Inam et al., 2007). However, for its size, Ali and De Boer (2007) state that the Indus system is relatively understudied, and not much is known about the hydrology of this drainage basin. The Indus is fed by a number of large tributaries, including the Shyok Shigar, Gilgit and Kabul Rivers from the north, and the Jhelum, Chenab, Ravi, Beas and Sutlej Rivers from the east (figure 1.1; figure 2.1). Flow in these tributaries is driven primarily by monsoon precipitation and snow and ice melt in the upper parts of the drainage basin (e.g. Bookhagen, 2010). The upper Indus system is a braided stream, draining the Karakoram and Himalayan mountain ranges, whilst the Lesser and Greater Himalaya are drained by the major Punjab tributaries (Jhelum, Chenab, Ravi, Beas and Sutlej) (Inam et al., 2007). The steep relief and seasonal precipitation in the region results in high sediment yields (Ali and De Boer, 2007) and flow is highly seasonal. In the Punjab Plains, as topography becomes less severe (e.g. figure 2.1d), the tributaries become low gradient systems, and high hydrological output and sediment yield are still observed, as the monsoon becomes the greatest control on these systems (Ali and De Boer, 2007). The confluence of the Indus and the Punjab tributaries occurs in southern Punjab, where the river continues as a braided system before starting to meander in Sindh before reaching the Indus Delta near Karachi.

The Indus and the Punjab tributaries have been dynamic in the past. A number of former courses of the Indus can be observed in Sindh, and the Indus channel has migrated westwards since the last glacial maximum (Kazmi, 1984). The Punjab tributaries also appear to have been highly dynamic over time, with Wright et al. (2008) reporting the northwards migration of the Ravi River during the mid-Holocene. Alterations of the Beas course during the Late Harappan phase are suggested by Amundson and Pendall (1991), and abandoned courses of the Sutlej river can be easily identified on satellite imagery. One of the most studied regional hydrological changes is the Ghaggar-Hakra palaeochannel in Punjab, south of the Sutlej River. This channel is associated with a dense concentration of archaeology, suggesting some form of fluvial system may have been utilised by ancient human

civilisations (e.g. the Mature and Late Harappan; figure 1.12). Previous work on the Ghaggar-Hakra palaeochannel is reviewed in section 2.4.

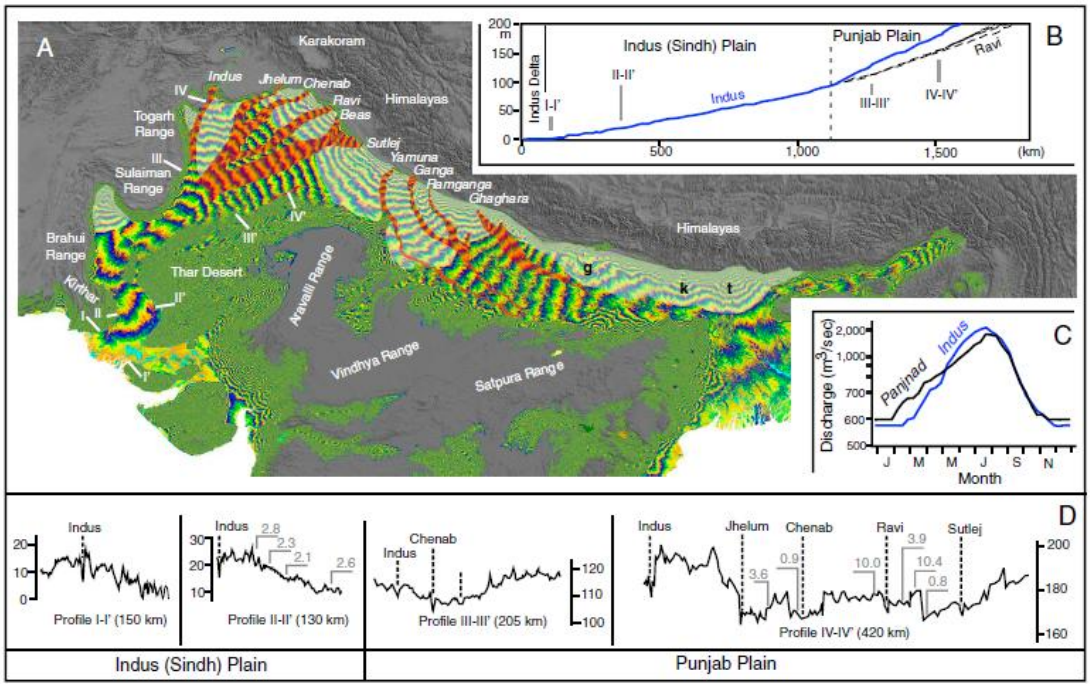

Figure 2.1: a) Large scale morphology of the Indo-Gangetic Plain from Shutter Radar Topography Mission (SRTM) data. For altitude, pattern of colours repeats every 10 m to 300 m, and higher landscape is shaded grey. Incisional landscapes have a red mask, and aggradational landscapes have a lighter mask. b) Along-channel longitudinal profiles for the Indus and its Punjab tributaries. c) Hydrographs for the influence and confluent Punjab tributaries (Panjnad River). d) Profiles across the extended Indus plain (m asl). River channel locations are shown in a) and ages of fluvial deposits (in ka) dated by Giosan et al. (2012) are given in grey. From Giosan et al. (2012)

2.2.2 The Thar/Cholistan Desert

The Thar Desert covers an area of approximately 200,000 km^2 and extends from the Aravalli mountain range in India to the Indus River in Pakistan (Roy et al., 2008). Although not a high-energy aeolian environment, sand dunes are widespread across the Thar Desert, with abundant source material including the alluvial plains of India and Pakistan, the coastline of the Arabian sea and the weathering of sandstone and granite outcrops (Derbyshire and Goudie, 1997). Drainage within the Thar is allogenic, with the exception of the Luni River in India (Deotare et al., 2004), and playas are often observed, particularly in the Indian state of Rajasthan, which may have occurred either by the blocking of drainage channels by dunes (e.g. the

Sambhar Lake; Sinha and Raymahashay, 2004), or through faulting (e.g. Pohedda Lake; Pandey and Chatterji, 1970).

The Cholistan Desert is an extension of the Thar Desert around the district of Bahawalpur in the Punjab state of Pakistan (figure 2.2). It extends over an area of ~26,000 km^2, and is ~480 km in length and the width varies between 23 km and 192 km (Akbar et al., 1996). It is generally divided into two regions (Akbar et al., 1996; Mughal, 1997; Akhtar and Arshad, 2006) based on topography and geomorphology, which has been mapped by Ahmad (2008) (figure 2.3), following a series of field seasons. The Lesser Cholistan is the area north of the Ghaggar-Hakra palaeochannel and is relatively flat with low sand dunes (Mughal, 1997). It contains remnants of some sandy terraces (Ahmad, 2008), and Akbar et al. (1996) describe this area as alluvial flats with alternating sandy ridges. The Greater Cholistan is the area south of the Ghaggar-Hakra palaeochannel and has a more diverse range of landforms according to Ahmad's (2008) mapping (figure 2.3). This area consists of low sand dunes, longitudinal ridges, transverse and alveolar ridges (figure 2.3), as well as partially covered channels. At present there are no natural bodies of surface water in the region, with groundwater at a depth of 30 – 50 m (Baig, 1980). Instead, modern fluvial activity is ephemeral, in response to monsoon precipitation and one of the more prominent features of the desert is the Ghaggar-Hakra palaeochannel (Mughal, 1997).

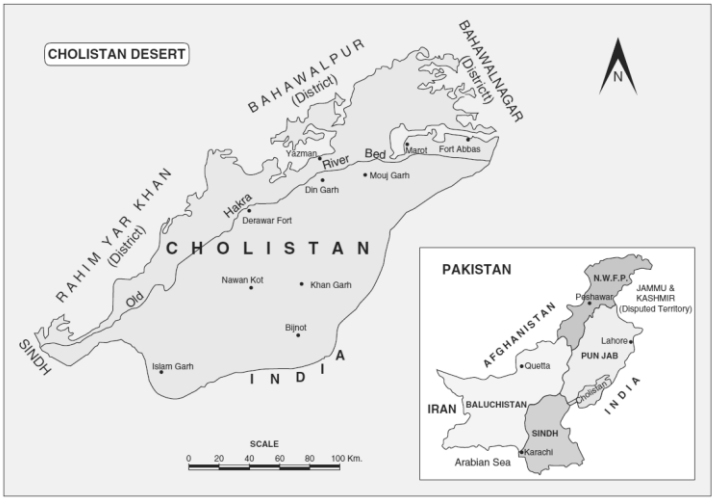

Figure 2.2: The Cholistan Desert and inset, the position of the desert within Pakistan. From Akhtar and Arshad (2007).

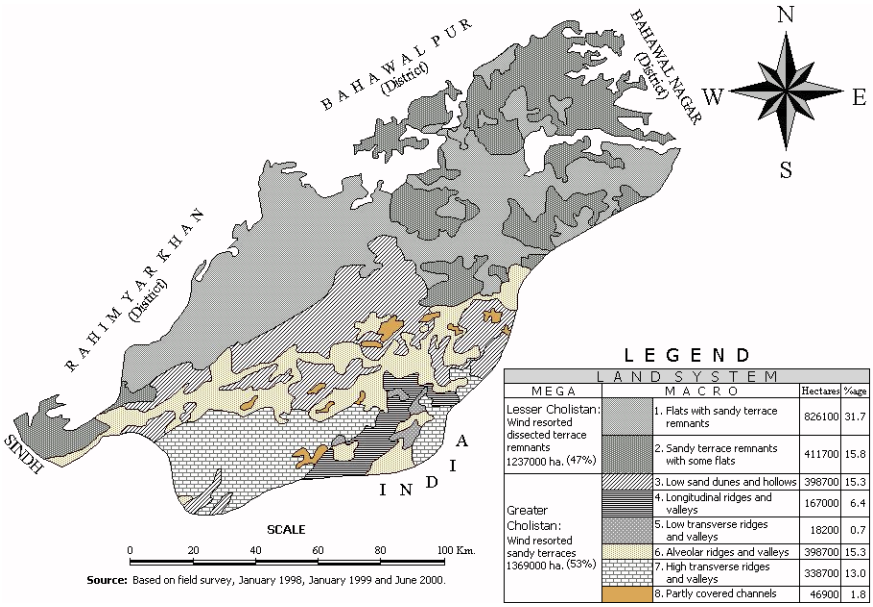

Figure 2.3: Geomorphological map of the Cholistan Desert, based on three field surveys. From Ahmad (2008).

One of the striking features of the Cholistan Desert is the subtlety of the topographic change. A digital elevation model (DEM) of Southern Punjab and Northern Sindh was provided by Dr Sam VanLaningham (Fairbanks University, Alaska) and is presented in figure 2.4. Using this DEM, the topographic change over the study area can be assessed. The width of the study area (e.g. the Ghaggar-Hakra transect; section 2.6) is approximately 175 km and over this distance, the altitude above sea level (asl) varies by 25 m, between 130 m and 105 m asl from east to west (figure 2.4). One of the original aims of this study was to produce a geomorphological map of the area prior to field work and sample collection, however the subtle topographic variability and the relatively small scale of the geomorphological features made this impracticable. The vertical resolution of the DEM is 2 – 3 m (VanLaningham, pers. comm.) and only the larger-scale topographic variability is highlighted. High resolution (15 m lateral scale) Advance Spaceborn Thermal Emission and Reflection (ASTER) images were acquired for mapping, however, the vertical resolution of these images was not sufficient to allow the identification of smaller-scale geomorphological features.

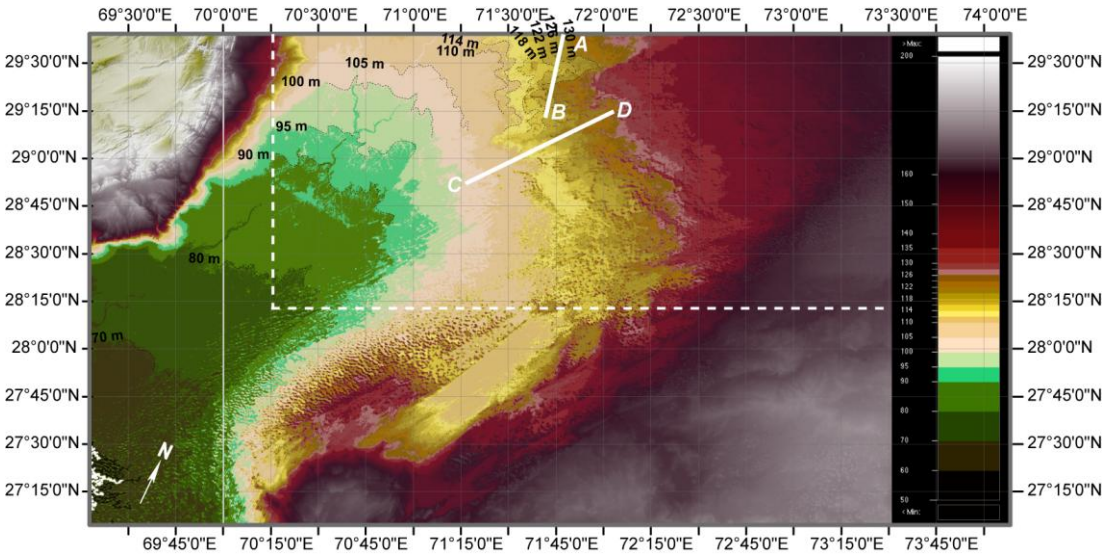

Figure 2.4: Digital elevation model of the region, provided by Dr Sam VanLaningham (Fairbanks University, Alaska). The satellite picture shown in figure 2.10 is shown by the dotted lines, as well as the Sutlej (A-B) and Ghaggar-Hakra (C-D) transects (sections 2.7 and 2.6).

2.2.2.1 Modern climate of the Cholistan Desert

The climate of the Thar and Cholistan Deserts is strongly influenced by the Asian Monsoon, and regionally, the majority of annual precipitation is received between June and September from the monsoon (e.g. Bookhagen, 2010). A strong rainfall gradient exists across the Punjab and Rajasthan districts (Prasad and Enzel, 2006; figure 2.5b). At the eastern margin of the Thar Desert, annual precipitation is approximately 450 mm (Roy et al., 2008), as opposed to approximately 100 mm per annum in Cholistan at the western fringe of the Thar Desert (Mughal, 1997; Prasad and Enzel, 2006; figure 2.5b). During the winter months, the northern areas of Pakistan are influenced by the westerly weather system, where mid-latitude cyclones forced by the westerlies cross the region at latitudes of ~28°N – 30°N, which brings winter precipitation to the region. Typically, winter precipitation accounts for approximately 20% of the annual precipitation delivered to Pakistan, which makes this region particularly sensitive to fluctuations in the strength and position of the summer monsoon (Prasad and Enzel, 2006). In the Thar Desert region, mean maximum summer temperatures range between 40°C – 45°C, with minimum mean temperatures of 3°C – 10°C (Roy et al., 2008). For the Cholistan region specifically, Mughal (1997) notes that summer temperatures have risen to

51.6°C, and during winter months, temperatures can fall below freezing. The majority of annual precipitation falls in July and August, and annual average precipitation is 137 mm (Mughal, 1997).

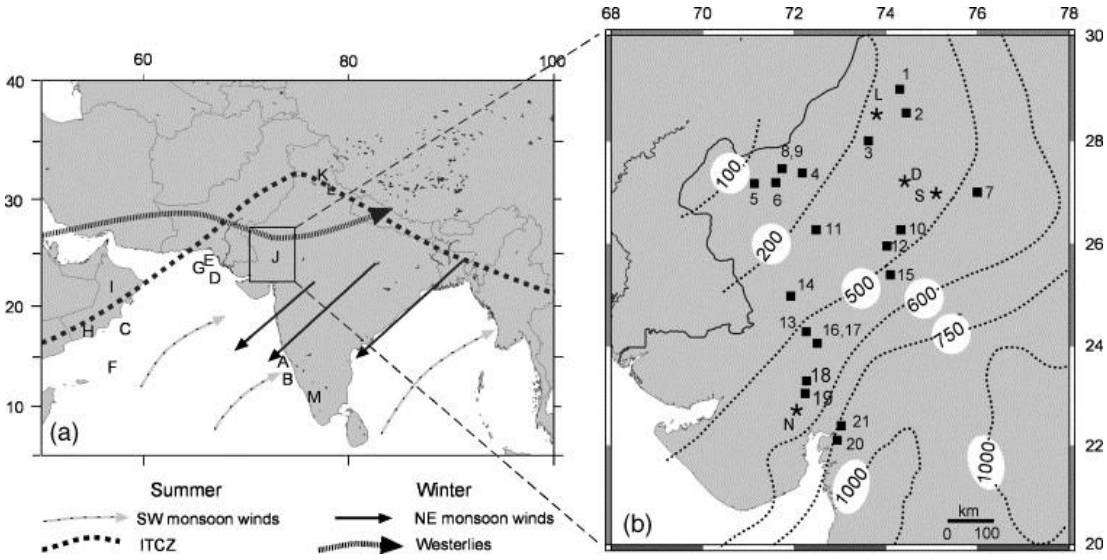

Figure 2.5: a) Schematic representation of the major winds in SW Asia. b) Annual rainfall isohyets (mm) in NW India. From Prasad and Enzel (2006). Letters and symbols refer to sites referred to by Prasad and Enzel (2006), and these are not referred to in this study.

2.3 The South Asian Monsoon system

According to Singhvi and Kale (2009), the Indian subcontinent is one of the largest monsoon dominated areas in the world, and the seasonal reversal of winds over the subcontinent is the dominant control on both the modern climate and the climate of the late Quaternary. The monsoon system occurs due to the differential warming of the South Asian continent and the surrounding oceans, and is driven by the seasonal reversal of winds, which deliver precipitation and cause upwelling along the continental margin (Thamban et al., 2007). Low seasonal insolation and high albedo characterise the winter monsoon, and result in the production of a high pressure cell over South Asia, creating northeasterly winds over the Arabian Sea (e.g. Clemens et al., 1996). These winds are weak and dry, travelling over land to the ocean. The summer monsoon occurs due to the differential heating of the continental and oceanic regions, which results in the production of a low pressure system over the northern and central Indian sub-continent (Thamban et al., 2007), and winds originating from the Bay of Bengal move to deliver precipitation over the

subcontinent. The delivery of monsoon precipitation varies spatially, depending on atmospheric circulation patterns (Singhvi et al., 2010a) and temporal and spatial variations in modern mean precipitation values of ±30% are usual (Singhvi and Kale, 2009).

The monsoon system is driven by the differential heating of the Asian continent and the surrounding Indian and Pacific Oceans, and the Asian Monsoon would have been a feature of the regional climate system over tectonic timescales (Clift and Plumb, 2008). The intensity of this system prior to the formation of the Himalaya would have been less strong over these longer timescales (Wang, 2004), due to the higher sea levels and relatively lower land mass, which would have resulted in a reduction in the temperature differential and a less intense monsoon system. The construction of the modern Asian landscape was caused by the collision of the Asian and Indian continental plates, which resulted in the uplift of the Himalaya and the creation of the Tibetan plateau. This occurred during the Cenozoic, possibly around 45 – 50 Ma (Rowley, 1996), but no later than 35 Ma (Ali and Aitchison, 2005). The uplift of the Tibetan plateau resulted in the intensification of the Asian Monsoon system (e.g. Raymo et al., 1988; Raymo and Ruddiman, 1992) and Prell and Kutzbach (1992) recognised that uplift of the Tibetan plateau had the potential to disrupt local, regional and possibly even global atmospheric circulation. The initial intensification of the Asian Monsoon system is dated to ~24 – 22 Ma (Clift, 2006).

2.3.1 Monsoon intensity during the late Quaternary

Clift and Plumb (2008) state that the Asian Monsoon varies not only over tectonic timescales (10^6 – 10^7 years), but over millennial and shorter timescales as well. Liu et al. (2006) comment that insolation change related to orbital forcing (e.g. Milankovitch cycles) plays a primary role in driving periodic monsoon variability. The Asian Monsoon has been shown to have varied greatly in intensity during the Quaternary (Van Campo et al., 1982; Clemens et al., 1991; Sirocko et al., 1993), and both geological and modelling studies have shown that this variability occurs in response to insolation (Ruddiman, 2001). Prell (1984) was one of the first

researchers to investigate the impact of orbital forcing on the summer monsoon system, using the abundance of planktonic foraminifera from an ocean core in the Arabian Sea as a proxy for upwelling driven by variability in the winds of the summer monsoon. Clemens and Prell (2003) also investigated the link between orbital forcing and monsoonal variability during the late Quaternary using physical, chemical, isotopic and biological proxies, finding a link between fluctuations in oceanographic and atmospheric systems and insolation. The link between the East Asian Monsoon and insolation has also been established using Chinese Loess records (e.g. Liu et al., 1999), palynological records from oceanic cores (Morley and Heusser, 1997) and marine geochemical proxies (e.g. Wehausen and Brumsack, 2002). It is now accepted that orbital forcing is the primary factor driving variability in the monsoon system during the late Quaternary.

The Asian Monsoon is linearly responsive to the obliquity (41 ka) and precession (23 ka) components of orbital forcing, albeit with a lag (Prell, 1984; Clemens et al., 1991; Imbrie et al., 1992; Clemens et al., 1996). To some degree, monsoon intensity is sensitive to the extent of northern hemispheric glaciation, although the exact nature of this link has yet to be established (e.g. Liu et al., 2006). Over the past 350 ka, peak monsoon strength has been found to occur slightly after maximum precession, and there is a near-simultaneous response of the monsoon to obliquity maxima (e.g. Berger et al., 2010). Clemens and Prell (2003) suggest that whilst insolation maxima is one of the key factors in monsoon intensity, the latent heat export from the ocean system also needs to be considered, and that this may explain the observed lag. Despite a slight delay in the response of the monsoon system to variability in the amount of insolation received, there is a clear relationship between monsoon intensity and orbital forcing. As a region dominated by the Asian Monsoon, the climate of Pakistan during the late Quaternary would have been highly sensitive to changes in orbital forcing.

2.3.2 The Asian Monsoon during the Holocene

During the early Holocene insolation was at a peak and glacial boundary conditions were at a minimum, resulting in a period of strengthened monsoon, and therefore increased precipitation in the Indian sub-continent region (e.g. Clemens et al., 1991; Sirocko et al., 1993; 2000; Overpeck et al., 1996; Thamban et al., 2002). Peak summer monsoon activity is observed between 9.5 – 5.5 ka according to Sirocko et al. (1993) and Overpeck et al. (1996), who analysed marine records from the Arabian Sea. Throughout the mid and late Holocene, insolation decreases (e.g. Berger and Loutre, 1991; 1999), and the summer monsoon becomes less intense, culminating in an arid phase at ~4 ka, which is seen in both terrestrial and marine records (e.g. Overpeck et al., 1996; Gupta et al., 2003; Fleitmann et al., 2003; Staubwasser et al., 2003; Wang et al., 2005). Insolation continues to decrease throughout the mid and late Holocene, resulting in a period of regional aridity in the Indian subcontinent (e.g. Clift and Plumb, 2008). The relationship between insolation and monsoon intensity during the Holocene can be clearly seen in figure 2.6, where the northern hemisphere insolation record of Berger and Loutre (1999) and the $\delta^{18}O$ record from the Dongge Cave speleothem, which is used as a proxy for palaeoprecipitation, and hence monsoon intensity (Wang et al., 2005), are plotted. The trend for decreasing insolation from ~9 ka is mirrored in the palaeoprecipitation record, with a decrease in $\delta^{18}O$ values observed until the late Holocene.

Superimposed onto the trend of decreasing insolation throughout the Holocene, multi-decadal to centennial scale, high magnitude oscillations can be observed in many proxy records of monsoon intensity (e.g. figure 2.6). These records include marine sediments from the Arabian sea (Sirocko et al., 1993; Schulz et al., 1998; Gupta et al., 2003), cave deposits from Oman (Fleitmann et al., 2003), deltaic sediments in the Indus Basin (Staubwasser et al., 2003) and the Bay of Bengal (Kudrass et al., 2001) and cave speleothem records (Wang et al., 2005; figure 2.6). Gupta et al. (2003; 2005) and Wang et al. (2005) suggest that these abrupt fluctuations relate to North Atlantic climate, and particularly Bond events (e.g. Bond et al., 1997; figure 2.6). This implies that North Atlantic ice rafting events may lead

to a reorganisation of the thermohaline circulation, which in turn results in a change in temperature and moisture gradient in the Indian Ocean (e.g. Hong et al., 2003). Bond events are plotted in figure 2.6 and high-magnitude fluctuations in monsoon intensity do appear to coincide with some events (e.g. 2.8 ka, 4.2 ka, 8.2 ka), suggesting that a teleconnection between the monsoon system and northern hemispheric ice-rafting events may exist. Other authors have suggested that variations in solar activity over shorter timescales may be responsible for variability in the amplitude of the summer monsoon (Neff et al., 2001; Fleitmann et al., 2003). There is also a link between monsoon intensity and the El Niño Southern Oscillation (ENSO) during the Holocene (e.g. Shukla and Paolina, 1983; Webster et al., 1998), with ENSO forcing changes in Pacific sea surface temperatures. Variability in the monsoon in response to ENSO is not straightforward, and appears to not only be affected by the magnitude of the ENSO event, but also the timing (Zhang et al., 1996).

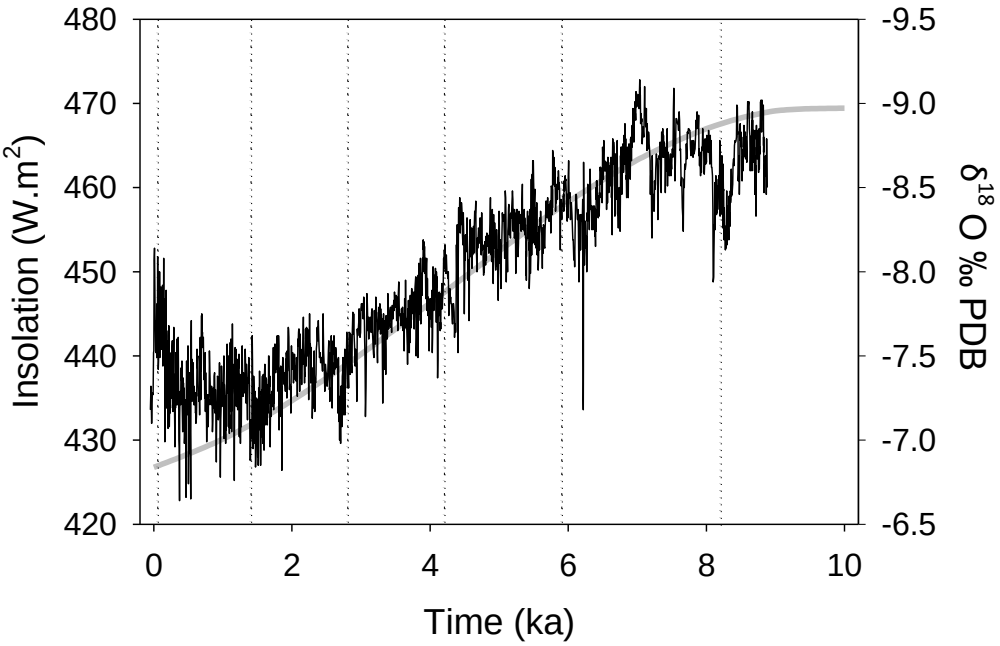

Figure 2.6: Comparison of the $\delta^{18}O$ record from Dongge Cave, a proxy for the Asian Monsoon (Wang et al., 2005), shown by the black line and the summer insolation record (during June at 30°N) of Berger and Loutre (1999) (solid grey line). North Atlantic Bond events (Bond et al., 1997) are marked by the dotted lines.

Despite the view that climate during the Holocene has been relatively stable, the palaeoprecipitation record of Wang et al. (2005), shown in figure 2.6, suggests that high frequency and magnitude variability in the Asian Monsoon is characteristic of

the epoch. As the dominant control on the climate of the Asian sub-continent, the fluvial and biological systems in the region would have been extremely sensitive to variability in the monsoon system. As complex societies were developing in Asia throughout the early and mid Holocene, they would have been impacted by water availability and the weakening of the Asian Monsoon (Clift and Plumb, 2008).

2.4 The Ghaggar-Hakra Palaeochannel

The geologist R.D. Oldham was the first researcher to record evidence for a 'lost river' in the Cholistan Desert (Sinha et al., in press), describing a dry river bed which was kilometres wide, which previously flowed through the now arid region of northwest India and east Pakistan (Oldham, 1886). This palaeochannel is clearly visible in satellite imagery (figure 2.7), flowing through the Indian state of Haryana and into the Pakistani state of Punjab. Mark Aurel Stein was the first to survey the archaeological remains along the palaeochannel, connecting the dense concentration of sites in Punjab to the mega-cities of the Mature Harappan Civilisation (Stein, 1942). Since the development of the radiocarbon dating technique in the 1950s, the archaeology along the Ghaggar-Hakra has been well dated, and sites are predominantly connected with the Early, Mature and Late Harappan phases (figure 1.3; section 1.3) (e.g. Mughal, 1997; Possehl, 2002; Gangal et al., 2010; Giosan et al., 2012). However, a chronology of fluvial activity in the Ghaggar-Hakra in Pakistan has not yet been confirmed (Wright, 2010), and therefore hypotheses linking the collapse of the Harappan in Punjab to a change in the fluvial system of the Ghaggar-Hakra remain speculative.

The presence of the dense concentration of sites has led many authors to suggest that a fluvial system supported the predominantly riverine Mature Harappan civilisation (Giosan et al., 2012) and this hypothesis has been discussed intensively in the literature (e.g. Stein, 1942; Wilhelmy, 1969; Gupta, 1996; Mughal, 1997; Chakrabarti and Saini, 2009; Gangal et al., 2010; Giosan et al., 2012). The Mature Harappan flourished against a backdrop of the mid-Holocene weakening of the Asian Monsoon system (section 2.3.2), and many workers have suggested that a

gradual recession and ultimate cessation of flow in this palaeochannel contributed to the collapse of the Mature Harappan civilisation at ~1900 BC. That climatic variability was a key factor in the collapse of the Mature Harappan has been proposed by researchers including Stein (1942), Singh (1971), Singh et al. (1974), Mughal (1997), Lal et al. (2003), and Staubwasser et al. (2003). However Sinha et al. (in press) state that these ideas remain speculative and have been contested widely in the literature (e.g. Agrawal, 1964; Wilhelmy, 1969; Misra, 1984; Kenoyer, 1998; Possehl, 2002; Madella and Fuller, 2006).

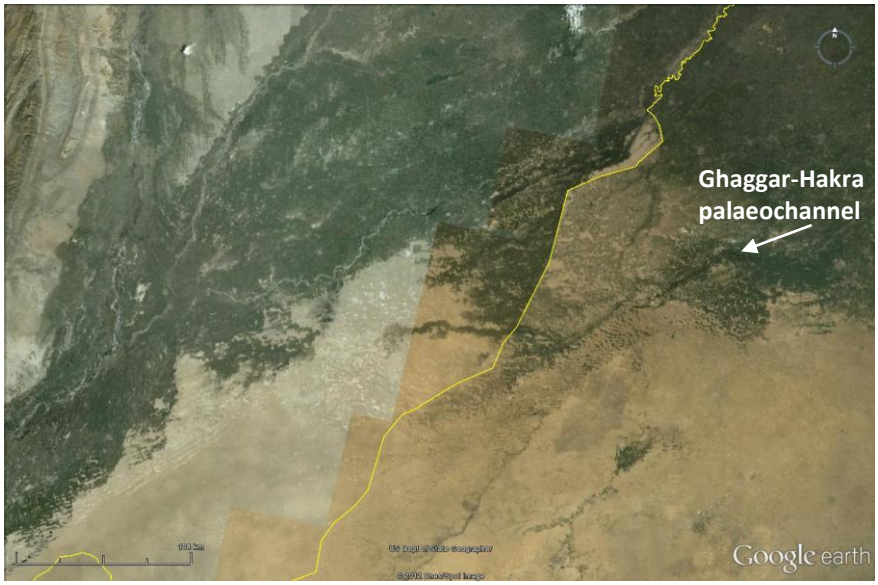

Figure 2.7: Satellite image of the Ghaggar-Hakra palaeochannel around the Pakistan-India border (solid yellow line). The satellite image is from Google earth.

2.4.1 Settlement along the Ghaggar-Hakra palaeochannel

Whilst the major urban cities of the Harappan (such as Mohenjo-Daro and Harappa) were located along the course of the Indus and its larger tributaries (Giosan et al., 2012), the area around the hypothesised former course of the Ghaggar-Hakra palaeochannel contains one of the densest concentrations of Mature Harappan sites in the region (e.g. figure 1.12). It is generally believed that this palaeochannel supported some of the major sites in what has been termed the 'bread-basket of the Mature Harappan (Possehl, 1997), and sites along the palaeochannel are predominantly associated with industry and craft (Mughal, 1990; Mughal, 1997). Archaeologist M.R. Mughal carried out extensive excavations and investigations in

the Cholistan Desert and reports 169 Mature Harappan sites and 50 Late Harappan sites in the region (Mughal, 1997), and these sites have been plotted in figure 1.3. Whilst subsequent research has revealed higher numbers of both Mature and Late Harappan sites along the palaeochannel (e.g. Gangal et al., 2010; figure 1.11; figure 1.12), Mughal's surveys remain the most detailed studies to date, providing information on the site use. It is likely that the key trends in land use and relative numbers of sites has been captured by Mughal's surveys (e.g. Possehl, 2002) and this is why this data is presented here in preference to more recent research. During the Mature Harappan phase, the majority of sites are associated with industry, with very few sites used as settlements (figure 2.8a). During the Late Harappan phase, far fewer sites have been recovered, and in comparison with the Mature Harappan, relatively few sites are used for industry. More common are camp sites and kilns for local use (Mughal, 1997; figure 2.8b), and these sites were multi-purpose, indicative of a less complex social set-up. This change in land use and population density in the area has been interpreted as evidence for a reduction in the availability of water, causing upstream migration of the Late Harappan (figure 1.12; section 1.4.1).

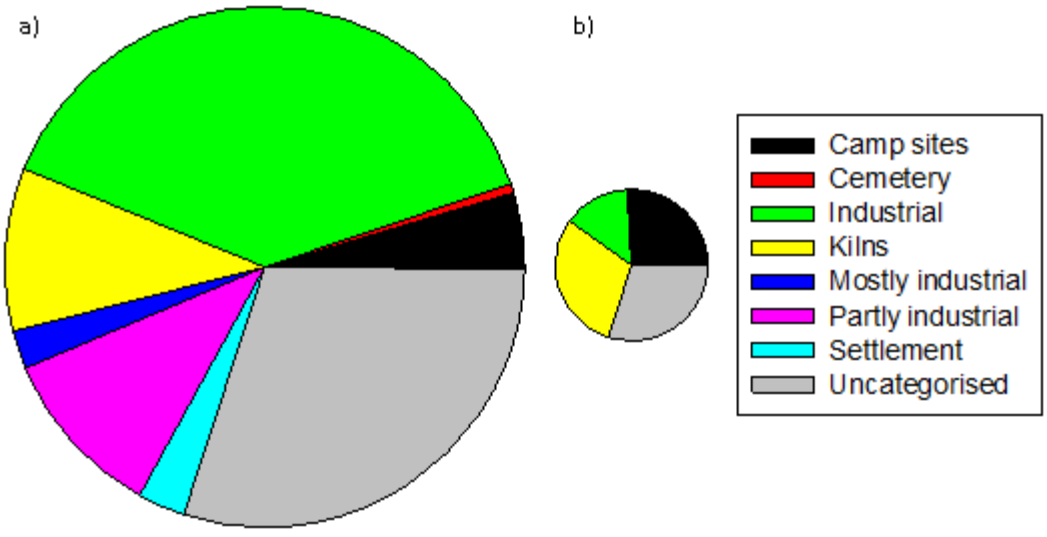

Figure 2.8: Pie charts for the types of sites surveyed by Mughal (1997) in the Cholistan Desert region from the a) Mature Harappan and b) Late Harappan phases. The size of the pie chart relates to the number of sites recorded.

2.4.2 Studies of the Ghaggar-Hakra palaeochannel

Investigations into the hydrological changes of the Ghaggar-Hakra have been ongoing for over a century (Mughal, 1997). In terms of the archaeological evidence, the Ghaggar-Hakra floodplain was densely populated during the Harappan phase, and agricultural yield in the region must have been reliable enough to support the mega-city Ganiwerala to the south of Fort Derawar, and the numerous sites along the channel itself (Mughal, 1997). Stein (1942) pointed out that relatively few sites are found by the widest part of the palaeochannel, between Fort Abbas and Fort Marot, and he interprets this as evidence for high energy perennial flow in this section of the channel during the Harappan phase. As discussed in section 1.4.1, the Mature Harappan collapse (or undergo a transformation) at approximately 1900 BC, and settlements from the Late Harappan are smaller in size and migration upstream into India is observed (e.g. Gangal et al., 2010). Many workers have suggested that hydrographic changes meant that fluvial activity in the Ghaggar-Hakra was significantly reduced or cut off at the time of the Mature Harappan collapse, and this change resulted in the upstream migration of the Late Harappan in search of more reliable (and perennial) water sources (e.g. Enzel et al., 1999).

Previous studies of the Ghaggar-Hakra palaeochannel have been concerned with mapping the former course of the channel and trying to reconstruct past hydrological conditions. Stein (1942) mapped the channel between Kalibangan in India and Fort Derawar in Pakistan based on fieldwork, suggesting the channel terminated as an inland delta south of Fort Derawar, and hypothesised that the Sutlej River fed the Ghaggar-Hakra system through at least one anabranch. Wilhelmy (1969) also mapped the channel, proposing that the uppermost tributaries of this system originated in the Siwalik Hills, with multiple braided channels through India before flowing through the Cholistan desert, through Fort Abbas, Fort Marot and Fort Derawar before connecting with the Nara channel, adjacent to the Indus River in Sindh. Using LANDSAT satellite imagery, Ghose et al. (1979) map the former Ghaggar-Hakra (which they refer to as the Saraswati) (figure 2.9). Like Wilhelmy (1969), Ghose et al. (1979) map a system which has its source in

the Himalaya, suggesting a glacier-fed system. They also suggest that the Ghaggar-Hakra connected to the Indus Delta through the Nara channel in Sindh (figure 2.9a), but also by connecting with the Luni River in India (figure 2.9b). Many studies since (e.g. Yash Pal et al., 1980; Sood and Sahai, 1983; Sahai, 1999; Radhakrishna and Merh, 1999; Gupta et al., 2004) have plotted the course of the Ghaggar-Hakra on the basis of satellite imagery, although corroboration of this type of mapping with field-based investigation has rarely been undertaken.

Whilst the Ghaggar-Hakra has been studied intensively over the past century, the majority of the palaeohydrological features suggested cannot be substantiated due to a lack of geomorphological and sedimentological investigation (Saini and Mujtaba, 2010). More crucially, a chronology of fluvial activity in the Ghaggar-Hakra in Pakistan has not been developed, and therefore, whether hydrological changes were a factor in the collapse of the Mature Harappan cannot be tested. The section of the palaeochannel between Fort Abbas and Fort Derawar is the most consistently mapped part of the Ghaggar-Hakra palaeochannel in the remote sensing studies, and it is also the region in which marked archaeological change has been documented. For these reasons, this section of the palaeochannel was selected for study and to address the project research aim (section 1.1.1).

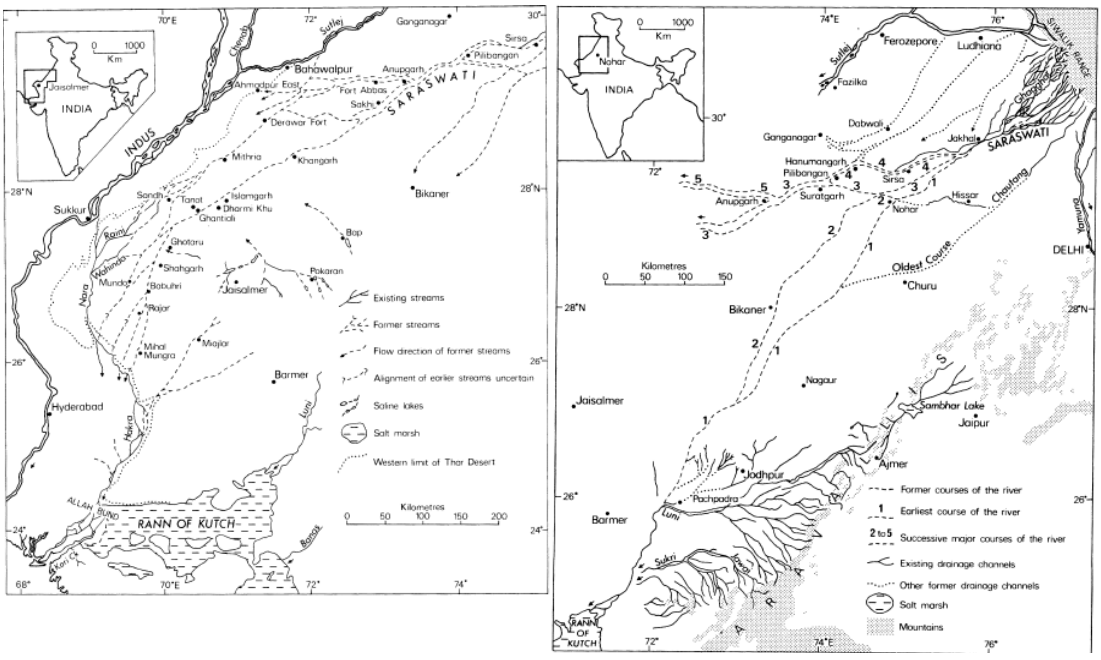

Figure 2.9: Former course of the Ghaggar-Hakra (referred to as the Saraswati in this figure), mapped using LANDSAT satellite imagery by Ghose et al. (1979).

2.5 Field sites and samples

The Ghaggar-Hakra palaeochannel is clearly visible in satellite imagery (e.g. figure 2.7) and is associated with a dense concentration of archaeological sites associated with the Mature and Late Harappan (section 1.4.1). The presence of this palaeochannel in the environment suggests wetter conditions in the past than at present and fieldwork to this region was undertaken with the principle aim of establishing a geochronology of presumed Holocene age river channels and dune deposits. To achieve this aim, two objectives were established for fieldwork. The first was to improve the understanding of Holocene river and dune development in the area, and the second, to sample fluvial and aeolian deposits for optically stimulated (OSL) dating and where available, radiocarbon (^{14}C) dating, to develop a regional chronology of fluvial dynamics.

2.5.1 Sampling strategy and collection

A firm chronology of past fluvial activity does not exist for the Ghaggar-Hakra palaeochannel (Wright, 2010) and it is the primary research aim of this project to address this (section 1.1.1). Therefore, this palaeochannel and the surrounding area was the focus during fieldwork, with the aim of identifying sites with evidence of deposition by fluvial processes, and where possible, the transition between deposition by fluvial and aeolian processes. At these sites, the sediment stratigraphy was investigated and logged (appendix A) and the sediments were sampled for OSL and ^{14}C dating. The availability of organic material for ^{14}C dating was limited, but where found, was sampled to provide independent age control to compare with the OSL ages. In total, twelve sites were sampled for OSL and ^{14}C dating and the location of these sites are shown in figure 2.10 and detailed in table 2.1. These sites were sampled along two transects, the Ghaggar-Hakra and the Sutlej anabranch transects, and sites along these transects are discussed in further detail in sections 2.6 and 2.7 respectively.

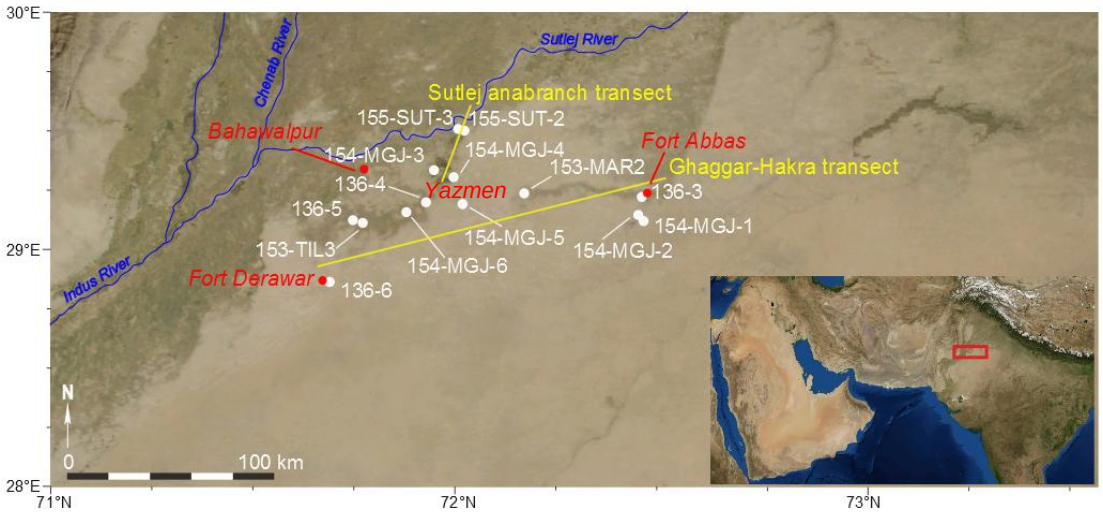

Figure 2.10: Field sites in the Bahawalpur region of the Punjab, Pakistan, and inset, the location of the field area in relation to the Near and Middle East. Satellite images from NASA World Wind 1.4.

2.5.1.1 Sampling for OSL dating

The majority of samples for OSL dating were taken using 25 cm lengths of opaque, plastic drainpipe. The tubes were stuffed with newspaper at one end before being hammered into the sediment unit (figure 2.11). Once packed with sediment, the tubes were carefully removed and the other end was filled with newspaper to ensure that sediment mixing did not occur during transportation or storage, which could result in the mixing of light exposed grains into the sample. At Fort Abbas (153-MAR2-5B) and Yazmen (153-TIL3-2), sediments were cored to a depth of approximately 40 m at two locations (sections 2.6.1 and 2.6.2; appendix A). Clear, plastic core liners were used during coring and the sediment cores were transported and stored in these liners in light conditions until they were sampled for OSL dating. To sample them, sections of the core containing sandy units were removed and light-exposed sediments from the section ends were removed. Sediment from the centre of the core which had not been exposed to light was then excavated and prepared for dating, leaving the light-exposed layer in contact with the core liner intact.

Table 2.1: Samples taken and presented in this study for OSL and ^{14}C dating. Samples are ordered according to sample name and depth and are referred to in the text by sample name.

Site Name	Sample Name[a]	Depositional Environment	Sample Material	Depth (m)	Altitude (m asl)	Latitude (dd, mm, ss)	Longitude (dd, mm, ss)
Optically stimulated luminescence dating							
Fort Abbas	136-3-1	Fluvial	Coarse grain sand	2.22	148	29° 11' 24.54"	72° 52' 54.54"
Fort Abbas	136-3-4	Fluvial	Coarse grain sand	3.07	148	29° 11' 24.54"	72° 52' 54.54"
Fort Abbas	136-3-9	Fluvial	Coarse grain sand	3.99	148	29° 11' 24.54"	72° 52' 54.54"
Alkasur Cotton Jinner	136-4-1	Fluvial	Coarse grain sand	2.32	121	29° 09' 54.42"	71° 51' 19.50"
Alkasur Cotton Jinner	136-4-2	Fluvial	Coarse grain sand	3.91	121	29° 09' 54.42"	71° 51' 19.50"
Basti	136-5-1	Fluvial	Coarse grain sand	2.27	116	29° 05' 42.29"	71° 34' 03.50"
Basti	136-5-3	Fluvial	Coarse grain sand	2.70	116	29° 05' 42.29"	71° 34' 03.50"
Basti	136-5-6	Fluvial	Coarse grain sand	3.87	116	29° 05' 42.29"	71° 34' 03.50"
Fort Derawar	136-6-1	Fluvial	Coarse grain sand	2.08	104	28° 45' 50.40"	71° 20' 06.40"
Fort Derawar	136-6-2	Fluvial	Coarse grain sand	2.33	104	28° 45' 50.40"	71° 20' 06.40"
Fort Derawar	136-6-3	Fluvial	Coarse grain sand	2.60	104	28° 45' 50.40"	71° 20' 06.40"
Fort Derawar	136-6-5	Fluvial	Coarse grain sand	3.08	104	28° 45' 50.40"	71° 20' 06.40"
Fort Derawar	136-6-6	Fluvial	Coarse grain sand	3.42	104	28° 45' 50.40"	71° 20' 06.40"
Fort Derawar	136-6-7	Fluvial	Coarse grain sand	3.81	104	28° 45' 50.40"	71° 20' 06.40"
Marot Core	153-MAR2-5B	Fluvial	Coarse grain sand	10.88	134	29° 12' 48.96"	72° 20' 28.50"
Marot Core	153-MAR2-13B	Fluvial	Coarse grain sand	34.42	134	29° 12' 48.96"	72° 20' 28.50"
Tilwalla Core	153-TIL3-2	Fluvial	Coarse grain sand	3.76	111	29° 05' 44.64"	71° 34' 05.46"
Tilwalla Core	153-TIL3-8B	Fluvial	Coarse grain sand	17.16	111	29° 05' 44.64"	71° 34' 05.46"
Tilwalla Core	153-TIL3-10A	Fluvial	Coarse grain sand	21.02	111	29° 05' 44.64"	71° 34' 05.46"

Site Name	Sample Name[a]	Depositional Environment	Sample Material	Depth (m)	Altitude (m asl)	Latitude	Longitude
Tilwalla Core	153-TIL3-18	Fluvial	Coarse grain sand	44.68	111	29° 05' 44.64"	71° 34' 05.46"
Fort Abbas	154-MGJ-1-1	Fluvial	Coarse grain sand	0.67	146	29° 06' 27.00"	72° 54' 32.52"
Fort Abbas	154-MGJ-1-2	Fluvial	Coarse grain sand	1.00	146	29° 06' 27.00"	72° 54' 32.52"
Fort Abbas	154-MGJ-1-3	Fluvial	Coarse grain sand	1.29	146	29° 06' 27.00"	72° 54' 32.52"
Fort Abbas	154-MGJ-1-4	Fluvial	Coarse grain sand	1.57	146	29° 06' 27.00"	72° 54' 32.52"
Fort Abbas	154-MGJ-1-5	Fluvial	Coarse grain sand	1.79	146	29° 06' 27.00"	72° 54' 32.52"
Fort Abbas	154-MGJ-1-6	Fluvial	Coarse grain sand	2.16	146	29° 06' 27.00"	72° 54' 32.52"
Fort Abbas	154-MGJ-1-7	Fluvial	Coarse grain sand	2.54	146	29° 06' 27.00"	72° 54' 32.52"
Fort Abbas	154-MGJ-1-8	Fluvial	Coarse grain sand	2.90	146	29° 06' 27.00"	72° 54' 32.52"
Fort Abbas	154-MGJ-2-1	Fluvial	Coarse grain sand	0.30	147	29° 06' 00.54"	72° 54' 33.36"
Fort Abbas	154-MGJ-2-2	Fluvial	Coarse grain sand	1.00	147	29° 06' 00.54"	72° 54' 33.36"
Fort Abbas	154-MGJ-2-3	Fluvial	Coarse grain sand	2.00	147	29° 06' 00.54"	72° 54' 33.36"
Fort Abbas	154-MGJ-2-4	Fluvial	Coarse grain sand	2.50	147	29° 06' 00.54"	72° 54' 33.36"
Fort Abbas	154-MGJ-2-5	Fluvial	Coarse grain sand	3.25	147	29° 06' 00.54"	72° 54' 33.36"
Lal Suhanrai dune	154-MGJ-3-1	Aeolian	Coarse grain sand	0	122	29° 24' 29.00"	71° 57' 59.30"
Lal Suhanrai dune	154-MGJ-3-2	Aeolian	Coarse grain sand	100	122	29° 24' 29.00"	71° 57' 59.30"
Lal Suhanrai dune	154-MGJ-3-3	Aeolian	Coarse grain sand	220	122	29° 24' 29.00"	71° 57' 59.30"
Lal Suhanrai dune	154-MGJ-3-4	Aeolian	Coarse grain sand	305	122	29° 24' 29.00"	71° 57' 59.30"
Lal Suhanrai dune	154-MGJ-3-5	Aeolian	Coarse grain sand	425	122	29° 24' 29.00"	71° 57' 59.30"
Lal Suhanrai dune	154-MGJ-3-6	Aeolian	Coarse grain sand	540	122	29° 24' 29.00"	71° 57' 59.30"

Site Name	Sample Name[a]	Depositional Environment	Sample Material	Depth (m)	Altitude (m asl)	Latitude	Longitude
Lal Suhanrai forest	154-MGJ-4-2	Fluvial/Pluvial	Coarse grain sand	1.37	121	29° 15' 50.10"	71° 54' 19.39"
Lal Suhanrai forest	154-MGJ-4-4	Fluvial/Pluvial	Coarse grain sand	1.66	121	29° 15' 50.10"	71° 54' 19.39"
Lal Suhanrai forest	154-MGJ-4-5	Fluvial/Pluvial	Coarse grain sand	2.10	121	29° 15' 50.10"	71° 54' 19.39"
Yazmen Road	154-MGJ-5-1	Aeolian	Coarse grain sand	0.40	123	29° 10' 04.90"	72° 01' 08.90"
Yazmen Road	154-MGJ-5-1B	Aeolian	Coarse grain sand	0.40	123	29° 10' 04.90"	72° 01' 08.90"
Yazmen Road	154-MGJ-5-1	Aeolian	Coarse grain sand	0.40	123	29° 10' 04.90"	72° 01' 08.90"
Yazmen Road	154-MGJ-5-2	Aeolian	Coarse grain sand	0.85	123	29° 10' 04.90"	72° 01' 08.90"
Yazmen Road	154-MGJ-5-3	Aeolian	Coarse grain sand	1.43	123	29° 10' 04.90"	72° 01' 08.90"
Yazmen Road	154-MGJ-5-4	Aeolian	Coarse grain sand	1.83	123	29° 10' 04.90"	72° 01' 08.90"
Yazmen Road	154-MGJ-5-5	Aeolian	Coarse grain sand	2.55	123	29° 10' 04.90"	72° 01' 08.90"
Yazmen brick pit	154-MGJ-6-2	Fluvial	Coarse grain sand	0.95	118	29° 07' 20.90"	71° 46' 16.60"
Yazmen brick pit	154-MGJ-6-3	Fluvial	Coarse grain sand	1.25	118	29° 07' 20.90"	71° 46' 16.60"
Sutlej overbank	155-SUT-2-1	Fluvial	Coarse grain sand	2.20	126	29° 28' 54.90"	72° 02' 03.00"
Sutlej overbank	155-SUT-3-1	Fluvial	Coarse grain sand	6.30	125	29° 28' 55.86"	72° 01' 43.80"
Radiocarbon dating							
Fort Abbas (136-3)		Channel infill	Gastropod	3.45	148	29° 11' 24.54"	72° 52' 54.54"
Alkasur Cotton Jinner (136-4)		Channel infill	Gastropod	3.81	121	29° 09' 54.42"	71° 51' 19.50"
Basti (136-5)		Channel infill	Gastropod	0.75	116	29° 05' 42.29"	71° 34' 03.50"
Basti (136-5)		Channel infill	Gastropod	2.65	116	29° 05' 42.29"	71° 34' 03.50"

Site Name	Sample Name[a]	Depositional Environment	Sample Material	Depth (m)	Altitude (m asl)	Latitude	Longitude
Tilwalla Core (153-TIL3)		Channel infill	Plant/wood	43.7	111	29° 05' 44.64"	71° 34' 05.46"
Fort Abbas (154-MGJ-1)		Channel infill	Gastropod	2.59	146	29° 06' 27.00"	72° 54' 32.52"
Fort Abbas (154-MGJ-1)		Channel infill	Gastropod	2.96	146	29° 06' 27.00"	72° 54' 32.52"
Yazmen Road (154-MGJ-5)		Channel infill	Plant/wood	1.10	123	29° 10' 04.90"	72° 01' 08.90"
Yazmen Road (154-MGJ-5)		Channel infill	Plant/wood	1.40	123	29° 10' 04.90"	72° 01' 08.90"
Yazmen brick pit (154-MGJ-6)		Channel infill	Gastropod	2.70	118	29° 07' 20.90"	71° 46' 16.60"
Yazmen brick pit (154-MGJ-6)		Channel infill	Gastropod	3.20	118	29° 07' 20.90"	71° 46' 16.60"

[a] Radiocarbon dates were prepared and measured by Dr Liviu Giosan and are referred to in this study by site name and depth.

2.5.1.2 Sampling for ^{14}C dating

A small number of samples were collected for ^{14}C dating (table 2.1), where sufficient biomass for dating was present. Gastropod and plant/wood remains were transferred directly from the section into sampling bags using a trowel to minimise the possibility of contamination with modern carbon. All samples were prepared and measured by Dr Liviu Giosan at the National Ocean Sciences Accelerator Mass Spectrometry Facility (NOSAMS) at the Woods Hole Oceanographic Institution, Massachusetts. Details of the preparation and measurement protocols are published on the NOSAMS (2012) website.

Figure 2.11: Sampling for OSL dating. a) Hammering the sampling tube into the sediment at 154-MGJ-1 and b) sampling tubes before removal from the section at 154-MGJ-4. Both photos taken by Julie Durcan.

2.5.1.3 Sedimentological interpretation

Prior to sampling for dating, the sedimentology at each site was studied to inform the best sampling strategy for dating. At each site, the section was cleaned and the major sedimentological units were logged (appendix A) and categorised into sediments deposited by fluvial or aeolian processes. Fluvial sediments were typically fine in nature (usually fine sands or silts) and contained features such as rip up clasts or horizontal bedding structures. Aeolian sediments were generally slightly coarser in nature, and were deposited as massive units or had cross bedding structures preserved.

2.6 The Ghaggar-Hakra transect

The Ghaggar-Hakra transect measures approximately 175 km, from the Pakistan-India border to Fort Derawar (figure 2.10) and was sampled to follow the former course of the Ghaggar-Hakra channel, identified in satellite imagery (figure 2.7). The transect was sampled to reconstruct fluvial activity in the channel and to help ascertain how migration of archaeological sites may have been linked to changes in fluvial activity. In total, nine sites along this transect were selected for sampling, and the majority of sediments sampled are inferred to have been deposited by fluvial processes. Samples were predominantly taken for OSL dating at these sites (table 2.1), although organic material suitable for ^{14}C dating was found at seven of these sites and eleven samples were taken (table 2.1). These sites are described in more detail in the following sections, where the sites are described in three groups; Fort Abbas, Yazmen and Fort Derawar. The sites at the most easterly extreme of the transect are described first, progressing to the most westerly sites, following the direction of flow along the channel.

2.6.1 Fort Abbas

Three sites, 154-MGJ-1, 154-MGJ-2 and 136-3, were sampled close to the Pakistan-India border, close to the town of Fort Abbas (figure 2.10). This area represents the most eastern part of the Ghaggar-Hakra palaeochannel in Pakistan and was targeted to determine when this part of the channel was active during the Holocene. Painted Grey Wares sites (1500 – 1100 BC) have been found within the former course of this channel in this area (Mughal, 1997; figure 1.3), indicating that this part of the tributary was not active between at least 3.5 – 3.1 ka. Gangal et al. (2010) observe the migration of sites along this channel prior to 3.5 ka (figure 1.12) and therefore understanding the timing of change in the fluvial activity in this part of the channel is important for understanding how changes in water availability may have impacted the change in population dynamics observed.

In the Fort Abbas area, two possible distributaries of the Ghaggar-Hakra diverge (figure 2.10), one of which crosses the Pakistan-India border and continues almost due west and the other continues in a south-westerly direction on the Indian side of the border. The sites 154-MGJ-1 and 154-MGJ-2 were chosen to evaluate whether there had been flow in either of these channel belts during the Holocene. Inspection of satellite imagery shows a high sinuosity channel containing sandy bars and small islands within a larger depression and one of the channels within this depression was sampled as the 154-MGJ-1 site. A pit was dug to a depth of approximately 3.5 m (figure 2.12b), and the sediment stratigraphy was analysed and is shown in figure 2.13. At this site, a basal silt is overlain by alternating flat bedded sand units and thin discontinuous silts, some of which have been desiccated, broken up and then incorporated into the overlying sand unit. The top of the sequence is a silt unit similar in character to the one found at the base. This sequence suggests alteration in flow frequency and magnitude, with the sandier units indicative of stronger flows.

Seventy metres to the north of 154-MGJ-1, one of the nearby islands was investigated as site 154-MGJ-2. A 3.8 m pit was dug into the deposit and the stratigraphy at this site was analysed and described (appendix A). The sediment stratigraphy at this site is similar to 154-MGJ-1 (figure 2.12b), and is made up of a thick upper sand unit overlaying silts, and underlain by a lower sand unit with alternating silt units. A clay-silt unit was observed at the bottom of the sequence.

Site 136-3 at Marot town provides further lateral coverage of the northern branch of the Ghaggar-Hakra tributary in the Fort Abbas area. This site was identified as being within the course of the former channel and a digger was used to expose a trench approximately 4 m in depth. The sedimentology was described (appendix A) and consists of two major units. The underlying unit consists of fine to medium fluvial sands, which is overlain by a massive silt, containing fine sand lenses at the base and fining upwards. The section is overlain by dune sands (appendix A). At site 153-MAR2 at Fort Marot a core 40 m in length was taken for sedimentological analysis and sampled for dating. Sampling this site further extends the spatial

coverage of the Ghaggar-Hakra palaeochannel, but also provides a record from the late Pleistocene. The uppermost 12 – 15 m of sediments are predominately silts, but with alternating fine sandy layers, and these are inferred to have been deposited by fluvial processes, in the absence of thicker, well sorted sandy units. The sampling of this core for OSL dating was limited due to the fine nature of sediments, and only two samples were suitable for coarse grain OSL dating from the top 11 m of sediments (table 2.1; appendix A).

Figure 2.12: Photographs of site 154-MGJ-1. a) View of the relationship between the channel deposit (154-MGJ-1) and the island deposit (154-MGJ-2). There is a vertical difference of ~1 m between the two sites, which are 70 m apart (photo taken by Geoff Duller). b) The pit dug to a depth of 3.4 m at 154-MGJ-1 and a view of the sediment stratigraphy detailed in figure 2.13. Photo taken by Julie Durcan.

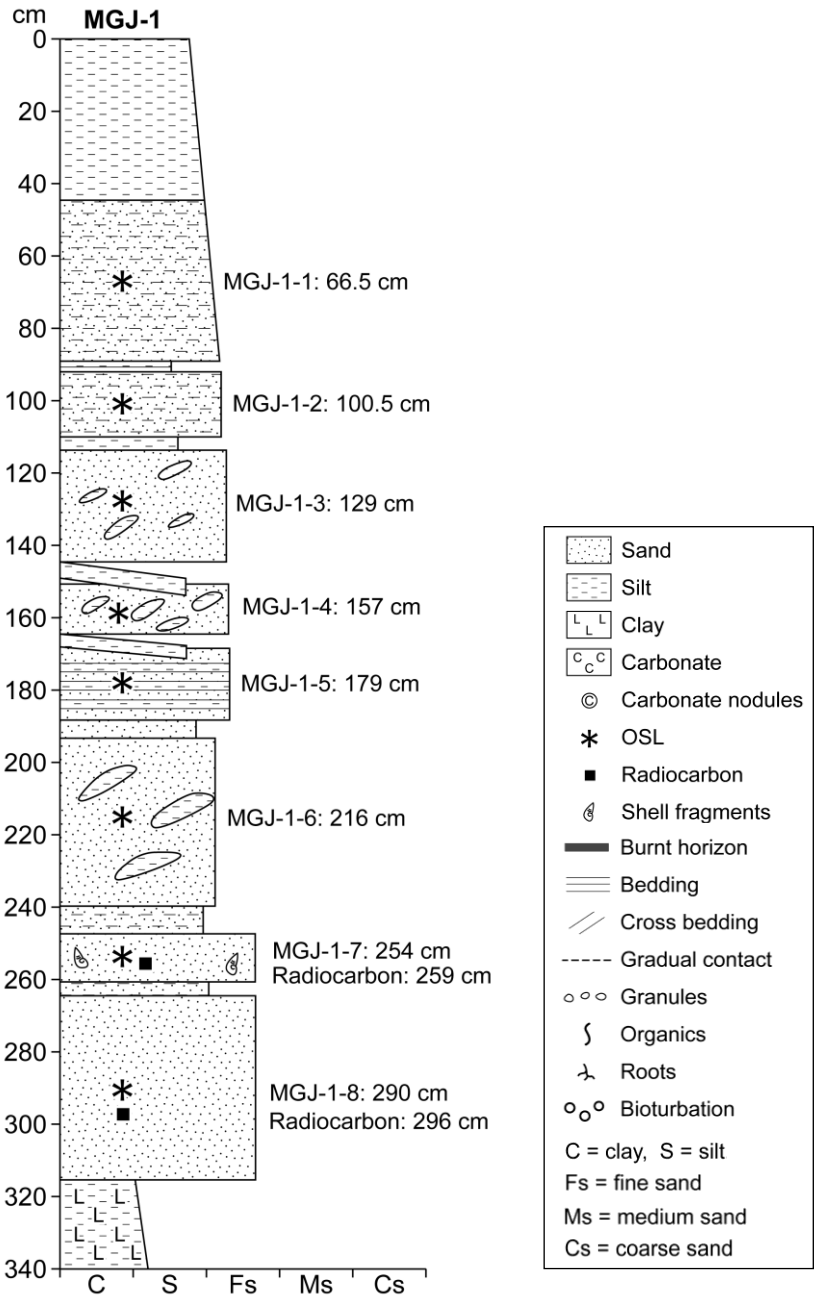

Figure 2.13: Stratigraphic log of site 154-MGJ-1 and the position of samples taken for OSL and ^{14}C dating. Note, not all symbols shown in the legend appear in this log because the legend is applicable to all sites logged (appendix A).

2.6.2 Yazmen

Three sites, 154-MGJ-5, 136-4 and 154-MGJ-6 (figure 2.10), were sampled in the area around the town of Yazmen in the central area of the Ghaggar-Hakra transect. After the abandonment of Mature Harappan age sites, this area is occupied by the Late Harappan, and sampling in the area may help to determine how crucial water availability may have been in the patterns of site migration seen. Sites 136-4 and

154-MGJ-6 are sites where evidence of deposition by fluvial processes is observed, and these sites were selected to further develop the history of fluvial activity along the Ghaggar-Hakra palaeochannel. 154-MGJ-5 is a dune which is part of a larger dune field which crosses the former course of the Ghaggar-Hakra. Therefore, dating at this site may provide a minimum age for the termination of fluvial deposition in this area.

Between the towns of Yazmen and Fort Abbas, a road has been constructed, and was still being built in some places during fieldwork in February 2009. The area between the two towns is flat and uncultivated (figure 2.14a), and contains dunes and a number of red mounds, which are Early, Mature and Late Harappan sites according to Mughal (1997). At site 154-MGJ-5, the road has cut through a dune, leaving an exposure (figure 2.14a) which was sampled for OSL and ^{14}C dating. This site appears to contain records of at least two phases of aeolian activity. The lower unit consists of fine sand and contains deflation surfaces. The upper unit is slightly coarser, fine to medium sand and cross-bedding structures are observed. Both units were sampled for OSL dating to establish the timing of aeolian deposition.

Figure 2.14: a) Dune site 154-MGJ-5. The dune exposure was created during construction of the nearby Yazmen Road and the interdune area is evident in the top right hand area of the photograph. b) Site 154-MGJ-6, where the transition between fluvial and aeolian depositional processes can be observed. Both photos were taken by Julie Durcan.

At Alkasur Cotton Jinner, close to Yazmen town, a site within the former course of the Ghaggar-Hakra was selected for sampling (136-4), which provides further coverage of the Ghaggar-Hakra palaeochannel. This site also appears to be at a

possible confluence between the Ghaggar-Hakra palaeochannel and the Desert Branch canal, which may have been the course of an anabranch of the Sutlej River in the past (section 2.7). Dating at this site may help ascertain whether fluvial activity in the Sutlej anabranch depression contributed to the Ghaggar-Hakra during the Holocene. A JCB digger was used to expose a trench approximately 4 m in depth (appendix A). The sediments at this site mostly consist of clayey-silts interspersed with silt and fine sand lenses, however, two sandy units were observed and sampled for OSL dating. A gastropod was recovered from the base of the unit and sampled for ^{14}C dating.

Site 154-MGJ-6 at Yazmen brick pit is the site at which the cessation of fluvial activity is most clear from the stratigraphy. This site extends the lateral coverage of the Ghaggar-Hakra palaeochannel, but may also provide a date for the cessation of fluvial activity in the central part of the transect. At this site, a section was exposed after excavation of material to supply the nearby brick pit. At the base of this 3.2 m exposure (figure 2.14b), a clay and silt unit are overlain by a unit of fine, fluvial sands (appendix A). An unconformity then separates the fluvial sand unit from a 2 m unit of coarser dune sand (figure 2.14b). This transition from fluvial to aeolian deposition was sampled in order to date the transition from fluvial and aeolian processes. Material for ^{14}C dating was collected from the clay unit at the base of this site (table 2.1).

2.6.3 Fort Derawar

The area around Fort Derawar represents the most western section of the Ghaggar-Hakra transect sampled and is the location of the densest concentration of Mature Harappan sites in the study area. Late Harappan sites have not been found in this area (e.g. Mughal et al., 1997; figure 1.3) and this may be a key region for comparing the fluvial activity in the Ghaggar-Hakra palaeochannel and settlement patterns at the time of the Mature Harappan collapse.

Sites 153-TIL3 and 136-5 were sampled close to the town of Basti (figure 2.10) to provide lateral coverage of the western extent of the Ghaggar-Hakra palaeochannel. Site 153-TIL3 is a core site, where approximately 50 m of sediments have been recovered (appendix A), and provides a depositional history extending into the late Quaternary. As with the core at Marot (section 2.6.1), the uppermost 10 – 15m are predominantly composed of silts with alternating fine sand lenses. The fine nature of the sediments in this core meant that only one sample was taken from the uppermost section of the core, however, a coarsening of sediments can be observed with depth and more samples were taken from greater depths (table 2.1). Site 136-5 is located close to the 153-TIL3 core site and at this site, a JCB digger was used to expose a trench approximately 4 m in depth. At this site, a massive clayey-silt unit is overlain by a number of alterations between silts and sands, suggesting variability in the magnitude of flow over the deposition period. The sandy units in the lower part of this site were sampled for OSL dating.

The Fort Derawar site (136-6) of the Ghaggar-Hakra transect was sampled from an area where a high concentration of Mature Harappan sites have been recorded. At this site, a 4 m deep trench was exposed using a JCB digger and sampled for OSL dating. The stratigraphy of the lower 2 m of sediment at this site indicates deposition by fluvial processes, with a unit of alternating sand and silt layers, and occasional clay laminae (appendix A), and this unit was sampled for OSL dating. The upper 2 m of sediment is finer, with a silt unit containing clay laminae, indicating a reduction in fluvial energy. The high concentration of Mature Harappan sites may indicate that this was the limit of flow during Harappan times, and determining a chronology for fluvial deposition at this site will help inform whether activity is coincident with the flourishing of the Mature Harappan, and also whether a reduction in the magnitude of flow coincides with the timing of the collapse.

2.7 The Sutlej anabranch transect

The Sutlej anabranch transect measures approximately 30 km in length, and consists of three sites sampled from the edge of the terrace which constitutes the

current land surface (figure 2.10). This transect was sampled to follow the course of the Desert branch canal, set in a depression which may have been a former course of the Sutlej River. Some authors (e.g. Mughal, 1997) have suggested that this anabranch was active during ancient times, supplementing the flow in the Ghaggar-Hakra channel and the aim of sampling these sites was to establish whether there was connection between the Sutlej River and the Ghaggar-Hakra palaeochannel during the mid-Holocene. By establishing a chronology for the timing of the most recent fluvial deposition, this hypothesis can be tested. Two samples were taken at the edge of the terrace from exposed sections of a cliff section relating to a former course of the Sutlej River (section 7.2.1) and two sites, one dune and one site of fluvial deposits, were sampled to establish when fluvial processes were last active in the depression. No organic material suitable for ^{14}C dating was recovered at any of the four sites.

2.7.1 Sutlej overbank

At the northern end of the Sutlej transect lies a cliff exposed by lateral erosion of the Sutlej River, and whilst this anabranch is not currently active, the terrace surface is flooded during extreme flooding events. This overbank site was chosen to constrain the maximum age of incision of the Sutlej River in its current position and to constrain the beginning and the end of the fluvial sedimentation that created the terrace that the Desert Branch canal has been constructed on. Two exposures at the top (155-SUT-2) and at the base (155-SUT-3) of the cliff were chosen for sampling. At SUT-2, the unit sampled consists of approximately 2 m of clayey-silts and sample 155-SUT-2-1 (table 2.1) was taken from a bioturbated sandy unit approximately 2.2 m below the surface of the cliff. Site 155-SUT-3 is from the same overbank sediment sequence, but further to the east. The sandy unit in 155-SUT-2 can be traced across the cliff face and was used as a marker horizon (figure 2.15a), and a bioturbated 2 m sandy unit (5.5 m below the cliff surface) was sampled (figure 2.15b).

Figure 2.15: Photographs of the Sutlej anabranch overbank cliff section. a) View of the cliff section, photo taken by Anwar Alizai. b) Photograph of site 155-SUT-3, with the unit sampled at 155-SUT-2 visible. Photo taken by Julie Durcan.

2.7.2 Lal Suhanrai forest

Two sites were selected adjacent to the Desert Branch canal and the nearby Lal Suhanrai forest and because they are on the terrace surface, these sites may overlay sediments related to a former anabranch of the Sutlej. Site 154-MGJ-3 is a dune within a large dune field bordering the Desert Branch canal (figure 2.16a), and at this site, more than 5 m of dune material was exposed (figure 2.16b). The sediments were considered in the field, but the site is made up of a massive unit of fine sand and no stratigraphic changes were observed. The initial purpose of sampling this site was to uncover fluvial deposits to sample sediments relating to the last phase of fluvial activity in the depression, however inspection of nearby wells showed that this aeolian material extends to a depth of over 10 m below the current ground surface. Beneath this is approximately 7 m of silts, overlying 10 m of fluvial sands. Dating the dune sediments will provide a minimum age for the cessation of fluvial deposition along this corridor.

Site 154-MGJ-4 was taken from within the Lal Suhanrai forest (figure 2.17a), next to the Desert Branch canal, and from within a depression which may mark one of the former courses of the Sutlej River. At this site, a 1.3 m pit was dug, which consisted of strongly indurated silts containing carbonate concretions, which overlay a unit of fine grey sands (appendix A; figure 2.17b). The sands were sampled for OSL dating

to help determine whether there was a fluvial channel which linked the Sutlej River system and the Ghaggar-Hakra palaeochannel.

Figure 2.16: Photographs of site 154-MGJ-3. a) The dune field with the Lal Suhanrai forest in the background (photo taken by Geoff Duller). b) Sampling the dune at site 154-MGJ-3 (photo taken by Julie Durcan).

Figure 2.17: Site 154-MGJ-4 in the Lal Suhanrai forest. a) The context of the site and b) the site stratigraphy. Both photos were taken by Julie Durcan.

2.8 Summary

This chapter has outlined some of the physiographic features of Pakistan, including the modern fluvial system of the Indus River and its tributaries. The Ghaggar-Hakra palaeochannel in the Cholistan Desert is associated with a dense concentration of Mature Harappan age archaeological sites. The Mature Harappan collapsed at ~1900 BC, and some authors have attributed this collapse to a change in fluvial activity, relating to the mid-Holocene weakening of the Asian Monsoon. Whilst the Ghaggar-Hakra palaeochannel has been studied by many researchers for over a

century, the lack of chronology for fluvial activity in the channel has not allowed this hypothesis to be tested.

The primary research aim of this study is to develop a chronology of fluvial activity in the Ghaggar-Hakra palaeochannel using the optically stimulated luminescence signal from quartz. Ten sites along a transect of the Ghaggar-Hakra were selected and sampled for both OSL and ^{14}C dating. A north to south transect from the Sutlej overbank cliff was also sampled, to test the hypothesis of Mughal (1997), who suggested that fluvial activity in an anabranch of the Sutlej River contributed to flow in the Ghaggar-Hakra during the Holocene. The following chapters discuss the calculation of OSL ages, beginning with the calculation of the environmental dose rate in chapter 3.

3. Measurement of the environmental dose rate

3.1 Introduction

Accurate determination of the environmental dose rate is important in luminescence dating because the dose rate forms the denominator of the age equation used to derive a luminescence age (equation 1.1; Olley et al., 1996). Exposure of mineral grains to ionising radiation results in electron trapping in defects in the crystal structure of the grain (Wintle, 2008) and the nature and amount of exposure to this radiation is of fundamental importance when calculating an age. Sources of this ionising radiation can be internal to a grain (e.g. from a radioactive element present in the mineral structure of the grain) or derived from the external environment. External sources include the contribution from radionuclides occurring naturally in the environment, primarily Uranium (U), Thorium (Th), Potassium-40 (^{40}K) and Rubidium-87 (^{87}Rb), as well as cosmic rays. Ionising radiation is delivered to a grain in the form of alpha (α) particles, beta (β) particles, gamma (γ) rays and cosmic rays. Alpha, beta and gamma irradiation occurs during the decay of the ^{232}Th, ^{235}U and ^{238}U decay chain series (figure 3.1) and beta and gamma irradiation is also produced during the decay of ^{40}K and ^{87}Rb. For the majority of samples, the dose rate is provided in equal parts by U, Th and K (Aitken, 1985), with a nominal contribution from cosmic rays and a negligible contribution from ^{87}Rb.

This chapter outlines the methods used to calculate the environmental dose rates used for age calculation in this study. Emission counting, in the form of thick source alpha and beta counting (TSAC and TSBC), was used to determine chemical concentrations of U, Th and K. The infinite-matrix beta dose rate and gamma dose rate were calculated from radionuclide concentrations, using the conversion factors of Adamiec and Aitken (1998) calculated from nuclear tables. Calculation of the contribution from cosmic rays has been made following the work of Prescott and Hutton (1994; 1998) and the effects of grain size and water content in attenuating ionising radiation are considered. The total environmental dose rates used in age calculation in this study are given in table 3.1.

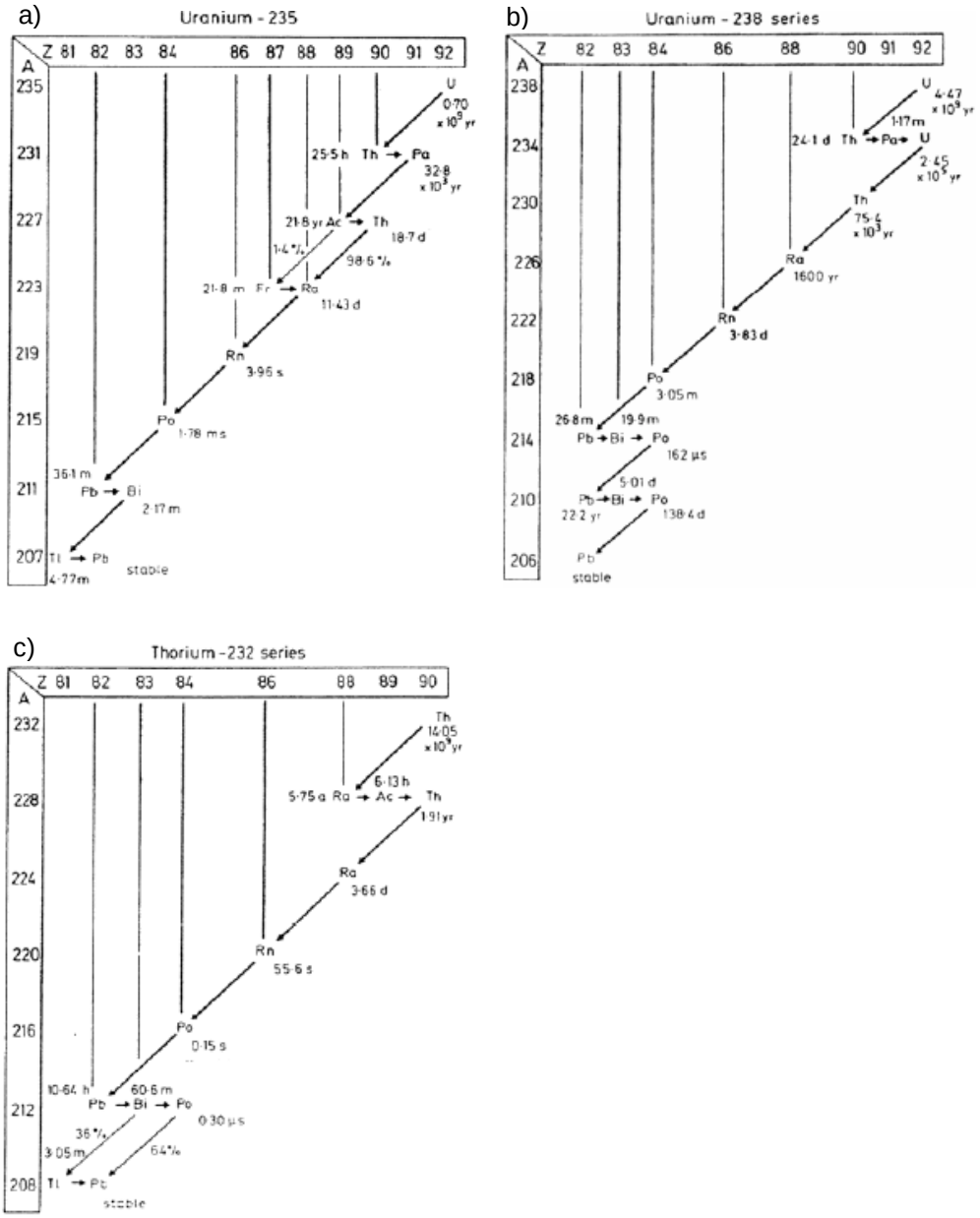

Figure 3.1: The decay series for a) ^{235}U, b) ^{238}U and c) ^{232}Th from Aitken (1985). The long arrows indicate alpha decay and the short arrows, beta decay. The half-lives of the isotopes are given and the isotopic number (y axis) and atomic number (x axis) are also shown.

Table 3.1: Parameters used for the calculation of the sample environmental dose rates. All values have been rounded to two decimal places, with calculations made prior to rounding.

Sample name	Depth (cm)	Water content	Th (ppm)[a]	U (ppm)[a]	K (%)[b]	IM beta dose rate (Gy.ka^{-1})[c]	Beta attenuation factor[d]	Gamma dose rate (Gy.ka^{-1})[c]	Cosmic dose rate (Gy.ka^{-1})[e]	Environmental dose rate (Gy.ka^{-1})
136-3-1	222	0.05 ± 0.02	14.45 ± 1.69	3.39 ± 0.51	1.20 ± 0.14	1.83 ± 0.06	0.91 ± 0.02	1.36 ± 0.10	0.15 ± 0.02	3.01 ± 0.13
136-3-9	399	0.05 ± 0.02	9.84 ± 1.35	3.52 ± 0.41	1.32 ± 0.12	1.81 ± 0.06	0.91 ± 0.02	1.19 ± 0.08	0.13 ± 0.01	2.81 ± 0.11
136-4-1	232	0.05 ± 0.02	12.95 ± 1.55	3.17 ± 0.47	1.60 ± 0.13	2.07 ± 0.07	0.91 ± 0.02	1.36 ± 0.10	0.15 ± 0.02	3.22 ± 0.13
136-4-2	291	0.05 ± 0.02	15.00 ± 2.00	4.40 ± 0.60	1.87 ± 0.17	2.51 ± 0.08	0.91 ± 0.02	1.67 ± 0.12	0.14 ± 0.01	3.88 ± 0.16
136-6-1	208	0.05 ± 0.02	11.99 ± 1.53	4.26 ± 0.46	1.85 ± 0.14	2.40 ± 0.08	0.91 ± 0.02	1.50 ± 0.10	0.16 ± 0.02	3.64 ± 0.14
136-6-7	381	0.05 ± 0.02	12.36 ± 1.23	4.63 ± 0.37	1.19 ± 0.12	1.95 ± 0.06	0.93 ± 0.02	1.40 ± 0.08	0.13 ± 0.01	3.06 ± 0.11
153-MAR2-5B	1086 – 1092	0.25 ± 0.05	15.37 ± 2.12	5.05 ± 0.64	2.66 ± 0.19	3.24 ± 0.10	0.93 ± 0.02	1.95 ± 0.13	0.06 ± 0.01	3.87 ± 0.19
153-MAR-12A	3005 – 3012	0.25 ± 0.05	17.23 ± 2.23	4.97 ± 0.67	1.17 ± 0.17	2.11 ± 0.07	0.91 ± 0.02	1.67 ± 0.14	0.02 ± 0.00	2.78 ± 0.15
153-MAR2-13B	3433 – 3438	0.25 ± 0.05	16.27 ± 2.08	4.23 ± 0.62	1.52 ± 0.17	2.25 ± 0.07	0.91 ± 0.02	1.62 ± 0.13	0.01 ± 0.00	2.84 ± 0.15
153-TIL3-2	367 – 371	0.25 ± 0.05	13.10 ± 1.57	3.62 ± 0.47	1.85 ± 0.14	2.33 ± 0.08	0.91 ± 0.02	1.48 ± 0.10	0.13 ± 0.01	2.91 ± 0.14
153-TIL3-8B	1707 – 1715	0.25 ± 0.05	13.62 ± 1.85	4.59 ± 0.56	2.12 ± 0.17	2.70 ± 0.09	0.93 ± 0.02	1.68 ± 0.12	0.04 ± 0.00	3.26 ± 0.16
153-TIL-10A	2094 – 2102	0.25 ± 0.05	17.92 ± 2.15	4.65 ± 0.65	1.97 ± 0.18	2.71 ± 0.09	0.93 ± 0.02	1.86 ± 0.13	0.03 ± 0.00	3.39 ± 0.17
153-TIL3-18	4468 – 4474	0.25 ± 0.05	10.85 ± 0.99	3.71 ± 0.30	1.83 ± 0.12	2.27 ± 0.07	0.91 ± 0.02	1.38 ± 0.06	0.01 ± 0.00	2.67 ± 0.12
154-MGJ-1-1	66.5	0.05 ± 0.02	7.83 ± 1.28	5.16 ± 0.39	1.53 ± 0.13	2.17 ± 0.07	0.91 ± 0.02	1.33 ± 0.08	0.19 ± 0.02	3.31 ± 0.12
154-MGJ-1-4	157	0.05 ± 0.02	8.65 ± 1.21	3.36 ± 0.37	1.35 ± 0.11	1.79 ± 0.06	0.90 ± 0.02	1.12 ± 0.08	0.17 ± 0.02	2.74 ± 0.10
154-MGJ-1-8	290	0.05 ± 0.02	10.26 ± 1.39	4.11 ± 0.42	1.20 ± 0.12	1.82 ± 0.06	0.91 ± 0.02	1.25 ± 0.09	0.14 ± 0.01	2.89 ± 0.11
154-MGJ-2-1	30	0.05 ± 0.02	12.42 ± 1.52	4.24 ± 0.46	1.43 ± 0.13	2.08 ± 0.07	0.90 ± 0.02	1.42 ± 0.10	0.22 ± 0.02	3.33 ± 0.13
154-MGJ-2-5	325	0.05 ± 0.02	12.53 ± 1.57	3.48 ± 0.47	1.36 ± 0.13	1.91 ± 0.06	0.90 ± 0.02	1.32 ± 0.10	0.14 ± 0.01	3.01 ± 0.12
154-MGJ-3-1	235	0.05 ± 0.02	11.82 ± 1.50	4.21 ± 0.45	1.35 ± 0.13	1.99 ± 0.07	0.91 ± 0.02	1.37 ± 0.09	0.11 ± 0.01	3.11 ± 0.12
154-MGJ-3-6	0	0.05 ± 0.02	9.82 ± 1.35	3.89 ± 0.41	1.43 ± 0.12	1.96 ± 0.06	0.91 ± 0.02	1.26 ± 0.08	0.28 ± 0.03	3.16 ± 0.12
154-MGJ-4-2	137	0.05 ± 0.02	13.03 ± 1.72	4.03 ± 0.52	1.82 ± 0.15	2.37 ± 0.08	0.91 ± 0.02	1.51 ± 0.11	0.17 ± 0.02	3.63 ± 0.14
154-MGJ-4-5	210	0.05 ± 0.02	9.96 ± 1.63	5.31 ± 0.50	1.24 ± 0.14	2.02 ± 0.07	0.91 ± 0.02	1.34 ± 0.10	0.16 ± 0.02	3.16 ± 0.13
154-MGJ-5-1	40	0.05 ± 0.02	10.99 ± 1.46	4.23 ± 0.44	1.07 ± 0.12	1.75 ± 0.06	0.91 ± 0.02	1.26 ± 0.09	0.21 ± 0.02	2.91 ± 0.12
154-MGJ-5-1B	40	0.05 ± 0.02	10.99 ± 1.46	4.23 ± 0.44	1.07 ± 0.12	1.75 ± 0.06	0.88 ± 0.02	1.26 ± 0.09	0.21 ± 0.02	2.85 ± 0.11
154-MGJ-5-5	255	0.05 ± 0.02	12.28 ± 1.47	2.68 ± 0.44	1.52 ± 0.13	1.92 ± 0.06	0.91 ± 0.02	1.26 ± 0.09	0.15 ± 0.02	2.98 ± 0.12
154-MGJ-6-2	95	0.05 ± 0.02	9.16 ± 1.33	4.23 ± 0.40	1.38 ± 0.12	1.95 ± 0.06	0.91 ± 0.02	1.25 ± 0.08	0.18 ± 0.02	3.04 ± 0.11

Table 3.1: *(continued)*

Sample name	Depth (cm)	Water content	Th (ppm)[a]	U (ppm)[a]	K (%)[b]	IM beta dose rate ($Gy.ka^{-1}$)[c]	Beta attenuation factor[d]	Gamma dose rate ($Gy.ka^{-1}$)[c]	Cosmic dose rate ($Gy.ka^{-1}$)[e]	Environmental dose rate ($Gy.ka^{-1}$)
154-MGJ-6-3	125	0.05 ± 0.02	12.12 ± 1.50	4.03 ± 0.45	1.64 ± 0.14	2.20 ± 0.07	0.91 ± 0.02	1.43 ± 0.09	0.17 ± 0.02	3.42 ± 0.13
155-SUT-2-1	220	0.05 ± 0.02	10.31 ± 1.38	3.98 ± 0.42	1.51 ± 0.13	2.05 ± 0.07	0.88 ± 0.02	1.31 ± 0.09	0.15 ± 0.02	3.08 ± 0.12
155-SUT-3-1	630	0.05 ± 0.02	13.50 ± 1.79	4.07 ± 0.54	2.30 ± 0.16	2.76 ± 0.09	0.88 ± 0.02	1.66 ± 0.11	0.10 ± 0.01	3.95 ± 0.15
Mean			***12.50 ± 2.54***	***4.29 ± 0.87***	***1.64 ± 0.43***	***2.25 ± 0.43***		***1.47 ± 0.43***	***0.14 ± 0.06***	***3.31 ± 0.54***

[a] U and Th concentrations (ppm) were calculated using TSAC.
[b] K concentrations (%) were calculated using TSAC and TSBC.
[c] Infinite-matrix (IM) beta and gamma dose rates were calculated using radionuclide concentrations derived from TSAC and TSBC and the attenuation factors of Adamiec and Aitken (1998).
[d] Beta dose rate attenuation factors are the combined factors of Mejdahl (1979) and Bell (1979).
[e] Cosmic dose rates were calculated using the equations of Prescott and Hutton (1998).

3.2 Internal dose rate

Quartz grains may contain very low levels of U, Th and K (e.g. Mejdahl, 1987) and it is possible that individual grains may receive a slight alpha dose rate (D_α) from within the grain. In most studies, the contribution of the internal D_α to the environmental dose rate is assumed to be negligible (Aitken, 1998) due to the low alpha efficiency of quartz (Ree-Jones and Tite, 1997). In some studies, an assessment of the internal D_α has been made by using either TSAC or instrumental neutron activation analysis (INAA). Using TSAC, Jacobs et al. (2003a) measured the internal D_α of South African quartz as 0.04 $Gy.ka^{-1}$, which is comparable to the range of internal D_α values of 0.01 – 0.05 $Gy.ka^{-1}$ measured from Congolese quartz by Feathers and Migliorini (2001). Similarly, using INAA to determine the U and Th concentrations of quartz separates, Vandenberghe et al. (2008) calculated an upper limit for the internal D_α of 0.01 ± 0.00 $Gy.ka^{-1}$ for the Dutch floodplain sediments investigated in their study.

Vandenberghe et al. (2008) suggest that an evaluation of the internal D_α should be made when assessing chronologies from low external dose rate environments. Whilst the assessment of the internal D_α would help to reduce systematic error in the calculation of the environmental dose rate, in this study the limited amount of material available for measurement did not allow for an assessment of the internal D_α. The external dose rates in this study are high (table 3.1) and not taking into account an internal D_α of 0.01 $Gy.ka^{-1}$ (Vandenberghe et al., 2008) makes negligible difference to the mean environmental dose rate of 3.31 ± 0.54 $Gy.ka^{-1}$ (table 3.1). As this internal D_α contribution would be minor in comparison to the contribution from the external dose rate, the internal D_α of quartz has not been taken into account in the calculation of the environmental dose rates of samples in this study (as suggested by Aitken, 1985).

3.3 External dose rate

Environmental irradiation is provided to a sample in the form of alpha and beta particles, gamma rays and cosmic rays. The cosmic ray contribution to the total

environmental dose rate can be calculated by taking into account parameters such as geographic location and sample overburden (see section 3.3.6), however, the contribution from alpha, beta and gamma irradiation (provided by the decay of radionuclides within the sediment matrix) requires laboratory measurement. In this study, emission counting has been used to calculate U, Th and K activity within the sample material, and the gamma (D_γ) dose rate was calculated using these activities. The infinite-matrix beta dose rate (D_β) is derived directly from TSBC, and the environmental dose rate is calculated by combining the D_β and D_γ values, as well as the contribution from cosmic rays, whilst making appropriate corrections for palaeo-water content, grain size and the effect of mineral etching. The external D_α has not been taken into account because the alpha-affected outer layers of the quartz grain are removed by mineral etching with HF acid (see section 4.2.5).

As stated, TSAC and TSBC were used for calculating radionuclide concentrations for the samples in this study, using the Daybreak 583 alpha counters (section 3.3.1.1) and Risø GM-25-5 beta counter (section 3.3.2.1) in the Aberystwyth Luminescence Research Laboratory (ALRL), although there are a number of other methods available for dose rate determination. For example, neutron activation and chemical analysis techniques, such as high resolution gamma spectrometry (HRGS), are well established techniques used to calculate chemical concentrations of the parents of radioactive series (Aitken, 1985). A number of authors have undertaken investigations to assess the comparability of dose rate determinations made using different techniques. De Corte et al. (2008) measured the D_α, D_β and D_γ dose rates of Belgian loess using INAA, HRGS and emission counting. They found that for all three dose rates calculated using the various techniques, determinations were within two sigma of each other, and they conclude that dose rates calculated using the different methods are consistent. Jacobs (2004) also undertook extensive comparison of the dose rates calculated from South African cave sediments. Comparing D_β values derived from TSBC using the ALRL beta counter and HRGS, Jacobs (2004) calculated a mean ratio between the two of 0.99 ± 0.04 for 9 samples. For D_γ values derived from emission counting (see section 3.3.4.1) and HRGS, she determined a ratio of 1.04 ± 0.01 (for 9 samples). Both studies indicate that emission counting methods provide

dose rate determinations comparable with those derived using other techniques, and that this is the case for the emission counting undertaken using the equipment at ALRL.

3.3.1 Thick source alpha counting

3.3.1.1 Sample Measurement

TSAC was undertaken using Daybreak 583 low-level alpha scintillation counters 4 and 5 in the ALRL to measure the alpha activity of a sample. TSAC measures this activity by counting the number of scintillations produced by alpha particles when they come into contact with a zinc sulphide (ZnS) screen. As an alpha particle (from the decay series of U and Th; figure 3.1) comes into contact with the ZnS screen used during measurement (figure 3.2), a scintillation is produced, causing a burst of photoelectrons to be emitted from the photocathode of the photomultiplier (PM) tube. These are converted into electrical pulses and are recorded as counts by the alpha counter (Aitken, 1985). The number of 'pairs' is also recorded, which takes into consideration alpha particles which are emitted in quick succession of each other (taking into account the probability of this occurring at random). This takes place when the new nucleus produced by the alpha emission is also an alpha emitter with a short half-life (Aitken, 1985). 'Slow pairs' are recorded from the decay of ^{220}Radon (Rn) to ^{216}Polonium (Po) in the ^{232}Th series (figure 3.1c) and fast pairs are recorded from the decay of ^{219}Rn to ^{215}Po in the ^{235}U series (figure 3.1a)

Prior to measurement, samples were dried overnight at 50°C and were homogenised using a ball mill. Each sample was measured in a Perspex sample holder containing a ZnS screen (figure 3.2). A retaining ring was used to ensure that the counting area of 15.45 cm^2 was consistent for each sample and the milled sample was spread over this area with a depth of ~1 mm. Once the sample has been loaded, the holder lid is fitted loosely to allow the 'unsealed' alpha counts to be measured. Following this measurement, the sample holder is completely sealed, and the 'sealed' counts recorded. 'Unsealed' counts are measured until a minimum of 3,000 counts have

been recorded and 'sealed' until 1,000 counts have been measured. Prior to sample measurement, the number of background counts from the ZnS screens are counted for at least 24 hours.

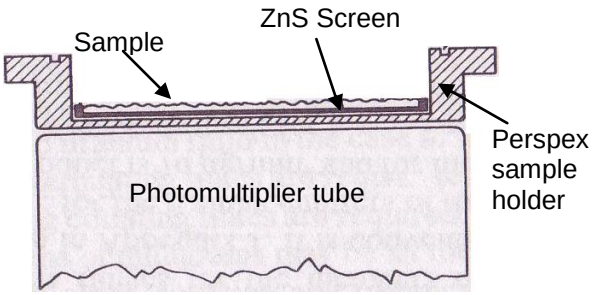

Figure 3.2: Schematic view of the sample arrangement in relation to the PM tube on a Daybreak alpha counter (modified from Aitken, 1985).

3.3.1.2 Calculation of the concentration of U and Th

The concentration (ppm) of U and Th in a sediment can be determined from TSAC (Aitken, 1985). As stated in section 3.3.1.1, the alpha counter counts the number of 'slow' pairs associated with the decay of ^{220}Rn to ^{216}Po (with a half-life of 0.145 s) in the ^{232}Th series. According to Aitken (1990), 3% of all alpha emissions associated with the ^{232}Th decay chain are emitted in this manner, and by comparing the slow pairs count with the total alpha count, the alpha activity from ^{232}Th can be calculated, based on the slow pair count rate (cts/ks/cm^2) expected from 1 ppm Th. Of the U, Th, K and Rb decay series, the U and Th decay series are the only ones with alpha emitting daughter products. Therefore, the Th activity can be subtracted from the total alpha count to calculate the alpha activity from U. Using the conversion factors of Adamiec and Aitken (1998) (table 3.2), the concentration of U and Th can be calculated from the activity. U and Th concentrations (with a systematic error of 10% applied) were calculated using TSAC for each sample in this study, and a worked example of this calculation is outlined in appendix B.

Table 3.2: Dose rate data from Adamiec and Aitken (1998) used for the calculation of environmental dose rates in this study. The alpha, beta and gamma dose produced per unit of the parent radionuclide is given.

	Alpha (Gy.ka^{-1})	Beta (Gy.ka^{-1})	Gamma (Gy.ka^{-1})
Th 1ppm	0.732	0.0273	0.0476
Nat U 1ppm	2.78	0.146	0.113
K 1%	-	0.782	0.243

3.3.1.3 Instrumental reproducibility

To assess the reproducibility of measurements made on the ALRL alpha counters, a series of measurements were made of a test source. A uranium ore standard was used, with a ^{238}U radioactivity of 1068 ± 20 pCi.g^{-1}, which has been used as the standard for alpha counter reproducibility tests since the establishment of the ALRL. This standard was made by Andrew Murray whilst he was at the Research Laboratory for Archaeology and the History of Art in the late 1970s (Murray, 1981). To maintain consistency, the same ZnS screen has been kept for use during reproducibility measurements. During measurement, the ZnS screen was placed directly on the PM tube and the uranium standard was rested on the screen, centred over the PM tube. The standard was measured two to three times on each counter for a period of 1000 s and the total counts recorded.

Table 3.3 shows data measured as part of this study, along with historical measurements made by Dr Helen Roberts and Professor Ann Wintle. Over the 12 year period of testing, measurement of the uranium ore standard suggests that the alpha counters provide reproducible measurements. On average, approximately 3,750 scintillations are counted over the 1,000 s measurements period, and repeat measurements can be consistently reproduced, indicated by the relative standard deviations (RSD) ranging between 0.75% and 2.06% over the 12 year period of measurement (table 3.3). Measurement of the uranium ore standard provides consistent results on both counters. Compared with counts measured on counter 4 in April 2010, relative mean counts vary between 0.99 and 1.02 on counter 4 and 0.98 and 1.01 on counter 5, consistent with the RSD for all ten measurements made over the 12 year period of 1.40% and 1.44% (counter 4 and 5 respectively). For all measurements made on both counters, a mean of 3773 counts with a RSD of 2.55%

has been calculated, again indicating consistency between the two counters over time. It is evident from table 3.3 that counter 4 measures slightly higher than counter 5, typically recording ~2 – 4% more counts. These differences reflect instrumental uncertainty, however, the systematic 10% error applied to U and Th concentrations derived from TSAC (section 3.3.1.2) accounts for this slight inter-counter variability.

Table 3.3: Reproducibility measurements made using the uranium ore standard. The mean total counts and the relative standard deviation (RSD) for each counter are shown, as well as the counts relative to the mean counts measured in April 2010. The ratio between the mean counts measured on counters 4 and 5 is also shown.

		Counter 4			Counter 5			
Date	**No. repeat meas.**	**Mean counts**	**RSD (%)**	**Counts relative to Apr 10**	**Mean counts**	**RSD (%)**	**Counts relative to Apr 10**	**Mean counts ratio (4:5)**
Feb 99	3	3894	1.14	1.02	3728	0.44	1.01	1.04
Mar 03	2	3794	0.75	0.99	3729	1.03	1.01	1.02
Apr 09	2	3859	0.77	1.01	3609	0.69	0.98	1.07
Apr 10	3	3822	2.06	1.00	3698	0.59	1.00	1.03
Mean	*10*	*3848*	*1.40*	*1.01*	*3692*	*1.44*	*1.00*	*1.04*

3.3.2 Thick source beta counting

3.3.2.1 Sample Measurement

Measurement of the infinite-matrix beta dose rate was made by TSBC using a Risø GM-25-5 beta counter (Bøtter-Jensen and Mejdahl, 1988) at the ALRL. The GM-25-5 beta counter is a gas flow (99% argon, 1% isobutane) counter, consisting of five Geiger-Muller counter elements and a common guard counter (Bøtter-Jensen and Mejdahl, 1988; figure 3.3). Using an anticoincidence technique, and having the equipment placed within a 100mm thick lead shielding, the contribution from ambient background radiation (e.g. from cosmic rays) is reduced by the guard counter, and allows for an assessment of D_β to be made.

Prior to measurement, samples were dried overnight in the oven at 50°C and homogenised using a ball mill. Three Perspex pots, with an internal diameter of 21 mm and an internal depth of 7mm, were packed with the homogenised sediment and the top levelled off to form a smooth and even surface. The packed sediment

was covered with cling film to protect the equipment from possible contamination during the loading and unloading of samples. Measurements were made over a period of at least 24 hours, with counts collected in 1 hour time slices. Three replicate pots of each sample were measured, as well as two standards of known radioactivity: milled Shap granite, with a D_β of 5.99 Gy.ka^{-1} and magnesium oxide powder (MgO) with a D_β of 0.00 Gy.ka^{-1}. The detection efficiency of each GM counter varies slightly, and therefore raw counts were corrected, based on the monthly analysis of a beta-emitting ^{36}Cl standard.

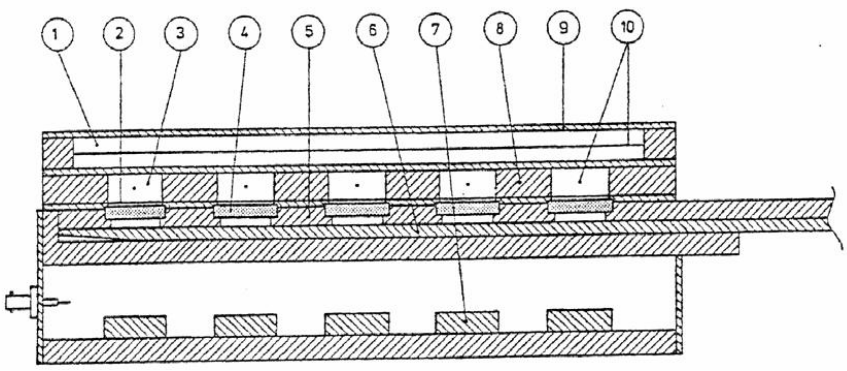

Figure 3.3: Schematic view of the GM-25-5 beta counting. (1) Guard counter (2) aluminised Mylar window (3) sample counter (4) sample (5) sample slide (6) lift slide (7) pre-amplifier (8) acrylic frame (9) Cu plate (10) anode cores. From Bøtter-Jensen and Mejdahl (1988).

3.3.2.2 Calculation of the infinite-matrix beta dose rate

The mean and standard deviation of the position corrected counts (PCC) from each of the three subsamples was calculated, and samples with a standard deviation greater than 0.1 Gy.ka^{-1} were re-measured to check for erroneous measurement. The D_β of each sample was calculated through interpolation between the inert MgO standard ($D_{\beta MgO}$ = 0.00 Gy.ka^{-1}) and the Shap standard ($D_{\beta Shap}$ = 5.99 Gy.ka^{-1}). Using equation 3.1, the D_β was calculated.

$$D_{\beta Sample} = D_{\beta Shap}\,[(\text{Sample PCC} - \text{MgO PCC})/(\text{Shap PCC} - \text{MgO PCC})] \quad \text{(Equation 3.1)}$$

The calculated D_β values range between ~1.7 Gy.ka^{-1} and 3.2 Gy.ka^{-1} and are given in table 3.1. The associated error is derived from counting statistics and the incorporation of a systematic error of 3% (section 3.3.2.3).

3.3.2.3 Instrumental reproducibility

To investigate the reproducibility of measurements made on the GM-25-5 beta counter, three pots of sample 136-3-1 were each measured five times to calculate five measurements of D_β for the same three pots of sample. The mean D_β from these five measurements ranged between 1.93 ± 0.07 and 2.02 ± 0.02 (figure 3.4), with a mean of 1.96 ± 0.03 and relative standard deviation of 1.78% for the five D_β determinations. For the same sample, the infinite-matrix beta dose rate was then measured five times, using fifteen unique subsamples. From these measurements, the mean D_β was calculated as 1.86 ± 0.07 $Gy.ka^{-1}$, with a relative standard deviation of 3.8%. Variability within these measurements is comprised of the systematic uncertainty from measurement reproducibility, the uncertainty from counting statistics and natural variability within the sample.

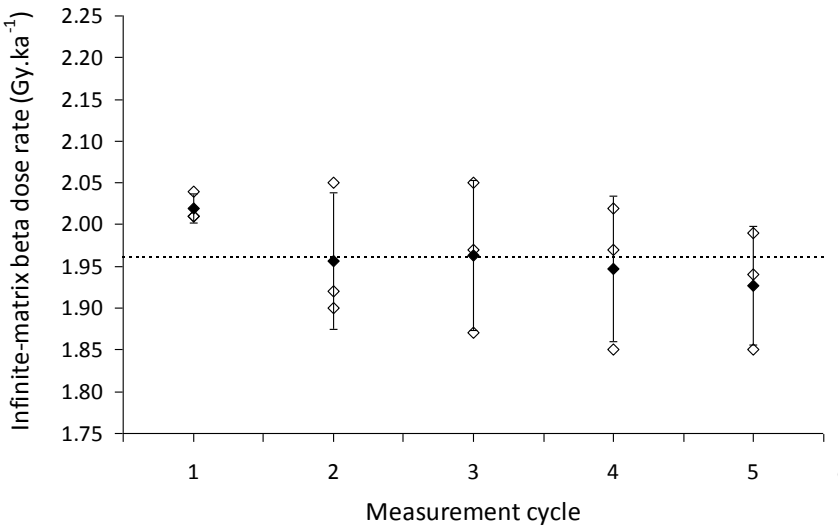

Figure 3.4: Infinite-matrix beta dose rate determinations from the same three subsamples of sample 136-3-1 measured five times (measurement cycle). The open symbols show the value for each subsample and the filled symbol, the mean D_β calculated from the three subsamples. The standard deviation is also shown. The mean dose rate is indicated by the dashed line.

The infinite-matrix beta dose rate was calculated for twenty nine samples in total, with three subsamples of each sample used, as discussed in section 3.3.1.1. The D_β was calculated for each subsample, from which the mean and standard deviation was calculated (section 3.3.1.2). The relative standard deviation can be calculated for each sample (figure 3.5), which ranges between 0.3 – 5.1%, with a mean of 2.2%.

Rodnight (2006) conducted the same set of experiments using South African samples with the ALRL beta counter. Based on her measurements, Rodnight (2006) applied a systematic error of 3% to beta dose rates, to account for instrument reproducibility. The variability evident in the infinite-matrix beta dose rate from the repeated measurement of sample 136-3-1 and across the suite of samples measured is in line with that measured by Rodnight (2006) and therefore the 3% systematic error that she applies to her beta dose rate calculations is considered appropriate and has been applied in this study (section 3.3.2.2).

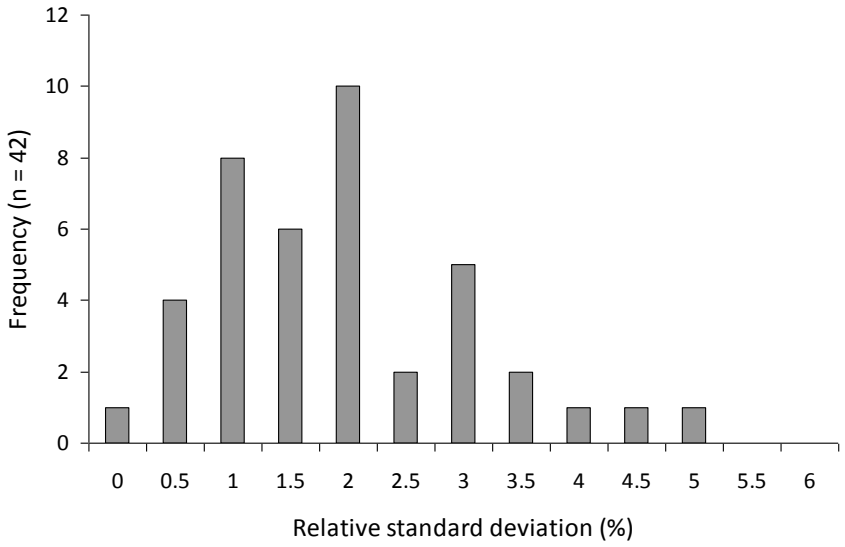

Figure 3.5: The relative standard deviation of the mean infinite-matrix beta dose rates for the forty-two measured samples.

3.3.2.4 Calculation of the K concentration

Concentrations of U and Th have been derived from TSAC in this study, and by using the conversion factors of Adamiec and Aitken (1998), the contribution from the beta emissions from these radionuclides can be calculated. The combined beta dose rate from U and Th can then be subtracted from the total infinite-matrix beta dose rate, leaving the beta dose rate from K. Again, using the Adamiec and Aitken (1998) conversion factors (table 3.2) the concentration of K (%) can be derived. The K concentration for each sample in this study is given in table 3.1 and a worked example of this calculation is available in appendix B.

3.3.2.5 Attenuation of the beta dose rate

The decay of the U, Th and K series produces beta emissions of various energies, and therefore the degree of attenuation within the grain varies according to the relative contribution from these different sources. Mejdahl (1979) investigated the absorbed beta dose fractions of ^{40}K, ^{232}Th and ^{238}U for spherical grains of quartz with diameters ranging between 5 – 10,000 μm. He calculated the attenuation factors for various grain sizes, based upon an assumed concentration of 12 ppm of Th, 3 ppm of U and 1% of K_2O. Similarly, the process of HF etching (see section 4.2.5) to remove the alpha-irradiated outer layer of the mineral grains will reduce the grain size and impact upon the beta dose rate attenuation factor. Bell (1979) calculated the effect of etching on the beta emissions for each of the decay chains. The values used in this study to account for attenuation of the beta dose by grain size and the effect of mineral etching (assuming a 10 μm layer has been removed by HF etching) are based on the work of Mejdahl (1979) and Bell (1979) respectively and are calculated in the LDB database written by Professor Geoff Duller. The attenuation factor applied to each sample is listed in table 3.1, and an error of 2%, as recommended by Murray and Olley (2002) has been applied to these attenuation factors and this error propagated in quadrature.

3.3.3 Radionuclide concentrations

As stated, the concentrations of U, Th and K have been determined using TSAC and TSBC, and are given in table 3.1. Concentrations of U vary between 2.7 and 5.2 ppm, with a mean value of 4.3 ± 0.9 ppm, with Th varying between 7.8 and 17.9 ppm and a mean of 12.5 ± 2.5 ppm. The percentage concentration of K varies between 1.1 and 2.7%, with a mean value of 1.6 ± 0.4%. Whilst there is some variability in the concentration of the radionuclides between samples (as would be expected), the measured values are in line with the typical abundance ratios of 12 ppm Th, 3 ppm U and either 1 or 2% of K_20 used in early dosimetry work (e.g. Mejdahl, 1979) and are close to mean concentration values found in crustal rock.

3.3.4 Calculation of the gamma dose rate

3.3.4.1 Calculation of the gamma dose rate from element concentrations

Using the U and Th concentrations calculated from TSAC and the K concentration derived from TSBC, D_γ can be calculated using the conversion factors of Adamiec and Aitken (1998) (table 3.2). The calculated gamma dose rates ranged between 1.1 $Gy.ka^{-1}$ and 2.0 $Gy.ka^{-1}$ and are given in table 3.1. All errors were propagated in quadrature and a worked example of the calculation from radionuclide concentrations to the gamma dose rate is given in appendix B.

3.3.5 Correction for water content

The D_β and D_γ dose rates should be corrected for water content, as water within sediment pore space attenuates radiation which would otherwise contribute to the bulk sediment dose rate. From nuclear tables, Zimmerman (1971) calculated the absorption spectra for water in comparison to pottery for alpha and beta particles and gamma rays, and following this work, and the work of Aitken and Xie (1990), the dose rates in this study have been corrected for water content using the following formulae:

$$D_\beta = \frac{D_{\beta\,dry}}{1+(1.25WF)} \qquad D_\gamma = \frac{D_{\gamma\,dry}}{1+(1.14WF)}$$

Where D_β and D_γ refer to the corrected 'wet' beta and gamma dose rates respectively. W refers to the saturation water content and F the mean saturation level in a sample over the burial time. WF has been substituted for the water content (%) defined below.

The water content of each sample at the time of sample collection was calculated by the change in mass of a subsample of sediment between opening the sample and drying the sediment in the oven. The change in mass was calculated as a percentage, and the reduction was attributed to water loss. In this study, the measured water

content of the samples from the cores (sample prefixes 153-MAR2 and 153-TIL3) varied between 24 and 30%. A water content of 25 ± 5% was used for dating calculations for the core samples to reflect the difficulty in estimating palaeo-water content over the burial period. All other samples (prefixes 136, 154-MGJ and 155-SUT) were corrected for a water content of 5 ± 2%. These samples were essentially dry when sampled in the field, reflected in measured water contents varying between 0.1% and 3.3%, and the slightly elevated water content of 5 ± 2% was considered to be a reasonable estimate of water content since burial.

3.3.6 Calculation of the contribution from cosmic rays to the environmental dose rate

Although small, the contribution from cosmic rays to the environmental dose rate is not negligible (Prescott and Hutton, 1998) and should be included in the calculation of the dose rate calculation. The contribution from cosmic rays is made up of two components – the 'soft' and 'hard' component. The 'soft' component is composed mainly of energy from electrons, and is typically absorbed by the upper 50 cm of overburden sediment (Aitken, 1985). The 'hard' component penetrates to greater depths and is composed of muons. In the appendix of their paper, Prescott and Hutton (1998) outline the suggested calculation protocol required for determination of the cosmic ray dose rate. This protocol involves the calculation of the cosmic dose rate at the depth of sampling, calculation of the geomagnetic latitude and the application of a correction for altitude and geomagnetic latitude and is outlined below.

1) The equation of Prescott and Hutton (1994) after Barbouti and Rastin (1983) can be used to calculate the cosmic dose rate from muons (e.g. the hard component, effective after 150 gcm^{-2})

$$D_0 = \frac{6072}{((x+11.6)^{1.68}+75)\,(x+212)} \exp(-5.50\times10^{-4}x)$$

Where D_0 is the uncorrected cosmic dose rate in $Gy.ka^{-1}$ and x is the depth in units of 100 gcm^{-2}.

The depth dependence of the 'soft' component (above 150 gcm^{-2}) can be calculated by a fourth order polynomial fitted to the data in Prescott and Hutton (1998):

$$D_0 = 3.21\times10^{-2}x^4 - 1.35\times10^{-1}x^3 + 2.21\times10^{-1}x^2 - 2.07\times10^{-1}x + 0.295$$

Where D_0 is the uncorrected cosmic dose rate in $Gy.ka^{-1}$ and x is the depth in units of 100 gcm^{-2}.

2) The cosmic ray dose rate is corrected for geomagnetic latitude (λ) using Eq. 4 in Prescott and Hutton (1998):

$$\sin\lambda = 0.203\cos\theta\cos(\phi-291) + 0.979\sin\theta$$

Where λ is the geomagnetic latitude, θ is the geographic latitude and ϕ the geographic longitude (north latitudes and east longitudes are positive).

3) The corrected cosmic dose rate (D_c) is then corrected for altitude and geomagnetic latitude using:

$$D_c = D_0\left[F + J\exp\left(\frac{h}{H}\right)\right]$$

Where D_0 is the cosmic dose rate prior to geomagnetic latitude correction, F, J and H are derived from figure 3.6 and h is the altitude (km).

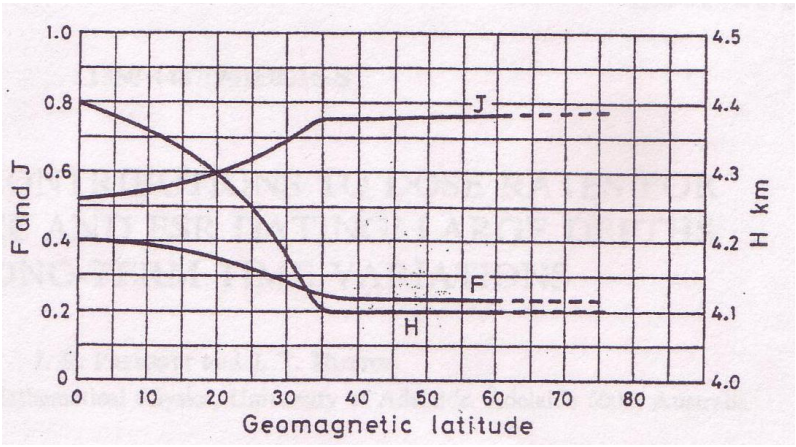

Figure 3.6: The parameters required to calculate the cosmic dose rate correcting for altitude and geomagnetic latitude, after Prescott and Stephan (1982) in Prescott and Hutton (1998).

In this study, the cosmic dose rate has been calculated using the COSMIC program, written by Dr Robert Clark, University of Durham. The cosmic dose rate can fluctuate over longer term time scales (Prescott and Hutton, 1994) as a result of variation in galactic primary comic rays, solar modulation and changes in the geomagnetic dipole moment. Prescott and Hutton (1994) state that over the past 500 ka, the variation in primary cosmic rays is thought to be less than 10% and that variation in the solar cycle (with a cyclicity 7 – 11 years) is likely to average itself out over the timescales considered in this study. Changes in the geomagnetic dipole moment are greatest at high latitudes and at geomagnetic latitudes of less than 35°. In this study, the samples were taken at altitudes of less than 150 m asl, and therefore the effects of variations in the geomagnetic dipole moment will be negligible at this altitude. Samples were taken from sites between 28.7° and 29.4°N and although Prescott and Hutton (1994) state that variation at latitudes less than 35° may cause up to a ±3% variation in the cosmic ray dose rate, the impact should decrease with distance from the equator, so is likely to be negligible for the samples in this study, over the time period that is being considered. To address possible fluctuations in the dose rate over time and errors associated with sample depth and geographical location, a systematic error of ±10% has been applied to each cosmic dose rate calculated and propagated in quadrature through the calculation of the environmental dose rate.

3.4 Calculation of the environmental dose rate

For the samples measured in this study, concentrations of U (ppm), Th (ppm) and K (%) have been determined using TSAC and TSBC. Using the conversion factors of Adamiec and Aitken (1998), the contributions from each of these radionuclides to the beta and gamma dose rates ($Gy.ka^{-1}$) have been calculated, assuming an infinite sediment matrix, where the rate of energy emission is equal to the rate of energy absorption in a volume with dimensions greater than the ranges of the radiation (Aitken, 1985). As stated in section 3.3, the contribution from the alpha dose rate has not been included in the calculation of the environmental dose rate because the alpha-irradiated outer layers of the quartz grains have been removed by chemical etching in this study. The sum of the beta and gamma dose rates (corrected for water content and attenuation as appropriate) and the contribution from cosmic rays has been used as the environmental dose rate. The errors associated with each of these calculations have been propagated in quadrature to provide an estimate of the error, and all dose rates were calculated using the LDB2005 database written by Professor Geoff Duller. A worked example of the conversion from radionuclide concentrations to the final environmental dose rate is shown in appendix B and the calculated parameters are given in table 3.1. Environmental dose rates are relatively high in this region, with dose rates varying between 2.7 and 4.0 $Gy.ka^{-1}$, with the associated errors ranging between 3.5 and 5.5%, and are in line with the dose rates measured by other workers in the region (e.g. Saini et al. 2010).

3.5 Conclusions

An accurate determination of the environmental dose rate is of equal importance to that of the equivalent dose determination in luminescence dating (Li et al., 2008). In this chapter, the emission counting based methods used to calculate the environmental dose rate have been outlined and the results presented in table 3.1. All calculations have been made with the assumption that environmental dose rates have remained unchanged since deposition. The dose rates calculated are relatively high, but are in line with measurements made in other studies in the region (e.g.

Saini et al., 2010) and the dose rates given in table 3.1 have been used in subsequent OSL age calculation in this study.

4. Measurement of the luminescence signal

4.1 Introduction

Quartz is one of the most abundant minerals in the continental crust of the Earth (Preusser et al. 2009), and is a commonly used dosimeter for luminescence dating. Quartz has been chosen for use in this study as it is not subject to the phenomenon of anomalous fading (Wintle, 2008), which affects feldspars (Wintle, 1973). The fast component of quartz is readily bleachable in nature and the composite quartz signal is reset more rapidly than feldspar (e.g. Godfrey-Smith et al., 1988; figure 1.14), which is an important consideration when dating fluvial sediments where incomplete bleaching may lead to overdispersion in equivalent dose (D_e) distributions (e.g. Rodnight et al., 2006).

This chapter describes the laboratory procedures applied to the sample to isolate the quartz component of the bulk-mineral sample prior to measurement. This chapter also outlines the equipment used for measurement of the luminescence signal and the technical specifications of the beta irradiation, light detection and optical sources are given. The stimulation power of the blue LEDs, used for the stimulation of the luminescence signal is considered in more detail and methods for measurement of both the relative and absolute power are presented. The results obtained are compared to the values supplied by the manufacturer at the time of equipment purchase and the stimulation power values used in this study are defined. A summary of the SAR protocol used for measurement of the luminescence signal is outlined and is defined by taking into account the inherent assumptions applied when using this protocol and testing these to ensure that the adopted SAR protocol can successfully recover a known dose.

4.2 Preparation of samples for OSL dating

After collection in the field, the samples were stored in their opaque sampling tubes until required for preparation. The ends of the tubes were stuffed with newspaper

immediately after collection and then securely wrapped with duct tape to prevent light exposure of the sample during transport and storage. All samples were opened and prepared in subdued red light conditions in the ALRL, and to ensure that none of the material destined for OSL dating had been exposed to light, the first 2.5 cm of material at either end of the sampling tube was removed and used for measurement of the environmental dose rate (chapter 3). Unless explicitly stated in the text, all samples for OSL dating were prepared using the full preparation (FP) protocol (figure 4.1) (e.g. Wintle, 1997). This protocol is outlined below. An alternative protocol for rapid age estimation called range-finder (RF) OSL dating (e.g. Roberts et al., 2009; Durcan et al., 2010) is presented in chapter 7.

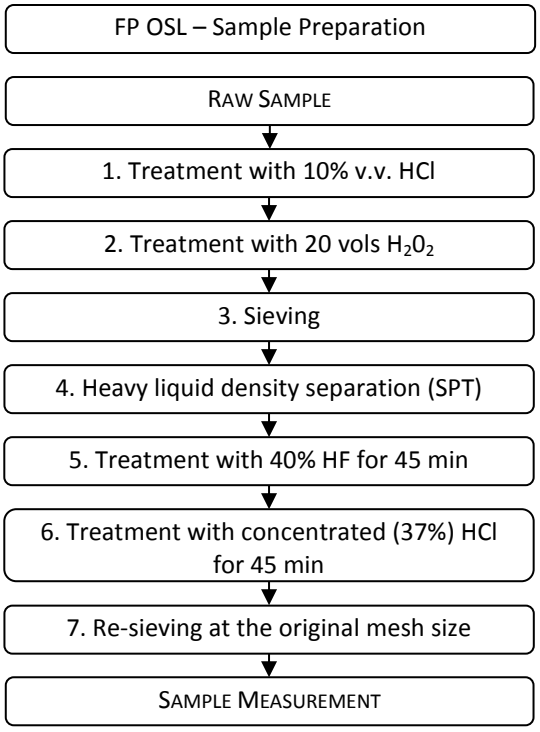

Figure 4.1: Summary of the laboratory treatment used to prepare samples for FP OSL dating.

4.2.1 Removal of carbonate material

Once the sample had been opened and the material decanted into a glass beaker, the first stage of sample preparation was to remove carbonate material using hydrochloric (HCl) acid. A 10% v.v. solution was made up and added to the dry sample. The sample and acid were stirred regularly and the acid was regularly replaced to ensure the continuation of the chemical reaction to completion. Once

no visible or audible reaction was evident upon the addition of fresh acid, the reaction was considered complete, and the sample rinsed three times with distilled water. The samples prepared for this PhD project did not react vigorously with HCl acid and generally, samples were in HCl acid for no more than three weeks.

4.2.2 Removal of organic material

Organic matter was removed by immersing the sample in 20 volumes hydrogen peroxide (H_2O_2). The sample was stirred regularly, and the H_2O_2 refreshed intermittently to ensure the continuation of the reaction. No vigorous reaction was noted upon the addition of the acid to any of the samples, however reaction times varied between two and six weeks. Once the reaction was considered complete, the samples were rinsed three times with distilled water.

4.2.3 Sieving

Once the carbonates and organic matter had been chemically removed, the samples were dried in the oven at 50°C. Once dry, each sample was sieved, using a set of six sieves of mesh size 90, 125, 150, 180, 212, 250 µm, and, where necessary, a 63 µm sieve was also used. The sieves were stacked and shaken in an automatic sieve shaker for 30 minutes. The fraction with the greatest mass (generally the 90 – 125 µm or the 125 – 150 µm) was used in subsequent stages of sample preparation.

4.2.4 Heavy liquid density separation

To isolate the quartz component of the sample, heavy liquid density separation using sodium polytungstate (SPT) was undertaken. Two separations were carried out, one using SPT with a density of 2.70 $g.cm^{-3}$, to remove the heavy mineral fraction ($\rho > 2.70$ $g.cm^{-3}$) and the other, using a SPT with a density of 2.62 $g.cm^{-3}$ to remove the feldspathic fraction ($\rho < 2.62$ $g.cm^{-3}$). The quartz fraction (2.62 $g.cm^{-3} < \rho < 2.70$ $g.cm^{-3}$) was retained for further laboratory treatment.

4.2.5 Mineral etching

To remove the alpha-irradiated outer layer of the quartz grains, and any feldspar grains not successfully removed during density separation, the separated quartz fraction was placed in a 40% solution of hydrofluoric (HF) acid for 45 minutes. This was followed by treatment with concentrated (37%) HCl acid for 45 minutes to remove any fluoride precipitates produced during the reaction between the sample and the HF. Once both stages were complete, the sample was rinsed three times with distilled water. This treatment was carried out by Mrs Lorraine Morrison (Aberystwyth University). Once dry, the etched material was resieved at its original grain size.

Once the steps outlined were complete, the purified quartz fraction was used for OSL dating and experimental work. When not in use, the prepared fractions were stored in light-tight opaque bags in a light-tight container to avoid accidental exposure to light.

4.3 Disc preparation

Sub-samples, or aliquots, of the prepared material used for OSL measurement were mounted on 9.7 mm diameter aluminium discs. It is rarely the case that the whole area of the disc is covered with mineral grains, and therefore at least part of the surface of the aluminium disc is exposed to light during optical stimulation.

4.3.1 Checking blank discs for an OSL signal

The aluminium discs initially used for measurement were taken from a stock pot in the ALRL. Prior to commencement of the experimental work, the discs (of various age) were checked to ensure no interfering signals were present. This was considered prudent, because if using small aliquots (2 mm in diameter; see section 4.3.4), only 4.25% of the surface area of the aluminium disc is covered with mineral grains. The discs were stored in white light conditions, so if contaminated (e.g. if a

grain was trapped in an imperfection on the disc surface) or if a luminescence signal was produced by the aluminium disc itself (e.g. Schmidt et al., 2011), a signal would not be produced when measuring the natural or 0 Gy dose. However, once applied, regenerative doses would result in the contaminating grains contributing to the OSL signal from that aliquot.

To check for contamination, a selection of discs from the stock pot (referred to as 'old' discs) were used for measurement. The discs were cleaned by immersing the discs in ethyl methyl ketone to dissolve the silicone oil (used to make the grains stay on the disc during measurement (section 4.3.4)) and to loosen and remove the grains from the disc. The discs were rinsed in methanol and left to dry, and wiped with methanol prior to use. The blank old discs were measured using a basic single SAR protocol (see section 4.8.3), to check for signal. Two SAR cycles were run, with regenerative doses of 0 Gy and 20 Gy applied, followed by a pre-heat of 220°C for 10 s and measurement of the OSL signal at 125°C for 40 s. This was followed by a test dose of 5 Gy, a cut heat of 160°C for 0 s and measurement of the OSL signal.

Signals were measured from 144 blank old discs and the measured OSL signal varied. As stated, the discs were stored in white-light conditions when not in use, and typically background-like signals were recorded after a 0 Gy regenerative dose (figure 4.2). In some cases, this was the case after a 20 Gy dose (indicating that that disc was free from luminescent grains), however in some cases a decaying signal, significantly above the background level was evident (e.g. figure 4.2). The inset of figure 4.2 shows a histogram displaying the number of counts recorded during the first 0.8 s of stimulation of the 144 blank old discs measured. In some cases, significant signals were recorded (in excess of 4000 counts), which if contributing to the signal from a mineral grain for D_e measurement would result in an underestimation of the equivalent dose (D_e).

To test whether a more rigorous cleaning protocol would solve this issue, the discs were put in an ultra sonic bath for 30 minutes in ethyl methyl ketone to dissolve the silicone oil, prior to rinsing with methanol fives times, before being dried and stored

in an air tight container. A selection of the originally measured discs were remeasured, however visibly decaying signals were still evident from some of the discs, albeit from a smaller proportion of discs. Figure 4.3 shows photographs of one disc (after cleaning), which has a mineral grain trapped on it and which produces a visibly decaying signal after irradiation, similar in form and magnitude to the signal shown in figure 4.2.

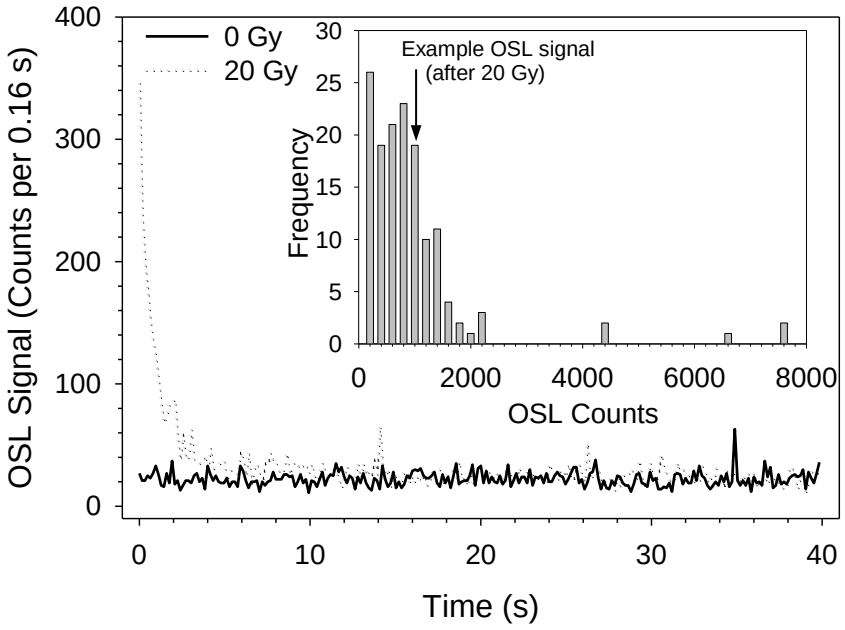

Figure 4.2: An example background corrected OSL signal from a blank old disc after a 0 Gy and 20 Gy irradiation. Inset, a histogram showing the number of background corrected counts recorded during the first 0.8 s of stimulation after a regenerative dose of 20 Gy (n = 144; bin width = 200 counts). The position of the example 20 Gy OSL signal is marked on the histogram with an arrow.

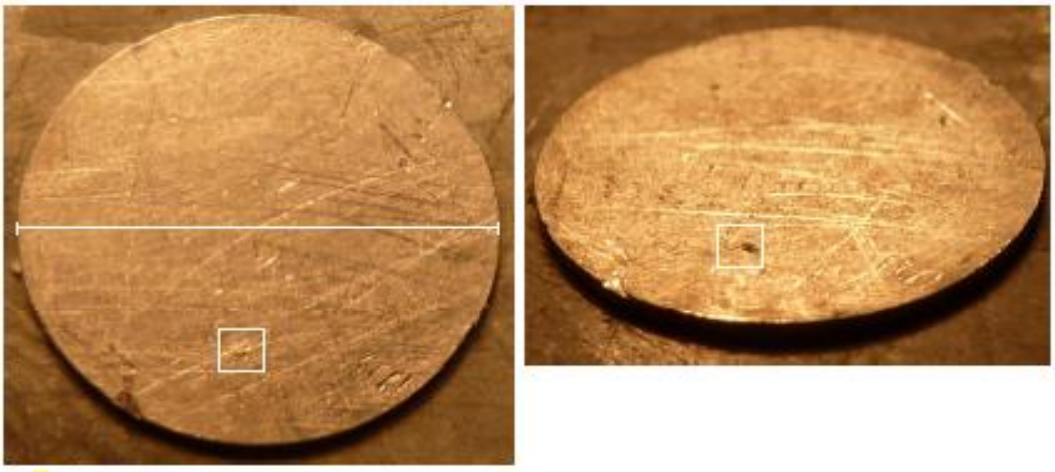

Figure 4.3: An example old disc after cleaning, with a mineral grain that had been trapped in one of the surface imperfections (see box; the grain was removed from the hole manually prior to photography to be more visible in the photograph).

The old discs were considered unsuitable for use in this study, given the use of small aliquots (see section 4.3.4) and the relatively low signal obtained from the sample material meaning that contamination from the disc surface may have a significant impact upon data collected using these discs. Therefore, newly purchased 'new' aluminium discs (made of aluminium with a very similar mass and the same dimensions as the old discs) were checked for contamination and the potential for thorough cleaning prior to use. A suite of 48 new discs were cleaned and measured in the same manner outlined above (e.g. two SAR cycles of 0 Gy and 20 Gy) on both sides. No discernible decaying signals were evident in any of the 96 measurements made. Figure 4.4 shows the signal measured from a new disc after a 0 and 20 Gy irradiation, as well as the measurement of an empty position in the carousel to provide a comparison between the measured signals and the background. It is clear that the new discs do not give a signal above the level of the machine background and are considered suitable for use in this study.

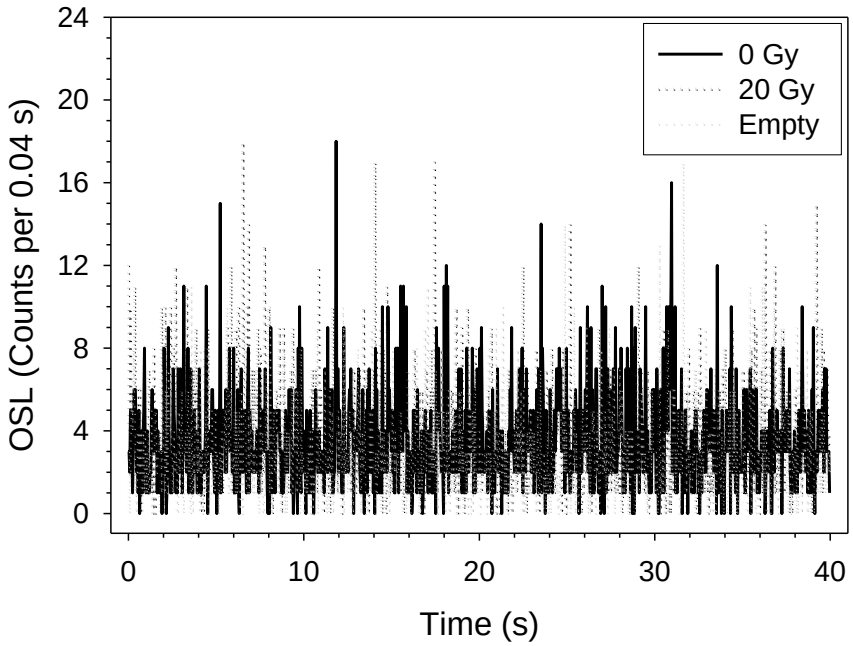

Figure 4.4: The OSL signal from a clean, blank new disc after a 0 and 20 Gy irradiation. The signal from an empty carousel position (i.e. the background) is also shown for comparative purposes.

To check that the more rigorous cleaning protocol was sufficient to clean the discs, a sample from the United Arab Emirates (Aber/UAE6225), which produced a relatively large luminescence signal after irradiation was used. Forty-eight blank new discs were checked for contamination on both sides of the disc using a dose of

20 Gy. Discs that had a signal greater than 50 counts in the first channel (0 – 0.16 s) or a visually decaying signal on either side were rejected. The accepted discs were then used to measure medium aliquots of sample Aber/UAE6225, which recorded in excess of 16,000 counts in the first channel (0 – 0.16 s) after a 20 Gy irradiation. With a signal of this magnitude, any luminescent material left on a disc after cleaning should be obvious. The discs were cleaned and the signals from the blank discs (both sides) were re-measured after a 20 Gy irradiation. Signal levels from these discs were of a similar magnitude to those measured prior to the measurement of the bright Aber/UAE6225 sample. All counts in the first channel (0 – 0.16 s) were below 50, and it is therefore concluded that the cleaning protocol is able to clean the new discs. It is possible that old discs were not cleaned as thoroughly due to the increased number of imperfections on the disc surface (e.g. figure 4.3), which act to trap the mineral grains (e.g. figure 4.3a).

4.3.2 Implications of using contaminated discs

Figure 4.5 shows two radial plots (see section 6.4.1 for further explanation) of the D_e distribution of the range-finder sample 136-3-9-RF (see chapter 7 for range-finder OSL dating). Initial measurement of twelve aliquots of sample 136-3-9-RF were made in June 2008, with measurement of a further forty eight aliquots made in November 2008, with both sets of aliquots measured using old discs. From figure 4.5a, it is clear that the mean D_e calculated from the two sets of measurements are not in good agreement. In figure 4.5a, the measurement of the further forty-eight aliquots of this sample made later using old discs produces a distinctive population of D_e values significantly lower (mean of 6.0 Gy) than the D_e values from the initial twelve aliquots (mean of 14.9 Gy). The mean D_e from the initial set of twelve aliquots is in line with the D_e calculated using fully FP OSL dating (14.94 ± 0.58 Gy; see table 6.5). Measurement of a further forty eight aliquots using new discs was made (figure 4.5b), and a mean D_e of 16.1 Gy was calculated, which is in line with FP D_e value and the value from the original twelve aliquots. All aliquots were medium in size, made up from the same batch of prepared material and measured on the same reader (Risø 4). The only difference between the signals measured was the

type of disc used to hold the sample, suggesting that disc contamination is a problem for this dataset. That said, this apparent underestimation of D_e did not manifest itself in the other range-finder samples measured at the same time or experimental work done previously using the old discs and the same reader, and therefore it is not suggested that this issue had remained undetected in the laboratory prior to these measurements. At this time, the number of discs available for use in the ALRL was limited and discs were recycled intensively and rapidly. Therefore, it is likely that a rapid deterioration of the quality of discs at this time due to the intensity of use is the most likely reason for this issue.

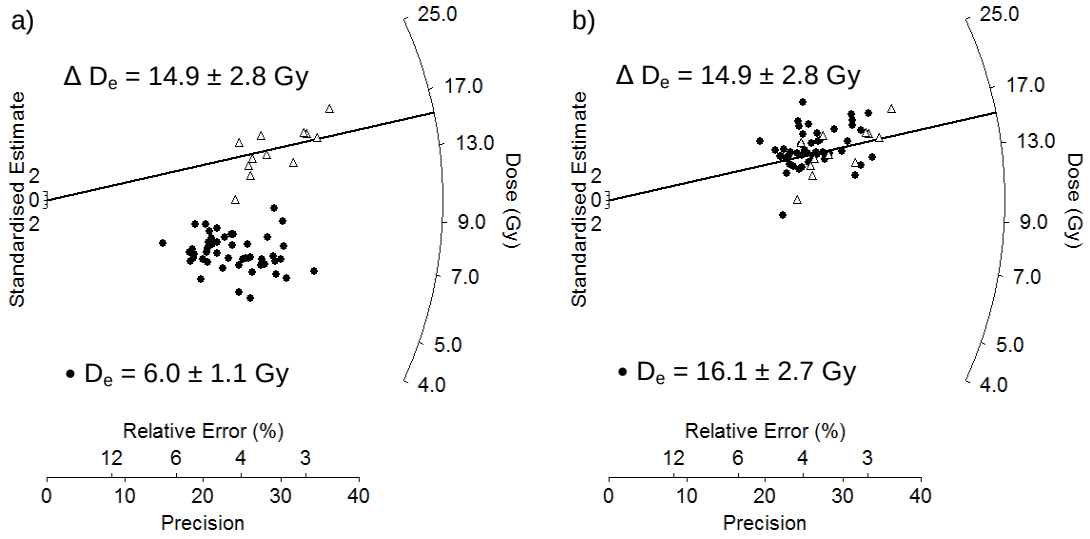

Figure 4.5: The impact of disc contamination on the D_e distribution of sample 136-3-9-RF. The D_e values from the initial measurement of 12 aliquots are shown by the open symbols in both figures. a) D_e values from the measurement of a further 48 aliquots are shown by the filled symbols (measured on old discs) and b) the 48 D_e values measured on new discs are shown by the filled symbols. In both figures, the FP D_e (14.94 ± 0.58 Gy) is shown by the black line. The mean D_e and standard deviation are shown for the 12 aliquots measured initially and the subsequent measurements of 48 more aliquots.

4.3.3 Disc screening protocol

After the identification of the potential contamination issues with the old discs, the use of these discs was discontinued in this study. Ideally, blank discs would be screened prior to every measurement to check for contamination, however

pressure on equipment time does not permit this. Therefore, after use, discs were cleaned with the more stringent cleaning protocol outlined in section 4.3.1 and a random sample measured regularly to check for contamination by measuring the OSL signal after a dose of 20 Gy to check the signal produced. The majority of the discs screened this way did not show a visibly decaying signal (e.g. figure 4.4). Occasionally, a decaying signal, similar in form to that of a quartz OSL decay curve was evident (e.g. figure 4.2). When these signals were identified, the discs were re-washed and visibly inspected under a microscope to ensure the disc was clean.

4.3.4 Preparation of aliquots

Aluminium discs with a diameter of 9.7 mm were used to make up multiple grain aliquots. A mask with circles of 2, 5 or 8 mm diameter, to create small, medium or large aliquots respectively (figure 4.6), was placed over the disc, and the exposed area sprayed with Silkospray silicone oil. To attach the sample to the disc, the surface sprayed with the oil was placed into the sample, to allow the purified quartz sample to stick to the oil, and the disc tapped lightly to remove any loose grains. The grains form a monolayer across the oiled area, and are then ready for measurement. Duller (2008b) suggests that for a grain size of 100 um, a small aliquot (e.g. 2mm diameter) will contain approximately 600 grains (figure 4.7), which is similar to the mean value of 425 (rounded to the nearest 25 grains) counted from 24 small aliquots of sample 154-MGJ-5-1 (size fraction 90 – 125 µm).

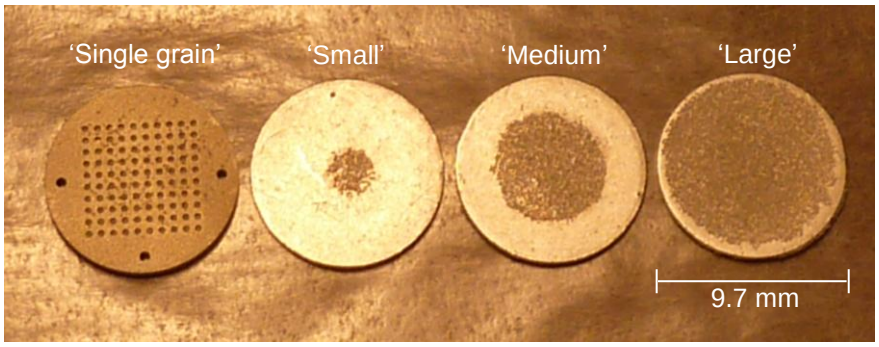

Figure 4.6: Photograph of the four aliquot sizes used in this study. A small aliquot consists of a grain monolayer 2 mm in diameter, a medium 5 mm in diameter and a large 8 mm in diameter. A single grain disc has one hundred holes. All aluminium discs have a diameter of 9.7 mm.

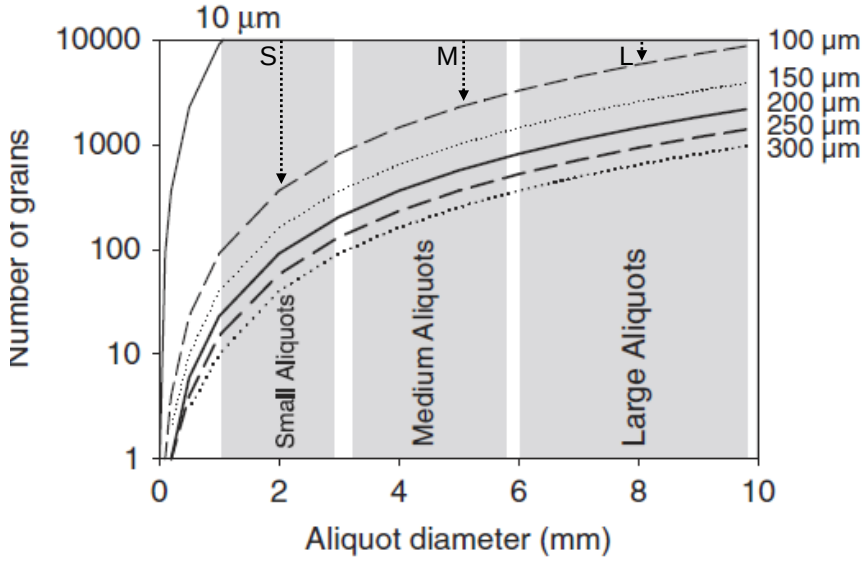

Figure 4.7: The number of grains on an aliquot as a function of aliquot diameter and grain size. The number of grains per aliquot size has been calculated as the maximum number of spherical grains that could inhabit a monolayer of the aliquot area. The small (S), medium (M) and large (L) aliquot sizes used in this study are shown for reference. Modified from Duller (2008b).

For single grain measurements, aluminium discs 9.7 mm in diameter were used. Drilled into the surface are 100 holes, arranged in a ten by ten grid (figure 4.6), and each hole is 300 µm in diameter and 300 µm deep. To ensure that each hole contains only one grain, grains with a diameter greater than 180 µm should be used for single grain measurement; using smaller grains makes it impossible to guarantee only one grain per hole. To make up a single grain disc, grains were carefully poured onto the surface of the disc and a fine-tipped brush was used to brush the grains gently across the surface of the disc. Any grains not retained in one of the holes were then brushed off the disc surface. After measurement, the discs were inspected with a microscope, and in the majority of cases, at least 95% of the holes were filled with grains. It is likely that during the movement of the disc both to and from the reader and to the microscope that some grains become dislodged and lost, however great care was taken when transferring the discs, so this should not be an issue.

4.4 Risø luminescence reader

All luminescence measurements were made using a Risø TL-DA 15 or TL-DA 20 luminescence reader. These readers are able to measure up to 48 aliquots per

measurement run, have a hot plate with a temperature range between room temperature and 700°C and can provide optical stimulation using a variety of light sources in the form of continuous wave (CW-), linearly modulated (LM-) and pulsed (P) OSL. Measurements are controlled through the "Mini-Sys" computer system developed by Markey et al. (1997), which automates all aspects of the measurement (e.g. heating, irradiation, stimulation). Figure 4.8 provides a schematic view of the OSL unit in the Risø TL-DA 20 reader. In this study, multiple grain aliquots were measured on either Risø 3, Risø 4 or Risø 6 (see table 4.1 for reader specifications) and single-grain aliquots, using the single grain system attachment on Risø readers 3 and 4.

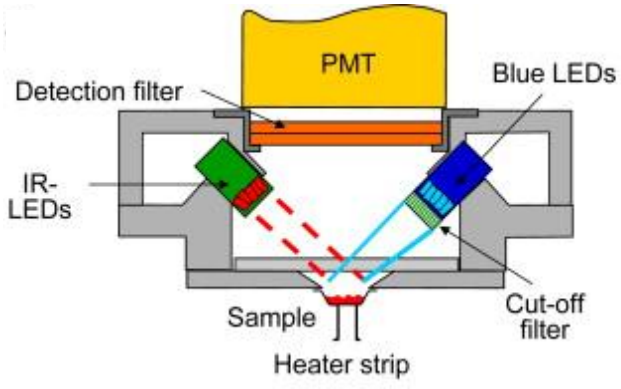

Figure 4.8: A schematic view of the OSL unit in the Risø TL-DA 20 luminescence reader (from Bøtter-Jensen et al., 2010).

4.5 Beta irradiation

Laboratory irradiations were made in situ using a strontium/yttrium (^{90}Sr/^{90}Y) beta source (1.48 GBq) (Bøtter-Jensen et al., 2010). Beta particles with an energy of 0.54 MeV from the decay of ^{90}Sr to ^{90}Y are produced, but it is the beta emission produced by the decay of ^{90}Y to the stable ^{90}Zr with the greater energy (2.27 MeV), that is used for irradiation (Aitken, 1985). The sources fitted in each of the ALRL readers are all of different age, and therefore deliver a different dose rate per time (table 4.1). All three Risø readers used in this study utilise a rotating source, with the source mounted on a rotating stainless steel wheel (described in more detail by Markey et al. 1997), creating a smaller distance between the source and sample than older systems and the delivery of a higher dose rate. Due to the relatively close

proximity of the source to the sample (~5 mm), cross-talk (e.g. the dose rate received by non-irradiated samples in adjacent positions on the carousel) is limited. Bøtter-Jensen et al. (2000) report that using a carousel with 48 positions and a beta source delivering a dose rate of ~5 Gy/min, aliquots in adjacent positions to the irradiated sample will receive 0.174 ± 0.004% of the irradiated dose.

Table 4.1: Technical specifications of the Risø readers used for dating in this study.

	Risø 3	**Risø 4**	**Risø 6**
Risø Model	TL-DA 15	TL-DA 15	TL-DA 20
Installation date	3rd Sept 1999	1st Jan 1989	22nd Nov 2007
Beta Irradiation			
Source Type	$^{90}Sr/^{90}Y$ (1.48 GBq)	$^{90}Sr/^{90}Y$ (1.48 GBq)	$^{90}Sr/^{90}Y$ (1.48 GBq)
Distance between source and sample	5 mm	5 mm	5 mm
Dose rate on 1st January 2011 (Gy/min)	4.77 ± 0.02	2.25 ± 0.03	5.68 ± 0.06
Light Detection			
PM tube model	9635Q	9635Q	9635Q
OSL filters	3 * 2.5mm Hoya U340	3 * 2.5mm Hoya U340	3 * 2.5mm Hoya U340
Optical Stimulation			
IR LEDs			
Number of diodes	24	24	22
Emission wavelength	870 nm	870 nm	870 nm
Quoted stimulation power (at 90%)[a]	110 $mW.cm^{-2}$	110 $mW.cm^{-2}$	116 $mW.cm^{-2}$
Distance from sample	20 mm	20 mm	20 mm
Blue LEDS			
Number of diodes	28	28	28
Emission wavelength	470 Δ 20 nm	470 Δ 20 nm	470 Δ 20 nm
Quoted stimulation power (at 90%)[a]	- $mW.cm^{-2}$ [c]	30.6 $mW.cm^{-2}$	45 $mW.cm^{-2}$
Stimulation power (at 90%)[b]	34.1 $mW.cm^{-2}$	27.7 $mW.cm^{-2}$	30.8 $mW.cm^{-2}$
Distance from sample	20 mm	20 mm	20 mm

[a] supplied by the manufacturer at the time of purchase
[b] calculated in this study (see section 4.7.4.3)
[c] the manufacturer's value of the stimulation power of the blue LEDs in Risø 3 is not known because the clusters have been replaced since purchase

The degree of homogeneity in the delivered dose rate across the surface of an aliquot has been a cause for concern for some authors (e.g. Spooner and Allsop, 2000), with non-uniformity in the dose rate across the aliquot leading to over-dispersion in the D_e distribution (Lapp and Thomsen, 2010). The beta sources in the ALRL have been checked and heterogeneity across the surface of the disc is not significant (Duller, pers. comm). Using Calibration Quartz, Li et al. (2011) measured the dose rate specific to each single grain position on Risø 4 to assess whether there was variability in the beta dose delivered to different positions on the disc. 1000 grains were measured, providing 10 repeat measurements of each single grain position and the weighted mean D_e was calculated for each position. The central age model (see section 6.4.2.1) was applied and an overdispersion of 3.6% was calculated, suggesting that a slight spatial heterogeneity of the dose rate across the surface of the disc would contribute an overdispersion of 3.6% to all D_e distributions calculated on Risø 4. Approximately 85% of single grain positions are consistent within ±2σ of the CAM D_e, with the majority of heterogeneity beyond the area of the disc which would be covered if a small aliquot was measured.

During the course of this study, the beta sources of each of the luminescence readers in the ALRL have been calibrated regularly to ensure accurate dose rates are used for D_e calculation. Calibration Quartz (CalQtz) (sensitised quartz from Jutland, Denmark) obtained from Professor Andrew Murray of the Nordic Laboratory for Luminescence Dating (NLLD) was used to calibrate the beta sources. A standard SAR protocol (section 4.8.3) was used to measure at least three medium aliquots of the calibration quartz to obtain a D_e in seconds. The D_e obtained is compared to the gamma-irradiated dose given to the calibration quartz using a ^{137}Cs gamma source at the NLLD to calculate the given dose and calibrate the source. As the half-life ($\tau_{½}$) of $^{90}Sr/^{90}Y$ is known to be 28.89 ± 0.04 years (MacMahon, 2006), the beta dose rate between calibrations can be calculated (in Gray) by

$$N(t) = N_0 e^{-\lambda t} \qquad \text{(Equation 4.1)}$$

where N_0 is the dose rate at time (t) = 0, and λ is the probability of decay per unit of time ($\lambda = 0.693/\tau_{1/2}$) (Aitken, 1985, p59).

4.6 Light detection

Light detection took place using a EMI bialkali 9635Q photomultiplier (PM) tube, which uses the single photon counting technique (described by Bøtter-Jensen, 1997). In this study, the quartz OSL signal has been detected through three 2.5 mm Hoya U340 filters, with an emission window of 340 Δ 80 nm (Singarayer and Bailey, 2003). This is designed to maximise OSL detection (the quartz luminescence signal peaks at around 365 nm wavelength (Huntley et al., 1991)). In addition, a GG-420 green long-pass filter was in front of each of the blue LED clusters. This combination of filters protects the PM tube from directly scattered blue light originating from the relatively long tail in the blue LED emission spectrum, whilst maximising OSL detection (figure 4.9) (Bøtter-Jensen et al., 1999a).

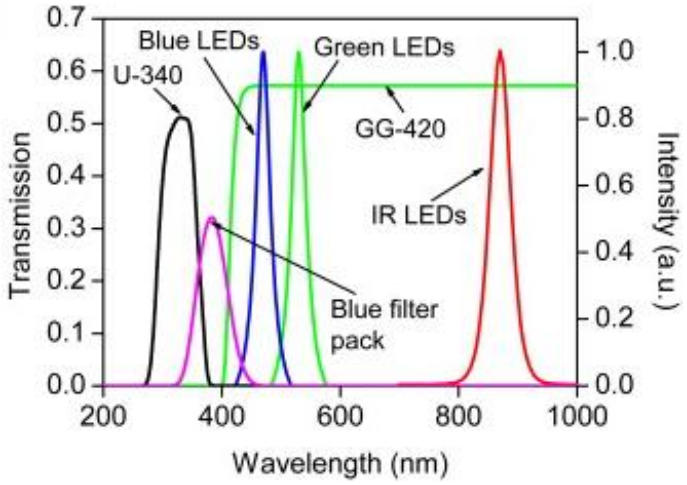

Figure 4.9: LED transmission and filter characteristics (from Bøtter-Jensen et al. (2010)).

4.7 Optical stimulation

4.7.1 IR stimulation

In the past, IR stimulation has taken place using an IR laser diode emitting at 830 nm (Bøtter-Jensen et al., 2000). Some of the issues surrounding stimulation with the

laser are discussed in more detail by Bøtter-Jensen et al. (2003a), however more recently, the IR laser has been replaced with light emitting diodes (LEDs) for the measurement of multi-grain aliquots in newer systems. In such systems, e.g. the Risø TL-DA 15 and -DA 20 readers used in this project, IR stimulation takes place using a set of three clusters, each of seven IR LEDs, emitting at wavelengths of 870 nm (Bøtter-Jensen et al., 2003a). These diodes offer a much more efficient means of stimulation, due to the peak in IR resonance (~870 nm) found in feldspars (Bøtter-Jensen et al., 1994).

4.7.2 Blue stimulation

During early OSL research, a range of light sources were used for optical stimulation, including argon lasers and halogen lamps. In 1999, Bøtter-Jensen et al. (1999a) presented the possibility of using blue LEDs as a stimulation source. The use of LEDs offers a number of advantages over the previously used sources, including their low heat dissipation and their comparably shorter switch on/off times, as well as their being software controlled to allow variations in power and illumination (Bøtter-Jensen et al., 1999b). Modern Risø readers are fitted with blue LEDs for optical stimulation as standard, and this is the case for the readers used in this study. Twenty-eight NISHIA blue LEDs (emitting at 470 Δ 20 nm) are arranged in four clusters of seven, approximately 20 mm from the sample The stimulation power (according to the manufacturer's information at the time of purchase) varies and table 4.1 details the stimulation powers for each of the readers used in this study (see also section 4.7.4).

4.7.3 Stimulation sources for single grain measurement

OSL dating in this project has been undertaken using multiple grain aliquots. Single grain OSL dating offers the potential for measuring a large number of OSL signals and identifying heterogeneous bleaching within a dose distribution (e.g. Jacobs and Roberts, 2007; Duller, 2008b). However, the samples dated in this study were fine sands, which were too fine for single grain analysis (the modal grain size analysed

was the 90 – 125 μm fraction). Analysis of single grain signals was undertaken for the one sample where an appropriate grain size fraction was available to assess the number of grains producing a luminescence signal (section 6.2). To make single grain measurements, a green solid-state diode-pumped laser was used (emitting at a wavelength of 532 nm) for optical stimulation. The laser beam focuses on a spot of approximately 20 μm in diameter (Bøtter-Jensen et al., 2010), and it is estimated that a power of 50 $W.cm^{-2}$ is delivered to the grain once the scattering within the grain hole is taken into account (Duller et al., 2003). IR stimulation was undertaken using an IR laser with a wavelength of 830 nm and an effective stimulation power of ~500 $W.cm^{-2}$ once reflection within the single grain hole has taken place (Duller et al., 2003).

4.7.4 Stimulation power of the blue LEDs

The rate of optical eviction of charge from a trap is a function of the photo ionisation cross-section (σ) of the trap and the light intensity (I_0) (Bulur, 2000), with I_0 (in photons $s^{-1}.cm^{-2}$) being linearly dependent upon the stimulation power (e.g. Choi et al., 2006). Calculation of the photo ionisation cross-section of different components of quartz (see section 5.3.1 for further details) is directly dependent upon an accurate determination of stimulation power.

An accurate measurement of stimulation power is not only important for photo ionisation cross-section calculation, but should also be considered during D_e calculation. The default setting of the Sequence Editor program (used to collect data on the Risø system) is that the OSL signal is measured for 40 s, with 250 data points recording the signal at intervals of 0.16 s. The default signal integration interval (L_x) in the Analyst data processing software consists of the signal collected from channels 1 to 5 or 0 to 0.8 s. For consistent D_e determination, where multiple readers are used for measurement, integration intervals should be varied according to the energy delivered to the sample. Figure 4.10 shows five synthetic CW-OSL curves, generated with the photo ionisation cross-section (σ) values and initial trapped charge population (n_0) values of Durcan and Duller (2011), but with

stimulation power (p) (and therefore I_0) varied. It is evident from figure 4.10 that the rate of optical eviction varies significantly with stimulation power. For example, the signal from the first five channels makes up 50% of the signal simulated over a 40 s period when the power is 50 mW.cm^{-2}, as opposed to 22% when the power is 10 mW.cm^{-2} (figure 4.10). The contribution of the various components during a fixed time period also varies with stimulation power (inset figure 4.10). After 0.8 s of stimulation with 50 mW.cm^{-2} (equivalent to 40 mJ.cm^{-2} of energy), 52% of the simulated signal originating from the fast component remains, in contrast to 80% with stimulation of 10 mW.cm^{-2} over 0.8 s (or 8 mJ.cm^{-2}). Whilst the differing rates of charge eviction do not directly impact upon D_e calculation, appropriate integration intervals according to the energy delivered (not time) should be applied where stimulation powers differ (e.g. where aliquots of the same sample have been measured using different equipment), and this is the approach applied in this study.

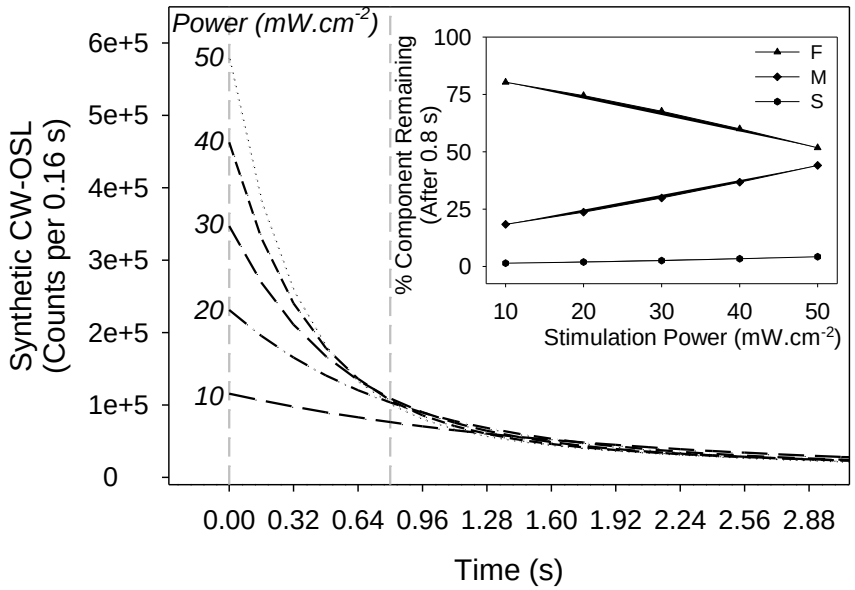

Figure 4.10: A synthetic CW-OSL signal, generated by varying the stimulation power and using the photo ionisation cross-section and n_0 values of Durcan and Duller (2011). The signal is made up of the fast, medium and slow2 components. The default integration interval in the Analyst (0 – 0.8 s) is shown by the dashed lines. Inset, the percentage of the signal originating from the fast (F), medium (M) and slow2 (S) components remaining after 0.8 s of stimulation, as stimulation power varies.

The stimulation power of the blue LEDs is measured using an optical power meter by the manufacturer when the equipment is purchased. However, it is not known whether this value remains constant over time. To assess the stimulation power of the blue LEDs used for optical stimulation in this study, a number of absolute and

relative measurements were made to ascertain whether the effective stimulation power can be precisely measured, and if it remains constant over time. Stimulation power determination was made on the four Risø TL-DA 15/20 readers (Risø 3 – 6) in the ALRL.

4.7.4.1 Half-time calculation

One method that has been applied to assess stimulation power is the calculation of the decay half-time of the OSL signal (e.g. Armitage, 2003; Rodnight, 2006). The half-time (measured in seconds) represents the time taken for the CW-OSL signal to reduce by a factor of two, and the calculation of this time can provide a relative measure of stimulation power between different readers. The half-time can be calculated by plotting the initial part of the OSL decay curve as the natural logarithm of the intensity (I) divided by the initial intensity (I_0) as a function of stimulation time (figure 4.11). By fitting this relationship with a linear function, the half-time (s) can be calculated where

The linear function is described as	$y = mx$
The half-time is	$y = ln\ (0.5) = -0.693$
The half-time is calculated from	$x = -0.693/m$

To calculate the half-time of the four readers, three aliquots of annealed calibration quartz batch 8 (CalQtz8) were irradiated with a 5 Gy dose and measured, with the same aliquots of sample measured on each reader in turn. Figure 4.11 shows an example decay curve measured on Risø 3 and the transformed data.

As the CW-OSL signal is composed of a number of exponential signals (e.g. Smith and Rhodes, 1994), the natural logarithm transformation does not result in a linear relationship, and the half-time should be calculated from the initial part of the signal. After only 1.12 s of stimulation, the transformation diverges from a linear relationship, due to the decay of the medium and slow components. The linear function can be fitted better to data from the initial 0.48 s of stimulation, where the

relationship between stimulation time and $Ln(I/I_0)$ can still be approximated reasonably well by the linear function. Therefore, half-times have been calculated using this shorter stimulation period. Table 4.2 gives the optical half-times of each of the four readers in seconds for the three aliquots measured, as well as the mean. The measured CW-OSL signals for all three aliquots of CalQtz8 produce mean half-times between 0.24 ± 0.02 and 0.36 ± 0.06 s. The almost identical mean half-time values for Risø 3 and 6 suggest very similar stimulation powers for these readers. Risø 4 and 5 have slightly higher mean half-times, indicative of less powerful LEDs. Calculation of the half-time provides a relative estimate of stimulation power, and therefore an absolute measure of power can not be made using this technique.

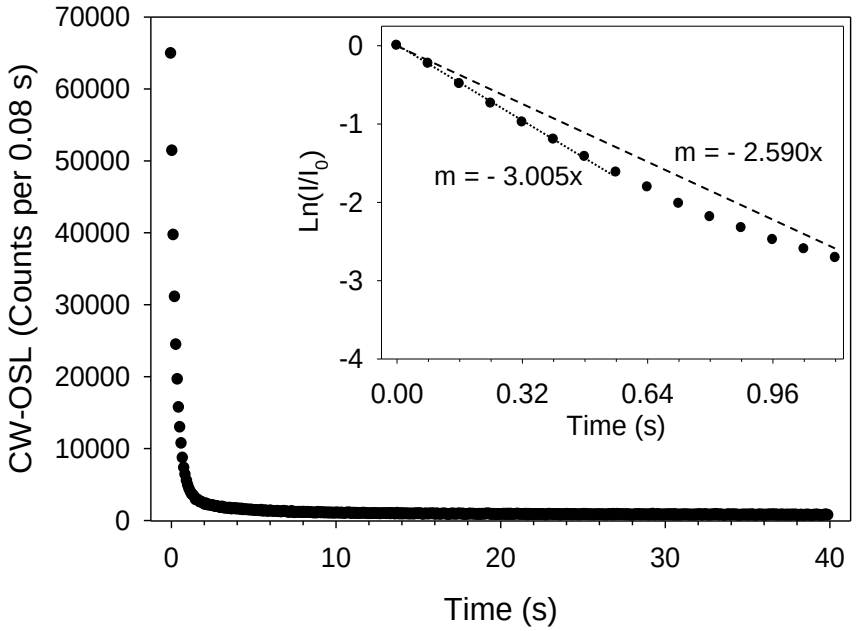

Figure 4.11: The CW-OSL signal of CalQtz8 (disc 1) after a 5 Gy irradiation, measured on Risø 3. Inset, the data transformed by taking the natural logarithm of the intensity divided by the initial intensity. The linear function fit of the initial 0.48 and 1.12 s of stimulation are shown.

Table 4.2: The calculated half-times (s) of each of the three aliquots of CalQtz8, based upon the first 0.48 s of stimulation with data collected every 0.08 s. The gradient of the linear function fitted (m) is also shown.

	Risø 3		Risø 4		Risø 5		Risø 6	
	m	**half-time (s)**	**m**	**half-time (s)**	**m**	**half-time (s)**	**m**	**half-time (s)**
Disc 1	-3.00	0.23	-2.28	0.30	-2.05	0.34	-2.89	0.24
Disc 2	-2.98	0.23	-2.30	0.30	-2.01	0.35	-2.86	0.24
Disc 3	-2.56	0.27	-2.16	0.32	-1.78	0.39	-2.48	0.28
Mean	*-2.85*	*0.24*	*-2.25*	*0.31*	*-1.95*	*0.36*	*-2.74*	*0.25*
Standard Deviation	*0.25*	*0.02*	*0.08*	*0.01*	*0.14*	*0.03*	*0.23*	*0.02*

4.7.4.2 The detrapping probability of the fast component

The CW-OSL quartz signal can be described by a sum of exponential functions (Smith and Rhodes, 1994), and it was concluded by Bailey et al. (1997) that this represents multiple OSL signals from distinct sources, each of which can be described by a single exponential decay. Early work into these sources identified a number of components that contribute to the OSL signal (named the fast (F), medium (M) and slow components (S)) (Bailey et al. 1997), each of which have unique bleaching, thermal stability and dose saturation characteristics (Tsukamoto et al., 2003). The quartz OSL components are discussed in more detail in section 5.2.

Assuming first order kinetics, Bulur (2000) describes the signal from each component as

$$L_{(t)} = n_0 b \exp(-bt)$$

where, $L(_t)$ is the luminescence intensity as a function of stimulation time t (s), n_0 is the initial trapped charge population, b is the detrapping probability (where $b = \sigma I_0$) σ is the photo ionisation cross-section (cm^2) and I_0 is the maximum light intensity ($s^{-1}.cm^{-2}$).

The maximum light intensity, I_0, can be calculated by multiplying the maximum stimulation power ($W.cm^{-2}$) by the energy of a photon, which is calculated by multiplying Planck's constant by the frequency of light (speed of light divided by the

wavelength) (e.g. Choi et al., 2006). I_0 and therefore the detrapping probability (e.g. the rate of decay) is linearly dependent upon the stimulation power. Therefore, by fitting a CW-OSL with a sum of exponentials, the detrapping probability of each component can be derived (e.g. b_F, b_M… etc), and can be used as a measure of relative power of the blue LEDs.

4.7.4.2.1 The detrapping probability derived from the same aliquots

The CW-OSL signals from each of the CalQtz8 aliquots measured in section 4.7.4.1 were used for analysis. Signal deconvolution took place using SigmaPlot (version 7.0), with the initial value of n_N for all components set to 10^5, n_N and b_N constrained to be more than 0 (Durcan and Duller, 2011). The sum of three exponentials plus a constant was used to fit each of the three signals measured on the four readers. The fitted b_F values are given in table 4.3 and an example CW-OSL curve with the fitted components is shown in figure 4.12.

Larger b_F values indicate a greater detrapping probability and a more rapid decay of the luminescence signal upon exposure to stimulation. The greatest mean b_F is seen for aliquots measured on Risø 6, indicating that this reader is fitted with the most powerful set of blue LEDs. The mean b_F values for these signals indicate similar trends to the half-time calculations (section 4.7.4.1), with Risø 3 and 6 having comparable stimulation powers, and Risø 4 and 5 having less powerful blue LEDs. As is the case with the half-time calculation, determination of the detrapping probability does not provide a quantitative estimate of LED stimulation power, instead providing a means of comparison.

Table 4.3: The b_F values for the same three aliquots of CalQtz8 measured on each of the Risø readers in turn. The mean, standard error (SE) and relative standard error (RSE) are also shown.

	Risø 3			**Risø 4**			**Risø 5**			**Risø 6**		
Disc	1	2	3	1	2	3	1	2	3	1	2	3
b_F (s^{-1})	3.52	3.33	3.60	2.81	2.89	2.93	2.78	2.40	2.46	4.05	3.88	3.61
Mean b_F	3.48			2.88			2.54			3.85		
SE b_F	0.08			0.04			0.12			0.13		
RSE b_F	2.26%			1.25%			4.67%			3.33%		

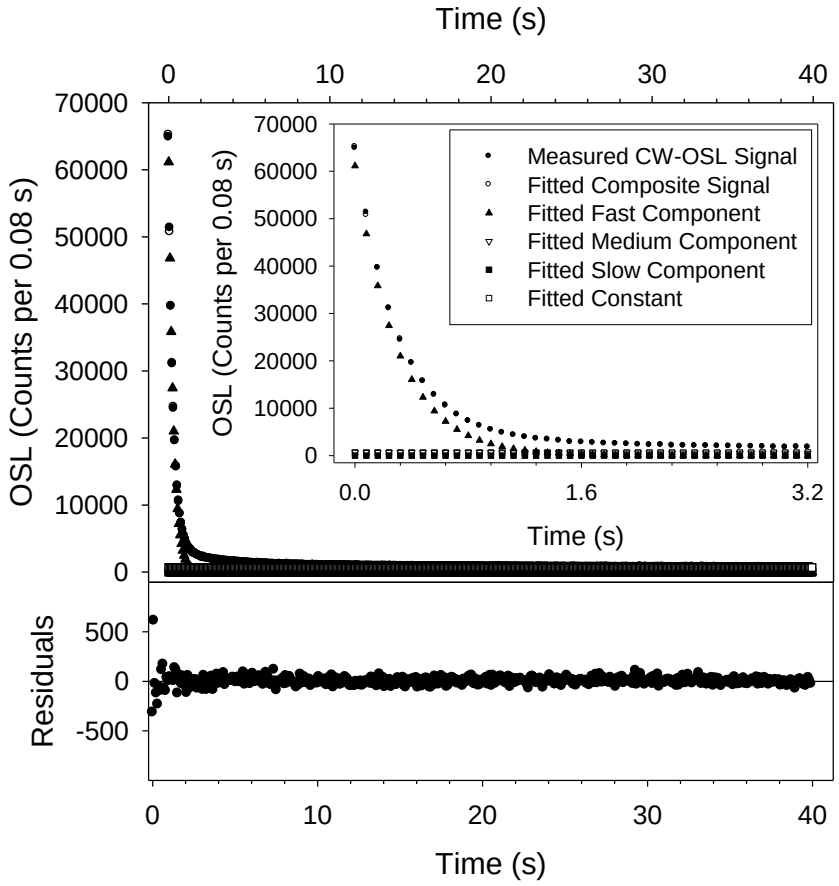

Figure 4.12: The CW-OSL curve of CalQtz8 (disc 1) measured on Risø 3 after a 5 Gy irradiation. The fitted components are shown and inset, a magnification of the first 3.2 s of stimulation for illustrative purposes. The residuals (e.g. the difference between the actual and fitted data) are also shown.

Fitted b_F values vary between aliquots slightly, with relative standard deviation values ranging between 1.3 and 4.7% (table 4.3). As photo ionisation cross-sections should be fixed, this variability is likely to be a reflection of the uncertainties associated with curve fitting. To assess how reproducible the process of curve deconvolution was using SigmaPlot, five repeat measurements of each of the three aliquots of CalQtz8 CW-OSL signals were made on Risø 3. The b_F and standard deviation for each of the three aliquots 3.38 ± 0.03, 3.25 ± 0.01, and 3.64 ± 0.01 (s^{-1}) (inset figure 4.13). Relative standard deviations of less than 1% for each aliquot indicates that the process of curve fitting does not introduce significant uncertainty. To check the parameters derived from curve deconvolution could be reliably reproduced, data was exchanged with Miss Ann Rowan (University of Manchester) for a 'blind' test of the curve fitting. The signals were fitted on SigmaPlot and by Ann Rowan using Matlab, using the sum of three exponentials plus a constant. Figure 4.13 compares the b_F values derived from curve deconvolution of the repeat CW-

OSL signals by different people, using the two different software programs The fitted b_F values derived using the two programs are very similar: all fifteen fitted b_F values are within 1% of each other (figure 4.13). Although this is not necessarily surprising, given that the same algorithm was used to model the data, it is comforting to know that the results can be reproduced by other users, using alternative software.

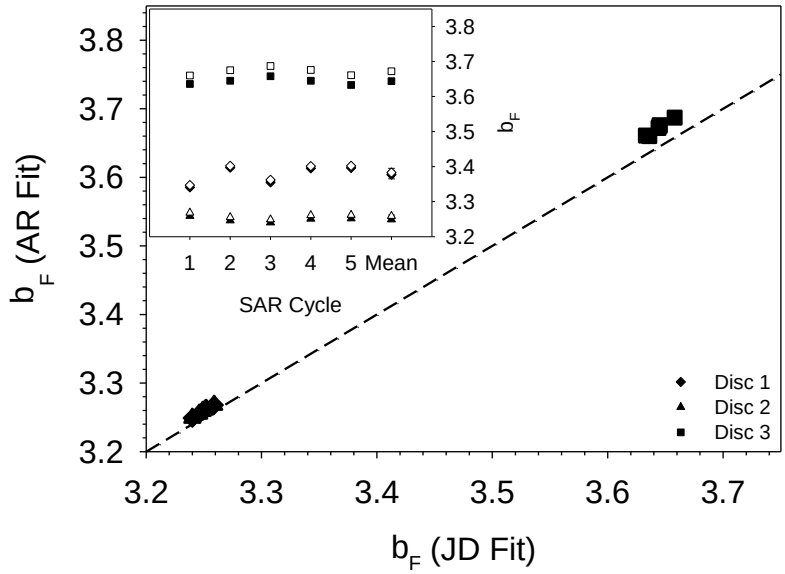

Figure 4.13: The relationship between the fitting of CalQtz8 in this study (JD Fit) and by Ann Rowan (AR Fit). Unity is indicated by the dashed line. Inset, the fitted values across the SAR cycles are shown, along with the mean and standard error. JD values are shown by the filled symbols and AR values by the open symbols.

4.7.4.2.2 The detrapping probability derived from the same sample

To provide another assessment of relative stimulation power for the blue LED units in the ALRL Risø readers, the CW-OSL signals from different aliquots of Calibration Quartz batch 25 – 26 (CalQtz25 – 26) were fitted to derive b_F values. Medium aliquots of CalQtz25 – 26, which had previously been used for beta source calibration were re-used, with the CW-OSL signals measured and fitted using the protocol outlined in section 4.7.4.2.1.

Table 4.4 shows the fitted b_F values obtained from the unique aliquots of CalQtz25 – 26. The fitted b_F values are similar to those calculated for the CalQtz8 signals, which is expected because the CalQtz samples are from the same bulk sample, with the

batch numbers referring to subsamples taken at different times for gamma irradiation (section 4.5). For these signals, b_F values indicate that Risø 3 has the most powerful set of LEDs, although the similar b_F value for Risø 6 suggests that the LED units for these two readers are of comparable strength. Relative standard deviation values are similar to those seen for CalQtz8 (table 4.3), again suggesting that uncertainties in curve fitting may be the cause of this variability.

Table 4.4: The b_F values for aliquots of CalQtz25 – 26 measured on each of the Risø readers. The mean, standard error (SE) and relative standard error (RSE) are also shown.

	Risø 3			**Risø 4**			**Risø 5**			**Risø 6**		
Disc	1	2	3	1	2	3	1	2	3	1	2	3
b_F (s^{-1})	3.67	3.57	3.79	3.01	2.69	2.63	2.06	2.27	2.12	3.47	3.36	3.52
Mean b_F	3.68			2.77			2.15			3.45		
SE b_F	0.06			0.12			0.06			0.05		
RSE b_F	1.72%			4.20%			2.91%			1.39%		

4.7.4.3 Absolute measurement with a power meter

To provide an absolute measurement of stimulation power, a Thorlabs PM100D power and energy meter fitted with a S120VC silicon photodiode sensor was used to measure the stimulation power from the blue LEDs of Risø 3 – 6. The Thorlabs S120VC sensor, with a power range of 50 nW – 50 mW and wavelength range of 200 – 1100 nm, measures at a 1 nW resolution, and has a measurement uncertainty of ±3% at wavelengths above 450 nm (±5% at wavelengths of 200 – 450 nm) according to the manufacturers instructions. The sensor has a diameter of 9.5 mm (figure 4.14) and a surface area of 0.709 cm^2, and for comparative purposes, all measurements have been converted in to $mW.cm^{-2}$. The sensor is held in place within a protective plastic casing, beneath a ND filter, and the surface of the sensor is 0.22 mm beneath the plastic casing.

To position the photodiode sensor to approximate the sample position during stimulation as closely as possible, the PM tube and filters were removed from the Risø reader. The sensor was visually centred and held against the flange that supports the quartz interface window (figure 4.15), and measurements were made whilst holding the sensor in place in this position. The power meter was set to

measure at a wavelength of 470 nm and the % power of the LEDs was altered manually at regular intervals using the Risø Control program and absolute power measurements were made.

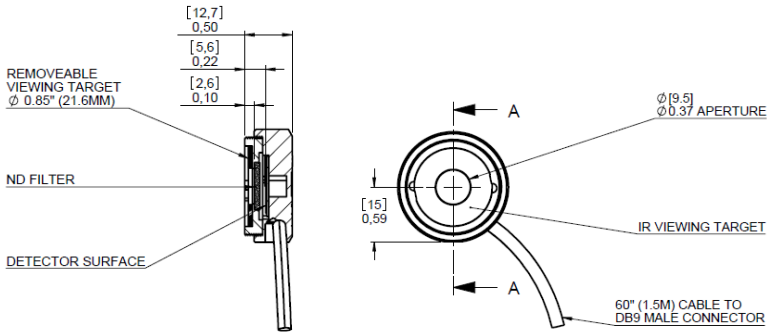

Figure 4.14: The technical diagram of the photodiode sensors (Thorlabs, 2008).

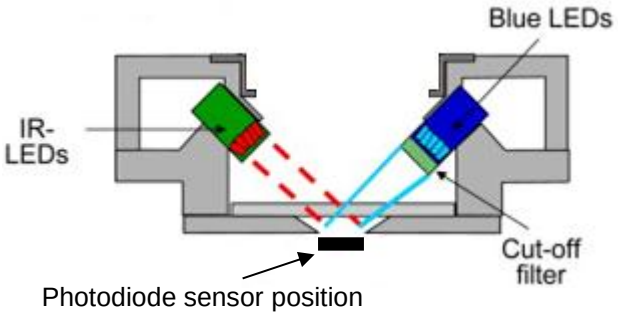

Figure 4.15: Positioning the photodiode sensor for power measurement. Schematic view of the OSL unit in the Risø reader modified from Bøtter-Jensen et al. (2010).

Absolute measurements of power for Risø 3 – 6 are shown in figure 4.16 and table 4.5. As was the case for the half-time calculations (section 4.7.4.1) and the detrapping probability derivations (section 4.7.4.2), Risø 3 and Risø 6 are the readers with the highest power and are fitted with diode units of similar power. Power meter measurements are considered reliable because they return a 0 $mW.cm^{-2}$ power when the diodes are off and the measured power increases linearly with the controlled power (figure 4.16). The stimulation powers measured are within the range of the photodiode sensor, and the sensor is precise even at the lower extreme of its range. Repeat measurements were made on different days following the same method outlined on Risø 4 and indicate that stimulation power is precisely measured (table 4.5).

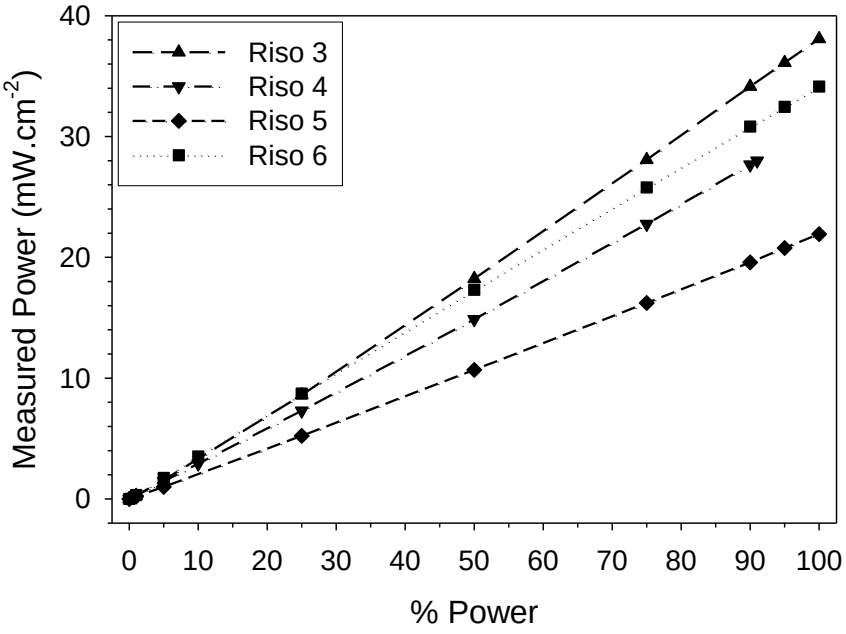

Figure 4.16: Absolute stimulation power of Risø 3 – 6, measured using a power meter as % power is varied manually using the Control program.

Table 4.5: Stimulation powers measured on Risø 3 – 6 using the power meter as diode power is varied using the program Control. Measurement of Risø 4 was repeated and these results are also shown. In Risø 4 and 5, the diodes cut out before 100% Control power is reached.

Control power (%)	Risø 3 ($mW.cm^{-2}$)	Risø 4 ($mW.cm^{-2}$)	Repeat Risø 4 ($mW.cm^{-2}$)	Risø 5 ($mW.cm^{-2}$)	Risø 6 ($mW.cm^{-2}$)
0	0.00	0.00	0.00	0.00	0.00
1	0.27	0.27	0.28	0.19	0.32
5	1.56	1.43	1.45	0.99	1.74
10			2.91		3.51
25	8.61	7.18	7.29	5.22	8.72
50	18.23	14.60	14.87	10.68	17.31
75	28.08	22.34	22.76	16.22	25.79
90	34.14	27.17	27.67	19.58	30.83
91		27.99	27.99	20.77	
95	36.12			21.92	32.46
100	38.09				34.14

4.7.4.4 Comparison of the four measurement protocols

Four methods for both relative and absolute measurement of stimulation power have been presented, the results of which are shown in figure 4.17. All four techniques (e.g. half-time calculation, calculation of b_F values for the same aliquots and the same sample and power meter measurements) show similar trends, with Risø 3 and 6 having similar stimulation powers, and lower powers seen from the

LEDs installed in Risø 4 and 5. Relative measurements of power are not directly comparable however, and therefore in figure 4.17, the results are presented relative to the Risø 5 value measured for each technique.

Of the three methods for relative power measurement, half-time calculation (section 4.7.4.1; table 4.2) is likely to be the least reliable, given the difficulty of fitting a linear function when more than one exponential decay is present. Most preferable of the relative methods is to derive the b_F value from the CW-OSL signal, because the rate of decay of the OSL signal is linearly dependent on stimulation power. For consistency and to reduce uncertainties as much as possible, it is preferable to use the same aliquots for relative power determination (e.g. section 4.7.4.2.1; table 4.3). Where the equipment is available, the preferred method of measurement is by making absolute measurements using a power meter (section 4.7.4.3). This technique allows a direct measurement of power at a fixed position as opposed to relying upon the measurement of a CW-OSL signal, subject to instrumental error and uncertainties associated with curve deconvolution. Whilst the direct measurement of power with a meter is not straightforward, with measurements made complex by the large angle of divergence of the light from the LEDs and the need to measure the power at precisely the position of the sample, the quantification of the stimulation power is valuable e.g. when calculating photo ionisation cross-sections.

One of the aims of conducting these sets of experiments was to determine whether the strength of the blue diodes in each reader had remained constant since measurement by the manufacturers. Comparison between the power meter measurements made in this study (table 4.5) and the manufacturer's values suggests change between the time of installation and measurement (table 4.6). The manufacturer's value is not available for Risø 3, as the LED cluster has been updated since purchase. The measured value is within 10% of the manufacturer's value for Risø 4, although is significantly lower for Risø 5 and 6 (table 4.5). At present, an explanation can not be offered for this disparity, although some of the equipment used is over 10 years old and maintenance operations may have altered the LED

output. It is possible that the power of the LEDs weakens over time, but Risø 6 is the newest reader in the laboratory and by this argument, the measured value should be much higher. It may also be possible that slight differences in the internal geometry (e.g. flange thickness) between the DA-15 and DA-20 models may affect the positioning of photodiode sensor in relation to the diodes, but the measured values of Risø 5 and Risø 6 are approximately two thirds of the manufacturer's values. The discrepancy between the power measurements made in this study and those made by the manufacturer cannot be resolved at present. However, the manufacturers use a power meter in the same way as has been done in this study to make their measurements of stimulation power (Duller, pers. comm.).

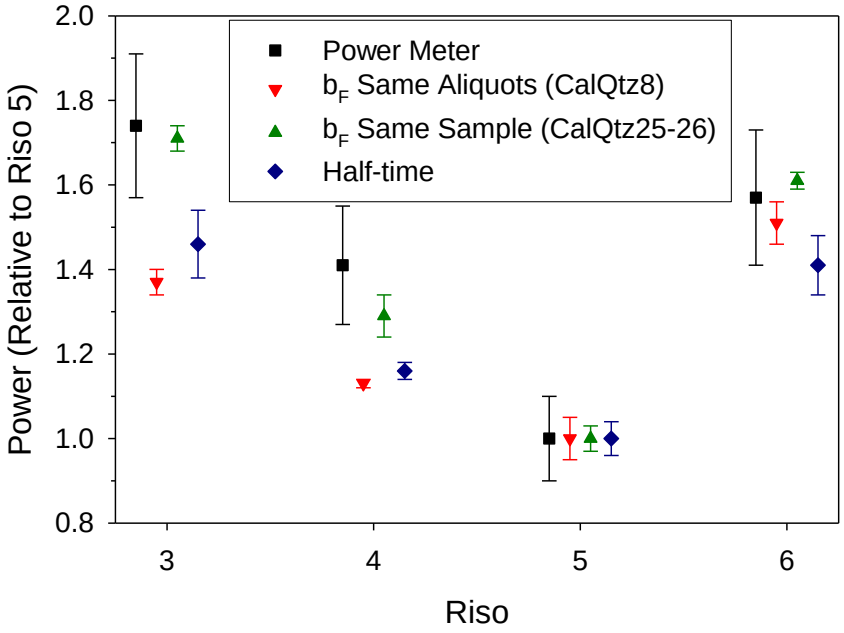

Figure 4.17: Comparison of the power of Risø 3, 4 and 6, relative to Risø 5. An arbitrary error of ± 10% is given to measurements made using the power meter to incorporate the ± 3% measurement error, as well as uncertainties associated with the positioning of the meter in relation to the LEDs. The relative mean half-time and b_F values along with the standard error are displayed.

As stated, absolute measurement of the stimulation power is extremely useful, and repeat measurements made using the power meter suggest that this technique is precise. Therefore, in this study, the values measured using the power meter (table 4.5 and 4.6) will be used as the stimulation power values, because these measurements are contemporaneous with the dating and experimental work carried out.

Table 4.6: Comparison between the stimulation power measured in this study and the manufacturer's values supplied at the time of purchase.

	Risø 3	**Risø 4**	**Risø 5**	**Risø 6**
Risø model	DA-15	DA-15	DA-15	DA-20
Manufacturers value (90%)	-[a]	30.6 $mW.cm^{-2}$	30 $mW.cm^{-2}$	45 $mW.cm^{-2}$
Measured in this study (90%)	34.1 $mW.cm^{-2}$	27.7 $mW.cm^{-2}$	19.6 $mW.cm^{-2}$	30.8 $mW.cm^{-2}$
Ratio of Measured and Manufacturer value		0.91	0.65	0.68

[a] the blue LED stimulation power is not known for Risø 3 as the LED clusters have been changed since the reader was bought.

4.8 Measurement of the equivalent dose

Integral to the calculation of a luminescence age is an estimation of the amount of radiation that the sample has absorbed during the burial period (often referred to as the natural or palaeodose). The laboratory estimate of the palaeodose is termed the equivalent dose (D_e) and is measured in units of Gray (Gy), where 1 Gy is equivalent to 1 $J.kg^{-1}$ (Duller, 2004). As the numerator of the age equation (equation 1.1), the accurate and precise measurement of D_e is critical for luminescence dating. Methods for D_e calculation were initially based on protocols used in TL dating, but have developed rapidly with advances in technology and understanding of the quartz OSL signal. There is no absolute relationship between the natural dose received and the level of OSL signal (Duller, 2004), and for each sample, at least one measurement of the regenerated OSL signal (in response to a laboratory administered dose) is required to calibrate the material.

Measurement protocols for the estimation of the equivalent dose were originally based on multiple aliquot techniques, which involved the use of many aliquots (typically 24 – 48) to derive one estimate of D_e (Duller, 2008b), with both additive and regenerative dose methods employed (Bøtter-Jensen et al., 2003b). Huntley et al. (1985) were the first to suggest the concept of a single aliquot based protocol for D_e estimation and the first single aliquot protocol was presented by Duller (1991). The single aliquot regenerative dose (SAR) protocol was first developed by Murray and Roberts (1998) as a single aliquot protocol which could monitor sensitivity change, and was subsequently modified by Murray and Wintle (2000). The SAR

protocol of Murray and Wintle (2000), since developed by Wintle and Murray (2006) has been widely employed during the past decade and is now routinely applied for OSL dating (Rhodes, 2011).

4.8.1 The SAR protocol

The main advantage of the SAR protocol over previous protocols is the ability to monitor and correct for any sensitivity change that occurs during measurement (e.g. during irradiation, heating and stimulation with light). The generalised SAR protocol of Wintle and Murray (2006) is outlined in table 4.7. Using the SAR protocol, the sample is pre-heated prior to the measurement of the OSL signal to remove charge from shallow, unstable traps and OSL signal is measured at a temperature of 125°C to prevent the re-trapping of charge in the 110°C TL trap during measurement (Murray and Wintle, 2003). Each SAR cycle is made up of the pre-heat, followed by the measurement of the natural (L_n) or a regenerative signal (L_x), which is the OSL measured after a laboratory irradiation. To monitor and correct for sensitivity change, after each L_n/L_x measurement the sample is given a fixed laboratory irradiation (termed the test dose) and the OSL signal (T_n or T_x) is measured after a thermal treatment termed the cut-heat. The cut-heat is usually conducted at a lower temperature than the pre-heat and the aliquot is cooled immediately, making this thermal treatment less severe than the pre-heat. The SAR cycle containing the measurement of the natural signal is followed by the measurement of a series of laboratory irradiations measured using the SAR protocol on the same aliquot. The sensitivity corrected luminescence from the regenerative doses (e.g. L_x/T_x) is used to construct a dose response curve (figure 4.18c), and L_n/T_n is interpolated on to this dose response curve to calculate the D_e for that aliquot.

The SAR protocol has now been widely applied to quartz samples from a variety of environments and to sediments of a range of ages (Wintle and Murray, 2006). In an extensive study by Murray and Olley (2002), 53 OSL ages obtained using the SAR protocol were compared to ages calculated using other techniques (mainly radiocarbon dates). The authors found excellent agreement between the majority

of the OSL ages and the independent age estimates. A more extensive comparison, using the data of Murray and Olley (2002) and Rittenour (2008) has been presented by Rhodes (2011) and is shown in figure 4.19. Rhodes (2011) concludes that there is excellent agreement between the SAR OSL ages and the independent age control available and comments that deviation from unity is likely to be a result of incomplete bleaching of the OSL signal as opposed to the inability of the measurement protocol to measure the true D_e.

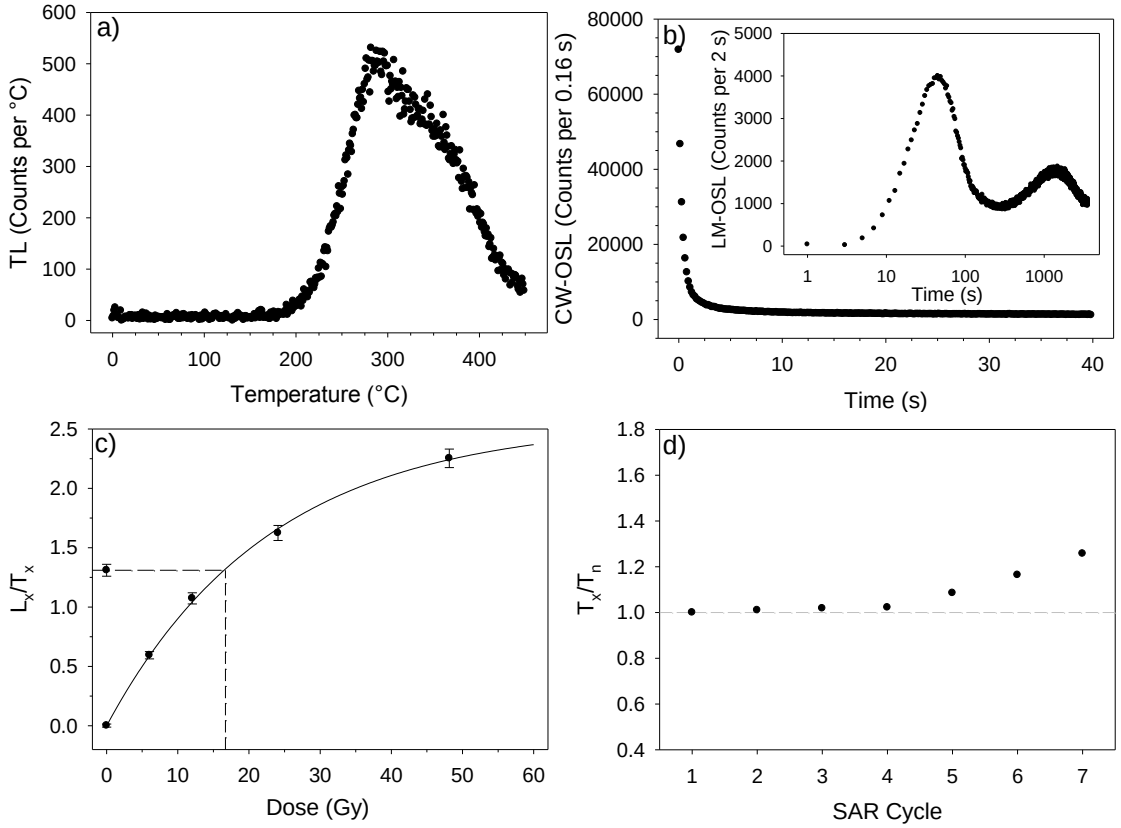

Figure 4.18: Example measurements made using a medium aliquot of sample 154-MGJ-1-1. a) The TL curve measured after a 42 Gy dose and a pre-heat of 220°C for 10 s. b) The CW-OSL signal after a 50 Gy dose and inset, the LM-OSL signal after the same sized dose. c) The dose response curve constructed from the L_x/T_x sensitivity corrected luminescence (shown by the filled symbols), fitted with a saturating exponential function. The natural signal (open symbol) can be interpolated on to the dose response curve and a D_e of 16.8 Gy is calculated (grey dashed line). d) Sensitivity change (T_x/T_n) monitored over the SAR measurement cycle used to construct the dose response curve. Unity is shown by the dashed line.

Table 4.7: The generalised SAR protocol (Wintle and Murray (2006)).

Step	Treatment	Observed
1	Give dose, D_i	
2	Preheat (160 – 300°C for 10 s)	
3	Stimulate for 40 s at 125°C	L_i
4	Give test dose, D_T	
5	Heat (160 – 300°C)	
6	Stimulate for 40 s at 125°C	
7	Stimulate for 40 s at 280°C	
8	Return to step 1	T_i

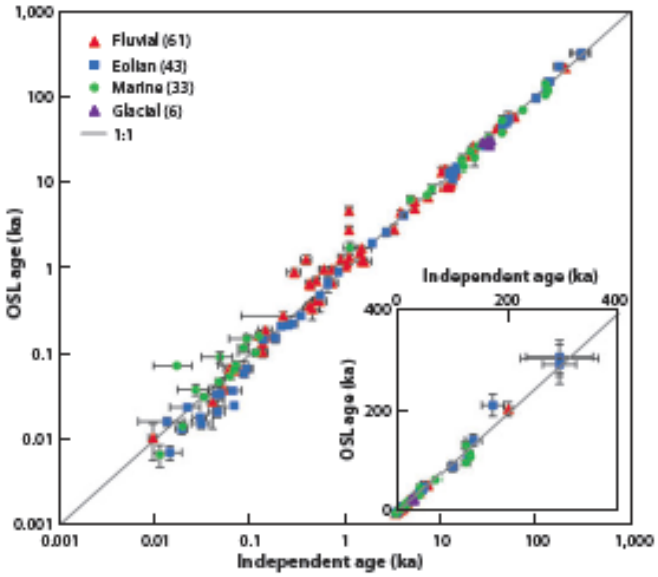

Figure 4.19: A comparison between SAR OSL ages and independent geochronological control (n=143) from a variety of environments. The line of unity is show for comparison and inset, the same data plotted using linear axes. The figure is taken from Rhodes (2011) and was constructed using data from Murray and Olley (2002) and Rittenour (2008).

4.8.2 Use of the SAR protocol for equivalent dose determination

One of the fundamental assumptions underlying the use of the SAR protocol for D_e determination is that sensitivity change is adequately monitored and corrected for using the test dose response (Murray and Wintle, 2000; 2003). As discussed, sensitivity change is monitored by normalising the natural and regenerative doses to a fixed test dose. The degree of sensitivity change can be monitored throughout a SAR cycle by comparing the test dose response e.g. T_x/T_n (figure 4.18d). In this study, for the signals which satisfied the set of rejection criteria described in section 6.3.3, sensitivity change increases through the SAR cycle, with the final T_x measurement typically ~30 – 40% greater than the initial T_n. The form of the T_x/T_n

chart shown in figure 4.18d is typical of the sensitivity change seen for the majority of samples, with little change in the first four to five SAR cycles and the majority of change occurring in the final cycles. Whilst there is no laboratory test which can confirm that sensitivity is being adequately corrected for (Wintle and Murray, 2006), it can be indirectly checked using a dose recovery test (section 4.8.2.1.2) which assesses the ability of the SAR protocol to recover a known dose.

A second assumption when using the SAR protocol is that the sample being analysed is dominated by the fast component, and dominance of a component other than the fast component often results in inaccurate D_e estimation when using the SAR protocol (e.g. Tsukamoto et al., 2003; Li and Li, 2006a; Pawley et al., 2010). The slow component can usually be eliminated by making an appropriate background subtraction (Wintle and Murray, 2006), and the ultrafast component (Choi et al., 2003; Jain et al., 2003) by using an appropriate thermal treatment (Jain et al., 2008), but the medium component cannot be separated from the fast component under usual CW-OSL measurement conditions. Therefore, the presence of a dominant fast component is commonly assumed or judged visually on a qualitative basis (Durcan and Duller, 2011). Qualitative inspection of the TL (e.g. figure 4.18a) and OSL signals (e.g. figure 4.18b) in this study suggest that the signals used for dating have a dominant fast component. In figure 4.18b, the rapid decay of the CW-OSL signal to background levels within the initial few seconds of measurement is consistent with a dominant fast component, and the peak in the LM-OSL signal (inset of 4.18b) after approximately 50 s of stimulation is consistent with charge originating from the fast component measured with blue light (e.g. Singarayer and Bailey, 2003). The fast component in quartz originates from the 325°C TL peak (Murray and Wintle, 1999) and figure 4.18a shows evidence of a peak in the TL glow curve at 325°C, albeit it with relatively low thermoluminescence response to the 42 Gy given dose. Durcan and Duller (2011) developed the fast ratio to provide a quantitative assessment of the dominance of the fast component in CW-OSL signals, negating the need for assuming dominance of the fast component. This is discussed further in chapter 5.

4.8.2.1 Testing the appropriateness of the SAR protocol

The internal checks that can be used to assess measurement reliability are one of the benefits of using the SAR protocol for quartz OSL dating (Roberts, 2008) and offer a method for validating the underlying assumptions. These checks allow for the identification and removal of erroneous signals which may lead to inaccurate D_e estimates. Roberts (2008) suggests that for OSL ages calculated from samples which satisfy these internal checks, the need for independent age control is negated. Wintle and Murray (2006) suggest three tests to assess the appropriateness of a SAR protocol for D_e determination; the recycling ratio test, the recuperation test and the dose recovery test. In this study, the recycling ratio and test for recuperation are routinely applied to individual D_e measurements, as part of a set of rejection criteria used to identify signals suitable for dating and these are discussed in section 6.3.3. The application of the dose recovery test to samples in this study is discussed below, as well as the selection of the most appropriate thermal pre-heat temperature for dating measurement sequences

4.8.2.1.1 Pre-heat plateau test

Thermal treatment in the form of pre-heats and cut-heats are integral to the SAR protocol for the removal of charge from thermally unstable traps (e.g. the TL 110°C trap; Murray and Wintle, 2003). However, these thermal treatments can impact upon D_e values in two ways (Ward et al., 2003). The first is through thermal transfer, or the transfer of charge from light insensitive traps to thermally stable, OSL traps (Wintle and Murray, 1999). The second is through sensitivity change, where luminescence emission per unit dose or the concentration of radiative recombination centres can change (Wintle and Murray, 1998; Murray and Wintle, 1999; Ward et al., 2003). Inherent in the SAR protocol is the ability to monitor and correct for sensitivity change, and therefore, thermal transfer and the dependence of D_e upon pre-heat temperature can be investigated by using a pre-heat plateau test. During a pre-heat plateau test, the D_e of aliquots given a range of pre-heat temperatures can be measured.

4.8.2.1.2 Combined dose recovery and pre-heat plateau test

In this study, the majority of samples were taken from sedimentary units believed to have been deposited by fluvial processes and it is possible that heterogeneous bleaching may affect D_e distributions. Therefore, it is not appropriate to apply a pre-heat plateau test to such samples, because the scatter in D_e values will obscure any temperature dependence. To address this, a combined dose recovery and pre-heat plateau test was used to assess the most suitable pre-heat temperature for use in the SAR protocol. For each sample analysed, twenty four medium sized aliquots had their natural signals removed (see section 4.8.2.1.3 for dose recovery test details), were given a laboratory dose and measured using the SAR protocol to assess the effect of pre-heat temperature on D_e. Three aliquots were pre-heated at a range of temperatures between 160°C and 300°C (at 20°C intervals) for 10 s prior to measurement of the OSL signal for 40 s at 125°C. A cut heat of 160°C for 0 s was applied as standard prior to the measurement of the test dose signal. The set of rejection criteria outlined in section 6.3.3, including the recycling ratio (Murray and Wintle, 2000), a check for recuperation (Murray and Olley, 2002), the OSL IR depletion ratio of Duller (2003) and the fast ratio (Durcan and Duller, 2011) were used to screen the measured OSL signals.

The samples analysed using the combined dose recovery and pre-heat plateau test are shown in figure 4.20. The ratio between the recovered and administered dose is shown as a function of pre-heat temperature. Pre-heat plots of samples 136-3-9, 154-MGJ-5-5 and 155-SUT-2-1, show D_e values that are consistent over the temperature range of 160 – 220°C, but recuperation of the signal due to thermal transfer (Murray and Wintle, 2000) becomes more significant at temperatures above 280°C. For sample 154-MGJ-1-1, D_e values are consistent at pre-heat temperatures up to 240°C, after which point, thermal transfer becomes more significant and a greater dose is recovered than was administered. For sample 154-MGJ-5-1, consistent D_e values (within errors) are observed when pre-heats of 160°C to 240°C are applied, but the administered dose is not fully recovered at higher temperatures and this may be attributable to thermal depletion of the OSL signal at

higher temperatures (e.g. Kim et al., 2009). Thermal depletion may also be significant in the D_e underestimation at a pre-heat of 300°C for sample 153-MAR2-13B. For all eight samples, a plateau in recovered D_e values exists when using pre-heat temperatures between 180°C and 220°C (figure 4.20), suggesting that any pre-heat temperature within this range is appropriate for use in the SAR protocol. D_e values following pre-heats of 220°C are typically the most consistent with unity, and therefore, this pre-heat temperature has been adopted for use for all samples in this study.

4.8.2.1.3 Dose recovery test

The dose recovery test is a powerful internal check for assessing the appropriateness of the SAR measurement protocol. According to Wintle and Murray (2006), the greatest change in luminescence sensitivity occurs after a sample is first heated and the dose recovery allows an assessment of the appropriateness of the first sensitivity measurement (T_n) to the preceding measurement of the natural signal (L_n) (Wintle and Murray, 2006). This test involves bleaching the natural signal from a sample, administering a known laboratory dose, and applying the SAR protocol, treating the administered dose as the natural signal and testing the ability of the SAR protocol to recover the known dose. This is a stringent test because the known dose is applied prior to thermal treatment and thus any sensitivity change. However it should be noted that the laboratory dose is delivered a factor of ~10^9 faster than in nature (Murray and Olley, 2002).

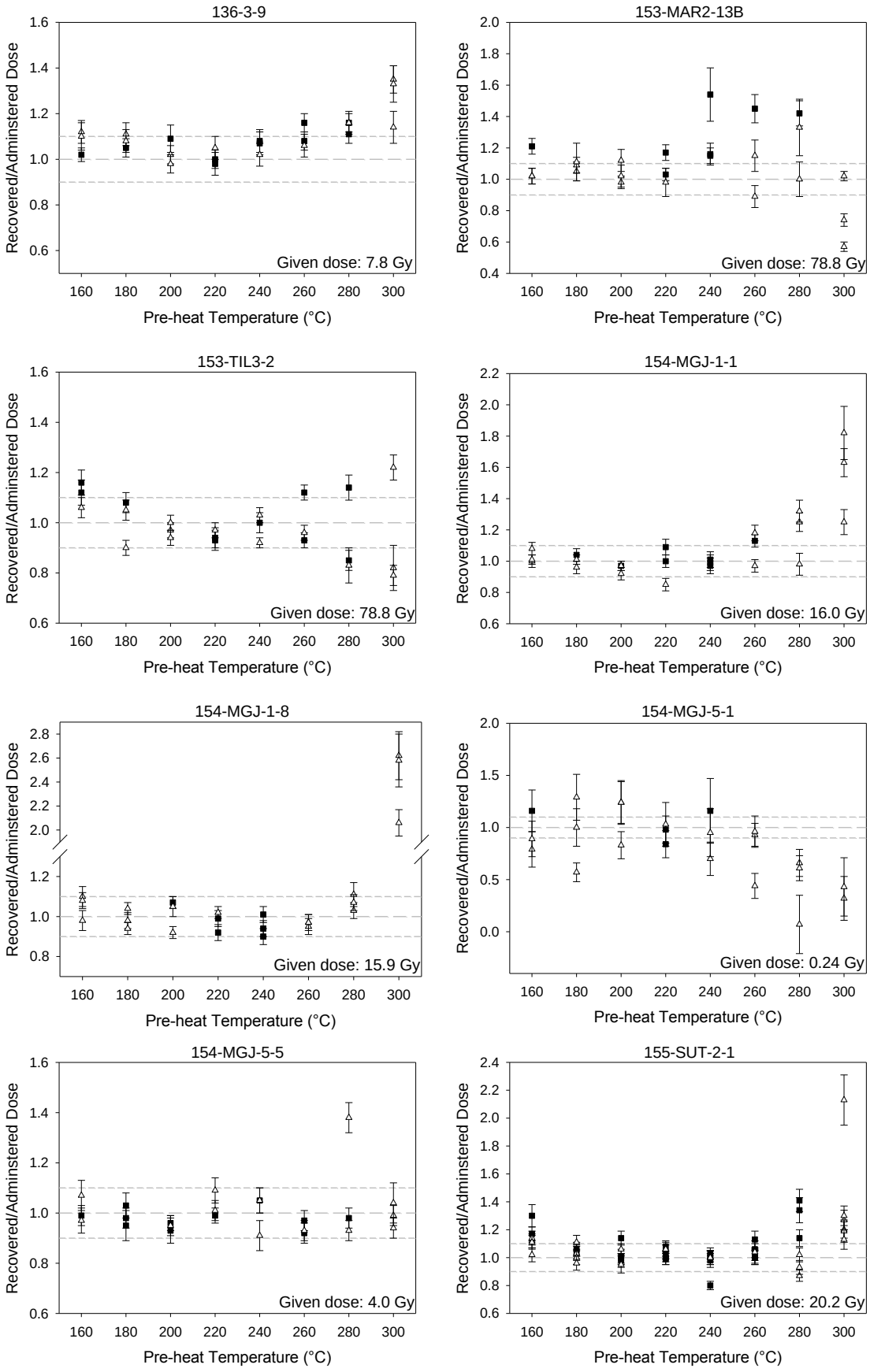

Figure 4.20: Combined dose recovery and pre-heat plateau tests. Filled symbols indicate aliquots that passed all rejection criteria and open symbols, aliquots that failed one or more rejection criteria (see appendix B). The dashed lines represent unity between the recovered and administered dose and ±10%.

For the dose recovery tests carried out in this study, the natural signal from the medium sized aliquots of sample were bleached using two stimulations with blue LEDs for 100 s at room temperature, with a 10,000 s pause between the two stimulations to allow time for any charge transferred into the 110°C trap to thermally decay (Murray and Wintle, 2003). The aliquots were then irradiated with a known dose, chosen to be close to the expected natural dose of the sample. A SAR protocol was run, using a pre-heat of 220°C for 10 s, a cut-heat of 160°C followed by immediate cooling and with OSL measured for 40 s at a temperature of 125°C. All data was screened using the rejection criteria outlined in section 6.3.3 and the ratio of the mean recovered dose to the administered dose was calculated.

The ratio between the administered and recovered dose should be close to unity if the SAR protocol is working correctly (Wintle and Murray, 2006). Figure 4.21 shows the results from dose recovery tests on 11 samples in the study. All samples are within 10% of unity (taking uncertainties into account), and the majority of samples are within 5% of unity, indicating that the SAR protocol is successfully recovering the administered dose. The given doses and number of aliquots used in each of the dose recovery tests is given in appendix C.

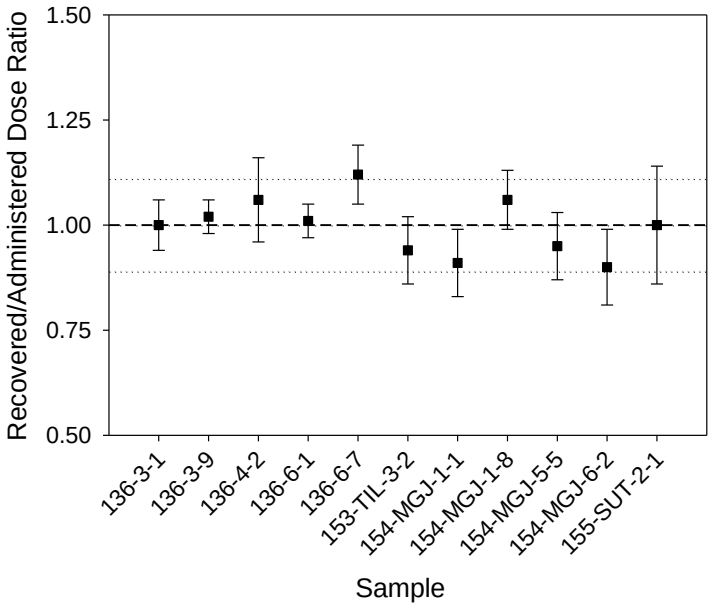

Figure 4.21: The mean ratio between the administered dose and dose recovered using the SAR protocol for the dose recovery tests carried out on 11 samples. The ratios have been calculated from aliquots which passed the rejection criteria. Unity is shown by the dashed line and ±10% by the dotted lines. The given doses are listed in appendix B.

4.8.3 The SAR protocol used in this study

The SAR protocol used in this study is summarised in table 4.8. A pre-heat of 220°C, held for 10 s was used for all dating measurement following the pre-heat plateau tests (section 4.8.2.1.2). A less severe cut-heat of 160°C followed by immediate cooling was used for all samples prior to the measurement of the test dose. All CW-OSL measurements were performed at an elevated temperature of 125°C (Murray and Wintle, 1998) to prevent the re-trapping of charge in the trap corresponding to the 110°C TL peak. Typically, the natural signal was measured, followed by the measurement of 5 – 7 regenerative doses to characterise the form of the dose response curve, before the repeat measurement of 0 Gy dose (to check for recuperation), and the repeat measurement twice of the first non-zero dose to check the recycling ratio and OSL IR depletion ratio (the rejection criteria used are discussed fully in section 6.3.3).

Table 4.8: The SAR protocol used in this study (after Murray and Wintle, 2000; Wintle and Murray, 2006).

Step	Treatment	Observed
1	Regenerative dose	
2	Pre-heat (220°C[a] for 10 s)	
3	CW-OSL stimulation (for 40 s at 125°C)	Ln[b], Lx
4	Test dose	
5	Cut-heat[b] (160°C for 0 s)	
6	CW-OSL stimulation (for 40 s at 125°C)	Tn[b], Tx

[a] All samples were given a pre-heat of 220°C following the pre-heat plateau tests outlined in section 4.8.2.1.2.

[b] The OSL signals from the natural dose and associated test dose are referred to as L_n and T_n. Subsequent regenerative doses and their test doses are replied to as L_x and T_x.

4.9 Conclusions

This chapter has outlined the treatment of samples for OSL dating, including the chemical and mechanical treatment in the laboratory to yield pure quartz. An investigation into whether a signal can be measured from clean, blank discs was undertaken, and the impact of using blank discs emitting a luminescence signal was investigated and shown to lead to dramatic D_e underestimation. Based on this work, new aluminium discs were used for measurements in this study and a more

rigorous disc cleaning protocol used. The technical specifications of the Risø readers used for luminescence measurements have been discussed, including methods for both the relative and absolute measurement of the stimulation power of the blue LED units in the Risø reader. Absolute measurement of the stimulation power with a power meter are shown to be precise, although produce results which are lower than the value provided by the manufacturers at the time of purchase. It is suggested that the power of the LEDs may change over time, however further work over a longer time period is required to investigate this further. In subsequent work, unless otherwise stated, the stimulation powers measured using the power meter are used.

The SAR protocol of Murray and Wintle (2000) and Wintle and Murray (2006) used for D_e determination has been outlined in detail. Dose recovery tests have been applied to multiple samples to check that the SAR protocol can successfully recover an administered laboratory dose and combined dose recovery and pre-heat plateau tests have been run to ascertain the most appropriate pre-heat temperature that should be applied. It is concluded that the SAR protocol can successfully recover known doses from this suite of samples when using a pre-heat temperature of 220°C and this protocol is used for dating in this project. The application of dose recovery and pre-heat plateau tests, along with the application of rejection criteria such as the recycling ratio, allows some of the fundamental assumptions made when using the SAR protocol to be checked. Another assumption made when using the SAR protocol is that the OSL signal is dominated by the fast component, and an objective measure for assessing the dominance of the fast component using the CW-OSL signal is discussed in the next chapter.

5. The fast ratio: testing the dominance of the fast component in the quartz OSL signal

5.1 Introduction

The quartz OSL signal has been shown to consist of a number of discrete components (e.g. Smith and Rhodes, 1994; Bailey et al., 1997; Jain et al., 2003; Singarayer and Bailey, 2003). Each of these components has unique thermal and optical properties, and it is the fast component which is considered most suitable for dating using the SAR protocol (Wintle and Murray, 2006). For signals where the initial part of the OSL signal is not dominated by the fast component, using the SAR protocol for equivalent dose (D_e) determination may result in inaccurate results. It is therefore important that the relative contribution of components within OSL signals used for dating be considered. The fast ratio is a ratio that provides a quantitative assessment of the dominance of the fast component in the initial part of the continuous wave OSL signal, and can be easily and routinely applied as a screening criterion for OSL signals used for dating. In this chapter, the development of the fast ratio (Durcan and Duller, 2011) is outlined and the application of the fast ratio as a rejection criterion is discussed.

5.2 The components of the quartz OSL signal

The quartz OSL signal decays monotonically under a constant stimulation power (figure 5.1a) but can not be fitted with a single exponential decay. Assuming first order kinetics (e.g. Chen and McKeever, 1997), this suggests that signals from a number of traps make up the composite OSL signal. Smith and Rhodes (1994) were the first to fit the continuous wave (CW-) OSL signal with the sum of exponentials, and these components were subsequently termed ‘fast’, ‘medium’ and ‘slow’ by Bailey et al. (1997), based on the rate of charge eviction of each component (figure 5.2). Bulur (2000) determined that each quartz OSL component could be mathematically described by:

$$L_{(t)} = n_0 b \exp(-bt) \qquad \text{(Equation 5.1)}$$

where $L_{(t)}$ is the luminescence intensity as a function of stimulation time t (s), n_0 is the initial trapped charge population, b is the de-trapping probability, where $b = \sigma I_0$, σ is the photo ionisation cross-section (cm^2) and I_0 is the light intensity (in photons $s^{-1}.cm^{-2}$). This equation allows the physical parameters of each OSL component to be defined.

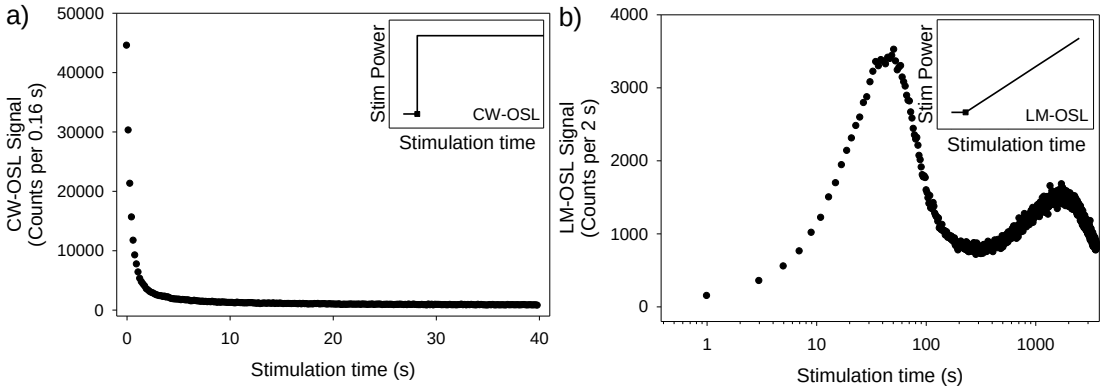

Figure 5.1: The OSL signal from a large aliquot of sample 136-4-1 after a 50 Gy regenerative dose, using a) constant wave (CW-) and b) linearly modulated (LM-) stimulation power (note the logarithmic scale on the x-axis). Inset, a schematic representation of each stimulation mode, with the filled symbol marking the LED switch-on time.

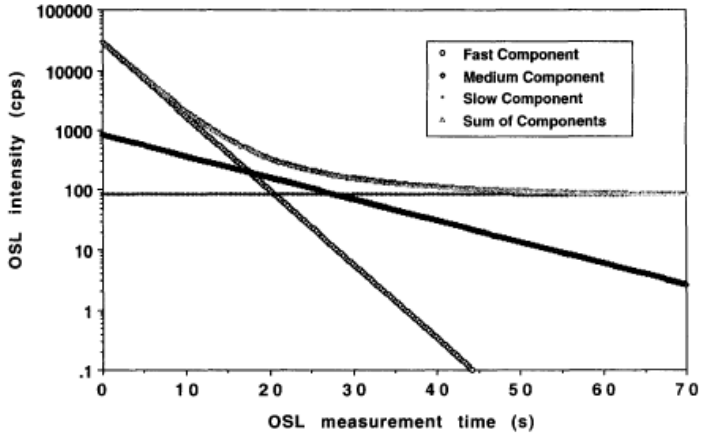

Figure 5.2: The CW-OSL signal from Moroccan Chaperon Rouge quartz (measured using green light with a wavelength of 514 nm). Three exponential functions have been fitted. From Bailey et al. (1997).

Bulur (1996) was the first to measure the OSL signal using linearly increasing power (figure 5.1b inset). By measuring the linearly modulated (LM-) OSL signal, the charge from each component is evicted relative to excitation power (figure 5.1b), with the

easier to bleach components being depleted after relatively less energy. Where the OSL signal has been measured using linearly modulated stimulation power, each component can be described by the equation (Bulur, 1996):

$$L_{(t)} = n_0 \frac{b}{P} t \exp\left(\frac{bt^2}{2P}\right) \qquad \text{(Equation 5.2)}$$

where $L_{(t)}$ is the luminescence intensity as a function of stimulation time t (s), n_0 is the initial trapped charge population, b is the de-trapping probability ($b = \sigma I_0$), I_0 is the maximum light intensity (photons $s^{-1}.cm^{-2}$) and P is the total stimulation time (s).

Bulur et al. (2000) found that the slow component of Bailey et al. (1997) was not one unique component, but appeared to contain signal from at least two slow components and following on from this work, Singarayer and Bailey (2003) identified five quartz OSL components (including three slow components; table 5.1). In 2003, Choi et al. identified an ultrafast component from Korean quartz and Jain et al. (2003) suggested that up to seven components (the ultrafast, fast, medium, slow1-4; table 5.1) could be present in sedimentary quartz. The combination of components present seems to vary between samples, and can be determined using curve deconvolution of the CW- or LM-OSL signal. Table 5.1 lists the components and respective photo ionisation cross-sections identified by Jain et al. (2003) and Singarayer and Bailey (2003).

Table 5.1: Absolute (cm^2) and relative ($\sigma:\sigma_F$) photo ionisation cross-sections (σ) for each component, calculated by Jain et al. (2003) and Singarayer and Bailey (2003).

Jain et al. (2003)			**Singarayer and Bailey (2003)**		
Component	**σ (cm^2)**	**Relative σ**	**Component**	**σ (cm^2)**	**Relative σ**
Ultrafast	2.90×10^{-16}	13			
Fast	$2.32 \pm 0.16 \times 10^{-17}$	1	Fast	$2.5 \pm 0.3 \times 10^{-17}$	1
Medium	$5.59 \pm 0.44 \times 10^{-18}$	0.2	Medium	$5.9 \pm 2.0 \times 10^{-18}$	0.2
Slow1	$1.33 \pm 0.26 \times 10^{-18}$	0.06	-	-	-
Slow2	$2.08 \pm 0.46 \times 10^{-19}$	0.01	Slow 1	$2.1 \pm 0.5 \times 10^{-19}$	0.01
Slow3	$2.06 \pm 0.16 \times 10^{-20}$	0.001	Slow 2	$1.2 \pm 0.2 \times 10^{-20}$	0.001
Slow4	$2.76 \pm 0.17 \times 10^{-21}$	0.0001	Slow 3	$1.9 \pm 2.9 \times 10^{-21}$	0.0001

5.2.1 The importance of the fast component for OSL dating

Each of the quartz OSL components has unique thermal and optical properties (Singarayer and Bailey, 2003) and the fast component is considered preferable for dating for a number of reasons (Jain et al., 2005). The signal from the fast component is considered stable and has a mean lifetime of up to 850 Ma at 20°C (Wintle and Murray, 1998). It also has relatively low recuperation in comparison to the other components (Jain et al., 2003), and the integration of signal from components with higher recuperation when calculating D_e values can result in D_e underestimation (Watanuki, 2002; Jain et al., 2003). Some of the other components (e.g. the slow3 component of Jain et al., 2003) have lower thermal stabilities, and also lower dose saturation points (Singarayer and Bailey, 2003). Different OSL components may also sensitise at different rates (Jain et al., 2003). It has therefore been concluded that the OSL signal originating from the fast component is usually preferable for dating, given its stable thermal properties (e.g. Singarayer and Bailey, 2003) and because it is readily bleachable in nature. The SAR protocol was also developed (Murray and Wintle, 2000) and tested extensively (e.g. Murray and Olley, 2002) on samples with CW-OSL signals dominated by the fast component in the initial part of the signal, and it is generally the case that OSL signals dominated by the fast component provide accurate age estimates (Bailey, 2010).

The CW-OSL signal is made up of signals originating from the various components present within a sample and it is not possible to separate these components under normal measurement conditions (Wintle and Murray, 2006). Whilst the initial part of the CW-OSL signal is usually dominated by the fast component (Jain et al., 2005), there will be a contribution from the other, less light sensitive signals (Jain et al., 2003) when a constant wave stimulation power is used (Li and Li, 2006a). This is seen in figure 4.10, where the simulated CW-OSL signal after 0.8 s of stimulation is dominated by signal originating from the fast component, but contains a contribution from the medium component and a small contribution from the slow component.

5.2.2 Utilising the signal from the fast component

The dominance of the fast component within a signal is preferred for OSL dating using the SAR protocol (Wintle and Murray, 2006), and it is generally accepted that the most reliable D_e estimates are determined from samples which are dominated by the fast component. There are a number of techniques which have been developed to isolate the signal from the fast component and/or to optimise the contribution from the fast component. Some of the most commonly applied techniques are discussed below, however these methods are often complex and time-consuming to apply to a large number of signals (Durcan and Duller, 2011).

5.2.2.1 Curve deconvolution

Both the CW-OSL and LM-OSL signal from quartz can be mathematically deconvolved, using equations 5.1 and 5.2 respectively, to determine the physical parameters of each OSL component. By fitting a sum of exponentials to either a CW- or LM-OSL signal, the de-trapping probability (b) and trapped charge population (n_0) can be derived and the photo ionisation cross-section (σ) of each component can be calculated (appendix D). Choi et al. (2006) provide a comprehensive outline of their protocol for the curve deconvolution of the LM-OSL signals from Kenyan and Australian quartz. Using this approach, the OSL signal from the fast component can be calculated and used for D_e determination. Li and Li (2006b) used curve deconvolution of LM-OSL signals for D_e determination using solely the fast component of quartz and found good agreement with D_e values determined using the SAR protocol applied to the composite CW-OSL signal. Li and Li (2006b) state that the curve deconvolution of LM-OSL signals can be advantageous for quartz samples with a weak fast component or samples which are poorly bleached (e.g. Agersnap-Larsen et al., 2000). However, they note that significant measurement and analysis times are required to undertake this form of data analysis.

Many authors have fitted the CW-OSL signal using curve deconvolution (e.g. Steffen et al., 2009; Pawley et al., 2010) and calculated the equivalent dose from the parameters derived. The measurement time required to make a CW-OSL measurement is significantly shorter than LM-OSL and Wallinga et al. (2008) and Bos and Wallinga (2009) suggest that curve deconvolution of the LM-OSL provides no better separation than of the CW-OSL signal. However, the curve fitting of both the LM- and the CW-OSL signal is time consuming, but more significantly curve fitting is both technically complex, and can introduce errors that are difficult to quantify (e.g. Jain et al., 2003).

5.2.2.2 Fast component isolation using IR stimulation

The quartz OSL signal has been found to respond to IR stimulation at elevated temperatures (e.g. Spooner, 1994; Bailey, 1998) and Singarayer and Bailey (2004) were the first to investigate the response of the individual components to IR stimulation after establishing a dependency of the photo ionisation cross-section on stimulation energy (Singarayer and Bailey, 2003; figure 5.3). Singarayer and Bailey (2004) stimulated quartz with IR at 160°C (chosen to provide sufficient levels of luminescence signal but not invoke sensitivity change in the sample during measurement) and found depletion of the OSL signal with extended IR stimulation times (figure 5.4a). By fitting the LM-OSL curves in figure 5.4a, Singarayer and Bailey (2004) observed that whilst the fast component depleted after ~6 – 8 ks, there was no significant decay in the medium component (e.g. figure 5.4b). They hypothesised that IR stimulation at 160°C is sufficient for the depletion of the fast component, but is below the minimum stimulation threshold energy required to deplete the medium component (e.g. figure 5.3). They therefore suggested the use of elevated temperature IR stimulation as a means of separating the fast and medium quartz OSL components.

Jain et al. (2005) established that the fast component is the only component stimulated by exposure to IR at temperatures between 120°C and 190°C and developed a differential-OSL SAR protocol cycle based upon the standard SAR

protocol of Murray and Wintle (2000). This protocol involves the measurement of the OSL signal using an elevated temperature IR stimulation in between two pulses of blue light stimulation. This protocol was tested on a selection of 'well behaved' (e.g. fast dominated OSL signals) samples and poorly behaved samples (non-fast dominated signals). For the well behaved samples, there was good agreement between the differential-OSL SAR and standard SAR D_e values, with excellent recycling ratios and recuperation was reduced to less than 1% (lower than the standard SAR measurements). For the poorly behaved samples, dose recovery tests carried out using the differential-OSL SAR protocol were consistent with unity, in comparison to the same tests undertaken using the standard SAR protocol, which were between 30 – 40% offset from unity.

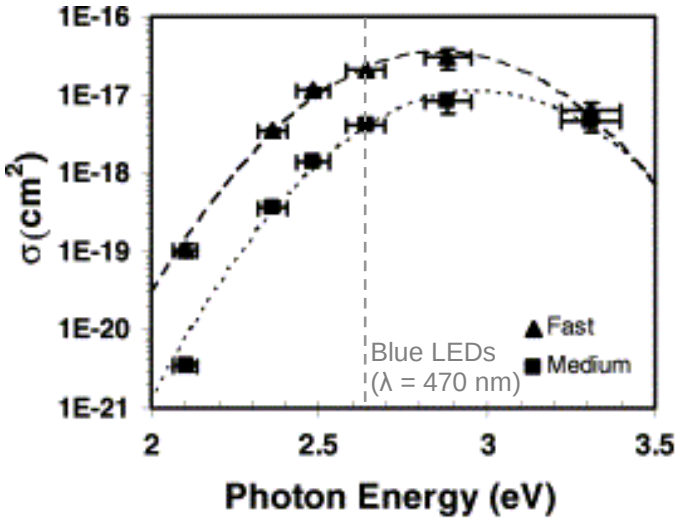

Figure 5.3: The dependency of the photo-ionisation cross-section (σ) on stimulation photon energy (at room temperature). From Singarayer and Bailey (2003). Note, IR stimulation at a wavelength of 880 nm has an energy of 1.41 eV and the photon energy of the blue LEDs used in this study (470 nm) is shown by the dashed line.

The differential-OSL SAR protocol of Jain et al. (2005) is time-consuming, with extended stimulation times required to deplete the fast component. Full depletion of the fast component using IR stimulation (with a power of 400 $mW.cm^{-2}$) takes approximately 6,000 s, whereas stimulation under blue light (470 nm) with a power of 36 $mW.cm^{-2}$ results in near complete depletion of the fast component in ~2 s (Bailey, 2010). This is due to the strong wavelength dependence of the photo ionisation cross-sections (figure 5.3), which results in the impracticably long stimulation times required to evict the fast component charge using IR. To address

this, Bailey (2010) proposed the use of a relatively short IR stimulation (~20 s) to assess only part of the quartz IRSL decay. The IRSL signal of quartz at 160°C originates from the trap associated with the fast component and will therefore decay exponentially (Singarayer and Bailey, 2004; Bailey, 2010). Bailey (2010) suggests that if this decay rate is known, only a portion of the IRSL signal needs to be measured, and from this, the full IRSL signal can be reconstructed and used for D_e determination.

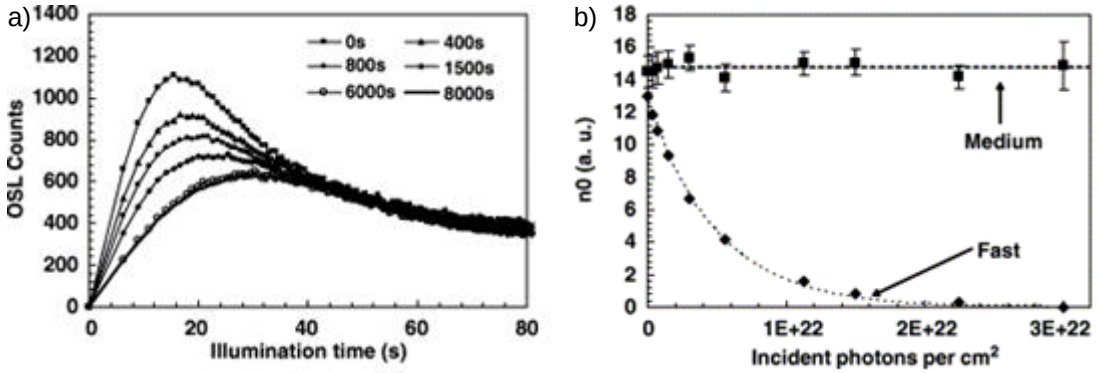

Figure 5.4: a) Blue light stimulated pseudo LM-OSL curves following IR stimulation at 160°C for various periods. b) The curve fitting of the fast and medium components from the signals in a). Both figures are from Singarayer and Bailey (2004).

The use of the IR stimulation for D_e determination makes the protocols of Jain et al. (2005) and Bailey (2010) highly sensitive to the presence of feldspar grains and Bailey (2010) recommends that for samples where feldspar can not be chemically removed, these techniques are not appropriate and curve fitting should be used to separate the components. The quartz IRSL signal is not very bright and for samples where the OSL signal is dim, these methods may not be appropriate for D_e determination. Whilst these studies provide successful techniques for component separation in some samples, it is not feasible to apply them routinely for D_e determination.

5.2.2.3 Early background analysis

To increase the relative contribution of the fast component within a CW-OSL quartz signal, Ballarini et al. (2007) applied the early background (EBG) subtraction

method, where the background signal is taken immediately after the initial signal integration interval, instead of later in the decay curve (figure 5.5). This approach is designed to maximise the contribution of the fast component by subtracting the contribution from the medium component, as well as the slow components and background. Ballarini et al. (2007) report that using the EBG method, the contribution of the medium and slow components to the composite signal are reduced by 83% and 99% respectively (in comparison to taking a late background). However, the net signal used in D_e calculation is also lower, resulting in reduced D_e precision. Cunningham and Wallinga (2010) tested further the use of integration intervals to maximise the contribution from the fast component, suggesting that the background signal should be taken immediately adjacent to the signal integration interval and should be 2.5 times the length of the initial interval. For four samples, Cunningham and Wallinga (2010) compare ages calculated using an EBG and late background (LBG) against independent age control. They suggest that for three samples, the application of the EBG results in D_e values which are more comparable with independent age control and have less dispersed dose distributions. For the fourth sample, the EBG and LBG D_e values are comparable. The focus of this study was young samples and Cunningham and Wallinga (2010) suggest that the application of the EBG to older samples will aid in the removal of unstable components (e.g. the medium or slow3 component of Jain et al., 2003), which may result in age underestimation.

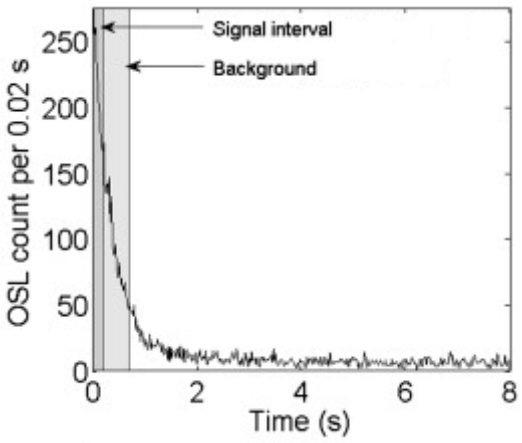

Figure 5.5: Schematic view of the application of an early background (modified from Cunningham and Wallinga, 2010).

Whilst the EBG method has the potential to improve the accuracy of OSL age estimates as Cunningham and Wallinga (2010) suggest, the application of an EBG significantly reduces the amount of signal used for D_e calculation and can impact upon the uncertainty associated with counting statistics and therefore the precision of D_e derivations. Whilst the aim of this treatment is to maximise the contribution of the fast component, the presence and relative dominance of the fast component within a signal is not verified.

5.2.3 Use of non-fast dominated OSL signals for dating

A dominant fast component is not necessarily present in all sedimentary quartz and it has been suggested that the presence of the fast component may be related to sedimentary history as opposed to provenance (Tsukamoto et al., 2011). Whilst the fast component is preferable for OSL dating, many authors have utilised alternative components for D_e determination. The slow 3 component (of Singarayer and Bailey, 2003; table 5.1) was used for age calculation by Rhodes et al. (2006) because it has a much higher dose saturation point than the fast component (Singarayer et al., 2000), and therefore has the potential to date much further back in time. The OSL signal from this component bleaches much less rapidly in nature than the fast component and this is a potential barrier to its use in extending the age range of quartz OSL dating. Rhodes et al. (2006) use this component for the dating of aeolian sediments from Morocco and see good agreement between the component resolved D_e calculations from the fast and slow 3 component, as well as the composite OSL signal. However, the uncertainties associated with the slow 3 D_e values are substantially greater than the fast and composite D_e values. The calculated ages are in stratigraphic order, but lack precision, possibly due to the difficulty in isolating this signal (Wintle, 2010), however, dating using the slow 3 component offers the potential to calculate D_e values far beyond the range of the fast component.

The medium component has also been used for D_e determination in some studies. Li and Li (2006a) deplete the fast component using an elevated temperature IR

stimulation for 7,000 s before measuring the OSL from the medium and slow components with blue light stimulation. The D_e values calculated from the medium component are systematically lower than those calculated using the signal from the fast component and Li and Li (2006a) suggest that this is due to the thermal instability of the medium in the samples they analyse. Solongo et al. (2006) also use elevated temperature IR stimulation to isolate the signals from the fast and medium components. In their study, D_e values measured from the fast and medium component are comparable, although the D_e values from the medium component were typically more scattered. Solongo et al. (2006) believe that their protocol provides a method for D_e estimation in samples that do not have a dominant fast component, but that the thermal instability of their medium component complicates D_e determination using this component.

5.3 The fast ratio

One of the underlying assumptions when using the SAR protocol for quartz OSL dating is that the OSL signal has a dominant fast component (Wintle and Murray, 2006). Whilst the SAR protocol incorporates a number of internal checks to ensure the protocol can accurately measure the luminescence signal (section 4.8.2.1), the dominance of the fast component is often only qualitatively assessed from a CW-OSL signal (Durcan and Duller, 2011). As discussed above, there are a number of ways in which the signal from the fast component can be isolated or maximised, but these can be technically complex, and introduce sources of error that are difficult to quantify and cannot be routinely applied to a large number of aliquots. Integration of the OSL signal from the initial part of the decay curve is designed to maximise the contribution from the fast component in quartz, but it will inevitably include signals from the medium and some slower components. Therefore, in the majority of studies using the OSL signal from quartz to date sediments, complex approaches such as those described in section 5.2.2 are not used and the dominance of the fast component is assumed but rarely verified (Durcan and Duller, 2011). A particular problem can occur where the medium component makes a significant contribution to the initial part of the decay curve used for dating quartz (e.g. Steffen et al. 2009),

because a number of studies have indicated that the medium component may have a much shorter lifetime than the fast component (e.g. Li and Li, 2006b; Steffen et al., 2009).

A ratio, termed the fast ratio, has been developed to provide a simple numerical measure for assessing the dominance of the fast component in the initial part of a CW-OSL signal (Durcan and Duller, 2011). This measure characterises the OSL signal measured under constant-wave stimulation and could be used to inform further analysis of the signal, such as the most appropriate integration intervals to use for dating or as a rejection criterion that can be applied as part of a suite of checks routinely applied to CW-OSL signals used for dating. The measure is a ratio based upon one devised by Madsen et al. (2009), where the photon count rate over a period of time dominated by the fast component (minus the background signal) was divided by the photon count rate of a time period dominated by the medium component (again with the background subtracted) (figure 5.6). However, Madsen et al. (2009) did not provide any clear rationale for their choice of integration intervals, nor how they selected the threshold value that they chose as a criterion for accepting an aliquot. Their approach cannot therefore be easily applied to other studies. The fast ratio developed by Durcan and Duller (2011) and presented here takes into account the stimulation power of the measurement equipment used and the photo ionisation cross-sections of the quartz OSL components. This ensures that results are comparable with measurements made on other aliquots (and samples) and/or made with other measurement equipment. To achieve this, it is first necessary to determine whether photo ionisation cross-section (σ) values are consistent between quartz from different samples. In section 5.3.1, this is explored by measuring the σ values of quartz from a variety of geographic locations, and based upon this, the integration intervals required to characterise the fast and medium components, and the background are considered. In section 5.3.2, these integrals are defined, and the relationship between the fast ratio and the relative dominance of the fast component within a signal is investigated.

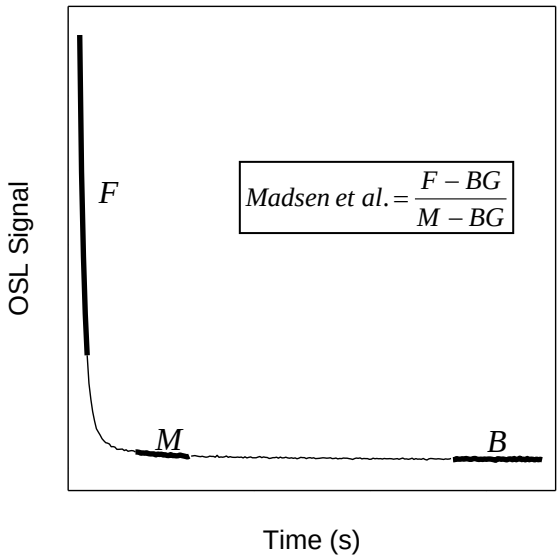

Figure 5.6: A schematic view of the ratio presented by Madsen et al. (2009). F refers to the period selected to represent the fast component, M, the medium component, and BG, the background. From Durcan and Duller (2011).

5.3.1 Measuring the photo ionisation cross-section

The photo ionisation cross-section (σ) is one of the most fundamental parameters relating to OSL (Bøtter-Jensen et al., 2003b), governing the stability of a particular trap during optical stimulation and therefore the probability of charge being evicted (Bøtter-Jensen et al., 2003b). The purpose of the fast ratio is to provide a rapid, easily applicable method of assessing whether the fast component is dominant in a signal measured with continuous wave stimulation, without prior knowledge of the sample specific σ parameters. A number of studies have published absolute and relative values for σ (e.g. table 5.1) and if σ values can be considered consistent, a set of standard σ values could be used for the calculation of the fast ratio. To test this, a number of samples were measured using LM-OSL, and from this, the σ values calculated by deconvolution.

5.3.1.1 Checking the linearity of the stimulation power

Measurement of the LM-OSL signal is based on the assumption that stimulation power is increased linearly during measurement, and the mathematics of Bulur (1996) relies upon this assumption. Choi et al. (2006) tested the linearity of power

on their measurement equipment by replacing the U340 density filters used to optimise the quartz luminescence signal (section 4.6) with an opaque disc containing a pinhole in order to allow a small proportion of the stimulating light to reach the PM tube. Three neutral density filters, ND3.0, ND1.0 and ND1.0, were then fitted to attenuate the signal and ensure the PM tube was not blinded during measurement and the reflection from a blank aluminium disc was measured to assess the intensity of the blue LEDs during LM-OSL measurement. Using the same experimental conditions, the linearity of the blue LEDs on Risø 4 was checked prior to signal measurement and analysis. Figure 5.7 shows the LM-OSL signal measured from a blank disc as blue LED power is increased linearly between 0 and 90% over the 3600 s measurement period on Risø 4. Power was increased in increments of 0.05% per 2 s to a maximum power of 90% (30.6 $mW.cm^{-2}$) to duplicate sample measurement conditions (section 5.3.1.2). The data can be fitted with a linear function, giving an r^2 value of 0.998, and a slightly better fit is seen when fitting using a quadratic function (r^2 = 0.999). There are some signs of slight non-linearity in this data, however all measurements were carried out on the same measurement equipment, which means that any uncertainty will be systematic throughout the OSL measurements made. It is likely that any uncertainty introduced will be small, and photo ionisation cross-sections calculated in this study (section 5.3.1.4) are consistent with published data (table 5.1).

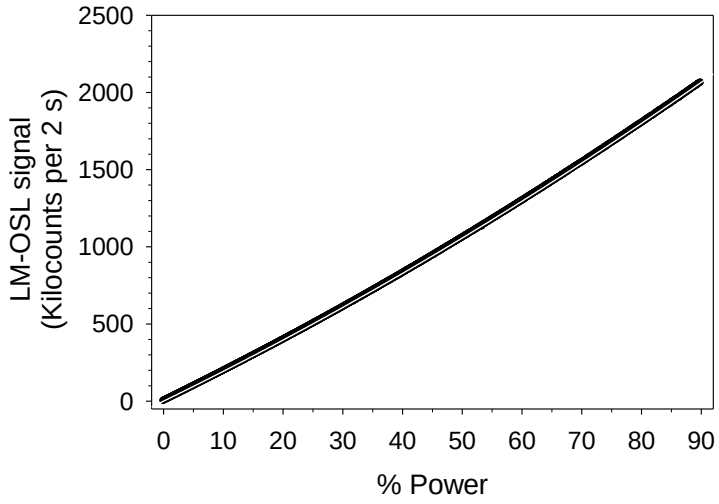

Figure 5.7: The LM-OSL signal measured from a blank aluminium disc through an opaque disc with a pinhole and neutral density filters ND3.0, ND1.0 and ND1.0. LM-OSL was measured for 3600 s and LED power was increased linearly between 0 and 90% power on Risø 4. The fitted quadratic function (r^2 = 0.999) is shown.

5.3.1.2 Sample measurement

Ten samples were chosen for analysis and 2 to 3 aliquots of each quartz sample were measured. Samples were chosen to reflect a variety of depositional settings, to be geographically dispersed (table 5.2) and to have a mixture of fast and non-fast component dominated OSL signals. All samples were prepared in subdued red light conditions in the ALRL, using the coarse grain sediment preparation procedure described in figure 4.1. Large aliquots (~8 mm diameter) of each sample were prepared, containing between ~1,000 and 10,000 grains (depending on grain size) (figure 4.7; Duller, 2008b), except for samples WIDG8, 135/NL19 and TNE9726, where medium aliquots (~5 mm diameter and ~500 – 1,000 grains; Duller, 2008b) were measured (table 5.2).

Table 5.2: Summary of the quartz samples measured. Medium aliquots are 5mm in diameter and large aliquots are 8 mm in diameter. From Durcan and Duller (2011).

Location	Sample name	Aliquot size	Grain size (μm)	Aliquots[a]	Depositional context
Australia	WIDG8	Medium	90 – 125	2	Desert sand
Cal. Quartz	CalQtz	Large	180 – 250	2	Annealed sediment
Cyprus	108/AGN2	Large	180 – 212	2	Coastal, beach sand
Cyprus	109/MAZ2	Large	180 – 212	2	Coastal, beach sand
Pakistan	136-3-9	Large	90 – 125	2	Fluvial, palaeochannel sand
Pakistan	136-4-1	Large	90 – 125	2	Fluvial, palaeochannel sand
Sudan	135/NL19	Medium	125 – 180	2	Fluvial, palaeochannel sand
Tasmania	TNE9726	Medium	150 – 250	3	Aeolian dune sand
UK	78/NO4	Large	180 – 212	2	Glaciofluvial outwash
USA	84/LSM6	Large	180 – 212	3	Beach barrier overwash sand

[a] number of aliquots measured

All measurements were made using Risø 4 (see table 4.1 for reader specification) using blue LEDs (470 Δ 20 nm) with a stimulation power of 30.6 $mW.cm^{-2}$ (at 90% power) to stimulate the OSL signal. Each aliquot was bleached at 280°C for 100 s prior to measurement to remove any residual signal. Samples were then irradiated with ~50 Gy, pre-heated to 220°C for 10 s and the luminescence signal measured. LM-OSL measurements were made at a temperature of 125°C for a period of 3600 s (photon counts measured every 2 s), with the stimulation power linearly increased from 0 $mW.cm^{-2}$ to 30.6 $mW.cm^{-2}$ (0 – 90% power). The optical bleach and pre-heat were then repeated and the CW-OSL signal measured using a constant power of

30.6 mW.cm^{-2} (90% power) for 40 s (photon counts recorded every 0.16 s) at 125°C. Prior to curve deconvolution, the recorded dark counts were subtracted from the LM-OSL signal.

5.3.1.3 LM-OSL curve deconvolution

Curve deconvolution of the LM-OSL signal was carried out using the software package SigmaPlot version 7.0, following the protocol outlined by Choi et al. (2006). This protocol uses the equation of Bulur (1996) (equation 5.2) to define the LM-OSL curve. For curve deconvolution, the initial value of n_N for all components was set to 10^5, n_N and b_N were constrained to be greater than 0 and the maximum number of iterations and step size were set to 10^5 and 10^2 (Choi et al., 2006). Where appropriate, up to six components were fitted, and the best mathematical fit was selected following the approach of Choi et al. (2006), which seeks to minimise the residuals relating to the fit and maximise the associated r^2 value (appendix D). Figure 5.8 shows an example of the measured LM-OSL curve of sample 136-4-1, along with the calculated components and residuals.

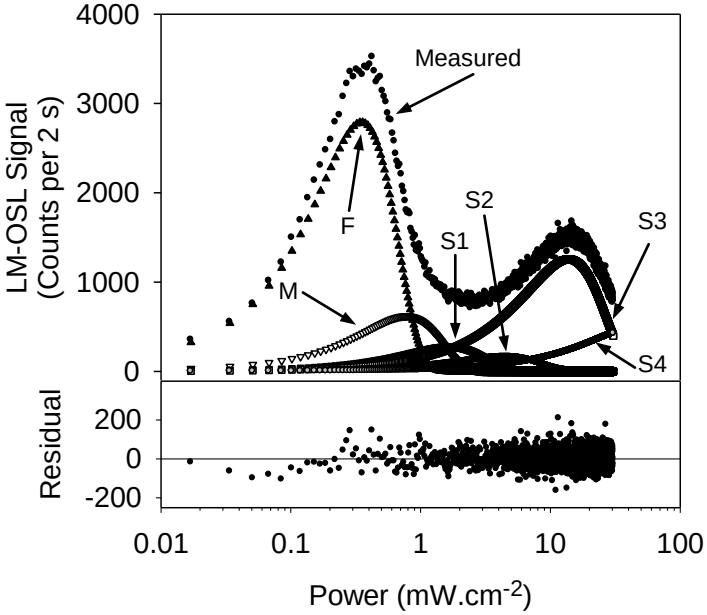

Figure 5.8: The LM-OSL signal of sample 136-4-1, the six components fitted by curve deconvolution and the residual between the measured and fitted data. From Durcan and Duller (2011).

5.3.1.4 The consistency of the photo ionisation cross-sections of quartz from a variety of geographic locations

Figure 5.9 shows the σ values for the fast (F), medium (M), slow1 (S1) and slow2 (S2) components of each aliquot measured. The mean values for each of these components are shown, along with the values of Jain et al. (2003) and Singarayer and Bailey (2003) reported in table 5.1. The observed σ values (figure 5.9) for the fast component are consistent between aliquots, and the mean value (σ_F = 2.60 ± 0.06 x 10^{-17} cm^2) calculated in this study is similar to those obtained in the other two studies (table 5.1). There is a little more variability in the cross-sections of the medium component (mean σ_M = 4.28 ± 0.35 x 10^{-18} cm^2) and intra-sample variability becomes more apparent when observing cross-sections of the slower components. The relative standard errors of the mean σ values vary between 2 and 20% (table 5.3) (with larger relative standard errors tending to be associated with the slower components) and this level of uncertainty is in line with that observed by Jain et al. (2003). One explanation Jain et al. (2003) propose for this variance is a difference in the average opacity of quartz grains in different samples, which would alter the light intensity delivered to the sample. However, if this were the case, each component within a sample would be expected to be equally affected, and the relative standard errors to be more similar. It is also possible that the LM-OSL measurement period of 3600 s (equivalent to 55 $J.cm^{-2}$ of energy), is only capturing the initial parts of the slow components, making it more difficult to accurately calculate their physical parameters (Singarayer and Bailey, 2003). In table 5.3, the relative cross-sections (where σ is normalised to σ_F) are shown, and these relative σ values compare well with the published values of Jain et al. (2003) and Singarayer and Bailey (2003) shown in table 5.1. It is therefore concluded that the photo ionisation cross-sections of the fast and medium components in sedimentary quartz can be considered consistent. The mean σ_F and σ_M from all aliquots measured in this study (table 5.3) have therefore been adopted for use in the calculation of the fast ratio.

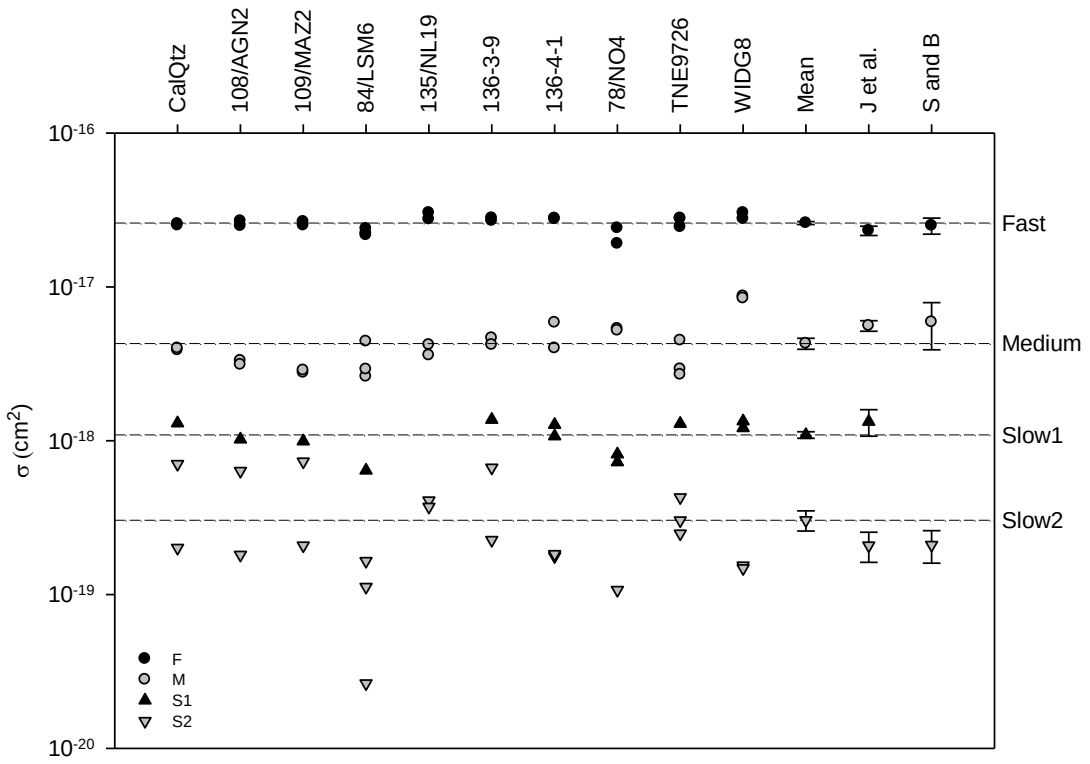

Figure 5.9: Photo ionisation cross-sections for each of the aliquots measured, as well as the mean values of Jain et al. (2003) (J et al. on the x-axis) and Singarayer and Bailey (2003) (S and B). Errors shown for the mean values are the standard errors. From Durcan and Duller (2011).

Table 5.3: Absolute (cm^2) and relative ($\sigma:\sigma_F$) photo ionisation cross-sections calculated by Durcan and Duller (2011) and in this study (mean and standard deviation).

Component	σ cm^2	Relative σ
Fast	$2.60 \pm 0.06 \times 10^{-17}$	1
Medium	$4.28 \pm 0.35 \times 10^{-18}$	0.16
Slow1	$1.09 \pm 0.05 \times 10^{-18}$	0.04
Slow2	$3.04 \pm 0.46 \times 10^{-19}$	0.01
Slow3	$3.39 \pm 0.64 \times 10^{-20}$	0.001
Slow4	$9.06 \pm 0.75 \times 10^{-21}$	0.0003

5.3.2 Selecting the points on a CW-OSL curve to use in the fast ratio

In quartz, the rate of optical eviction of charge from a trap is a function of σ and I_0 (equations 5.1 and 5.2; Bulur, 1996; 2000). As I_0 is linearly dependent upon the stimulation power (appendix D), the rate of decay of a quartz OSL signal varies with stimulation power. For the development of the fast ratio, the integration intervals of the fast ratio are defined in energy ($mJ.cm^{-2}$), as opposed to the time intervals used by Madsen et al. (2009), and by making this conversion, the ratio becomes transferrable between different measurement equipment.

5.3.2.1 Defining the points to use for the fast ratio calculation

The emptying of the traps associated with each component does not occur independently (Kuhns et al., 2000), and therefore the points at which the fast and medium components are at their greatest relative dominance are sought for use in the fast ratio. Figure 1 of Li and Li (2006a) plots the relative contribution from the fast, medium and slow components to the CW-OSL signal during stimulation. A similar plot is shown in figure 5.10 using the photo ionisation cross-section values derived in this study (table 5.3). The fast component is dominant during the initial seconds of stimulation, and during this time, the relative contribution from the medium and slow gradually increases. Therefore, the photon count from the first channel of stimulation has been selected to represent the fast component (L_1) in the fast ratio calculation, because the relative contribution from the fast component to the total signal at this point will be at a maximum. In figure 5.10, there is a peak in the relative contribution of the medium component, which occurs at ~100 $mJ.cm^{-2}$. The position of this peak is weakly dependent upon the relative magnitude of the different components ($n_{F,\ M,\ S1...etc}$) (Steffen et al., 2009), but tends to occur when the fast component has been reduced to approximately 1% of its initial signal. Therefore, the point where the fast component has reduced to 1% of its initial signal has been selected to represent the medium component (L_2). In order to improve the reliability with which the background (L_3) is determined, the signal is averaged over a range of channels. To isolate the medium component effectively, L_3 is averaged over the interval where the medium component has been reduced to 1% and 0.1% of its initial signal.

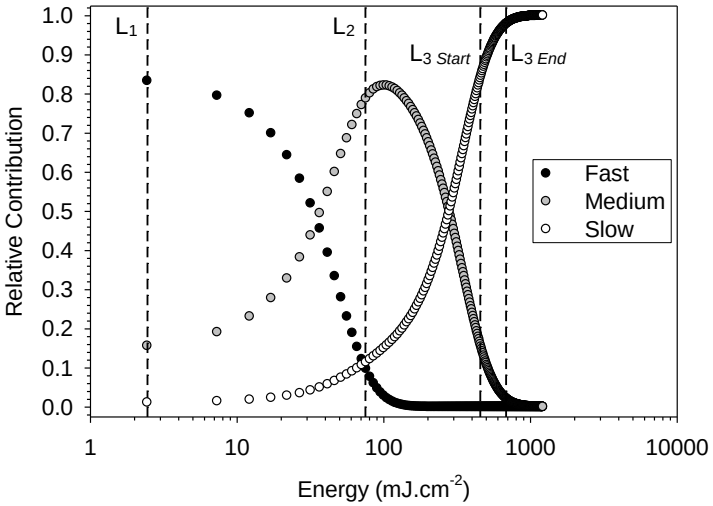

Figure 5.10: The relative proportion of the fast, medium and slow (slow2) components to the composite OSL signal. The proportions have been calculated using the σ values calculated in this study (table 5.3) and setting n_0 to $1x10^6$ for all three components. The position of L_1, L_2 and L_3 are also shown. L_1 is equal to the photon counts from the first channel of stimulation, e.g. when power/time is equal to zero, and is shown in this figure at ~2.4 mJ.cm^{-2}, which is midway through the first channel. From Durcan and Duller (2011).

By rearranging equation 5.2, the energy required to reduce the signal from a particular component (c) to x% of its initial level can be calculated by

$$E = \frac{-\ln\left(\frac{x}{100}\right)}{\sigma_c}\lambda_{470} \qquad \text{(Equation 5.3)}$$

where E is energy (mJ.cm^{-2}), x is the percentage of the initial signal level required (e.g. for 1%, x = 1), σ_c is the photo ionisation cross-section (cm^2) of the component of interest, and λ_{470} is the energy per photon of the blue (470 nm) LEDs used for optical stimulation (mJ per photon) and has a value of 4.23 x 10^{-16} mJ per photon (appendix D). Table 5.4 lists the energy required to reduce the six components (F, M, S1, S2, S3, S4) to a given percentage of their initial signals.

As stated, L_1 is taken from channel one, therefore $t_{(L1)}$ is set as 0 s, and using equation 5.3, L_2 is defined as the photon counts after 75 mJ.cm^{-2}, and L_3 as the mean photon counts between 455 and 683 mJ.cm^{-2} (table 5.4). The equivalent time (s) of L_2 and L_3 can be calculated by:

$$t_{(L1)} = 0 \qquad \text{(Equation 5.4a)}$$

$$t_{(L2)} = \frac{1.95 \times 10^{-15}}{\sigma_F p} \qquad \text{(Equation 5.4b)}$$

$$t_{(Start\ L3)} = \frac{1.95 \times 10^{-15}}{\sigma_M p} \quad t_{(End\ L3)} = \frac{2.92 \times 10^{-15}}{\sigma_M p} \qquad \text{(Equation 5.4c)}$$

where $t_{(L2)}$ is the time (s) where L_2 occurs, $t_{(Start\ L3)}$ and $t_{(End\ L3)}$ is the time period that L_3 should be averaged over, σ_F and σ_M are the photo ionisation cross-sections (cm^2) of the fast and medium component respectively (table 5.3), and p is the stimulation power ($mW.cm^{-2}$).

Therefore, the fast ratio can be calculated by

$$Fast\ ratio = \frac{L_1 - L_3}{L_2 - L_3} \qquad \text{(Equation 5.5)}$$

using the photon counts from the channels containing L_1, L_2 and L_3, as defined above. The error associated with the fast ratio can be calculated using the counting statistics relating to the measurement of the photon count. Using equation 3 of Galbraith (2002) (equation 6.1 in this thesis), the relative standard error for both the numerator and the denominator of the fast ratio can be calculated, and these errors are propagated to provide the standard error associated with the fast ratio calculation.

Table 5.4: Calculation of the energy required to reduce an individual component to x% of its original signal. The photo ionisation cross-sections are those derived in this study (summarised in table 5.3). The stimulation time (s) required (when p = 30.6 mW.cm^{-2}) is also shown for comparative purposes. From Durcan and Duller (2011).

		Comp	F	M	S1	S2	S3	S4
		σ (cm^2)	2.60x10^{-17}	4.28x10^{-18}	1.09x10^{-18}	3.04x10^{-19}	3.39x10^{-20}	9.06x10^{-21}
Percentage reduction of the initial signal	50%	mJ.cm^{-2}	11	69	269	965	8,649	32,362
		s	*0.4*	*2.2*	*8.8*	*31.5*	*283*	*1,058*
	25%	mJ.cm^{-2}	23	137	538	1,929	17,298	64,724
		s	*0.8*	*4.5*	*17.6*	*63.0*	*565*	*2,115*
	10%	mJ.cm^{-2}	38	228	894	3,204	28,731	107,504
		s	*1.2*	*7.4*	*29.2*	*105*	*939*	*3,513*
	5%	mJ.cm^{-2}	49	296	1,163	4,168	37,380	139,867
		s	*1.6*	*9.7*	*38.0*	*136*	*1,222*	*4,571*
	2.5%	mJ.cm^{-2}	60	365	1,432	5,133	46,029	172,229
		s	*2.0*	*11.9*	*46.8*	*168*	*1,504*	*5,628*
	1%	mJ.cm^{-2}	75	455	1,787	6,408	57,463	215,009
		s	*2.5*	*14.9*	*58.4*	*209*	*1,878*	*7,027*
	0.1%	mJ.cm^{-2}	112	683	2,681	9,612	86,194	322,514
		s	*3.7*	*22.3*	*87.6*	*314*	*2,817*	*10,540*

5.3.2.2 The impact of channel width on the fast ratio

The instantaneous photon count rate from the points calculated (e.g. $t_{(L1)}$, $t_{(L2)}$ etc) cannot be used directly because the OSL signal is not measured continuously, but instead is collected over set intervals of power or time, known as channels. The width of the channel is set prior to measurement; in this study the channel width was set to 4.9 mJ.cm^{-2} (equivalent to 0.16 s, when stimulation power (p) is 30.6 mW.cm^{-2}). For calculation of the fast ratio, the photon counts from the channel containing the points discussed above are taken. For example in this study, L_1 is equal to the photon counts between 0.0 and 4.9 mJ.cm^{-2}, and L_2 from 73.4 – 78.3 mJ.cm^{-2}. The channel width is an important variable to consider and will impact upon the calculated value of the fast ratio.

To explore the relationship between channel width and the calculated fast ratio, samples WIDG8 and 136-4-1 were measured with a channel width of 0.5 mJ.cm^{-2} (0.016 s, when p = 30.6 mW.cm^{-2}) and by combining the photon counts from adjacent channels, the data were combined to give OSL signals with channels of various widths (e.g. 1, 2, 4 … 64 mJ.cm^{-2}) (figure 5.11). From these combined signals, the fast ratio and standard error can be calculated. As channel width increases, the

fast ratio decreases, as does the standard error. A higher fast ratio is obtained with a narrower channel as this maximises the contribution from the fast component (in comparison to the other components) in the first channel, but the associated error will be higher than that observed for greater channel widths because of counting statistics. There is therefore a compromise between a higher fast ratio value versus minimising the standard error. A channel width of around 5 mJ.cm^{-2} is suggested as a compromise between these two factors, because once a channel wider than ~5 mJ.cm^{-2} is used, the calculated fast ratio begins to reduce rapidly (figure 5.11).

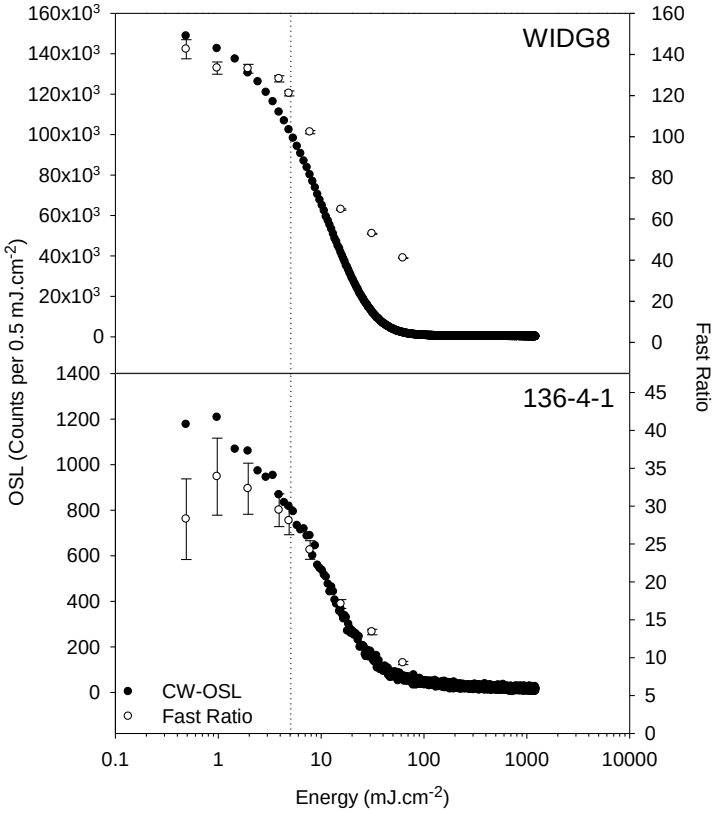

Figure 5.11: The CW-OSL signal of samples WIDG8 and 136-4-1, measured every 0.5 mJ.cm^{-2} (filled circles). These datasets were combined into signals with different channel widths and the fast ratio (and standard error) from these signals are also plotted (open circles). The CW-OSL signal can be read from the y-axis on the left, and the fast ratio on the right. The dashed line indicates the recommended channel width of ~5 mJ.cm^{-2}. From Durcan and Duller (2011).

5.4 Investigating the utility of the fast ratio

5.4.1 Testing the fast ratio using simulated data

Naturally occurring quartz from different provenances and with different depositional histories are likely to exhibit a high variability in both the absolute

intensity of OSL signals from different components, and in the relative proportion of these components. To test the impact of such variability upon the fast ratio and explore its ability to differentiate between fast and non-fast component dominated signals, CW-OSL signals were modelled from equation 5.1 using the mean σ values (table 5.3). Samples dominated by different components were simulated by varying n_F, n_M and n_S, and the fast ratio of these modelled signals (equation 5.5) was calculated (using the photon counts from the channels identified in section 5.3.2.1). Additionally the percentage contribution of the fast component to the signal in the first channel was calculated from these modelled data using equation 5.1. In the model, 2,500 simulations were undertaken, varying n_F, n_M, and n_{S2} values randomly between $1x10^3$ and $1x10^7$, and the signal from the fast, medium and slow2 components were calculated. The slow1 component was not included in the signal calculation as it is not present in all samples (figure 5.9 and appendix D) and slow3 and slow4 were also excluded, because their contributions will vary little in the range from zero to 683 $mJ.cm^{-2}$ (the end of L_3) and so they will not impact upon the fast ratio (table 5.4). Figure 5.12 shows these data plotted for each of the 2,500 simulations. As the contribution from the fast component to the net signal in the first channel increases, the fast ratio increases, with only limited scatter due to variations in the combination of n_0 values modelled.

To examine the scatter due to variations in the combination of n_0 more closely, the inset to figure 5.12 shows the region around a fast ratio value of 20 in more detail. In the modelled dataset (shown as filled symbols), a small number of simulations yield a percentage of signal from the fast component in the first channel (0.0 – 4.9 $mJ.cm^{-2}$) that is lower than is typical of the fast ratio from the modelled data. These simulations are most evident when the fast ratio is between ~10 and 25. Upon further investigation, it was found that for these simulations, n_{S2} made up the majority of the total trapped charge population (e.g. the sum of n_F, n_M and n_{S2}), with a negligible n_M, but a n_F sufficient to result in a relatively high contribution from the fast component to the total signal in the first channel. For measured data, where a large slow component exists, its impact will be minimised by subtraction of the background (either as L_3 in this instance, or as the background used in SAR analysis).

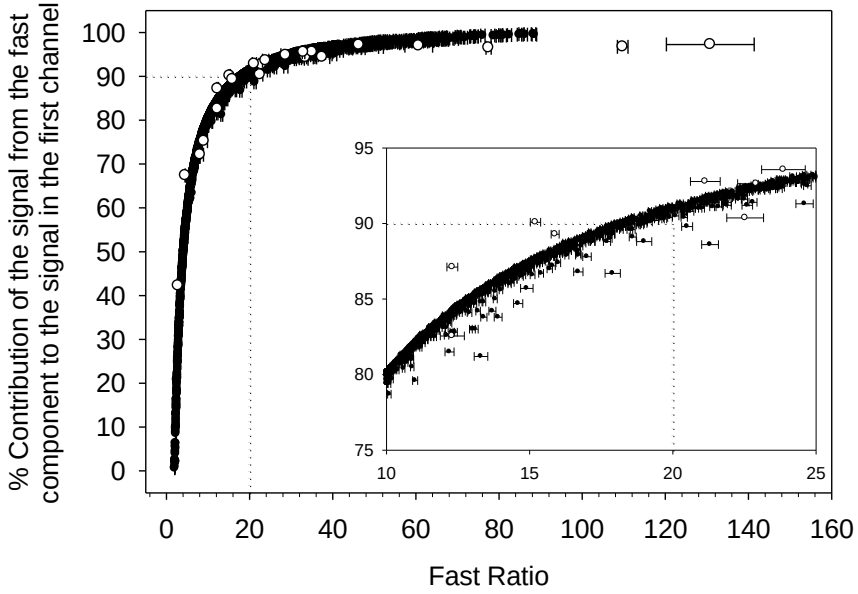

Figure 5.12: Filled circles show the % signal contribution of the fast component to the net signal in the first channel (0 – 5 mJ.cm^{-2}) calculated from modelled data where n_F, n_M and n_{S2} were randomly varied (2,500 simulations), as a function of the fast ratio (and standard error). Inset,the area where the suggested fast ratio threshold of 20 lies. The open circles show the fast ratio calculated from the CW-OSL signals measured in this study (table 5.2) and the contribution of the fast component signal to the net signal in the first channel, calculated from the σ and n_0 values determined from LM-OSL curve deconvolution. From Durcan and Duller (2011).

From figure 5.12, a fast ratio value of 20 indicates that at least 90% of the signal in the first channel originates from the fast component, and this value for the fast ratio is proposed as a threshold to discriminate between fast dominated and non-fast dominated samples.

5.4.2 Comparing the results of component fitting with the fast ratio

Figure 5.13 shows three normalised CW-OSL signals and their corresponding LM-OSL signals (inset) from measurements made on samples listed in table 5.2 and used to create figure 5.9. For sample 109/MAZ2, subjective observations of both the CW- and LM-OSL signals suggest that the signal is not dominated by the fast component; the CW-OSL signal decays slowly and the peak of the LM-OSL signals requires more stimulation power to reach its maximum than samples with a dominant fast component (e.g. CalQtz, figure 5.13). The calculated fast ratio of 2.8 ± 0.0 provides an objective confirmation of these subjective observations, and suggests that not more than 20% of the signal in the first channel is from the fast

component (figure 5.12). Using the σ and n_0 values derived for this sample from LM-OSL curve deconvolution, the percentage of signal in the first channel which originates from the fast component is 42%. The CW-OSL signals from sample 136-4-1 and the CalQtz decay much more rapidly, giving fast ratios of 21.1 ± 0.5 and 46.3 ± 0.5 respectively. Peaks in the LM-OSL signal of these aliquots occur at a lower stimulation power than for 109/MAZ2 (figure 5.13, inset), and dominance of the fast component is confirmed by the fast ratio. The percentage of signal originating from the fast component in the first channel is 93 and 97% for these samples respectively, calculated from σ and n_0 values derived from curve deconvolution. These examples indicate that the fast ratio is successfully distinguishing between samples that are fast dominated (136-4-1 and CalQtz) and non-fast dominated (109/MAZ2).

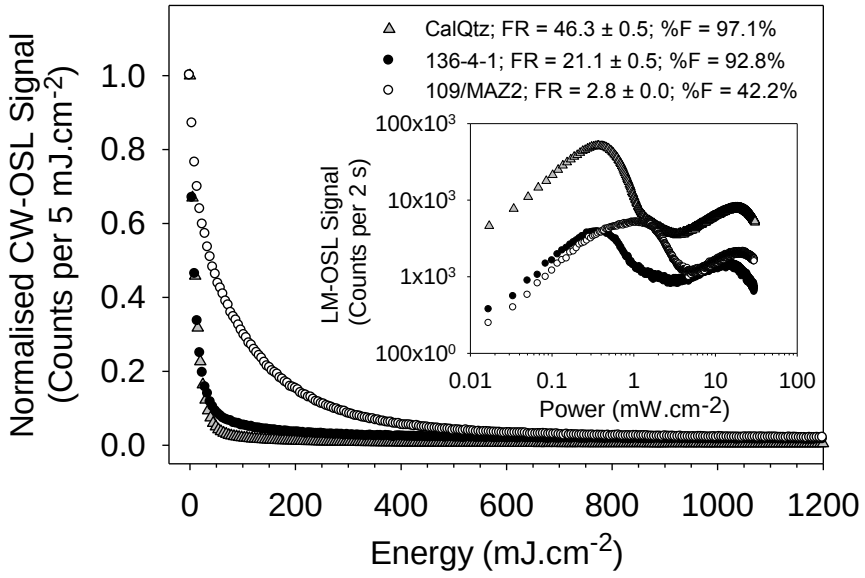

Figure 5.13: The normalised CW-OSL signals of samples CalQtz, 136-4-1 and 109/MAZ2 with the respective LM-OSL curves shown inset. The fast ratio (FR), calculated from the CW-OSL signal and the % of signal originating from the fast component in the first channel (%F), calculated from the LM-OSL signal are also shown. From Durcan and Duller (2011).

The fast ratio values calculated from the CW-OSL data of the 22 aliquots listed in table 5.2 have been plotted in figure 5.12 against the percentage of signal in the first channel originating from the fast component, calculated using the σ and n_0 values derived by deconvolution of the LM-OSL signal. The experimental data (open symbols) fall close to the line described by the modelled data (filled symbols). For all

samples, a threshold value for the fast ratio of 20 distinguishes samples with more than 90% of the signal in the first channel originating from the fast component, consistent with the simulated data. In the modelled data (figure 5.12, filled symbols) outliers tended to be associated with high values of n_{S2}, low values of n_M and intermediate values of n_F. This combination does not occur in the 22 aliquots measured in this study (table 5.2). Fourteen of these 22 aliquots had a fast ratio of above 20, and a n_F value which made up at least 45% of the total trapped charge population. In the instances where this was not the case, dominance of the n_M component (>60%), resulted in the lowest fast ratio values calculated (<10.0; figure 5.12). In the one sample (84/LSM6) where the n_{S2} population was dominant (89%), a low fast ratio (12.3 ± 0.4) was also calculated (figure 5.12). Therefore, for the signals measured in this study, the combination of components that gives rise to the outliers in the modelled data (filled symbols, figure 5.12) does not occur.

From the LM-OSL signals of some of their Chilean samples, Steffen et al. (2009) note that the relative contribution of the fast and medium component varies in the natural and regenerated signals, with the medium component contributing less to the natural signal. The authors attribute this to instability of the medium component, causing charge from this component to reduce over geological time in the natural signal, but to be present during laboratory measurements which take place immediately after irradiation. Therefore when applying the fast ratio to screen a suite of data, a prudent approach is to apply the fast ratio to both the natural and to one of the regenerated CW-OSL signals of the SAR protocol. Discrepancy in the fast ratio values calculated from these signals may also help infer the presence of other undesirable, thermally unstable quartz components, such as the ultrafast (e.g. Jain et al. 2008). The regenerative signal used for screening should be bright enough that the separation between the signal and the background is not an issue, however, this selected regenerative signal should not be taken from a dose which is close to the saturation of the fast component. Thus a regenerative dose which is less than the D_0 value (Wintle and Murray, 2006) of the signal dose response curve should be selected.

5.4.3 Effect of an inaccurate assessment of stimulation power on the fast ratio

Critical to the calculation of the fast ratio is that the stimulation power is known, and uncertainties in this value will impact upon the calculated fast ratio. Using an inaccurate stimulation power value in the fast ratio calculation affects the channels that L_2 and L_3 are located in, and sensitivity tests indicate that on average a 1% uncertainty in stimulation power will result in approximately 1% variability in the fast ratio (figure 5.14). However, because the fast ratio is calculated using photon counts from channels containing L_2 and L_3, there is a step-change in this variability. Where the stimulation power is known within approximately ±4% (and L_2 is located at the midpoint of the channel), the fast ratio is unaffected (figure 5.14), and where stimulation power is known within ±10%, the fast ratio varies by approximately ±9% (figure 5.14). Using a stimulation power value which is higher than the true power value (positive power error values in figure 5.14) means that the L_2 channel is relatively closer to L_1, which results in a lower fast ratio.

The stimulation power of the LED unit is usually provided by the manufacturer at the point of purchase and whilst ideally measurement of the stimulation power would also be routinely undertaken ahead of measurement, this is not straightforward (section 4.7.4.4) and further work is required to establish a means for accurately measuring this parameter. A prudent approach, where users of the fast ratio are uncertain of the stimulation power of their equipment, would be to measure photo ionisation cross-sections of a sample known to be dominated by a fast component (e.g. calibration quartz) and compare them to the mean photo ionisation cross-sections measured by Durcan and Duller (2011).

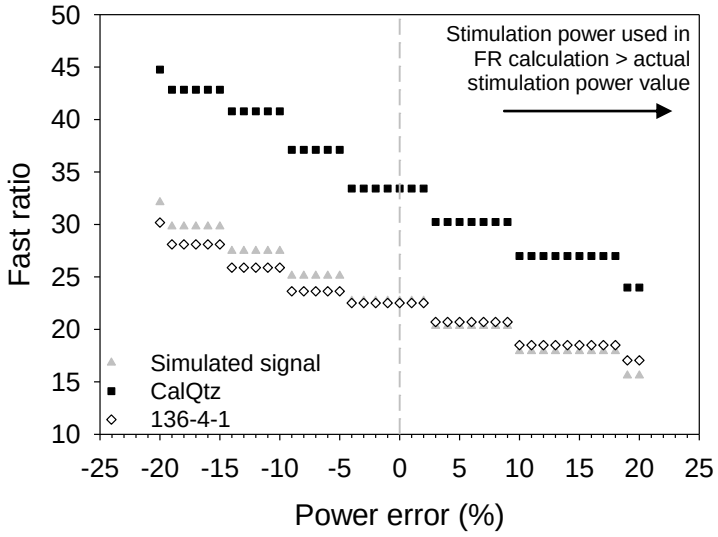

Figure 5.14: The impact of uncertainty in the stimulation power value on the fast ratio for a simulated OSL signal and signals from aliquots of samples CalQtz and 136-4-1. Power error (%) refers to the extent to which the stimulation power is over- or under-estimated. Positive values indicate the power value used in the fast ratio calculation is greater than the actual power and negative values, that the power value used is less than the actual. The dashed line at zero shows where the actual and used power are equal.

5.5 Using the fast ratio as a rejection criterion

It has been demonstrated in section 5.4 that the fast ratio can differentiate between CW-OSL signals that are dominated by the fast component (where dominated is taken to mean that at least 90% of the signal measured after 5 mJ.cm^{-2} of energy originates from the fast component). The comparison between the CW-OSL and LM-OSL signal (figure 5.13) from the same aliquot of samples allows this assessment to be made. The routine application of the fast ratio removes the need for LM-OSL measurement or complex treatment of the CW-OSL and the following sections assess the application of the fast ratio to CW-OSL signals measured for dating. The application of rejection criteria, such as the recycling ratio and OSL IR depletion ratio (discussed further in section 6.3.3.3 and 6.3.3.4) are designed to remove aliquots from a dose distribution which may provide erroneous D_e estimates on the basis of their luminescence characteristics, and Durcan and Duller (2011) suggest that the fast ratio can be added to this suite of rejection criteria.

5.5.1 Signal levels and the fast ratio

Theoretically, the fast ratio is not dependent on signal levels and/or the magnitude of the equivalent dose. The fast ratio uses the mean photo ionisation cross-section values of Durcan and Duller (2011) to fix the points used on a CW-OSL curve and the photon counts in the L_1 and L_2 channels are compared, with a background/slow component subtraction incorporated. Fast ratios calculated from the modelled data in figure 5.12 range between 0.5 and 100, with relative standard errors between 0.5 and 2%. For the 22 signals used to develop the fast ratio, fast ratio values were calculated from the CW-OSL signals range between 3 and 131, and have associated relative standard errors between 1 and 3%. CW-OSL measurements were made using medium aliquots and fast ratios calculated from a signal after a 50 Gy regenerative dose, resulting in bright luminescence signals. Not all signals that the fast ratio will be applied to will be of this magnitude, and the application of the majority of signal analysis tools can be challenging when considering signals which are close to the equipment detection limits. When applying the fast ratio to CW-OSL signals as a rejection criteria, two types of anomalous fast ratio values are sometimes observed. The first is a negative fast ratio and the second is an inflated fast ratio value, where the value exceeds 1000.

5.5.1.1 Negative fast ratio values

In figure 5.15, the fast ratio is plotted as a function of $L_2 - L_3$ for 552 signals from six samples (section 5.5.3). Of the 552 aliquots plotted, 48 negative fast ratios were calculated. Negative fast ratio values are calculated where $L_2 - L_3$ is negative, and this typically occurs for young and/or dim signals, where the photon counts in the L_2 channel are not discernible from the average counts over the interval representing L_3. Occasionally, a negative $L_2 - L_3$ value is calculated from a signal which qualitatively appears to be dominated by the fast component. For these signals, L_2 does not exceed L_3 and this signal is interpreted as having a relatively weak contribution from the medium component (e.g. figure 5.16a). For this type of signal, $L_1 - L_3$ is generally relatively high and the negative fast ratio occurs as a result of a

mathematical artefact due to the close proximity of L_2 and L_3, which results in a negative value. In this study, the approach taken has been to exclude signals with negative fast ratios from dose distribution analysis. This may lead to a small number of signals removed on the basis of counting statistics and not due to a lack of dominance by the fast component. However, of the 552 aliquots plotted in figure 5.15, 48 negative fast ratio values are calculated and 31 of these aliquots fail at least one other rejection criteria, and would be removed from the sample dose distribution in any case. In studies where young and/or dim samples are being dated routinely, the fast ratio could be altered slightly by taking L_2 from a range of values, in the same way L_3 is calculated. This would make the ratio less vulnerable to fluctuations in the number of recorded photon counts when measured close to the background.

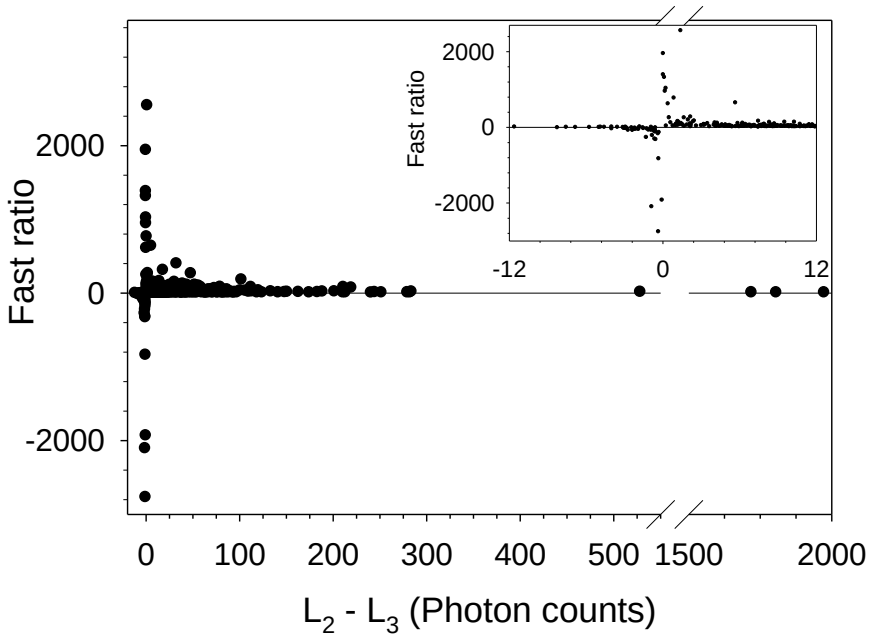

Figure 5.15: The values of L_2 - L_3 plotted against the fast ratio for 552 signals from six samples (table 5.5). A fast ratio of 20 is shown for reference by the black line. Inset, a magnified view of the fast ratios calculated as $L_2 – L_3$ converges on zero.

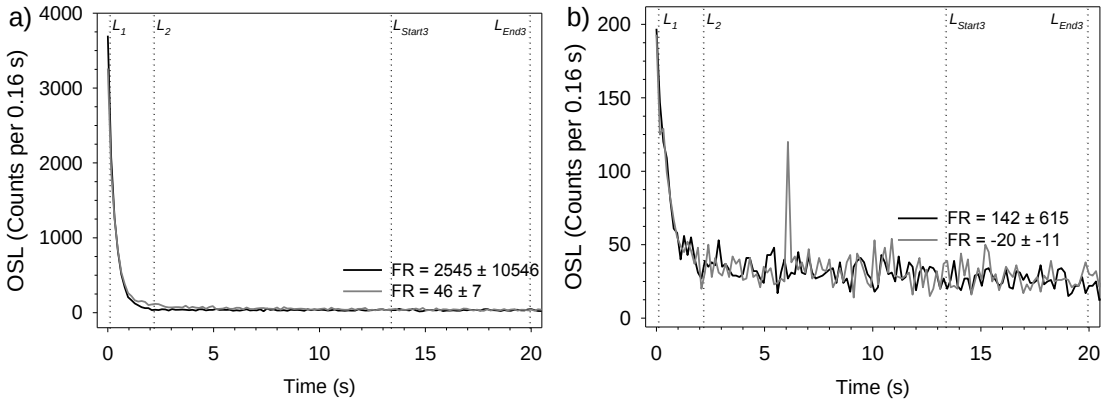

Figure 5.16: OSL signals from sample 153-TIL3-2 and the fast ratio (FR) values calculated from them. For reference, the position of L_1, L_2 and L_3 (start and end) are shown. The fast ratio and standard error are rounded to the nearest integer.

5.5.1.2 Inflated fast ratio values

Very high, or inflated, fast ratio values are ratios in excess of 1000, and are occasionally calculated (figure 5.15), with 1.5% of the 552 signals plotted producing inflated fast ratio values (both positive and negative). As the denominator of the fast ratio equation (equation 5.5), there is some sensitivity of the calculated fast ratio to the convergence of the number of photon counts in the channels representing L_2 and L_3. Inflated fast ratio values are observed as $L_2 - L_3$ becomes increasingly small, and positive and negative inflated ratios are calculated depending whether L_2 or L_3 is greater (figure 5.15). This often occurs for young and/or dim signals, where L_2 is likely to be close to the background of the reader. An inflated fast ratio can also be calculated for a very fast dominated signal, in combination with a relatively weak medium component. Figure 5.16b shows two OSL signals from sample 153-TIL3-2 which are similar in magnitude and form, but give different fast ratio values. Both signals decay rapidly to background levels within the first few seconds of stimulation and qualitative assessment of these curves suggests that they both should be OSL signals dominated by the fast component, with fast ratios greater than 20 expected. For the first signal (black line in figure 5.16b), a fast ratio of 2545 ± 10546 is calculated, where L_1 is 3699, L_2 is 35 and L_3 is 34 photon counts. The second signal (grey line in figure 5.16b) has a fast ratio of 46 ± 7 with L_1, L_2 and L_3 values of 3261, 110 and 40 photon counts

respectively. The similarity in L_2 and L_3 in the first signal contributes to the inflated fast ratio value, but also the extremely large standard error. Extremely high standard errors are calculated for these types of signals, and can be used to diagnose inflated fast ratio values calculated as a result of the close proximity of L_2 and L_3. High fast ratio values may also be calculated from extremely bright, fast dominated OSL signals, although these ratios typically have a standard error of approximately 3% (e.g. figure 5.12).

Jain et al. (2003) measured the photo ionisation cross-section of the ultrafast component as 2.90 x 10^{-16} cm^2 (table 5.1), and under a stimulation power of 30.6 $mW.cm^{-2}$, the signal from the ultrafast component will have reduced to 1% of its original signal after 0.22 s. The presence of the ultrafast component in a regenerated OSL signal could therefore also result in an inflated fast ratio value because the number of photon counts in the first channel of measurement would contain signal from the fast and ultrafast component. Inflated fast ratio values need not be immediately interpreted as evidence for the presence of an ultrafast component, however the ratio values for the natural and regenerative signals of an aliquot should be examined, and a discrepancy between the two may be indicative of the presence of an undesirable component.

Theoretically, the fast ratio is not dependent on signal levels because the photo ionisation cross-sections are fixed physical parameters and the fast ratio compares the amount of charge evicted at points in the OSL decay curve which have been chosen to represent the fast and medium components. However, it is important that the signal at L_2 can be distinguished from the background, and this means that there is a slight sensitivity of the fast ratio to the value of L_2. In this study, inflated fast ratio values have been interpreted as a sign of a relatively weak medium component, and all aliquots with fast ratios in excess of 20 were included in dose distribution analysis if all other rejection criteria were satisfied. From the 552 aliquots plotted in figure 5.15, 5 fast ratio values in excess of 1000 are calculated, 4 of which pass all other rejection criteria and would be included in a dose

distribution. All 5 fast ratio values have extremely high standard deviations, indicating that the close proximity of L_2 and L_3 values cause the inflated ratio value.

5.5.2 Applying the fast ratio to natural and regenerative signals

Durcan and Duller (2011) recommend that the fast ratio be applied to the natural and at least one regenerative signal (section 5.4.2) because the relative contribution of the fast and medium component may vary between the natural and regenerative signals (Steffen et al., 2009). Discrepancy between fast ratio values of the natural and regenerative signals may indicate the presence of undesirable, thermally unstable quartz components, and the presence of such components may result in D_e under-estimation because charge from the unstable component will not contribute to the natural signal but will constitute part of the regenerative signals. It is therefore prudent that the fast ratio of both the natural and regenerative signals are checked to avoid erroneous D_e estimates.

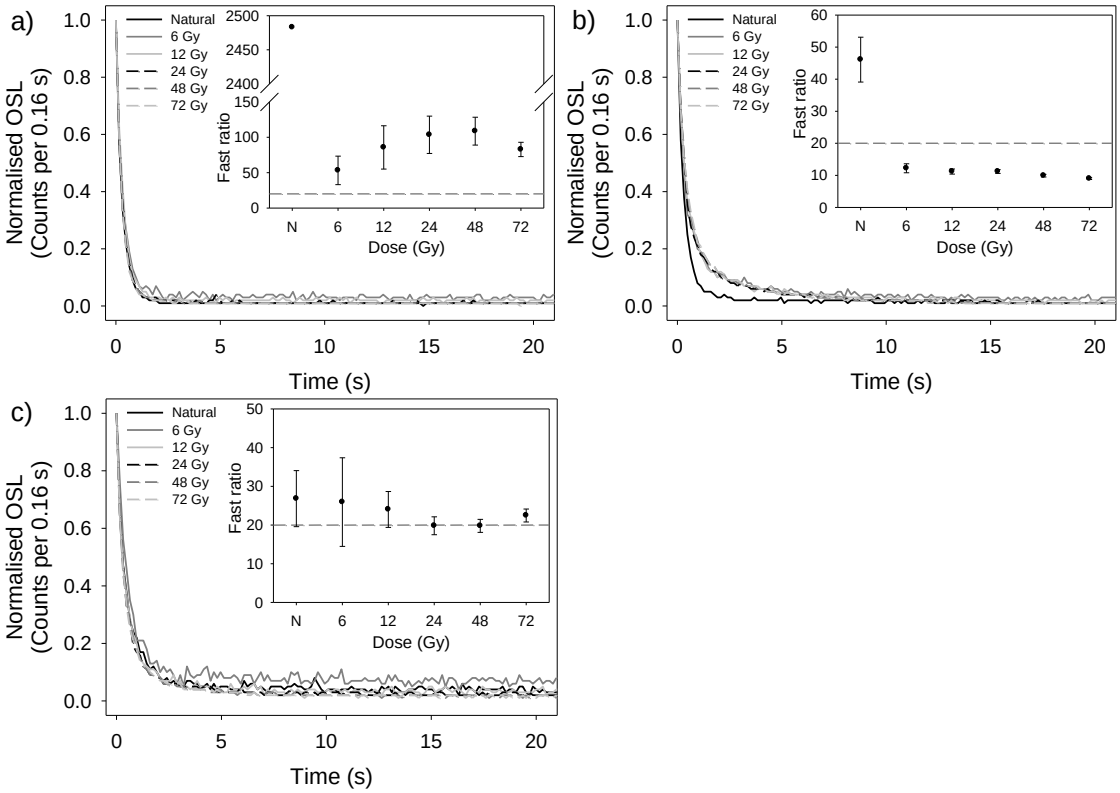

Figure 5.17: The natural and regenerative signals measured over a SAR cycle from three aliquots of sample 153-TIL3-2. Inset, the fast ratio calculated from the natural signal (N) and each regenerative signal (plotted by dose given). The fast ratio acceptance threshold of 20 is shown by the dashed line. Note, in a) the relative error of the fast ratio from the natural signal (2483 ± 10064) is omitted for display purposes.

Figure 5.17 shows the natural and regenerative OSL signals measured using the SAR protocol for three aliquots of sample 153-TIL3-2. The OSL signals have been normalised to the first data point of each OSL decay curve so that their shapes can be compared. Both the natural and regenerative signals in figure 5.17a decay exponentially to background levels within a few seconds of stimulation and fast ratios in excess of 20 for all measured signals confirm that these signals are dominated by the fast component. The fast ratio of the natural signal is very high due to the small difference in the photon counts from L_2 and L_3 (see section 5.5.1) and although there is variability in the fast ratios of the regenerative dose signals, the ratios are consistent within errors. In figure 5.17b, the fast ratio of the natural signal is in excess of 20 and is considered to be dominated by the fast component (which is reflected in the shape of the decay curve). However, the regenerative signals decay much less rapidly (figure 5.17b) and the fast ratio of each of the regenerative signals is consistently below the acceptance threshold of 20 (figure 5.17b inset). The discrepancy in fast ratio values between the natural and regenerative signals indicates the possible contribution of a thermally unstable component to the regenerative signals, which is not present in the natural, and further analysis (e.g. signal deconvolution) would be required to confirm the exact nature of this additional component. Aliquots which have natural signals which pass the fast ratio and regenerative doses which fail are not suitable for inclusion in dose distribution analysis, due to the possibility of D_e under-estimation and these aliquots are excluded from distribution analysis and age calculation in this study. In figure 5.17c, a more typical aliquot is shown, with natural and regenerative signals similar in form, and the calculated fast ratio values in good agreement and within errors.

5.5.3 Impact of applying the fast ratio to dose distributions

The fast ratio can be easily and rapidly applied to CW-OSL signals. To assess the impact of applying the fast ratio to dose distributions, six samples have been selected for analysis. These samples have been chosen to have a range of D_e and overdispersion (σ_d) values (table 6.3) and to have a D_e value calculated using a

variety of different age models. Dose distribution analysis is discussed fully in chapter 6, however all OSL signals used for dating have been screened using a standard set of five rejection criteria (e.g. Jacobs et al., 2006; section 6.3.3), which include the recycling ratio (Wintle and Murray, 2006), the OSL IR depletion ratio (Duller, 2003), assessing the amount of recuperation (Murray and Olley, 2002) and two means of checking signal levels. Figure 5.18 shows radial plots of dose distributions for the six selected samples. D_e values calculated from signals which satisfy all five standard rejection criteria and the fast ratio are shown by the filled symbols. Equivalent doses from signals which pass all five standard criteria but fail the fast ratio are shown by the open symbols.

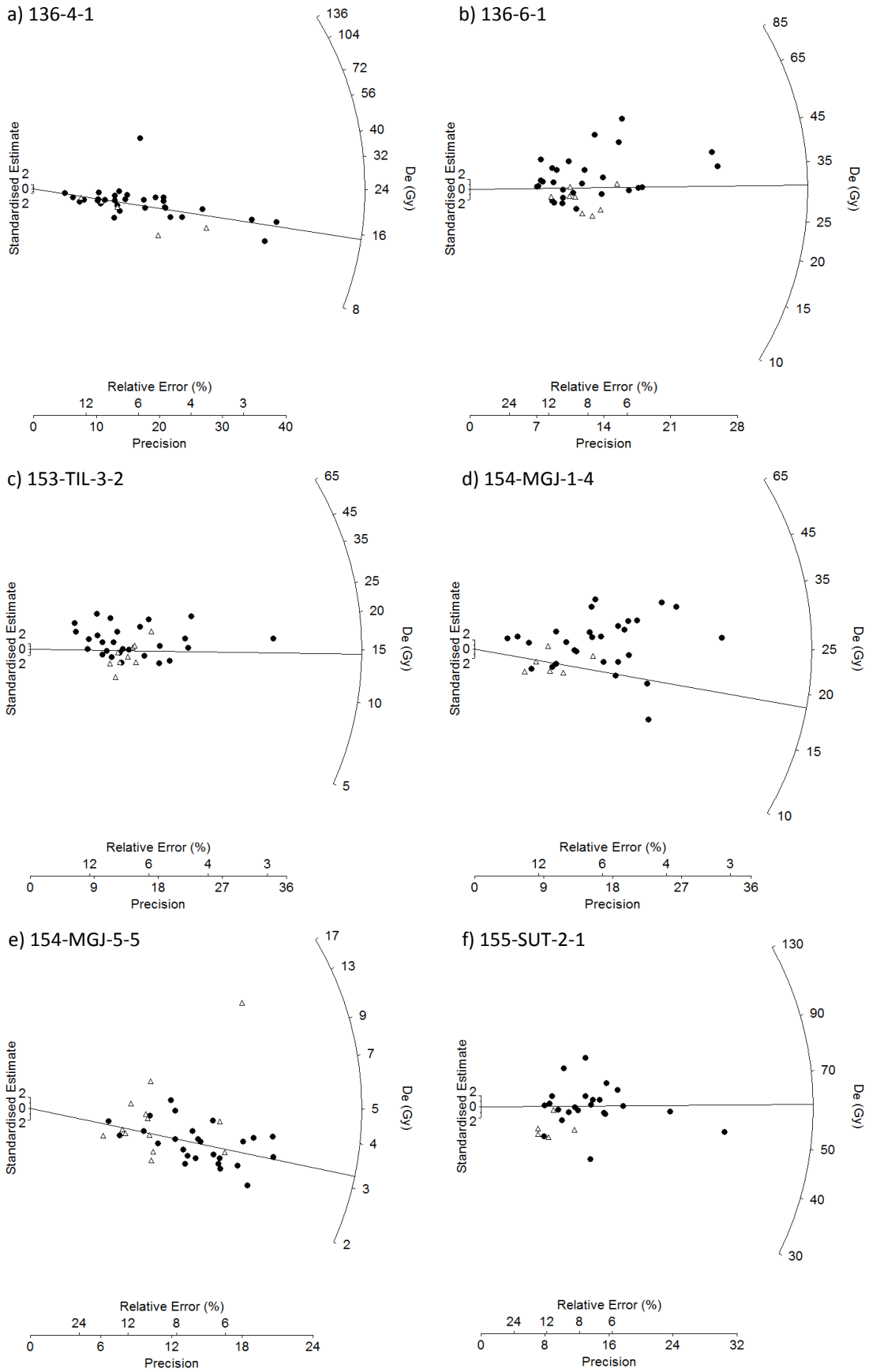

Figure 5.18: Radial plots showing the impact of applying the fast ratio to D_e distributions. The filled symbols show D_e values calculated from signals passing the five standard criteria and the fast ratio. The open symbols indicate signals which passed the standard criteria but not the fast ratio. The FP D_e value (calculated from signals passing all six rejection criteria) is shown by the black line.

Table 5.5: Summary of overdispersion (σ_d) and D_e values calculated from signals which pass all five standard rejection criteria (standard) and signals which pass all standard criteria and the fast ratio (standard & FR). The age model used for D_e calculation is shown, and where the FMM was used, the number of components (k) and the percentage of signals in the dominant component (%) is also given. Dose distributions are shown in figure 5.18. Age models are discussed in section 6.4.2.1; CAM refers to the central age model and FMM, the finite mixture model. σ_d is reported to 1 d.p. and D_e to 2 d.p..

Sample	# Aliquots (standard)[a]	# Aliquots (standard & FR)[a]	% Fast ratio removal[b]	Fast ratio rejected in lowest[c]		σ_d (%) (Standard)	σ_d (%) (Standard & FR)	σ_d ratio	Age model	D_e (Gy) (Standard)	k (#,%)	D_e (Gy) (Standard & FR)	k (#,%)	D_e Ratio
				33%	50%									
136-4-1	36	31	14	60	100	37.0 ± 0.8	37.5 ± 0.9	1.02	FMM	15.41 ± 0.84	3, 90	15.38 ± 0.47	2, 70	1.00
136-6-1	36	28	22	75	88	32.3 ± 0.7	31.7 ± 0.9	0.98	FMM	28.80 ± 1.09	2, 76	30.79 ± 1.36		1.07
153-TIL3-2	36	27	25	56	67	46.1 ± 0.9	45.2 ± 1.2	0.98	FMM	13.57 ± 0.57	4, 62	14.15 ± 0.66	3, 60	1.04
154-MGJ-1-4	34	28	18	67	100	34.5 ± 0.8	32.4 ± 0.9	0.94	FMM	18.05 ± 1.13	2, 35	18.70 ± 1.33		1.04
154-MGJ-5-5	39	26	33	23	54	34.9 ± 0.7	20.0 ± 0.6	0.57	CAM	3.47 ± 0.20		3.25 ± 0.14		0.94
155-SUT-2-1	28	23	18	80	100	31.8 ± 0.9	28.2 ± 0.9	0.89	FMM	59.86 ± 5.32	3, 74	60.86 ± 2.40	3,83	1.02

[a] number of signals which satisfy the standard five rejection criteria (standard) and the number of signals which satisfy the fast ratio in addition to the standard criteria (standard & FR). Standard rejection criteria are discussed in section 6.3.3 and include the recycling ratio (Murray and Wintle, 2000) and the OSL IR depletion (Duller, 2003).

[b] % of signals which pass the standard rejection criteria but fail the fast ratio.

[c] % of signals removed (on the basis of fast ratio failure) which fall within the lowest 33% and 50% of D_e values of the sample.

From figure 5.18, it is evident that the application of the fast ratio as a rejection criterion removes aliquots from dose distributions which would not be removed if solely applying the standard rejection criteria (section 6.3.3), with up to a third of aliquots removed which pass all other criteria but fail the fast ratio (e.g. sample 154-MGJ-5-5; table 5.5). This highlights the importance of testing signals for the dominance of the fast component and that dominance should not be assumed or qualitatively assessed. Signals which are not dominated by the fast component can pass all other screening criteria, but may not be suitable for inclusion in dose distribution analysis, because one of the fundamental assumptions made when applying the SAR protocol is that the signal is dominated by the fast component (Murray and Wintle, 2000).

Typically lower D_e values are calculated from the signals which pass all standard rejection criteria, but fail the fast ratio. In table 5.5, the percentage of D_e values removed on the basis of fast ratio which are in the lowest third and half of the dose distribution are shown. For samples 136-4-1, 154-MGJ-1-4 and 155-SUT-2-1, all signals removed on the basis of the fast ratio are within the lowest 50% of D_e values, and this is the case for the vast majority of removed signals for sample 136-6-1 (table 5.5). For samples 136-6-1 and 155-SUT-2-1, 75% and 80% of signals removed are from the lowest third of the dose distribution, and it is the case for the other samples presented (with the exception of 154-MGJ-5-5) that the majority of signals removed on the basis of the fast ratio threshold are amongst the lowest third of D_e values in the dose distribution. That the fast ratio removes signals which produce relatively lower D_es is consistent with the conclusions drawn by Li and Li (2006b), who state that a greater relative dominance of the medium component leads to D_e underestimation because of thermal instability.

For the younger sample 154-MGJ-5-5, the fast ratio removes signals from across the dose distribution. Of the 13 signals which pass all standard criteria, but fail the fast ratio, three signals produce equivalent doses within the lowest third of the dose distribution, and 7 out of 13 aliquots are within the lower half of the distribution. The other 6 signals are amongst the highest quartile of D_e values, including two D_e

values which are much greater than the majority of D_e values (open symbols in figure 5.18e). This is likely to be due to incomplete bleaching of the OSL signal, the effects of which are more pronounced in samples with lower D_e values. Singarayer and Bailey (2004) found that signal from the fast component decayed at a much more rapid rate than the medium component under illumination and Bailey et al. (2003) found that samples with a greater relative dominance of the medium component were more prone to be incompletely bleached. The fast ratio removes signals which have a greater relative dominance of the medium component, and for signals removed on the basis of the fast ratio which have high D_e determinations, incomplete bleaching of the signal is a probable cause.

The removal of signals from the extremes of the dose distribution by the fast ratio typically results in lower overdispersion (σ_d) values (table 5.5), indicating that complexity in the underlying dose distribution is reduced by the application of the fast ratio as a rejection criteria. This is further apparent in dose distributions where the finite mixture model (FMM) has been applied and for samples 136-4-1, 153-TIL3-2 and 155-SUT-2-1, applying the fast ratio as a screening criterion provides dose distributions that can be fitted with fewer components (e.g. samples 136-4-1 and 153-TIL3-2) or where more signals constitute the component used for dating (e.g. sample 155-SUT-2-1). In table 5.5, the D_e values derived from signals which pass all standard rejection criteria and signals which pass the fast ratio in addition to the standard criteria are compared. The greatest disparity between the two D_e determinations is seen when the CAM has been applied, and the application of the fast ratio can result in an increase in D_e of up to 7% (e.g. sample 136-6-1; table 5.5). For the samples where the FMM has been applied, there is less variability between the two D_e values. This is because D_e calculation using the FMM is usually based upon the most dominant component within the dose distribution in this study (table 6.3). The fast ratio removes D_e values from the extremes of the distribution, and therefore the dominant component is not significantly affected.

5.5.4 Feldspar contamination and the fast ratio

The fast ratio allows comparison of the form of CW-OSL curves measured on different measurement equipment and between different aliquots/samples, and in some respects, can be viewed as a means for comparing the shape of luminescence curves. Godfrey-Smith et al. (1988) investigated the bleaching properties of quartz and feldspar and found that the process of de-trapping was much more rapid in quartz than in feldspar (e.g. figure 1.14) and the difference in the de-trapping rate between the two minerals results in luminescence signals which differ in form. A quartz OSL signal dominated by the fast component consists of a rapid decay of signal to background levels within the first few seconds of stimulation with light (Roberts, 2007). The feldspar IRSL signal decays much less rapidly and requires longer exposure times to light to reduce the signal to background levels (Godfrey-Smith et al., 1988). However, quartz OSL signals which are not dominated by the fast component are similar in form to an IRSL feldspar signal and consequently quartz OSL signals which fail the OSL IR depletion and the fast ratio can be similar in shape. It is therefore possible that the fast ratio is affected by the level of feldspar contamination within a signal.

Despite the potential similarities between feldspar-contaminated quartz OSL signals and non-fast component dominated signals, the fast ratio is not entirely dependent on the OSL IR depletion ratio (Duller, 2003; section 6.3.3.4). In figure 5.19, three OSL signals of sample 136-4-1 are shown. One signal passes all six rejection criteria (the five standard measures and the fast ratio), one signal fails only the OSL IR depletion ratio (with a ratio of 0.70 ± 0.03), and one signal which fails only the fast ratio (fast ratio of 16.76 ± 2.18). Both signals which fail only one criterion are very similar in form, evidence that signals failing the OSL IR depletion ratio do not necessarily fail the fast ratio. However, the signal which has a fast ratio of 16.76 ± 2.18 only just fails the fast ratio threshold, and an OSL IR depletion ratio of 0.70 ± 0.03 is well above the ~0.0 – 0.2 values that would be expected from a signal almost completely contaminated by feldspar. It is therefore likely that as signals become either more

dominated by non-fast components or contain a greater contribution from feldspar, the more likely that a signal will fail both the fast ratio and IR OSL depletion ratio.

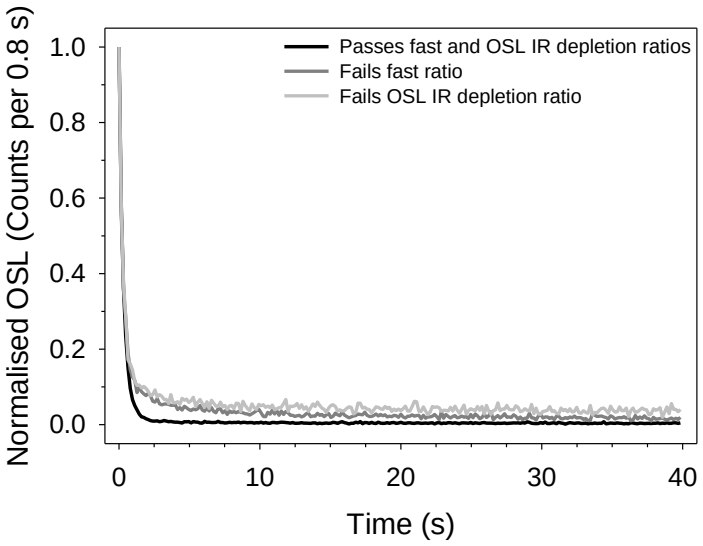

Figure 5.19: Example OSL decay curves measured from sample 136-4-1 which have been screened using the five standard rejection criteria and the fast ratio. The black line shows the signal which satisfies all six criteria and the two grey lines show the signals which fail either the fast ratio or the OSL IR depletion ratio only.

A total of 552 signals were measured to calculate the OSL ages for the six samples listed in table 5.5. In figure 5.20, the OSL IR depletion ratio of each of these signals is plotted against the fast ratio. No clear, linear relationship between the fast ratio and OSL IR depletion ratio is apparent, but a number of observations can be made. For signals with an OSL depletion ratio below ~0.70, the vast majority of aliquots fail the fast ratio threshold of 20. Not all signals with an OSL IR depletion ratio of less than 0.70 fail the fast ratio, but the number satisfying the fast ratio increases as the OSL IR depletion ratio approaches unity. That said, a greater OSL IR depletion ratio does not result in a fast ratio in excess of 20, and of the 258 signals which have OSL IR depletion ratios within 10% of unity (within errors), 33% do not satisfy the fast ratio threshold. Therefore, whilst signals which have a low OSL IR depletion ratio are extremely like to fail the fast ratio (because L_2 will have a greater number of photon counts, in relation to L_1, than would be expected for a fast dominated quartz OSL signal), the fast ratio can differentiate between fast and non-fast dominated quartz signals which have intermediate to high (approaching unity) OSL IR depletion ratios.

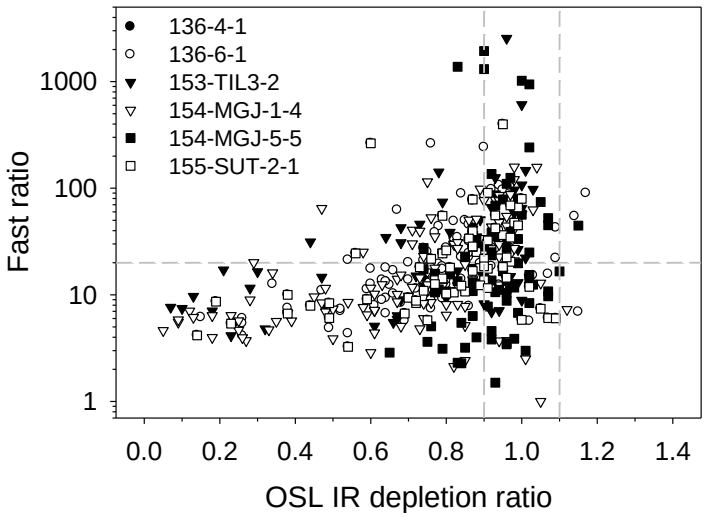

Figure 5.20: Relationship between the OSL IR depletion ratio and the fast ratio for 552 signals measured from 6 samples (table 5.5). Standard errors are not shown for clarity and only positive fast ratio values are shown. The fast ratio threshold of 20 and the OSL IR depletion ratio thresholds of ±10% of unity are shown by the grey dashed lines for reference.

5.6 Conclusions

The fast ratio has a number of applications. By incorporating the photo ionisation cross-section and stimulation power of the measurement equipment into the ratio, the ratio is transferrable between aliquots, samples and readers, making comparison of signals straightforward. The fast ratio can also be applied as a rejection criterion used as part of a suite of tests routinely applied to signals used for dating, and a threshold fast ratio value of 20 has been suggested to distinguish between CW-OSL signals where the initial part of the signal is dominated by the fast or other components. It is recommended that where used for data screening, the ratio is applied to both the natural and a regenerative dose signal; discrepancy between the two fast ratios may indicate the presence of signal from thermally unstable components. Calculated fast ratio values may also be used to indicate the need for further, more complex, forms of analysis aimed at isolating the signal from the fast component, such as component fitting of the OSL signal (Li and Li, 2006a) or variation of the integration intervals used for dating (Cunningham and Wallinga, 2010). Whilst the fast ratio has been shown to be able to distinguish between fast and non-fast dominated CW-OSL signals (figure 5.12), it does not replace curve deconvolution of OSL signals, or other techniques utilised in the investigation of the

quartz OSL components and their properties. Similarly, the fast ratio characterises CW-OSL curves, but it does not provide information about the optimal integration interval for use during dating. The fast ratio provides a rapid, quantitative and transferrable measure for assessing the dominance of the fast component in quartz OSL signals and is therefore applied to dose distributions in this study as a rejection criterion, in addition to the standard set of criteria typically applied (e.g. Jacobs et al., 2006). The fast ratio has an extremely valuable application for not only testing the assumption that OSL signals used for dating are dominated by the fast component, but for reducing complexity in dose distributions and improving the precision and accuracy of calculated D_e values and therefore age calculations.

6. Equivalent dose determination and age calculation

6.1 Introduction

The precise and accurate calculation of the equivalent dose (D_e) is critical for luminescence dating because the D_e forms the numerator of the age equation required to calculate an OSL age (equation 1.1). Recent equipment and experimental advances have facilitated the development of single aliquot techniques, which allow the routine and rapid measurement of multiple D_e determinations for one sample, allowing dose distributions for a sample to be investigated. Ideally, all luminescence signals from all measured aliquots would be suitable for dating using the SAR protocol and would provide individual D_e estimates consistent with one value (within measurement uncertainties). However, this is rarely the case and dose distributions can be complex and statistical analysis can reveal the presence of multiple equivalent dose populations within one measured sample. Factors contributing to heterogeneity of D_e values include incomplete bleaching, variations in the environmental dose rate within the sediment matrix (e.g. Jacobs et al., 2006) and post-depositional mixing (e.g. Bateman et al., 2007). Therefore, the calculation of the equivalent dose for a sample may not be straightforward.

In this chapter, single grain measurements are made to allow an estimate of the number of grains giving rise to the luminescence signal seen from the small aliquots used for dating in this study. This chapter then focuses upon the analysis of the OSL signal from an individual aliquot used to calculate a D_e and the removal of signals which may provide erroneous D_e determinations. Signals that do not satisfy the suite of rejection criteria applied may not be suitable for dating using the SAR protocol (e.g. Wintle and Murray, 2006) or may be contaminated by luminescence signals from other minerals, such as feldspars (Duller, 2003) and the removal of such signals will provide more reliable D_e determinations (Roberts, 2008). After the measurement of a large number of individual D_e estimates, the statistical treatment required to calculate the sample D_e is considered. Whilst the majority of samples

investigated in this project are expected to date from the Holocene, the natural signal from some aliquots of a number of samples appear to be in saturation. The definition of a saturated signal and sample is discussed and a method for calculating a minimum age is described. In the final sections of this chapter, the calculated D_e values and OSL ages are presented.

6.2 Number of grains giving a measureable luminescence signal

Duller (2008b) states that the most striking finding arising from the OSL measurement of single grains is the variability of luminescence properties between grains, noting that the brightness of the luminescence signal can vary by up to four orders of magnitude within the same sample. The proportion of grains contributing to the luminescence signal varies greatly between samples (e.g. figure 6.1; Duller et al., 2000), as does the mean brightness of grains. Variability can also be seen in the dose saturation point (D_0) of a dose response curve (Roberts et al., 1999) and the relative balance of components within the quartz OSL signal seen in signals from grains of the same sample (Bulur et al., 2002). For the purpose of using an OSL signal for dating, the number of grains which produce a measurable luminescence signal should be taken into consideration because the OSL signal from a small aliquot of sample could be potentially dominated by signal from very few grains (Duller, 2008b). Duller et al. (2000) were the first to investigate this variability for seven quartz samples and presented this graphically in figure 6.1. Their data shows that for a geographic range of quartz samples, between 5 and 50% of grains constitute 95% of the total light sum (figure 6.1). Subsequent work has confirmed this variability. Jacobs et al. (2003b) found that approximately 10% of their South African dune sands gave rise to 90% of the OSL signal and a similar value was calculated from South African fluvial sediments by Rodnight (2006). Harrison et al. (2008) found that a substantially smaller number of quartz grains (between 0.6 and 1.8%) from Chilean glacial sediments yielded measureable OSL signals. In Southern India, Jaiswal et al. (2009) did not calculate the number of grains giving rise to the luminescence signal but state there was an extremely low occurrence (<1%) of bright luminescence signals from slackwater deposits.

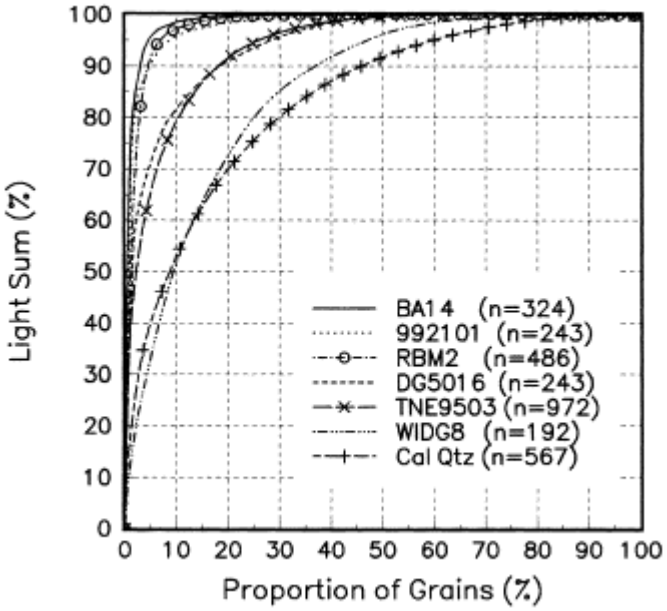

Figure 6.1: Distribution of signal intensity of single grains from seven quartz samples. The data are plotted as a function of the total light sum that originates from the specified percentage of the brightest grains. From Duller et al. (2000).

The single grain discs (figure 4.6) are made up of an array of 100 holes, each of which has a diameter of 300 µm and a depth of 300 µm (Duller, 2008b). To ensure only one mineral grain per hole, grains from the sieved fraction of 180 – 212 µm diameter or greater should be used for single grain measurement. The samples in this study are typically composed of fine sand and only one sample, 154-MGJ-5-1, yielded sufficient mass in the size fraction 180 – 212 µm (or greater) for single grain analysis and is referred to as 154-MGJ-5-1B to differentiate it from the 90 – 125 µm size fraction of 154-MGJ-5-1 used for dating. To assess the number of grains giving a luminescence signal, the response of 900 grains to a laboratory irradiation of 45.6 Gy was measured using a standard SAR protocol (section 4.8.3). The OSL IR depletion ratio (section 6.3.3.4) was also calculated for each grain using a laboratory dose of 8.6 Gy.

Figure 6.2 shows the signal intensity of grains from sample 154-MGJ-5-1B. The data has been ranked according to signal intensity (the OSL counts measured during the first 0.15 s of stimulation with a mean background calculated from the last 0.2 s subtracted) and plotted against the proportion of the brightest grains after Duller et al. (2000). The rapid increase in signal intensity is indicative of an OSL signal

dominated by the signal from a small number of grains and of the 900 grains measured, 44 grains or 4.8% of grains constitute 90% of the total OSL signal. In the inset of figure 6.2, the signal intensity of these 44 grains is shown and confirms that the signal is dominated by a few relatively bright grains, with the brightest 5 grains constituting 52% of the signal measured from the 900 grains.

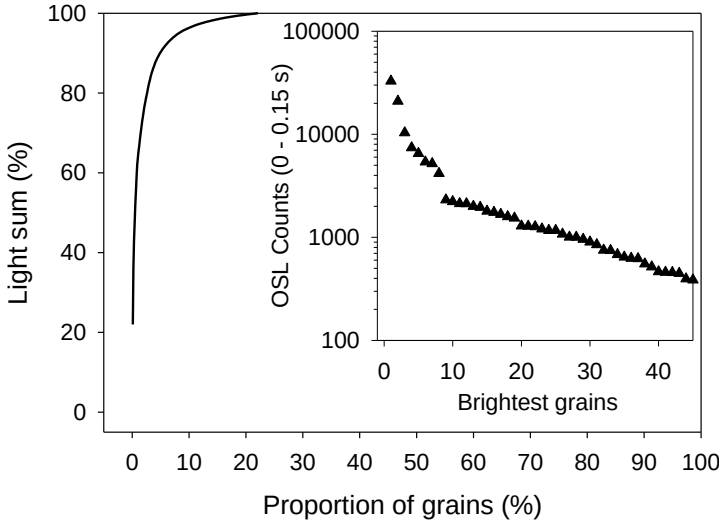

Figure 6.2: The percentage of the total light sum (following a 45.6 Gy dose) as a function of percentage of grains (n = 900) for sample 154–MGJ-5-1B. Inset, the number of OSL counts measured during the initial 0.15 s of green light stimulation for the 44 brightest grains which constitute 90% of the total light sum.

The OSL IR depletion ratio of Duller (2003) is used to differentiate between OSL signals from quartz and (presumably) feldspar signals by comparing the signals from the repeated measurement of two identical regenerative doses, one of which has been exposed to IR prior to measurement with blue LEDs. Duller (2003) found that grains of feldspar and quartz could be differentiated on the basis of this ratio, with feldspar grains having low ratios, typically between 0 and 0.2 and quartz grains exhibiting a slightly broader range of values around unity (figure 6.3).

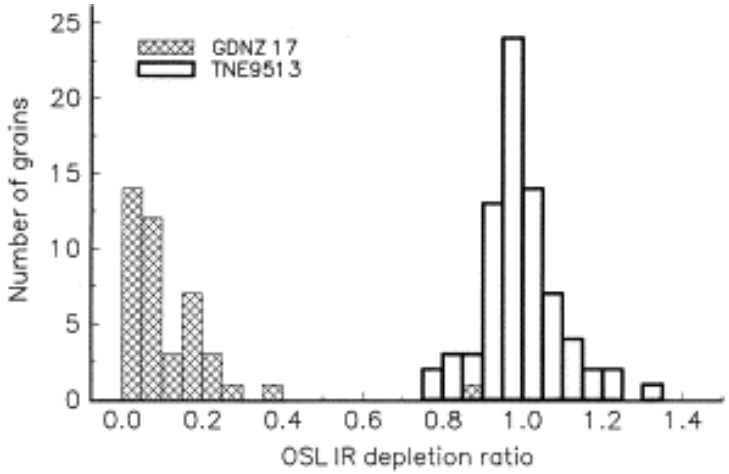

Figure 6.3: The OSL IR depletion ratio measured from single grains of feldspar (GDNZ 17) and quartz (TNE9513). Ratio values of approximately unity are indicative of an OSL signal which is unaffected by IR stimulation. From Duller (2003).

The OSL IR depletion ratios of the brightest 44 grains from 154-MGJ-5-1B, which constitute 90% of the OSL signal, have been calculated and the data presented as a scatter plot in figure 6.4, allowing the uncertainty associated with each ratio to be displayed. The ratios from these grains form two distinct groups; those grains that have a ratio of approximately unity (within errors) and grains which have a ratio of between 0 and 0.2 (figure 6.4). The ratios calculated from the less bright luminescence signals become more variable and this is most likely to due to the uncertainties associated with counting statistics. Duller (2003) interprets grains with low OSL IR depletion ratios as grains of feldspar or other minerals, such as zircons, tourmaline and garnets, which have luminescence signals stimulated by IR. It is therefore concluded that despite the thorough laboratory treatment applied to isolate the quartz mineral fraction, this sample contains many non-quartz mineral grains which contribute to the luminescence signal. Of the 44 grains which make up 90% of the luminescence signal, 19 grains have OSL IR depletion ratios within 10% of unity (taking the uncertainty into account) and are considered to be quartz grains. Therefore, 2% of quartz grains make up 90% of the OSL signal for this sample, and this sample contains significant contamination from non-quartz mineral grains. Whilst this sample is contaminated by feldspar, the clear separation between the quartz and feldspar OSL IR depletion ratios suggests that contamination of the quartz OSL signal by feldspathic inclusions within the quartz grains is not an issue. The potential for contamination of the quartz OSL signal by

feldspar means that the application of the OSL IR depletion ratio to every aliquot will be necessary in order to reject those where feldspars dominate the signal (section 6.3.3.4).

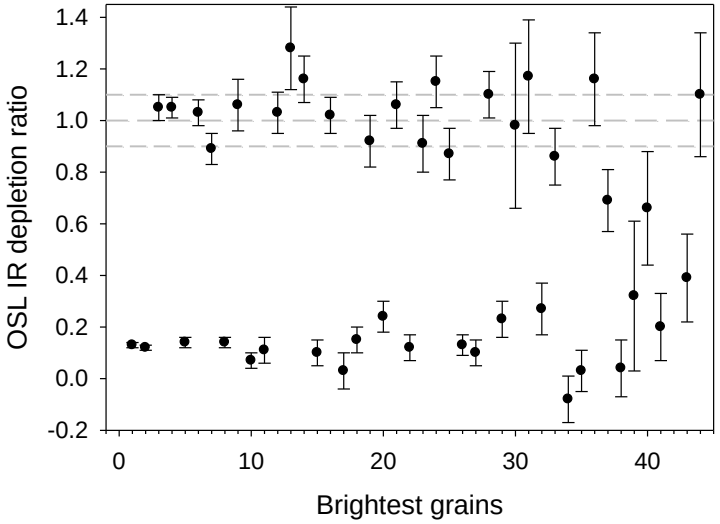

Figure 6.4: OSL IR depletion ratio of the 44 grains (ranked in order of brightness) which make up 90% of the OSL signal of sample 154-MGJ-5-1B. The dashed lines indicate unity and the ±10% ratio thresholds.

Unfortunately, the fine particle size of the other samples in this study does not allow for the single grain analysis of any other samples. However, the types and brightness of luminescence signals from multiple grain aliquots in the other samples analysed in this study do not vary greatly from those seen from sample 154-MGJ-5-1. Therefore there is no reason to believe that there is a considerable difference in the number of grains that contribute to the luminescence signal in the other samples. It has been suggested that small aliquots containing less than 100 grains (e.g. Rittenour, 2008) should be used for the dating of samples from fluvial and colluvial environments and Olley et al. (1998) argue that the use of larger aliquots may result in incomplete bleaching going undetected. In this study, fine grain sand has been dated, so even on a small aliquot, as many as 500 grains may be present (Duller, 2008b; section 4.3.4). However, with only 2% of quartz grains producing a luminescence signal and assuming a small aliquot is packed with a monolayer of spherical grains, 10 grains will constitute the signal if the mean grain size is 100 µm and 4 grains if it is 150 µm. Therefore, this aliquot size should be suitable for detecting spread in sample dose distributions, if present, in this study.

6.3 Calculation of individual D_e values

In this study, a standard SAR protocol (section 4.8.3) has been used to measure the luminescence signal of small aliquots of sample. Multiple determinations of D_e were made for each sample, however, not all measured aliquots provided OSL signals suitable for use when calculating a sample D_e and signals were screened using a rigorous suite of rejection criteria to ensure that only appropriate signals were used for dating. This section outlines the measurement and analysis undertaken to calculate the D_e from a single aliquot and discusses the rejection criteria applied, the calculation of the uncertainty associated with each D_e and summarises the types of signal used for dating.

6.3.1 Measurement conditions and signal analysis

Equivalent dose measurements were made using the SAR protocol (Murray and Wintle, 2000; Wintle and Murray, 2006) outlined in table 4.8. As discussed, the natural signal (L_n) was measured, followed by the measurement of a fixed laboratory test dose (T_n). Following this set of measurements, the OSL response to a series of regenerative doses (L_x) was measured and sensitivity change was monitored by the repeat measurement of the test dose (T_x) after each L_x measurement. Dose response curves were fitted by plotting the normalised OSL signal (L_x/T_x) as a function of the regenerative dose, and depending on which function provided the best fit, either an exponential or an exponential plus linear function was fitted to describe the relationship of the dose response curve. The natural dose was calculated by interpolation of the natural signal onto the dose response curve (e.g. figure 4.18c). Typically, between five and eight regenerative doses were measured to characterise the dose response curve and the repeated measurement of the 0 Gy dose and two repeat measurements of the first regenerative dose point were made to assess the recuperation (section 6.3.3.2), recycling ratio (section 6.3.3.3) and OSL IR depletion ratio (section 6.3.3.4) respectively.

All D_e measurements were made using small aliquots (section 4.3.4), using either Risø 3, Risø 4 or Risø 6 in the ALRL (see table 4.1 for individual machine specifications). For dating using Risø 4, the OSL signal was taken from the first 5 channels (0 – 0.8 s, equivalent to ~22 $mJ.cm^{-2}$ of stimulation energy) and a background subtraction was made, where the background was the mean counts taken from the final 50 channels of measurement (8 s or ~268 $mJ.cm^{-2}$). Where luminescence measurements were made on Risø 3 or Risø 6, the integration and background intervals were varied according to the stimulation power (section 4.7.4.3).

6.3.2 Calculation of the uncertainty associated with individual D_e values

The level of precision with which a D_e can be calculated varies within a sample (Duller, 2007) and in order to combine multiple D_e determinations to produce an equivalent dose for a sample, the uncertainty associated with the individual D_e determinations must be accurately quantified (Bailey and Arnold, 2006). This is of particular importance if statistical analysis is weighted according to the precision of the individual D_e results (Duller, 2007), which is the case for commonly applied age models, including the central age and finite mixture models of Galbraith et al. (1999) and Galbraith and Green (1990). The random errors associated with the measurement of the luminescence signal and subsequent equivalent dose calculation in this study have been calculated using Analyst v3.24 (written by Professor Geoff Duller) and include uncertainties associated with counting statistics, curve fitting and instrument reproducibility.

The relative standard error (RSE) resulting from the counting statistics associated with the measurement of each luminescence signal can be calculated using equation 6.1 (Galbraith, 2002). This equation was updated from the equation first proposed by Banerjee et al. (2000) and the uncertainties calculated for L_x and T_x individually can be propagated in quadrature to produce the L_x/T_x error. In this study, L_n/T_n and L_x/T_x errors are calculated in Analyst by:

$$RSE = \frac{\sqrt{Y_0 + (\bar{Y}/k)}}{Y_0 - \bar{Y}} \qquad \text{(Equation 6.1)}$$

where Y_0 refers to the number of OSL counts, $\bar{Y}$ refers to the mean number of background counts and k refers to the number of channels used for Y_0 (Galbraith, 2002).

The uncertainty associated with the fitting of the dose response curve is also incorporated into the D_e uncertainty. The deviation of the predicted values from the dose response curve from the actual data is used in equation 6.2 (Duller, 2007) and this is calculated in Analyst and combined with the L_n/T_n error.

$$Average\ deviation = \frac{\sqrt{\sum_{i=1}^{i=n} (predicted\ \ L_x/T_x - actual\ \ L_x/T_x)^2}}{n} \qquad \text{(Equation 6.2)}$$

where n is the number of regenerated doses.

Also incorporated into the uncertainty associated with a D_e determination is the uncertainty which arises from measurement of the signal (Duller, 2007). Instrumental uncertainty can be assessed by making a series of repeat measurements of an OSL signal after a fixed irradiation dose (Duller, 2007) and values for the instrumental uncertainty of the equipment in ALRL has been reported to range between 1 and 2.5% (e.g. Armitage et al., 2000; Jacobs et al., 2006; Rodnight et al., 2006). In this study, a 1.5% instrumental uncertainty has been incorporated into the D_e uncertainty.

6.3.3 Removal of OSL signals using rejection criteria

As discussed in section 4.8.2.1, the internal checks available when using the SAR protocol provide a powerful tool to assess measurement reliability (Roberts, 2008). These checks allow for the identification and removal of erroneous signals which may lead to inaccurate D_e determinations and for samples with ages calculated

from signals which satisfy these internal checks, corroboration of ages with independent age control is not required (Roberts, 2008). Wintle and Murray (2006) suggest three tests to assess the appropriateness of a SAR protocol for D_e determination; the recycling ratio test, the recuperation test and the dose recovery test (section 4.8.2.1.3). In this study, the recycling ratio and test for recuperation are routinely applied to individual D_e measurements, as part of a set of rejection criteria used to identify signals unsuitable for routine dating discussed below.

6.3.3.1 Signal levels

The brightness of the luminescence signal of grains varies both between and within samples and measurement uncertainties are usually reduced when brighter signals are measured. 'Dim' OSL signals can still provide accurate D_e determinations, however signals need to be discernible from the background of the measurement equipment and to ensure that this is the case for signals measured in this study, two rejection criteria are routinely applied. To ensure the test dose signals can be repeatedly measured to normalise the natural and regenerative dose OSL signals, the uncertainty associated with the test dose is calculated in Analyst (Duller, 2007) following the protocol of Banerjee et al. (2000), and signals with a test dose error in excess of 10% have been excluded from dose distribution analysis. The background rejection criterion of Jacobs et al. (2006) has also been used to identify and remove OSL signals which are not distinguishable from the background. Signals where the first test dose signal (T_n) is less than three times the standard deviation of the background (e.g. $T_n<3\sigma BG$) have also been removed from dose distribution analysis.

6.3.3.2 Recuperation

Recuperation refers to the amount of luminescence that is measured after a zero dose has been given (e.g. Aitken and Smith, 1988). Heating, irradiation and OSL measurement carried out during the SAR protocol may result in the transfer of charge from deep traps, which could cause this signal to be above zero (Wintle and Murray, 2006). To monitor the level of recuperation, a zero dose is measured as

part of the SAR cycle, and the sensitivity corrected signal from this measurement is compared with the natural signal. The percentage of recuperation (e.g. $[L_0/T_0]/[L_n/T_n]$) should be no more than 5% for the aliquot to be accepted (Murray and Wintle, 2000; Murray and Olley, 2002). For young samples, calculating recuperation as a percentage of the natural may result in an exaggerated recuperation value, due to the calculation of a percentage from a small value (e.g. Reimann et al., 2012). Therefore, for samples less than 500 years old (with a D_e of less than 1.65 Gy), recuperation is calculated as an absolute value (in Gy) and aliquots which have a regenerated dose greater than 0.25 Gy after a 0 Gy dose are excluded from dose distribution analysis.

6.3.3.3 Recycling ratio

The recycling ratio (Murray and Wintle, 2000) provides a check that the SAR protocol is successfully correcting for any sensitivity change occurring during the measurement procedure. The ratio between the sensitivity corrected luminescence signal from one of the first regenerative doses is compared to one of the final, identical regenerative doses, because sensitively change is considered progressive, and a ratio between one of the first and last measurements will provide the widest range of sensitivity change (Wintle and Murray, 2006). Murray and Wintle (2000) suggest a range of acceptability within ±10% of unity, and this threshold (taking uncertainties into account) has been applied in this study.

6.3.3.4 OSL IR depletion ratio

The luminescence signal from quartz and feldspar have significantly different behaviours (Duller, 2003), and despite density separation and etching with HF, the presence of feldspar (either as grains or inclusions) in a purified quartz sample is still a possibility. Single grain analysis of sample 154-MGJ-5-1B (section 6.2) suggests that contamination by feldspar may be an issue for the samples in this study. Therefore, it is prudent to incorporate a procedure into the measurement protocol to check for feldspathic contamination. Duller (2003) developed the OSL IR

depletion ratio, which compares the L_x/T_x from two identical regenerative doses, with the OSL measurement from the second dose immediately preceded by stimulation with IR. Quartz gives only a limited signal when stimulated with IR (Spooner, 1994), and therefore, if quartz is the only source of the luminescence signal, the two L_x/T_x values should be equal. If present, the feldspar signal will be reduced by the IR stimulation and the ratio between the two sensitivity corrected signals will be less than unity. In this study, aliquots with OSL IR depletion ratios which differ from unity by more than 10% (within errors) have been excluded from D_e calculation.

6.3.3.5 The fast ratio

The quartz CW-OSL signal is composed of signal originating from the fast, medium and slow components (section 5.2), and it is generally considered that OSL signals dominated by the fast component provide more accurate age estimates (Bailey, 2010). The fast ratio of Durcan and Duller (2011), presented in chapter 5, has been developed to identify fast dominated quartz OSL signals and can be applied as a rejection criterion. In this study, a fast ratio of 20 or more (within errors) has been used to identify signals which are dominated by the fast component (where 90% of the signal in the first channel originates from the fast component). Aliquots which have a fast ratio below 20 (within errors) for the natural signal and/or the largest regenerative signal (up to D_0) have been excluded from D_e calculation.

6.3.4 Signal assessment

A large number of the aliquots measured during the course of this study failed to satisfy at least one of the rejection criterion outlined in section 6.3.3 and were excluded from dose distribution analysis. For each sample, each rejection criterion was applied to all measured signals, with the majority of signals failing at least one criterion, but more often two or more criteria. Table 6.1 summarises the screening of the 126 signals measured for sample 154-MGJ-1-4. Of the 126 measured signals, 28 (22%) of signals pass all 6 rejection criteria and are used to calculate the sample

D_e. The remaining 98 signals fail one or more rejection criteria and were excluded from subsequent analysis, with 70 signals failing at least two criteria. Approximately one third of signals (39 of 126) fail both the OSL IR depletion ratio and the fast ratio (table 6.1), with feldspar contamination appearing to be a particular problem for this sample, and 77 of the 126 measured signals failing the OSL IR depletion in total (table 6.1). The radial plot in figure 6.5 shows the dose distribution of D_e values from the accepted (filled symbols) and rejected (open symbols) signals for this sample, and shows that application of the suite of rejection criteria removes D_e determinations which are not precisely known (i.e. points which fall to the left of the plot) and D_e calculations that do not appear to be consistent with the sample D_e calculated for this sample (table 6.3).

Table 6.1: Data screening summary of the 126 signals measured from sample 154-MGJ-1-4. Pass indicates the number of rejection criteria (out of 6) that are met, where only signals passing all six criteria are used for D_e determination. The suite of rejection criteria are shown, with X indicating that the criteria was not satisfied for the number (n) of samples. The percentage of measured aliquots which meet the number of rejection criteria are also shown.

Pass (of 6)	Signal levels	Recup-eration	Recycling ratio	OSL IR depletion ratio	Fast ratio	n		% Measured aliquots	
6						28		22.2	
5				X		17	28	13.5	22.2
					X	6		4.8	
	X					2		1.6	
			X			2		1.6	
		X				1		0.8	
4				X	X	39	52	31.0	41.3
		X		X		3		2.4	
	X				X	2		1.6	
	X			X		2		1.6	
		X			X	2		1.6	
			X	X		2		1.6	
	X	X				1		0.8	
			X		X	1		0.8	
3		X		X	X	6	15	4.8	11.9
	X	X			X	3		2.4	
	X			X	X	2		1.6	
	X	X		X		1		0.8	
	X		X	X		1		0.8	
		X	X	X		1		0.8	
		X	X		X	1		0.8	
2	X	X		X	X	2	3	1.6	2.4
		X	X	X	X	1		0.8	
Total	16	22	9	77	65	126	126	100	100

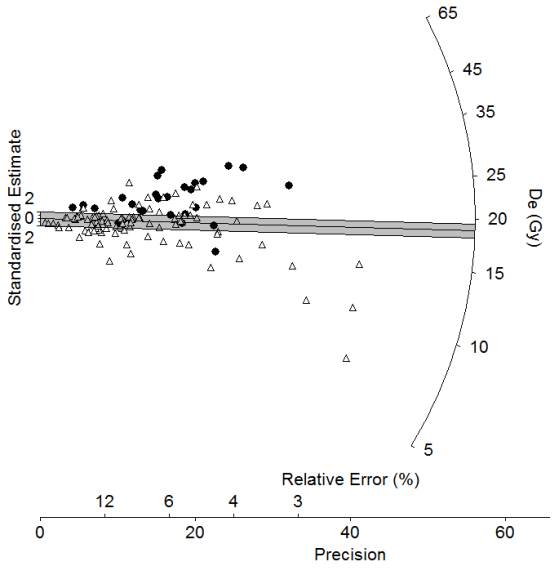

Figure 6.5: Radial plot of sample 154-MGJ-1-4. D_e determinations from signals which satisfy all six rejection criteria are shown by the filled symbols and those that fail one or more rejection criteria are shown by the open symbols. The sample D_e of 18.70 Gy (calculated using the finite mixture model) and a ±2σ confidence interval are shown by the solid black line and grey shaded area.

For each sample dated in this study, table 6.2 shows the number of signals measured, the percentage of signals which satisfied all six rejection criteria and a breakdown of the number of signals which failed to satisfy each criterion. Figure 6.6 shows examples of the types of signals which fail each of the rejection criteria. On average, 34% of all measured aliquots were used for D_e calculation and dating, ranging between 17% and 90% for individual samples (table 6.2). For some samples, less than 20% of the measured aliquots were used for D_e calculation (e.g. 136-6-7, 153-TIL3-18), although a larger number of aliquots were accepted for some samples, including 136-4-2 (60%) and 154-MGJ-4-2 (62%). Generally, relatively few aliquots were rejected on the basis of signal levels, and for samples where a higher than average number of signals are rejected (e.g. samples 136-4-1 and 155-SUT-3-1), this is likely to reflect a low number of grains providing a luminescence signal. Similarly, relatively few signals were rejected on the basis of recuperation, although higher numbers are seen for samples with a low D_e, which may reflect the sensitivity of low doses to recuperation caused by thermal transfer (Murray and Olley, 2002). Whilst the exclusion of signals with a low D_e on the basis of recuperation alone may lead to bias in the dataset, in this study, signals which failed on the basis of the recuperation ratio usually failed at least one other criterion (e.g. sample 154-MGJ-1-4, table 6.2). On average, 18% of signals were rejected on the

basis of the recycling ratio (table 6.2) and it was rare to see a signal fail only the recycling ratio criterion, e.g. only 2 of the 126 aliquots for sample 154-MGJ-1-4 (table 6.2). More usual was that a signal would fail two or more rejection criteria as well as the recycling ratio, indicating that the SAR protocol could not be successfully used to measure that signal.

Table 6.2: Summary of the percentage of aliquots failing each rejection criterion per sample and the total number and percentage of aliquots measured and accepted (shown in parenthesis).

Sample	Signal Levels	Recup-eration	Recycling ratio	OSL IR depletion ratio	Fast ratio	# Measured (accepted)	% Accepted
136-3-1	5.0	13.3	3.3	48.3	30.0	60 (21)	35
136-3-9	29.2	16.7	18.8	35.4	22.9	96 (44)	46
136-4-1	3.6	19.1	7.1	45.2	29.8	84 (31)	37
136-4-2	2.4	6.0	9.6	24.1	12.1	83 (50)	60
136-6-1	14.8	6.5	16.7	43.5	40.7	108 (28)	26
136-6-7	23.2	10.2	18.5	52.8	57.4	108 (21)	19
153-MAR2-5B	0.0	0.0	10.4	2.1	0.0	48 (43)	90
153-MAR2-13B	0.0	2.1	28.1	28.1	56.3	96 (34)	35
153-TIL3-2	4.2	9.7	11.1	44.4	44.4	72 (27)	38
153-TIL3-8B	8.3	4.2	20.8	37.5	66.7	48 (15)	31
153-TIL-10A	13.6	21.2	21.2	28.8	68.2	66 (12)	18
153-TIL3-18	16.7	16.7	16.7	50.0	69.2	120 (20)	17
154-MGJ-1-1	0.0	6.3	8.3	31.3	27.1	48 (22)	46
154-MGJ-1-4	12.7	17.5	7.1	61.1	51.6	126 (28)	22
154-MGJ-1-8	6.7	3.3	16.7	18.3	25.0	60 (31)	52
154-MGJ-2-1	11.5	32.3	15.6	18.8	45.8	96 (35)	36
154-MGJ-2-5	20.8	21.9	21.9	33.3	50.0	96 (28)	29
154-MGJ-3-1	14.6	8.3	10.4	25.0	18.8	48 (26)	54
154-MGJ-3-6	8.3	20.8	13.9	22.2	23.6	72 (40)	56
154-MGJ-4-2	4.6	4.6	15.2	21.2	12.1	66 (41)	62
154-MGJ-4-5	15.3	11.1	15.3	22.2	37.5	72 (29)	40
154-MGJ-5-1	24.2	34.3	38.2	31.9	48.5	204 (47)	23
154-MGJ-5-5	10.4	34.4	27.1	18.8	49.0	96 (26)	27
154-MGJ-6-2	5.6	13.9	26.4	23.6	33.3	72 (31)	43
154-MGJ-6-3	18.5	28.7	26.9	38.0	38.9	108 (29)	27
155-SUT-2-1	2.4	3.6	14.3	34.5	38.1	84 (23)	27
155-SUT-3-1	25.6	9.0	21.8	19.2	41.0	78 (34)	44
Mean	*14.1*	*13.9*	*18.7*	*33.6*	*41.0*	*2315 (816)*	*35*

Measured signals most commonly failed on the basis of the OSL IR depletion ratio and/or the fast ratio (table 6.2). The fast ratio is not completely independent of the OSL IR depletion ratio (section 5.5.4), particularly when the OSL IR depletion ratio is low, and therefore many aliquots which fail one of these criteria will fail the other. However, as demonstrated in section 5.5.4, the two criteria are not completely dependent and many aliquots fail solely on the basis of the OSL IR depletion ratio

(17 signals for sample 154-MGJ-1-4; table 6.2) or the fast ratio (6 signals of 154-MGJ-1-4). Therefore, whilst more signals are rejected on the basis of the fast ratio overall in this study (table 6.2), the presence of significant feldspar contamination is a contributory factor. If both the OSL IR depletion ratio and fast ratio are viewed as a proxy for OSL decay form, many signals measured in this study do not have the typical, rapid, near exponential decay to background levels which is expected from a quartz OSL signal dominated by the fast component.

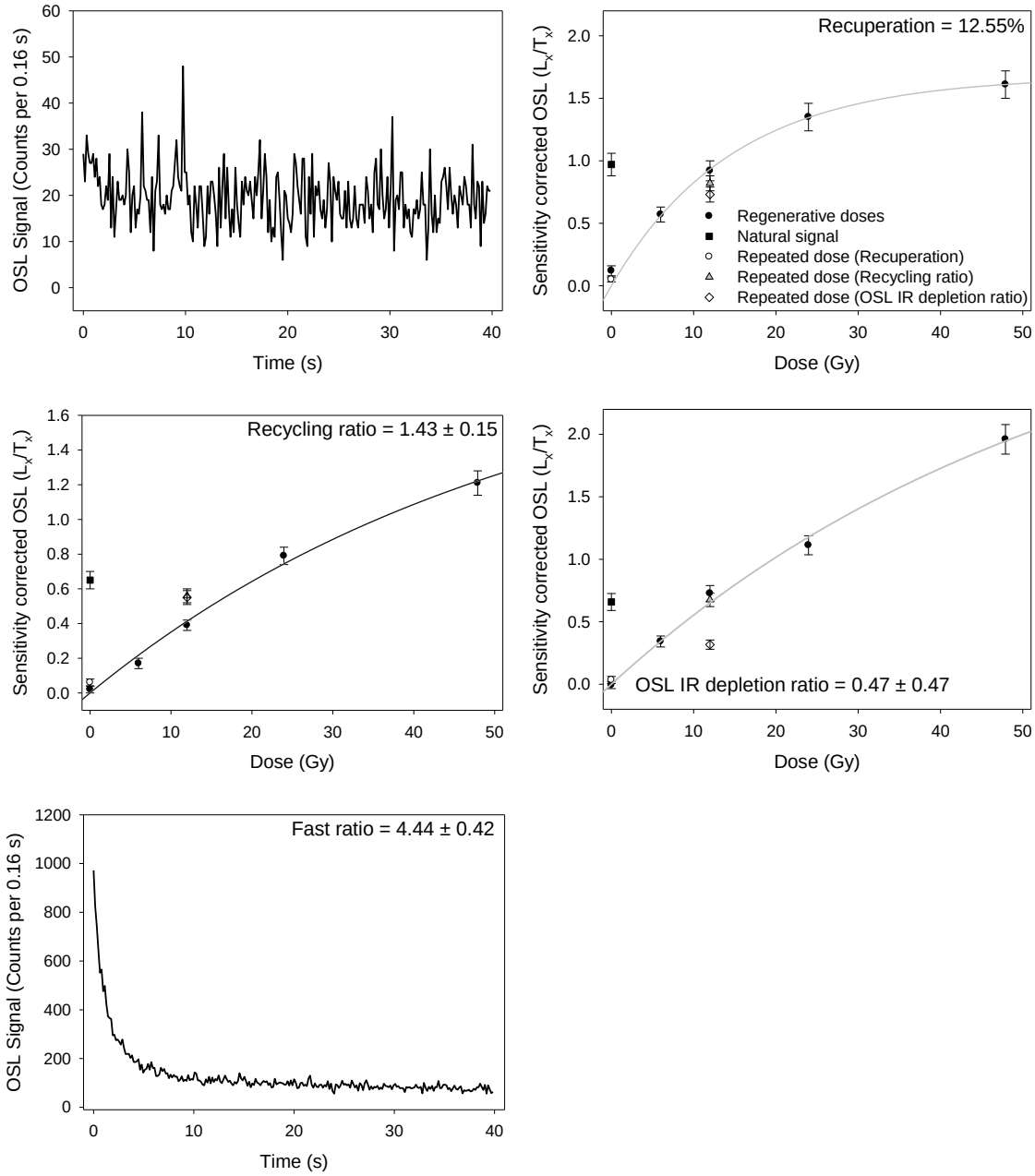

Figure 6.6: Graphs showing the type of signals that did not satisfy the suite of rejection criteria: a) The signal is not discernible from the background after a 10 Gy dose. b) A measureable OSL signal after the 0 Gy regenerative dose indicates thermal transfer and recuperation. c) The recycling ratio is not consistent with unity. d) The OSL IR depletion ratio is not consistent with unity. e) The OSL signal does not satisfy the fast ratio threshold. The legend shown in b) is applicable to c) and d).

6.3.4.1 Feldspar contamination

The luminescence characteristics of quartz and feldspars are not similar and when dating using coarse grains, it is usually desirable to isolate the two minerals prior to measurement of the luminescence signal (Wintle, 1997). Thomsen et al. (2008) summarise the reasons for separating the two mineral fractions, stating that feldspar usually has a much stronger luminescence signal than quartz and that the bleaching characteristics are different (with the OSL signal of quartz depleting much more rapidly in daylight). Feldspar and quartz may also record different doses, with the internal ^{40}K content of some feldspar grains causing dose overestimation if not taken into account. Failure to account for anomalous fading of the feldspar signal can cause D_e underestimation.

In this study, the laboratory treatment undertaken to isolate the quartz fraction from the bulk mineral sample is discussed in section 4.2. However, the single grain measurement of sample 154-MGJ-5-1B suggests feldspar contamination (section 6.2) and the large number of signals which fail to satisfy the OSL IR depletion ratio also suggests this (table 6.2). On average, over a third of signals measured during the OSL dating of samples in this study were rejected due to the OSL IR depletion ratio not being within 10% of unity (table 6.2) and for the majority of samples, a significant number of aliquots are rejected on the basis of this ratio alone. As discussed in section 4.2.4, heavy liquid density separation was undertaken to isolate the quartz grains from the bulk mineral sample, with mineral grains separated into fractions with densities of less than 2.62 $g.cm^{-3}$, between 2.62 and 2.70 $g.cm^{-3}$ and more than 2.70 $g.cm^{-3}$. For each sample, figure 6.7a shows the proportion of the 'feldspar' (ρ < 2.62 $g.cm^{-3}$), 'quartz' (2.62 < ρ < 2.70 $g.cm^{-3}$) and 'heavy mineral' (ρ < 2.70 $g.cm^{-3}$) fractions separated from the bulk mineral sample. For the samples in this study, between 9 and 70% of the bulk sample separated was composed of grains with densities between 2.62 and 2.70 $g.cm^{-3}$, and for all samples, on average, 43% of the material separated came from the quartz fraction. In figure 6.7b, the mass of purified quartz obtained after density separation, HF etching and 2nd sieving (e.g. figure 4.1) as a fraction of the amount of material separated is shown. For the

samples analysed, between 1% and 30% of the original mass separated is retained as purified quartz suitable for dating, and typically, this amount is less than 15% per sample. This means for samples where 5 g of material was originally separated using heavy liquid density separation, on average 0.75 g remained for dating at the end of the laboratory treatment. Alizai et al. (2011) measured isotopic variability of K-feldspar grains from samples taken at Fort Abbas, Marot, Fort Derawar and the Sutlej. Whilst they did not confirm absolute amounts of quartz and feldspar in these samples, Alizai et al., (2011) comment that K concentration, usually associated with K feldspars, is present in abundance in these samples. It can therefore be concluded that for many samples in this study, quartz is not present in large amounts.

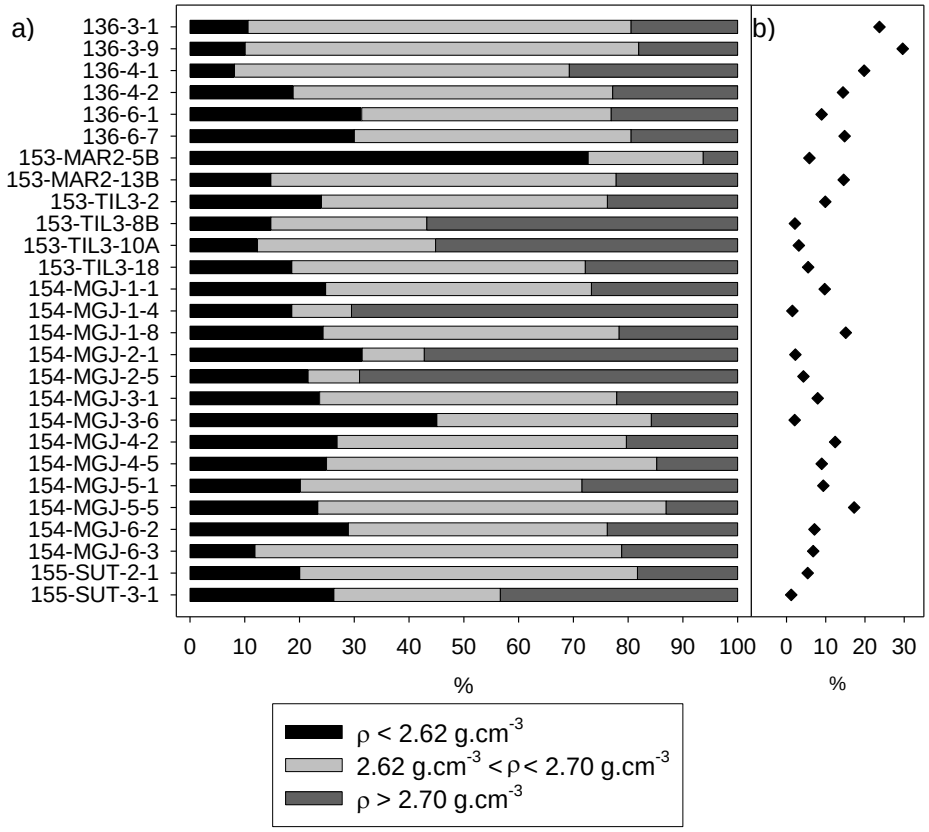

Figure 6.7: a) The percentage of mass separated during heavy liquid density separation. Quartz should be isolated in the $2.62 < \rho < 2.70$ g.cm^{-3} fraction. b) The percentage of purified quartz retained for dating as a percentage of the mass treated using density separation, chemical etching and second sieving.

For each sample, figure 6.8 shows the relationship between the amount of material separated in the feldspar fraction and the percentage of signals which fail the OSL IR depletion ratio. A weak negative correlation ($r^2 = 0.32$) is observed, and typically,

samples from which a relatively low amount of feldspar has been separated have a high number of signals which fail the OSL IR depletion ratio. For example, for sample 153-MAR2-5B, 73% of the mass separated had a density less than 2.62 g.cm^{-3}, with 21% of the mass having a density between 2.62 and 2.70 g.cm^{-3} (figure 6.7a) and for this sample, less than 5% of signals fail the OSL IR depletion ratio. Conversely, for sample 136-3-1, 70% of the separated mass was between 2.62 and 2.70 g.cm^{-3} (figure 6.7a), but 48% of signals failed the OSL IR depletion ratio (table 6.2). Therefore, for some samples, it appears that heavy liquid density separation and HF etching does not completely isolate the quartz mineral fraction. For samples where feldspar contamination was prevalent, a second HF etch was undertaken. However, this usually resulted in less than 0.1 g of material remaining after the etch for dating, and this approach was not applied routinely. However, the significant reduction in mass after a second HF etch provides further evidence for contamination by feldspar. Further investigation is required to determine the reason for this contamination. The single grain measurement of sample 154-MGJ-5-1B (section 6.2) suggests that feldspathic inclusions within the quartz grains are not the issue, and it may be that the feldspar in the samples in this study has a density more similar to that of quartz.

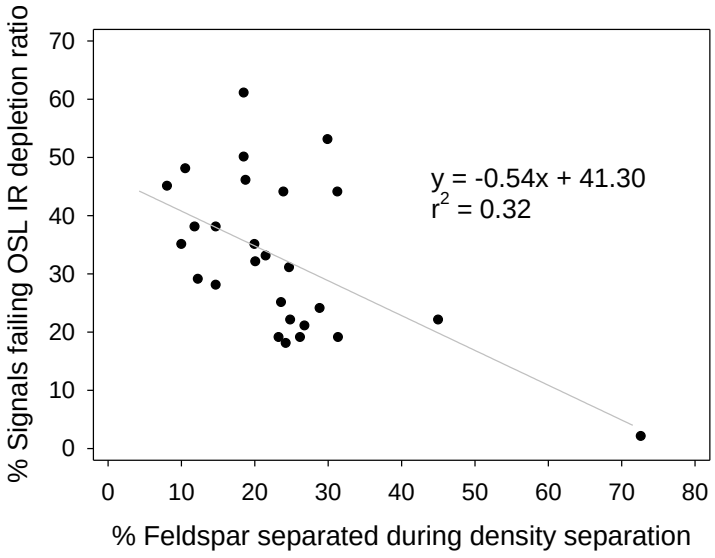

Figure 6.8: The percentage of feldspar (or material with densities of $\rho < 2.62$ g.cm^{-3}) removed during heavy liquid density separation as a function of the percentage of measured signals failing the OSL IR depletion ratio for each sample. The linear function fitted and the correlation co-efficient are also shown.

6.4 Calculation of a sample D_e

The measurement of a number of individual D_e values for one sample allows trends within a dose distribution to be identified. The most appropriate means of statistical treatment can be established on the basis of visual inspection of the distribution and statistical assessment of the spread in the dose distribution (Galbraith et al., 2005). Analysis of dose distributions is complex and there are many factors which may contribute to inconsistency in D_e values from the same sample, including heterogeneous bleaching, microdosimetry and post-depositional mixing. To further complicate this analysis, it is reported in the literature that samples which should have been well bleached at deposition can exhibit great variability (Thomsen et al., 2005; Jacobs et al., 2006). This section outlines the statistical analysis undertaken to calculate a sample D_e from a large number of individual D_e determinations.

6.4.1 Radial plots

Single grain and single aliquot measurement protocols allow a large number of D_e determinations to be calculated rapidly and routinely for a single sample. The graphical display of these data is necessary to help identify trends within the data and to inform which individual D_e determinations are most likely to represent the 'true' D_e (Galbraith and Roberts, 2012). There are a number of ways that dose distributions can be presented and in the past variants of scatterplots, histograms and radial plots have been used. These presentation methods have been discussed in detail by Duller (2008b) and Galbraith (2010), but critical to the method used is that the precision associated with each individual D_e determination is presented (Galbraith and Roberts, 2012). According to these authors, the radial plot (figure 6.9) allows different levels of precision to be graphically presented. The radial plot was initially designed for use in fission-track dating by Galbraith (1988; 1990) and has since been suggested for use in luminescence dating (Galbraith et al., 1999).

When used for the presentation of D_e determinations, the radial plot displays both the D_e value and the associated uncertainty. This allows 'outliers' to be identified

visually and provides a graphical means of assessing whether individual D_e determinations are consistent with the 'true' dose. In a radial plot, the precision is plotted on the x-axis against the standardised estimate on the y-axis. The D_e of any given point can be read off by drawing a straight line from the origin to the scale of slopes (the radial axis) and the precision (the reciprocal of the standard error) can be read from the x-axis. D_e values with small errors (high precision) will plot towards the right of the diagram, with less precisely known D_e values plotted to the left. Where the y-axis is plotted between 2 and -2 standardised units, its length is equivalent to a two sigma error bar, which can be applied to any point plotted on the radial plot (Galbraith and Roberts, 2012).

In this study, radial plots have been used for data presentation. Figure 6.9 shows an example radial plot for sample 136-3-9. Log D_e determinations are plotted on the radial scale and the relative standard error is plotted on the x-axis. Individual D_e values that plot within the grey area are within 2σ of the 14.94 Gy D_e calculated for this sample. Using the radial plot to present this dose distribution allows a number of observations to be made. The majority of individual D_e values are consistent within ±2σ of the sample D_e of 14.94 Gy, although the level of precision varies. Not all measured D_e values are consistent and a number of D_e estimates are visually distinctive from the main population.

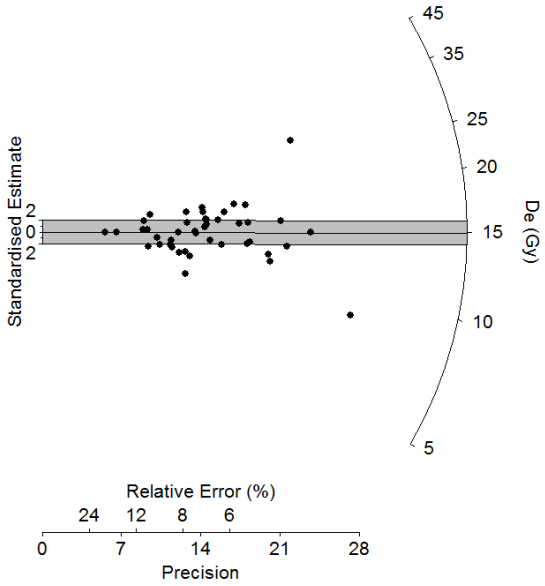

Figure 6.9: A radial plot of sample 136-3-9. All points within the grey shaded area are within 2σ of the 14.94 Gy D_e (shown by the solid line).

6.4.2 Statistical derivation of D_e

The development and application of single aliquot dating protocols has permitted the rapid and routine measurement of many aliquots from a sample, which allows the underlying dose distribution of a sample to be assessed. Single grain analysis of aeolian sediments has shown that variability in dose distributions is evident even in samples that were thought to have been completely bleached at the time of burial (Jacobs et al., 2006). For many fluvial samples, broad, asymmetric dose distributions have been observed (e.g. Murray et al., 1995; Olley et al., 1998; 1999; Wallinga, 2002), and these are often attributed to incomplete bleaching. The use of single grains or small aliquots when dating fluvial sediments has been advocated by many authors (e.g. Olley et al., 1998; 1999; Wallinga, 2002), however, for all samples irrespective of depositional history, calculating individual D_e estimates using the luminescence signal from a small number of grains will allow complexity in the dose distribution of a sample to be investigated (e.g. Galbraith et al., 2005).

Visual inspection of a dose distribution can help inform to some extent, the factors contributing to complexity (Rodnight et al., 2006). However, the calculation of a sample D_e from a dose distribution which is non-Gaussian can be challenging, and simply taking the mean value is not likely to be appropriate, with more complex statistical treatment required (Wallinga, 2002). Statistical treatments to derive the 'true' D_e have been presented in many studies and approaches have varied. These approaches include i) taking the mean of the lowest 5% of D_e values (Olley et al., 1998), ii) calculating D_e from values which only fall within a fixed standard deviation of the mean (Fuchs and Lang, 2001) and iii) the leading edge model of Lepper and McKeever (2002) which plots the dose distribution as a histogram, fits a Gaussian distribution to the leading edge of the distribution and a second derivative of this Gaussian is used to calculated the D_e. Whilst these treatments provided OSL ages in good agreement with independent age control in the studies which they were presented in, the precision associated with each individual D_e is not taken into account.

The age models of Professor Rex Galbraith and co-workers are considered to be the most robust of the published age models to date (Bailey and Arnold, 2006; Arnold et al., 2009) because the precision of each individual D_e determination is taken into consideration (Galbraith et al., 1999) and the variability, or overdispersion (section 6.4.2.2) is incorporated into the calculation of the D_e and uncertainty (Galbraith and Roberts, 2012). A number of age models have been devised by Professor Rex Galbraith and these are often applied in luminescence dating. The central age model (Galbraith et al., 1999), the minimum age model (Galbraith and Laslett, 1993; Galbraith et al., 1999) and the finite mixture model (Galbraith and Green, 1990; Roberts et al., 2000) are described in the following section.

6.4.2.1 The Galbraith age models

The common age model outlined by Galbraith et al. (1999) assumes that all D_e values are consistent with a common value (e.g. figure 6.10b) and that 'within' aliquot measurement errors account for variability in the dose distribution (Galbraith et al., 2005). In reality, the dose distributions of quartz samples (from single grain and multiple grain signals) exhibit variability which cannot be explained by measurement uncertainties alone (Galbraith and Roberts, 2012). This inherent spread in the underlying dose distribution is described by a parameter called overdispersion (σ_d) and overdispersion values of up to 22% have been reported for single grain measurements of samples believed to have been well bleached at deposition (Jacobs et al., 2006). Using the central age model (CAM) of Galbraith et al. (1999), it is not assumed that measurement uncertainties account for all of the variability in D_e values observed (Galbraith and Roberts, 2012). When applying the CAM, it is assumed that the logarithm of the D_e values form a normal distribution and the mean (δ) and standard deviation (σ) are calculated. These parameters are calculated by simultaneously solving equations 6.3 and 6.4 presented in section 6.4.2.2.

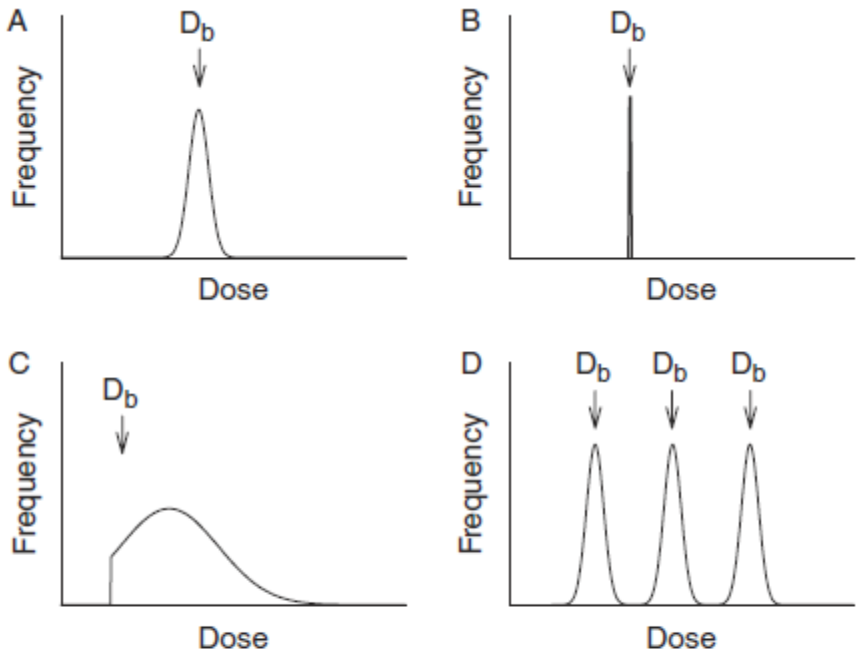

Figure 6.10: Schematic representation of the a) central age model, b) common age model, c) minimum age model and d) finite mixture model. The curves show the theoretical distribution of D_e values for a sample and D_b indicates the sample D_e which would be used for age calculation using each model. Modified from Rodnight (2006) in Duller (2008b)

The minimum age model (MAM) was first outlined by Galbraith and Laslett (1993) and was presented with reference to luminescence dating by Galbraith et al. (1999). This model was developed for use with samples that are incompletely bleached (Galbraith et al., 1999) and assumes that some signals have been fully bleached prior to deposition and burial, whilst other signals contain residual charge from previous burial events, leading to higher equivalent doses (figure 6.10c). To apply this model, the calculation of four parameters and their errors are required: the proportion of fully bleached grains, the point of truncation in the distribution (the logarithm of D_e), the mean value of the distribution if a Gaussian distribution were fitted and the overdispersion of the distribution. A maximum likelihood method is used to estimate these parameters. A three parameter MAM can be applied where the values for the truncation point and mean are equal. Galbraith et al. (1999) note that the application of the MAM may not be appropriate in all instances and if low D_e determinations do not relate to incomplete bleaching, but for example post-depositional mixing (e.g. bioturbation) or microdosimetry (e.g. an inhomogeneous beta matrix), an estimate of the minimum equivalent dose population may not be desirable.

The finite mixture model (FMM) was described by Galbraith and Green (1990) for identifying discrete populations within a dataset for fission track dating. In luminescence dating, it can be applied to dose distributions containing discrete populations (e.g. figure 6.10d; Jacobs et al., 2006) and for heterogeneously bleached samples where a continuum of D_e values is evident (Roberts et al., 2000). This model identifies populations or components (k) of D_e determinations that are consistent with each other (according to a user defined value of σ_d) and assuming a Gaussian distribution. The mean and standard deviation of each component is calculated from the logarithm of the D_e determinations. For each component, the mean and standard deviation are calculated, as well as the proportion of individual D_e determinations that make up each component, with a one component FMM being identical to the CAM. The model should be run fitting two components, then three components and so on, with the maximum log likelihoods obtained from the fitting used to assess how well the model fits the data (Galbraith and Roberts, 2012). The Bayes Information Criterion (BIC) provides a useful means of assessing the fit of the model and takes into account the maximum log likelihoods and the number of fitted components. The BIC value will decrease as more components are fitted but will increase as the increase in maximum log likelihood is counteracted by the number of modelled components (Galbraith and Roberts, 2012). Therefore, Galbraith (2005) states that the fit with the lowest BIC value should be selected for D_e calculation.

6.4.2.2 Overdispersion

The overdispersion (σ_d) value of Galbraith et al. (1999) provides a measure of the relative standard deviation of the underlying dose distribution after measurement uncertainties have been taken into account, where an σ_d of 0%, means that all log D_e values are equal (within errors). This parameter is now widely used in OSL dating to assess and compare dose distributions and is calculated as part of the calculation of the CAM of Galbraith et al. (1999). σ_d and the CAM can be calculated by simultaneously solving the equations of Galbraith et al. (1999):

$$\delta = \frac{\sum_{i=1}^{n} w_i \hat{\delta}_i}{\sum_{i=1}^{n} w_i} \qquad \text{(Equation 6.3)}$$

$$\sum_{i=1}^{n} w_i^2 (\hat{\delta}_i - \delta)^2 = \sum_{i=1}^{n} w_i \qquad \text{(Equation 6.4)}$$

$$where\ w_i = \frac{1}{\sigma^2 + s_i^2}$$

where σ is the overdispersion, $\hat{\delta}_i$ is the natural logarithm of the D_e, s is the standard error and w is the weight. n refers to the number of aliquots/grains.

Olley et al. (2004a; 2004b) reason that once measurement uncertainties have been taken into account, σ_d should equal zero if they were the only source of variability in D_e. However, σ_d values of between 9 and 22% have been reported for single grain dose distributions from samples which were considered to have been well bleached at deposition (see Jacobs et al., 2006 and references therein). Olley et al. (2004a) conclude that σ_d values of less than 20% are consistent with a single component dose population and advocate the application of statistical treatment with this as its underlying assumption. According to Olley et al. (2004b), σ_d values in excess of 20% are indicative of substantial spread in the dose distribution that can not be explained solely by measurement uncertainties. The variability in such dose distributions may originate from a number of possible sources including heterogeneous bleaching at the time of deposition, post depositional mixing (e.g. bio- or pedo-turbation) and the variations in the dose rate over the micro-scale, or a combination of these sources (Rhodes, 2011). Such distributions should be considered as having at least two dose populations and treated in a statistically appropriate manner.

The overdispersion has been calculated for each sample using equations 6.3 and 6.4, and these values are listed in table 6.3. σ_d varies between 12 and 110% with the majority of samples having an σ_d of less than 45%. The greatest σ_d is seen in the two young aeolian samples, 154-MGJ-3-6 and 154-MGJ-5-1, where the D_e is less than 0.5

Gy. Large percentage overdispersion is commonly seen in young samples, and for example, Arnold et al. (2009) report overdispersion values of between 73% and 208% for samples less than 350 years of age. The impact of incomplete bleaching and residual doses will likely have the greatest impact on young samples (Duller, 2008b) and this is the likely cause of the large overdispersion values for samples 154-MGJ-3-6 and 154-MGJ-5-1. With the exception of these two samples, there is no discernible relationship between D_e and σ_d for the samples measured in this study (figure 6.11c).

Rittenour (2008) recommends that coarser grain sizes be used when dating fluvial deposits, as many authors have reported better bleaching of coarser sand (e.g. Olley et al., 1998; Colls et al., 2001; Wallinga, 2002). Rittenour (2008) argues that the aggregation of finer grains and mud coatings may hinder the amount of light reaching the grain during a transport event and that the deposition environments formed by coarser grains (such as channel bars) should be sampled to increase the likelihood of the full resetting of the OSL signal. The samples in this study were predominately made up of fine sands and silts and the coarser grain size fractions (e.g. the 180 – 212 µm fraction) were absent. Despite this, there is no obvious relationship between particle size and σ_d for the samples in this study (figure 6.11a), although the majority of dating has been undertaken using the 90 – 125 µm fraction. There is also no clear difference in σ_d according to the inferred depositional process (figure 6.11b). The σ_d of samples taken from sedimentological units implying aeolian distribution varies between 20 and 37% (excluding the two young aeolian samples discussed above), and for fluvial samples, a range of 12 to 57% is seen (figure 6.11c; table 6.3).

Table 6.3: The σ_d (%) of each of the samples measured in this study. The D_e (Gy) calculated from the CAM, MAM and FMM are also shown, alongside the mode of deposition inferred from the site sedimentology. For the FMM, the number of components, k, and the proportion of individual D_e determinations in the selected component are given. The age model used for the D_e determination is shown in bold. Saturated samples are discussed further in section 6.4.4. D_e distributions are shown in appendix E. Samples are listed by site and in stratigraphic order. Further details are given in section 2.6 and 2.7 and in table 2.1.

Sample	Deposition	σ_d (%)	CAM (Gy)	MAM (Gy)	FMM (Gy)	FMM (k, %)
136-3-1	Fluvial	39.7 ± 1.4	17.85 ± 1.58	12.03 ± 3.21	**16.49 ± 0.62**	2, 95
136-3-9	Fluvial	22.5 ± 0.4	14.20 ± 0.78	12.02 ± 0.74	**14.94 ± 0.54**	2, 46
136-4-1	Fluvial	37.5 ± 0.9	16.21 ± 1.12	11.24 ± 2.95	**15.38 ± 0.47**	2, 70
136-4-2	Fluvial	42.6 ± 0.6	23.26 ± 1.41	15.14 ± 2.71	**19.19 ± 0.71**	3, 70
136-6-1	Fluvial	31.7 ± 0.9	35.59 ± 2.23	24.92 ± 2.19	**30.79 ± 1.36**	2, 76
136-6-7	Fluvial	25.2 ± 1.0	36.89 ± 2.15	14.94 ± 0.54	**33.35 ± 1.80**	2, 80
153-MAR2-5B	Fluvial	11.7 ± 0.2	**23.99 ± 0.47**	23.33 ± 1.21	Not calc	-
153-MAR2-13B	Fluvial	**Saturated**				
153-TIL3-2	Fluvial	45.2 ± 1.2	19.20 ± 1.70	11.35 ± 1.25	**14.15 ± 0.66**	3, 60
153-TIL3-8B	Fluvial	**Saturated**				
153-TIL-10A	Fluvial	**Saturated**				
153-TIL3-18	Fluvial	43.7 ± 1.9	122.74 ± 13.33	114.05 ± 89.73	**116.15 ± 7.42**	3, 73
154-MGJ-1-1	Fluvial	24.8 ± 0.9	25.77 ± 1.44	3.25 ± 0.14	**22.25 ± 1.39**	2, 65
154-MGJ-1-4	Fluvial	32.4 ± 0.9	27.11 ± 1.72	18.54 ± 1.81	**18.70 ± 1.33**	2, 35
154-MGJ-1-8	Fluvial	27.3 ± 0.7	25.15 ± 1.29	18.62 ± 1.55	**20.75 ± 1.42**	2, 57
154-MGJ-2-1	Fluvial	42.0 ± 0.9	2.67 ± 0.20	1.66 ± 0.17	**2.07 ± 0.11**	3, 62
154-MGJ-2-5	Fluvial	28.8 ± 0.8	24.79 ± 1.41	18.26 ± 1.64	**25.81 ± 0.68**	2, 92
154-MGJ-3-1	Aeolian	28.2 ± 0.9	30.14 ± 1.75	30.42 ± 11.31	**27.37 ± 2.45**	2, 52
154-MGJ-3-6	Aeolian	78.3 ± 1.5	0.75 ± 0.01	Not calc	**0.37 ± 0.03**	4, 44
154-MGJ-4-2	Fluvial	57.0 ± 1.0	55.35 ± 5.03	27.53 ± 2.48	**30.67 ± 2.44**	4, 27
154-MGJ-4-5	Fluvial	43.1 ± 1.2	46.13 ± 3.85	26.84 ± 2.80	**29.21 ± 2.49**	3, 35
154-MGJ-5-1	Aeolian	110.0 ± 2.6	0.34 ± 0.07	Not calc	**0.25 ± 0.02**	3, 78
154-MGJ-5-5	Aeolian	20.0 ± 0.6	**3.25 ± 0.14**	2.69 ± 0.22	3.04 ± 0.17	2, 82
154-MGJ-6-2	Aeolian	29.8 ± 0.7	4.79 ± 0.27	27.11 ± 1.72	**4.26 ± 0.15**	2, 82
154-MGJ-6-3	Fluvial	37.1 ± 1.0	5.31 ± 0.38	3.52 ± 0.31	**4.84 ± 0.16**	2, 90
155-SUT-2-1	Fluvial	28.2 ± 0.9	60.80 ± 3.73	45.43 ± 4.23	**60.86 ± 2.40**	3, 83
155-SUT-3-1	Fluvial	**Saturated**				

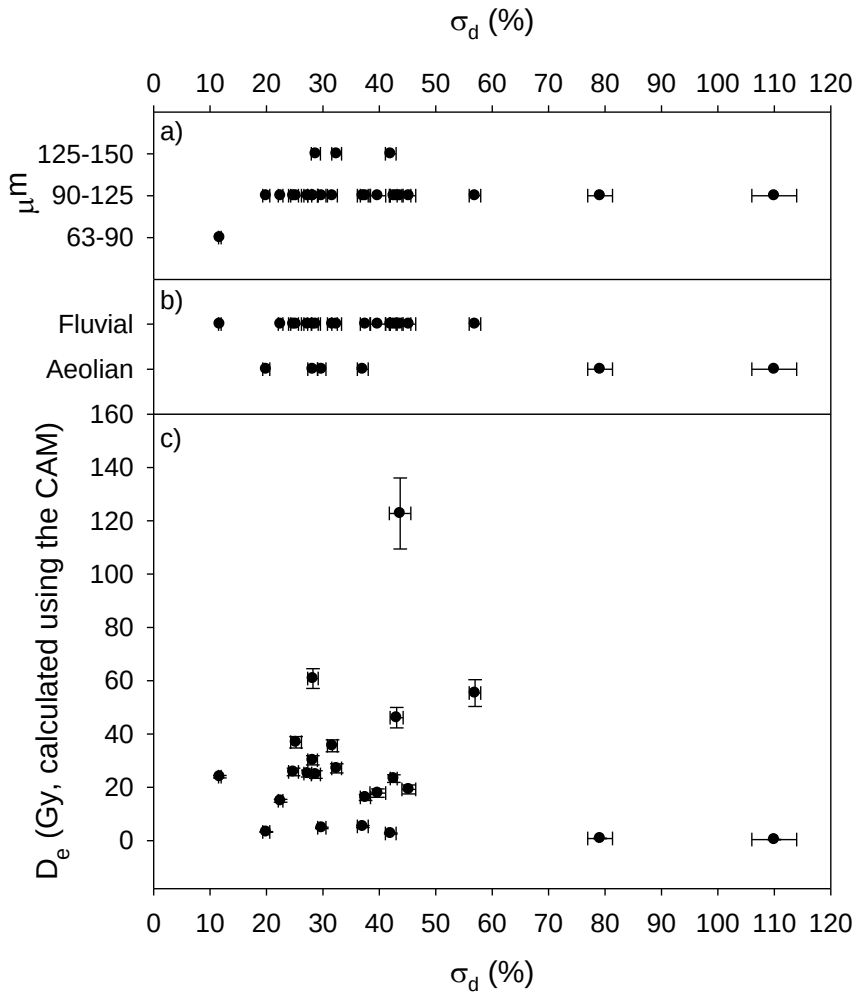

Figure 6.11: Comparison of the σ_d for each sample with a) the particle size used for dating, b) the inferred depositional environment and c) the CAM D_e in Gy.

6.4.3 Age model selection protocol

Selecting the most appropriate age model for D_e determination is not straightforward, and a number of approaches have been applied in recent studies. Olley et al. (2004b) suggest that the overdispersion of a dose distribution should be used to select the most appropriate statistical model to apply for D_e determination and recommend that the CAM of Galbraith et al. (1999) should only be applied to dose distributions with an σ_d of less than 20%. Rowan et al. (2012) do not apply this approach, and instead use the CAM for all of their New Zealand samples. They suggest that whilst overdispersion values of up to 31% are observed, the dose distributions are symmetrical around a central value, and reason that the CAM can be applied to this type of dose distribution. Rodnight et al. (2006) adopt a similar approach to Olley et al (2004b), using a threshold for σ_d of 10% to differentiate

between well and heterogeneously bleached sediments. Using simulated OSL signals, Bailey and Arnold (2006) designed an age model decision tree based on σ_d, skewness and kurtosis. They state that the σ_d value of a dose distribution cannot be used as a sole diagnostic criterion for age model choice and that the CAM can be applied to dose distributions with σ_d of up to 50%, as long as no significant skewness is observed.

For all samples, the CAM, MAM and FMM were applied to dose distributions to calculate equivalent doses using each model (table 6.3). In this study, the approach of Rodnight et al. (2006) has been adopted for age model selection, having been tested on fluvial samples with independent age control in the form of ^{14}C ages. This protocol uses the CAM and FMM for D_e determination, applying the CAM to dose distributions with overdispersion of less than 10% and the FMM model distributions where σ_d is greater than 10%. In this study however, this threshold has been increased to the 20% σ_d CAM threshold of Olley et al. (2004b). The minimum age model is not used because it can be strongly influenced by a few low D_e values (Rodnight et al., 2006), and such low outliers are sometimes observed in this study (e.g. figure 6.12; appendix E), possibly as a result of bioturbation or variability in micro-dosimetry. To apply the FMM, Rodnight et al. (2006) suggest running the model with an increasing number of components, until the best fit is found, using the fit with the lowest BIC value and selecting the lowest component composed of at least 10% of the accepted aliquots for D_e calculation.

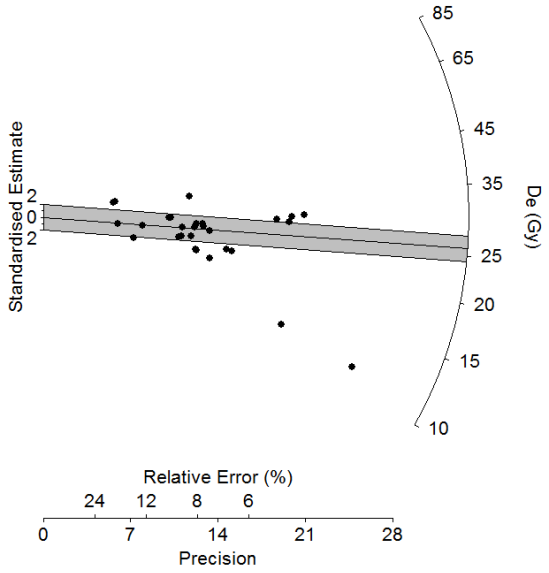

Figure 6.12: Radial plot of sample 154-MGJ-2-5. The FMM D_e of 25.81 ± 0.68 Gy is shown by the black line and the ±2σ confidence interval is shown by the grey shading. The presence of two low D_e outliers suggests that the MAM would underestimate the burial dose.

6.4.3.1 Age model application

Calculation of both the CAM and the FMM was made in the software package R, using age models provided by Professor Rex Galbraith. The CAM was applied to all dose distributions to calculate the σ_d of the dose distribution by solving equations 6.3 and 6.4 simultaneously. Of the twenty seven samples dated in this study, only samples 153-MAR2-5B and 154-MGJ-5-5 had overdispersion values below 20% (table 6.3) and therefore, the CAM D_e was used only for these samples. Radial plots of the dose distribution for these samples are presented in appendix E. The FMM of Galbraith and Green (1990) was applied to all samples and the FMM D_e was used for twenty one measured samples (table 6.3), with dose distributions with σ_d values ranging between 25 and 110%. For all samples, up to five components were fitted, assuming an underlying σ_d of 15%. The fit with the lowest BIC was selected for use and the lowest component containing at least 10% of individual D_e determinations has been used as the FMM D_e value.

6.4.3.2 Indirect assessment of the extent of bleaching

As stated, age model selection is not straightforward and a variety of approaches have been published with the aim of selecting the most appropriate model for a dose distribution (section 6.4.3). However, by using the Olley et al. (2004) 20% σ_d value as a threshold for use of the CAM in this study, the implication is that the majority of samples measured in this study were not completely bleached at deposition and asymmetry in the dose distribution requires treatment with statistical models, such as FMM which can be applied to non-Gaussian distributions. Murray et al. (2012) state that there are no unambiguous ways of testing older samples for incomplete bleaching and comment that only indirect methods are available, such as dating known age deposits expected to be completely bleached or comparison with dose distributions of modern samples. In this study, neither a modern/young fluvial analogue from the Ghaggar-Hakra palaeochannel nor an older sample with independent age control were available and therefore the suggested tests cannot be undertaken.

Murray et al. (2012) suggest that a comparison between the CAM D_e and the preferred D_e (e.g. the D_e calculated using the statistical model of choice) can be used to help inform the degree of incomplete bleaching for a suite of samples. For a well bleached sample, Murray et al. (2012) state that the D_e values calculated from the CAM and preferred model will be in good agreement. This comparison has been plotted for the samples in this study in figure 6.13, where the CAM D_e is compared with the preferred D_e, predominantly calculated using the FMM (table 6.3). The D_e values calculated from the CAM and FMM are generally in good agreement with each other, with a strong positive correlation of 0.90 between the two D_e determinations. This implies the amount of excess dose (attributable to incomplete bleaching or some other mode of mixing) is on average 10% of the burial dose for this suite of samples. However, there are two samples for which there is a greater discrepancy between the CAM D_e and FMM D_e (samples 154-MGJ-4-2 and 154-MGJ-4-5; figure 6.13), and the removal of these two outliers results in a correlation of 0.95 for the dataset. The strong relationship between the CAM and preferred D_e

values implies that incomplete bleaching of the OSL signal is not an extensive problem for the majority of samples measured.

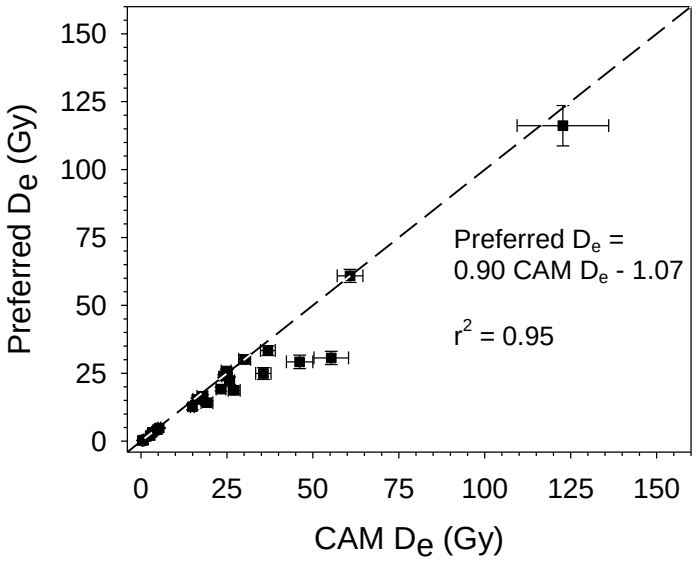

Figure 6.13: Relationship between the CAM D_e and the preferred D_e values calculated for the samples in this study (the FMM was preferred for 21 samples and the CAM for 2 samples). Unity is shown by the dashed line, with the implication that well bleached samples should fall close to this line.

The majority of dose distributions were best fitted with a two or three component FMM (table 6.3), and for many of these fits, the component used for D_e determination according to the protocol of Rodnight et al. (2006) was the dominant component, containing the majority of accepted aliquots (table 6.3). This again suggests that incomplete bleaching of the luminescence signal is not an extensive problem within the dataset, and that greater overdispersion values are often calculated as a result of a small number of outliers for many samples (e.g. figure 6.12). Therefore, it is concluded that whilst overdispersion for the majority of samples in this study exceeds 20%, incomplete bleaching is not significant for many of the samples measured.

6.4.4 Determining D_e from samples containing OSL signals in saturation

Whilst the upper age limit for thermoluminescence dating has been reported to be around 500 ka (Prescott and Robertson, 1997), the upper age limit when using the OSL signal of quartz is for the most part restricted to the late Quaternary period

(Yoshida et al., 2000). The upper limit for quartz OSL dating is based upon the environmental dose rate and the dose saturation properties of the sample being dated, with the longest dateable age range coming from samples in areas with low environmental dose rates and with above average dose saturation characteristics. As discussed in chapter 3, the magnitude of the environmental dose rate is predominantly dependent upon the concentrations of the radionuclides (U, Th, K) naturally occurring in the sediment. The dose saturation properties of the luminescence signal can be assessed by considering the luminescence response to a dose. This section considers the treatment of dose distributions containing OSL signals which are considered to be in saturation.

6.4.4.1 Quartz OSL signals in saturation

Assuming a single trap, the dose response of the signal from each of the quartz OSL components can be fitted with a single saturating exponential function in the form $I = I_0(1 – \exp^{-D/D0})$, where I is the OSL intensity after a dose (D), I_0 is the saturation intensity and D_0 is the dose level characteristic of the dose response curve (Wintle and Murray, 2006). For Moroccan dune sand, Singarayer and Bailey (2003) fitted each of the five observed components with single saturating exponential functions and determined that D_0 varies for each of the quartz OSL components. For the fast component, they calculated a D_0 value of 190 Gy and recent calculations of D_0 for fast dominated OSL samples vary from 55 Gy (Roberts and Duller, 2004) to 69 Gy (Singarayer and Bailey, 2004) and 75 Gy (Banerjee et al., 2003). Whilst a saturating exponential function should describe the quartz OSL signal if a single trap is assumed, many authors have reported that the dose response curve is better fitted with an exponential plus linear function (e.g. Roberts and Duller, 2004; Murray et al., 2008; Pawley et al., 2008) or in some cases the sum of two saturating exponentials (Murray et al., 2007; Pawley et al., 2010). For these grains that pass all rejection criteria but exhibit this type of behaviour, the process which gives rise to these additional components is still under investigation (Wintle, 2008b; Lowick et al., 2010). Usually at these higher doses, interpolation from the dose response curve will result in large and asymmetric uncertainties in D_e (Murray et al. 2002) and

therefore Wintle and Murray (2006) recommend that a prudent approach when dating using the quartz OSL signal is to use $2D_0$ as an upper limit for D_e.

6.4.4.2 Using $2D_0$ as an upper limit for D_e

In this study, two types of OSL signal are defined as saturated and are shown in figure 6.14. The first type of signal is from the 'class 3' grains described by Yoshida et al. (2000), where the natural OSL signal does not intersect with the dose response curve (figure 6.14a) and for which a D_e cannot be interpolated from the dose response curve. The cause of this type of behaviour in a quartz OSL signal which passes all rejection criteria and is considered suitable for dating using the SAR protocol has not been resolved. Yoshida et al. (2000) suggest that if the test dose intensity increases whilst the regenerative dose remains relatively constant during the SAR protocol, the sensitivity corrected OSL signal at higher doses may decrease. Yoshida et al. (2000) also propose that radiation quenching at high doses may be a factor. Bailey (2004) suggests another possible cause may be differences in charge competition during natural and laboratory irradiation. Despite these suggestions, the mechanics leading to this type of behaviour have not yet been resolved. The second type of signal considered saturated is where the natural signal intersects with the dose response curve, but at a point that is greater than the $2D_0$ limit recommended by Wintle and Murray (2006) (figure 6.14b). As discussed in the previous section, interpolation of the natural signal onto the dose response curve at higher doses is likely to result in large and asymmetric uncertainties in D_e, because the uncertainties associated with the natural will be magnified on the saturating dose response curve (Athanassas, 2011).

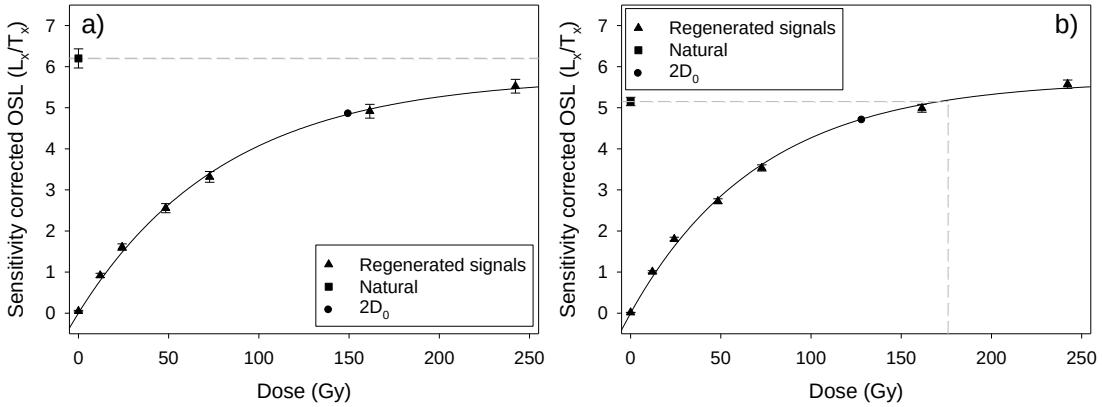

Figure 6.14: Examples of two dose response curves where the natural OSL signal is considered to be in saturation. a) The natural signal does not intercept the dose response curve and b) D_e exceeds $2D_0$.

In many studies, the approach taken is to exclude signals where the natural sensitivity corrected signal does not intercept the dose response curve (e.g. Jacobs et al., 2006; Armitage et al., 2011) and in these studies, the D_e is calculated from signals which provide a quantitative D_e value. In some studies, the second type of saturated signal outlined (e.g. figure 6.14b) are included in dose distribution analysis, and the $2D_0$ upper limit of D_e used in this study is not applied (e.g. Armitage et al., 2011). Other authors define samples which contain saturated signals as undateable and use alternative luminescence signals for dating (e.g. Alappat et al., 2010). In this study, a signal is considered to be saturated if the natural signal can not be interpolated from the dose response curve or if the D_e exceeds $2D_0$, given the potential for the derivation of imprecise and inaccurate equivalent doses (e.g. figure 6.15). However, these signals provide geochronological information, and therefore, it is considered preferable to calculate a minimum D_e and age for a sample as opposed to defining it as undateable.

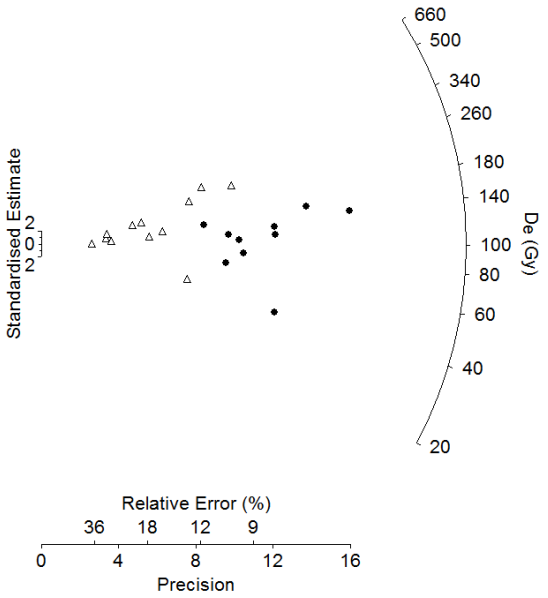

Figure 6.15: Radial plot of saturated sample 153-MAR2-13B. 34 aliquots passed all six rejection criteria, 10 of which had D_e determinations less than $2D_0$ (filled symbols), 12 signals had D_e values in excess of $2D_0$ (open symbols) and 12 signals had a natural signal which could not be interpolated from the dose response curve and are not plotted.

For the samples measured in this study, the environmental dose rates range between 2.7 and 4.0 Gy.ka^{-1} (table 3.1), which are relatively high and will restrict the upper limit of quartz OSL dating. For example, the mean environmental dose rate of 3.31 Gy.ka^{-1} when applied to a signal with a D_0 of 70 Gy would result in an upper dating limit of ~42 ka. However, whilst D_0 values for fast dominated signals have been reported to range between 55 Gy and 75 Gy (section 6.4.4.1), these values have typically been measured from medium and large aliquots and therefore the effect of averaging is likely to mask a greater variability in D_0. Four samples in this study are considered to be in saturation and are discussed in further detail in section 6.4.4.3. For each of these samples, the D_0 obtained for each accepted aliquot (n=92) was calculated by fitting a saturating exponential function to each dose response curve (e.g. figure 6.16). The mean D_0 for all 92 aliquots is 70 Gy, with the mean D_0 for each sample ranging between 62 and 82 Gy. These values are consistent with those quoted in the literature but greater variability is observed from the signals measured from each small aliquot, with D_0 varying between 14 and 181 Gy (figure 6.17). This implies a very variable dating limit between aliquots from the same sample and highly variable forms of dose response curves within the same sample (figure 6.16).

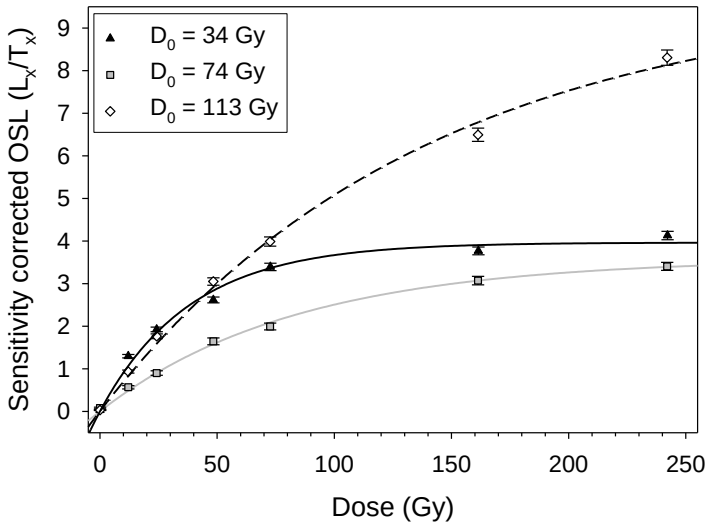

Figure 6.16: Three dose response curves from aliquots of sample 153-MAR2-13B. All three signals pass all rejection criteria but have dose saturation characteristics and dose response curves that differ greatly.

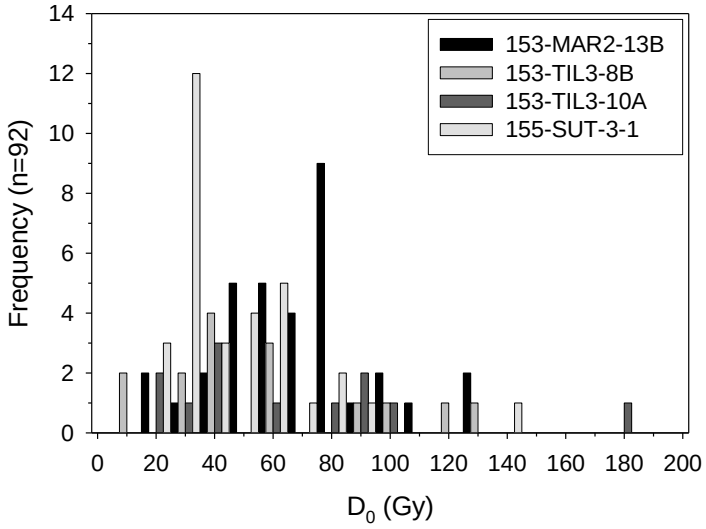

Figure 6.17: D_0 (in Gy) of 92 signals (from 4 samples) calculated by fitting a saturating exponential function to each dose response curve.

6.4.4.3 Calculation of a minimum D_e

A sample was defined as saturated if more than 50% of accepted aliquots were saturated, as defined in this study and this is the case for four samples (table 6.4). As the D_e and uncertainty of the saturated signals is unknown, it is not possible to statistically calculate a finite age, and calculating an equivalent dose from the non-saturated signal would introduce bias into the D_e determination. However, these signals still contain geochronological information in the form of a minimum age. In this study, the approach has been to calculate the D_0 value for each aliquot of a

sample by fitting a single saturating exponential and to use the mean $2D_0$ value for the sample as the minimum D_e (table 6.4). Minimum ages are quoted to the nearest integer and without an error term to reflect the unknown level of uncertainty associated with the estimate.

Table 6.4: Samples defined as saturated and for which a minimum OSL age has been calculated. All calculations were made prior to rounding and the D_e and age are quoted to the nearest integer to reflect the reduced precision associated with these estimates. The number of measured (meas) and accepted (acc) aliquots are shown, along with the number of accepted signals which are saturated. $2D_0$ is derived from the mean D_0 values from all accepted signals.

Sample	Meas (acc)	# Accepted saturated signals	% Accepted saturated signals	Environmental dose rate ($Gy.ka^{-1}$)	$2D_0$ (Gy)	Minimum age (ka)
153-MAR2-13B	96 (34)	24	70.6	2.84 ± 0.15	140	49
153-TIL3-8B	48 (15)	11	73.3	3.26 ± 0.16	127	39
153-TIL3-10A	66 (12)	8	66.6	3.40 ± 0.17	140	41
155-SUT-3-1	78 (33)	18	54.5	3.95 ± 0.15	129	33

6.5 Age calculation

OSL ages have been calculated using equation 1.1, using the environmental dose rates calculated in chapter 3 (table 3.1) and the equivalent doses detailed in this chapter (tables 6.3 and 6.4). Table 6.5 gives the calculated ages, which have been rounded to the nearest two decimal places. The samples dated in this study range in age between 0.09 ± 0.01 ka to 43.59 ± 3.41 ka, with the majority of samples dating from within the Holocene epoch. In addition, there are four samples which were defined as saturated and therefore a minimum age only has been calculated (section 6.4.4.3). The age uncertainty was calculated by propagating in quadrature both the random and measurement uncertainties associated with the equivalent dose and environmental dose rate. Age uncertainties vary between 4.7 and 11.1%, with a mean of 6.6% and typically, the larger uncertainties are associated with the younger ages that have more overdispersed dose distributions, dim signals and lower equivalent doses (e.g. Madsen and Murray, 2009).

Table 6.5: OSL ages calculated in this study. The number of measured (meas) and accepted (acc) aliquots are shown as well as the overdispersion (σ_d), the age model used for D_e calculation and the environmental dose rate. Ages are shown in ka and were calculated in 2011.

Sample	Meas (acc)	σ_d (%)	Age model (k, %)[a]	D_e (Gy)[b]	Environmental dose rate (Gy.ka^{-1})[b]	Age (ka)[b]
136-3-1	60 (21)	39.7	FMM (2, 95)	16.49 ± 0.62	3.01 ± 0.13	5.47 ± 0.31
136-3-9	96 (44)	22.5	FMM (2, 46)	14.94 ± 0.54	2.81 ± 0.11	5.32 ± 0.28
136-4-1	84 (31)	37.5	FMM (2, 70)	15.38 ± 0.47	3.22 ± 0.13	4.78 ± 0.24
136-4-2	83 (50)	42.6	FMM (3, 70)	19.19 ± 0.71	3.88 ± 0.16	4.95 ± 0.27
136-6-1	108 (28)	31.7	FMM (2, 76)	30.79 ± 1.36	3.64 ± 0.13	8.46 ± 0.49
136-6-7	108 (21)	25.2	FMM (2, 80)	33.35 ± 1.80	3.06 ± 0.11	10.88 ± 0.70
153-MAR2-5B	48 (43)	11.7	CAM	23.99 ± 0.47	3.87 ± 0.19	6.17 ± 0.32
153-MAR2-13B	96 (34)	-	Saturated	140	2.84 ± 0.15	> 49
153-TIL3-2	72 (27)	45.2	FMM (3, 60)	14.15 ± 0.66	2.91 ± 0.14	4.87 ± 0.32
153-TIL3-8B	48 (15)	-	Saturated	127	3.26 ± 0.16	> 39
153-TIL-10A	66 (12)	-	Saturated	140	3.39 ± 0.17	> 41
153-TIL3-18	120 (20)	43.7	FMM (3, 73)	116.15 ± 7.42	2.66 ± 0.12	43.59 ± 3.41
154-MGJ-1-1	48 (22)	24.8	FMM (2, 65)	22.25 ± 1.39	3.31 ± 0.12	6.72 ± 0.49
154-MGJ-1-4	126 (28)	32.4	FMM (2, 35)	18.70 ± 1.33	2.74 ± 0.10	6.82 ± 0.54
154-MGJ-1-8	60 (31)	27.3	FMM (2, 57)	20.75 ± 1.42	2.89 ± 0.11	7.19 ± 0.56
154-MGJ-2-1	96 (35)	42.0	FMM (3, 62)	2.07 ± 0.11	3.33 ± 0.13	0.62 ± 0.04
154-MGJ-2-5	96 (28)	28.8	FMM (2, 92)	25.81 ± 0.68	3.01 ± 0.12	8.58 ± 0.40
154-MGJ-3-1	48 (26)	28.2	FMM (2, 52)	27.37 ± 2.45	3.11 ± 0.12	9.68 ± 0.68
154-MGJ-3-6	72 (40)	78.3	FMM (4, 43)	0.37 ± 0.03	3.16 ± 0.12	0.12 ± 0.01
154-MGJ-4-2	66 (41)	57.0	FMM (4, 27)	30.67 ± 2.44	3.63 ± 0.14	9.59 ± 0.85
154-MGJ-4-5	72 (29)	43.1	FMM (3, 35)	29.21 ± 2.49	3.16 ± 0.13	9.14 ± 0.85
154-MGJ-5-1	204 (47)	110.0	FMM (3, 78)	0.25 ± 0.02	2.91 ±0.16	0.09 ± 0.01
154-MGJ-5-5	96 (26)	20.0	CAM	3.25 ± 0.14	2.98 ± 0.12	1.09 ± 0.06
154-MGJ-6-2	72 (31)	29.8	FMM (2, 82)	4.26 ± 0.15	3.04 ± 0.11	1.40 ± 0.07
154-MGJ-6-3	108 (29)	37.1	FMM (2, 90)	4.84 ± 0.16	3.42 ± 0.13	1.42 ± 0.07
155-SUT-2-1	84 (23)	28.2	FMM (3, 83)	60.86 ± 2.40	3.08 ± 0.12	19.74 ± 1.08
155-SUT-3-1	78 (34)	-	Saturated	129	3.95 ± 0.15	> 33

[a] Where the FMM has been used, the number of fitted components (k) and the percentage of individual D_e determinations in the selected component are given.
[b] Quoted to 2 d.p. for all finite determinations. For saturated signals, D_e and the age are reported to the nearest integer. All calculations were performed prior to rounding.

6.5.1 Assessing the reliability of the calculated OSL ages

There are a number of means of assessing the reliability of the calculated OSL ages (table 6.5). These include comparison with another form of independent age control, checking that ages are in stratigraphic order and are sensible in terms of geomorphological processes and to check that modern samples provide a modern age. No modern samples were collected from the Ghaggar-Hakra palaeochannel because this system is no longer active, and whilst recent fluvial activity has been documented in the Sutlej channel adjacent to the overbank site (155-SUT-2 and

155-SUT-3), the dating of these modern sediments was not undertaken because the source area and sediment properties differ greatly between the Sutlej and Ghaggar-Hakra sediments. Therefore, assessment of the reliability of the OSL ages is undertaken using stratigraphic control and the availability of radiocarbon dates.

Figure 6.18 presents a schematic view of the geochronology at the twelve sites where OSL and radiocarbon (^{14}C) dating has been applied. More detailed sedimentological logs are presented in appendix A, and the sites are discussed in section 2.6 and 2.7. Material suitable for ^{14}C dating was limited across the study area, however samples were collected at seven sites for radiocarbon dating. These ages were prepared and measured by Dr Liviu Giosan at Woods Hole Oceanographic Institute, Massachusetts, USA and are presented by Giosan et al. (2012) and in table 6.6. All dates were converted to calendar ages (2 sigma range) using the Calib 5.0.1 software (Stuiver et al., 1998) and the IntCal04 calibration curve (Reimer et al., 2004) with a 60 year positive correction in order to make them comparable with the OSL ages that were calculated using a datum of 2010. The ^{14}C ages calculated by Giosan et al. (2012) provide a means of independent age control for the OSL ages calculated in this study. Material sampled for ^{14}C dating was usually found in finer clay and/or silt units, which were not sampled for OSL dating, and therefore a direct comparison between the two dating methods cannot be made. Only at site 154-MGJ-1 were samples for OSL and ^{14}C dating taken from the same horizon. However, the calibrated ^{14}C ages are approximately 6 ka older than the OSL ages. Giosan et al. (2012) state that because the ^{14}C ages were calculated from mollusc fragments, that these are likely to have been reworked, and therefore overestimate the deposition age of the unit.

At the majority of sites, OSL ages increase with depth and ages, both radiocarbon and OSL, are in good stratigraphic agreement (e.g. sites 136-4, 154-MGJ-4, 154-MGJ-5). It is therefore concluded that the protocols adopted in this study for OSL dating provide accurate OSL ages. However, at two sites, age inversions are observed. At Fort Abbas site 136-3, the OSL age at the base of the section is slightly younger (5.32 ± 0.28 ka), albeit within errors, than the OSL age taken ~2m above

(5.47 ± 0.31 ka). At this site, a radiocarbon age of 5.85 ± 0.12 ka is available (table 6.6) and whilst slightly older than the two OSL ages (figure 6.18), the ages of all three samples agree within two standard deviations, and it is concluded that the sediments at this site accumulated rapidly. At site 154-MGJ-4 in the Lal Suhanrai forest, another age inversion occurs between the two OSL samples, although again, the ages agree within errors, and suggests that the two units sampled were deposited at a similar time. Overall, the OSL chronology developed in this thesis provides ages that are in stratigraphic order for the majority of sites. Where an age inversion is observed, the inverted ages are within errors of each other, and this is interpreted as a period of rapid sediment accumulation. Whilst a comparison between the OSL and ^{14}C ages cannot be made for the same unit at any of the sites, the stratigraphic relationship between the two types of dates is in good broad agreement (figure 6.18), and therefore, the OSL ages are considered to be accurate.

Table 6.6: AMS radiocarbon dates sampled within the study area. Samples were measured by Dr Liviu Giosan at the Woods Hole Oceanographic Institute, Massachusetts and are presented in Giosan et al. (2012).

Site Name	Depth (m)	Sample material	Radiocarbon age (kyr)	Calibrated age (cal kyr BP)[a]
Fort Abbas (136-3)	3.45	Gastropod	5.05 ± 0.35	5.85 ± 0.12
Alkasur Cotton Jinner (136-4)	3.81	Gastropod	6.01 ± 0.50	6.92 ± 0.07
Basti (136-5)	0.75	Gastropod	5.05 ± 0.20	5.88 ± 0.08
Basti (136-5)	2.65	Gastropod	5.88 ± 0.20	6.76 ± 0.04
Tilwalla Core (153-TIL3)	43.7	Plant/wood	45.10 ± 6.70[b]	
Fort Abbas (154-MGJ-1))	2.59	Gastropod	11.90 ± 0.50	13.84 ± 0.13[c]
Fort Abbas (154-MGJ-1))	2.96	Gastropod	12.00 ± 0.70	13.93 ± 0.15[c]
Yazmen Road (154-MGJ-5)	1.10	Plant/wood	0.15 ± 0.25	0.20 ± 0.14
Yazmen Road (154-MGJ-5)	1.40	Plant/wood	0.32 ± 0.3	0.44 ± 0.08
Yazmen Brick Pit (154-MGJ-6)	2.70	Gastropod	3.81 ± 0.02	4.25 ± 0.09
Yazmen Brick Pit (154-MGJ-6)	3.55	Gastropod	4.13 ± 0.02	4.74 ± 0.14

[a] Calendar ages relative to 2010. Ages calibrated using the IntCal04 calibration curve (Reimer et al., 2004).

[b] This age has not been calibrated because it is close to measurement detection limits and the limit of the calibration curve.

[c] Ages calculated from mollusc fragments. Giosan et al. (2012) state that these are most probably reworked and are not used in age models or for environmental interpretations. They are therefore not included in further analysis in this study.

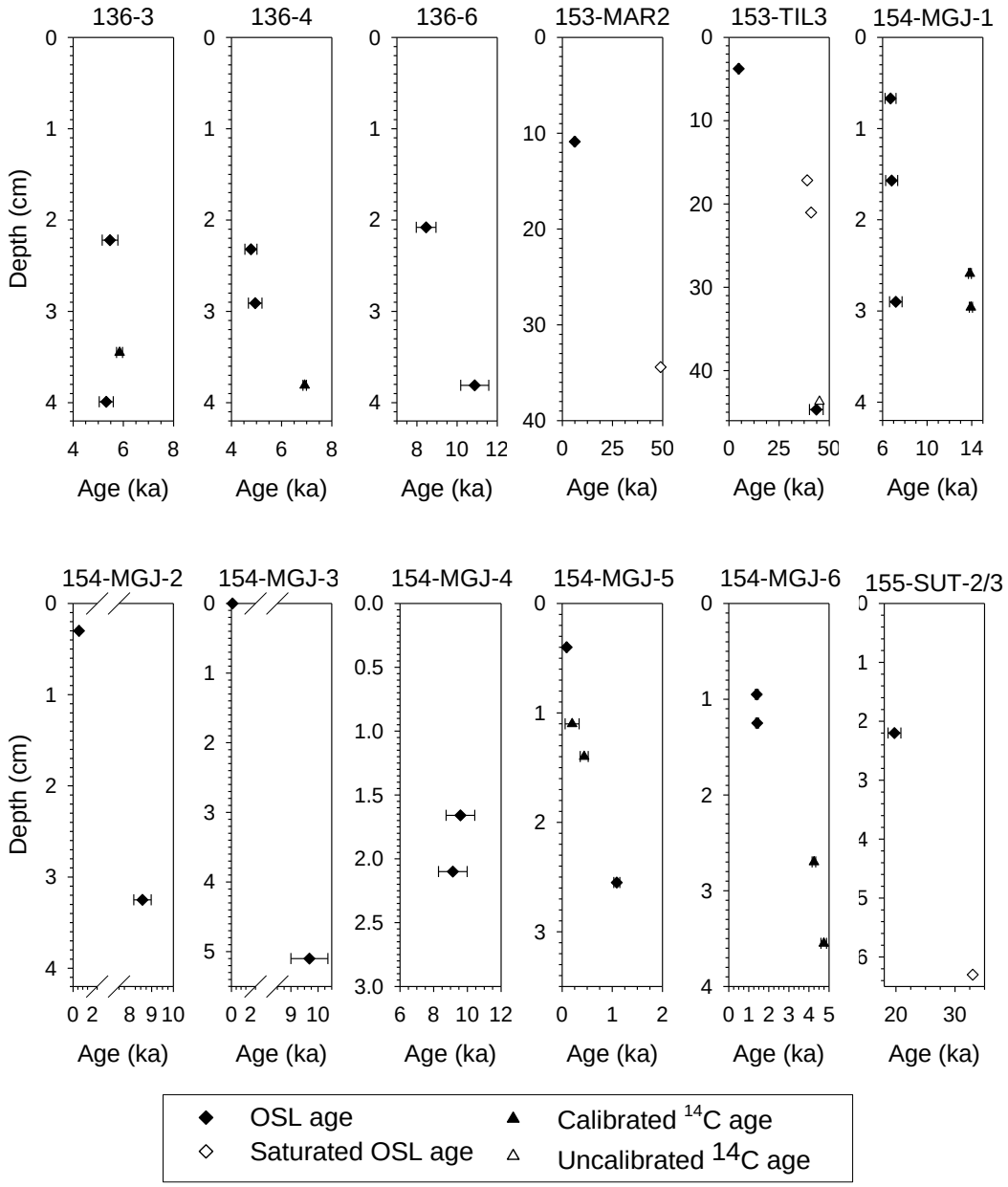

Figure 6.18: Schematic view of OSL ages calculated in this study (tables 6.4 and 6.5) and the radiocarbon ages calculated by Giosan et al. (2012) (table 6.6).

6.6 Conclusions

A relatively low proportion of the aliquots measured during the course of this study have been used for D_e calculation, with on average 34% of measured signals used for age calculation. Despite thorough and careful laboratory preparation, feldspar contamination is prevalent, with large numbers of aliquots excluded on the basis of the OSL IR depletion ratio of Duller (2003). During single grain analysis of sample 154-MGJ-5-1B, half of the brightest 44 grains failed this ratio and are considered to

be non-quartz mineral grains. From this sample, it was calculated that 2% of quartz grains provide a luminescence signal.

The overdispersion parameter of Galbraith et al. (1999) has been used as a measure of variability in the dose distributions of samples. Across the range of samples dated σ_d varies between 12% and 110%, with larger values associated with samples with low D_e values (<1 Gy), and lower values (typically less than 45%) for samples with greater equivalent doses. The σ_d value was used to inform the choice of age model used following the protocol of Rodnight et al. (2006), with the central age model (Galbraith et al., 1999), and the finite mixture model (Galbraith and Green, 1990; Roberts et al., 2000) used for statistical derivation of the sample D_e. For the majority of samples, the FMM was applied and investigation of the dose distribution for many of these samples showed that overdispersion in the distribution was caused by the presence of a small number of outliers as opposed to extensive incomplete bleaching. For four samples, a minimum D_e and age was calculated because in excess of 50% of accepted signals were considered to be in saturation. The calculation of a minimum age differs from the approach in some studies, where D_e values in excess of $2D_0$ are included in D_e calculation, however it seems prudent to calculate a minimum age given the large, asymmetric uncertainties associated with interpolation from a dose response curve in saturation (Murray et al., 2002).

The calculated OSL ages have been presented in table 6.5. The majority of samples date within the Holocene, although there are some samples of late Pleistocene age. For the samples where a minimum age was calculated, relatively high environmental dose rates limit the upper limit for finite age calculation to the late Quaternary. The uncertainties associated with the ages vary between approximately 5% and 9%, with higher levels of uncertainty typically associated with the younger samples, reflecting the challenges of measuring dim signals and low equivalent doses (Madsen and Murray, 2009). The OSL ages calculated in this study are considered to be accurate, as they are in good stratigraphic agreement and where available, compare well with ^{14}C ages (figure 6.18). In conclusion, this chapter has presented the data analysis undertaken to calculate equivalent doses and ages

for samples once the luminescence signal has been measured (chapter 4) and environmental interpretations using these dose distributions and ages are presented in chapter 8.

7. Range-finder OSL dating: a protocol for rapid age estimation

7.1 Introduction

The calculation of an OSL age from sample collection to final age calculation can be a lengthy process. In many instances, where only an estimate of the true age is required, a method for rapidly producing OSL age estimates would be welcome. This chapter outlines the development of the range-finder (RF) OSL dating protocol (Roberts et al., 2009), and the testing and application of this dating protocol, which has the potential to produce RF age estimates from a batch of eight to ten samples within a fortnight. This chapter discusses the rapid estimation of the environmental dose rate and D_e before comparing the RF ages with fully prepared (FP) OSL ages and independent age control in the form of radiocarbon dates. The discussion below develops further the work presented by Durcan et al. (2010).

7.2 Methods for rapid OSL age estimation

The calculation of a quartz OSL age typically takes between two and six months, but can take longer (Roberts et al., 2009) and thorough laboratory treatment is required in order to isolate a purified mineral fraction suitable for D_e measurement (e.g. figure 4.1). Measurement of the luminescence signal can take days to weeks, depending on the age of the sample, the equipment specifications (e.g. stimulation power and source dose rate), the number of aliquots required and the measurement protocol used (Roberts et al., 2009). In addition to the calculation of the D_e, the environmental dose rate also requires measurement, and again, this can take a substantial amount of time depending on the method used and the dose rate of the sample. There are some instances where an estimation of age is all that is required, e.g. for a pilot field study or to determine the resolution required for a dating campaign and/or processing of laboratory samples (Roberts et al., 2009) and in these situations, being able to provide an approximate age without the lengthy preparation time of a FP OSL age would be extremely useful.

Some authors have proposed methods for reducing the time taken to obtain an OSL age. Sanderson et al. (2001; 2003) and Burbidge et al. (2007) applied a pared-down laboratory procedure, termed luminescence profiling, to sediment sequences to aid the selection of sites and units upon which to focus. However, in these studies, the focus was to obtain information principally to inform sedimentological and archaeological interpretations as opposed to calculating ages based on the luminescence signal. Roberts and Duller (2004) investigated the development of a standardised growth curve (SGC) which if successful, would have defined the form of a quartz OSL dose response curve, and meant that only measurement of the natural and residual signals would have been required for D_e calculation. For quartz at low regenerative doses, the SGC can be successfully applied because the dose response of quartz is essentially linear (Roberts and Duller, 2004). However, at larger regenerative doses, the point of saturation in quartz becomes variable and the form of the dose response curve can vary considerably between samples. D_0 is reported to vary between 55 and 75 Gy by various authors quoted in Wintle and Murray (2006), and varies significantly for the samples analysed in this study (figure 6.18). Therefore a single SGC cannot be universally applied. Denby et al. (2006) and Thomsen et al. (2008) proposed the use of the pulsed OSL (POSL) signal as a means for rapid assessment of D_e because sample preparation is not required. This technique utilises the difference in the luminescence lifetimes of quartz and feldspar and uses pulsed stimulation to differentiate between the quartz and feldspar luminescence signals within a polymineral sample. Whilst this technique achieves POSL D_e values comparable to CW-OSL D_e values from fully prepared quartz (Thomsen et al., 2008), to apply this technique specialised equipment is required to control LED pulsing (e.g. Denby et al., 2006).

Roberts et al. (2009) sought to develop a protocol which could optimise existing methods for calculating the environmental dose rate and D_e to rapidly produce OSL age estimates. They developed the range-finder (RF) OSL dating protocol, which was successfully applied to a range of samples from a variety of locations. Using their most successful pared-down treatment procedure, for the eight samples where the RF and FP OSL ages were compared against each other, a mean ratio of 0.9 ± 0.3

was calculated, seven of which were within 30% of the target FP OSL age. Their range-finder protocol provides a means for rapid age estimation using OSL dating, although Roberts et al. (2009) acknowledge that the dating of young samples or dim signals using the RF protocol may be challenging. For example, in their study, the measurement of a young sample, with a FP OSL age of 50 ± 3 a, yielded an RF OSL age of 110 ± 115 a. Whilst this represents a large age overestimation (most likely due to the application of a relatively high pre-heat temperature of 220°C to a young sample, giving rise to the recuperation of charge), Roberts et al. (2009) argue that in this instance the RF OSL dating protocol fulfilled its purpose by indicating that the sample was very young. Durcan et al. (2010) applied this protocol to sediment sequences from three sites in Pakistan, two of which had independent age control in the form of radiocarbon (^{14}C) dating. The range-finder protocol produced RF OSL age estimates which were in stratigraphic order and in good agreement with the ^{14}C dating. This data and further development and application of the RF dating protocol is discussed below.

7.3 RF environmental dose rate determination

The environmental dose rate received by a sample is composed of the energy originating from alpha and beta particles and gamma and cosmic rays (see chapter 3), and the measurement of these activities can take days or even weeks depending on the dose rate of the sample and the method used. In this study, the FP environmental dose rate was calculated using radionuclide concentrations determined from emission counting. Thick source alpha counting (TSAC) typically took between 4 – 7 days per sample and thick source beta counting (TSBC), at least 24 hours per sample. Concentrations of U and Th were determined from TSAC (section 3.3.1.2) and the total infinite-matrix beta dose rate (D_β) was derived from TSBC, from which the K concentration was calculated (sections 3.3.2.2 and 3.3.2.4 respectively). The gamma dose rate (D_γ) was calculated from these radionuclide concentrations (section 3.3.4.1), using the conversion factors of Adamiec and Aitken (1998). The D_β and $D_{\gamma,}$ once corrected for grain size attenuation and water content, were combined with the contribution from cosmic rays to calculate the

environmental dose rate (section 3.4). For the samples in this study, approximately one week of measurement time per sample was required to calculate the environmental dose rate, which is relatively quick, due to the high dose rates of the samples in this study (table 3.1). However, a procedure for a more rapid estimation of the environmental dose rate is integral to a successful and useful RF OSL dating protocol. Roberts et al. (2009) investigated the relationship between the infinite-matrix beta and gamma dose rate with the aim of calculating the gamma dose rate from the beta dose rate and removing the need for TSAC for determining radionuclide determinations.

To calculate the FP gamma dose rate, the conversion factors of Adamiec and Aitken (1998) are applied to the radionuclide concentrations of U, Th and K derived from emission counting. Based on 427 observations of samples measured in the ALRL, Roberts et al. (2009) calculated a ratio of 0.59 ± 0.13 between D_γ and D_β (figure 7.1). Ankjærgaard and Murray (2007) obtained a similar ratio of 0.50, based on the measurement of approximately 3,700 samples and conclude that the infinite-matrix beta dose rate can be successfully used to approximate the gamma dose rate. The concentrations of U, Th and K in the samples analysed in this study (table 3.1) are in line with standard concentrations (e.g. 12 ppm of Th, 3 ppm of U and 1% of K_2O of Mejdahl (1979)), and therefore, as long as D_β can be determined accurately, the resulting D_γ can be predicted with reasonable certainty. By calculating D_γ from D_β, the need for TSAC (and radionuclide concentration determination) is removed and measurement time is significantly reduced. In this study, the factor of Roberts et al. (2009) has been adopted and the RF D_γ has been calculated by multiplying D_β by 0.59. A comparison between the RF D_γ and the FP D_γ values calculated from the same sample is presented in section 7.3.3.

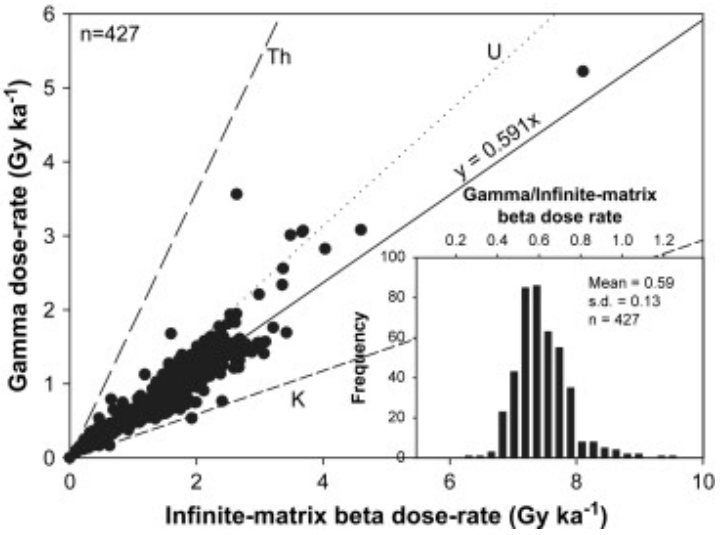

Figure 7.1: The gamma dose rate determined from TSAC and TSBC plotted as a function of the infinite-matrix beta dose rate (derived from TSBC). The fitted linear function is shown by the solid line. The dashed lines show the maximum theoretical values if the dose rates were derived solely from U, Th or K. Inset, a histogram of the ratio between D_γ and D_β. From Roberts et al. (2009).

7.3.1 RF TSBC

RF TSBC was undertaken using a Risø GM-25-5 beta counter (Bøtter-Jensen and Mejdahl, 1988) and the measurement equipment and calculation of the D_β is outlined fully in section 3.3.2. Reducing the time taken to determine the RF D_β will significantly speed up the time taken to produce a RF OSL age estimate. To investigate the optimum measurement time for D_β determination using TSBC, a number of RF samples were measured for 12 hours, with data collected in hourly time slices. Figure 7.2 shows the variation in the calculated D_β ($Gy.ka^{-1}$) as the measurement period is varied between 1 and 12 hours for a selection of samples. Typically, the greatest variability is seen in the first hour or two of measurement (e.g. sample 136-3-9-RF and 154-MGJ-3-5-RF; figure 7.2), but D_β becomes more consistent after 3 – 4 hours of measurement and does not dramatically vary as measurement time is increased, suggesting that RF D_β precision is not improved radically with an extended measurement time period. Durcan et al. (2010) found that the measurement uncertainty relating to counting statistics was typically reduced to less than 4% after 4 hours counting, and less than 2% after 24 hours. The compromise between this improved uncertainty and measurement time is not a critical consideration for RF dose rate calculation and the reduced measurement

time is preferred. Therefore, a 4 hour period is considered sufficient for the measurement of the RF D_β.

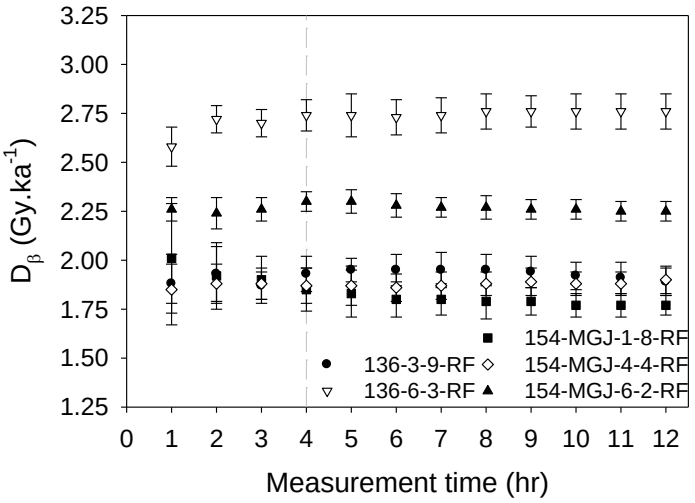

Figure 7.2: RF D_β calculated as RF TSBC measurement time is varied between 1 and 12 hours. The mean and standard deviation from three subsamples is shown. The selected measurement time of 4 hours is indicated by the dashed line.

To further streamline the time taken to measure the RF D_β, measurements were undertaken to assess whether unmilled samples could be used for beta counting (Durcan et al., 2010). As discussed in section 3.3.2.1, prior to measurement sediment is milled to homogenise the sediment matrix across the range over which beta particles travel. Eight samples were first dried overnight at 50°C before being beta counted in an uncrushed state for 4 hours. The sediment was then milled using a ball mill and the sample was remeasured in its crushed state, allowing the D_β to be calculated for the uncrushed and crushed sample. A comparison between the uncrushed and crushed beta dose rates is shown in figure 7.3. Taking into account the errors arising from counting statistics and a systematic instrumental uncertainty of ±3%, for each of the eight samples measured, the infinite-matrix beta dose rates calculated are within 10% of each other (figure 7.3) and the mean crushed to uncrushed ratio is 1.00 ± 0.07 (Durcan et al., 2010). For the purpose of RF OSL dating, milling appears to be unnecessary.

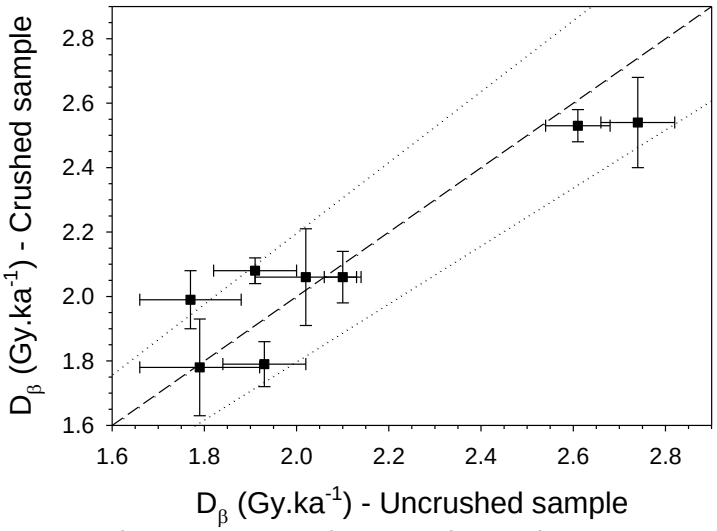

Figure 7.3: Comparison of RF D_β calculated after 4 hrs of TSBC of crushed and uncrushed sample. The dashed line represents unity and the dotted lines ±10%.

7.3.2 Calculation of the RF environmental dose rate

Calculation of the RF environmental dose rate is based upon TSBC to calculate the infinite-matrix beta dose rate and the gamma dose rate. D_β was calculated from the TSBC measurement of unhomogenised sediment for 4 hours and the D_γ by multiplying D_β by 0.59 (Roberts et al., 2009; Durcan et al. 2010). Prior to calculation of the RF environmental dose rate, both D_β and D_γ were corrected for water content and D_β was also corrected for attenuation within the grains (e.g. Bell, 1979; Mejdahl, 1979). The samples for RF OSL dating are not sieved, and it is not possible to apply a grain size specific attenuation factor to the calculated D_β. Therefore an attenuation factor of 0.90, recommended by Aitken (1985) for general use, has been applied (Durcan et al., 2010). The cosmic dose rate was calculated from sample depth, altitude, latitude and longitude (Prescott and Hutton, 1998), and this calculation is described in section 3.3.6. The RF environmental dose rate is the sum of beta, gamma and cosmic dose rate and the calculated dose rates are given in table 7.1. The uncertainty associated with the infinite-matrix beta dose rate is discussed in section 3.3.2.3 and ±10% uncertainty has been applied to both the gamma and the cosmic dose rate. All errors have been propagated in quadrature to give the quoted uncertainties in table 7.1, although the level of uncertainty quoted with an RF OSL age estimate is discussed further in section 7.5.1. Calculated RF dose rates range between 2.8 and 4.1 Gy.ka^{-1} for the 37 samples measured, which are in

line with the FP dose rate values of 2.7 and 4.0 Gy.ka^{-1} (table 3.1) and a more detailed comparison between RF and FP dose rates is discussed in section 7.3.3.

7.3.3 Comparison of the RF and FP environmental dose rates

Figure 7.4 shows a comparison between the beta, gamma and environmental dose rates calculated for 15 samples using both the RF and FP protocols. In figure 7.4a, the RF and FP D_β values are compared and a good correlation between the two protocols is observed. The mean ratio of 1.03 ± 0.08 between the RF and FP calculated D_β values indicates that the RF protocol approximates the FP infinite-matrix beta dose rate well, with all fifteen RF samples falling within 10% (within errors) of the FP values. Figure 7.4b shows the relationship between the calculated RF gamma dose rate and the FP gamma dose rate calculated from radionuclide concentrations. All fifteen RF gamma dose rates (within errors) are within 10% of their FP counterparts, confirmed by a mean ratio of 0.92 ± 0.08 and it is concluded that the beta to gamma ratio of Roberts et al. (2009) provides a good approximation of the FP gamma dose rate.

The calculated environmental dose rates are compared in figure 7.4c. As the beta dose rate constitutes approximately two thirds of the total environmental dose rate, the trends evident in the D_β comparison (figure 7.4a) can be observed in the environmental dose rate comparison (figure 7.4c). In general, the environmental dose rate calculated using the RF protocol compare extremely well with those calculated using the FP protocol. The mean ratio between the RF and FP environmental dose rates is 1.01 ± 0.07 and all fifteen samples have calculated RF environmental dose rates within ±10% of unity of the FP environmental dose rate. Based on this, the pared-down protocol for environmental dose rate calculation is considered suitable for dose rate calculation for RF OSL dating.

Table 7.1: RF environmental dose rates. D_β was calculated from the TSBC of uncrushed sample for 4 hours, D_γ from D_β and the cosmic dose rate using the equations of Prescott and Hutton (1998). Dose rates were corrected for a water content 5 ± 4% and an attenuation factor of 0.9 was applied to D_β. Dose rates are quoted to two decimal places and all calculations were made prior to rounding. FP environmental dose rates have also been calculated for the samples marked *.

Sample	Depth (cm)	Infinite-matrix beta dose rate ($Gy.ka^{-1}$)	Gamma dose rate ($Gy.ka^{-1}$)	Cosmic dose rate ($Gy.ka^{-1}$)	Environmental dose rate ($Gy.ka^{-1}$)
136-3-1-RF*	222	2.02 ± 0.09	1.20 ± 0.12	0.15 ± 0.02	3.06 ± 0.16
136-3-4-RF*	307	1.91 ± 0.08	1.13 ± 0.11	0.13 ± 0.01	2.88 ± 0.15
136-3-9-RF*	399	2.09 ± 0.09	1.24 ± 0.12	0.12 ± 0.01	3.13 ± 0.17
136-4-1-RF*	232	2.10 ± 0.09	1.24 ± 0.12	0.15 ± 0.02	3.16 ± 0.17
136-4-2-RF*	291	2.62 ± 0.11	1.55 ± 0.16	0.14 ± 0.01	3.90 ± 0.21
136-5-1-RF*	227	1.77 ± 0.08	1.05 ± 0.11	0.15 ± 0.02	2.70 ± 0.14
136-5-3-RF*	270	2.37 ± 0.10	1.40 ± 0.14	0.14 ± 0.01	3.47 ± 0.19
136-5-6-RF*	387	2.75 ± 0.11	1.63 ± 0.16	0.12 ± 0.01	4.08 ± 0.12
136-6-2-RF	233	1.90 ± 0.09	1.12 ± 0.11	0.15 ± 0.02	2.88 ± 0.15
136-6-3-RF	260	2.15 ± 0.08	1.27 ± 0.13	0.15 ± 0.02	3.24 ± 0.17
136-6-5-RF	308	1.87 ± 0.09	1.11 ± 0.11	0.14 ± 0.01	2.82 ± 0.16
136-6-6-RF	342	2.17 ± 0.10	1.29 ± 0.13	0.13 ± 0.01	3.26 ± 0.18
154-MGJ-1-1-RF*	66.5	1.97 ± 0.09	1.16 ± 0.12	0.19 ± 0.02	3.02 ± 0.11
154-MGJ-1-2-RF	100.5	2.03 ± 0.09	1.20 ± 0.12	0.18 ± 0.02	3.10 ± 0.12
154-MGJ-1-3-RF	129	2.16 ± 0.10	1.28 ± 0.13	0.17 ± 0.02	3.29 ± 0.18
154-MGJ-1-5-RF	179	1.77 ± 0.06	1.05 ± 0.11	0.16 ± 0.02	2.88 ± 0.15
154-MGJ-1-6-RF	216	1.95 ± 0.09	1.16 ± 0.12	0.16 ± 0.02	3.15 ± 0.17
154-MGJ-1-7-RF	254	1.96 ± 0.09	1.16 ± 0.12	0.15 ± 0.02	2.96 ± 0.16
154-MGJ-1-8-RF*	290	1.90 ± 0.08	1.12 ± 0.11	0.14 ± 0.01	2.87 ± 0.15
154-MGJ-2-1-RF*	30	1.97 ± 0.09	1.16 ± 0.12	0.22 ± 0.02	3.05 ± 0.16
154-MGJ-2-2-RF	100	1.96 ± 0.09	1.16 ± 0.12	0.18 ± 0.02	3.00 ± 0.16
154-MGJ-2-3-RF	200	1.97 ± 0.09	1.17 ± 0.12	0.16 ± 0.02	3.00 ± 0.16
154-MGJ-2-4-RF	250	1.98 ± 0.07	1.17 ± 0.12	0.15 ± 0.02	3.00 ± 0.15
154-MGJ-3-1-RF*	540	2.01 ± 0.09	1.19 ± 0.12	0.11 ± 0.01	3.00 ± 0.16
154-MGJ-3-2-RF	425	1.93 ± 0.07	1.14 ± 0.14	0.13 ± 0.01	3.00 ± 0.15
154-MGJ-3-3-RF	305	2.11 ± 0.09	1.25 ± 0.13	0.14 ± 0.01	3.29 ± 0.15
154-MGJ-3-4-RF	220	2.00 ± 0.09	1.18 ± 0.12	0.15 ± 0.02	3.14 ± 0.14
154-MGJ-3-5-RF	100	1.90 ± 0.07	1.12 ± 0.11	0.18 ± 0.02	3.01 ± 0.13
154-MGJ-3-6-RF*	0	2.22 ± 0.10	1.32 ± 0.13	0.28 ± 0.02	3.60 ± 0.16
154-MGJ-4-4-RF	165	2.25 ± 0.08	1.33 ± 0.13	0.17 ± 0.02	3.41 ± 0.18
154-MGJ-5-1-RF*	40	1.78 ± 0.08	1.01 ± 0.11	0.21 ± 0.02	2.87 ± 0.13
154-MGJ-5-2-RF	85	1.85 ± 0.09	1.09 ± 0.11	0.18 ± 0.02	2.94 ± 0.14
154-MGJ-5-3-RF	143	2.18 ± 0.10	1.29 ± 0.13	0.17 ± 0.02	3.42 ± 0.16
154-MGJ-5-4-RF	183	1.94 ± 0.09	1.15 ± 0.12	0.16 ± 0.02	3.06 ± 0.14
154-MGJ-5-5-RF*	255	2.15 ± 0.08	1.28 ± 0.13	0.15 ± 0.02	3.36 ± 0.15
154-MGJ-6-2-RF*	90	2.06 ± 0.07	1.22 ± 0.12	0.18 ± 0.02	3.14 ± 0.16
154-MGJ-6-3-RF*	125	2.25 ± 0.08	1.33 ± 0.13	0.17 ± 0.02	3.53 ± 0.15

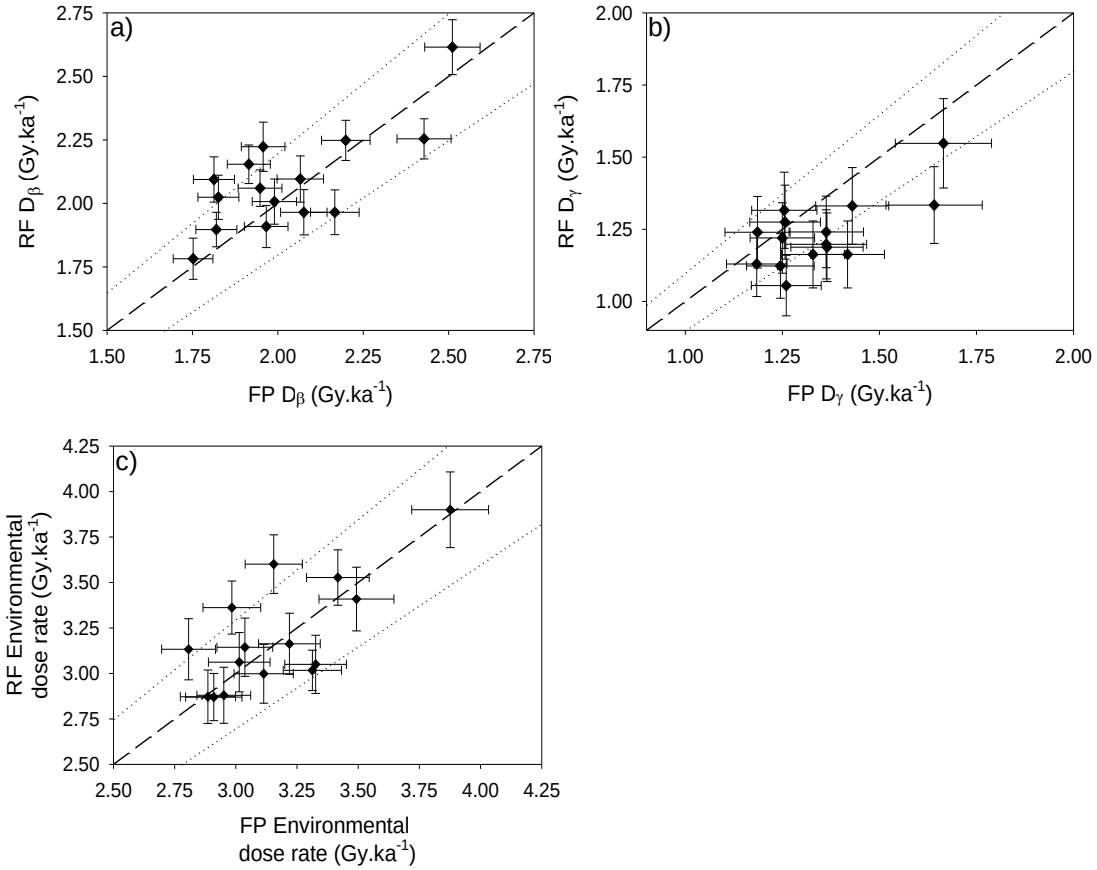

Figure 7.4: A comparison between the FP and RF dose rates for 15 samples. a) FP and RF D_β values, b) FP and RF D_γ values and c) FP and RF environmental dose rates. In all three figures, the dashed line represents unity and the dotted lines ± 10%.

7.4 Optimising RF D_e determination

7.4.1 Development of a RF protocol for D_e measurement

Roberts et al. (2009) investigated the effect of streamlining the coarse grain quartz OSL sample preparation by comparing RF D_e values obtained after various preparation procedures using two samples. Of the various combinations of laboratory treatments and measurement protocols that were tested, Roberts et al. (2009) undertook further testing of two possible protocols by applying them to a wider range of samples. The first protocol was the application of the double-SAR protocol (e.g Roberts and Wintle, 2001) to untreated sample, and the second, the SAR protocol applied to sediment which had been treated with HF and HCl. In this study, the two protocols have been applied to eight samples with the aim of

defining a RF protocol for D_e estimation. Given the extremely reactive and dangerous nature of HF (Kirkpatrick et al., 2005), the RF SAR protocol applied to HF treated sample (section 7.4.2.2) has been modified slightly from the protocol suggested by Roberts et al. (2009) to include a 1 hour treatment with concentrated (50%) HCl prior to HF etching.

7.4.2 Testing the suitability of RF D_e measurement protocols

7.4.2.1 The double-SAR protocol applied to raw sample

Roberts et al. (2009) found that the application of the double-SAR protocol to dried, raw sample provided excellent agreement with the target FP D_e values for the samples used in their study. To test the suitability of this method to the samples in this study, eight samples were selected (Durcan et al., 2010) and two aliquots of each were prepared with sediment that had been dried overnight at 50°C, but was otherwise untreated. Medium sized aliquots of sample were prepared and although there is potentially a wide range of grain sizes present in the prepared material, a modal grain size of 150 µm would imply ~800 grains per aliquot (Duller, 2008b). A double-SAR protocol (Banerjee et al., 2001; Roberts and Wintle, 2001) was applied to this raw material, stimulating with IR at 50°C for 500 s prior to OSL stimulation with blue diodes at 125°C for 125 s to measure the post-IR OSL signal. A pre-heat of 220°C held for 10 s, and a cut-heat of 160°C followed by immediate cooling were used. A test dose of 11.9 Gy and regeneration doses of 0, 9.9, 19.8, 39.7 Gy were applied, followed by a repeat measurement of a 0 Gy dose to assess the extent of recuperation and the 19.8 Gy dose to give the recycling ratio which monitors the efficacy of the correction for sensitivity change. Feldspar contamination was assessed using the OSL IR depletion ratio (Duller, 2003) by adding two additional cycles repeating the regeneration does of 19.8 Gy (Roberts, 2007). In the first cycle, stimulation was with blue LEDs only, while in the second cycle, IR stimulation was added before measurement of the signal resulting from the regenerative dose. In both cycles, the test dose signal was stimulated with blue LEDs only.

Figure 7.5 shows the [post-IR] OSL signal and dose response curve from an aliquot of sample 136-5-1-RF, typical of the eight samples measured using this protocol. The gradual decay of the [post-IR] OSL signal implies contamination by feldspar and OSL IR depletion ratios between 0.03 and 0.06 from aliquots of these samples also indicate this. The dose response curve (figure 7.5, inset) does not pass through the origin, and therefore D_e interpolation cannot be considered accurate. For these samples, it appears that the 500 s stimulation with IR prior to measurement of the OSL signal is not sufficient to bleach the signal from the feldspar (Durcan et al., 2010). Alternatively, it is possible, there is a component of the trapped charge in the feldspar signal which is responsive only to stimulation with blue diodes (e.g. Duller & Bøtter-Jensen, 1993). With this in mind, it was concluded that the application of a double-SAR protocol to raw, polymineral material is not appropriate for RF D_e determination for the samples in this study.

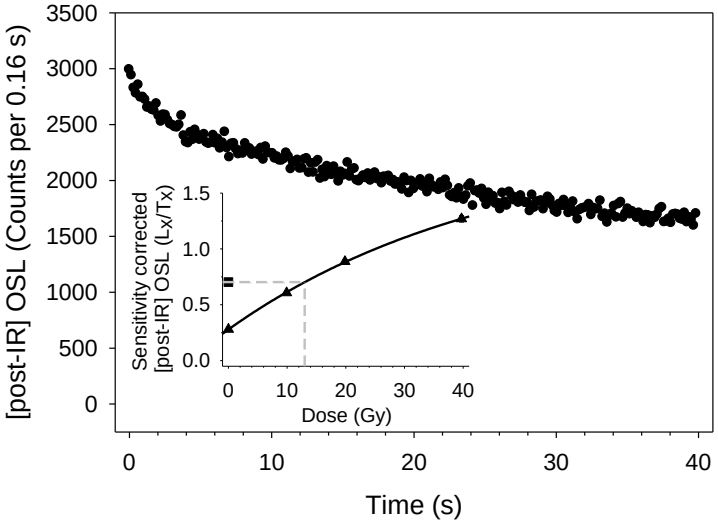

Figure 7.5: A typical [post-IR] OSL signal from raw material (sample 136-5-1-RF) after a 9.9 Gy regenerative dose and inset, the corresponding dose response curve. The sensitivity corrected natural [post-IR] OSL signal is shown by the filled square and the sensitivity corrected regenerative doses by the triangles.

7.4.2.2 The SAR protocol applied to HF treated sample

The suitability of the second RF protocol suggested by Roberts et al. (2009) was also tested on the same eight samples, given the potential issue with feldspathic contamination in the samples in this study (section 6.3.4.1). Raw sample was dried overnight at 50°C before being treated for 1 hour with concentrated (50%) HCl. The

sample was then treated with 40% HF for 45 minutes, followed by 45 minutes in concentrated (37%) HCl to remove the build up of any fluorides created during the reaction. Twelve medium sized aliquots of the HF treated material were prepared for each of the samples. A standard SAR protocol (e.g. table 4.8; Murray and Wintle, 2000) was used for measurement, using a pre-heat of 220°C held for 10 s and a cut-heat of 160°C followed by immediate cooling, and stimulation with blue diodes at 125°C for 125 s. Regenerative doses of 0, 9.9, 19.8, 39.7 Gy and a test dose of 11.9 Gy were applied, followed by the repeat measurement of the 0 Gy and 19.8 Gy doses to check the recuperation and recycling ratio. Feldspar contamination was checked using the OSL IR depletion ratio of Duller (2003).

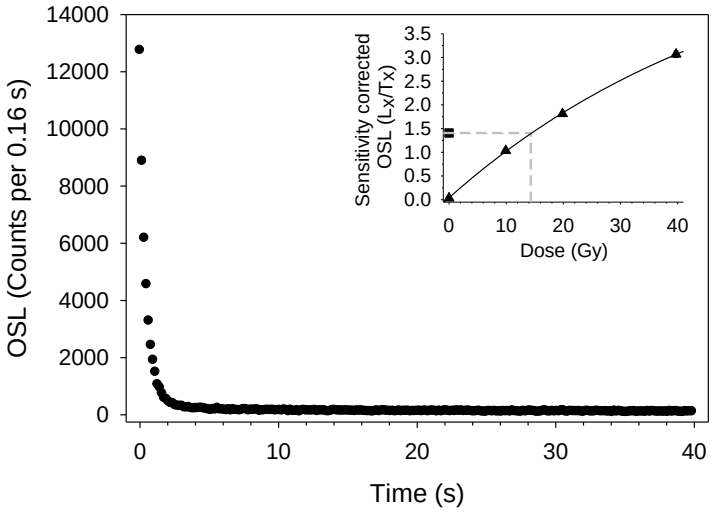

Figure 7.6: A typical OSL signal from HF treated material (sample 136-5-1-RF) after a 9.9 Gy regenerative dose. Inset, the corresponding dose response curve. The sensitivity corrected natural OSL signal is shown by the filled square and the sensitivity corrected regenerative doses by the triangles.

Figure 7.6 shows an OSL signal and dose response curve from sample 136-5-1-RF which is typical of the signals seen from samples in this study measured using this RF protocol. The rapid initial decay of the OSL signal to a low background level and the non-linearity of the dose response curve is typical of an OSL signal dominated by the signal from quartz (Roberts, 2007; Roberts et al., 2009) and the high OSL IR depletion ratios (between 0.91 and 0.99 for the aliquots measured) confirm that the contribution from feldspar has been significantly reduced by the HF etching (Durcan et al., 2010). Recycling ratios are within the ±10% limits suggested by Murray and

Wintle (2000), indicating that the SAR protocol successfully corrected for any sensitivity change occurring through the measurement procedure.

7.4.2.3 The RF D_e measurement protocol used in this study

Whilst the application of the RF double-SAR protocol to untreated, dry sample produced D_e estimates close to the target FP D_e in the study by Roberts et al. (2009), it has not proved appropriate in this study. For some reason, whether due to insufficient IR stimulation time or feldspar signals responsive only to blue light, the OSL signal measured using this protocol is not one of pure quartz. Therefore, the RF protocol which involves the HF etching of sample material, followed by D_e measurement using the SAR protocol has been adopted for use in this study (section 7.4.2.2). This is in line with the conclusions made by Roberts et al. (2009) who found that the treatment of raw material with HF and HCl acid was the most successful of the pared-down treatment procedures investigated. The RF laboratory preparation procedure used is summarised in figure 7.7. In comparison with the FP procedure, the time taken to prepare the sample sediment for RF dating is significantly reduced due to the omission of the H_20_2 treatment, sieving and heavy liquid density separation, stages that can each be lengthy.

7.4.3 RF D_e determination

All RF D_e measurements were made on Risø 3 or 4 (see table 4.1 for Risø reader specifications). A standard SAR protocol (table 4.8; Murray and Wintle, 2000; Wintle and Murray, 2006) was used for measurement of the RF D_e, and is described in section 7.4.2.2. The recycling ratio was monitored and feldspar contamination was checked using the OSL IR depletion ratio of Duller (2003).

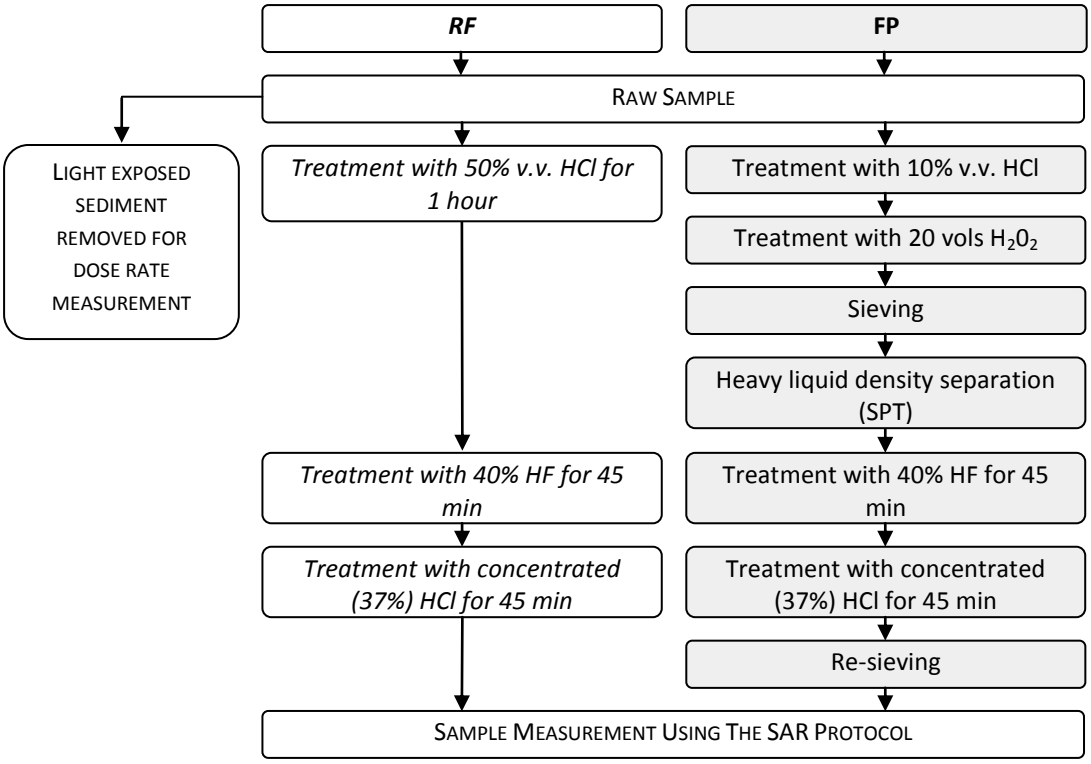

Figure 7.7: Comparison of the sample preparation procedure for the RF and FP OSL dating protocols.

7.4.3.1 Aliquot size and number

Olley et al. (1998) suggest small aliquots (~100 grains per disc) of sample should be used for dating samples from fluvial and colluvial environments. They argue that the measurement of a larger number of grains per aliquot for samples which are incompletely bleached will result in overestimation of the true burial dose. The impact of averaging the signal from individual grains on the same multiple grain aliquot can result in incomplete bleaching going undetected, however, this is also dependent on the number of grains which contribute to the luminescence signal. In this study, a relatively low number of grains (~2%) constitute 90% of the OSL signal (figure 6.2). Therefore, the OSL signal from a small sized aliquot of sample (containing 200 grains, assuming a modal grain size of 150 µm; Duller (2008b)) will originate from ~4 grains and ~16 grains will make up the signal from a medium sized aliquot. Whilst small sized aliquots have been used elsewhere in this study for FP OSL dating, medium sized aliquots have been selected for the RF OSL dating protocol because the signal levels are greater.

To investigate the impact of using medium sized aliquots on dose distributions of samples, the D_e distributions measured using the FP and RF protocols are compared for samples 136-3-1-RF, 136-3-9-RF, 136-4-1-RF and 136-4-2-RF using the radial plots in figure 7.8. FP D_es were calculated from the luminescence signal from small aliquots and the RF D_es were calculated using medium aliquots. Individual D_e values tend to be more precise for the RF aliquots due to the brighter luminescence signal from the larger aliquot and the associated reduction in error with counting statistics. For samples 136-3-1-RF, 136-3-9-RF and 136-4-1-RF (table 7.2), visually the RF and FP dose distributions are similar (figure 7.8a-c). The RF D_e calculated from these samples are within 10% of the FP D_e value, and it is concluded that for samples with a relatively simple distribution of D_e values, the use of medium aliquots does not appear to affect the calculated D_e value.

Sample 136-4-2 has a more complex dose distribution, with a FP σ_d of 43% and when the finite mixture model is applied to the FP dose distribution, three distinct components are identified, with 70% of accepted aliquots making up the dominant component (table 6.3). This complexity is not evident in the RF D_e distribution, where the RF σ_d is 21% (table 7.2). This is likely to be a result of the effect of averaging over the larger aliquot size. Nonetheless, the RF D_e is within 2% of the FP D_e. Whilst the dose distribution calculated from D_es measured using the RF protocol does not identify the intricacies of the FP dose distribution, it has identified the crucial characteristic; the dose population identified by the FMM which has been used for FP age calculation. Based on the similarity between the RF and FP D_e values calculated, it is concluded that using medium sized aliquots can identify the main features of a dose distribution. Nonetheless, age overestimation by the RF protocol is possible for samples that have been heterogeneously bleached, and the extent of overestimation will depend upon the sample dose distribution and the number and dominance of dose components.

Table 7.2: Comparison of RF and FP D_e and σ_d values for the listed samples. RF D_e values were calculated by taking the mean value of 60 medium sized aliquots and the standard error is given. FP D_e values were calculated using the FMM, using the number of aliquots given in brackets.

	RF			FP			RF: FP D_e
Sample	**# of aliquots**	**D_e (Gy)**	**σ_d (%)**	**# of aliquots**	**D_e (Gy)**	**σ_d (%)**	
136-3-1-RF	60	16.4 ± 0.5	22	60 (23)	16.49 ± 0.62	39.7	0.99
136-3-9-RF	60	15.8 ± 0.3	16	96 (46)	14.94 ± 0.54	22.5	1.06
136-4-1-RF	60	15.4 ± 0.6	29	60 (26)	15.38 ± 0.47	37.5	1.00
136-4-2-RF	60	18.9 ± 0.4	21	107 (54)	19.19 ± 0.71	42.6	0.98

a) 136-3-1

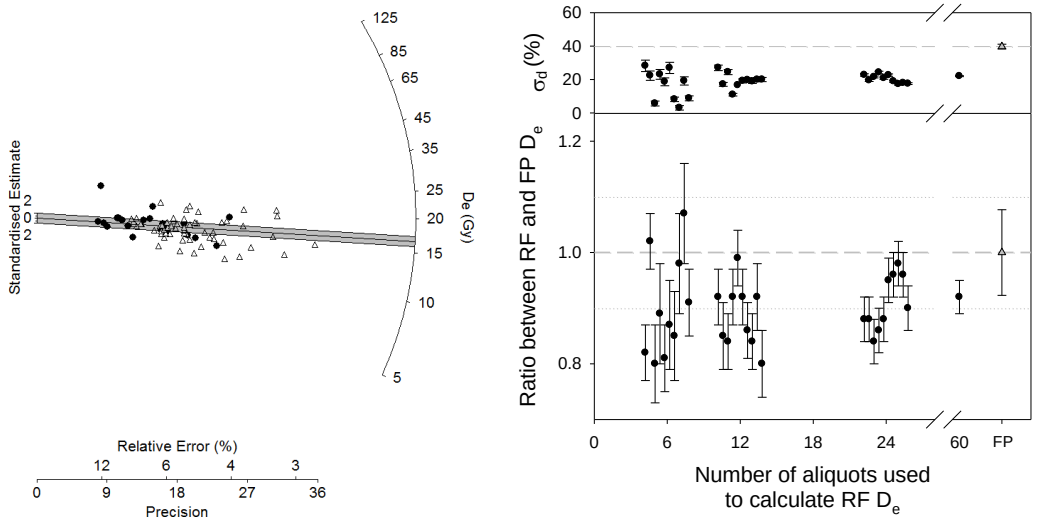

b) 136-3-9

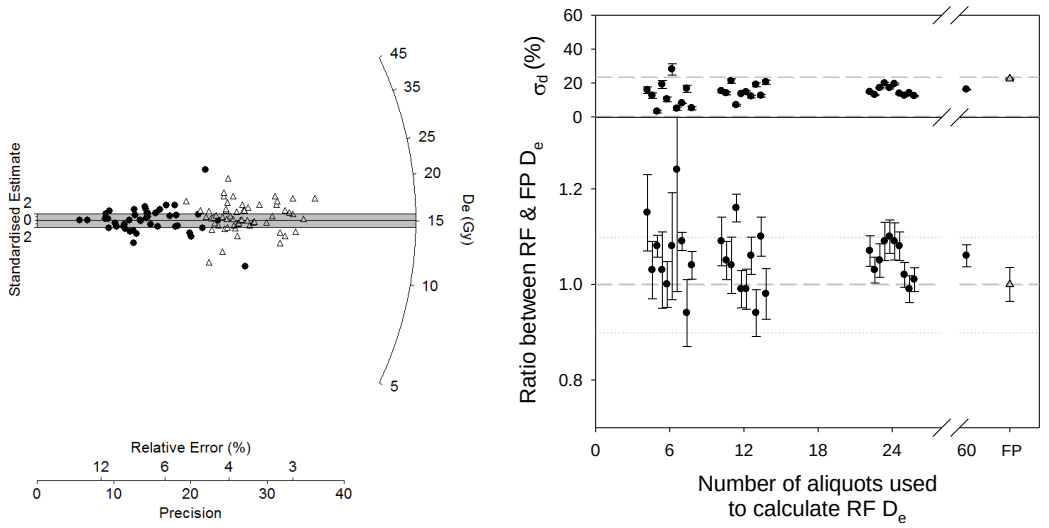

Figure 7.8: *Figure caption on page 242.*

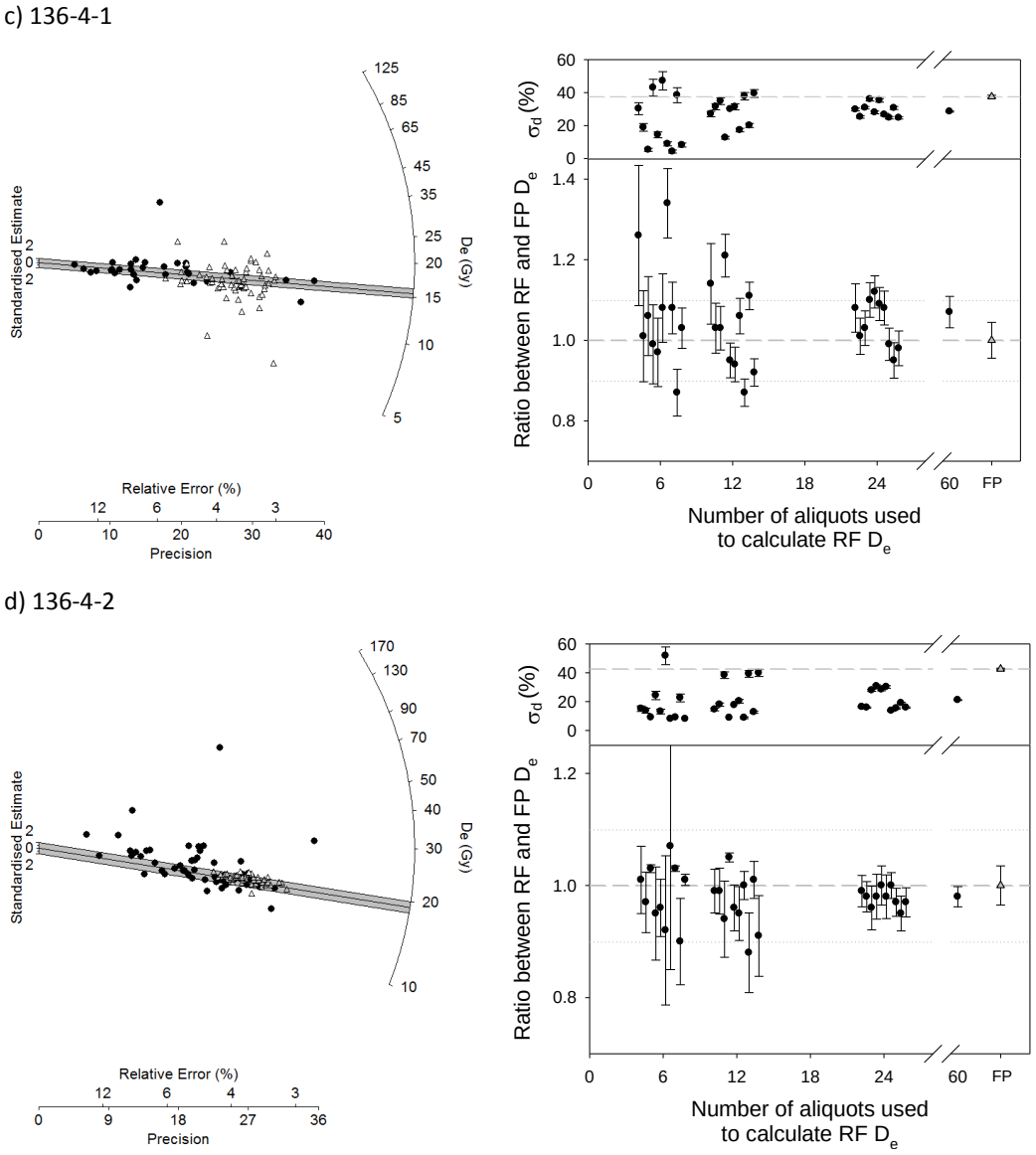

Figure 7.8: Left) Radial plots of the RF (open symbols) and FP (filled symbols) dose distributions for samples 136-3-1-RF, 136-3-9-RF, 136-4-1-RF and 136-4-2-RF. For each sample 60 RF aliquots and at least 23 accepted FP aliquots were used for D_e calculation. The shaded area shows the FP D_e ± 2σ. Right) The RF D_es (black symbols) were calculated by taking the mean of 6, 12 and 24 randomly selected aliquots (ten times) and 60 aliquots from the 60 RF aliquots measured (the standard error is also shown). For illustrative purposes, the FP D_e and ± 10% is shown by the dashed and dotted lines respectively. σ_d is shown for each RF simulation and the FP distribution.

Furthering the work of Durcan et al. (2010), where calculation of the RF D_e was based upon 12 aliquots, 60 aliquots of the samples listed in table 7.3 were measured to investigate the impact of varying the number of aliquots used for RF D_e calculation. The aim when using the RF protocol is that D_e estimates are reproducible and the effect of using fewer aliquots to calculate a RF D_e was investigated by randomly selecting ten sets of 6, 12 and 24 aliquots from the 60 measured and using these to calculate the mean RF D_e and associated σ_d. The

results of these simulations are shown alongside the FP D_e visually in figure 7.8 and in table 7.3. The scatter plots in figure 7.8 show the ratio between the FP D_e and the RF D_e calculated using different numbers of aliquots. Also shown is the FP σ_d and the RF σ_d calculated for each set of D_e values. Figures 7.8a-c show data for samples 136-3-1-RF, 136-3-9-RF and 136-4-1-RF. Similar trends in D_e and σ_d are observed for all three samples. When 6 aliquots are used for D_e determination, variability in both the calculated D_e and σ_d is observed (table 7.3) and D_e estimates can be up to 135% of the FP D_e (e.g. figure 7.8c). However D_e estimates become much more reproducible when twelve or more aliquots are used for calculation, and this is reflected by the lower standard deviation values in table 7.3. The majority of D_e estimates calculated with 12 or more aliquots for all three samples are within ±10% of the target FP D_e. When considering variability within the different sets, reproducibility does not improve when increasing numbers of aliquots are used, and neither do the D_e estimates become significantly closer to the FP target. Similar trends are seen for sample 136-4-2-RF (figure 7.8d), suggesting that even for a sample with a more complex dose distribution, the measurement of a relatively small number of aliquots is sufficient for D_e estimation. Whilst the measurement of more aliquots in FP OSL dating is preferable, there is a compromise between the number of aliquots measured and measurement time, and therefore the measurement of the 12 aliquots used by Durcan et al. (2010) is considered an appropriate number to use to calculate a RF D_e.

Table 7.3: The mean ratio between the RF D_e (based on 10 simulations), calculated as the number of aliquots used is varied, and the FP D_e. The mean and standard deviation are given.

Sample	6 Aliquots		12 Aliquots		24 Aliquots		60 Aliquots	
	D_e	σ_d	D_e	σ_d	D_e	σ_d	D_e	σ_d
136-3-1-RF	1.01 ± 0.12	16%	0.97 ± 0.09	19%	0.99 ± 0.06	20%	0.99 ± 0.03	22%
136-3-9-RF	1.07 ± 0.08	12%	1.04 ± 0.07	15%	1.05 ± 0.04	15%	1.06 ± 0.02	16%
136-4-1-RF	1.00 ± 0.13	22%	0.96 ± 0.10	28%	0.98 ± 0.06	29%	1.00 ± 0.04	29%
136-4-2-RF	1.02 ± 0.02	11%	1.03 ± 0.02	12%	1.02 ± 0.01	18%	0.98 ± 0.02	21%

7.4.3.2 Rejection criteria

In this study, the application of a suite of rejection criteria to OSL signals measured using the FP OSL dating protocol have been used to identify and remove signals

which may give an erroneous D_e value. Many OSL signals have been excluded from dose distribution analysis on the basis of these criteria, including the recycling ratio and OSL IR depletion ratio to ensure that only signals which behave in an acceptable manner considered suitable for dating are used for FP D_e determination. OSL signals are only rejected after careful laboratory treatment and measurement and because the aim of the RF OSL dating protocol is to provide rapid estimates of age, the application of numerous stringent data screening checks does not seem appropriate to signals that have been measured from material which has been rapidly prepared. Therefore, only two of the rejection criteria outlined in section 6.3.3 are applied to RF signals; the recycling ratio and the OSL IR depletion. The recycling ratio is applied because it is an underlying assumption when using the SAR protocol that it can successfully account for sensitivity change during measurement (Wintle and Murray, 2006). Aliquots with a recycling ratio within 10% (including errors) of unity were accepted for RF D_e calculation, and for the majority of samples, all measured aliquots passed this criteria (table 7.4). As discussed in section 6.3.4.1, the OSL signals observed from samples in this study are often not those of a pure quartz OSL signal, and despite thorough laboratory preparation, a large number of aliquots were rejected on the basis of the OSL IR depletion ratio (section 6.3.3.4). With feldspar contamination identified as an issue for the FP samples in this study, it is prudent that a check for contamination be part of the RF dating protocol, particularly because the density separation stage of standard laboratory treatment has been omitted. Therefore, the OSL IR depletion ratio of Duller (2003) has been used as a rejection criterion in the RF OSL dating protocol, with signals rejected if they have a ratio in excess of 10% of unity (including errors).

Table 7.4: Summary of the RF OSL ages calculated in this study.

Sample	Aliquots[a]	D_e (Gy)[b,c]	σ_d (%)	Dose rate (Gy.ka^{-1})[b]	Age (ka)[d,e]
136-3-1	12 (12)	16.72 ± 1.21	25.0 ± 1.5	3.06 ± 0.16	5.5 ± 1.1
136-3-4	12 (11)	15.54 ± 1.20	24.0 ± 1.6	2.88 ± 0.15	5.4 ± 1.1
136-3-9	12 (11)	15.19 ± 0.70	15.5 ± 1.0	3.13 ± 0.17	4.9 ± 1.0
136-4-1	12 (11)	13.31 ± 1.08	32.4 ± 2.1	3.16 ± 0.17	4.2 ± 0.8
136-4-2	12 (12)	20.85 ± 0.30	3.6 ± 0.4	3.90 ± 0.21	5.4 ± 1.0
136-5-1	12 (12)	15.63 ± 0.39	8.4 ± 0.5	2.70 ± 0.14	5.8 ± 1.2
136-5-3	12 (10)	16.31 ± 0.64	11.7 ± 0.9	3.47 ± 0.19	4.7 ± 1.0
136-5-6	12 (9)	23.75 ± 1.73	21.5 ± 1.7	4.08 ± 0.20	5.8 ± 1.2
136-6-2	12 (9)	32.76 ± 1.41	9.3 ± 1.3	2.88 ± 0.15	11.4 ± 2.3
136-6-3	12 (11)	41.94 ± 1.87	12.4 ± 1.0	3.24 ± 0.17	13.0 ± 2.6
136-6-5	12 (12)	37.54 ± 1.65	13.1 ± 0.9	2.82 ± 0.16	13.3 ± 2.7
136-6-6	12 (7)	34.75 ± 2.60	14.6 ± 1.7	3.26 ± 0.18	10.7 ± 2.1
154-MGJ-1-1	12 (8)	29.28 ± 1.85	16.9 ± 1.7	3.02 ± 0.11	9.7 ± 2.0
154-MGJ-1-2	12 (11)	37.17 ± 3.46	30.2 ± 2.1	3.11 ± 0.12	12.0 ± 2.4
154-MGJ-1-3	*12 (0)*				
154-MGJ-1-5	12 (11)	31.33 ± 3.73	27.0 ± 1.8	2.71 ± 0.11	11.6 ± 2.3
154-MGJ-1-6	*12 (0)*				
154-MGJ-1-7	*12 (0)*				
154-MGJ-1-8	*12 (0)*				
154-MGJ-2-1	12 (5)	3.45 ± 0.51	28.9 ± 4.2	3.05 ± 0.16	1.1 ± 0.2
154-MGJ-2-2	12 (12)	4.18 ± 0.23	17.5 ± 1.1	3.00 ± 0.16	1.4 ± 0.3
154-MGJ-2-3	12 (10)	31.51 ± 1.30	11.2 ± 1.0	3.00 ± 0.16	10.5 ± 2.1
154-MGJ-2-4	12 (10)	28.86 ± 2.15	24.5 ± 1.5	3.00 ± 0.15	9.6 ± 1.9
154-MGJ-3-1	12 (10)	33.83 ± 1.86	10.0 ± 1.3	3.00 ± 0.16	11.3 ± 2.3
154-MGJ-3-2	12 (10)	37.91 ± 1.85	13.4 ± 1.1	3.00 ± 0.15	12.7 ± 2.5
154-MGJ-3-3	*12 (0)*				
154-MGJ-3-4	12 (11)	0.32 ± 0.08	61.0 ± 5.4	3.14 ± 0.14	0.1 ± 0.05
154-MGJ-3-5	12 (10)	0.37 ± 0.06	37.5 ± 3.3	3.01 ± 0.13	0.1 ± 0.05
154-MGJ-3-6	12 (11)	0.98 ± 0.47	85.8 ± 5.9	3.60 ± 0.16	0.3 ± 0.05
154-MGJ-4-4	12 (12)	63.96 ± 7.61	29.7 ± 1.8	3.41 ± 0.18	18.8 ± 3.8
154-MGJ-5-1	*12 (0)*				
154-MGJ-5-2	12 (12)	0.60 ± 0.11	61.7 ± 4.5	2.94 ± 0.14	0.2 ± 0.05
154-MGJ-5-3	*12 (0)*				
154-MGJ-5-4	12 (12)	1.86 ± 0.22	37.6 ± 2.3	3.06 ± 0.14	0.6 ± 0.1
154-MGJ-5-5	12 (11)	5.80 ± 0.93	43.1 ± 2.8	3.36 ± 0.15	1.7 ± 0.4
154-MGJ-6-2	12 (12)	5.08 ± 0.92	31.2 ± 2.0	3.14 ± 0.16	1.6 ± 0.3
154-MGJ-6-3	12 (12)	5.89 ± 0.38	18.2 ± 1.1	3.53 ± 0.15	1.7 ± 0.3

[a] The number of aliquots measured, with the number passing the rejection criteria in brackets. All measured aliquots of the samples in italics failed the rejection criteria and were not dated.
[b] Rounded to 2 d.p. All calculations were made prior to rounding.
[c] The quoted uncertainty is the standard error
[d] Ages reported to the nearest 1 d.p., unless the figure is less than 0.1, where it is rounded to 2 d.p.. Calculations were made prior to rounding.
[e] RF ages are quoted with a ±20% uncertainty, see section 7.5.2.

Figure 7.9 shows examples of two samples where there appears to be an issue with contamination of the quartz OSL signal on the basis of the OSL IR depletion ratio values. Figure 7.9a shows D_e values from sample 154-MGJ-1-1-RF, which has a FP D_e

of 22.25 Gy. The 12 RF OSL signals measured (filled symbols in figure 7.9a) have OSL IR depletion ratios ranging between 0.31 ± 0.03 and 1.05 ± 0.07 and D_e values varying between 13.3 and 36.0 Gy, and there is a strong positive correlation between samples with low depletion ratios and D_e estimates which underestimate the target FP D_e ($r^2 = 0.82$). For sample 154-MGJ-1-3-RF (figure 7.9b), a FP D_e has not been calculated, although the sample was taken from beneath sample 154-MGJ-1-1-RF and a D_e equal to or greater than 22.25 Gy is expected. However, all 12 RF aliquots give D_e values between 13 and 17 Gy (closed symbols figure 7.9b), with OSL IR depletion ratios not exceeding 0.33 ± 0.01. It appears that the measured RF D_e values for this sample are underestimating the true D_e, and failure to apply the OSL IR depletion ratio (or some other check for signal contamination) would result in age underestimation.

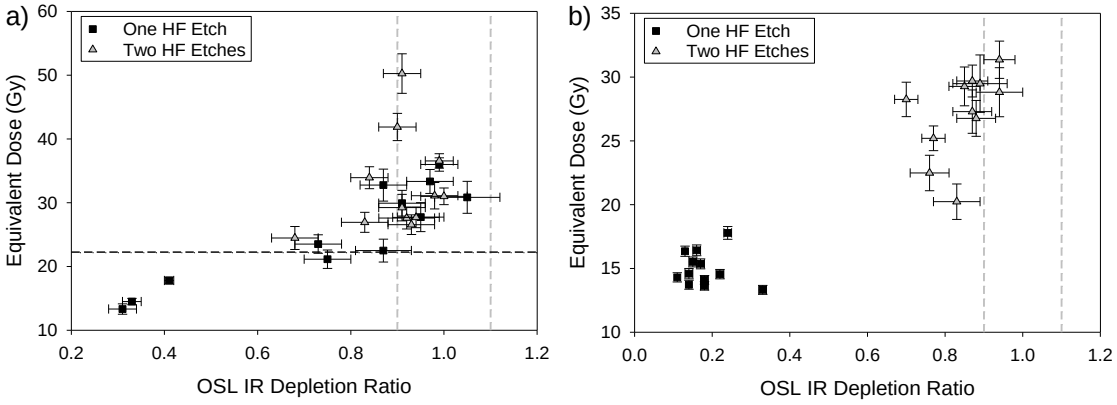

Figure 7.9: D_e plotted as a function of the OSL IR depletion ratio for sample a) 154-MGJ-1-1-RF and b) 154-MGJ-1-3-RF. The FP D_e of 154-MGJ-1-1 is shown by the black dashed line in a) and the limits of the rejection criteria (±10% of unity) are shown in both plots by the grey dashed lines. The measured D_es after one HF etch are shown by the square symbols and after a second HF etch by the triangle symbols.

In light of the apparent contamination issues, samples 154-MGJ-1-1-RF and 154-MGJ-1-3-RF were re-etched in HF acid and concentrated HCl to ascertain whether the contamination could be removed. Twelve aliquots of each sample were re-measured and are plotted in figure 7.9. For both samples, a second etch considerably improves the OSL IR depletion ratios, however many aliquots of each sample still do not satisfy the rejection criterion. This test has illustrated the importance, in this study at least, that signals should originate from pure quartz signals to provide accurate D_e estimates. It also demonstrates the importance of

screening signals for contamination. In the case of both of these samples, further treatment is required to purify the signals, but repeated etching would undermine the original purpose of the RF OSL dating protocol, which is to provide rapid estimates of age.

7.4.3.3 Statistical calculation of D_e

The application of complex age models (such as the finite mixture model) has been used elsewhere in this study to deal with complex dose distributions, based on the geomorphological context from which the sample was taken and the σ_d value (Galbraith et al., 1999). Without careful sample preparation and the measurement of numerous aliquots, the application of this complex analytical tool is not appropriate to the simplified sample preparation process undertaken. Therefore, the application of a more simple statistical treatment in the form of the mean is used to calculate a D_e from RF OSL signals. The central age model of Galbraith et al. (1999) is essentially a weighted mean that takes into account the underlying overdispersion within a dose distribution. Therefore, taking the mean value for samples which do not have large σ_d values will not dramatically impact upon the accuracy of the RF D_e estimation. Even in cases where the FP σ_d indicates a wide range of D_es, the RF value is likely to identify the most dominant component within the distribution (e.g. sample 136-4-2-RF; table 7.2), although overestimation of the true D_e is possible for samples that are at least moderately incompletely bleached.

7.4.4 Comparison of RF and FP D_e values

Figure 7.10 shows a comparison between the calculated FP D_e values and the RF D_e estimates of eleven samples. The RF D_e estimates approximate the FP D_e determinations well, regardless of the age model used for FP D_e calculation and the majority of RF D_e estimates are within 20% of the FP value. A mean ratio of 1.30 ± 0.52 between the RF and FP D_e values is calculated and the individual ratios are presented in figure 7.11. This mean ratio includes sample 154-MGJ-3-6 which has a FP D_e of 0.37 Gy (table 6.5). The RF protocol overestimates this D_e by a factor of

2.65, possibly because the effects of incomplete bleaching become more obvious at lower doses, and if this sample is excluded from the ratio, the RF:FP D_e ratio is 1.18 ± 0.29. In figure 7.11, the ratio between the RF and FP D_e estimates are compared against the FP D_e and it is evident that the RF protocol overestimates the FP D_e when the FP D_e is low (less than ~3 Gy). This is in line with the overestimation of young samples by the RF protocol found by Roberts et al. (2009), and it is concluded that whilst the RF protocol has a valuable application in determining whether a sample is young in age, it is likely that this protocol overestimates the true D_e.

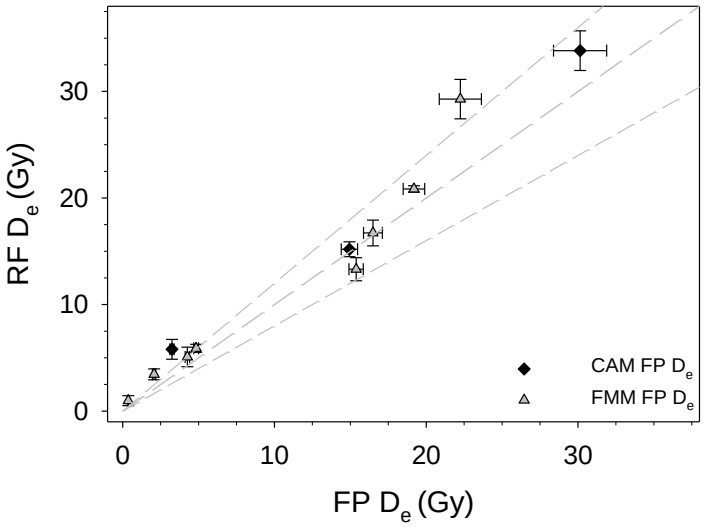

Figure 7.10: A comparison of the RF and FP measured D_e values. The level of uncertainty calculated by the CAM/FMM model is shown for the FP calculations and the standard error for the RF. Unity and ± 20% are shown by the grey dashed lines.

For samples with palaeodoses greater than ~3 Gy, the RF protocol estimates are within 20% of the FP D_e for the majority of compared samples, regardless of the level of overdispersion calculated from the FP dose distributions (figure 7.11). This suggests that despite the use of medium aliquots for samples with potentially complex dose distributions and the use of a relatively low number of signals for D_e calculation, the RF protocol can successfully estimate a FP D_e within 20%.

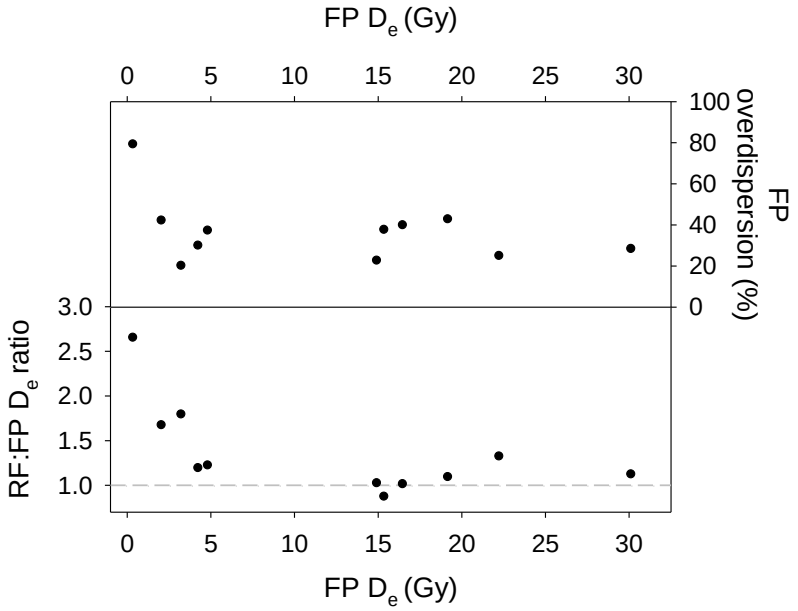

Figure 7.11: The ratio between the RF and FP D_e estimates plotted against the FP D_e (Gy). Also shown is the FP overdispersion as a function of FP D_e.

7.5 Calculation of a RF OSL age estimate

A RF OSL age is calculated in the same manner as a FP OSL age; by the division of the equivalent dose by the environmental dose rate (equation 1.1). Table 7.4 summarises the D_e, environmental dose rate and the RF age for the 30 samples measured using the RF OSL dating protocol. In section 7.5.2, a discussion of the uncertainty given for each RF age is given.

7.5.1 Comparison of the RF and FP OSL ages

Calculation of the environmental dose rate, using the RF protocol outlined in section 7.3.3, provides RF dose rate estimates that agree well with the FP target dose rates, with a mean ratio between RF and FP dose rates of 1.01 ± 0.07 (e.g. figure 7.4). As discussed in section 7.4.4, the comparison of RF D_e and FP D_e estimates are slightly more variable than the dose rates, with a mean ratio of 1.18 ± 0.29 (excluding sample 154-MGJ-3-6-RF). RF ages, calculated by dividing the RF D_e by the RF environmental dose rate, are presented in table 7.4 and for samples where an FP OSL age has been calculated, FP and RF ages are compared to the FP ages in figure 7.12. RF age estimates are in good agreement with the FP ages from

the same sample and the RF age is within 20% of the target FP age for most samples, with a mean ratio between RF and FP ages of 1.27 ± 0.47. The greatest discrepancy between the RF and FP ages occurs when young samples are dated and more specifically, where the FP age is less than approximately 1 ka (figure 7.12). It is therefore recommended that RF ages of approximately 1 ka or less be treated as maximum ages only. A ratio of 1.06 ± 0.19 is calculated when the samples with a FP age of 1 ka or less are excluded. This ratio suggests a good agreement between ages calculated using the two OSL protocols, with variability of ~20% within the dataset.

7.5.2 Defining the uncertainty associated with a RF OSL age

The level of uncertainty associated with a FP OSL age is carefully calculated and takes into account sources of systematic and random error in all aspects of equivalent dose and dose rate calculation. The calculation of uncertainty in this manner for RF OSL age estimates is not possible because there are many aspects of the measurement where the level of uncertainty is unknown. These sources of potential error include the impact of using a wide variety of grain sizes on beta dose attenuation and the impact on the dose rate due to variability in the beta to gamma ratio. Based on comparison of seven RF OSL age estimates to target FP OSL ages, Roberts et al. (2009) suggested that a value of 30% should be quoted as the error term for RF OSL ages, based on the comparison between the RF and FP ages in their study. In this study, eleven samples were measured using the RF and FP OSL dating protocols and a mean ratio between the RF and FP ages of 1.27 ± 0.47 has been calculated, or 1.06 ± 0.19 for samples with an FP age in excess of 1 ka. Based on this standard deviation of 0.19, it is suggested that RF ages older than 1 ka have a ±20% uncertainty applied to them, with younger RF ages treated as maximum ages only.

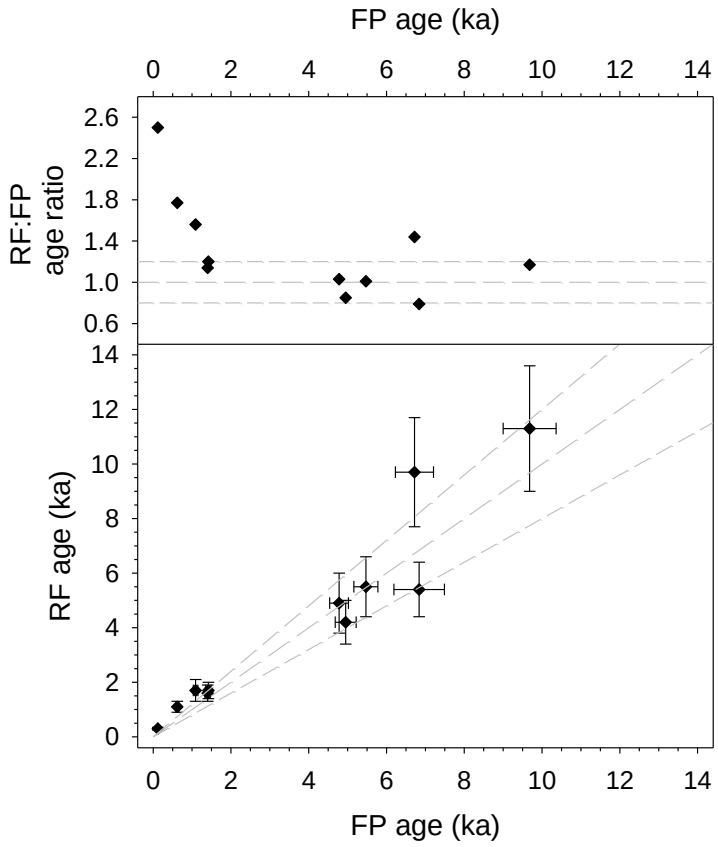

Figure 7.12: Comparison between the FP and RF ages. Also shown is the ratio between RF and FP ages as a function of the FP age. The line of unity and ±20% are shown by the grey dashed lines.

7.5.3 Reporting a RF OSL age estimate

Durcan et al. (2010) describe RF OSL ages as rough estimates of the true age. They are not presented as precise or accurate OSL age determinations and this notion is reiterated here. In this study, FP equivalent doses, dose rates and ages have been presented rounded to two decimal places. To reflect the reduced precision of the final RF OSL ages, RF ages and the associated uncertainties have been rounded to the nearest 100 years to distinguish them from FP OSL ages (table 6.5). Sample codes have been supplemented with the '-RF' notation to differentiate them from FP dates, and figures and tables which present RF data have been drawn to differentiate between a RF OSL age estimate and a FP OSL age.

7.6 Assessing the accuracy of the RF OSL dating protocol

Figure 7.13 presents a schematic view of the nine sites where a combination of RF OSL dating, FP OSL dating and ^{14}C dating has been applied. More detailed sedimentological logs are shown in appendix A, but the purpose of these simplified logs is to allow the geochronological data to be displayed more clearly. Using stratigraphic control to compare RF OSL ages estimates to FP OSL and ^{14}C ages provides a further test of the RF dating protocol and makes it possible to assess the accuracy of RF OSL ages of samples where no FP OSL age has been calculated. The RF dating protocol appears to work extremely well at sites 136-3, 136-4, 154-MGJ-3, 154-MGJ-5 and 154-MGJ-6 (figure 7.13). At these sites, the RF OSL ages are in excellent agreement with the FP OSL ages, and the ^{14}C ages (figure 7.13). At these sites, the RF ages are in stratigraphic order and agree within errors of the independent age control at the sites where a comparison can be made.

At some of the other sites, there is some discrepancy between the RF OSL age estimates and the independent age control. At site 154-MGJ-4 (figure 7.13), the RF OSL age of sample 154-MGJ-4-4-RF is 18.8 ± 3.8 ka, which appears to be an overestimation of the true burial age, because the samples above and below the position of the RF sample have FP OSL ages of 9.59 ± 0.85 ka and 9.14 ± 0.85 ka respectively. The σ_d values for these FP samples are 57% and 43% respectively, indicative of complexity in the dose distribution, and assuming that the underlying dose distribution of sample 154-MGJ-4-4-RF is similar, the use of a small number of medium sized aliquots may cause age overestimation. At this site, whilst the agreement between RF and FP ages is not as precise as some other sites, the purpose of the RF OSL dating protocol is to provide a rapid estimate of age, and at this site, this is achieved by highlighting that sample 154-MGJ-4-4-RF dates from the early-Holocene/late Pleistocene. Similarly, at site 136-6 (figure 7.13), the RF OSL age estimates appear to overestimate age in comparison to the FP OSL ages at this site. At this site, FP D_e determinations were calculated using the finite mixture model (table 6.3), and complexity in the D_e distributions may be indicative of heterogeneous bleaching, and therefore overestimation by the RF OSL ages can be

expected, due to the effects of averaging across a larger aliquot size and using the mean for RF D_e calculation.

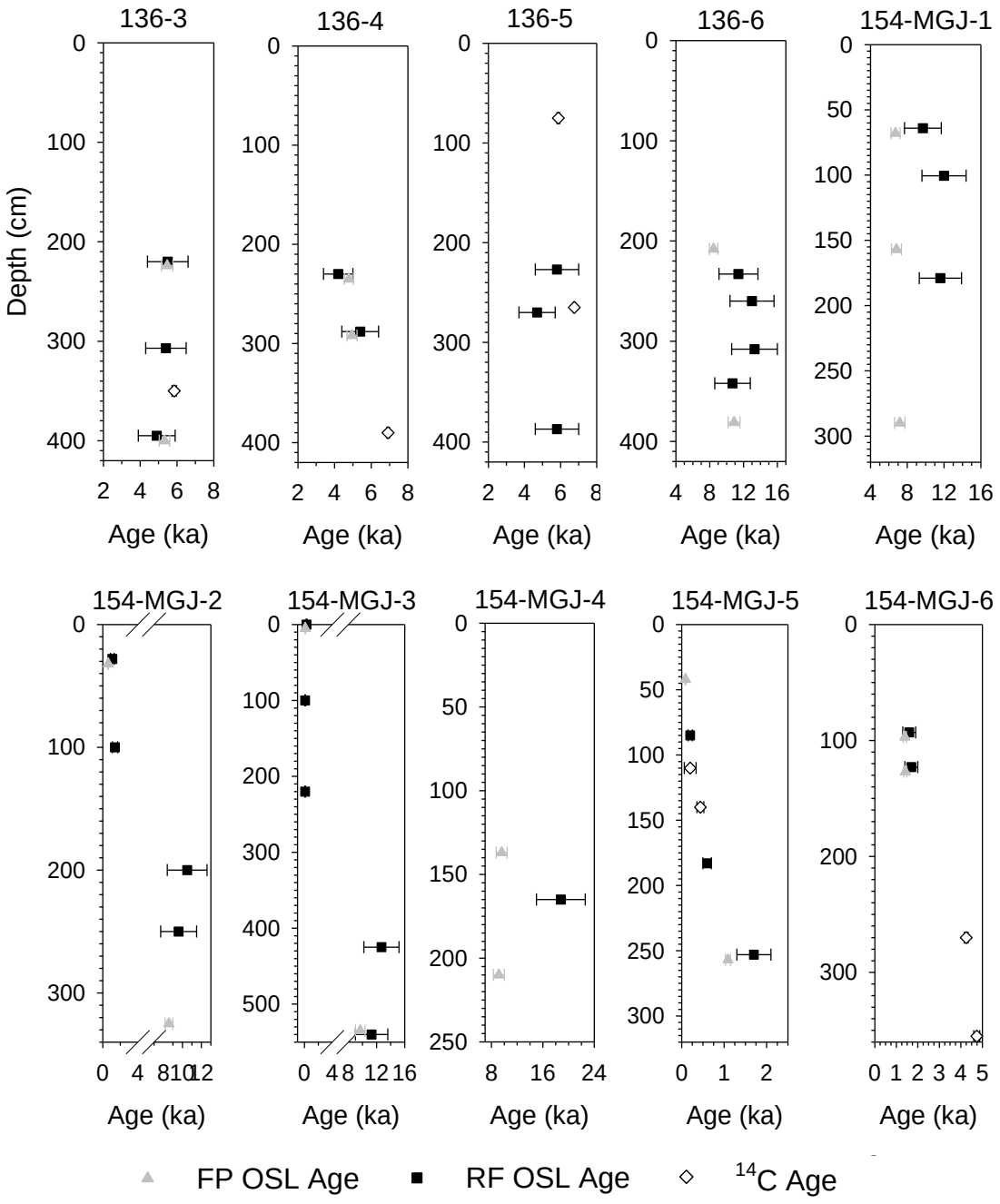

Figure 7.13: Schematic views of the sites where a combination of RF OSL, FP OSL and radiocarbon dating has been used for age determination. Details of the plotted RF and FP OSL ages are listed in tables 7.5 and 6.5 and the ^{14}C dates in table 6.6.

7.7 Conclusions

This chapter has presented the development and testing of the novel range-finder OSL dating protocol first suggested by Roberts et al. (2009). The study of Roberts et al. (2009) was based only aeolian sediments and this chapter has presented the more extensive testing and application of the RF dating protocol to fluvial samples with more complex depositional histories. This chapter has also systematically tested the protocol of Roberts et al. (2009) using samples that have a FP OSL age. Some of these samples were presented in the paper by Durcan et al. (2010), but this study was limited to three sites with only two ^{14}C dates available as independent age control. The application of the RF OSL dating protocol to samples with complex dose distributions has been considered, as well as the most appropriate number of aliquots that should be used for D_e calculation. The ±30% error advocated by Roberts et al. (2009) has been revised, and an uncertainty of ±20% has been applied to RF OSL age estimates in this study.

At the ten sites in this study where RF OSL dating has been applied, the protocol provides age estimates that are generally in good agreement with FP OSL ages and ^{14}C dating, particularly considering that sample preparation has been radically pared-down and the calculated ages are based on the mean value of 12 medium sized aliquots (subject to two rejection criteria). There is some suggestion of age overestimation at some of the sites considered. At these sites, data collected using the FP OSL dating protocol indicates that incomplete bleaching is present in many of these fluvial samples, and the combination of the larger sized aliquot and calculation of the mean for D_e calculation is likely to be responsible for the age overestimation. It is therefore suggested that the RF OSL dating protocol is not applied to samples in isolation, but to sediment sequences and that the depositional context (and probability of complexity in the dose distribution) is taken into consideration when analysing the subsequent RF OSL age estimates.

Whilst the RF OSL dating protocol has been proven to provide age estimates in good agreement with independent age control, these dates are presented as estimates of

age only. They do not replace the meticulous treatment and analysis required to calculate an FP OSL age. However, they do provide valuable geochronological information and are therefore used to support the palaeoenvironmental interpretations presented in chapter 8 and supplement the FP OSL ages calculated in this study and the radiocarbon ages.

8. Reconstructing fluvial activity in the Punjab: chronology, climate and archaeology

8.1 Introduction

The absolute dating of both fluvial and aeolian deposits along two transects in the Ghaggar-Hakra region has been undertaken using optically stimulated luminescence (OSL) and radiocarbon (^{14}C) dating. In response to the research aims and objectives presented in sections 1.1.1 and 1.6, this chapter presents a chronology of fluvial activity in the Ghaggar-Hakra palaeochannel. This chronology is compared to published proxies of regional climate change to assess whether past changes in the Ghaggar-Hakra palaeochannel correlate with palaeoclimatic variability. The chronology is also compared with documented records of archaeological change (e.g. Mughal, 1997; Gangal et al., 2010; Giosan et al., 2012). Whilst many authors have hypothesised a link between changing fluvial activity in the Ghaggar-Hakra palaeochannel and the collapse of the Mature Harappan, a chronology of geomorphological change for this system in Pakistan has not been published. This study allows for the first time, a comparison between the published settlement dynamics during the Mature and Late Harappan transformation and an assessment of the role of changing fluvial activity and climatic variability in the observed spatial and temporal patterns of archaeological change.

8.2 Developing chronologies of fluvial activity in the Punjab

The majority of work presented in this thesis has been concerned with the development of a robust geochronological framework of past fluvial activity using the OSL signal from quartz, and both fully prepared (FP) OSL and range-finder (RF) OSL ages have been used to develop the chronologies presented in this chapter, with ^{14}C dating utilised where possible. The calculated ages are presented with the aim of developing an understanding of the timing of phases of fluvial activity in both the Ghaggar-Hakra transect (section 2.6) and the Sutlej anabranch transect (section 2.7).

8.2.1 The Ghaggar-Hakra transect

The Ghaggar-Hakra transect (section 2.6) follows the course of the Ghaggar-Hakra palaeochannel in the district of Bahawalpur, Punjab. Ten field sites were selected with the aim of reconstructing past fluvial activity in the channel, and sediments indicative of deposition by fluvial processes were predominantly sampled. The calculated ages at sites along this transect are presented in figure 8.1. In section 2.6, the Ghaggar-Hakra palaeochannel was described in three sections, Fort Abbas to the east, Yazmen in the centre of the transect, and Fort Derawar to the west. The following sections discuss the geochronology at sites in each of these sections, before discussing fluvial activity across the transect as a whole.

8.2.1.1 Fort Abbas

The Fort Abbas area represents the most eastern section of the Ghaggar-Hakra palaeochannel in Pakistan (section 2.6.1), and four sites have been selected for study in this area. Pits at 154-MGJ-1, MGJ-2 and 136-3 were sampled for OSL and ^{14}C dating, and a sample for OSL dating was taken from the upper part of the core drilled at Marot (153-MAR2). All samples for dating were taken from units inferred to have been deposited by fluvial processes, with the aim of developing a chronology of fluvial activity in this part of the channel. Early and mid-Holocene fluvial deposition is observed across the area. At site 154-MGJ-1, the FP OSL ages range between 6.72 ± 0.49 ka and 7.19 ± 0.56 ka (figure 8.1), suggesting the rapid deposition of a series of fine sand and silty units at this site. The lower units of nearby site 154-MGJ-2 also suggest early Holocene fluvial deposition, with the FP OSL age of 8.58 ± 0.40 ka complimented by RF OSL ages that are within errors of this date (figure 8.1). Fluvial deposits from the upper most units at this site are relatively modern, with an FP OSL age of 0.62 ± 0.04 ka indicating a reactivation of fluvial deposition during the medieval period, which may explain the large number of medieval age forts built regionally (e.g. figure 1.3d). The ~2 m of fluvial sands deposited at the Fort Abbas site 136-3 appears to have been deposited within a relatively short period of time during the mid-Holocene, with OSL ages of 5.47 ±

0.31 ka and 5.32 ± 0.28 ka respectively. A slightly older age is recorded in the Marot core, where the fine sand unit has been dated to 6.17 ± 0.32 ka (figure 8.1).

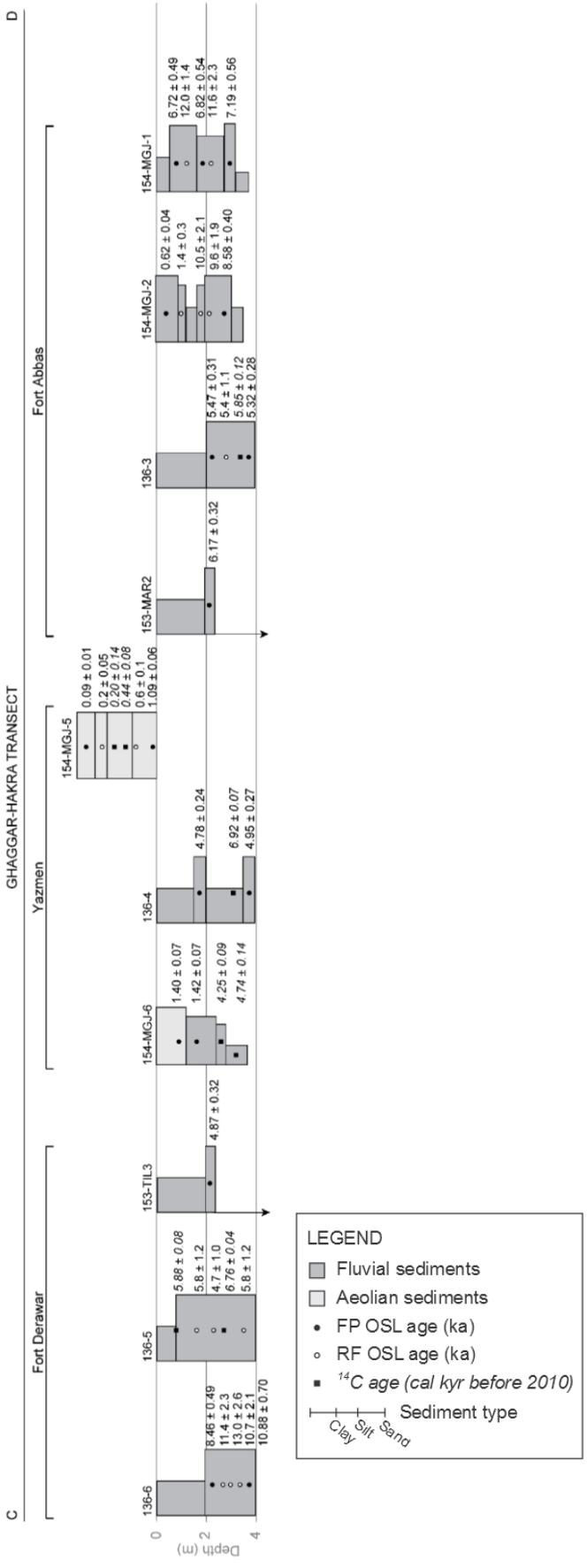

Figure 8.1: Core logs and the geochronology of sites along the Ghaggar-Hakra transect. The position of this transect in relation to the study area can be seen in figures 2.4 and 2.10.

8.2.1.2 Yazmen

The three sites 136-4 (Alkasur Cotton Jinner), 154-MGJ-5 (Yazmen Road) and 154-MGJ-6 (Yazmen Brick Pit) close to the town of Yazmen make up the central section of the Ghaggar Hakra transect (section 2.6.2). At these sites, a combination of fluvial and aeolian sediments were sampled, including the transition between fluvial and aeolian deposition identified at site 154-MGJ-6. The sediments at Alkasur Cotton Jinner are predominantly fine silts (appendix A), however FP OSL ages were calculated from two units of fine sand, and ages of 4.78 ± 0.24 ka and 4.95 ± 0.27 ka, imply mid-Holocene deposition of fluvial sands in this area. The ^{14}C sample taken between these two OSL ages provides an age of 6.92 ± 0.07 cal kyr BP. This sample is similar in age to both the radiocarbon and OSL ages for fluvial deposition at the Fort Derawar sites (section 8.2.1.3), however, because the OSL ages are consistent at this site, it is likely that the gastropod used for ^{14}C dating was reworked, hence the age inversion. Mid-Holocene fluvial deposits have also been dated at site 154-MGJ-6 (figure 8.1), using radiocarbon dating. Two ^{14}C ages of 4.25 ± 0.09 cal kyr BP and 4.74 ± 0.14 cal kyr BP have been calculated from gastropod shells sampled from a silt and a clayey silt unit at the base of the Yazmen brick pit site. The fine nature of sediments is indicative of a low energy system, and the probable terminal end of a phase of fluvial activity. The OSL age of 1.42 ± 0.07 ka from the unit of fluvial sands at this site indicates a later phase of fluvial deposition during the late Holocene, and the OSL age from the base of the overlying aeolian sand of 1.40 ± 0.07 ka places the transition between these depositional states at ~1.4 ka. At site 154-MGJ-5, two phases of aeolian activity are identified using FP and RF OSL dating. At the base of this dune site, aeolian deposition is dated to 1.09 ± 0.06 ka, which may be an extension of the aeolian phase observed at the Yazmen Brick Pit. More recent aeolian deposits overly this unit, with deposition within the past ~0.4 ka (figure 8.1).

8.2.1.3 Fort Derawar

The most western extent of the Ghaggar-Hakra transect sampled is the area around Fort Derawar, where a dense concentration of Mature Harappan settlements are

observed (Mughal, 1997). Sampling in this area focused on three sites, 136-5 (Basti), 136-6 (Fort Derawar) and the core site at Tilwalla (153-TIL3), with fluvial sediments sampled at all three sites. Fluvial deposition at Fort Derawar is dated to the early Holocene, with the fine sand unit at the base of this site deposited between 8.46 ± 0.49 ka (sample 136-6-1) and 10.88 ± 0.70 ka (sample 136-6-7) (figure 8.1). The finer silt unit overlying the dated deposits was not sampled, but the upwards fining in particle size indicates a reduction in flow magnitude during the mid-Holocene, and a later reactivation of fluvial sedimentation is not observed in the sediments at this site. Further to the east at sites 136-5 and 153-TIL3, fluvial sediments were also sampled and dated using a combination of FP OSL, RF OSL and ^{14}C dating (figure 8.1). At these sites, fluvial deposition is dated to the mid-Holocene, with an FP OSL age of 4.87 ± 0.32 ka for sample 153-TIL3-2. At site 136-5, RF OSL ages were calculated and suggest deposition of the ~3 m of fluvial sands between 4.7 ± 1.0 ka and 5.8 ± 1.2 ka (figure 8.1). ^{14}C ages from the top and the base of this unit suggest channel infill between 5.88 ± 0.08 cal kyr BP and 6.76 ± 0.04 cal kyr BP (figure 8.1). The geochronology of these two sites at Basti suggests fluvial activity between approximately 4.7 and 6.7 ka.

8.2.1.4 Fluvial activity in the Ghaggar-Hakra palaeochannel

The fluvial deposits dated along the Ghaggar-Hakra palaeochannel are predominantly early and mid-Holocene in age and are suggestive of strengthened fluvial activity in this palaeochannel during the past. In figure 8.2, the OSL and ^{14}C ages calculated from both aeolian and fluvial sediments are plotted as a function of their position along the palaeochannel, and from this, a number of observations can be made. The earliest evidence of fluvial activity is seen at Fort Derawar, where the deposition of a thick sand unit occurs between 10.88 ± 0.70 ka and 8.46 ± 0.49 ka. However, fluvial deposition is not observed at this site after 8.46 ± 0.49 ka, and recession of flow is inferred. Stein (1942) suggested the presence of an inland delta in the region around Fort Derawar at some time during the past, and the continued accumulation of silts at this site may be suggestive of a floodout system, such as those described in Central Australia by Tooth (1999), where channelised flow

ceases, and unchanneled floodwaters spread out and ultimately dissipate. The dense concentration of Mature Harappan sites in this area implies that during the Harappan phase (~4.5 – 3.9 ka), the area must have been secure enough from catastrophic and/or uncontrollable flooding to allow the construction of permanent settlements and structures. Early Holocene deposition is also observed in Fort Abbas, in sites 154-MGJ-1 and 154-MGJ-2 and it is suggested that during the early part of the Holocene, the Ghaggar-Hakra was a perennial system across the sampled transect area.

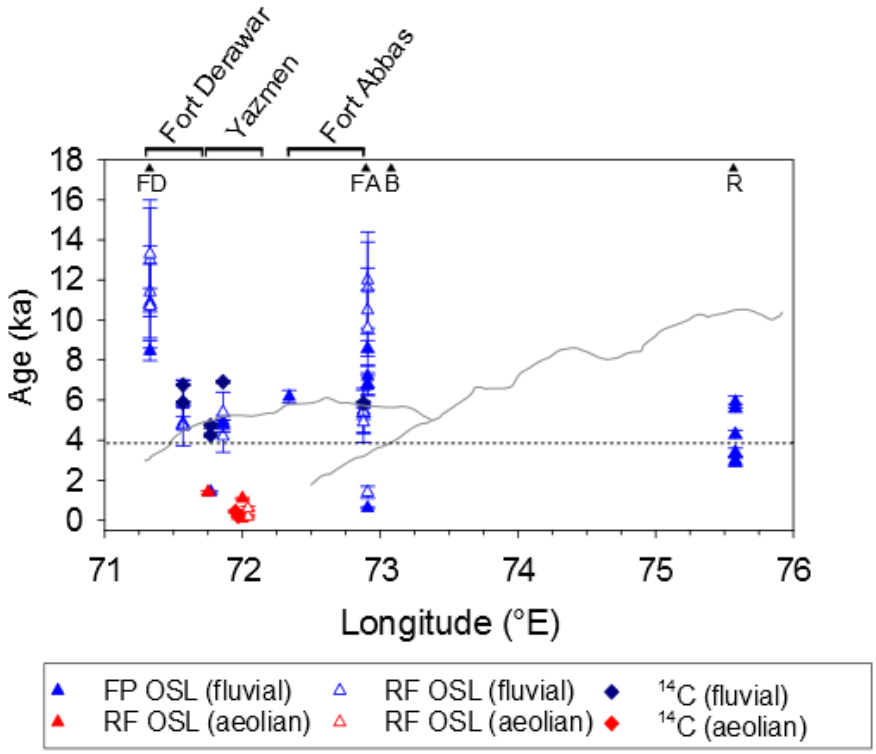

Figure 8.2: Geochronology calculated from samples taken along the Ghaggar-Hakra transect. Samples are plotted according to their position along the palaeochannel and an outline of the channel, mapped from satellite imagery, is overlain. The positions of Fort Derawar (FD), Fort Abbas (FA) and the Pakistan-India border (B) where it transects the palaeochannel are shown, as well as the transect areas discussed in the text. The OSL ages of Saini et al. (2009) taken from the palaeochannel close to the town of Radhakrishna (R) in Haryana, India are also plotted. The collapse of the Mature Harappan at 3.9 ka is shown by the dashed line.

Mid-Holocene deposition between approximately 7 and 5 ka is observed from Fort Abbas (154-MGJ-1 and 154-MGJ-2) to Basti (136-5) and Tilwalla (153-TIL3-2) (e.g. figure 8.2). During this phase, recession of flow upstream from Fort Derawar is observed, and the system was likely to have been perennial during this period, with thick sandy units deposited (e.g. sites 136-5, 136-3) across the transect (figure 8.1).

At some time around 5 ka, a weakening in fluvial activity is inferred. Overlying the fluvial sands at Basti (136-5) and Fort Abbas (154-MGJ-1 and 154-MGJ-2) are silts, suggesting a weakening of fluvial energy, and a reduction in flow at these sites. In the central parts of the Ghaggar-Hakra, relatively shallow units of fluvial sands are deposited at Tilwalla (153-TIL3-2) and Alkasur Cotton Jinner (136-4), with OSL ages of 4.87 ± 0.32 ka (sample 153-TIL3-2), 4.95 ± 0.27 ka (136-4-2) and 4.78 ± 0.24 ka (136-4-1), providing evidence for lower magnitude and possibly intermittent fluvial activity between ~5 and 4.5 ka. At site 154-MGJ-6 at Yazmen Brick Pit, ^{14}C ages of 4.25 ± 0.09 cal kyr BP and 4.74 ± 0.14 cal kyr BP from silt and clay silt units are interpreted as the final phases of fluvial deposition and/or permanent water bodies in the transect and evidence for recession of perennial flow upstream in the Ghaggar-Hakra (figure 8.3).

A hiatus in deposition between 4 ka and 1.5 ka is evident from figure 8.2, although continued fluvial activity is documented further upstream in Haryana by Saini et al., (2009) (e.g. figure 8.2). This hiatus coincides with both the collapse of the Mature Harappan at 1900 BC and the observed migration of Late Harappan sites (e.g. Mughal, 1997; Gangal et al., 2010; Giosan et al., 2012). The lack of fluvial deposition, and presumably reduced amount of regional water availability provides a compelling reason for the collapse of the Mature Harappan. More recently, a reactivation of fluvial activity is observed at Yazmen (site 154-MGJ-6) at ~1.4 ka. Another phase of deposition at site 154-MGJ-2 at Fort Abbas is observed through the deposition of a ~1 m unit of fluvial sands, and this implies a period of strengthened channel flow at ~0.6 ka. As mentioned in section 8.2.1.1, this coincides with a period of medieval fort building in the study area (e.g. Fort Abbas, Fort Marot and Fort Derawar), and more reliable water availability locally may explain the reoccupation of this region.

In figure 8.3, a reconstruction of the early and mid-Holocene fluvial activity in the Ghaggar-Hakra palaeochannel is presented. Further sampling is required to make this geographically accurate, however, this figure summarises the key trends identified in this study. Fluvial activity across the transect area is inferred in the

early Holocene (figure 8.3a), and whilst evidence of the deposition of thick fluvial sand units is observed between ~7 – 5 ka, there is no deposition of sand at Fort Derawar at this time (figure 8.1). Instead, thick units of silt are deposited after 8.5 ka, and the presence of a floodout system is suggested (figure 8.3b). Recession of flow at 4.5 ka is inferred, with a hiatus of deposition in the Pakistan reach of the Ghaggar-Hakra between 4.5 and 1.4 ka. Fluvial deposition between ~5 and 3.5 ka is documented by Saini et al. (2009) in the Haryana Ghaggar-Hakra, which provides further evidence for mid-Holocene recession of flow upstream.

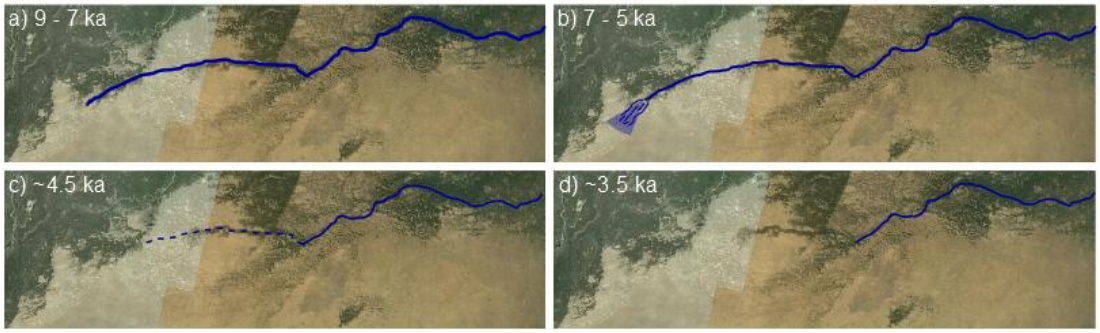

Figure 8.3: Reconstruction of fluvial activity in the Ghaggar-Hakra during the Holocene. Denser solid lines are indicative of inferred greater strength of the fluvial system, with stronger activity suggested during the early Holocene. The proposed floodout is shown in b) and the dashed line in c) indicates the likely terminal phase of fluvial activity. This figure is intended as a schematic view of the overall changes in fluvial activity in the palaeochannel.

8.2.1.5 The Ghaggar-Hakra palaeochannel within the regional fluvial context

In many previous mapping studies of the Ghaggar-Hakra system, the upper tributaries of this system are plotted in the Siwalik Hills, a sub-Himalayan mountain range in India (e.g. Wilhelmy, 1969; Ghose et al., 1979; Kar and Ghose, 1984; Gupta et al., 2004; Bhadra et al., 2009). This implies that at some point during the past, the Ghaggar-Hakra system was glacier-fed, with possible additional sources including the Sutlej River and/or Yamuna River systems (Giosan et al., 2012). Using U-Pb zircon dating, Clift et al. (2012) suggest that whilst the Yamuna River may have contributed to sediments in the region in the past, possibly during the last glacial period, sediments from the Yamuna drainage basin are not found in the Holocene age sediments sampled from the Ghaggar-Hakra palaeochannel. Therefore, capture of waters by the Yamuna River is not the cause of the reduction in fluvial activity in the Ghaggar-Hakra during the Holocene. Using OSL dating, Giosan et al. (2012)

demonstrate that the larger Punjab tributaries (the Chenab, Jhelum, Ravi and Sutlej Rivers) were incisional during the Holocene and the OSL age of 19.74 ± 1.08 ka at the top of the Sutlej overbank site (section 8.2.2.1) indicates that the interfluve that the Ghaggar-Hakra flows upon formed during the last glacial period. Giosan et al. (2012) suggest that the lack of large-scale incision within the Ghaggar-Hakra drainage basin provides evidence that the Ghaggar-Hakra was not a large scale, glacier-fed system during the Holocene.

The nature of the fluvial sediments observed during fieldwork further suggest that the Ghaggar-Hakra was a lower energy system during the Holocene in comparison to the larger Punjab tributaries. The fluvial sediments deposited in the former course of the channel are fine in nature, predominantly fine sands and silts, and in conjunction with the subtle topographic change of the area sampled (figure 2.4), this is indicative of a low gradient, low energy system. The dense concentration of archaeological sites along the palaeochannel is also suggestive of a system less powerful than its Punjab counterparts during the mid-Holocene. Occupation of the floodplain around the channel would have been improbable had this been a powerful system, and Giosan et al. (2012) suggest that settling along the Ghaggar-Hakra palaeochannel is a very good example of an adaptation strategy which took advantage of smaller, monsoon driven floods, which were not augmented by glacial meltwater.

8.2.2 The Sutlej anabranch transect

The Sutlej anabranch transect (section 2.7) consists of samples taken from three sites: the Sutlej overbank section, where the top and base of the cliff section were sampled (samples 155-SUT-2-1 and 155-SUT-3-1) and the two sites by the Lal Suhanrai forest next to the Desert Branch canal. The samples taken from the Sutlej overbank site were taken in order to date the most recent incision of the Ghaggar-Hakra interfluve by the Sutlej River. The two sites by Lal Suhanrai were sampled with the aim of dating fluvial activity in the depression that the Desert Branch canal has been constructed within. This will ascertain whether flow in an anabranch of

the Sutlej contributed to the Ghaggar-Hakra channel during the Holocene, which has been suggested by Stein (1942) and Mughal (1997). The OSL based geochronology for the samples dated at each of these sites is presented in figure 8.4.

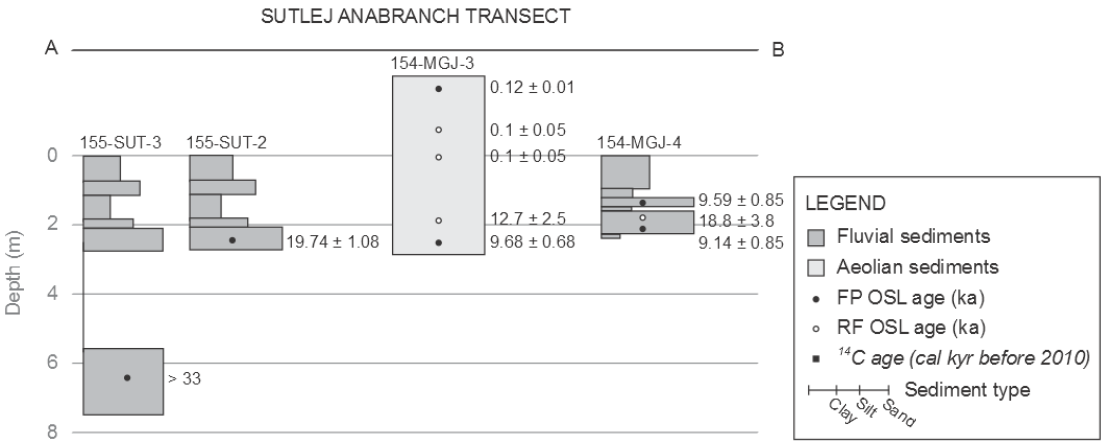

Figure 8.4: Core logs and the geochronology of sites along the Sutlej anabranch transect. The position of this transect in relation to the study area can be seen in figure 2.4 and 2.10.

8.2.2.1 Investigating the presence of a Sutlej anabranch during the Holocene

The OSL age of 19.74 ± 1.08 ka calculated from sample 155-SUT-2-1 constrains the age of the Ghaggar-Hakra interfluve, demonstrating that the last incision of the Sutlej River into the contemporary land surface (near Bahawalpur) occurred during the Last Glacial Maximum (LGM). The chronology at this site is not well constrained because access to the cliff face was limited, and the only other unit that could be sampled was at the base of the overbank section (sample 155-SUT-3-1). The majority of accepted aliquots from this sample were considered to be saturated (section 6.4.4), and a minimum age of 33 ka was calculated. This anabranch has been mapped by researchers since Stein (1942), leading many researchers to hypothesise that fluvial activity in this anabranch supplemented the Ghaggar-Hakra during the Holocene (e.g. Mughal, 1997). The sandy unit that 155-SUT-2-1 was sampled from can be traced along this overbank terrace, and provides evidence that this anabranch of the Sutlej River was not active after ~20 ka.

As discussed, sites 154-MGJ-3 and 154-MGJ-4 at Lal Suhanrai were sampled on either side of the depression which the Desert Branch canal has been constructed

within. The aim when sampling these sites was to identify fluvial deposits which could be dated, allowing phases of fluvial activity in this depression to be determined. Site 154-MGJ-3 was an aeolian dune, sampled from within a dune field on the western edge of the depression. The original aim was to identify the transition between fluvial and aeolian sedimentation, however, discussion with local well diggers revealed that fluvial sands lay approximately 20 m beneath the current land surface. OSL dating at this site indicates two phases of aeolian activity, one at approximately 10 ka, indicated by both FP and RF OSL dating (figure 8.4), and a more recent second phase, within the past 100 years. Phases of aeolian deposition between these time periods has not been recorded at this site.

Site 154-MGJ-4 was sampled from within the Lal Suhunrai Forest on the western edge of the Desert Branch depression. At this site, the majority of units were composed of silts or clays. At the base of the unit, a finely laminated clay was observed, and deposition by pluvial processes is inferred at this site, not only because of the presence of fine sediments, but also the high proportion of carbonate nodules and calcretions observed. The FP OSL ages of 9.59 ± 0.85 ka and 9.14 ± 0.85 ka for the samples 154-MGJ-4-2 and 154-MGJ-4-5 (table 6.5; figure 8.4) suggest the presence of a water body, and pluvial deposition during the early Holocene is inferred. However, these dates coincide with aeolian deposition at the nearby 154-MGJ-3 site, as well as fluvial deposition at Fort Derawar (figure 8.1).

The application of OSL dating along the Sutlej transect has sought to ascertain whether there is evidence of fluvial activity in this depression, and if so, whether this activity can be dated to the Holocene and linked to fluvial activity further south in the Ghaggar-Hakra palaeochannel. Authors such as Stein (1942) and Mughal (1997) have suggested that this anabranch of the Sutlej River was active during the Harappan phase. However, OSL dating at the top of the Sutlej overbank terrace constrain the age of this land surface at the northern most point of the proposed anabranch to 19.74 ± 1.08 ka. At least one phase of dune building occurred within the anabranch depression during the early Holocene, however, there is also evidence for pluvial deposition nearby, and further dating of this depression is

required to further refine this chronology. No evidence of fluvial sedimentation was observed in the area, and there is no evidence to suggest that this anabranch was connected with the Ghaggar-Hakra palaeochannel during the Holocene.

8.3 The Ghaggar-Hakra fluvial chronology within the regional context

The chronology developed for the Ghaggar-Hakra palaeochannel (section 8.2.1.4) suggests fluvial activity during the early to mid-Holocene between ~9 – 5 ka, with a period of decreased flow magnitude and recession around ~4.5 ka. In this section, regional palaeoenvironmental reconstructions are presented to assess whether the geochronology developed in this study is similar to trends observed in other regional palaeoenvironmental studies. Wright et al. (2008) suggest that studies from the Thar Desert are too distant to be representative of the Harappan areas of occupation. However, palaeoenvironmental studies in Pakistan are limited, and MacDonald (2011) argues that because the Thar Desert is within the same major precipitation and monsoonal gradients, palaeoenvironmental records from this area may reflect larger-scale environmental and climatic trends which would have affected the Harappan-occupied areas of Pakistan. In this section, the studies of Saini et al. (2009) and Saini and Mujtaba (2010) are presented, as the only other geochronological studies of Ghaggar-Hakra sediments published to date. Lacustrine-based palaeoenvironmental reconstructions from northwest India and fluvial records from northwest and west India are also compared to the Ghaggar-Hakra chronology to assess whether the fluvial changes reconstructed in the palaeochannel are observed in regional records of environmental change. The location of these sites in relation to the Ghaggar-Hakra palaeochannel are shown in figure 8.5.

Figure 8.5: Map showing the location of key regional palaeohydrological records.

8.3.1 Other dating studies of the Ghaggar-Hakra palaeochannel

Geochronological study of the Ghaggar-Hakra palaeochannel in Pakistan has not been undertaken previously, and Saini et al. (2009) and Saini and Mujtaba (2010) were the first to publish OSL ages from channel sediments from part of the Ghaggar-Hakra in India. Saini et al. (2009) sampled part of the channel identified previously by Yash Pal et al. (1980) and Sahai (1999) in Haryana, India. Two sites were selected and three OSL ages were calculated from each site (figure 8.6). Using these OSL ages, Saini and Mujtaba (2010) suggest that this part of the channel was active between 6 and 4.3 ka, during a period of enhanced precipitation regionally. After 4.3 ka, the sediments fine to sandy silts and silts (figure 8.6), and Saini and Mujtaba (2010) suggest a weakening fluvial system between 4.3 and 3.4 ka, after which, the channel is abandoned, with localised ponding and pluvial deposition occurring in response to periods of enhanced humidity.

More systematic sampling and dating along the Ghaggar-Hakra palaeochannel is required, however the OSL ages of Saini et al. (2009) compliment the idea of

upstream recession of flow suggested in figure 8.3. As is the case in this study, Saini et al. (2009) and Saini and Mujtaba (2010) observe the deposition of fluvial sands at their sites between ~ 6 and 5 ka, after which, the sediments fine, concurrent with a reduction in flow magnitude. Saini and Mujtaba (2010) suggest cessation of flow at some time after 3.4 ka, almost 1 ka after channel abandonment is inferred at the Yazmen Brick Pit site (154-MGJ-6). This again is consistent with the idea of a recession of flow upstream and coincides with the Late Harappan phase of occupation in the area between 3.9 and 3.5 ka.

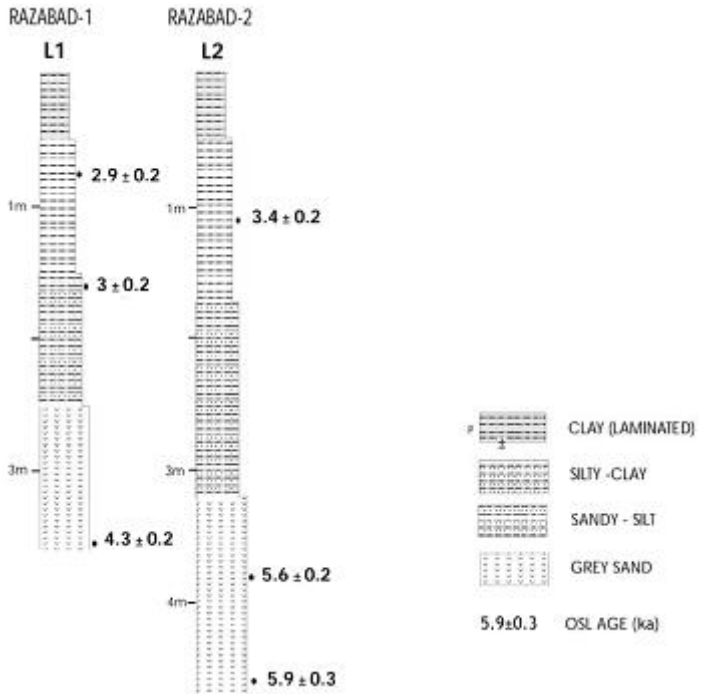

Figure 8.6: Sediment cores and OSL ages from part of the Ghaggar-Hakra palaeochannel in Haryana, India. From Saini et al. (2009).

8.3.2 Lake level reconstruction in northwest India

Gurdip Singh and co-workers were the first to initiate systematic palaeoclimatic research in northwest India (Prasad and Enzel, 2006) and focused on reconstructing palaeoenvironmental conditions based on the palynological records from Lakes Didwana, Lunkaransar and Sambhar in northwest India (e.g. Singh, 1971; Singh et al., 1972; Singh et al., 1973; Singh et al., 1974 and Singh et al., 1990). A number of key sites have provided important records of change since being first studied by Singh and his co-workers, and advances in radiocarbon dating have allowed the

chronologies at these sites to be better constrained (Prasad and Enzel, 2006). Environmental reconstructions have been based upon palynological investigation at Lakes Lunkaransar and Didwana in Rajasthan (Bryson and Swain, 1981) and the sedimentological, mineralogic and geochemical properties of the lake sediments at Didwana (Wasson et al., 1984), Lunkaransar (Enzel et al., 1999) and Nal Sarovar in Gujarat (Prasad et al., 1997).

A summary of reconstructed lake levels and palaeoprecipitation at Lakes Didwana and Lunkaransar, as well as a relative climate at Lake Nal Sarovar is presented by MacDonald (2011) and in figure 8.7, based on data from Bryson and Swain (1981), Wasson et al. (1984), Prasad et al. (1997) and Enzel et al. (1999). At all three sites, conditions during the late Holocene were arid in comparison to the timing of the Mature Harappan phase (4.5 – 3.9 ka) (figure 8.7). However, the timing of the inferred onset of aridity appears to differ between sites. At Lake Didwana, lowering lake levels are observed between ~6 – 4.5 ka, with the disappearance of the freshwater pollen *Typha* (cattail) at 4.5 ka (Singh et al., 1990). At Lake Lunkaransar, Enzel et al. (1999) propose a phase of drying from approximately 5 ka, with a switch from a perennial water body to a playa/episodic lake at ~4.7 ka (figure 8.8), however at Lake Nal Sarovar, environmental deterioration into aridity appears to occur later at ~ 3 ka (Prasad et al., 1997). Whilst these reconstructions may reflect local conditions, higher lake levels and palaeoprecipitation is inferred during the early and mid-Holocene at Lakes Didwana and Lunkaransar. Several other playas/ephemeral lakes have been investigated in northwest India, and sedimentological analysis suggests alternating climatic conditions during the past (e.g. Kajale and Deotare et al., 1997; Deotare et al., 1998; Roy et al., 2006; Roy et al., 2008). However, at present, palaeoenvironmental interpretations at these sites cannot be put into a geochronological framework due to a lack of dating (Prasad and Enzel, 2006).

The environmental record from these lakes is in good agreement with the reconstruction of fluvial activity in the Ghaggar-Hakra palaeochannel. Perennial flow across the Ghaggar-Hakra transect is inferred (figure 8.3a) during the early

Holocene, and relatively high lake levels are suggested at Lake Lunkaransar and Didwana, although the records do suggest alternations between low and high lake levels during the early Holocene (figures 8.6 and 8.7). High lake levels continue until approximately 5 ka, when a trend of drying is observed. The terminal phase of fluvial deposition during the mid-Holocene in the Ghaggar-Hakra transect occurs at ~4.5 ka, and at a similar time, Lake Lunkaransar becomes a playa (figure 8.8). Whilst the proxy record at these playas is likely to incorporate a mixture of local and regional factors, with climate being only one factor in the system, the environmental reconstructions appear to be in good agreement with the suggested model of fluvial activity in the Ghaggar-Hakra during the early and mid-Holocene (figure 8.3).

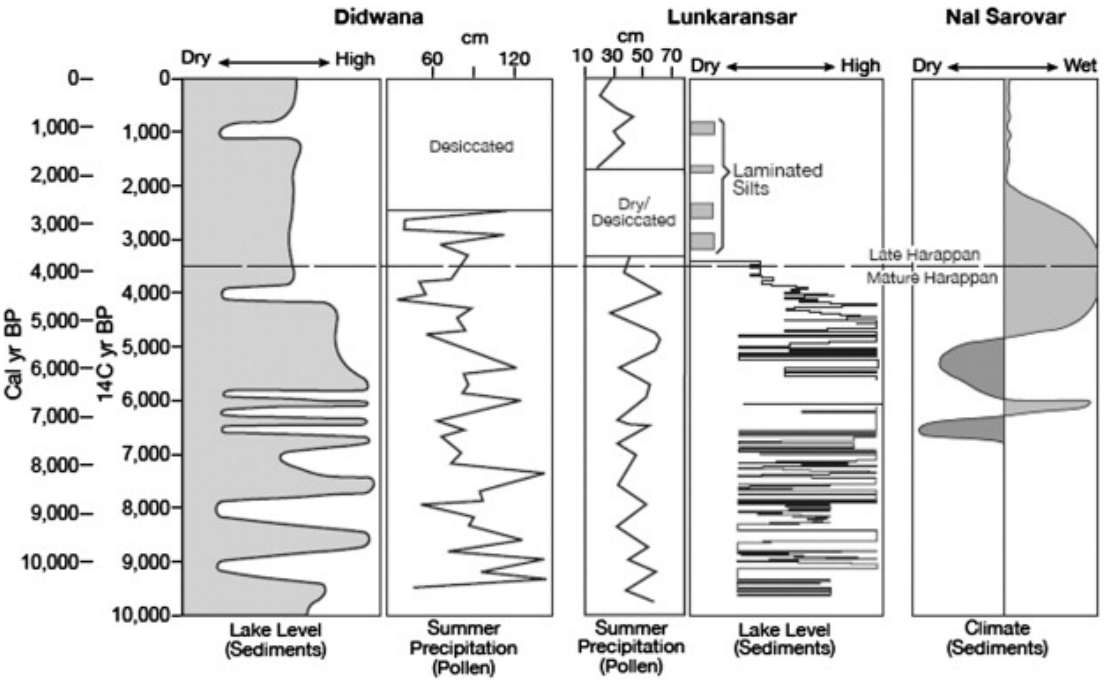

Figure 8.7: Summary of Indian lake level reconstructions from MacDonald (2011). Lake level and pollen based palaeoprecipitation reconstructions at Lake Didwana are from Wasson et al. (1984) and Bryson and Swain (1981) respectively. Lake level and pollen based palaeoprecipitation reconstructions at Lake Lunkaransar are from Enzel et al. (1999) and Bryson and Swain (1981) respectively. A climatic reconstruction based on the analysis of sediments at Lake Nal Sarovar by Prasad et al. (1997) is also shown. The dashed line indicates the collapse of the Mature Harappan at 3.9 ka.

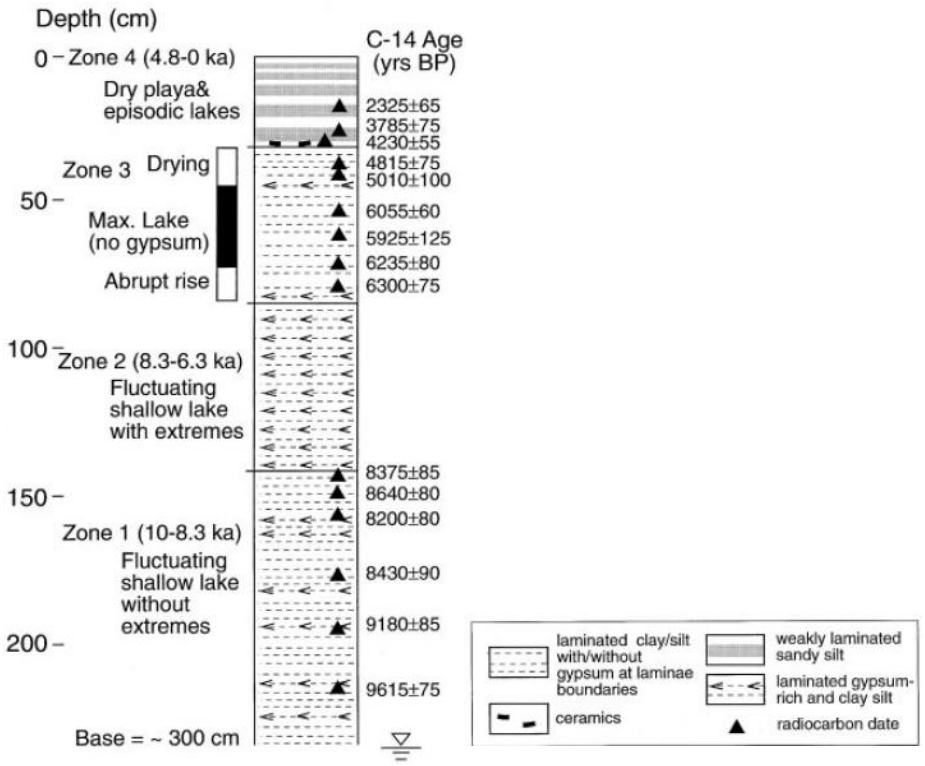

Figure 8.8: Stratigraphic zones at Lake Lunkaransar and uncalibrated ^{14}C ages. From Enzel et al. (1999).

8.3.3 Indian fluvial systems

Palaeohydrological records from the Thar Desert indicate a more humid period during the early Holocene (e.g. Bryson and Swain, 1981; Swain et al., 1983), with peak humidity between ~7.2 and 5.6 ka and desiccation at approximately 5 ka (Singh et al., 1974; Singh et al., 1990; Enzel et al., 1999). Aeolian records indicate enhanced aridity at ~3 ka (Kar et al., 1998; Thomas et al., 1999; Jain et al., 2004b), and this is also suggested by the lacustrine records from Lakes Lunkaransar and Didwana (figure 8.7). However, few Holocene palaeoenvironmental reconstructions based on fluvial records from the Thar Desert have been published. This may be due, in part, to the relative incompleteness of stratigraphic records (Jain et al., 2004b), however fluvial studies in the region tend to focus upon late Pleistocene reconstructions (e.g. Srivastava et al., 2001; Juyal et al., 2006; Juyal et al., 2009; Singhvi et al., 2010b) or concentrate on the late Holocene and historical period (e.g. Thomas et al., 2007; Kunz et al., 2010; Jayangondaperumal et al., 2012).

Holocene activity in the Luni, Sabarmati and Mahi Rivers has been reconstructed in a number of studies. Jain et al. (2004b) applied OSL dating at a number of sites along the ephemeral Luni River in Rajasthan and reconstructed late Pleistocene deposition based on luminescence dating and stratigraphic interpretation. From 12 ka to 5 ka, deposition by fluvial processes is observed generally, with the deposition of sand units, evidence for channel migration and sheets flows documented. Aeolian deposition occurs at approximately 3 ka at three of the four sites studied by Jain et al. (2004b), with no evidence of fluvial activity during this period. More recently, Jain et al. (2004b) see evidence for the reactivation of fluvial processes and incision within the last 1 ka at some sites. Many studies have focused along the perennial Mahi and Sabarmati systems, which flow through Gujarat into the Rann of Khambat (figure 8.5). Incision is observed in this system between 12 ka and 4.5 ka, possibly in response to climatic amelioration (Jain and Tandon, 2003). Tandon et al. (1997) use TL and OSL dating to date aeolian deposits in the Sabarmati River to 5 – 2 ka, inferring a dry phase during this period. These broad trends for relatively stronger fluvial activity during the early Holocene in the semi-arid fluvial systems of the Thar Desert are also seen in the Ghaggar-Hakra palaeochannel.

Thomas et al. (2007) use OSL dating to reconstruct a fluvial record over the past 2.9 ka in the uplands of the Penner River in central India (figure 8.5), a system driven by the Asian Monsoon. Between ~3 – 1 ka, Thomas et al. (2007) suggest a period of weakening in monsoon intensity, on the basis of the low occurrence of flood deposits and sediment aggradations within the palaeochannel sequence dated. They observe an increase in fluvial sedimentation and pedogenesis between 1 – 0.6 ka, which they attribute to an increase in monsoon intensity, coincident with the Medieval Warm Period. After 0.6 ka, aridity is indicated by aeolian sands. Increased fluvial deposition is also seen in the Narmada and Tapi river basins (figure 8.5) between 0.5 - 1 ka (Kale, 1999a) and in the Luni basin between 1 – 0.4 ka (Kale et al., 2000). In the Ghaggar-Hakra palaeochannel, fluvial deposition is observed at 0.6 ka, which coincides with this regional phase of relatively strengthened activity. Recent dune building in the Ghaggar-Hakra area occurs during a time when Thomas et al. (2007) also observe dune building in their central Indian record, and Ely et al.

(1996) and Kale (1999b) see a break in flood frequency from ~0.5 ka to present day in the Narmada, Tapi and Godavari River systems. Whilst it is difficult to link a number of different drainage systems, particularly because the response to external forcing factors can vary depending on size and sedimentary properties (e.g. Jain and Thandon, 2003), the recent aeolian and fluvial phases observed in the Ghaggar-Hakra are also seen in the arid fluvial systems of northwest and central India.

8.3.4 Summary of the Ghaggar-Hakra fluvial chronology within the context of regional terrestrial records

Terrestrial proxies for environmental change in northwest and west India are indicative of a region less arid during the early and mid-Holocene in comparison to contemporary conditions. From the palaeohydrological reconstructions from the playa systems in Rajasthan, high lake levels are inferred between approximately 8 – 5 ka. At this time, fluvial deposition and incision is observed in the Luni River in Rajasthan and the Mahi and Sabarmati Rivers in Gujurat, and this period is one of increased water availability regionally. Fluvial deposition is observed in the Ghaggar-Hakra system throughout the early and mid-Holocene, particularly during the period between 7 – 5 ka. The coincidence of these dates with the Indian terrestrial records suggests that fluvial activity in the Ghaggar-Hakra were driven by regional forcing factors, most likely climate (section 8.4.2) at this time. From 5 ka, falling lake levels and desiccation are observed at Lake Lunkaransar and Lake Didwana (figure 8.7). Fluvial deposition in the upper reaches of the Ghaggar-Hakra continues until 3.4 ka (Saini et al., 2009), but the fining of sediments is indicative of a weakening system, and aeolian deposits dating from ~ 3 ka are found overlying fluvial sediments of the Luni and Sabarmati Rivers. Weakening of fluvial activity in the Ghaggar-Hakra in Pakistan is observed earlier, at around 4.5 ka. This is consistent with a response to the weakening of the Asian Monsoon, which would have occurred along a west to east gradient. Local reactivation of fluvial systems at around 0.6 ka are observed in the Ghaggar-Hakra, Penner and Luni River systems and it is suggested that this was in response to a period of enhanced precipitation regionally. The trends observed in the Ghaggar-Hakra palaeochannel record

compare well with published records of geomorphological and hydrologic changes in northwest India. It is therefore concluded that the Ghaggar-Hakra system during the Holocene was responsive to the same regional stimuli that caused the observed changes in India.

8.4 Comparing the fluvial chronology with regional proxies of climatic variability

One of the research aims of this study is to compare the chronology of fluvial activity in the Ghaggar-Hakra palaeochannel to other proxies of climatic variability to ascertain whether there is a link between fluvial processes in the Ghaggar-Hakra and palaeoclimatic change during the Holocene. In this section, the chronology is considered against proxies of monsoon intensity to make this comparison. The Asian Monsoon is the dominant control on the contemporary climate of the Indian sub-continent (e.g. Singhvi and Kale, 2009), and is likely to have been a primary factor controlling the palaeoclimate of the region. As discussed in section 2.3.3, in response to orbital forcing, the Asian Monsoon weakened during the Holocene from a peak intensity at around 9 ka (section 2.3.2), followed by a gradual decline in intensity. The '4.2 ka' event is a prominent North Atlantic climatic event which coincides with the collapse of other Bronze Age civilisations in the near and far east. Whilst chronological control in this study, both in terms of the fluvial chronology and the uncertainties associated with the archaeological chronologies, is not sufficient to directly correlate the collapse of the Harappan with the 4.2 ka event, proxy records are considered and an assessment of how this event may have affected the Harappan is discussed in this section.

8.4.1 Monsoon intensity during the Last Glacial Maximum

OSL dating of the Sutlej overbank site dates the last major incision of the Sutlej near Bahawalpur to 19.74 ± 1.08 ka (section 8.2.2.1), implying a period of at least locally strengthened fluvial activity and incision of the Ghaggar-Hakra interfluve. There are many factors which may contribute to strengthened fluvial activity, including tectonic activity and drainage capture, increases in glacier meltwater and climate.

The hydrology of the Punjab tributaries of the Indus River is highly influenced by the Asian Monsoon, with up to 80% of precipitation regionally delivered by the monsoon system (e.g. Rao, 1976), and variability in the intensity of the monsoon is likely to impact upon regional fluvial systems. Reconstructions of monsoon activity during the Pleistocene are not plentiful, although a number of high resolution proxies for the monsoon from China are available. From the Jintanwan Cave, in Central China, Cosford et al. (2009) have reconstructed the East Asian Monsoon during MIS 2 based on the $\delta^{18}O$ record from a stalagmite. The LGM occurred between 23 and 19 ka in the Northern Hemisphere at a time when insolation was at a minimum (Berger, 1978) and the Jintanwan record indicates a weakened Asian Monsoon in the early part of the LGM (~23 – 20 ka) and an intensification from ~20 ka onwards, with peak intensity between 19.2 and 17.4 ka (Cosford et al., 2009). This interpretation is consistent with Chinese stalagmite records (e.g. the Hulu cave; Wu et al., 2009), a period of warmer northern hemispheric temperatures (Koutavas et al., 2002) and a decrease in global ice volume (Yokoyama et al., 2000).

Terrestrial records of monsoon intensity from the Indian subcontinent are limited, fragmentary and suffer from poor geochronological control (Juyal et al., 2009), and the records that are available also indicate variability in monsoon strength during the LGM. From lake deposits taken from Lake Sambhar in Rajasthan, Sinha et al. (2006) suggest an arid phase between 24 and 20 ka, inferred from the $\delta^{18}O$ and MgO/CaO ratio of lake sediments. Hypersaline conditions are indicated from pollen records nearby at Lake Didwana by Wasson et al. (1984) and Singh et al. (1990) during the LGM. Prevalent shallow lake conditions between 20 and 16 ka are interpreted by Sinha et al. (2006) as evidence for a gradual strengthening of the monsoon (as modelled by Prell and Kutzbach (1987)). Palynological analysis at Wadda Lake in northern India also indicates a shift from a more arid LGM period to more humid conditions from between 21.7 and 18.2 kyr BP (Kotlia et al., 2000).

Whilst proxies for the intensity of the Asian Monsoon suggest variable climatic conditions during the LGM, the general trend appears to be enhanced aridity between ~ 23 – 20 ka, and an increase in monsoon intensity from 20 ka onwards.

The incision of the Sutlej River into the Ghaggar-Hakra interfluve at the top of the anabranch transect coincides with this period of regional precipitation and therefore, it is likely that fluvial activity at this time was driven by intensification of the Asian Monsoon system at the end of the LGM.

8.4.2 Monsoon variability during the Holocene

Variation of the monsoon over the Holocene is of most relevance to this study to allow a comparison between monsoon intensity and the Ghaggar-Hakra fluvial chronology. In figure 8.9a, the modelled change in northern hemisphere insolation of Berger and Loutre (1991) is plotted. Also shown is the Qunf Cave (Fleitmann et al., 2007) and Dongge Cave (Wang et al., 2005) speleothem records (figures 8.8c-d), both of which are proxies for monsoon intensity (e.g. Giosan et al., 2012). Both records show a trend of decreasing intensity of the monsoon throughout the Holocene, in response to the decline in insolation (figure 8.9a). The Asian Monsoon is the dominant control of the regional climate of the Indian sub-continent and as discussed in sections 8.3.2 and 8.3.3, the early and mid-Holocene, when the monsoon is most intense (Sirocko et al., 1993), is a period of greater fluvial activity and higher lake levels in northwest India. When comparing the fluvial chronology of the Ghaggar-Hakra (figure 8.9e) with the Qunf and Dongge Cave records, fluvial dynamics in the Ghaggar-Hakra do appear to be responsive to periods of strengthened monsoon. Peak monsoon intensity in both records occurs during the early-Holocene, coincident with the deposition of fluvial sand units in the Ghaggar-Hakra transect.

Staubwasser et al. (2003) analysed the $\delta^{18}O$ of planktonic foraminfera from a core taken in the Indus Delta. This record is used as a proxy for oceanic salinity change and therefore of output of the Indus River during the Holocene. This record suggests that Indus output during the early to mid-Holocene was relatively consistent, although the Indus River and its major tributaries are fed by both monsoon precipitation and glacier meltwaters. However, after 4.5 ka, Indus output becomes highly variable (figure 8.9b), which Staubwasser et al. (2003) suggest is

indicative of a rapid weakening of monsoon driven precipitation. Large fluctuations in the $\delta^{18}O$ records from the Dongge Cave (figure 8.9d) are also seen during this period, indicating a period where large scale fluctuations in monsoon intensity were set against a backdrop of a general trend for weakening of the monsoon system. In the Ghaggar-Hakra chronology, weakened fluvial activity, consistent with drying and flow recession upstream, is recorded at 4.5 ka, and after this date, there is a hiatus in fluvial deposition until 1.4 ka.

The trends of fluvial activity dated in the Ghaggar-Hakra palaeochannel are consistent with other terrestrial records of palaeohydrological change (section 8.3), which are set against a backdrop of weakening of the Asian Monsoon system (e.g. figure 8.9c-d). The majority of dated fluvial activity occurs during a period of strengthened monsoon activity and because the Ghaggar-Hakra was not a glacier-fed system during the Holocene (Giosan et al., 2012; section 8.2.1.5), this system would have been highly responsive to changes in the availability of monsoon precipitation.

8.4.3 The 4.2 ka event

The 4.2 ka event is a globally observed climatic event (Staubwasser and Weiss, 2006), which coincides with Bond event 3 at 4.2 ka (e.g. Bond et al., 1997). The exact nature of the teleconnection between Asian climatic variability and North Atlantic ice rafted debris events has yet to be determined. Whilst there appears to be a response of the East Asian Monsoon to Bond events (Wang et al., 2005), a response is not observed in the Qunf Cave record of the South West Asian Monsoon (Staubwasser and Weiss, 2006). Terrestrial records from the Mediterranean and low-latitude Asia show a period of enhanced aridity centred around 4.2 ka, and this is coincident with the collapse of some of the largest Bronze Age civilisations, including the Akkadians, the Chinese Neolithic and the Egyptians (section 1.2), leading many Quaternary Scientists to hypothesise a link between climate and collapse (Madella and Fuller, 2006).

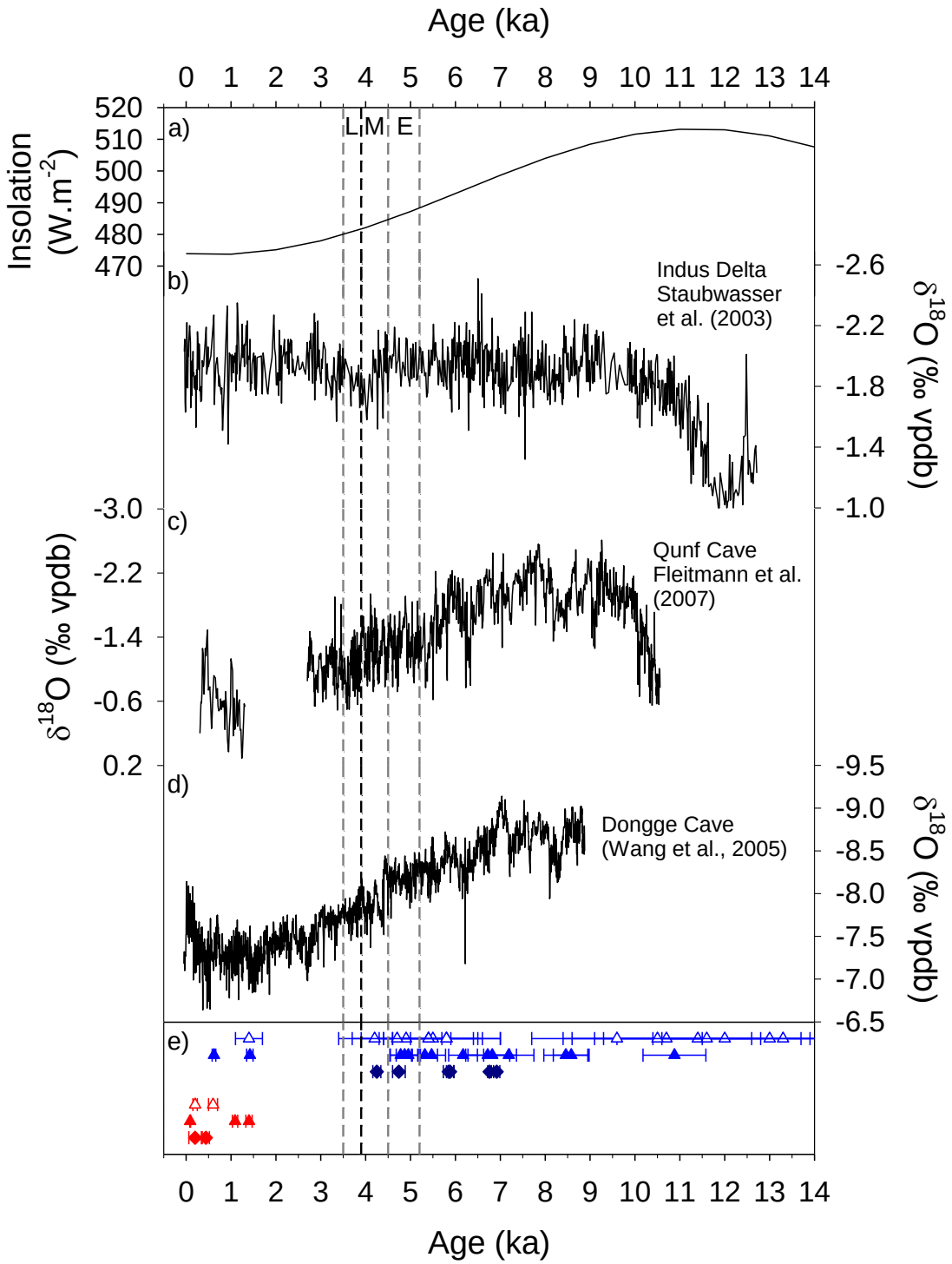

Figure 8.9: Reconstructions of insolation, proxies of Asian Monsoon intensity and the Ghaggar-Hakra chronology developed in this study. a) Insolation values for 30°N from Berger and Loutre (1991). b) $\delta^{18}O$ of *Globigerinoides ruber* foraminifera from the Indus Delta (Staubwasser et al., 2003). c) Qunf cave $\delta^{18}O$ speleothem record (Fleitmann et al., 2007). d) Dongge cave $\delta^{18}O$ speleothem record (Wang et al., 2005). e) Ghaggar-Hakra chronology developed in this study (see figure 8.2 for legend). The Early (E), Mature (M) and Late (L) Harappan phases are indicated by the dashed lines, with the timing of the collapse of the Mature Harappan indicated by the black dashed line.

Palaeoenvironmental proxies from the region indicate a period of reduced precipitation and drought. Measuring the mass of dolomite in a sediment core from

the Gulf of Oman, Cullen et al. (2000) observe a dramatic increase in the amount of aeolian material at 4.2 ka and suggest that this indicates a period of strengthened aeolian activity. Staubwasser et al. (2003) see a increase in salinity at ~4.2 ka, which they interpret as evidence for lowered Indus output and a period of enhanced aridity in Pakistan (section 8.4.2). Analysing the palynology of an alpine peat in the Central Himalaya, Phadtare (2000) infers a cooler, more arid environment from ~4 ka. Within the wider region, there are many environmental studies where enhanced aridity has been inferred at ~ 4.2 ka, including the speleothem record at Soreq Cave, Israel (Bar-Matthews et al. (1997), lowered lake levels in Turkey (Lemcke and Sturm, 1997) and the onset of arid pedogenesis in the Caucasus (Alexandrovskiy et al., 2001). Prasad and Enzel (2006) comment that given the chronological uncertainties associated with the majority of regional proxy records, it is not possible to correlate Indian archives with short-term events. However, there is a clear indication that, within chronological uncertainties, the Asian subcontinent experienced enhanced aridity around the time of 4.2 ka, and during this period, there is no fluvial deposition recorded at any sites taken along the Ghaggar-Hakra transect. Within chronological uncertainties, this period of intense aridity coincides with a phase of inferred drying of the palaeochannel and recession of the channel upstream.

8.5 Changing fluvial activity and implications for the collapse of the Mature Harappan

The systematic sampling and dating of fluvial sediments from the Ghaggar-Hakra palaeochannel has allowed a chronology of fluvial activity to be developed and this activity appears to have varied in response to the intensity of the Asian Monsoon. Fluvial deposition coincides with the Holocene peak in the intensity of the monsoon system, which progressively weakens in response to changes in orbitally forced insolation. The role of hydrological and climate change more generally has been suggested by many researchers as a key factor in the collapse of the Mature Harappan at 1900 BC (e.g. Singh, 1971; Singh et al., 1974; Mughal, 1997; Enzel et al., 1999; Prasad and Enzel, 2006; Staubwasser and Weiss, 2006; MacDonald, 2011). The chronology developed in this study has been calculated on the basis of a highly

focused study of the Ghaggar-Hakra palaeochannel, and therefore allows the comparison of palaeohydrological changes in this channel, which appear to be driven by Asian Monsoon intensity, with documented records of archaeological change. In this section, the hydrological changes are considered in the context of the archaeological changes, and the role of climate change in the collapse of the Harappan is discussed.

8.5.1 Harappan settlement dynamics and fluvial activity

Climatic deterioration during the mid-Holocene appears to have facilitated the flourishing of the Mature Harappan, with aridity driving the need for social complexity and urbanisation (Giosan et al., 2012). Unlike the Akkadian Empire, where civilisation collapse coincides with climate deterioration at 4.2 ka (Weiss et al., 1993; Cullen et al., 2000), the aridification of the Punjab region appears to have facilitated the use of the fertile floodplains of the Ghaggar-Hakra palaeochannel, and allowed the development of inundation agriculture (Giosan et al., 2012). The timing of the Mature Harappan phase between 4.5 and 3.9 ka coincides with an inferred period of reduction in flow magnitude and recession in the Ghaggar-Hakra palaeochannel (section 8.2.1.4), and it is suggested that at this time, the Mature Harappan were utilising a system where flooding was regular and controllable. The Mature Harappan occupied the Ghaggar-Hakra area at a time when OSL dating indicates a reduction in fluvial activity, recession in flow upstream and a possible switch to ephemeral activity. The Mature Harappan utilised this area until ~3.9 ka, when further aridification appears to have become detrimental. After 3.9 ka, the Late Harappan migrate upstream, presumably in search of more reliable waters to maintain agriculture.

It is suggested that climate played an important role in the collapse of the Mature Harappan along the Ghaggar-Hakra palaeochannel. The flourishing of the Mature Harappan in this region occurred within a narrow window of opportunity, where floods along the Ghaggar-Hakra system were reliable and controllable. However, climatic deterioriation, driven by the weakening of the Asian Monsoon, would have

led to the eventual aridification of this area. This appears to have occurred at ~3.9 ka, where migration upstream towards the upper parts of the Ghaggar-Hakra drainage basin, which would have received more reliable monsoon rains is observed. Weber (2003) suggests that a change in agriculture occurred between the Mature and Late Harappan, with the Late Harappan favouring drought resistant crops, such as millet. These behaviours are suggestive of coping mechanisms to deal with hydroclimatic stresses, and provides further evidence for the regional aridification of the Punjab at the time of the Mature Harappan collapse.

8.5.2 Climate change as a hypothesis for the collapse of the Mature Harappan

The collapse of the Mature Harappan did not occur instantaneously, temporally or spatially, and therefore, suggesting climate change as the reason for the collapse of the entire Mature Harappan would be an oversimplified explanation of a complex process which occurred over a prolonged period. Unlike the Akkadian empire (see Weiss et al., 1993; Cullen et al., 2000), the Mature Harappan do not appear to have been affected by the 4.2 ka event, and instead, the beginning of this period of aridity coincides with the flourishing of the Mature Harappan and peak social complexity. Giosan et al. (2012) comment that adaptation to increasing aridity during the mid-Holocene most likely drove social complexity and urbanism, and that during this period, increasingly arid conditions may have allowed inundation agriculture to expand along the Indus and its tributaries, including the Ghaggar-Hakra palaeochannel. However, the continuing aridification of the region, in response to the weakening of the Asian Monsoon system would have made floodwater farming difficult as water availability became increasingly less reliable.

The purpose of this thesis has been to undertake a focused study of one palaeochannel where marked archaeological change has been documented. Clearly, for the Mature Harappan inhabitants of this area, hydrological change driven by climatic variability was a key factor in the occupation and abandonment of the area around the Ghaggar-Hakra palaeochannel. As an area considered to have been the ‘bread-basket’ of the Mature Harappan, industrial and agricultural activity in this

area would have been reliant on consistent and controllable water availability. The changes in the fluvial activity in the Ghaggar-Hakra, driven by the weakening of the Asian Monsoon would have had a negative impact on Mature Harappan occupants of this area. Therefore, it is suggested that for this part of the Mature Harappan civilisation, hydrological change, forced by climatic variability led to the transformation of the Mature Harappan in this part of the Punjab. Further detailed study of the relationship of the rest of the Mature Harappan civilisation with this area, and the sensitivity of the Mature Harappan to hydrological change more generally needs to be undertaken to assess the role of climate change in the collapse of the Mature Harappan as a whole.

8.6 Conclusions

A chronology of fluvial activity for the Ghaggar-Hakra palaeochannel has been presented in this chapter, based predominantly on the optically stimulated luminescence dating of fluvial and aeolian sands. Fluvial deposition is inferred across the whole study transect from Fort Abbas in the east to Fort Derawar in the west during the early Holocene, at ~9 ka. The majority of fluvial deposition in the Ghaggar-Hakra occurs in the early and mid-Holocene, with a peak period of deposition between ~7 – 5 ka. However, deposition at the westerly extent of the transect is not observed after ~8.5 ka, and it is suggested that fluvial activity started to diminish around this time, resulting in the presence of an inland delta or floodout system at Fort Derawar. Thick units of fluvial sands are deposited up to around 5 ka, and these units are typically overlain with finer units of silts, indicative of a reduction in the magnitude of flow. It is therefore suggested that fluvial activity continued to weaken after 5 ka, with flow receeding from the central area of the study (at Yazmen Brick Pit) at ~4.5 ka. There is no evidence for fluvial deposition after 4.5 ka until 1.4 ka, and this hiatus in fluvial deposition coincides with the collapse of the Mature Harappan at 3.9 ka (1900 BC).

Fluvial activity in the Ghaggar-Hakra appears to have been driven by the intensity of the Asian Monsoon. The lack of large scale incision by this system suggests that the

Ghaggar-Hakra was not fed by glacial meltwaters during the Holocene, leaving monsoon precipitation as the dominant hydrologic control on the channel. The chronology of fluvial activity observed is similar to palaeohydrological patterns observed in terrestrial records from India, and this implies a regional response of fluvial activity to the Asian Monsoon. The response of the Mature Harappan civilisation to mid-Holocene regional aridification is not a simple one. Initially social development and complexity was driven by increasing aridity, and the weakening of the Ghaggar-Hakra fluvial system allowed this area to be used for inundation agriculture. However, continued aridity in response to the weakening of the Asian Monsoon resulted in the recession of flow upstream. The response of the Late Harappan to this was to migrate upstream to areas with more reliable water availability. In this area at least, changing fluvial activity driven by climate change did impact the Mature Harappan civilisation, and is likely to have driven the transformation of this civilisation to a less complex social state.

9. Conclusions

This body of work represents the first application of optically stimulated luminescence dating in the lowlands of Pakistan, and more specifically, the first geochronological study of the Pakistani section of the Ghaggar-Hakra palaeochannel. This palaeochannel has been the subject of research for over a century, and the role of changing fluvial activity in this channel has been hypothesised to have been a critical factor in the collapse of the Mature Harappan civilisation at ~3.9 ka. However, without a chronology for fluvial activity, a comparison between changing fluvial activity and the documented archaeological change has never been made. This thesis has sought to address this research problem, and use OSL dating as the basis for developing a fluvial chronology to allow this comparison.

9.1 Luminescence dating conclusions

The chronology of fluvial activity in the Ghaggar-Hakra palaeochannel developed in this study is predominantly based upon the OSL dating of quartz. The calculation of each OSL age requires the measurement of two parameters, the environmental dose rate and the equivalent dose (D_e). In this study, radionuclide concentrations derived from thick source alpha and beta counting have been used as the basis of environmental dose rate calculation. The calculated dose rates are relatively high, with a mean dose rate for the dataset of 3.3 ± 0.5 $Gy.ka^{-1}$, but are comparable with those calculated in other regional studies (e.g. Saini et al., 2009). For equivalent dose determination, the single aliquot regenerative dose (SAR) protocol of Murray and Wintle (2000) has been shown to be appropriate and this measurement protocol has been applied in this study.

A new criterion has been designed and developed to assess the extent to which OSL signals are dominated by the fast component of quartz. The fast ratio of Durcan and Duller (2011) has been shown to identify CW-OSL signals which are dominated by the fast component in the initial part of the signal, and has been applied as a

rejection criterion in this study to ensure that only fast-dominated OSL signals are used for D_e determination. The application of the fast ratio to dose distributions in this study suggests that some OSL signals which pass all other standard rejection criteria are not dominated by the fast component and these signals may not be suitable for measurement using the SAR protocol. The application of the fast ratio to D_e distributions has been shown to reduce complexity and for older samples, alters the calculated D_e by up to 7%. This demonstrates the importance of testing OSL signals for the dominance of the fast component using a criterion such as the fast ratio, particularly because signals containing a contribution from unstable quartz OSL components may result in D_e underestimation.

Single grain measurements have shown that approximately 2% of quartz grains provide a measurable OSL signal, and it is estimated that between 4 and 10 quartz grains provide the luminescence signal from the small aliquots of sample used for dating. The single grain measurements also highlighted significant contamination by feldspar, and the OSL IR depletion ratio of Duller (2003) has been routinely applied to each measured aliquot to ensure that only quartz OSL luminescence signals are used for D_e determination. The large number of aliquots which fail to satisfy the OSL IR depletion ratio indicates that despite thorough laboratory preparation, feldspar contamination is prevalent in this suite of samples. Future OSL dating of samples from this region should take these contamination issues into account.

Multiple individual D_e determinations were made for each sample using the SAR protocol, requiring the use of statistical analysis to calculate a D_e value for each sample. Age model selection was made according to the protocol of Rodnight et al. (2006), where either the central age model or finite mixture model was applied, depending on the level of overdispersion of each dose distribution. The overdispersion (σ_d) threshold of Rodnight et al. (2006) was revised slightly, and the CAM D_e was used for distributions with an overdispersion of less than 20%, and the FMM D_e (from the lowest component containing more than 10% of signals) for samples with an σ_d greater than 20%. The majority of samples had σ_d values in excess of 20%, implying that incomplete bleaching was a factor for the suite of

samples measured in this study, and the finite mixture model was almost exclusively applied. Rodnight et al.'s (2006) protocol was selected because it had been developed and tested using fluvial samples, however, many different strategies for dealing with complex dose distributions have been published in the luminescence dating literature. The assessment of incomplete bleaching and the application of statistical models to dose distributions is not straightforward, and further work to develop methods for quantifying the extent of incomplete bleaching and selecting the most appropriate age model may need to be undertaken on a community-wide level.

The OSL ages calculated in this study are predominantly Holocene in age, and taking into account intrinsic and extrinsic sources of uncertainty, have a mean uncertainty of approximately 6.5%. These OSL ages are generally in good stratigraphic agreement and compare well with ^{14}C ages, where available. This suggests that the age model choice for D_e determination was appropriate and it is concluded that the OSL dating protocols applied in this study provide accurate OSL ages and a robust geochronological framework.

The range-finder (RF) OSL dating protocol first presented by Roberts et al. (2009) has been further tested and developed in this study, using fluvial sediments bleached to a varying degree. The measurement of around twelve medium sized aliquots and taking the mean value of these D_e values was found to provide an acceptable estimate of the equivalent dose. Comparison of RF and FP OSL ages for a suite of samples resulted in a revised uncertainty of 20% being applied to range-finder OSL age estimates. Whilst range-finder OSL ages remain estimates of age only, and do not replace the thorough treatment and analysis required to calculate a fully prepared OSL age, RF OSL ages provide valuable geochronological information and are used as part of the geochronological framework presented.

9.2 Palaeoenvironmental conclusions and interpretations

The OSL-based chronology for fluvial activity developed in this study indicates perennial fluvial activity across the whole Ghaggar-Hakra transect during the early Holocene, prior to 8.5 ka. Fluvial activity continues between 7 and 5 ka, however, there is no evidence for fluvial deposition at Fort Derawar, at the western extent of the channel, later than 8.5 ka, suggesting that flow in the Ghaggar-Hakra started to recede from Fort Derawar during the early Holocene. Small fluvial deposits are observed in the central section of the Ghaggar-Hakra transect and have been dated to between 5 and 4.5 ka. This implies a weakening of fluvial processes in the area around Yazmen during the mid-Holocene, and the deposition of silts and clays dated to ~4.5 ka at Yazmen is interpreted as the final phase of mid-Holocene fluvial activity in this part of the channel and indicates continued recession of flow upstream. The OSL dating of Ghaggar-Hakra sediments in Haryana by Saini et al. (2009) shows fluvial deposition in the upper part of this system until 3.4 ka, and this provides further evidence for upstream flow recession. A hiatus in fluvial deposition between 4.5 and 1.4 ka suggests that between this period, fluvial activity was either absent or limited to low frequency and/or low magnitude events.

Comparison of the fluvial chronology with Indian palaeohydrological records, including lacustrine and fluvial systems, suggests that Holocene fluvial activity in the Ghaggar-Hakra system was responsive to regional stimuli. Indian palaeoenvironmental records show increased hydrological activity during the early to mid-Holocene and regionally, a period of aridification is observed from around 4.5 ka. The contemporary climate of Pakistan and India is dominated by the Asian Monsoon, and the palaeoenvironment of the Indian sub-continent is likely to have been influenced greatly by the monsoon. Peak monsoon intensity is observed at around 8.5 ka (e.g. Wang et al., 2005; Fleitmann et al., 2003, 2007), and weakens throughout the mid-Holocene in response to orbitally driven changes in insolation. From the comparability of the Ghaggar-Hakra chronology and the Indian terrestrial records, it is concluded that the Asian Monsoon was a major factor driving palaeoclimatic change in Pakistan and India during the late Quaternary, and fluvial

changes in the Ghaggar-Hakra palaeochannel are attributed to the insolation-driven weakening of the Asian Monsoon during the Holocene.

9.2.1 Implications for the collapse of the Mature Harappan

The flourishing of the Mature Harappan between 4.5 and 3.9 ka occurred during a period of intense aridification, with aridity appearing to drive the need for social complexity, urbanisation and development. The timing of this phase coincides with an inferred period of flow recession in the Ghaggar-Hakra palaeochannel after 4.5 ka, and it is suggested that during the Mature Harappan phase, flooding in the Ghaggar-Hakra system became regular and controllable and was utilised for inundation agriculture. As aridity intensified, this became detrimental to the Harappan and collapse and transformation to the Late Harappan occurs at ~3.9 ka. Late Harappan sites are concentrated further upstream, around the upper reaches of the Ghaggar-Hakra palaeochannel in India, and the Late Harappan favour drought resistant crops, suggesting that the Late Harappan were responding to lower water availability and more intense aridity. It is therefore concluded that monsoon-driven changes in fluvial activity in the Ghaggar-Hakra were a significant factor driving the collapse of the Mature Harappan in this area.

References

Adamiec, G. and Aitken, M.J., 1998. Dose rate conversion factors: update. Ancient TL, 16, 37-50.

Agersnap Larsen, N., Bulur, E., Bøtter-Jensen, L., and McKeever, S.W.S., 2000. Use of the LM-OSL technique for the detection of partial bleaching in quartz and feldspar. Radiation Measurements, 32, 419-425.

Agrawal, D.P., 1964. Harappa culture: new evidence for a shorter chronology. Science, 143, 950-952.

Agrawal, D.P., 2007. The Indus civilization: an interdisciplinary approach. Aryan Books International, New Delhi.

Agrawal, D.P. and Sood, R.K., 1982. Ecological factors and the Harappan Civilization. In: Possehl, G.L. (ed.). Harappan Civilization: a contemporary perspective. Oxford University Press, Oxford. Pp 223-231.

Ahmad, F., 2008. Runoff farming in reducing rural poverty in Cholistan Desert. Sociedade y Natureza, 20, 177-188.

Aitken, M.J., 1985. Thermoluminescence Dating. Academic Press, London.

Aitken, M.J., 1990. Science-based dating in archaeology. Longman, Essex.

Aitken, M.J., 1998. An introduction to optical dating: the dating of Quaternary sediments by the use of photon-stimulated luminescence. Oxford University Press, Oxford.

Aitken, M.J. and Smith, B.W., 1988. Optical dating: recuperation after bleaching. Quaternary Science Reviews, 7, 387-393.

Aitken, M.J. and Xie, J., 1990. Moisture correction for annual gamma dose. Ancient TL, 8, 6-9.

Akbar, G., Khan, T.N. and Arshad, M., 1996. Cholistan Desert, Pakistan. Rangelands, 18, 124-128.

Akhter, R. and Arshad, M., 2006. Arid rangelands in the Cholistan Desert, Pakistan, Secheresse, 17, 210-217.

Alappat, L., Tsukamoto, S., Singh, P., Srikanth, D., Ramesh, R. and Frechen, M., 2010. Chronology of Cauvery delta sediments from shallow subsurface cores using

elevated-temperature post-IR IRSL dating of feldspar. Geochronometria, 37, 37-47.

Alexandrovskiy, A.L., van der Plicht, J., Belinskiy, A. and Khoklova, O., 2001. Chronology of soil evolution and climatic changes in the dry steppe zone of the northern Caucasus, Russia, during the 3rd millennium BC. Radiocarbon, 43, 629-635.

Ali, J.R. and Aitchison, J.C., 2005. Greater India. Earth Science Reviews, 72, 169-188.

Ali, K.F. and De Boer, D.H., 2007. Spatial patterns and variation of suspended sediment yield in the upper Indus River basin, northern Pakistan. Journal of Hydrology, 334, 368-387.

Allchin, F.R., 1990. The end of the Harappan urban phase and its aftermath. Ancient Ceylon, 10, 25-40.

Allchin, B. and Allchin, F.R., 1997. Origins of a civilisation: the prehistory and early archaeology of South Asia. Viking, New Delhi.

Amundson, R. and Pendall, E., 1991. Pedology and Late Quaternary environments surrounding Harappa: a review and synthesis. In: Meadow, R.H. (ed.). Harappa Excavations 1986-1990: a multidisciplinary approach to third millennium urbanism. Monographs in World Archaeology, Madison. Pp. 13-27.

An, C.-B., Tang, L., Barton, L. and Chen, F.-H., 2005. Climate change and cultural response around 4000 cal yr B.P. in the western part of the Chinese loess plateau. Quaternary Research, 63, 347-325.

Ankjærgaard, C. and Murray, A.S., 2007. Total beta and gamma dose rates in trapped charge dating based on beta counting. Radiation Measurements, 42, 352-359.

Armitage, S.J., 2003. Testing and application of luminescence techniques using sediment from the southeast African coast. Unpublished PhD thesis, University of Wales, Aberystwyth.

Armitage, S.J., Duller, G.A.T. and Wintle, A.G., 2000. Quartz from southern Africa: sensitivity changes as a result of thermal pre-treatment. Radiation Measurements, 32, 571-577.

Armitage, S.J., Jasim, S.A., Marks, A.E., Parker, A.G., Usik, V.I. and Uerpmann, H.-P., 2011. The Southern Route 'Out of Africa': Evidence for an early expansion of modern humans into Arabia. Science, 331, 453-456.

Arnold, L.J., Roberts, R.G., Galbraith, R.F. and DeLong, S.B., 2009. A revised burial dose estimation procedure for optical dating of young and modern-age sediments. Quaternary Geochronology, 4, 306-325.

Athanassas, C., 2011. Constraints on the precision of SAR in equivalent dose estimations close to saturation in quartz. Geochronometria, 38, 413-423.

Baig, M.S., Akram, M. and Hassan, M.A., 1980. Possibilities for range development in Cholistan desert as reflected by its physiography and soils. Pakistan Journal of Forestry, 30, 61-71.

Bailey, R.M., 1998. Depletion of the quartz OSL signal using low photon energy stimulation. Ancient TL, 16, 33-36.

Bailey, R.M., 2004. Paper I – simulation of dose absorption in quartz over geological timescales and its implications for the precision and accuracy of optical dating. Radiation Measurements, 38, 299-310.

Bailey, R.M., 2010. Direct measurement of the fast component of quartz optically stimulated luminescence and implications for the accuracy of optical dating. Quaternary Geochronology, 5, 559-568.

Bailey, R.M. and Arnold, L.J., 2006. Statistical modelling of single grain quartz D_e distributions and an assessment of procedures for estimating burial dose. Quaternary Science Reviews, 25, 2475-2502.

Bailey, R.M., Smith, B.W. and Rhodes, E.J., 1997. Partial bleaching and the decay form characteristics of quartz OSL. Radiation measurements, 27, 123-136.

Bailey, R.M., Singarayer, J.S., Ward, S. and Stokes, S., 2003. Identification of partial resetting using D_e as a function of illumination time. Radiation Measurements, 37, 511-518.

Ballarini, M., Wallinga, J., Wintle, A.G. and Bos, A.J.J., 2007. A modified SAR protocol for optical dating of individual grains from young quartz samples Radiation Measurements, 42, 360-369.

Banerjee, D., Bøtter-Jensen, L. and Murray, A.S., 2000. Retrospective dosimetry: estimation of the dose to quartz using the single-aliquot regenerative-dose protocol. Applied Radiation and Isotopes, 52, 831-844.

Banerjee, D., Murray, A.S., Bøtter-Jensen, L. and Lang, A., 2001. Equivalent dose estimation using a single aliquot of polymineral fine grains. Radiation Measurements, 33, 73-94.

Banerjee, D., Hildebrand, A.N., Murray-Wallace, C.V., Bourman, R.P., Brooke, B.P and Blair, M., 2003. New quartz SAR-OSL ages from the stranded beach dune sequence in south-east South Australia. Quaternary Science Reviews, 22, 1019-1025.

Barbouti, A.I. and Rastin, B.C., 1983. A study of the absolute intensity of muons at sea level and under various thicknesses of absorber. Journal of Physics G: Nuclear and Particle Physics, 9, 1577-1595.

Bar-Matthews, M., Ayalon, A. and Kaufman, A., 1997. Late Quaternary paleoclimate in the eastern Mediterranean region from stable isotope analysis of speleothems at Soreq Cave, Israel. Quaternary Research, 47, 155-168.

Bateman, M.D., 2008. Luminescence dating of periglacial sediments and structures. Boreas, 37, 574-588.

Bateman, M.D., Boulter, C.H., Carr, A.S., Frederick, C.D., Peter, D. and Wilder, M., 2007. Detecting post-depositional sediment disturbance in sandy deposits using optical luminescence. Quaternary Geochronology, 2, 57-64.

Bell, W.T., 1979. Attenuation factors for the absorbed radiation dose in quartz inclusions for thermoluminescence dating. Ancient TL, 8, 2-13.

Berger, A., 1978. Long-term variations of daily insolation and Quaternary climates changes. Journal of the Atmospheric Sciences, 35, 2362-2367.

Berger, A. and Loutre, M.F., 1991. Insolation values for the climate of the last 10 million years. Quaternary Science Reviews, 10, 297-317.

Berger, A. and Loutre, M.F., 1999. Parameters of the Earths orbit for the last 5 million years in 1 kyr resolution. doi:10.1594/PANGAEA.56040.

Berger, A., Loutre, M.F. and Yin, Q., 2010. Total irradiation during any time interval of the year using elliptic integrals. Quaternary Science Reviews, 29, 1968-1982.

Bhadra, B.K., Gupta, A.K. and Sharma, J.R., 2009. Saraswati Nadi in Haryana and its linkage with the Vedic Saraswati river-integrated study based on satellite images and ground based formation. Journal Geological Society of India, 73, 273-288.

Bhan, K.K., 1989. Late Harappan settlements in Western India, with specific reference to Gujarat. In: Kenoyer, J.M. (ed.). Old problems and new perspectives in the archaeology of South Asia. Madison Department of Anthropology, University of Wisconsin. Pp. 219-234.

Blong, R. J and Gillespie, R., 1978. Fluvially transported charcoal gives erroneous ^{14}C ages for recent deposits. Nature, 271, 739-741.

Bond, G., Showers, W., Cheseby, M., Lotti, R., Almasi, P., de Menocal, P., Priore, P., Cullen, H., Hajdas, I. and Bonani, G., 1997. A pervasive millennial-scale cycle in North Atlantic Holocene and glacial climates. Science, 278, 1257-1266.

Bookhagen, B., 2010. Appearance of extreme monsoonal rainfall events and their impact on erosion in the Himalaya. Geomatics, Natural Hazards and Risk, 1, 37-50.

Bos, A.J. and Wallinga, J., 2009. Optically stimulated luminescence signals under various stimulation modes assuming first-order kinetics. Physical Review B, 79, 195118.

Bøtter-Jensen, L., 1997. Luminescence techniques: instrumentation and methods. Radiation Measurements, 27, 749-768.

Bøtter-Jensen, L. and Mejdahl, V., 1988. Assessment of beta dose rate using a GM multicounter system. Nuclear Tracks and Radiation Measurement, 14, 187-191.

Bøtter-Jensen, L., Duller, G.A.T. and Poolton, N.J., 1994. Excitation and emission spectrometry of stimulated luminescence from quartz and feldspars. Radiation Measurements, 23, 613-616.

Bøtter-Jensen, L., Duller, G.A.T., Murray, A.S. and Banerjee, D., 1999a. Blue light emitting diodes for optical stimulation of quartz in retrospective dosimetry and dating. Radiation Protection Dosimetry, 84, 335-340.

Bøtter-Jensen, L., Mejdahl, V. and Murray, A.S., 1999b. New light on OSL. Quaternary Geochronology, 18, 303-309.

Bøtter-Jensen, L., Bulur, E., Duller, G.A.T. and Murray, A.S., 2000. Advances in luminescence instrument systems. Radiation Measurements, 32, 523-528.

Bøtter-Jensen, L., Andersen, C.E., Duller, G.A.T. and Murray, A.S., 2003a. Developments in radiation, stimulation and observation facilities in luminescence measurements. Radiation Measurements, 37, 535-541.

Bøtter-Jensen, L., McKeever, S.W.S. and Wintle, A.G., 2003b. Optically stimulated luminescence dosimetry. Elsevier, Amsterdam.

Bøtter-Jensen, L., Thomsen, K.J. and Jain, M., 2010. Review of optically stimulated luminescence (OSL) instrumental developments for retrospective dosimetry. Radiation Measurements, 45, 253-257.

Briant, R. M., Bates, M. R., Schwenninger, J.-L. and Wenban-Smith, F., 2006. An optically stimulated luminescence dated middle to late Pleistocene fluvial sequence from the western Solent basin, southern England. Journal of Quaternary Science, 21, 507-523.

Brooks, N., 2006. Cultural responses to aridity in the Middle Holocene and increased social complexity. Quaternary International, 151, 29-49.

Bryson, R.A. and Swain, M.A., 1981. Holocene variations in monsoon rainfall in Rajasthan. Quaternary Research, 16, 135-145.

Bulur, E., 1996. An alternative technique for optically stimulated luminescence (OSL) experiment. Radiation Measurements, 26, 701-709.

Bulur, E., 2000. A simple transformation for converting CW-OSL curves to LM-OSL curves. Radiation Measurements, 32, 141-145.

Bulur, E., Bøtter-Jensen, L. and Murray, A.S., 2000. Optically stimulated luminescence from quartz measured using the linear modulation technique. Radiation Measurements, 32, 407-411.

Bulur, E., Duller, G.A.T., Solongo, S., Bøtter-Jensen, L. and Murray, A.S., 2002. LM-OSL from single grains of quartz: a preliminary study. Radiation Measurements, 35, 79-85.

Burbank, D.W., Beck, R.A. and Mulder, T., 1996. The Himalayan Foreland. In: An, Y. and Harrison, M. Asian Tectonics. Cambridge University Press, Cambridge. Pp. 149-188.

Burbidge, C.I., Sanderson, D.C.W., Housely, R.A. and Allsworth Jones, P., 2007. Survey of Palaeolithic sites by luminescence profiling, a case study from Eastern Europe. Quaternary Geochronology, 2, 296-302.

Caseldine, C.J. and Turney, C., 2010. The bigger picture: towards integrating palaeoclimate and environmental data with a history of societal change. Journal of Quaternary Science, 25, 88-93.

Chakrabarti, D.K. and Saini, S., 2009. The problem of the Sarasvati River and notes on the archaeological geography of Haryana and Indian Punjab. Aryan Books International, Delhi.

Chanda, R., 1916. The Indo-Aryan Races, Rajshahi.

Chapman, R., 2003. Archaeologies of complexity. Routledge, London.

Chen, R. and McKeever, S.W.S., 1997. Theory of thermoluminescence and related phenomena. World Scientific, Singapore.

Childe, V.G., 1934. New light on the most Ancient East. London.

Childe, V.G., 1950. The urban revolution. Town Planning Review, 21, 3-17.

Choi, J.H., Duller, G.A.T. and Wintle A.G., 2006. Analysis of quartz LM-OSL curves. Ancient TL 24, 9-20.

Choi, J.H., Murray, A.S., Jain, M., Cheong, C.-S. and Chang, H.W., 2003. Luminescence dating of well-sorted marine terrace sediments on the southeastern coast of Korea. Quaternary Science Reviews, 22, 407-421.

Clemens, S.C. and Prell, W.L., 2003. A 350,000 year summer monsoon multi-proxy stack from the Owen Ridge, Northern Arabian Sea. Marine Geology, 201, 35-51.

Clemens, S.C., Prell, W.L., Murray, D., Shimmield, G.B. and Weedon, G., 1991. Forcing mechanisms of the Indian Ocean monsoon. Nature, 353, 720-725.

Clemens, S.C., Murray, D.W. and Prell, W.L., 1996. Non-stationary phase of the Plio-Pleistocene Asian Monsoon. Science, 274, 943-948.

Clift, P.D., 2006. Controls on the erosion of Cenozoic Asia and the flux of clastic sediment to the ocean. Earth and Planetary Science Letters, 241, 571-580.

Clift, P.D. and Plumb, R.A., 2008. The Asian monsoon: causes, history and effects. Cambridge University Press, Cambridge.

Clift, P.D., Carter, A.C., Giosan, L., Durcan, J.A., Duller, G.A.T., Macklin, M.G., Alizai, A., Tabrez, A.R., Danish, M., VanLaningham, S. and Fuller, D.Q., 2012. U-Pb zircon dating evidence for a Pleistocene Sarasvati River and capture of the Yamuna River. Geology, 40, 211-214.

Colls, A.E., Stokes, S., Blum, M.D. and Straffin, E., 2001. Age limits on the Late Quaternary evolution of the upper Loire River. Quaternary Science Reviews, 20, 743-750.

Cosford, J., Qing, H., Lin, Y., Eglington, B., Mattey, D., Chen, Y.G., Zhang, M. and Cheng, H., 2009. The East Asian monsoon during MIS 2 expressed in a speleothem $\delta^{18}O$ record from Jintanwan Cave, Hunan, China. Quaternary Research, 73, 541-549.

Cullen, H.M., de Menocal, P.B., Hemming, S., Hemming, G., Brown, F.H., Guilderson, T. and Sirocko, F., 2000. Climate change and the collapse of the Akkadian empire. Evidence from the deep sea. Geology, 28, 379-382.

Cunningham, A.C. and Wallinga, J., 2010. Selection of integration time intervals for quartz OSL decay curves. Quaternary Geochronology, 5, 657-666.

Dales, G.F., 1964. The mythical massacre at Mohenjo-Daro. Expedition, 6, 36-43.

Dales, G.F., 1966a. Relation of Indus Valley floods to decline of Harappan Civilisation. American Philosophical Society Yearbook 1965. American Philosophical Society, Philadelphia.

Dales, G.F., 1966b. The decline of the Harappans. Scientific American, 214, 93-100.

Dales, G.F. and Raikes, R.L., 1968. The Mohenjo-Daro floods – a rejoinder. American Anthropologist, 70, 957-961.

De Corte, F., Vandenberghe, D., Hossain, S.M., De Wispelaere, A., Buylaert, J.-P. and Van den Haute, P., 2008. Preparation and characterization of loess sediment for use as a reference material in the annual radiation dose determination for luminescence dating. Journal of Radioanalytical and Nuclear Chemistry, 272, 311-319.

de Menocal, P., 2001. Cultural response to climate change during the late Holocene. Science, 292, 667-673.

Dearing, J.A., 2006. Climate-human-environment interactions: resolving our past. Climate of the Past, 2, 187-203.

Debenham, N.C., 1983. Reliability of thermoluminescence dating of stalagmitic calcite. Nature, 304, 154-156.

DeLong, S.B. and Arnold, L.J., 2007. Dating alluvial deposits with optically stimulated luminescence, AMS ^{14}C and cosmogenic techniques, western Transverse Ranges, California, USA. Quaternary Geochronology, 2, 129-136.

Denby, P.M., Bøtter-Jensen, L., Murray, A.S., Thomsen, K.J. and Moska, P., 2006. Application of pulsed OSL to the separation of the luminescence components from a mixed quartz/feldspar sample. Radiation Measurements, 41, 774-779.

Deotare, B.C., Kajale, M.D., Khirsagar, A.A. and Rajaguru, S.N., 1998. Geoarchaeological and palaeoenvironmental studies and Bap-Malar playa, district Jodhpur, Rajasthan. Current Science, 75, 316-320.

Deotare, B.C., Kajale, M.D., Rajaguru, S.N. and Basavaiah, N., 2004. Late Quaternary geomorphology, palynology and magnetic susceptibility of playas in western margin of the Indian Thar Desert. Journal of Indian Geophysical Union, 1, 15-25.

Derbyshire, E. and Goudie, A.S., 1997. Asia. In: Thomas, D.S.G. (ed.). Arid Zone Geomorphology: process form and change in drylands. John Wiley and Sons, Chicester. Pp. 487-506.

Diamond, J.M., 2005. Collapse: How societies choose to fail or succeed. Viking Books, New York.

Duller, G.A.T., 1991. Equivalent dose determination using single aliquots. Nuclear Tracks and Radiation Measurements, 18, 371-378.

Duller, G. A. T., 1994. Luminescence dating of poorly bleached sediments from Scotland. Quaternary Geochronology (Quaternary Science Reviews), 13, 521-524.

Duller, G.A.T., 2003. Distinguishing quartz and feldspar in single grain luminescence measurements. Radiation Measurements, 37, 161-165.

Duller, G.A.T, 2004. Luminescence dating of Quaternary sediments: recent advances. Journal of Quaternary Science, 19, 183-192.

Duller, G.A.T., 2007. Assessing the error on equivalent dose estimates derived from single aliquot regenerative dose measurements. Ancient TL, 25, 15-24.

Duller, G.A.T., 2008a. Luminescence dating: guidelines on using luminescence dating in archaeology. English Heritage, Swindon.

Duller, G.A.T., 2008b. Single-grain optical dating of Quaternary sediments: why aliquot size matters in luminescence dating. Boreas, 37, 589-612.

Duller, G.A.T., 2012. Improving the accuracy and precision of equivalent doses determined using the optically stimulated luminescence signal from single grains of quartz. Radiation Measurements, 47, 770-777.

Duller, G.A.T. and Bøtter-Jensen, L., 1993. Luminescence from potassium feldspars stimulated by infrared and green light. Radiation Protection Dosimetry, 47, 683-688.

Duller, G.A.T. and Wintle, A.G., 2012. A review of the thermally transferred optically stimulated luminescence signal from quartz for dating sediments. Quaternary Geochronology, 7, 6-20.

Duller, G.A.T., Bøtter-Jensen, L. and Murray, A.S., 2000. Optical dating of single sand-sized grains of quartz: sources of variability. Radiation Measurements, 32, 453-457.

Duller, G.A.T., Bøtter-Jensen, L. and Murray, A.S., 2003. Combining infrared and green-laser stimulation sources in single-grain luminescence measurements of feldspar and quartz. Radiation Measurements, 37, 543-550.

Duller, G.A.T., Penkman, K.E.H. and Wintle, A.G., 2009. Assessing the potential for using biogenic carbonates as dosemeters for luminescence dating. Radiation Measurements, 44, 429-433.

Durcan, J.A. and Duller, G.A.T., 2011. The fast ratio: an objective rejection criterion for testing the dominance of the fast component in quartz OSL signals. Radiation Measurements, 46, 1065-1072.

Durcan, J.A., Roberts, H.M. and Duller, G.A.T., 2010. Testing the use of range-finder OSL dating to inform field sampling and laboratory processing strategies. Quaternary Geochronology, 5, 86-90.

Ely, L.L., Enzel, Y., Baker, V.R., Kale, V.S. and Mishra, S., 1996. Changes in the magnitude and frequency of Late Holocene monsoon floods on the Narmada River, central India. Geological Society of America, 108, 1134-1148.

Enzel, Y., Ely, L., Misra, S., Ramesh, R., Amit, R., Lazar, B., Rajaguru, Baker, V.R. and Sandler, A., 1999. High-resolution Holocene environmental changes in the Thar Desert, northwestern India. Science, 284, 125-128.

Fairservis, W.A., 1956. Excavations in the Quetta Valley, west Pakistan. Anthropological Papers of the American Museum of Natural History, 45, 167-402.

Fairservis, W.A., 1967. The origin, character and decline of an early civilisation. Novitates 2055, New York. Pp. 1-55.

Feathers, J.K. and Migliorini, E., 2001. Luminescence dating at Katanda – a reassessment. Quaternary Science Reviews, 20, 961-966.

Fleitmann, D., Burns, S.J., Mudelsee, M., Neff, U., Kramers, J., Mangini, A. and Matter, A., 2003. Holocene forcing of the Indian monsoon recorded in a stalagmite from southern Oman. Science, 300, 1737-1739.

Fleitmann, D., Burns, S.J., Mangini, A., Mudelsee, M., Kramers, J., Villa, I., Neff U., Al-Subbary, A.A., Buettner, A., Hippler, D. and Matter, A., 2007. Holocene ITCZ and Indian monsoon dynamics recorded in stalagmites from Oman and Yemen (Socotra). Quaternary Science Reviews, 26, 170-188.

Frumkin, A., 1991. The Holocene climatic record of the salt caves of Mount Sedom, Israel. The Holocene, 1, 191-200.

Fuchs, M. and Lang, A., 2001. OSL dating of coarse-grain fluvial quartz using single-aliquot protocols on sediments from NE Peloponnese, Greece. Quaternary Science Reviews, 20, 783-787.

Fuchs, M. and Owen, L.A., 2008. Luminescence dating of glacial and associated sediments: review, recommendations and future directions. Boreas, 37, 636-659.

Fuller, D.Q. and Madella, M., 2000. Issues in Harappan archaeobotany: retrospect and prospect. In: Settar, S. and Korisettar, R. (eds.). Indian archaeology in retrospect, vol. III, archaeology and interactive disciplines. Indian Council of Historical Research, Manohar. Pp. 317-390.

Galbraith, R.F., 1988. Graphical display of estimates having differing standard errors. Technometrics, 30, 271-281.

Galbraith, R.F., 1990. The radial plot: graphical assessment of spread in ages. Nuclear Tracks and Radiation Measurements, 17, 207-214.

Galbraith, R.F, 2002. A note on the variance of a background-corrected OSL count. Ancient TL, 20, 49-51.

Galbraith, R.F., 2005. Statistics for fission track analysis. Chapman and Hall/CRC Interdisciplinary Statistics.

Galbraith, R.F., 2010. On plotting OSL equivalent doses. Ancient TL, 28, 1-10.

Galbraith, R.F. and Green, P.F., 1990. Estimating the component ages in a finite mixture. Nuclear Tracks and Radiation Measurements, 17, 197-206.

Galbraith, R.F. and Laslett, G., 1993. Statistical models for mixed fission track ages. Radiation Measurements, 21, 459-470.

Galbraith, R.F. and Roberts, R.G., 2012. Statistical aspects of equivalent dose and error calculation and display in OSL dating: An overview and some recommendations. Quaternary Geochronology, 11, 1-27.

Galbraith, R.F., Roberts, R.G., Laslett, G.M., Yoshida, H. and Olley, J.M., 1999. Optical dating of single and multiple grains of quartz from Jinmium rock shelter, northern Australia: part I, experimental design and statistical models. Archaeometry, 41, 339-364.

Galbraith, R.F., Roberts, R.G. and Yoshida, H., 2005. Error variation in OSL palaeodose estimates from single aliquots of quartz: a factorial experiment. Radiation Measurements, 39, 289-307.

Gangal, K., Vahia, M. and Adhikari, R., 2010. Spatio-temporal analysis of the Indus urbanisation. Current Science, 98, 846-852.

Ghose, B., Kar, A. and Hussain, Z., 1979. The lost courses of the Saraswati River in the Great Indian Desert: new evidence from Landsat Imagery. The Geographical Journal, 145, 446-451.

Gillespie, R., Prosser, I.P., Dlugokencky, E., Sparks, R.J., Wallace, G. and Chappell, J.M.A., 1992. AMS dating of alluvial sediments on the southern tablelands of New South Wales Australia. Radiocarbon, 34, 29-36.

Giosan, L., Clift, P.D., Macklin, M.G., Fuller, D.Q., Constantinescu, S., Durcan, J.A., Stevens, T., Duller, G.A.T., Tabrez, A., Gangal, K., Adhikari, R., Alizai, A., Filip, F., VanLaningham, S. and Syvitski, J.P.M., 2012. Fluvial landscapes of the Harappan civilisation. Proceedings of the National Academy of Sciences of the United States of America, doi:10.1073/pnas.1112743109.

Godfrey-Smith, D.I., Huntley, D.J. and Chen, W.-H., 1988. Optical dating studies of quartz and feldspar sediment extracts. Quaternary Science Reviews, 7, 373-380.

Gupta, S.K., 1996. The Indus-Saraswati civilisation: origins, problems and issues. Pratibha Prakashan, Delhi.

Gupta, A.K., Anderson, D.M. and Overpeck, J.T., 2003. Abrupt changes in the Asian southwest monsoon during the Holocene and their links to the North Atlantic Ocean. Nature, 421, 354-357.

Gupta, A.K., Sharma, J.R., Sreenivasan, G. and Srivastava, K.S., 2004. New findings on the course of River Saraswati. Journal of Indian Society of Remote Sensing, 32, 1-24.

Gupta, A.K., Das, M. and Anderson, D.M., 2005. Solar influence on the Indian summer monsoon during the Holocene. Geophysical Research Letters, 32, doi:10.1029/2005GL022685.

Harden, T., Macklin, M.G. and Victor, R., 2008. Holocene flood histories in south-western USA. Earth Surface Processes and Landforms, 35, 707-716.

Harrison, S., Glasser, N., Winchester, V., Haresign, E., Warren, C., Duller, G.A.T., Bailey, R.M., Ivy-Ochs, S., Jansson, K. and Kubik, P., 2008. Glaciar Leon, Chilean Patagonia: late-Holocene chronology and geomorphology. The Holocene, 18, 643-652.

Hodell, D.A., Brenner, M., Curtis, J.H. and Guilderson, T., 2001. Solar forcing of drought frequency in the Maya lowlands. Science, 292, 1367-1369.

Hodell, D.A., Brenner, M. and Curtis, J.H., 2005. Terminal classic drought in the northern Maya lowlands inferred from multiple sediment cores in Lake Chichancanab (Mexico). Quaternary Science Reviews, 24, 1413-1427.

Hodell, D.A., Brenner, M. and Curtis, J.H., 2007. Climate and cultural history of the Northeastern Yucatan Peninsula, Quintana Roo, Mexico. Climatic Change, 83, 215-240.

Holden, N.E., Bonardi, M.L., De Bievre, P., Renne, P. and Villa, I.M., 2011. IUPAC-IUGS common definition and convention on the use of the year as a derived unit of time (IUPAC Recommendations 2011). Pure Applied Chemistry, 83, 1159-1162.

Hong, Y.T., Hong, B., Lin, Q.H., Zhu, Y.X., Shibata, Y., Hirota, M., Uchida, M., Leng, X.T., Jiang, H.B., Xua, H., Wang, H. and Yi, L., 2003. Correlation between Indian Ocean summer monsoon and North Atlantic climate during the Holocene. Earth and Planetary Science Letters, 211, 371-380.

Huang, C.C., Pang, J., Zha, X., Zhou, Y., Su, H. and Li, Y., 2010. Extraordinary floods of 4100-4000 a BP recorded at the Late Neolithic ruins in the Jinghe river gorges,

middle reach of the Yellow river, China. Palaeogeography, palaeoclimatology, palaeoecology, 289, 1-9.

Huntley, D.J., Godfrey-Smith, D.I. and Thewalt, M.L.W., 1985. Optical dating of sediments. Nature, 313, 105-108.

Huntley, D.J., Godfrey-Smith, D.I. and Haskell, E.H., 1991. Light-induced emission spectra from some quartz and feldspars. International Journal of Radiation Applications and Instrumentation. Part D: Nuclear Tracks and Radiation Measurements, 18, 127-131.

Imbrie, J., Boyle, E.A., Clemens, S.C., Duffy, A., Howard, W.R., Kukla, G., Kutzbach, J., Martinson, D.G., McIntyre, A., Mix, A.C., Molfino, B., Morley, J.J., Peterson, L.C., Pisias, M.G., Prell, W.L., Raymo, M.E., Shackleton, N.J. and Toggweiler, J.R., 1992. On the structure and origin of major glaciation cycles 1: linear response to Milankovitch forcing. Paleoceanography, 7, 701-738.

Inam, A., Clift, P.D., Giosan, L., Tabrez, A.R., Tahir, M., Rabbani, M.M. and Danish, M., 2007. The geographic, geological and oceanographic setting of the Indus River. In: Gupta, A. (ed.). Large rivers: Geomorphology and management. John Wiley and Sons, Chichester. Pp. 333-346.

Istratov, A.A. and Vyvenko, O.F., 1999. Exponential analysis in physical phenomena. Review of Scientific Instruments, 70, 2, 1233-1257.

IUPAC-IUGS Task Group, 2006. Recommendations for isotope data in geosciences. [Online] http://www.iupac.org/projects/2006/2006-016-1-200.html [access date: 3rd July 2012].

Jacobs, Z., 2004. Development of luminescence techniques for dating Middle Stone Age sites in South Africa. Unpublished Ph.D. thesis, University of Wales, Aberystwyth.

Jacobs, Z. and Roberts, R. G., 2007. Advances in optically stimulated luminescence (OSL) dating of individual grains of quartz from archaeological deposits. Evolutionary Anthropology, 16, 210–223.

Jacobs, Z., Wintle, A.G. and Duller, G.A.T., 2003a. Optical dating of dune sand from Blombos Cave, South Africa: I – multiple grain data. Journal of Human Evolution, 44, 599-612.

Jacobs, Z., Duller, G.A.T. and Wintle, A.G., 2003b. Optical dating of dune sand from Blombos Cave, South Africa: II-single grain data. Journal of Human Evolution, 44, 613-625.

Jacobs, Z., Duller, G.A.T. and Wintle, A.G., 2006. Interpretation of single grain D_e distributions and calculation of D_e. Radiation Measurements, 41, 264-277.

Jain, M. and Tandon, S.K., 2003. Fluvial response to Late Quaternary climate changes, western India. Quaternary Science Reviews, 22, 2223-2235.

Jain, M., Murray A.S. and Bøtter-Jensen, L., 2003. Characterisation of blue-light stimulated luminescence components in different quartz samples: implications for dose measurement. Radiation Measurements, 37, 441-449.

Jain, M., Murray, A.S. and Bøtter-Jensen, 2004a. Optically stimulated luminescence dating: how significant is incomplete light exposure in fluvial environments? Quaternaire, 15, 143-147.

Jain, M., Tandon, S.K. and Bhatt, S.C., 2004b. Late Quaternary stratigraphic development in the lower Luni, Mahi and Sabarmati river basins, western India. Proceedings of the Indian Academy of Science, 113, 453-471.

Jain, M., Murray, A.S., Bøtter-Jensen, L. and Wintle, A.G., 2005. A single-aliquot regenerative-dose method based on IR (1.49 eV) bleaching of the fast OSL component in quartz. Radiation Measurements, 39, 309-318.

Jain, M., Choi, J.H. and Thomas, P.J., 2008. The ultrafast OSL component in quartz: Origins and implications. Radiation Measurements, 43, 709-714.

Jaiswal, M.K., Chen, Y.G., Kale, V.S. and Achyuthan, H., 2009. Residual luminescence in quartz from slack water deposits in Kaveri basin, south India. Geochronometria, 33, 1-8.

Jansen, M., 1979. City planning in the Harappa Culture. In: Hartel, H. (ed.). South Asian Archaeology. Dietrich Reimer, Berlin. Pp. 251-69.

Jansen, M., 1989. Water supply and sewage disposal at Mohenjo-Daro. World Archaeology, 21, 177-129.

Jarrige, C., 1995. Mergarh: Field reports 1974-1985 from Neolithic times to the Indus Civilisation. Department of Culture and Tourism, Government of Sindh, Karachi.

Jayangondaperumal, R., Murari, M.K., Sivasubramanian, P., Chandresekar, N. and Singhvi, A.K., 2012. Luminescence dating of fluvial and coastal red sediments in the SE coast, India, and implications for palaeoenvironmental changes and dune reddening. Quaternary Research, 77, 468-481.

Juyal, N., Chamyal, L. S., Bhandari, S., Bhushan, R. and Singhvi, A. K., 2006. Continental record of the southwest monsoon during the last 130 ka: evidence from the southern margin of the Thar Desert, India. Quaternary Science Reviews, 25, 2632-2650.

Juyal, N., Pant, R.K., Basavaiah, N., Bhushan, R., Jain, M., Saini, N.K., Yadava, M.G. and Singhvi, A.K., 2009. Reconstruction of Last Glacial to early Holocene monsoon variability from relict lake sediments of the Higher Central Himalaya, Uttrakhand, India. Journal of Asian Earth Science, 34, 437-449.

Kajale, M.D. and Deotare, B.C., 1997. Late Quaternary environmental studies on salt lakes in western Rajasthan, India: a summarised review. Journal of Quaternary Science, 12, 405-412.

Kale, V.S., 1999a. Late Holocene temporal patterns of palaeofloods in central and western India. Man and Environment, 24, 109-115.

Kale, V.S., 1999b. Long-period fluctuation in monsoon floods in the Deccan Peninsula, India. Journal of Geological Society of India, 53, 5-15.

Kale, V., 2007. Fluvio-sedimentary response of the monsoon-fed Indian Rivers to Late Pleistocene–Holocene changes in monsoon dynamics: reconstruction based on existing ^{14}C database. Quaternary Science Reviews, 26, 1610-1620.

Kale, V.S., Singhvi, A. K., Mishra, P. K. and Banerjee, D., 2000. Sedimentary records and luminescence chronology of Late Holocene palaeofloods in the Luni River, Thar Desert, northwestern India. Catena, 40, 337-358.

Kale, V.S., Mishra, S. and Baker, V.R., 2003. Sedimentary records of palaeofloods in the bedrock gorges of the Tapi and Narmada rivers, central India. Current Science, 84, 1072-1079.

Kar, A and Ghose, B., 1984. The Drishadvati river system of India: an assessment of new findings. The Geographical Journal, 150, 221-229.

Kar, A., Felix, C., Rajguru, S.N. and Singhvi, A.K., 1998. Late Holocene growth and mobility of a transverse dune in the Thar Desert. Journal of Arid Environments, 38, 175-185.

Kazmi, A.H., 1984. Geology of the Indus Delta. In: Haq, B.U. and Milliman, J.D. (eds.). Marine geology and oceanography of Arabian Sea and Coastal Pakistan. Reinhold, New York. Pp. 71-84.

Kenoyer, M.J., 1991. Urban process in the Indus tradition: A preliminary model from Harappa. In: Meadow, R.H. (ed.). Harappa Excavations 1986-1990. Prehistory Press, Madison. Pp. 29-60.

Kenoyer, M.J., 1996. Craft traditions of the Indus civilisation and their legacy in modern Pakistan. Lahore Museum Bulletin, IX, 1-8.

Kenoyer, J.M., 1998. Ancient cities of the Indus Valley Civilisation. Oxford University Press, Oxford.

Khan, F.A., 1965. Excavations at Kot Diji. Pakistan Archaeology, 2, 11-85.

Kim, J.C., Roberts, H.M., Duller, G.A.T., Lee, Y.I. and Yi, S.B., 2009. Assessment of diagnostic tests for evaluating the reliability of SAR D_e values from polymineral and quartz fine grains. Radiation Measurements, 44, 149-157.

Kirkpatrick, J.J.R., Enion, D.S. and Burd, D.A.R., 1995. Hydroflouric acid burns: a review. Burns, 21, 483-493.

Kotlia, B.S., Sharma, C., Bhalla, M.S., Rajagopalan, G., Subrahmanyam, K., Bhattacharyya, A. and Valdiya, K.S., 2000. Palaeoclimatic conditions in the late Pleistocene Wadda Lake, eastern Kumaun Himalaya (India). Palaeogeograpahy, Palaeoclimatology, Palaeoecology, 162, 105-118.

Koutavas, A., Lynch-Stieglita, J., Marchitto, T. and Sachs, J., 2002. El Niño-like pattern in ice age tropical Pacific sea-surface temperature. Science, 297, 226-230.

Kudrass, H.R., Hofman, A., Doose, H., Emeis, K. and Erlenkeuser, H., 2001. Modulation and amplification of climatic changes in the Northern Hemisphere by the Indian summer monsoon during the past 80 ky. Geology, 29, 63-66.

Kuhns, C.K., Agersnap Larsen, N. and McKeever, S.W.S., 2000. Characteristics of LM-OSL from several different types of quartz. Radiation Measurements, 32, 413-418.

Kunz, A., Frechen, M., Ramesh, R. and Urban, B., 2010. Luminescence dating of late Holcene dunes showing remnants of early settlement in Cuddalore and evidence of monsoon activity in south east India. Quaternary International, 222, 194-208.

Lahiri, N., 2000. Indus cities and the Aryans: Historical conquerors, mythical marauders or Vedic Harappans. In: Lahiri, N. (ed.). The decline and fall of the Indus civilisation. Permanent Black, Delhi. Pp. 1-36.

Lal, M., 2003. Global climate change: Indias monsoon and its variability. Journal of Environmental Studies and Policy, 6, 1-34.

Lamothe, M. and Auclair, M., 1999. A solution to anomalous fading and age shortfalls in optical dating of feldspar minerals. Earth and Planetary Science Letters, 171, 319-323.

Lapp, T. and Thomsen, K.J., 2010. Beta source uniformity in the Risø TL/OSL reader. UK TL/OSL/ESR Meeting, 8th-10th September 2010, Oxford University.

Lauer, T., Frechen, M., Hoselmann, C. and Tsukamoto, S., 2010. Fluvial aggradation phases in the Upper Rhine Graben – New insights by quartz OSL dating. Proceedings of Geologists Association, 121, 154-161.

Lawler, A., 2008. Boring no more – a trade savvy Indus emerges. Science, 320, 1276–1281.

Lemcke, G. and Sturm, M., 1997. $d^{18}O$ and trace element measurements as proxy for the reconstruction of climate changes at Lake Van (Turkey): preliminary results. In: Dalfes, H.N., Kukla, G. and Weiss, H. (eds.). Third millennium BC climate change and old world collapse. Springer, Berlin. Pp. 653-678.

Lepper, K. and McKeever, S.W.S., 2002. An objective methodology for dose distribution analysis. Radiation Protection Dosimetry, 101, 349-352.

Leroy, S.A.G., Jousse, H. and Cremaschi, M., 2006. Impact of rapid environmental changes on humans and ecosystems. Quaternary International, 150, 1-2.

Lewin, J., Macklin, M.G. and Johnstone, E., 2005. Interpreting alluvial archives: sedimentological factors in the British Holocene fluvial record. Quaternary Science Reviews, 24, 1873-1889.

Lewis, S. G., Maddy, D. and Scaife, R. G., 2001. The fluvial system response to abrupt climate change during the last cold stage: the Upper Pleistocene River Thames

fluvial succession at Ashton Keynes, UK. Global and Planetary Change, 28, 341-359.

Li, B. and Li, S-H., 2006a. Comparison of D_e estimates using the fast component and the medium component of quartz OSL. Radiation Measurements, 41, 125-136.

Li, S-H. and Li, B., 2006b. Dose measurement using the fast component of LM-OSL signals from quartz. Radiation Measurements, 41, 534-541.

Li, B., Li, S.-H. and Wintle, A.G., 2008. Overcoming environmental dose rate changes in luminescence dating of waterlain deposits. Geochronometria, 30, 33-40.

Li, B, Li, S.-H., Duller, G.A.T. and Wintle, A.G., 2011. Infrared stimulated luminescence measurements of single grains of K-rich feldspar for isochron dating. Quaternary Geochronology, 6, 71-81.

Liu, L., 1996. Settlement patterns chiefdom variability and the development of early states in North China. Journal of Anthropological Archaeology, 15, 237-288.

Liu, L., 2000. The development and decline of social complexity in northern China. Indo-Pacific Prehistory Association Bulletin, 4, 14-34.

Liu, T.S., Ding, Z.L. and Rutter, N., 1999. Comparison of Milankovitch periods between continental loess and deep sea records over the last 2.5 Ma. Quaternary Science Reviews, 18, 1205-1212.

Liu, X., Liu, Z., Kutzbach, J.E., Clemens, S.C. and Prell, W.L., 2006. Hemispheric insolation forcing of the Indian Ocean and Asian Monsoon: local versus remote impacts. Journal of Climate, 19, 6195-6208.

Lowick, S.E., Preusser, F. and Wintle, A.G., 2010. Investigating quartz optically stimulated luminescence dose-response curves at high doses. Radiation Measurements, 45, 975-984.

MacDonald, G., 2011. Potential influence of the Pacific Ocean on the Indian summer monsoon and Harappan decline. Quaternary International, 229, 140-148.

Macklin, M.G., Johnstone, E. and Lewin, J., 2005. Pervasive and long-term forcing of Holocene river instability and flooding in Great Britain by centennial-scale climate change. The Holocene, 15, 937-943.

Macklin, M.G., Benito, G., Gregory, K.J., Johnstone, E., Lewin, J., Michczynska, D.J., Soja, R., Starkel, L. and Thorndycraft, V.R., 2006. Past hydrological events reflected in the Holocene fluvial record of Europe. Catena, 66, 145–154.

Macklin, M.G., Jones, A.F. and Lewin, J., 2010. River response to rapid Holocene environmental change: evidence and explanation in British catchments. Quaternary Science Reviews, 29, 1555-1576.

Macklin, M. G., Jones, A. F. and Lewin, J., 2011. Comment: Cumulative probability functions and their role in evaluating the chronology of geomorphological events during the Holocene. Chiverrell, R.C., Thorndycraft, V.R. and Hoffmann, T.O., Journal of Quaternary Science, 26, 76-85. Journal of Quaternary Science, 26, 238-240.

MacMahon, D., 2006. Half-life evaluations for ^{3}H, ^{90}Sr and ^{90}Y. Applied Radiation and Isotopes, 64, 1417-1419.

Madella, M. and Fuller, D.Q., 2006. Palaeoecology and the Harappan Civilisation of South Asia: a reconsideration. Quaternary Science Reviews, 25, 1283-1301.

Madsen, A.T. and Murray, A.S., 2009. Optically stimulated luminescence dating of young sediments: a review. Geomorphology, 109, 3-16.

Madsen, A.T., Duller, G.A.T., Donnelly, J.P., Roberts, H.M. and Wintle, A.G., 2009. A chronology of hurricane landfalls at Little Sippewissett Marsh, Massachusetts, USA, using optical dating. Geomorphology, 109, 36-45.

Magny, M., Vanniere, B., Zanchetta, G., Fouache, E., Touchais, G., Petrika, L., Coussot, C., Walter-Simonnet, A.-V. and Arnaud, F., 2009. Possible complexity of the climatic event around 4300 – 3800 cal BP in the central and western Mediterranean. The Holocene, 19, 823-833.

Maisels, C.K., 2001. Early civilisations of the world. Routledge, London.

Mallah, Q.H., 2010. Current studies on the Indus Civilisation. In: Osada, T., Uesugi, A. (eds.). Indus Project Series, Manohar Publishers, India. Pp. 27-76.

Markey, B.G., Bøtter-Jensen, L. and Duller, G.A.T., 1997. A new flexible system for measuring thermally and optically stimulated luminescence. Radiation Measurements, 27, 83-89.

Marshal, J., 1931. Mohenjo-Daro and the Indus Civilisation. Probsthain, London.

Matthews, R., 2003. The archaeology of Mesopotamia: theories and approaches. Routledge, London.

McIntosh, J., 2007. The Ancient Indus Valley: new perspectives. ABC-CLIO, Santa Barbara.

Meadow, R.H., 1993. The past, present, and future of bioarchaeological studies in Pakistan with specific reference to Mohenjo-Daro and the Indus Civilisation. Pakistan Archaeology, 28, 183-215.

Meadow, R.H., 1998. The origins and spread of agriculture and pastoralism in northwestern South Asia. In Harris, D.R. (ed.). The origins and spread of agriculture and pastoralism in Eurasia. University College London Press, London. Pp. 309-412.

Mejdahl, V., 1979. Thermoluminescence dating: beta-dose attenuation in quartz grains. Archaeometry, 21, 61-72.

Mejdahl, V., 1987. Internal radioactivity in quartz and feldspar grains. Ancient TL, 5, 10-17.

Misra, V.N., 1984. Climate: a factor in the rise and fall of the Indus Civilisation. In: Lal, B.B. and Gupta, S.P. (eds.). Frontiers of the Indus Civilisation. Books and Books, New Delhi. Pp. 461-489.

Morley, J.J. and Heusser, L.E., 1997. Role of orbital forcing in east Asian monsoon climates during the last 350 kyr: evidence from terrestrial and marine climate proxies from core RC14-99. Paleoceanography, 12, 483-494.

Morrill, C., Overpeck, J.T. and Cole, J.E., 2003. A synthesis of abrupt changes in the Asian summer monsoon since the last deglaciation. The Holocene, 13, 465-476.

Mughal, M.R., 1990. Further evidence of the Early Harappan culture in the Greater Indus Valley. South Asian Studies, 6, 175-200.

Mughal, M.R., 1996. Archaeological sites and monuments in Punjab: preliminary results of explorations, 1992-1996. In Iqbal, F., Khan, M.A. and Hassan, M. (eds.). Pakistan Archaeology, Volume 29.

Mughal, M. R., 1997. Ancient Cholistan: archaeology and architecture. Ferozsons, Lahore.

Murray, A.S., 1981. Environmental radioactivity studies relevant to thermoluminescence dating. Unpublished PhD thesis, Oxford University.

Murray, A.S. and Roberts, R.G., 1998. Measurement of the equivalent dose in quartz using a regenerative-dose single-aliquot protocol. Radiation Measurements, 29, 503-515.

Murray, A.S. and Wintle, A.G., 1998. Factors controlling the shape of the OSL decay curve in quartz. Radiation Measurements, 29, 65-79.

Murray, A.S. and Wintle, A.G., 1999. Isothermal decay of optically stimulated luminescence in quartz. Radiation Measurements, 30, 119-125.

Murray, A.S. and Wintle, A.G., 2000. Luminescence dating of quartz using an improved single-aliquot regenerative-dose protocol. Radiation Measurements 32, 57-73.

Murray, A.S. and Olley, J. M., 2002. Precision and accuracy in the optically stimulated luminescence dating of sedimentary quartz: a status review. Geochronometria, 21, 1-16.

Murray, A.S. and Wintle, A.G., 2003. The single aliquot regenerative dose protocol: potential for improvements in reliability. Radiation Measurements, 37, 377-381.

Murray, A. S., Olley, J. M. and Caitcheon, G. G., 1995. Measurement of equivalent doses in quartz from contemporary water-lain sediments using optically stimulated luminescence. Quaternary Science Reviews 14, 365-371.

Murray, A.S., Wintle, A.G. and Wallinga, J., 2002. Dose estimation using quartz OSL in the non-linear region of the growth curve. Radiation Protection Dosimetry, 101, 371-374.

Murray, A.S., Svendsen, J.-I., Mangerud, J. and Astakhov, V.I., 2007. Testing the accuracy of quartz OSL dating using a known-age Eemian site on the river Sula, northern Russia. Quaternary Geochronology, 2, 102-109.

Murray, A.S., Buylaert, J.-P., Henriksen, M., Svendsen, J.-I. and Mangerud, J., 2008. Testing the reliability of quartz OSL dating beyond the Eemian. Radiation Measurements, 43, 776-780.

Neff, U., Burns, S.J., Mangini, A., Mudelsee, M., Fleitmann, D. and Matter, A., 2001. Strong coherence between solar variability and the monsoon in Oman between 9 and 6 kyr ago. Nature, 411, 290-293.

NOSAMS, 2012. National Ocean Sciences Accelerator Mass Spectrometry Facility. http://www.whoi.edu/nosams/page.do?pid=40135 [access date 13th July 2012].

O'Sullivan, P., 2008. The 'collapse' of civilizations: what palaeoenvironmental reconstruction cannot tell us, but anthropology can. The Holocene, 18, 45-55.

Oldham, R.D., 1886. On the probable changes in the geography of the Punjab and its rivers – historio-geographical study. Journal of Asiatic Society, 55, 322-343.

Olley, J.M., Murray, A.S. and Roberts, R.G., 1996. The effects of disequilibria in the uranium and thorium decay chains on burial dose rates in fluvial sediments. Quaternary Science Reviews (Quaternary Geochronology), 15, 751-760.

Olley, J.M., Caitcheon, G.G. and Murray, A.S., 1998. The distribution of apparent dose as determined by optically stimulated luminescence in small aliquots of fluvial quartz: implications for dating young sediments. Quaternary Geochronolgoy, 17, 1033-1040.

Olley, J.M., Caitcheon, G.G. and Roberts, R.G., 1999. The origin of dose distributions in fluvial sediments, and the prospect of dating single grains from fluvial deposits using optically stimulated luminescence. Radiation Measurements, 30, 207-217.

Olley, J.M., De Deckker, P., Roberts, R.G., Fifield, L.K., Yoshida, H. and Hancock, G., 2004a. Optical dating of deep-sea sediments using single grains of quartz: a comparison with radiocarbon. Sedimentary Geology, 169,175–189.

Olley, J.M., Pietsch, T. and Roberts, R.G., 2004b. Optical dating of Holocene sediments from a variety of geomorphic setting using single grains of quartz, Geomorphology, 60, 337–358.

Overpeck, J., Anderson, D.M., Trumbore, S. and Prell, W.L, 1996. The southwest Indian Monsoon over the last 18,000 years. Climate Dynamics, 12, 213-225.

Owen, L.A., Kamp, U., Spencer, J.Q. and Haserodt, K., 2002. Timing and style of Late Quaternary glaciation in the eastern Hindu Kush, Chitral, northern Pakistan: a review and revision of the glacial chronology based on new optically stimulated luminescence dating. Quaternary International, 97-98, 41-55.

Pandey, S. and Chatterji, P.C., 1970. Genesis of Mitha Ranns, Kharia Rann and Kanodurala Ranns in the Great Indian Desert. Annals of Arid Zone, 9, 175-180.

Pawley, S.M., Bailey, R.M., Rose, J., Moorlock, B.S.P., Hamblin, R.J.O., Booth, S.J. and Lee, J.R., 2008. Age limits on Middle Pleistocene glacial sediments from OSL dating, north Norfolk, UK. Quaternary Science Reviews, 27, 1363-1377.

Pawley, S.M., Toms, P., Armitage, S.J. and Rose, J., 2010. Quartz luminescence dating of Anglian Stage (MIS 12) fluvial sediments: comparison of SAR age

estimates to the terrace chronology of the Middle Thames valley, UK. Quaternary Geochronology, 5, 569-582.

Phadtare, N.R., 2000. Sharp decrease in summer monsoon strength 4000-3500 cal yr BP in the central higher Himalaya of India based on pollen evidence from alpine peat. Quaternary Research, 53, 122-129.

Possehl, G.L., 1994. Radiometric dates for South Asian archaeology, an occasional publication of the Asia section. University of Pennsylvania Museum, Philadelphia.

Possehl, G.L., 1996. Climate and the eclipse of the ancient cities of the Indus. In: Dalfes, H.N., Kukla, G. and Weiss, H. (eds.). Third millennium BC climate change and Old World collapse. (NATO ASI, Series 1: Global Environment Change, vol. 49.) Springer, New York. Pp. 193–244.

Possehl, G.L., 1997. The transformation of the Indus Civilisation. Journal of World Prehistory, 11, 425-472.

Possehl, G.L., 1998. Sociocultural complexity without the state: the Indus Civilisation. In: Feinman, G.M. and Marcus, J. (eds.). The archaic state. School of American Research, Santa Fe. Pp. 261-291.

Possehl, G.L., 1999. The Indus age: the beginnings. University of Pennsylvania Press, Philadelphia.

Possehl, G.L., 2002. The Indus civilisation: a contemporary perspective. Altamira Press, California.

Prasad, S. and Enzel, Y., 2006. Holocene paleoclimates of India. Quaternary Research, 66, 442-453.

Prasad, S., Kusumgar, S. and Gupta, S.K., 1997. A mid-late Holocene record of palaeoclimatic changes from Nal Sarovar – A palaeodesert margin lake in western India. Journal of Quaternary Science, 12, 153-159.

Prell, W.L., 1984. Variation of monsoonal upwelling: a response to changing solar radiation. In: Hansen, J.E. and Takahashi, T. (eds.). Climate processes and climate sensitivity. Geophysical Monograph Series, AGU Washington. Pp. 48-57.

Prell, W.L. and Kutzbach, J.E., 1987. Monsoon variability over the past 150,000 years. Journal of Geophysical Research, 92, 8411-8425.

Prell, W.L. and Kutzbach, J.E., 1992. Sensitivity of the Indian monsoon to forcing parameters and implications for its evolution. Nature, 350, 647-652.

Prescott, J.R. and Hutton, J.T., 1994. Cosmic ray and gamma ray dosimetry for TL and ESR. Nuclear Tracks and Radiation Measurements, 14, 223-227.

Prescott, J.R. and Robertson, B.G., 1997. Sediment dating by luminescence: a review. Radiation Measurements, 27, 893-922.

Prescott, J.R. and Hutton, J.T., 1998. Cosmic ray contributions to dose rates for luminescence and ESR dating: large depths and long-term time variations. Radiation Measurements, 23, 497-500.

Prescott, J.R. and Stephan, L.G., 1982. The contribution of cosmic radiation to the environmental dose for thermoluminescence dating. PACT, 6, 17-25

Preusser, F., Chithambo, M.L., Götte, T., Martini, M., Ramseyer, K., Sendezera, E.J., Susino, G.J., and Wintle, A.G., 2009. Quartz as a natural luminescence dosimeter. Earth-Science Reviews, 97, 184-214.

Radhakrishna, B.P. and Merh S.S., 1999. Vedic Saraswati: evolutionary history of a lost river of Northwestern India. Geological Society of India, Delhi.

Raikes, R.L., 1964. The end of the ancient cities of the Indus. American Anthropologist, 66, 284-299.

Raikes, R.L., 1965. The Mohenjo-Daro floods. Antiquity, 39, 193-2003.

Raikes, R.L., 1969. Kalibangan: Death from natural causes. Antiquity, 42, 286-291.

Rao, Y.P., 1976. South west Monsoon. India Meteorological Department, New Delhi.

Raymo, M.E. and Ruddiman, W.F., 1992. Tectonic forcing of the late Cenozoic climate. Nature, 359, 117-122.

Raymo, M.E., Ruddiman, W.F. and Froelich, P., 1988. Influence of late Cenozoic mountain building on ocean geochemical cycles. Geology, 16, 649-653.

Ree-Jones, J. and Tite, M.S., 1997. Optical dating results for British archaeological sediments. Archaeometry, 39, 177-187.

Reimann, T, Thomsen, K.J., Jain, M., Murray, A.S. and Frechen, M., 2012. Single-grain dating of young sediments using the pIRIR signal from feldspar. Quaternary Geochronology, 11, 28-41.

Reimer, P.J., Baillie, M.G.L., Bard, E., Bayliss, A., Beck, J.W., Bertrand, C.J.H, Blackwell, P.G., Buck, C.E., Burr, G.S., Cutler, K.B., Damon, P.E., Edwards, R.L., Fairbanks, R.G., Friedrich, M., Guilderson, T.P., Hogg, A.G., Hughen, K.A., Kromer, B., McCormac, G., Manning, S., Bronk Ramsey, C., Reimer, R.W., Remmele, S.,

Southon, J.R., Stuiver, M., Talamo, S., Taylor, F.W., van der Plicht, J. and Weyhenmeyer, C.E., 2004. IntCal04 terrestrial radiocarbon age calibration 0-26 cal kyr BP. Radiocarbon, 46, 1029-1058.

Renfrew, C., 1979. Systems collapse as social transformation: catastrophe and anastrophe in early state societies. In: Renfrew, C. and Cooke, K. (eds.). Transformations: mathematical approaches to culture change. Academic Press, New York. Pp. 481-506.

Rhodes, E.J., 2011. Optically stimulated luminescence dating of sediments over the past 200,000 years. Annual Review of Earth and Planetary Sciences, 39, 461-488.

Rhodes, E.J., Singarayer, J.S., Raynal, J.-P., Westaway, K.E. and Sbihi-Alaoui, F.Z., 2006. New age estimates for the Palaeolithic assemblages and Pleistocene succession of Casablanca, Morocco. Quaternary Science Reviews, 25, 2569-2585.

Richards, B.W.M., 2000. Luminescence dating of Quaternary sediments in the Himalaya and High Asia: a practical guide to its use and limitations for constraining the timing of glaciation. Quaternary International, 56-66, 49-61.

Rittenour, T.M., 2008. Luminescence dating of fluvial deposits: applications to geomorphic, palaeoseismic and archaeological research. Boreas, 37, 613-635.

Rittenour, T. M., Goble, R. J. and Blum, M. D., 2003. An optical age chronology of Late Pleistocene fluvial deposits in the Northern Lower Mississippi Valley. Quaternary Science Reviews, 22, 1105-1110.

Roberts, H.M., 2007. Assessing the effectiveness of the double-SAR protocol in isolating a luminescence signal dominated by quartz. Radiation Measurements, 42, 1627-1636.

Roberts, H.M., 2008. The development and application of luminescence dating to loess deposits: a perspective on the past, present and future. Boreas, 37, 483-507.

Roberts, H.M. and Wintle, A.G., 2001. Equivalent dose determinations for polymineralic fine-grains using the SAR protocol: application to a Holocene sequence of the Chinese Loess Plateau. Quaternary Science Reviews, 20, 859-863.

Roberts, H.M. and Duller, G.A.T., 2004. Standardised growth curves for optical dating of sediment using multiple-grain aliquots. Radiation Measurements, 38, 241-252.

Roberts, H.M., Durcan, J.A. and Duller, G.A.T., 2009. Exploring procedures for the rapid assessment of optically stimulated luminescence range-finder ages. Radiation Measurements, 44, 582-587.

Roberts, R.G., Galbraith, R.F., Olley, J.M., Yoshida, H. and Laslett, G.M., 1999. Optical dating of single and multiple grains of quartz from Jinmium rock shelter, northern Australia: part II, results and implications. Archaeometry, 41, 365-395.

Roberts, R.G., Galbraith, R.F., Yoshida, H., Laslett, G.M. and Olley, J.M., 2000. Distinguishing dose populations in sediment mixtures: a test of single-grain optical dating procedures using mixtures of laboratory-dosed quartz. Radiation Measurements, 32, 459-465.

Rodnight, H., 2006. Developing a luminescence chronology for late Quaternary fluvial change in South African floodplain wetlands. Unpublished PhD thesis, University of Wales, Aberystwyth.

Rodnight, H., Duller, G.A.T., Wintle, A.G. and Tooth, S., 2006. Assessing the reproducibility and accuracy of optical dating of fluvial deposits. Quaternary Geochronology, 1, 109-120.

Rose, J., 2007. The use of time units in Quaternary Science Reviews, 26, 1193.

Rowan, A.V., Roberts, H.M., Jones, M.A., Duller, G.A.T., Covey-Crump, S.J. and Brocklehurst, S.H., 2012. Optically stimulated luminescence dating of glaciofluvial sediments on the Canterbury Plains, South Island, New Zealand. Quaternary Geochronology, 8, 10-22.

Rowley, D.B., 1996. Age of initiation of collision between India and Asia; a review of stratigraphic data. Earth and Planetary Science Letters, 145, 1-13.

Roy, P.D., Smykatz-Kloss, W. and Sinha, R., 2006. Late Holocene geochemical history inferred from Sambhar and Didwana playa sediments, Thar Desert, India: comparison and synthesis. Quaternary International, 144, 84-98.

Roy, P.D., Smykatz-Kloss, W. and Morton, O., 2008. Geochemical zones and reconstruction of late Holocene environments from shallow core sediments of the Pachapadra palaeo-lake, Thar Desert, India. Chemie der Erde, 68, 313-322.

Ruddiman, W.F., 2001. Earths climate: past and future. W.H. Freeman and Co, New York.

Sahai, B., 1999. Unravelling the lost Saraswati. In: Radhakrishna, B.P. and Merh, S.S. (eds.). Vedic Saraswati: evolutionary history of a lost river of Northwestern India. Geological Society of India, 42, 121-141.

Saini, H.S. and Mujtaba, S.A.I., 2010. Luminescence dating of the sediments from a buried channel loop in Fatehabad area, Haryana: insight into vedic Saraswati River and its environment. Geochronometria, 37, 29-35.

Saini, H.S., Tandon, S.K., Mujtaba, S.A.I., Pant, N.C. and Khorana, R.K., 2009. Reconstruction of buried channel-floodplain systems of the northwestern Haryana Plains and their relation to the 'Vedic' Saraswati. Current Science, 97, 1634-1643.

Sanderson, D.C.W., Bishop, P., Houston, I. and Boonsener, M., 2001. Luminescence characterisation of quartz-rich cover sands from NE Thailand. Quaternary Science Reviews, 20, 893-900.

Sanderson, D.C.W., Bishop, P., Start, M.T. and Spencer, J.Q., 2003. Luminescence dating of anthropogenically reset canal sediments from Angkor Borei, Mekong Delta, Cambodia. Quaternary Science Reviews, 22, 1111-1121.

Schmidt, C., Kreutzer, S., Fattahi, M., Bailey, R.M., Zander, A. and Zoeller, L., 2011. On the luminescence signals of empty sample carriers. Ancient TL, 29, 65-74.

Schuldenrein, J., Wright, R.P., Mughal, M.R. and Khan, M.A., 2004. Landscapes, soils and mound histories of the Upper Indus Valley, Pakistan: new insights on the Holocene environments near ancient Harappa. Journal of Archaeological Science, 31, 777-797.

Schulz, H., von Rad, U., Erlenkeuser, H. and von Rad, U., 1998. Correlation between Arabian Sea and Greenland climate oscillations of the past 110,000 years. Nature, 393, 54-57.

Schumm, S. A., 1977. The Fluvial System. John Wiley and Sons, New York.

Shukla, J. and Paolina, D., 1983. The southern oscillation and long range forecasting of the summer monsoon rainfall over India. Monthly Weather Review, 111, 1830-1837.

Singarayer, J.S. and Bailey, R.M., 2003. Further investigations of the quartz optically stimulated luminescence components using linear modulation. Radiation Measurements, 37, 451-458.

Singarayer, J.S. and Bailey, R.M., 2004. Component-resolved bleaching spectra of quartz optically stimulated luminescence: preliminary results and implications for dating. Radiation Measurements, 38, 111-118.

Singarayer, J.S., Bailey, R.M. and Rhodes, E.J., 2000. Potential of the slow component for quartz OSL for age determination of sedimentary samples. Radiation Measurements, 32, 873-880.

Singh, G., 1971. The Indus Valley culture seen in the context of postglacial climatic and ecological studies in north-west India. Archaeology and Physical Anthropology of Oceania, 6, 177-189.

Singh, G., Joshi, R.D. and Singh, A.B., 1972. Stratigraphic evidence for the age and development of three salt lake deposits in Rajasthan, India. Quaternary Research, 2, 496-505.

Singh, G., Joshi, R.D. and Singh, A.B., 1973. Pollen-rain from the vegetation of northwest India. New Phytologist, 72, 191-206.

Singh, G., Joshi, R.D., Chopra, S.K. and Singh, A.B., 1974. Late Quaternary history of vegetation and climate in the Rajasthan Desert, India. Philosophical Transactions of the Royal Society of London, 267, 467-501.

Singhvi, A.K. and Porat, N., 2008. Impact of luminescence dating on geomorphological and palaeoclimate research in drylands. Boreas, 37, 536-558.

Singhvi, A.K. and Kale, V.S., 2009. Palaeoclimate studies in India: late ice age to present. Indian Science Academy, New Delhi.

Singhvi, A.K., Rupakumar, K., Thamban, M., Gupta, A.K., Kale, V.S., Yadav, R.R., Bhattacharya, A., Phadtare, N.R., Roy, P.D., Chauhan, M.S., Chauhan, O.S., Cahkravorty, S., Sheikh, M.M., Manzoor, N., Adnan, M., Ashraf, J., Khan, A.M., Quadir, D.A., Devkota, L.P. and Shrestha, A.B., 2010a. Instrumental, terrestrial and marine records of the climate of South Asia during the Holocene: present status, unresolved problems and societal aspects. In: Mitra, A.P. and Sharma, C. (eds.). Global environmental changes in South Asia: a regional perspective. Capital Publishing, New Delhi. Pp. 54-124.

Singhvi, A.K., Williams, M.A.J., Rajaguru, S.N., Misra, V.N., Chawla, S., Stokes, S., Chauhan, N., Francis, T., Ganjoo, R.K. and Humphreys, G.S., 2010b. A ~200 ka record of climatic change and dune activity in the Thar Desert, India. Quaternary Science Reviews, 29, 3095-3105.

Sinha, R. and Raymahashay, B.C., 2004. Evaporite mineralogy and geochemical evolution of the Sambhar Salt Lake, Rajasthan, India. Sedimentary Geology, 166, 59-71.

Sinha, R. and Sarkar, S., 2009. Climate-induced variability in the Late Pleistocene-Holocene fluvial and fluvio-deltaic successions in the Ganga plains, India. Geomorphology, 113, 173-188.

Sinha, R., Smykatz-Kloss, W., Stuben, D., Harrison, S.P., Berner, Z. and Kramar, U., 2006. Late Quaternary palaeoclimatic reconstruction from the lacustrine sediments of the Sambhar playa core, Thar Desert margin, India. Palaeogeography, Palaeoclimatology, Palaeoecology, 233, 252-270.

Sinha, R., Kuman, R., Sinha, S., Tandon, S.K. and Gibling, M.R., 2007. Late Cenozoic fluvial successions in northern and western India: an overview and synthesis. Quaternary Science Reviews, 26, 2801-2822.

Sinha, R., Yadev, G.S., Gupta, S., Singh, A. and Lahiri, S.K., in press. Geo-electric resistivity evidence for subsurface palaeochannel systems adjacent to Harappan sites in northwest India. Quaternary International, doi:10.1016/ j.quaint.2012.08.002.

Sirocko, F., Sarnthein, M., Erlenkeuser, H., Lange H., Arnold, M. and Duplessy, J.-C., 1993. Century scale events in monsoon climate over the past 24,000 years. Nature, 364, 322-324.

Sirocko, F., Garbe-Schonberg, D. and Devey, C., 2000. Processes controlling trace-element geochemistry of Arabian Sea sediments during the last 25,000 years. Global Planetary Change, 26, 217-303.

Smedley, R.K, Duller, G.A.T., Pearce, N.J.G. and Roberts, H.M., 2012. Determining the K-content of single-grains of feldspar for luminescence dating. Radiation Measurements, 47, 790-796.

Smith, B.W., 1988. Zircons from sediments: a combined OSL and TL auto-regenerative dating technique. Quaternary Science Reviews, 7, 401-406.

Smith, B.W. and Rhodes, E.J., 1994. Charge movements in quartz and their relevance to optical dating. Radiation Measurements, 23, 329-333.

Smith, B.W., Rhodes, E.J., Stokes, S. and Spooner, N.A., 1990. The optical dating of sediments using quartz. Radiation Protection Dosimetry, 34, 75-78.

Solongo, S., Wagner, G.A. and Galbaatar, T., 2006. The estimation of D_e using the fast and medium components in fired quartz from archaeological site Karakorum, Mongolia. Radiation Measurements, 41, 1001-1008.

Sood, R.K. and Sahai, B., 1983. Hydrographic changes in northwestern India. Man and Environment, 7, 166-169.

Spencer, J.Q. and Owen, L.A., 2004. Optically stimulated luminescence dating of Late Quaternary glaciogenic sediments in the upper Hunza valley: validating the timing of glaciation and assessing dating methods. Quaternary Science Reviews, 23, 175-191.

Spooner, N. A., 1994. On the optical dating signal from quartz. Radiation Measurements, 23, 593-600.

Spooner, N.A. and Questiaux, D.G., 2000a. Kinetics of red, blue and UV thermoluminescence and optically stimulated luminescence from quartz. Radiation Measurements, 32, 659-666.

Spooner, N.A. and Allsop, A., 2000b. The spatial variation of dose-rate from $^{90}Sr/^{90}Y$ beta sources used in luminescence dating. Radiation Measurements, 32, 49-56.

Spooner, N.A., Prescott, J.R. and Hutton, J.T., 1988. The effect of illumination wavelength on the bleaching of the thermoluminescence (TL) of quartz. Quaternary Science Reviews, 7, 325-329.

Srivastava, P., Juyal, N., Singhvi, A.K., Wasson, R.J. and Bateman, M.D., 2001. Luminescence chronology of river adjustment and incision of Quaternary sediments in the alluvial plain of the Sabarmati River, north Gujarat, India. Geomorphology, 36, 217-229.

Srivastava, P., Singh, I.B., Sharma, S., Shukla, W.K. and Singhvi, A.K., 2003. Late Pleistocene-Holocene hydrologic changes in the inter-fluve areas of the central Ganga Plain, India. Geomorphology, 54, 279-292.

Stanley, D.J., Chen, Z.Y. and Song, J., 1999. Inundation, sea-level rise and transition from Neolithic to Bronze Age culture, Yangtze delta, China. Geoarchaeology, 14, 15-26.

Staubwasser, M. and Weiss, H., 2006. Holocene climate and cultural evolution in late prehistoric-early historic West Asia. Quaternary Research, 66, 372-387.

Staubwasser, M., Sirocko, F., Grootes, P.M. and Segl. M., 2003. Climate change at the 4.2 ka BP termination of the Indus valley civilisation and Holocene south Asian monsoon variability. Geophysical Research Letters, 30, doi:10.1029/2002GL016822.

Steffen, D., Preusser, F. and Schlunegger, F., 2009. OSL quartz age underestimation due to unstable signal components. Quaternary Geochronology, 4, 353-362.

Stein, M.A., 1942. A survey of ancient sites along the 'lost' Sarasvati River. Geographical Journal, 99, 173-182.

Stirling, R.J., Duller, G.A.T. and Roberts, H.M., 2012. Developing a single-aliquot protocol for measuring equivalent dose in biogenic carbonates. Radiation Measurements, 47, 725-731.

Stokes, S. 1999. Luminescence dating application in geomorphological research. Geomorphology, 29, 153-171.

Stone, A.E. and Thomas, D.S.G., in press. Casting new light on late Quaternary environmental palaeohydrological change in the Namib Desert: a review of the application of optically stimulated luminescence in the region. Journal of Arid Environments, doi: 10.1016/j.aridenv.2012.01.009.

Stuiver, M., Reimer, P.J., Bard, E., Beck, J.W., Burr, G.S., Hughen, K.A., Kromer, B., McCormac, G., der Plicht, V.J. and Spurk, M., 1998. INTCAL98 radiocarbon age calibration, 24,000-0 cal BP. Radiocarbon, 40, 1041-1083.

Summa-Nelson, M. and Rittenour, T.M., 2012. Application of OSL dating to middle to late Holocene arroyo sediments in Kanab Creek, southern Utah, USA. Quaternary Geochronology, 10, 167-174.

Sun, X.J. and Chen, Y.S., 1991. Palynological records of the last 11,000 years in China. Quaternary Science Reviews, 10, 537-544.

Swain, A.M., Kutzbach, J.E. and Hastenrath, S., 1983. Monsoon climate of Rajasthan for the Holocene: estimates of precipitation based on pollen and lake levels. Quaternary Research, 19, 1-17.

Tainter, J., 1988. The collapse of complex societies. Cambridge University Press, Cambridge.

Tandon, S.K., Sareen, B.K., Someshwar Rao, M. and Singhvi, A.K., 1997. Aggradation history and luminescence chronology of Late Quaternary semi-arid sequences of the Sabarmati basin, Gujarat, Western India. Palaeogeography, palaeoclimatology, palaeoecology, 128, 339-357.

Taylor, T., 2008. Prehistory vs. archaeology: terms of engagement. Journal of Prehistory, 21, 1-18.

Templer, R.H and Smith, B.W., 1988. Auto-regenerative TL dating of zircon from fired minerals. Nuclear Tracks and Radiation Measurements, 14, 329-332.

Thamban, M., Rao, V.P. and Schneider, R.R., 2002. Reconstruction of late Quaternary monsoon oscillations based on clay mineral proxies using sediment cores from the western margin of India. Marine Geology, 186, 527-539.

Thamban, M., Kawahata, H. and Rao, V.P., 2007. Indian summer monsoon variability during the Holocene as recorded in sediments of the Arabian Sea: timing and implications. Journal of Oceanography, 63, 1009-1020.

Thomas, J.V., Kar, A., Kailath, A.J., Juyal, N., Rajguru, S.N. and Singhvi, A.K., 1999. Late Pleistocene-Holocene history of aeolian accumulation in the Thar Desert, India. Zeitschrift fur Geomorphologie, 116, 181-194.

Thomas, P.J., Juyal, N., Kale, V.S. and Singhvi, A.S., 2007. Luminescence chronology of late Holocene extreme hydrological events in the upper Penner River basin, South India. Journal of Quaternary Science, 22, 747-753.

Thomsen, K.J., Murray, A.S. and Bøtter-Jensen, L., 2005. Sources of variability in OSL dose measurements using single grains of quartz. Radiation Measurements, 39, 47-61.

Thomsen, K.J., Jain, M., Murray, A.S., Denby, P.M., Roy, N. and Bøtter-Jensen, L., 2008. Minimising feldspar contamination in quartz UV-OSL using pulsed blue stimulation. Radiation Measurements, 43, 752-757.

Thorlabs, 2008. S120VC Compact Photodiode Power Head with Silicon Detector [online]. Available at http://www.thorlabs.com/Thorcat/18300/18357-S01.pdf [Accessed 25th November 2010].

Thorndycraft, V.R. and Benito, G., 2006. The Holocene fluvial chronology of Spain: evidence from a newly compiled radiocarbon database. Quaternary Science Reviews, 25, 223-234.

Tian, G.J., 2000. The relationships between archaeological culture and ecological environment. In: Zhou, K.S. and Song, Y.Q. (eds.). Research of Environmental Archaeology. Science Press, Beijing. Pp. 72-80.

Tooth, S., 1999. Floodouts in Central Australia. In: Miller, A.J. and Gupta, A. (eds.). Varieties of Fluvial Form. Wiley and Sons, London. Pp. 219-247.

Tooth, S., 2012. Arid geomorphology: changing perspectives on timescales of change. Progress in Physical Geography, 36, 262-284.

Tooth, S., Rodnight, H., McCarthy, T.S., Duller, G.A.T. and Grundling, A.T., 2009. Late Quaternary dynamics of a South African floodplain wetland and the implications for assessing recent human impacts. Geomorphology, 106, 278-291.

Tsukamoto, S., Rink, W.J and Watanuki, T., 2003. OSL of tephric loess and volcanic quartz in Japan and an alternative procedure for estimating D_e from a fast OSL component. Radiation Measurements, 37, 459-465.

Tsukamoto, S., Nagashima, K., Murray, A.S. and Tada, R., 2011. Variations in OSL components from quartz from Japan sea sediments and the possibility of reconstructing provenance. Quaternary International, 234, 182-189.

Turner, J.N., Macklin, M.G., Jones, A.F. and Lewis, H., 2010. New perspectives on Holocene flooding in Ireland using meta-analysis of fluvial radiocarbon dates. Catena, 82, 183-190.

Van Campo, E., Duplessy, J.C. and Rossignol-Strick, M., 1982. Climatic conditions deduced from a 150-kyr oxygen isotope pollen record from the Arabian Sea. Nature, 296, 56-59.

Van der Plicht, H. and Hogg, A., 2006. A note on reporting radiocarbon. Quaternary Geochronology, 1, 237-240.

Vandenberghe, D., De Corte, F., Buylaert, J.-P., Kučera, J. and Van Den Haute, P., 2008. On the internal radioactivity in quartz. Radiation Measurements, 43, 771-775.

Vaughan, P.C., 1995. Functional analysis of samples of Neolithic, Chalcolithic and Bronze Age flints from Mehrgarh (Baluchistan, Pakistan). In: Jarrige, C., Jarrige, J.F., Meadow, R.H. and Quivron, G. (eds.). Mehrgarh: field reports 1974-1985 from Neolithic times to the Indus civilisation. Government of Sindh, Karachi. Pp. 614-625.

Vishnu-Mittre, 1993. The Harappan Civilisation and the need for a new approach. In Possehl, G. (ed.). Harappan Civilisation. Oxford and IBH Publishing, New Delhi. Pp.34-35.

Wallinga, J., 2002. Optically stimulated luminescence dating of fluvial deposits: a review. Boreas, 31, 303-322.

Wallinga, J., Bos, A.J.J. and Duller, G.A.T., 2008. On the separation of quartz OSL signal components using different stimulation modes. Radiation Measurements, 43, 742-747.

Wang, P., 2004. Cenozoic deformation and the history of sea-land interactions in Asia. In: Clift, P.D., Kuhnt, W., Wang, P. and Hayes, D.E. (eds.). Continent-ocean interactions within East Asian marginal seas. Geophysical Monograph Series, 149, 1-22.

Wang, Y., Cheng, H., Edwards, R.L., He, Y., Kong, X., An, Z., Wu, J., Kelly, M.J., Dykoski, C.A. and Li, X., 2005. The Holocene Asian Monsoon: links to solar changes and North Atlantic climate. Science, 308, 854-857.

Ward, S., Stokes, S., Bailey, R., Singarayer, J., Goudie, A. and Bray, H., 2003. Optical dating of quartz from young samples and the effects of pre-heat temperature. Radiation Measurements, 37, 401-407.

Wasson, R.J., 1984. The sedimentological basis of the Mohenjo-Daro flood hypothesis. Man and environment, 8, 88-90.

Wasson, R.J., 1987. The sedimentological basis of the Mohenjo-Daro flood hypothesis – a further comment. Man and environment, 11, 122-123.

Wasson, R.J., Smith, G.I. and Agrawal, D.P., 1984. Late Quaternary sediments, minerals and inferred geochemical history of Didwana lake, Thar desert, India. Palaeogeography, palaeoclimatology, palaeoecology, 46, 345-372.

Watanuki, T., 2002. Chronological study of loess palaeosol by improved method of luminescence dating and application to reconstruct past environmental changes. PhD Thesis, Tokyo Metropolitan University, unpublished.

Weber, S.A., 1999. Seeds of urbanism: palaeoethnobotany and the Indus Civilisation. Antiquity, 73, 813-826.

Weber, S.A., 2003. Archaeobotany at Harappa: indications for change. In: Weber, S.A. and Belcher, W.R. (eds.). Indus ethnobiology: new perspectives from the field. Lexington Books, Lanham. Pp. 175-198.

Webster, P.J., Magana, V.O., Palmer, T.N., Shukla, J., Tomas, R.A., Yanai, M. and Yasunari, T., 1998. Monsoons: processes, predictability and the prospects for prediction. Journal of Geophysical Research, 103, 14451-14510.

Wehausen, R. and Brumsack, H.J., 2002. Astronomical forcing of the East Asian monsoon mirrored by the composition of Pliocene South China Sea sediments. Earth and Planetary Science Letters, 201, 621-636.

Weiss, H. and Bradley, R.S., 2001. Archaeology. What drives societal collapse? Science, 291, 609-610.

Weiss, H., Courty, M.-A., Wetterstrom, W., Guichard, F., Senior, L., Meadow, R. and Curnow, A., 1993. The genesis and collapse of third millennium north Mesopotamian civilisation. Science, 261, 995-1003.

Wenxiang, W. and Tungshen, L., 2004. Possible role of the 'Holocene Event 3' on the collapse of Neolithic Cultures around the Central Plain of China. Quaternary International, 117, 153-166.

Wheeler, R.E.M., 1947. Harappan 1946: the defences and cemetery R-37. Ancient India, 3, 58-130.

Wheeler, R.E.M, 1953. The Indus Civilisation. Cambridge University Press, Cambridge.

Wilhelmy, H., 1969. The ancient river valley on the eastern border of the Indus Plain and the Saraswati problem. Zeitschrift fur Geomorphologie, 8, 76-93.

Williams, M.A.J., Williams, F.M., Duller, G.A.T., Munro, R.N., El Tom, O.A.M., Barrows, T.T., Macklin, M., Woodward, J., Talbot, M.R., Haberlab, D. and Fluin, J., 2010. Late Quaternary floods and droughts in the Nile valley, Sudan, new evidence from optically stimulated luminescence and AMS radiocarbon dating. Quaternary Science Reviews, 29, 1116-1137.

Wintle, A.G., 1973. Anomalous fading of thermoluminescence in mineral samples. Nature, 245, 143-144.

Wintle, A.G., 1978. A thermoluminescence dating study of some Quaternary calcite: potential and problems. Canadian Journal of Earth Sciences, 15, 1977-1986.

Wintle, A.G., 1997. Luminescence dating: laboratory procedures and protocols. Radiation Measurements, 27, 769-817.

Wintle, A.G., 2008a. Fifty years of luminescence dating. Archaeometry, 50, 276-312.

Wintle, A.G., 2008b. Luminescence dating: where it has been and where it is going. Boreas, 37, 471-482.

Wintle, A.G., 2010. Future directions of luminescence dating of quartz. Geochronometria, 37, 1-7.

Wintle, A.G. and Murray, A.S., 1997. The relationship between quartz thermoluminescence, photo-transferred thermoluminescence and optically stimulated luminescence. Radiation Measurements, 27, 611-624.

Wintle, A.G. and Murray, A.S., 1998. Towards the development of a pre-heat procedure for OSL dating of quartz. Radiation Measurements, 29, 81-94.

Wintle, A.G. and Murray, A.S., 1999. Luminescence sensitivity changes in quartz. Radiation Measurements, 30, 107-118.

Wintle, A.G. and Murray, A.S., 2006. A review of quartz optically stimulated luminescence characteristics and their relevance in single-aliquot regeneration dating protocols. Radiation Measurements, 41, 369-391.

Woodward, J.C., Macklin, M.G. and Welsby, D.A., 2001. The Holocene fluvial sedimentary record and alluvial geoarchaeology in the Nile Valley of northern Sudan. In: Maddy, D., Macklin, M.G. and Woodward, J.C. (eds.). River system basin sediments systems: archives of environmental change. Balkema, Rotterdam. Pp 327-355.

Wright, R.P., 2010. The ancient Indus. Cambridge University Press, Cambridge.

Wright, R.P., Schuldenrein, J. and Mughal, M.R., 2005. The emergence of satellite communities along the Beas drainage: Preliminary results from Lahoma Lal Tibba and Chak Purbane Syal. In Jarrige, C. (ed.). South Asian Archaeology. Recherche sur les Civilisations-ADF, Paris. Pp. 327-335.

Wright, R.P., Bryson, R.A. and Schuldenrein, J., 2008. Water supply and history: Harappa and the Beas regional survey. Antiquity, 82, 37-48.

Wu, W.X. and Liu, T.S., 2001. 4000 yr BP event and its implications for the origin of ancient Chinese civilisation. Quaternary Science, 5, 443-451.

Wu, J., Wang, Y., Cheng, H. and Edwards, L., 2009. An exceptionally strengthened East Asian summer monsoon event between 19.9 and 17.1 ka BP recorded in a Hulu stalagmite. Science in China series D: Earth Sciences, 42, 360-368.

Yah Pal, Sahai, B., Sood, R.K. and Agrawal, D.P., 1980. Remote sensing of the 'Lost' Saraswati River. Proceedings of the Indian Academy of Science, 89, 313-331.

Yoffee, N. and Cowgill, W., 1988. The collapse of the ancient Mesopotamian states and civilisations. University of Arizona Press, Tuscon.

Yokoyama, Y., Lambeck, K., DeDecker, P.l., Johnston, P. and Fifield, L., 2000. Timing of the Last Glacial Maximum from observed sea-level minima. Nature, 406, 713-716.

Yoshida, H., Roberts, R.G., Olley, J.M., Laslett, G.M. and Galbraith, R.F., 2000. Extending the age range of optical dating using single 'supergrains' of quartz. Radiation Measurements, 32, 439-446.

Zaicha, 2007. Hakra-Sutlej valley. [online] http://hakkra.blogspot.co.uk/ [access date 03rd July 2012].

Zhang, H.C., Ma, Y.Z., Wunnemann, B. and Pachur, H.J., 2000. A Holocene climatic record from arid northwestern China. Palaeogeography, palaeoclimatology, palaeoecology, 162, 389-401.

Zhang, R., Sumi, A. and Kimot, M., 1996. Impact of El Niño on the East Asian monsoon: a diagnostic study of the '86/87 and '91/92 events. Journal of the Meteorological Society of Japan. 74, 49-62.

Zhu, C., Yu, S.Y. and Lu, C.C., 1997. The study of Holocene environmental archaeological and extreme flood disaster in the Three Gorges of the Changjiang River and the Jianghan Plain. Acta Geographic Sinica, 52, 268-278.

Zhu, G.Y., Zhu, C., Shi, G.Y. and Sun, Z.B., 2008. Relations between man and nature reflected by the evolution of the Neolithic production tools in the Three Gorges region of the Yangtze River, China. Chinese Science Bulletin, 53, 95-106.

Zimmerman, D.W., 1971. Thermoluminescence dating using fine grains from pottery. Archaeometry, 13, 29-52.

Appendix A: Site stratigraphic logs

Stratigraphic logs of the sites sampled for OSL and ^{14}C dating. Sites with the prefixes 136-3, 136,-4, 136-6, 153-MAR-2 and 153-TIL-3 were sampled by Dr Anwar Alizai (Aberdeen University) in separate field trips and the logs for these sites were provided by him. A stratigraphic log for site 154-MGJ-3 was not drawn, because the dune site was composed of a massive sand unit, and instead a schematic profile of the dune, showing the depths sampled is presented.

Site prefix 136-

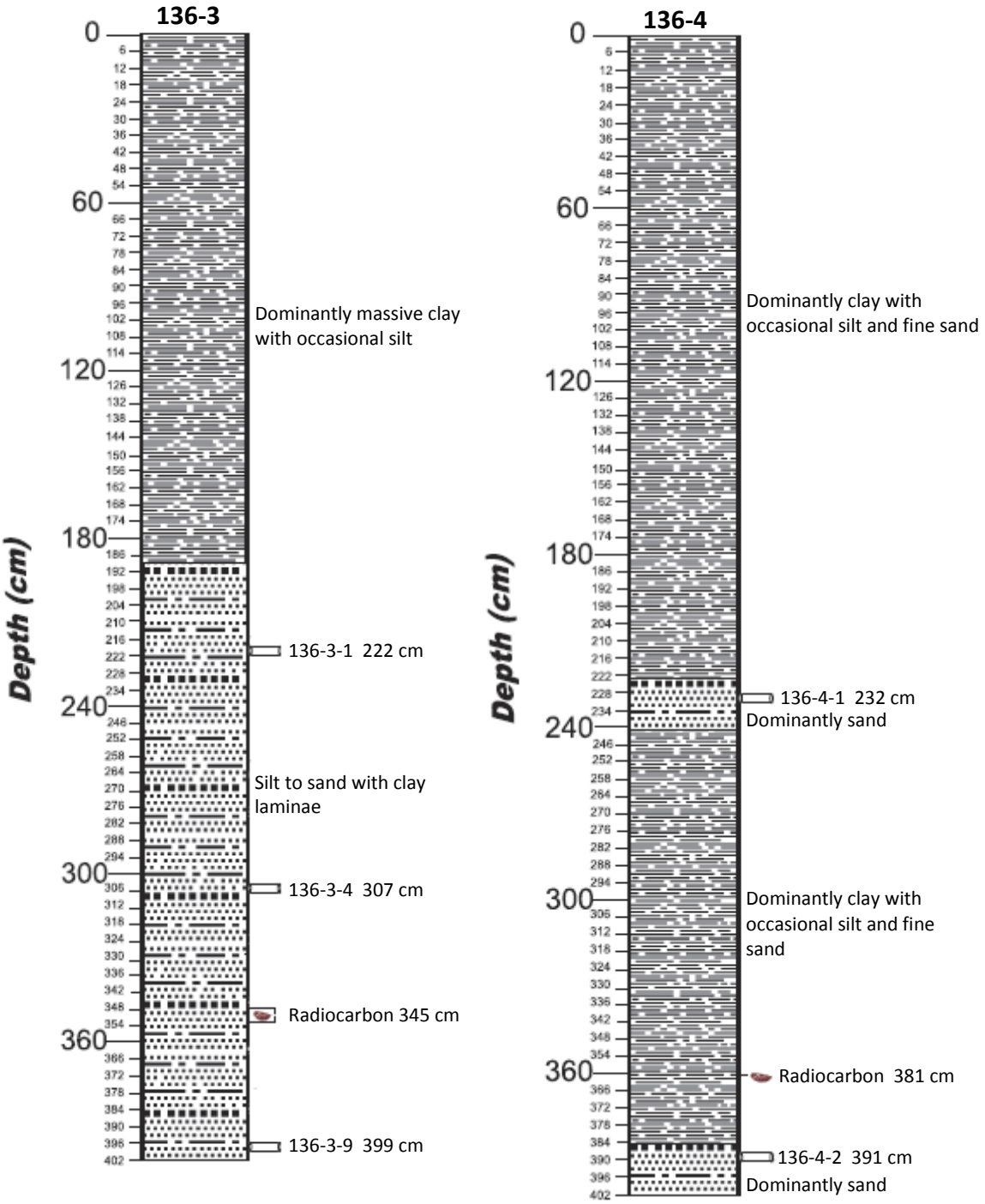

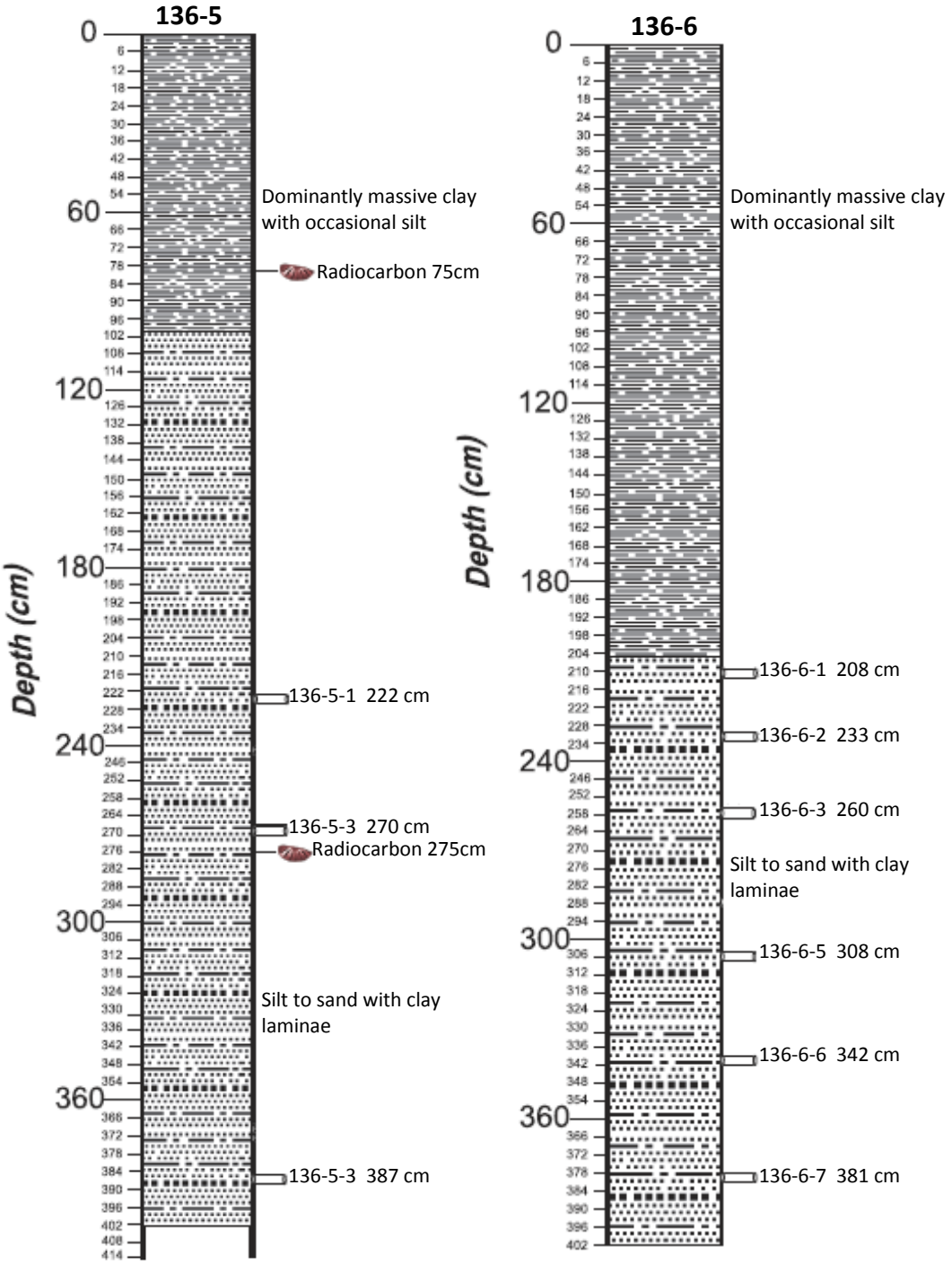
136-5
Depth (cm)
Dominantly massive clay with occasional silt
Radiocarbon 75cm
136-5-1 222 cm
136-5-3 270 cm
Radiocarbon 275cm
Silt to sand with clay laminae
136-5-3 387 cm
136-6
Depth (cm)
Dominantly massive clay with occasional silt
136-6-1 208 cm
136-6-2 233 cm
136-6-3 260 cm
Silt to sand with clay laminae
136-6-5 308 cm
136-6-6 342 cm
136-6-7 381 cm

Site prefix 153-

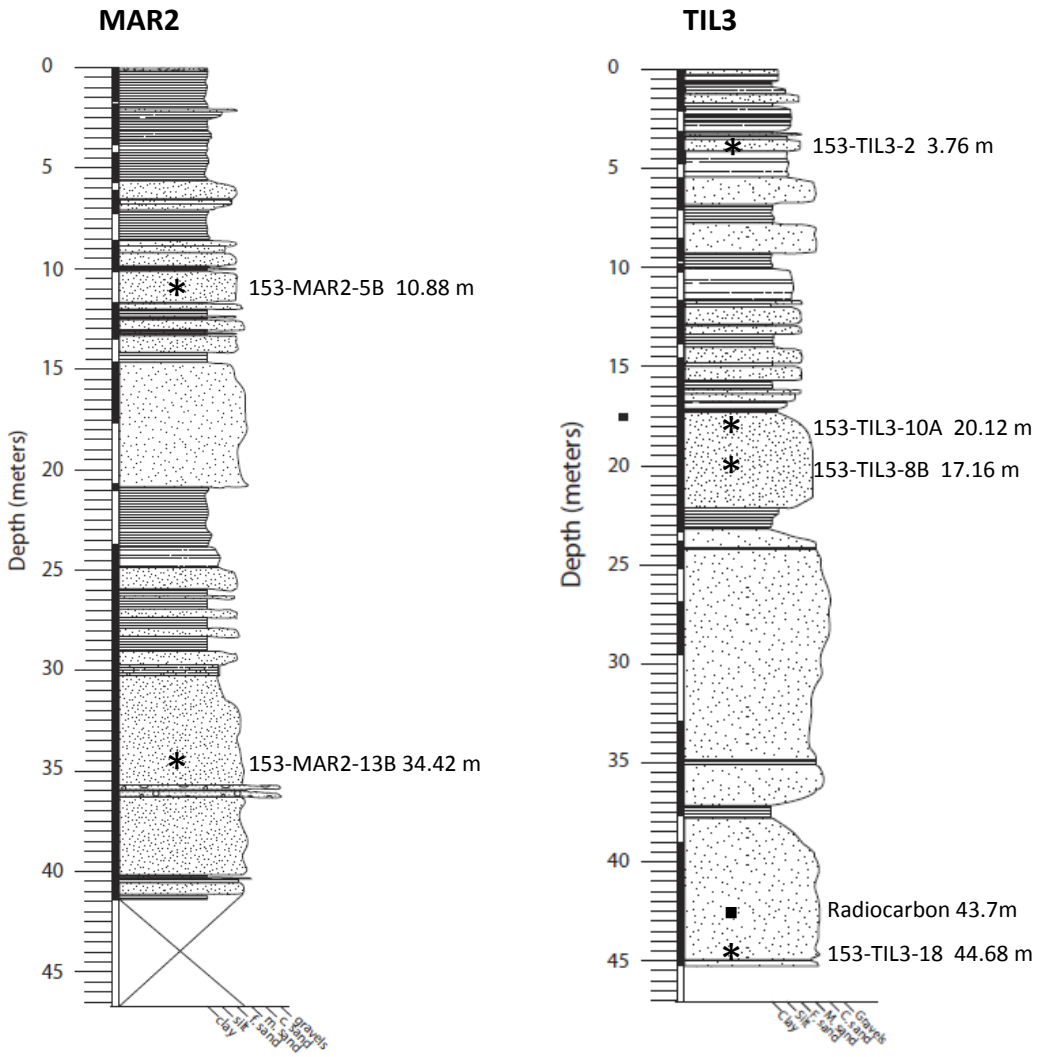

Site prefix 154-

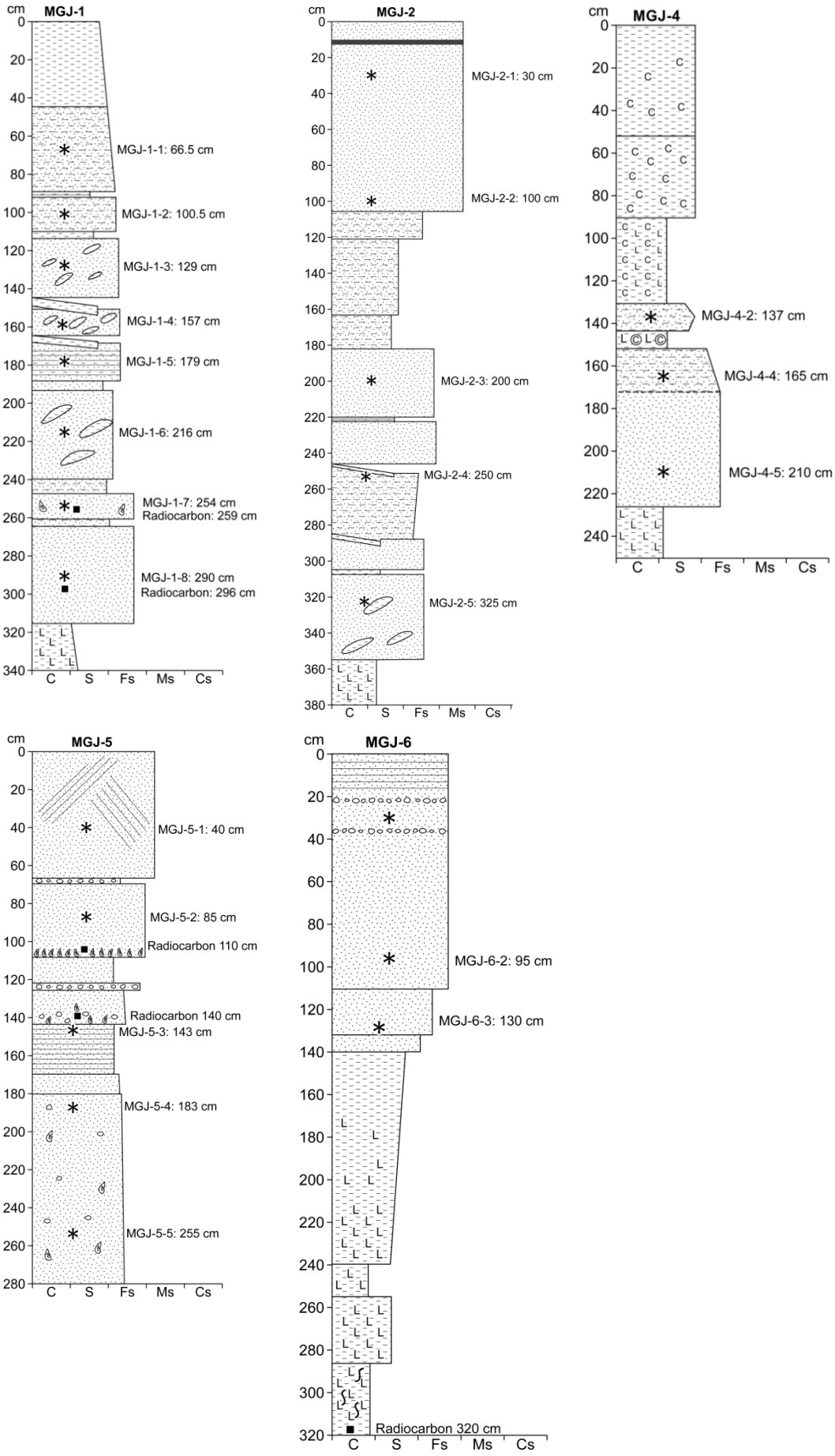

Site 154-MGJ-3

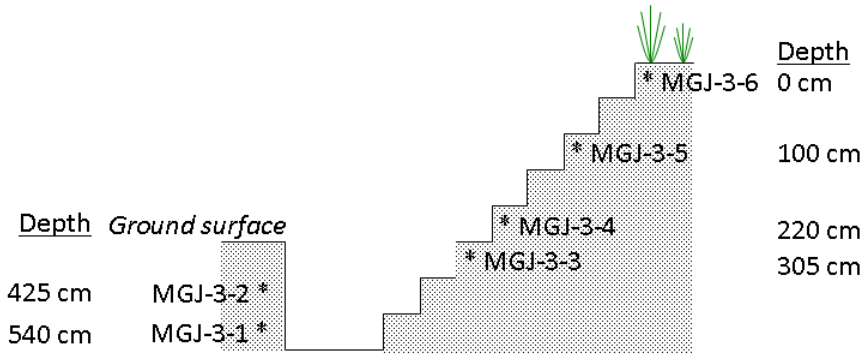

Site prefix 155-

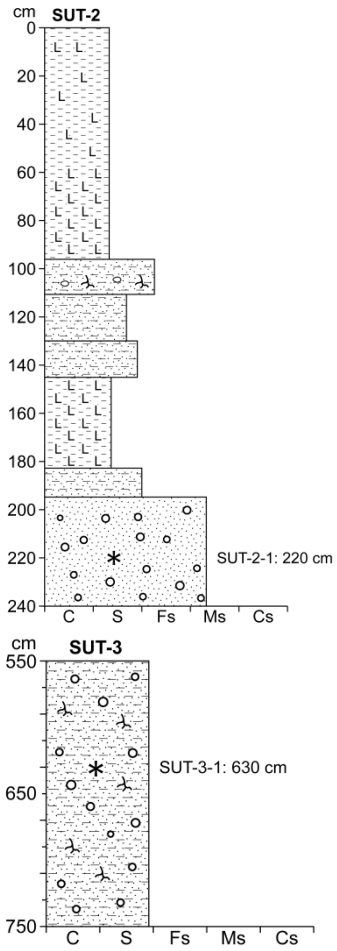

Legend for 154- and 155- stratigraphic logs

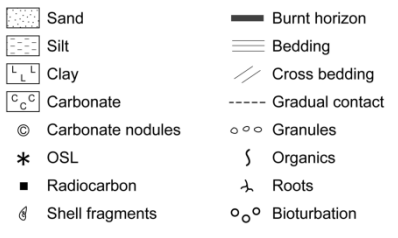

C = clay, S = silt, Fs = fine sand, Ms = medium sand, Cs = coarse sand

Appendix B: Calculation of the environmental dose rate

The environmental dose rates in this thesis have been calculated using the LDB2005 database written by Professor Geoff Duller. To ensure that the database is calculating the correct dose rate, a worked example for sample 136-3-1 is presented. The manual calculations match the values calculated in the database and provide a check that both methods of dose rate calculation are correct. All values have been rounded to two decimal places and all calculations were made prior to rounding.

Determination of the U and Th concentrations

The U and Th concentrations are determined using TSAC (section 3.3.1.2). For sample 136-3-1, the U and Th concentrations have been calculated as:

U	3.39 ± 0.51 ppm
Th	14.47 ± 1.69 ppm

Calculation of the K concentration

Using the conversion factors of Adamiec and Aitken (1998; table 3.2), the beta dose rate can be calculated from the U and Th concentrations:

U D_β	3.39 x 0.15 = 0.50 $Gy.ka^{-1}$
U D_β error	0.51 x 0.15 = 0.07 $Gy.ka^{-1}$
Th D_β	14.47 x 0.027 = 0.40 $Gy.ka^{-1}$
Th D_β error	0.40 x 0.027 = 0.05 $Gy.ka^{-1}$
U and Th D_β	0.50 + 0.40 = 0.890 $Gy.ka^{-1}$
U and Th D_β error	$\sqrt{(0.07^2 + 0.05^2)}$ = 0.09 $Gy.ka^{-1}$

The infinite-matrix beta dose rate has been determined from TSBC as

D_β	1.83 Gy.ka^{-1}
D_β error	0.06 Gy.ka^{-1}

The combined U and Th beta dose rates can be subtracted from the infinite-matrix beta dose rate to leave the K beta dose rate

K D_β	1.83 – 0.89 = 0.94 Gy.ka^{-1}
K D_β error	$\sqrt{(0.06^2 + 0.09^2)}$ = 0.11 Gy.ka^{-1}

Using the conversion factors of Adamiec and Aitken (1998), the concentration of K (%) can be calculated.

K (%)	0.94 / 0.78 = 1.20
K error (%)	1.20 x (0.11/0.94) = 0.14

Radionuclide concentrations

From TSAC and TSBC, the concentrations of U, Th and K have been calculated as:

U	3.39 ± 0.51 ppm
Th	14.47 ± 1.69 ppm
K	1.20 ± 0.14%

Calculation of the gamma dose rate

By applying the conversation factors of Adamiec and Aitken (1998) to the radionuclide concentrations, the gamma dose rate can be calculated:

U D_γ	3.39 x 0.11 = 0.38 Gy.ka^{-1}
U D_γ error	0.38 x (0.51/3.39) = 0.08 Gy.ka^{-1}
Th D_γ	14.47 x 0.05 = 0.69 Gy.ka^{-1}

Th D_γ error 0.69 x (1.69/14.47) = 0.08 Gy.ka^{-1}

K D_γ 1.20 x 0.24 = 0.29 Gy.ka^{-1}

K D_γ error 0.29 x (0.14/1.2) = 0.03 Gy.ka^{-1}

Total D_γ 0.38 + 0.69 + 0.29 = 1.36 Gy.ka^{-1}

Total D_γ error $\sqrt{(0.08^2 + 0.05^2 + 0.03^2)}$ = 0.10 Gy.ka^{-1}

Attenuation and water content correction

The beta and gamma dose rates have been calculated from U, Th and K concentrations as:

D_β 1.83 ± 0.06 Gy.ka^{-1}

D_γ 1.36 ± 0.10 Gy.ka^{-1}

The beta dose rate requires correcting for grain size (90 – 125 µm) and HF etching (section 3.3.2.5), and both the beta and gamma dose rates require correction for the water content.

To correct the beta dose rate of 1.83 ± 0.06 Gy.ka^{-1} for an attenuation factor of 0.91 ± 0.02

D_β 1.83 x 0.914 = 1.67 Gy.ka^{-1}

D_β error 1.67 x $\sqrt{((0.018/0.914)^2 + (0.914/1.83)^2)}$ = 0.06 Gy.ka^{-1}

To correct the beta dose rate for a water content of 5 ± 2% (section 3.3.5)

D_β 1.67 / (1+(1.25 x 0.05)) = 1.57 Gy.ka^{-1}

D_β error 1.57 x $\sqrt{((0.06/1.67)^2 + (0.03/1.06)^2)}$ = 0.07 Gy.ka^{-1}

To correct the gamma dose rate for a water content of 5 ± 2% (section 3.3.5)

D_γ 1.36 / (1+(1.12 x 0.05)) = 1.29 $Gy.ka^{-1}$

D_γ error 1.29 x √((0.03/1.06)^2 + (0.10/1.36)^2) = 0.10 $Gy.ka^{-1}$

Note: the values (0.02/1.06) and (0.03/1.06)) have been derived by propagating the error associated with the water content through the equation.

The cosmic dose rate

The cosmic dose rate has been calculated using the equations in Prescott and Hutton (1998) and using the COSMIC program (written by Dr Robert Clark) as:

D_c 0.15 ± 0.02 $Gy.ka^{-1}$

Calculation of the environmental dose rate

In summary, the beta, gamma and cosmic dose rates have been calculated as:

D_β 1.57 ± 0.07 $Gy.ka^{-1}$

D_γ 1.29 ± 0.10 $Gy.ka^{-1}$

D_c 0.15 ± 0.02 $Gy.ka^{-1}$

The environmental dose rate is the sum of these

$D_{136\text{-}3\text{-}1}$ 1.57 + 1.29 + 0.15 = 3.01 $Gy.ka^{-1}$

$D_{136\text{-}3\text{-}1}$ error √(0.07^2 + 0.10^2 + 0.02^2) = 0.13 $Gy.ka^{-1}$

The environmental dose rate of sample 136-3-1 is 3.01 ± 0.13 $Gy.ka^{-1}$

Appendix C: Combined pre-heat and dose recovery and dose recovery tests

Combined pre-heat and dose recovery tests

The table below summarises the combined pre-heat and dose recovery tests undertaken in this study (see section 4.8.2.1.2), including the given dose, the number of aliquots at each pre-heat temperature which satisfy all rejection criteria (section 6.3.3) and the mean ratio and standard deviation between the recovered and administered dose at the selected pre-heat temperature of 220°C.

			# Accepted Aliquots								
Sample	**Given Dose (Gy)**	**# Aliquots**	**160 °C**	**180 °C**	**200 °C**	**220 °C**	**240 °C**	**260 °C**	**280 °C**	**300 °C**	**Rec/Admin Dose**
136-3-9	7.8	24	1	1	2	3	2	3	2	0	1.01 ± 0.02
153-MAR2-13B	78.8	24	1	0	0	2	3	1	1	0	1.10 ± 0.10
153-TIL3-2	7.8	24	2	1	0	2	1	2	2	0	0.95 ± 0.01
154-MGJ-1-1	16	24	0	1	1	2	3	1	0	0	1.04 ± 0.00
154-MGJ-1-8	15.9	24	0	0	1	2	3	0	0	0	0.95 ± 0.04
154-MGJ-5-1	0.24	24	1	1	0	3	2	0	0	0	0.95 ± 0.10
154-MGJ-5-5	4.0	24	0	2	3	3	3	0	0	0	0.97 ± 0.02
155-SUT-2-1	20.2	48	2	2	4	5	5	5	3	0	1.02 ± 0.03

Dose recovery tests

The table below gives further details of the dose recovery tests carried out on the samples in this study (section 4.8.2.1.3), including the given dose, the number of aliquots measured and which pass the rejection criteria, and the mean ratio between the recovered and administered dose and the standard deviation.

Sample	**Given Dose (Gy)**	**# Aliquots**	**# Accepted Aliquots**	**Recovered/ Administered Dose**
136-3-1	7.8	36	15	1.00 ± 0.06
136-3-9	7.8	30	15	1.02 ± 0.04
136-4-2	7.8	12	10	1.06 ± 0.10
136-6-1	7.8	12	7	1.01 ± 0.04
136-6-7	7.8	18	12	1.12 ± 0.07
153-TIL3-2	7.8	15	12	0.94 ± 0.08
154-MGJ-1-1	16.0	30	12	0.91 ± 0.08
154-MGJ-1-8	16.0	21	19	1.06 0.07
154-MGJ-5-5	4.0	15	14	0.95 ± 0.09
154-MGJ-6-2	8.0	12	7	0.90 ± 0.09
155-SUT-2-1	20.2	18	11	1.00 ± 0.14

Appendix D: Calculation of I_0 and the selection of the best sum of exponentials fit for a LM-OSL signal

Calculation of I_0

Two parameters are derived through curve deconvolution of the OSL signal; the de-trapping probability, b, and the trapped charge population, n_0 (e.g. Bulur, 1996; 2000). b is calculated by the multiplication of the maximum light intensity (I_0, in photons per $s^{-1}.cm^{-2}$) and the photo ionisation cross-section. Therefore, by dividing b by I_0, σ can be calculated for each component.

The calculation of I_0 is outlined by Choi et al. (2006) and by the following steps:

The energy (E) of one photon is E = hv

Where, h is Planck's constant, equal to 6.63 x 10^{-34} $W.s^2$ and v is the frequency. v =c/λ, where c is the speed of light (3 x 10^8 $m.s^{-1}$), and for light with a wavelength of 470 nm, v = (3 x 10^8 $m.s^{-1}$)/(470 x 10^{-9} s^{-1}).

The energy of one photon produced from a blue LED (with a wavelength of 470 nm) is 4.23 x 10^{-19} W.s.

I_0 is calculated by dividing the stimulation power by the energy of a photon. Therefore, for a stimulation power of 30.6 $mW.cm^{-2}$, I_0 = (0.036 $W.cm^{-2}$)/(4.23 x 10^{-19}).

In this study, for blue LEDs with a stimulation power of 30.6 $mW.cm^{-2}$ and wavelength of 470 nm, **$I_0 = 7.23 \times 10^{16}$ $s^{-1}.cm^{-2}$**.

Selection of the best sum of exponentials fit

Curve deconvolution of the LM-OSL signal is discussed in section 5.3.1.3. For each LM-OSL signal, three, four, five and six components were fitted, with the best fit chosen by looking for the fit that minimised and removed structure from the residuals relating to the fit and those that maximised the r^2 value, ensuring that components were not duplicated. Below, an example of the selection of the best sum of exponentials fit is outlined for an aliquot of Pakistani sample 136-4-1. Table D.1 details the photo ionisation cross-section (σ), the cross-sections relative to the fast component ($\sigma:\sigma_F$) and the trapped charge population (n_0) for the three, four, five and six component fit. Figure D.1 shows plots of each of the modelled components in relation to the measured signal and the residuals relating to each fit.

Table D.1: The trapped charge population (n_0) and photo ionisation cross-section (σ) for each of the components fitted when three, four, five and six components were fitted to the LM-OSL signal from an aliquot of Pakistani quartz (sample 136-4-1). The selected fit is shown by italics.

136-4-1			3 Components	4 Components	5 Components	*6 Components*
Components	F	n_0	2.84×10^{5}	2.20×10^{5}	2.05×10^{5}	*1.94×10^{5}*
		σ (cm^2)	1.80×10^{-17}	2.53×10^{-17}	2.69×10^{-17}	*2.79×10^{-17}*
		$\sigma:\sigma_F$	1	1	1	*1*
	M	n_0	1.47×10^{5}	1.47×10^{5}	1.19×10^{5}	*9.43×10^{4}*
		σ (cm^2)	2.52×10^{-18}	2.52×10^{-18}	4.04×10^{-18}	*5.86×10^{-18}*
		$\sigma:\sigma_F$	0.1	0.1	0.2	*0.2*
	S1	n_0				*8.94×10^{4}*
		σ (cm^2)				*1.27×10^{-18}*
		$\sigma:\sigma_F$				*0.05*
	S2	n_0		2.92×10^{5}	1.15×10^{5}	*1.39×10^{5}*
		σ (cm^2)		1.11×10^{-19}	4.59×10^{-19}	*1.77×10^{-19}*
		$\sigma:\sigma_F$		0.04	0.02	*0.02*
	S3	n_0	2.95×10^{6}	4.57×10^{6}	7.30×10^{5}	*3.37×10^{6}*
		σ (cm^2)	2.47×10^{-20}	1.36×10^{-20}	4.05×10^{-20}	*1.88×10^{-20}*
		$\sigma:\sigma_F$	0.001	0.001	0.002	*0.001*
	S4	n_0	2.14×10^{8}		4.25×10^{6}	*4.20×10^{6}*
		σ (cm^2)	4.50×10^{-23}		1.14×10^{-20}	*1.77×10^{-21}*
		$\sigma:\sigma_F$	0.0000		0.0004	*0.0001*
		r^2	0.853	0.978	0.982	*0.983*

The fitting of a sum of exponentials is mathematically not simple (e.g. Istratov and Vyvenko, 1999), and whilst fitting a larger number of exponentials to an LM-OSL signal will result in a greater r^2 value, the fitting of a greater number of components does not necessarily make physical sense. Therefore, a number of factors were

considered when selecting the most appropriate fit. One key factor was the magnitude and form of the residual between the fitted and measured data, and the fit which minimised the residuals, but also removed any structure was sought. In figure D.1a-b, a clearly defined structure is evident in the residuals, and the three and four component fit (figure D.1 a and b respectively) were not considered as appropriate fit for the signal on this basis. Structure in the residuals indicates that the sum of exponentials does not fit the measured signal well, and this is apparent in figure D.1a, where the peak of the fitted fast component is not well aligned with the peak in the measured LM-OSL signal.

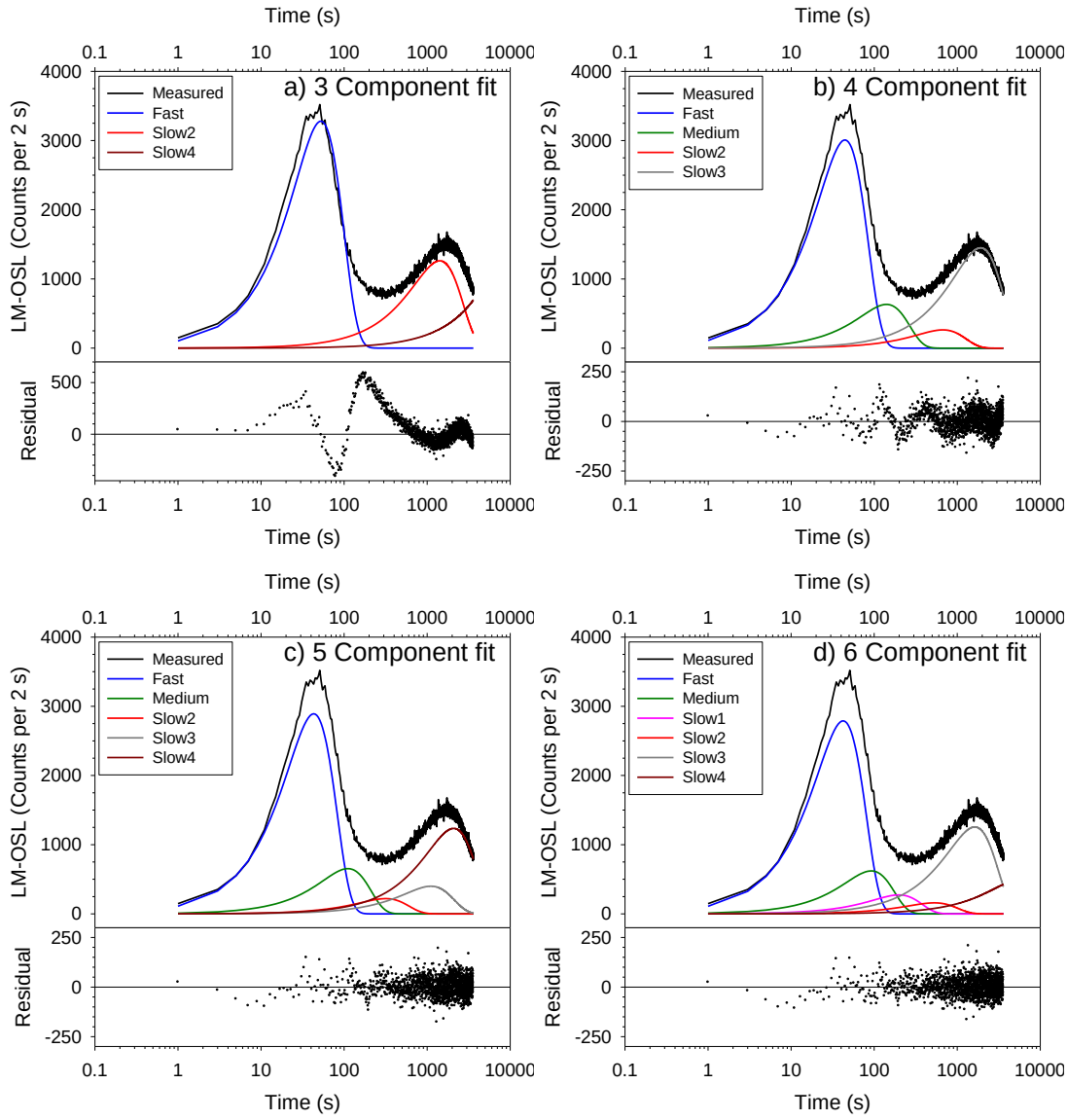

Figure D.1: The LM-OSL signal of sample 136-4-1, along with the a) three, b) four, c) five and d) six component fit by curve deconvolution. The residual between the measured and fitted data for each fit is also shown.

The calculated parameters were also a consideration when selected the most appropriate fit, and fits which contained anomalous components were not considered. For example, in the three component fit (table D.1; figure D.1a), the S4 component fitted suggests that an extremely large amount of charge originates from an extremely deep trap, and in reality, this amount charge is likely to originate from a number of traps. In some of the other signals fitted, a fit with more exponentials resulted in components (usually, the fast) being duplicated, and fits such as this were not considered. For the aliquot of 136-4-1 shown in table D.1, the physical parameters of the components of the five and six component fit are similar, and both appear to be appropriate values in comparison to published values (e.g. Jain et al., 2003; Singarayer and Bailey, 2003). For this signal, a six component fit was selected because the residuals in figure D.1c still retain some structure.

Appendix E: FP equivalent dose distributions

Radial plots of the equivalent dose distributions for the samples measured using FP OSL dating in this study. Individual D_e values are shown by the filled symbols, the sample D_e is indicated by the solid line and the shaded grey area represents the ±2σ confidence interval. Where a sample is considered saturated, D_e values from saturated signals are shown by the open symbols and the grey line represents the minimum D_e. The number of signals measured with a natural signal that does not intercept the dose response curve is shown next to a vertical arrow.

136-3-1

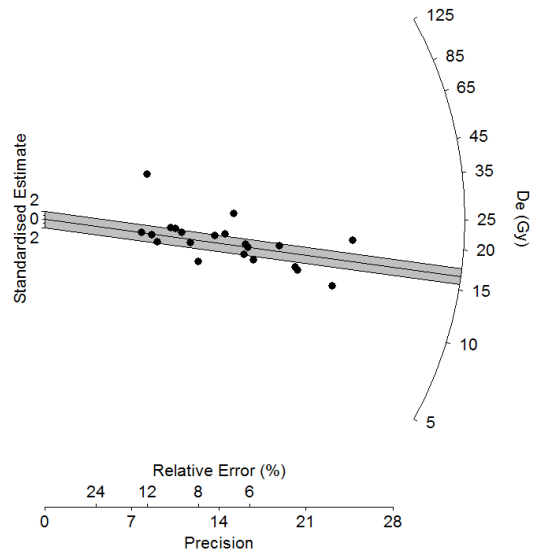

136-3-9

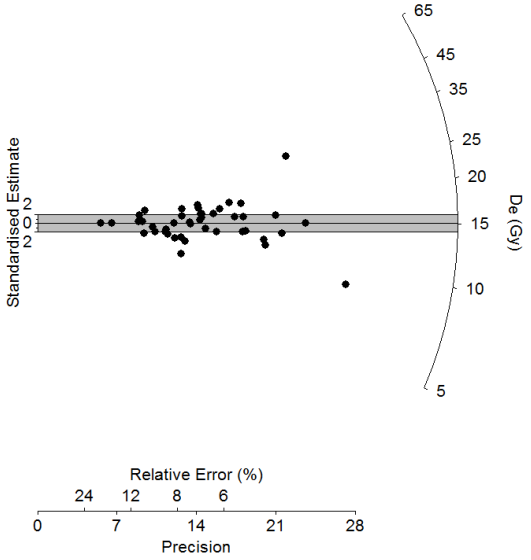

136-4-1

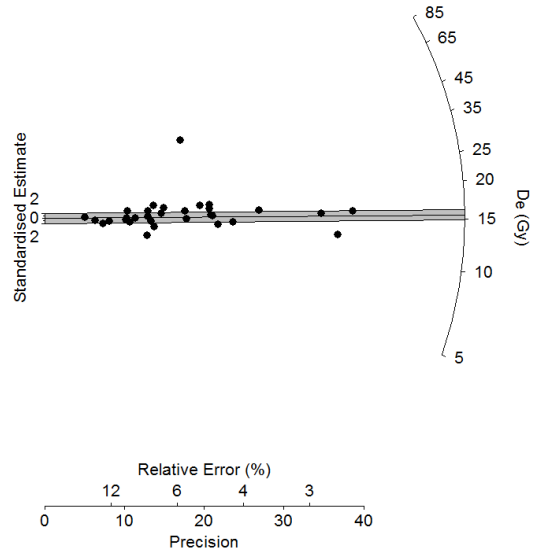

136-4-2

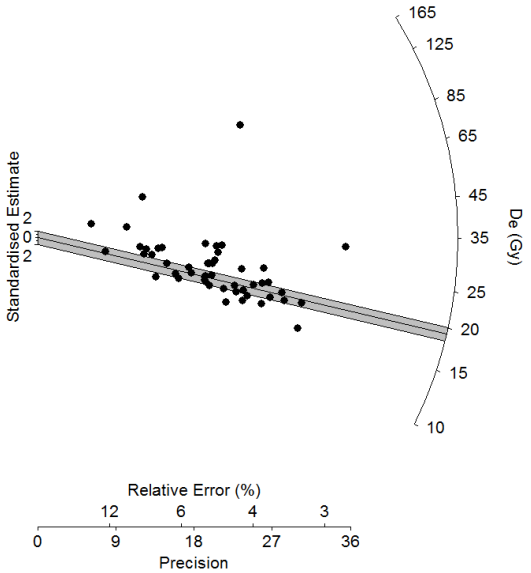

136-6-1

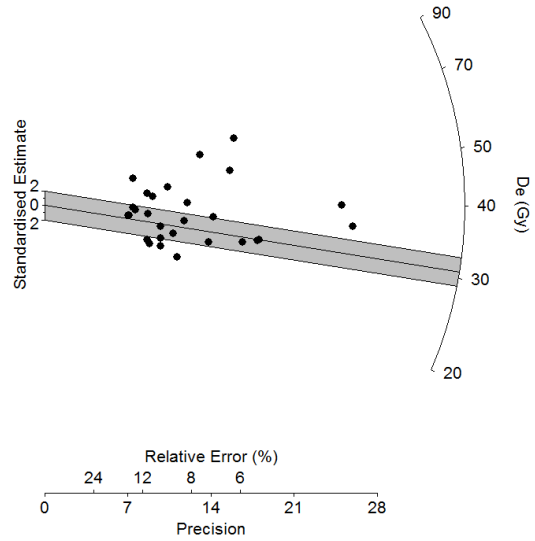

136-6-7

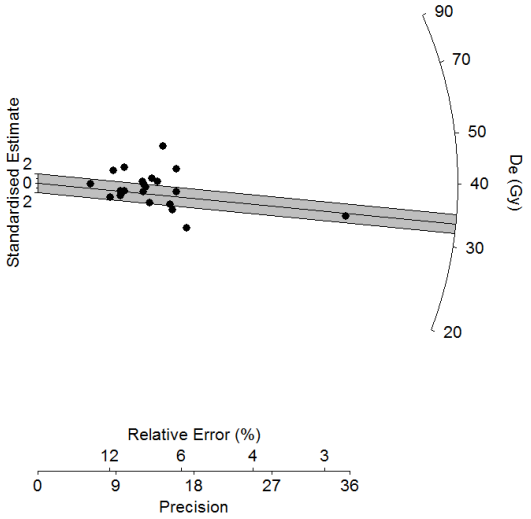

153-MAR2-5B

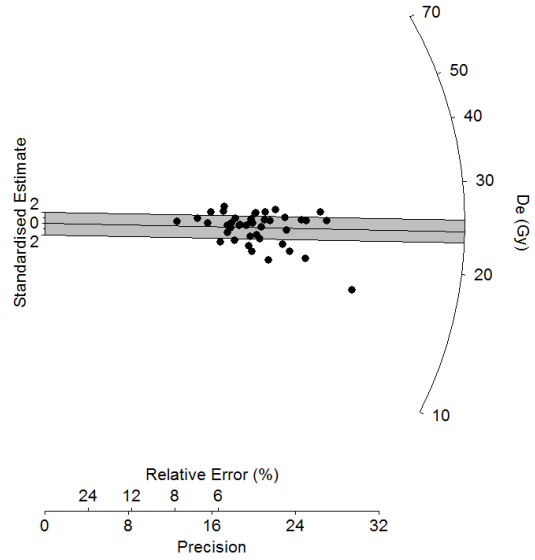

153-MAR2-13B

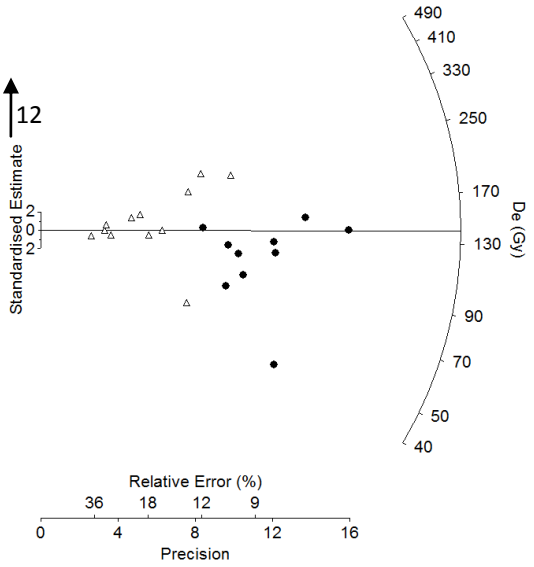

153-TIL3-2

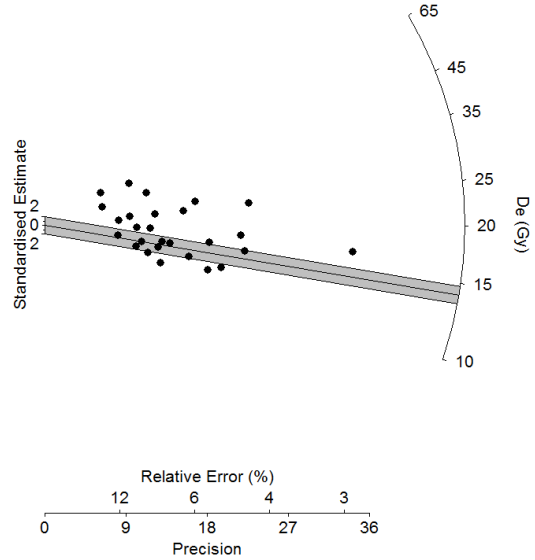

153-TIL3-8B

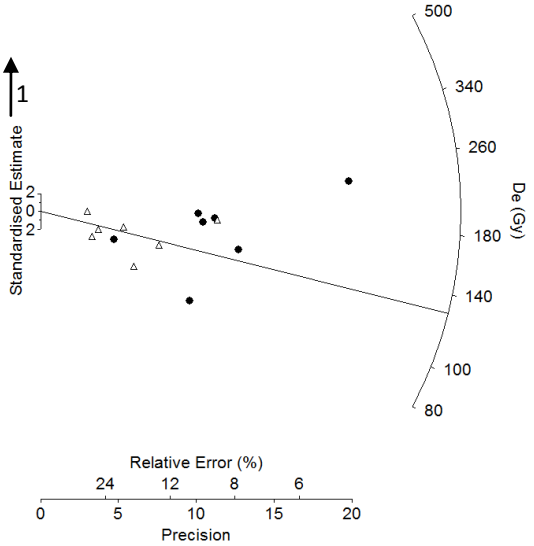

153-TIL3-10A

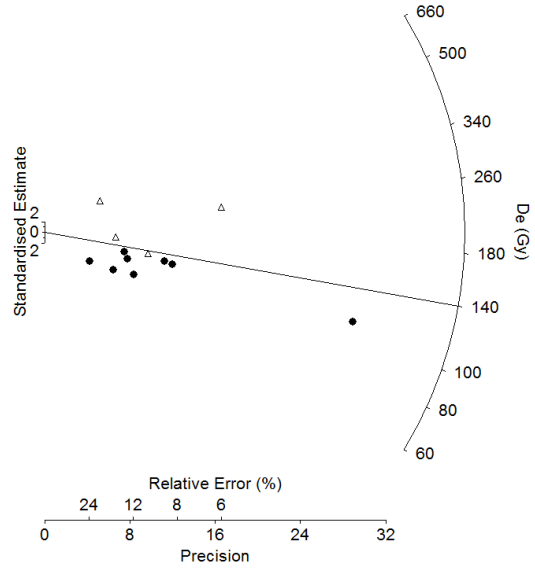

153-TIL3-18

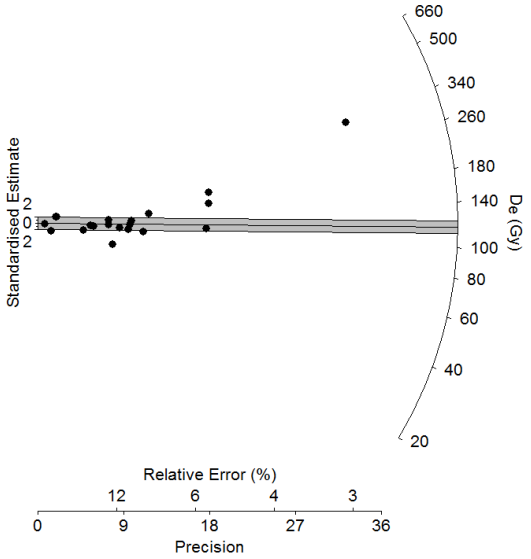

154-MGJ-1-1

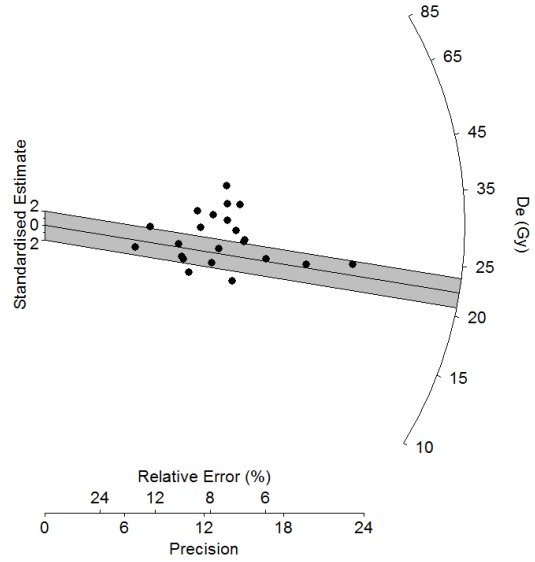

154-MGJ-1-4

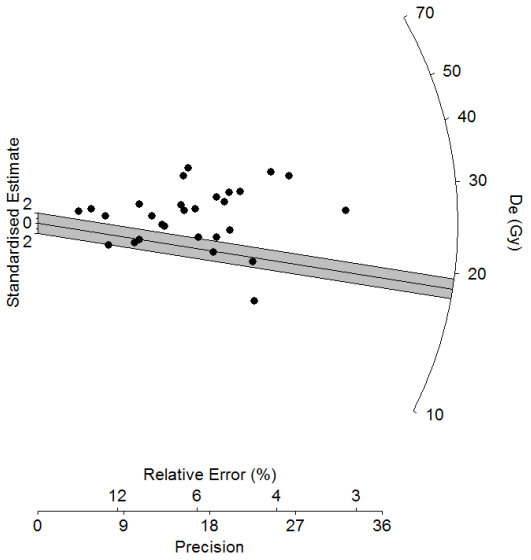

154-MGJ-1-8

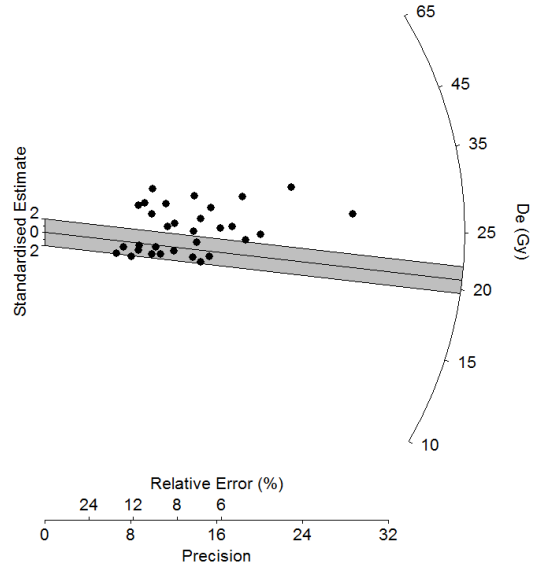

154-MGJ-2-1

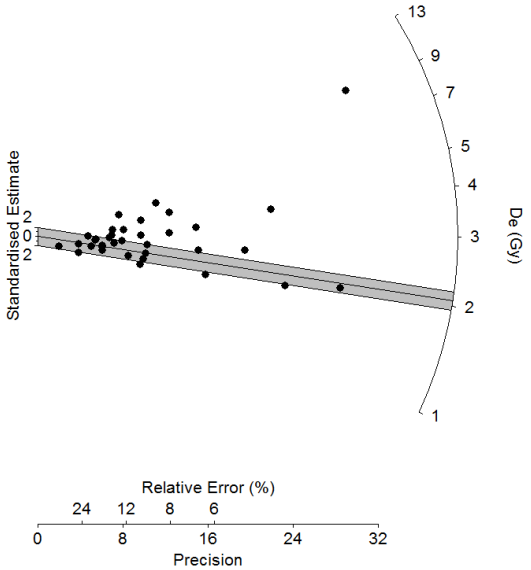

154-MGJ-2-5

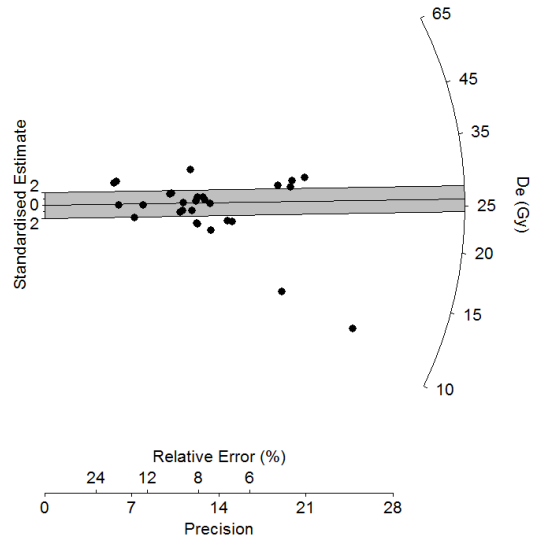

154-MGJ-3-1

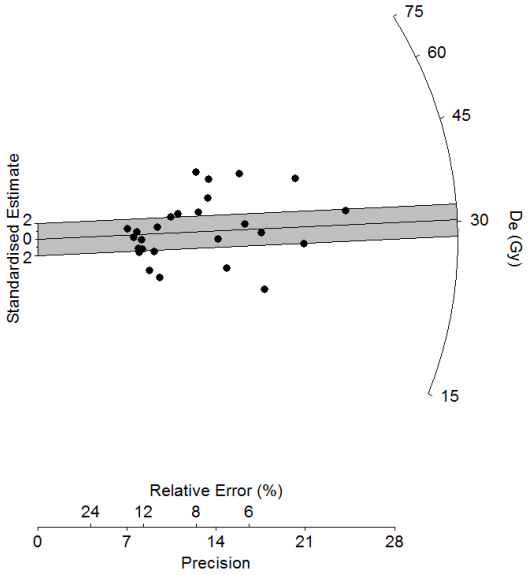

154-MGJ-3-6

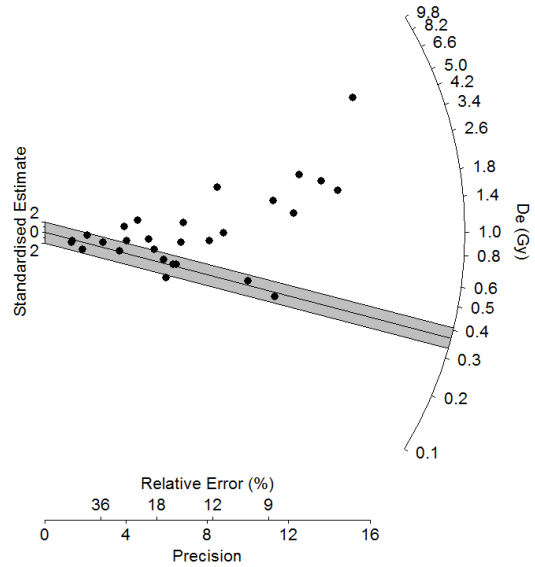

154-MGJ-4-2

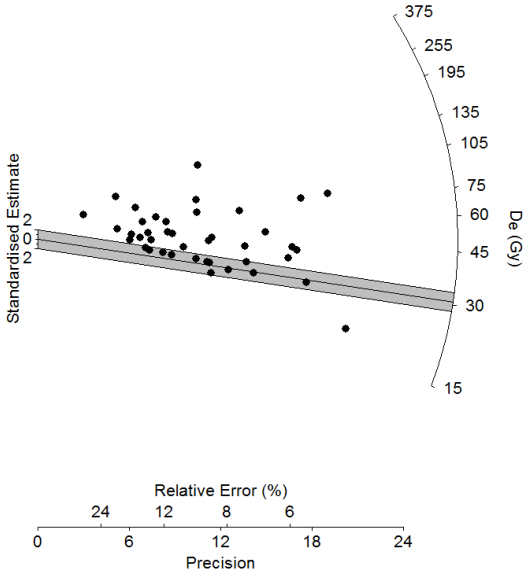

154-MGJ-4-5

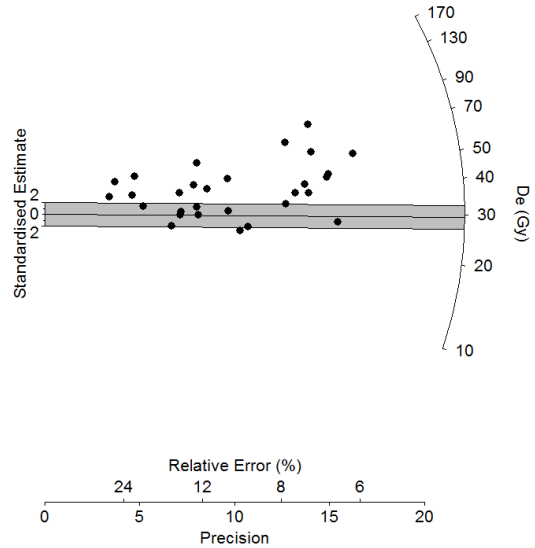

154-MGJ-5-1

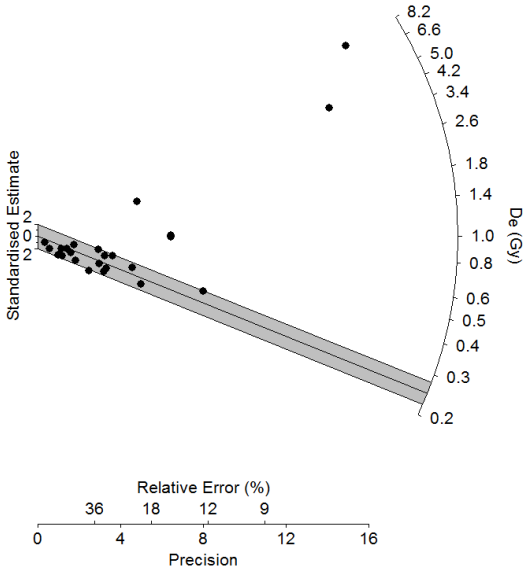

154-MGJ-5-5

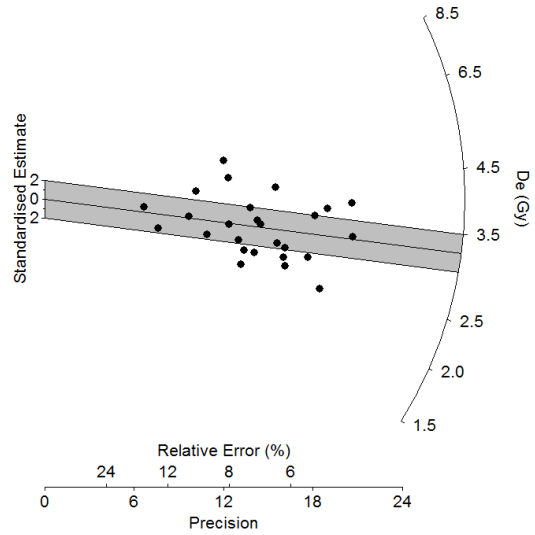

154-MGJ-6-2

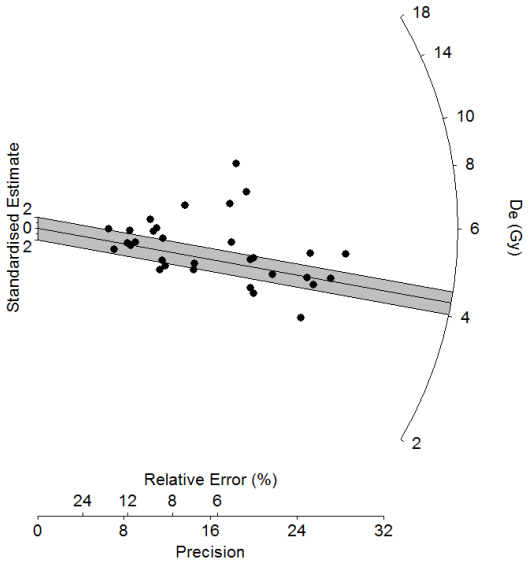

154-MGJ-6-3

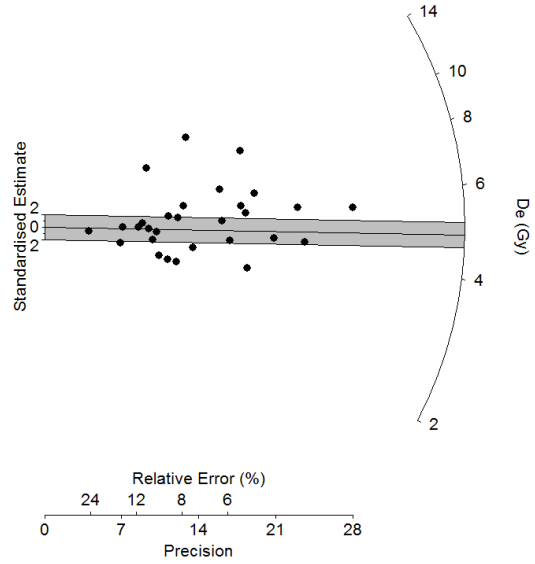

155-SUT-2-1

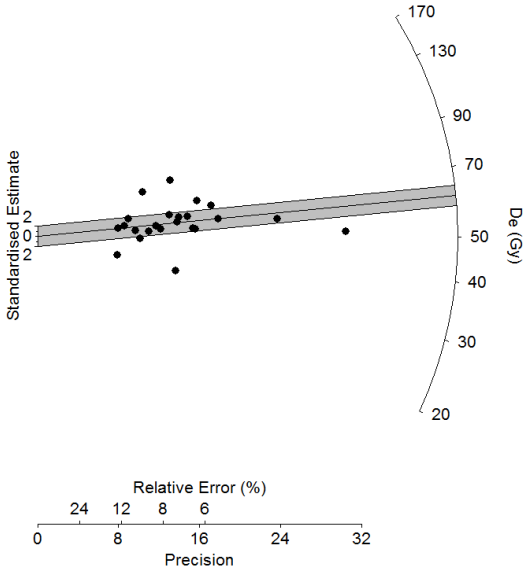

155-SUT-3-1